XLI Brazilian Meeting
on Nuclear Physics

XLI Brazilian Meeting on Nuclear Physics

02 to 06 September 2018

Maresias – São Sebastião – SP - Brazil

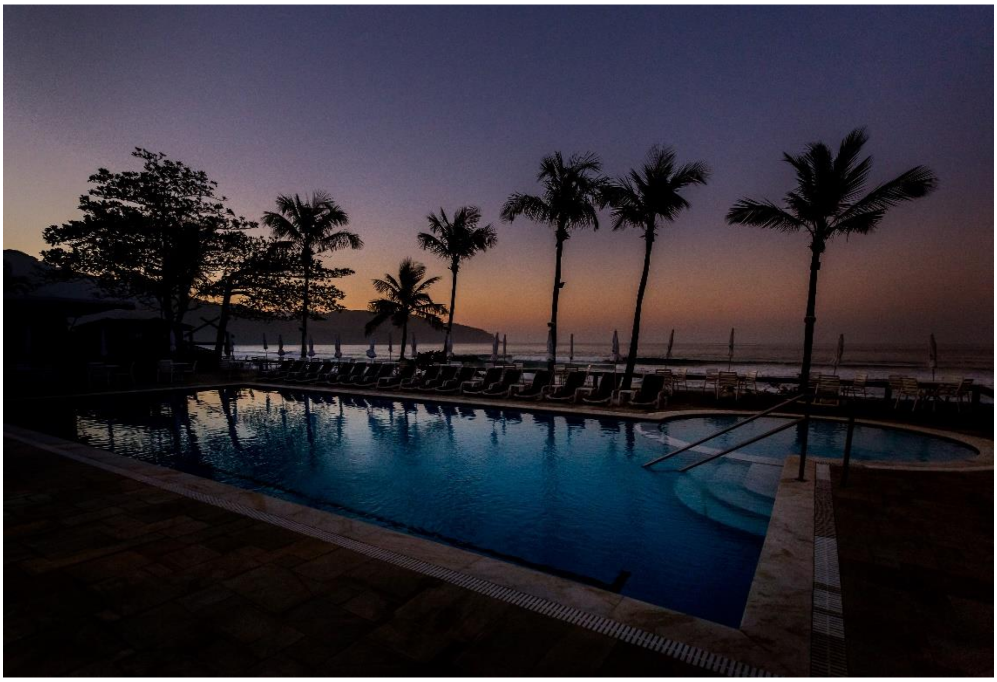

EDITORS

VALDIR GUIMARÃES

Instituto de Física - Universidade de São Paulo

FREDERICO GENEZINI

IPEN – Instituto Pesquisas Energéticas e Nucleares

JESUS LUBIAN

Instituto de Física – Universidade Federal Fluminense

MARLETE ASSUNÇÃO

Departamento de Física Universidade Federal de São Paulo

ADRIANA DELGADO

Instituto de Física – Universidade Federal de São Carlos

LUIS AUGUSTO TREVISAN

Departamento de Física – Universidade Federal de Ponta Grossa

PREFACE

In the present volume of Journal of Physics: Conference Series we publish the proceedings of the "XLI Brazilian Meeting on Nuclear Physics". The Brazilian Workshop on Nuclear Physics (RTFNB, acronym in Portuguese) is organized annually by the Brazilian Physics Society since 1978. This year, from 02-06 September, the 41th edition of this meeting was held in the Maresias Beach Hotel in the city of São Sebastião, São Paulo, Brazil. This hotel is located by the beach and it is surround by splendid natural beauty. Few steps separate the guest rooms from the beach and the ocean can be seen from any of the hotel areas. This pleasant and relaxing environment is just perfect for fruitful discussion of new projects, exchanging ideas and starting new collaborations.

The main motivation of this meeting is to promote Nuclear Physics research in Brazil, by stimulating and reinforcing collaborations between nuclear physicists from around the country together with some international invited researchers. Also, this meeting will serve to disseminate advances in nuclear physics research and its applications being performed in Brazil, disclose and evaluate the scientific production in this field and stimulate young Brazilian researchers and students in their first steps into scientific research. Also, renowned invited speakers from Brazil and from several countries present their most recent works.

The website of the event is: http://www.sbfisica.org.br/~rtfnb/xli/index.php/en/

The subjects on Nuclear Physics covered in the meeting were:

1) Hadron Physics

2) High Energy Physics

3) Nuclear Structure and Reactions at low energies

4) Nuclear Astrophysics

5) Applied Nuclear Physics

6) Instrumentation

7) Few-body Problems

The meeting involved 113 participants. Among the participants, undergraduate, graduate students, young and senior researchers from Brazil and some invited speakers from overseas (USA, Japan, Spain, Mexico, South Africa and Argentina). In the program we had plenary morning sessions with (10) review talks on recent developments in theory, experimentation and applications related to the many aspects of nuclear physics. In the afternoons we had parallel sections with (16) invited talks and (20) oral contributions. The posters were exhibited all the time nearby where the coffee breaks were offered and allowed the participants to check them in several opportunities. All the talks showed high level of professionalism of the research being carried on. The good level of professionalism was also presented in many of the 60 posters that were displayed during the event. We would like to give special thanks to all speakers and presenters as well as to the session chairpersons, who drove all the conference sessions on the right track, keeping them in time while permitting enriching discussions.

In this edition of the event we have introduced some sections on Few-Body problem in Physics. This field has been growing thanks to the new ideas and techniques of ab-initio calculations, which has also being applied to nuclear physics problems.

The XLI Brazilian Meeting on Nuclear Physics also included a short satellite event; a workshop devoted to the INCT (Instituto Nacional de Ciência e Tencologia) project of Nuclear Physics with some guest speakers. A roundtable discussion focusing on the future of the nuclear physics in Brazil.

The present proceedings contain 47 written contributions from participants presenting plenary and invited talks, oral contributions, as well as posters, during the event. These contributed papers, representing mainly the scientific activity of young physicists, were exhibited as posters and are included in the present volume. We would like to thank all participants who made the effort to present their results and write the contributions to the proceedings. We can say that the objectives of this meeting were achieved, given the quality of the presented contributions in the various area of the nuclear physics field.

This event was organized by the Brazilian Physical Society who did a good job in taking care of all logistic issues. Finally, but not least, the event was sponsored by Brazilian national agencies: Conselho Nacional de Desenvolvimento Científico e Tecnológico (CNPq); Coordenação de Aperfeiçoamento de Pessoal de Nível Superior (CAPES) and Fundação de Amparo à Pesquisa do Estado de São Paulo (FAPESP). Without the financial support of these foundations this event would not be possible.

Peer review statement

All papers published in this volume of *Journal of Physics: Conference Series* have been peer reviewed through processes administered by the proceedings Editors. Reviews were conducted by expert referees to the professional and scientific standards expected of a proceedings journal published by IOP Publishing.

IOP Conf. Series: Journal of Physics: Conf. Series **1291** (2019) 012001 doi:10.1088/1742-6596/1291/1/012001

^{236}U identification in the new AMS beamline at the TANDAR accelerator

J de Jesús[1], E de Barbará[1], A Arazi[1,2], J Fernández Niello[1,2,3], G V Martí[1], D Abriola[1], M A Cardona[1,2], F Gollan[1,2], D Hojman[1,2], A J Pacheco[1,2], N Samsolo[1]

[1] Laboratorio TANDAR, Comisión Nacional de Energía Atómica, Av. Gral. Paz 1499, BKNA1650 San Martín, Buenos Aires, Argentina

[2] Consejo Nacional de Investigaciones Científicas y Técnicas, Av. Rivadavia 1917, C1033AAJ Buenos Aires, Argentina

[3] Instituto de Investigación e Ingeniería Ambiental, Universidad Nacional de San Martín, 25 de Mayo y Francia, B1650BWA San Martín, Buenos Aires, Argentina

E-mail: `arazi@tandar.cnea.gov.ar`

Abstract. ^{236}U ($T_{1/2} = 23$ My) is an excellent monitor for nuclear contamination in the environment. Indeed, spent nuclear fuels present isotopic ratios ^{236}U/^{238}U several orders of magnitude higher than natural samples. ^{236}U also provides a useful fingerprint to identify and trace nuclear material for safeguards purposes. Here we describe a new beamline for the discrimination of ^{236}U using the accelerator mass spectrometry (AMS) technique. This system comprises a Wien velocity filter and a 6.7 m long time-of-flight (ToF) path with a focusing quadrupole. The ToF is determined by a time zero detector and a surface barrier detector, which also provides an energy measurement. The capability of the system to discriminate ^{236}U from the much more abundant isotopes ^{235}U and ^{238}U is shown. While sensitivity values of ^{236}U/^{238}U$\sim 10^{-8}$ were achieved, ongoing works aim to improve this performance.

1. Introduction

Radionuclides are useful tracers for several research fields since they provide not only spatial but also time information. Typical examples are the use of ^{14}C (5.7 ky) for archaeology, ^{10}Be (1.4 My) for geology and ^{129}I (16 My) for environmental and oceanographic studies [1]. To the latter application, ^{236}U (23 My) can add substantial information [2, 3].

^{236}U is mainly produced by thermal neutron capture on the abundant, primordial isotope ^{235}U. In nature, these neutrons can be provided by (α,n) reactions on light nuclei, induced fission of ^{235}U, spontaneous fission of ^{238}U and at Earth surface by cosmic rays. Thus, the production and concentration of ^{236}U are strongly dependent on the neutron flux, which in turn depends on several factors: concentration of light nuclei, the depth from the Earth surface, the amount of water in the ore necessary for an efficient neutron thermalization and the presence of elements with high neutron capture cross section. It is estimated that about 30 kg of naturally produced ^{236}U exists in the Earth surface and $\sim$0.5 kg in the oceans [4]. However, the anthropogenic contribution to the ^{236}U inventory is much larger than the natural one. Around 900 kg of ^{236}U have been released to the environment during the atmospheric nuclear weapon testing period between 1945 and 1963 [5], and about 10^6 kg were produced in power reactors [4], although only a fraction of the latter is expected to have leaked to the environment due to nuclear fuel reprocessing plants discharges (∼100 kg [6]) and accidents in power reactors.

In samples of preanthropogenical material, the isotopic ratio ^{236}U/^{238}U lies in the 10^{-14}-10^{-9} range, while in those stemming from man-made processes this ratio can be as high as 10^{-4}-10^{-2}. This feature makes the radionuclide ^{236}U a very sensitive monitor for nuclear contamination in the environment and a valuable tracer used to determine the origin of an unknown uranium material, contributing in this way to nuclear safeguards controls. In addition, in the past few years, the radionuclide ^{236}U became a complementary oceanographic tracer in conjunction with ^{129}I [2, 3].

Since its long half-life, sensitive measurements of ^{236}U abundances are not achievable by alpha-decay detection. On the other hand, molecular isobars, such as ^{204}Pb^{16}O$_2$ and ^{235}U^{1}H, interfere the measurement of low concentrations of ^{236}U by conventional mass spectrometry. Hence, accelerator mass spectrometry (AMS) turns out to be the most suitable technique for these measurements. When using a tandem accelerator, the stripper at the high-voltage terminal assures the dissociation of all molecular background.

In the following section, we describe the commissioning of a time-of-flight beamline at the TANDAR accelerator aimed at the detection of ^{236}U by the AMS technique. In section 3, the sample preparation and measurement procedures are explained. In section 4, results for detection of ^{236}U are shown and discussed. Summary and outlook are given in section 5.

2. Experimental setup

In fig. 1 schemes of the 20 MV TANDAR accelerator and of the new AMS beamline are shown. Negative atomic or molecular ions are produced by a 40-cathodes sputtering ion source. A first mass selection is performed at the injection double-focusing magnet (bending radius $\rho = 305$ mm and $(B\rho)^2_{max} = 17.5$ amu×MeV/e^2) which, in conjunction with a 10 mm slit, provides a selectivity of $\Delta m/m \sim 1\%$. After a preacceleration voltage of 165 kV, ions are injected into the main accelerator where terminal voltages of around 8 MV are used. Carbon foil strippers are often damaged by heavy ion beams and introduce large angular straggling to the beam. Instead, N$_2$ gas stripper (~ 1 μTorr, 1 m long) is used. The analyzing double-focusing magnet ($\rho = 2$ m and $(B\rho)^2_{max} = 500$ amu×MeV/e^2) selects the charge state of uranium ions ($q = 8+$ was used in these experiments). Using a 5 mm slit at the image focal point, a selectivity of $\Delta m/m \sim 0.2\%$ can be expected. The analyzing magnet mechanically rotates to direct the beam to each experimental line, without the use of a switching magnet.

It is worth mentioning that in the injection magnet the suppression of neighboring masses is not complete. In the mass region of interest (mass of ^{236}U^{16}O, 252 a.m.u) the selectivity of 1% allows the injection of molecules with mass between 250 and 254. An effective mass selection can be expected in the analyzing magnet, since its mass selectivity ($\Delta m/m \sim 0.2\%$) is adequate for discriminating mass 236 from 235. However, charge-exchange collisions in the high energy side of the accelerator can provide ^{235}U (and ^{238}U) ions the magnetic rigidity necessary to be accepted by the analyzing magnet (see Sect. 4).

In this facility, a new Wien velocity filter and a ToF system were installed in a beamline conducting to a QDD magnetic spectrometer. This setup is intended for the detection of ^{236}U and ^{129}I. These radionuclides suffer no interference from stable isobars[1], so they can be discriminated from their more abundant isotopes by a ToF measurement. The Wien filter, acquired from Danfysik®, is composed by a 1-m-long magnet and an electrostatic dipole with an electrode gap of 50 mm. Electric and magnetic forces counterbalance for a selected ion velocity, thus deviating interfering ions. The Wien filter was placed at the exit of the first magnetic quadrupole triplet following the analyzing magnet (MQ-L1, see fig. 1). Since the

---

[1] ^{129}Xe produces no negative ions in the ion source

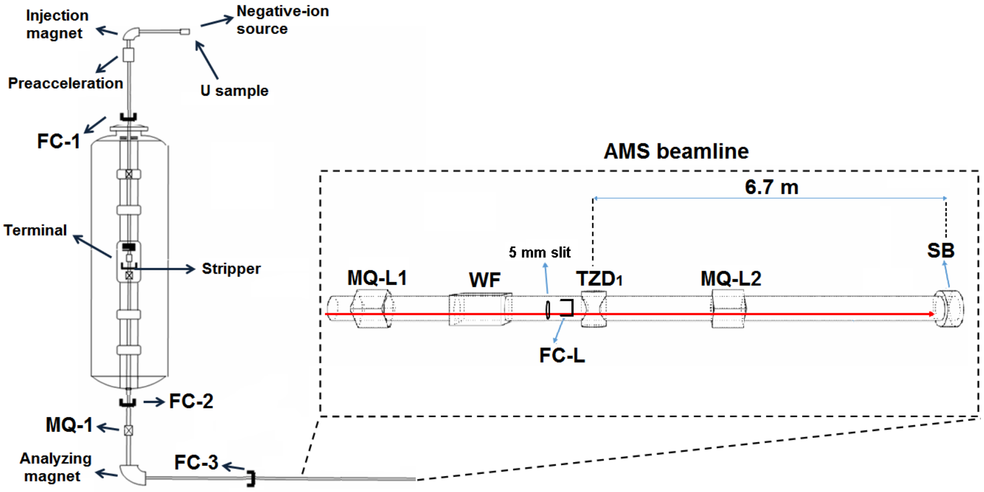

Figure 1. TANDAR accelerator and AMS beamline. MQ=magnetic quadrupole; WF=Wien filter; FC=Faraday cup; TZD=time zero detector; SB=surface barrier detector. Not in scale.

analyzing magnet selects the beam energy bending it in the vertical axis, the Wien filter was installed to exert its forces in the horizontal axis, so as to be decoupled. The maximum magnetic and electric fields are 0.3 T and 24 kV/cm, respectively. The coil current and electrodes voltages are set by PLC-controlled power supplies. For its initial calibration, ions of several masses (^{12}C, ^{35}Cl, ^{127}I and ^{197}Au) and velocities ($0.02 < v/c < 0.10$) were tuned. For selecting 70-MeV ^{236}U ions a coil current of 150 A (0.234 T) and electrode voltages of ±52 kV were adopted. Thus, under the condition in which ^{236}U is tuned, interfering ^{235}U and ^{238}U ions are deviated ~1.3 mm and ~2.6 mm at the image focal point of the quadrupole MQ-L1 (which is the start of the ToF system). At this point a 5 mm slit was placed to partially suppress these interferences.

The ToF system comprises a time zero detector (TZD) as start and a surface barrier silicon detector as stop, separated by 6.7 m. The silicon detector also provides an energy measurement. An alternative configuration using a second TZD (close to the surface barrier detector) to provide a faster stop signal was also tested, achieving lower total detection efficiency values.

The TZD is composed by a thin carbon foil ($\sim 20\ \mu$g/cm^2) and a Z-stack microchannel plate (MCP) assembly. Three different configurations were tested: a) direct collection of forward electrons, b) direct collection of backward electrons, and c) electrostatic mirror [7] (see Fig. 2). We run the measurements using the latter configuration since it showed a better intrinsic efficiency[2].

The surface barrier detector, which is 1 mm thick and 19.5 mm diameter, is over-biased to 220 V to improve its timing performance. Because the flight path of 6.7 m is rather large, a magnetic quadrupole triplet half-way between the TZD and the surface barrier detector was used to minimize the loss of ions due to angular straggling in the carbon foil.

The signal processing was performed with standard nuclear instruments electronic modules (NIM). The time signals from the TZD and the surface barrier detector were furnished to constant fraction discriminator modules to produce negative logic pulses. The output signal from the TZD discriminator was delayed about 1.5 μs using a gate and delay generator and was fed together with the output pulse from the surface barrier detector discriminator to a time-to-

---

[2] Defined as the ratio between the number of output signals and the number of impinging ions. The former is estimated by the coincidence events in the TZD and the surface barrier detector and the latter by the total events in the surface barrier detector.

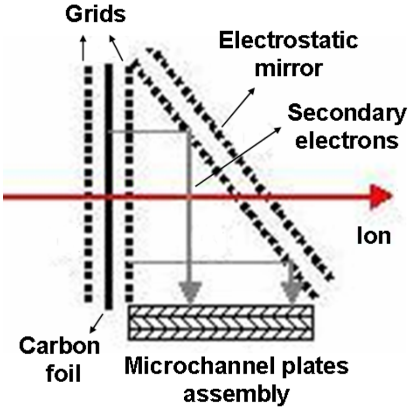

Figure 2. Electrostatic mirror configuration of the time zero detector.

amplitude converter (TAC) used in the inverse start-stop mode, i.e. the surface barrier detector starts the TAC and the TZD stops it. In this way, TAC dead time due to ions triggering the TZD but not reaching the surface barrier detector is avoided. This is important if the TZD rate is high, which is our case due to the high isotopic ratio of the samples used as standards.

3. Experimental procedure

The ToF detection system was characterized using samples with different content of uranium and concentrations of ^{236}U: (a) samples with 1-5 milligrams of non-enriched uranium, (b) samples with about 20 ng of non-enriched uranium, (c) samples ranging from 20 ng to 20 μg of enriched uranium, and (d) samples with 1-5 milligrams of enriched uranium with high ^{236}U concentration (^{236}U/U= 0.03%).

Samples (a) were used to generate a ^{238}U pilot beam (intensities of several nanoamperes) necessary for tuning the ion optic elements of the accelerator, including the Wien filter, by optimizing the reading in the Faraday cups (FC). Samples (b) and (c) were used for tuning low-intensity beams (rates $\lesssim$ 1 kHz) for the calibration of the detection system using the ^{235}U and ^{238}U ToF and energy signals. Samples (d) were used as calibration standards for the detection of ^{236}U. Measuring the ^{238}U beam intensity of these samples in FC-L1 (immediately before the TZD$_1$, see fig. 1) the beam transmission of the system can be determined. This transmission is necessary for correcting systematic effects when determining isotopic ratios ^{236}U/^{238}U of unknown samples. The use of a calibration standard corrects for any isotopic fractionation effect, even though it is expected to be negligible in this mass region.

Nanogram samples (b) and (c) were prepared dissolving 1 mg of uranyl nitrate ($UO_2(NO_3)_2$) in 1 l of a 10^{-4} M HCl solution and 50 mg of iron oxide (Fe_2O_3) in 50 ml of concentrated HCl (36.5% m/m). In these samples, iron is used as a carrier material for the coprecipitation and to form a macroscopic bulk for the handling of the sample material. An aliquot of 50 μl of the uranyl solution was added to 400 μl of the iron solution and, by the addition of NH_3, the solution was neutralized (pH $>$ 7). This induces coprecipitation of iron as iron hydroxide ($Fe(OH)_3$) and of uranium in the form of ammonium diuranate ($(NH_4)_2U_2O_7$). After centrifugation, the supernatant was extracted and the precipitate was washed and subsequently dried in vacuum at ~60°C. Then, it was transferred to a ~1 ml quartz crucible, where it was heated to 850°C in a muffle furnace to convert it into the oxide form. After cooling it at room temperature, approximately 1 mg of metallic aluminum powder was added to the crucible and mixed with the oxide, which is composed of ~0.5 mg of Fe_2O_3 and ~20 ng of uranium in the form of triuranium octoxide (U_3O_8). Finally, the solid was scrapped from the crucible and loaded in aluminum cathodes.

Milligram samples (a) and (d) were prepared heating 1-5 mg of uranyl nitrate to 800°C in a muffle furnace to convert it in U_3O_8. Once cool, the solid was mixed with ~2 mg of metallic aluminum powder and loaded in aluminum cathodes.

Uranium samples were loaded into the ion source, where uranium ions were extracted as UO^-. An initial tuning of accelerator beam optics can be done with a $^{197}Au^{7+}$ beam, which fits the same magnetic rigidity as $^{238}U^{8+}$ for a similar terminal voltage (see table 1). Gold samples deliver more intense beams than uranium ($I \sim 1\ \mu$A at FC-1, after the injection magnet), easing the optimization of the ion optics elements. After it, a pilot beam of $^{238}U^{8+}$ ($I \sim 50$ nA at FC-1) is tuned up to FC-L1 and optimized. Then, nanogram samples (b) are used to produce low-intensity beams of ^{235}U and ^{238}U which allow the calibration of the ToF system, determining the expected spectrum region for ^{236}U events. Finally, from samples (c) ^{236}U was tuned and their events were identified and discriminated from the interfering ^{235}U and ^{238}U events, which are originated in charge-exchange collisions within the accelerator tube (see Sect. 4).

While the terminal voltage can be regulated in slit mode when pilot beams ($I > 0.1$ nA) are tuned, low intensity beams require the use of the generating voltmeter (GVM). ^{235}U and ^{236}U tuning parameters were calculated from the pilot beam parameters, maintaining the same magnetic rigidity. Hence, the analyzing magnet and the high-energy side magnetic optic elements are kept constant. The magnetic field of the Wien filter is kept fixed as well. Thus, the parameters to be changed for switching different ion masses are the injection magnet field, the terminal voltage and the electric field of the Wien filter.

Table 1. Parameters used for the tuning of the different ions for a magnetic field of 11581 G in the analyzing magnet. M_{inj} is the molecular mass extracted from the ion source, B_{inj} is the magnetic field of the injection magnet, V_{Term} is the terminal voltage and V_{WF} is the plate voltage of the Wien filter.

Ion	M_{inj} (uma)	B_{inj} (G)	V_{Term} (MV)	Energy (MeV)	V_{WF} (kV)	ToF (ns)
$^{197}Au^{7+}$	197	7395	8.036	64.47	±53.9	842.6
$^{235}U^{8+}$	251	8348	7.880	70.58	±51.8	879.4
$^{236}U^{8+}$	252	8364	7.846	70.28	±51.7	883.2
$^{238}U^{8+}$	254	8398	7.780	69.69	±51.2	890.7

4. Results and discussion

The two dimensional spectrum shown in Fig.4(a) was taken tuning mass $A = 236$ from a sample containing 0.03% of ^{236}U and 3.5% of ^{235}U. Fig. 4(b) corresponds to the projection of uranium events onto the ToF axis. The interfering ^{235}U ions enter as molecules such as $^{235}U^{17}O^-$, $^{235}U^{16}O^-$ or $^{235}U^{16}O^1H^-$, while ^{238}U ions may stem from the low energy tail of the $^{238}U^{16}O^-$ beam. After stripping to a charge state 7+ or 9+, a subsequent charge-exchange collision with a residual gas molecule can result in $^{235}U^{8+}$ and $^{238}U^{8+}$ ions. When the collision occurs at a determined place of the high-energy side of the acceleration tube, these interfering ions may acquire the same magnetic rigidity as the tuned $^{236}U^{8+}$, and hence be accepted by the analyzing magnet [9]. Although the Wien filter slightly deviates interfering ^{235}U and ^{238}U (see sect. 2), a considerable amount of these ions still goes into the ToF, which must further discriminate their signals.

The events having the same ToF than uranium but approximately half of their energy can be identified as $^{118}Sn^{4+}$. When tuning $^{236}U^{8+}$, the ^{118}Sn present in trace amounts in the aluminum

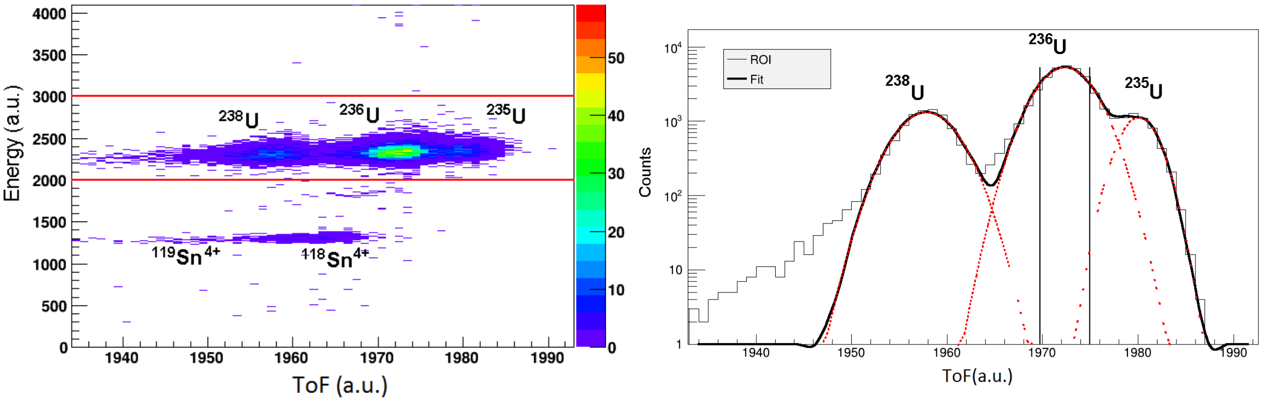

(a) (b)

Figure 3. (a) Energy vs. ToF two-dimensional spectrum. Horizontal lines show the gate used to project uranium events to the ToF axis. (b) Projection of uranium events into the ToF axis. Vertical lines show the ROI for the ^{236}U events. Dashed lines are the individual gaussian functions for each peak obtained by the fit. The solid line is the sum of the three gaussians.

alloy of the cathode can be extracted from the ion source as the molecular ion $^{118}\mathrm{Sn}_2^{18}\mathrm{O}^-$, which has the same mass of the tuned ion $^{236}\mathrm{U}^{18}\mathrm{O}^-$, thus being accepted by the injection magnet. After stripping to the 4+ charge state in the terminal, it will reach the analyzing magnet with half of the energy of the $^{236}\mathrm{U}^{8+}$ ions and, since both ions have the same mass to charge ratio, it will be accepted. Moreover, it will have the same velocity than $^{236}\mathrm{U}^{8+}$, so it will not be deviated by the Wien filter. However, these events are easily discriminated by the energy measurement and therefore pose no inconvenience to the ^{236}U identification.

The sensitivity, i.e. the minimum isotopic ratio $^{236}\mathrm{U}/^{238}\mathrm{U}$ that the system is capable to measure, is around $^{236}\mathrm{U}/^{238}\mathrm{U} = 10^{-8}$. This sensitivity was estimated as follows: the ToF spectrum of fig. 4(b) was fitted with a sum of three Gaussian functions. The region of interest (ROI) associated with the ^{236}U events was defined as the interval $\mu \pm \sigma$, where μ and σ are the mean and the standard deviation of the ^{236}U peak obtained by the fit. Using that the isotopic ratio of the sample was $^{236}\mathrm{U}/^{238}\mathrm{U}$=0.03%, it was determined that the tail of ^{235}U and ^{238}U peaks contribute at the level of 2×10^{-8} in the ratio.

Although the achieved sensitivity is still far from that of other dedicated AMS laboratories [8], there are many issues to be improved. The improvements will require the use of thinner carbon foils in the TZD$_1$ and a more restrictive vertical slit at image focal point of the quadrupole MQ-L1, to improve the Wien filter selectivity prior to the TZD$_1$. Additionally, the tuning of lower charge states, which have a higher yield at the stripper, will be tested. This will also make the difference between the ToF of the uranium isotopes larger, improving their discrimination. Due to the limitation in magnetic rigidity of the analyzing magnet and beam optic elements, the use of lower charge state as, for example, $q = 5+$, will require voltages of about 4 MV. Operating at such low voltages requires the use of shorting rods at the second half of both low- and high-energy sector of the accelerator.

5. Summary and perspective

In this work, we presented the commissioning and initial tests of a new dedicated AMS beamline at the TANDAR accelerator aimed at the detection of the radionuclide ^{236}U. It includes a Wien filter and a 6.7 m-long ToF system composed by a time zero detector and a silicon surface barrier detector, which also provides an energy measurement. To study the performance of this system, samples with different amounts of uranium and ^{236}U concentration were tested. Experimental results show that a sensitivity of ^{236}U/^{238}U=10^{-8} was achieved, but ongoing work is being done to improve this performance. The ToF system is also suitable for the detection of other radionuclides without interfering isobars, such as ^{129}I. For the discrimination of radionuclides that suffers from isobar interference, such as ^{10}Be, a segmented anode ionization chamber for atomic number discrimination and a gas-filled magnetic spectrometer are available at the end of this AMS beamline.

Acknowledgments

The authors are very grateful to E. Gautier and R. Servant from the Chemistry Division of the Comisión Nacional de Energía Atómica. Grants PICT-2016-3110 (FONCYT) and PIP00786CO (CONICET) are also acknowledged.

References

[1] Kutschera, W 2005 Progress in isotope analysis at ultra-trace level by AMS *Int. J. Mass Spectrom.* **242** pp 145-160

[2] Casacuberta, N, Masqu, P, Henderson, G, Rutgers van-der-Loeff, M, Bauch, D, Vockenhuber, C, Christl, M 2016 First ^{236}U data from the Arctic Ocean and use of ^{236}U/^{238}U and ^{129}I/^{236}U as a new dual tracer. *Earth Planet. Sci. Lett.* **440** pp 127-134.

[3] Castrillejo, M, Casacuberta, N, Christl, M, Garcia-Orellana, J, Vockenhuber, C, Synal, H-A, Masqu, P 2017 Anthropogenic ^{236}U and ^{129}I in the Mediterranean Sea: First comprehensive distribution and constrain of their sources. *Sci. Total Environ.*, **593** pp 745-759.

[4] Steier, P, Bichler, M, Keith Fifield, L, Golser, R, Kutschera, W, Priller, A, Maria Wild, E 2008. Natural and anthropogenic ^{236}U in environmental samples*Nucl. Instr. Meth. B*, **266** pp 2246-2250.

[5] Sakaguchi, A, Kawai, K, Steier, P, Quinto, F, Mino, K, Tomita, J,Yamamoto, M 2009 First results on 236U levels in global fallout *Sci. Total Environ.*, **407**, pp 4238-4242

[6] Christl, M, Casacuberta, N, Vockenhuber, C, Elssser, C, Bailly du Bois, P, Herrmann, J, Synal, H-A 2015 Reconstruction of the ^{236}U input function for the Northeast Atlantic Ocean: Implications for ^{129}I/^{236}U and ^{236}U/^{238}U-based tracer ages. *J. of Geophys. Res.: Oceans* **120** pp 7282-7299.

[7] Starzecki, W, Stefanini, A M, Lunardi, S, Signorini, C 1982 A compact time-zero detector for mass identification of heavy ions *Nucl. Instr. Meth.* **193** pp 499-505

[8] Fifield, L K, Tims, S G, Stone, J O, Argento, D C, De Cesare, M 2013 Ultra-sensitive measurements of ^{36}Cl and ^{236}U at the Australian National University *Nucl. Instr. Meth. B* **294** pp 126-131

[9] Fernández Niello, J O, Arazi, A, Capurro, O A, Abriola, D, Ferrero, A M J, Gladkis, L, Liberman, R G, Martí, G V, Pacheco, A J, Ramírez, M, Testoni, J E 2004 Spurious ionic charge states in a tandem accelerator *Nucl. Instr. Meth. B*, **223** pp 242-246

XLI Brazilian Meeting on Nuclear Physics (RTFNB) IOP Publishing
IOP Conf. Series: Journal of Physics: Conf. Series **1291** (2019) 012002 doi:10.1088/1742-6596/1291/1/012002

Big Bang Nucleosynthesis and the Lithium Problem

C.A. Bertulani

Department of Physics and Astronomy, Texas A&M University-Commerce, Commerce, TX 75429, USA

E-mail: `carlos.bertulani@tamuc.edu`

Abstract. I briefly describe the cosmological lithium problems followed by a summary of our recent theoretical work on the magnitude of the effects of electron screening, the possible existence of dark matter parallel universes and the use of non-extensive (Tsallis) statistics during big bang nucleosynthesis. Solutions within nuclear physics are also discussed and recent measurements of cross-sections based on indirect experimental techniques are summarized.

1. Introduction

The cosmological lithium problem has become one of the most intriguing open questions in cosmology due to inconsistencies between observation and calculations based on the standard Big Bang nucleosynthesis (BBN) for the primordial elemental abundances. The BBN model contains a few parameters such as the baryon-to-photon ratio $\eta = n_b/n_\gamma$, the neutron decay time τ_n, and the number of neutrino families N_ν (see, for instance, Ref. [1]). The parameter η relates to the baryon density of the universe by means of $\Omega_0 h^2 \simeq (\eta/10^{-10})/273$, with the Hubble dimensionless parameter h defined through the relation $H_0 = 100h$ km/s/Mpc, the index '0' meaning present time. The anisotropies of the cosmic microwave radiation (CMB) independently determine the value of η [1, 2, 3] when the universe was about 0.3 Myr after the Big Bang. Then photons decoupled and began steaming freely in the universe. Precise LEP experiments to deduce the number of neutrino families [4] lead to the value $N_\nu = 2.9840 \pm 0.0082$, and neutron lifetime measurements have inferred that $\tau_n \simeq 880.2 \pm 1.0$ s [5].

The observed abundances of light elements probe the universe at the very early stages, i.e., 3-20 minutes, of its existence. During this epoch, the light elements D, ^{3}He, ^{4}He, and ^{7}Li were produced and their abundances in selected astrophysical environments are telltales of the BBN epoch. The BBN model predictions also depend on the nuclear reaction network and magnitude of the nuclear cross sections. A few minutes ($\sim$ 3 min) after the Big Bang, deuterons were formed by neutron capture on protons, by means of the reaction p(n,γ)d. The formation of deuterons is strongly dependent on the value of η. Deuterons are promptly destroyed once they are formed leading to the formation of ^{3}He nuclei by means of the d(p,γ)^{3}He and d(d,n)^{3}He reactions. Deuterons also synthesize tritium by means of the d(d,p)t reaction. ^{4}He are then created by the ^{3}He(d,p)^{4}He and t(d,n)^{4}He reactions. In the end, the BBN model predicts that the universe should be composed of about 75% of hydrogen and 25% of helium with tiny traces of D, ^{3}He, ^{7}Li and ^{6}Li. The foundations of these results rely on the big bang prediction of the neutron-to-proton ratio n/p = 1/7 when the nucleosynthesis started, i.e., the BBN occurred in a proton-rich environment.

Table 1. Nuclear reactions of importance for big bang nucleosynthesis.

n ↔ p	p(n,γ)d	d(p,γ)^{3}He	d(d, p)t
d(d, n)^{3}He	^{3}He(n, p)t	t(d, n)^{4}He	^{3}He(d, p)^{4}He
^{3}He(α,γ)^{7}Be	t(α,γ)^{7}Li	^{7}Be(n, p)^{7}Li	^{7}Li(p,α)^{4}He

The standard BBN model predicts the ^{7}Li/H abundance ratio of the order of 10^{-10} and the ^{6}Li/H abundance ratio of the order of 10^{-14}. Much after the BBN epoch, ^{6}Li and ^{7}Li can be produced in spallation processes by cosmic rays and ^{7}Li can be synthesized in novae or during AGB stars pulsations. In Ref. [6] it was reported that the ^{7}Li abundance is independent of the metallicity in metal-poor stars with small Fe/H abundances relative to the sun. Such stars are warm ($5700 \leq T \leq 6250$ K) metal-poor dwarf stars observed in the galaxy halo. For low metallicity stars the ^{7}Li abundance is nearly constant and this behavior is known as the “Spite plateau” [6]. ^{7}Li is destroyed in red giants with core temperatures in excess of 10^6 K via the reaction ^{7}Li(p, α)^{4}He and that is why white dwarfs at moderate temperatures have been used in such observations. The Spite plateau provides a reasonable evidence that lithium is neither created nor destroyed in warm dwarfs and that such stars display the abundances of primordial ^{7}Li. On the other hand, it is worthwhile mention that recent observations in low-metallicity stars seem to contradict the conclusions drawn from the Spite plateau [7, 8]. The currently accepted value for the ^{7}Li BBN model abundance, calculated using $\eta = (6.07 \pm 0.07) \times 10^{-10}$ [3], corresponds to Li/H $= (4.16 - 5.34) \times 10^{-10}$ [10] while the observations from metal-poor halo stars yields Li/H $= (1.58 + 0.35 - 0.28) \times 10^{-10}$ [8, 9]. This is approximately a factor of 3 lower than expected and is the source of the lithium puzzle.

The second lithium puzzle involves the abundance of ^{6}Li produced during the BBN by means of the ^{2}H(α,γ)^{6}Li reaction. ^{6}Li nuclei formed in stars disappear quickly by means of other reactions. ^{6}Li is also created in cosmic ray interactions, and could also exist in the atmosphere of metal-poor warm dwarfs in the halo of the galaxy, surviving destruction by cosmic rays. But such assumptions are controversial, because they can also apply to ^{7}Li nuclei. The second lithium puzzle relates to the BBN predictions of the isotopic ratio ^{6}Li/^{7}Li $\sim 10^{-5}$ [10, 12], while observations report ^{6}Li/^{7}Li $\sim 5 \times 10^{-2}$ [14]. This puzzle is less robust because of the complexities involved in 3-dimension calculations involving convection and non-local thermodynamical equilibrium, in particular in the photo-sphere of metal-poor stars. Because they might have a large influence on the ^{6}Li/^{7}Li isotopic ratio, such complexities weaken the arguments for the existence of the second lithium problem which in some scenarios yields a better agreement with BBN predictions [15].

2. Nuclear reaction cross sections

During the BBN, the most relevant nuclear reactions are listed in Table 1. This network of reactions resulted in the production of D, ^{3}H, ^{3}He, ^{4}He, ^{6}Li, ^{7}Li and ^{7}Be. Only very small traces of carbon, nitrogen and oxygen were produced at the $10^{-15} - 10^{-25}$ abundance level. Therefore, there is no need to include reaction networks beyond those shown in Table 1, such as the famous CNO cycle, to tackle the lithium problem [9]. In Figure 1 we show the calculated BBN abundance of H, D, ^{3}H, ^{3}He, ^{4}He, ^{6}Li, ^{7}Li and ^{7}Be as a function of time [1]. Our calculations were performed with an extended code based on the Wagoner code [16] and similar to NUC123 [17]. The dashed blue curve represents the ^{4}He mass fraction, the red dashed curve represents the deuterium abundance, the green dashed curve represents the ^{3}He abundance, the solid black curve is the ^{3}H abundance, the red dashed curve is the ^{7}Be abundance and blue dashed curve is

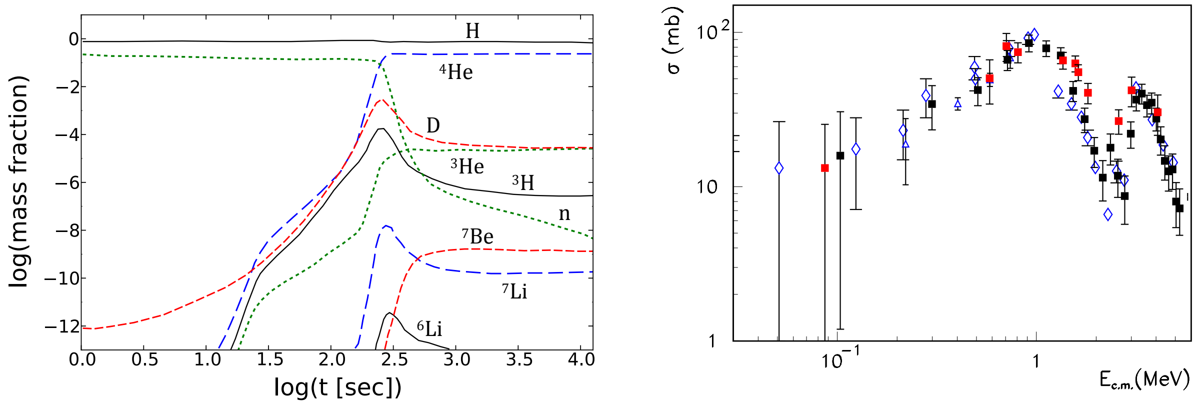

Figure 1. *Left:* Calculated BBN abundances of H, D, ^{3}H, ^{3}He, ^{4}He, ^{6}Li, ^{7}Li and ^{7}Be as a function of time [1]. *Right:* ^{7}Be(n,α) cross section deduced using the THM experimental data for the ^{7}Li(p,α)^{4}He mirror reaction (full red circles) and using ^{3}He THM breakup data (full black circles) [29]. The data compiled by Hou [26] is shown as empty blue circles, and data from Kawabata [28] are shown as full blue squares.

the ^{7}Li abundance. Recently, new experimental measurements of reactions of relevance for the BBN have been reported based on the use of the Trojan Horse Method (THM) [10].

The reaction cross sections at the low astrophysical energies are enhanced due to the electrons in the plasma. The cross sections in the plasma are enhanced by a factor $f(E) = \sigma_s(E)/\sigma_b(E)$, where σ_s is the screened and σ_b the bare (non-screened) cross section. The Debye-Hückel theory predicts a screened Coulomb potential of the form $V(r) = (e^2 Z_i/r) \exp(-r/R_D)$, where the Debye radius is given by $R_D = (1/\zeta)\,(kT/4\pi e^2 n)^{1/2}$, with n being the ion number density and $\zeta = \left[\sum_i X_i(Z_i^2/A_i) + \chi \sum_i X_i(Z_i/A_i)\right]^{1/2}$, with X_i the mass fraction of particle i and the temperature T_6 in units of 10^6 K. χ is a factor correcting for electron degeneracy effects [19]. During the big bang, the electron number density decreased strongly with the temperature, being up to 10^4 times larger than the number density in the core of the sun, $n_e^{sun} \sim 10^{26}/\text{cm}^3$. However, the baryon density was much smaller during the BBN epoch than at the core of the sun. The number of excess electrons during the BBN is nearly the same as those of protons. But most electrons were in balance with the number of positrons produced via $\gamma\gamma \to e^+e^-$ processes. In Ref. [20] the electron screening effects were included in the BBN reaction network. It was found that the modification of the BBN abundances are negligible. Evidently, it cannot be responsible for the lithium abundance deficiency. Worth mentioning is that recently it has been shown that clustering effects in reactions involving light nuclei at astrophysically relevant energies might also play an important role and could perhaps explain some of the discrepancies found in the experimentally deduced values of electron screening enhancement and theoretical calculations [21].

In Table 2 the BBN calculations are compared with observations. The mass fraction for ^{4}He, historically denoted by Y_p, is taken from Ref. [18], (b) the deuterium abundance $\text{D/H} = (2.527 \pm 0.03) \times 10^{-5}$ [22, 23], compatible with $100\Omega_b h^2$ (BBN) $= 2.225 \pm 0.016$ inferred from the measurements of the cosmic microwave background [3], (c) the ^{3}He abundance is taken from Ref. [24], and (d) the lithium abundance is taken from Ref. [8]. The BBN model result for the ^{7}Li abundance shown in Table 2 is in evident discordance (roughly by a factor 3) with the observation. One possibility for this discrepancy could be that ^{7}Be is further destroyed during the BBN. We recall that ^{7}Be decays in 53.22 ± 0.06 days by electron capture to ground and first excited (0.477 MeV) states of ^{7}Li. Therefore, all ^{7}Be produced during the big bang will count towards the ^{7}Li primordial abundance. If ^{7}Be is substantially destroyed by, e.g., (n,p) or (n,α) reactions, it could possibly explain the observed lithium depletion. This possibility has been investigated in Refs. [25, 26, 27, 28, 29]. In particular, Lamia et al. [29] have experimentally determined the ^{7}Be(n,α) reaction cross section using the THM experimental data for the ^{7}Li(p,α)^{4}He mirror reaction with corrections for Coulomb effects (see Figure 1). The new deduced data for ^{7}Be(n,α) using this technique lies within the Gamow window appropriate for BBN temperatures and the reaction rate using the new data is found to be lower by a factor ≈ 10 relative to the one used by Wagoner [16]. The new reaction rate yields a ^{7}Li/H abundance ratio of 2.845×10^{-11} and a ^{7}Be/H abundance ratio of 4.156×10^{-10}, leading to a total cosmological lithium abundance of 4.441×10^{-10}, and no appreciable change of the previously obtained BBN results is verified. More recently, a theoretical investigation of the impact of the ^{7}Be(α,γ) on ^{7}Be destruction was performed [30]. It was found that the ^{7}Be abundance would be compromised only if an unexpected strong resonance exists very close to threshold in this reaction channel. All odds are that such a resonant state does not exist.

Table 2. BBN calculations using fits to recent experimental data for BBN reactions compared with observations. The mass fraction for ^{4}He, historically denoted by Y_p, is taken from Ref. [18], (b) deuterium abundance D/H = $(2.527 \pm 0.03) \times 10^{-5}$ [22, 23], compatible with $100\Omega_b h^2$ (BBN) = 2.225 ± 0.016 inferred from the measurements of the cosmic microwave background [3], (c) ^{3}He abundance is taken from Ref. [24], and (d) the lithium abundance is taken from Ref. [8].

Yields	Calculation	Observation
Y_p	0.2485+0.001-0.002	$0.2565 \pm 0.006^{(a)}$
D/H ($\times 10^{-5}$)	2.692+0.177-0.070	$2.527 \pm 0.03^{(b)}$
^{3}He/H ($\times 10^{-6}$)	9.441+0.511-0.466	$\geq 11. \pm 2.^{(c)}$
^{7}Li/H ($\times 10^{-10}$)	4.283 +0.335-0.292	$1.58{+}0.35 - 0.28^{(d)}$

BBN predicts an isotopic ratio of ^{6}Li/^{7}Li $\sim 10^{-5}$, whereas observation yields ^{6}Li/^{7}Li $\sim 5 \times 10^{-2}$ [14]. In Ref. [12] a re-analysis of the reaction ^{4}He$(\mathrm{d},\gamma)^6$Li was performed, including new predictions for the gamma-ray angular distribution. This was done using a two-body potential model to calculate the S-factor for this reaction at the BBN energies [11, 12]. The potential parameters were chosen to reproduce experimental phase shifts and recently measured ANCs. A nice agreement was found with the experimental data of the LUNA collaboration [13]. This work reinforces BBN predictions for the lithium isotopic ratio and yields a new value of ^{6}Li/^{7}Li = $(1.5 \pm 0.3) \times 10^{-5}$. The second lithium puzzle seems to be alive although it is not impossible that lithium abundances might change appreciably due to astration.

We conclude this section by stating that it does not seem possible that both lithium puzzles can be solved by accurate measurements of nuclear reaction cross sections, combined with progresses in the theories for nuclear astrophysical reactions. There has been a considerable number of recent theoretical efforts to elucidate the lithium puzzle using a plethora of different ideas based on the premise that physics as we know today might have been different 13.8 billions years ago. New particles, new interactions, changes in fundamental constants, non-standard BBN models, and various intriguing ideas have been used and published elsewhere.

3. Dark matter

Most of the matter in the universe consists of an obscure kind of Dark Matter (DM) which interacts very weakly with the visible matter. In fact, we only know that it interacts gravitationally and large scale experimental searches are underway to identify if DM interacts with visible matter by other means [31, 32, 33]. The existence of DM is based on astronomical observations of galaxy clusters dynamics and on the anisotropies of the Cosmic Microwave Background (CMB). Perhaps Weakly Interacting Massive Particles (WIMPs), supersymmetric particles, sterile neutrinos, or any other hitherto undiscovered particles are responsible for its composition. It has also been hypothesized that DM is a mirror sector of particles such as dark photons, dark electrons, etc., which interact in nearly the same way as Standard Model (SM) particles, but only within their own sector. They interact very weakly across sectors, i.e. between the DM sector and the visible sector [34, 35, 36, 37, 38, 39, 41]. Besides, the particle copies in the dark sector do not need to have the same masses and couplings as in the visible sector, opening a huge number of possible scenarios for DM.

Astronomical observations yield the ratio of density parameters $\Omega_{DM}/\Omega_{visible} = 4.94 \pm 0.66$. Therefore, DM is 5 times more frequent than visible matter. In Ref. [39, 40, 41] this feature was used to explore the possible existence of 5 dark sectors instead of the single ubiquitous dark sector. A Weakly Interacting Massive Gauge Boson (WIMG) was also proposed to couple all dark sectors and ordinary matter. The massive, $E \sim 10$ TeV, WIMG does not modify the properties of the SM and gravity. It has to be consistent with BBN predictions and CMB observations, except maybe with the lithium abundance. Much below the electroweak scale energy, we can assume particles to be massless and group them in matter/charge fields with a similar structure for DM. The WIMG mass is generated by a real scalar field, with the condition that the WIMG has a short-range interaction. In this formalism, the number of dark sectors plays an important role which has been overseen in other BBN models. The new degrees of freedom of particles in the dark sector modify the early universe expansion rate [42] and the elemental abundance predictions. Additional dark sectors increase the effective number of degrees of freedom and their implications for BBN [39, 40, 41].

The basic idea of having additional dark sectors is that the radiation in the BBN epoch have densities and entropies given by $\rho(T) = (\pi^2/30)\, g_*(T)\, T^4$ and $s(T) = (2\pi^2/45)\, g_s(T)\, T^3$ with

$$g_*(T) = \sum_B g_B \left(\frac{T_B}{T}\right)^4 + \frac{7}{8}\sum_F g_F \left(\frac{T_F}{T}\right)^4, \quad \text{and} \quad g_s(T) = \sum_B g_B \left(\frac{T_B}{T}\right)^3 + \frac{7}{8}\sum_F g_F \left(\frac{T_F}{T}\right)^3, \tag{1}$$

where g_* and g_s are the number of degrees of freedom, with $g_{B(F)}$ being the fractions contributed by bosons (fermions) at temperatures $T_{B(F)}$. In this notation, T is the temperature of the radiation thermal bath.

For simplicity, we assume only two temperatures: T in the ordinary matter sector and T' in the dark sectors. By analogy, the energy $\rho'(T')$ and entropy $s'(T')$ densities in the dark sectors are also obtained with Eqs. (1) with $g_*(T) \to g'_*(T')$, $g_s(T) \to g'_s(T')$, and $T \to T'$. An independent variable $x = (s'/s)^{1/3} \sim T'/T$ emerges if one assumes conservation of entropy in all sectors. If each dark sector has the same matter content as in the visible sector, then $g_s(T_0) = g'_s(T'_0)$, leading to $x = T'/T$. The Friedman equation is $H(t) = \sqrt{(8\pi/3c^2)\; G_N\, \bar{\rho}}$, where $\bar{\rho}$ is the total energy density. Including the number of dark sectors, N_{DM}, it becomes $\bar{\rho} = \rho + N_{DM}\, \rho'$. Therefore, one has $H(t) = 1.66\, \sqrt{\bar{g}_*(T)}T^2/M_{Pl}$, with $\bar{g}_*(T) = g_*(T)\,(1 + N_{DM}\, a\, x^4)$, where M_{Pl} is the Planck mass and $a = (g'_*/g_*)\,(g_s/g'_s)^{4/3} \sim 1$, for a not too small T'/T [42]. At about 1 MeV, standard BBN assumes $g_*(T = 1 \text{ MeV}) = 10.75$, but with the additional dark particles it becomes $\bar{g}_* = g_*\,(1 + N_{DM}\, x^4)$. We can study the bounds for N_{DM} and x, or T'/T, by comparing BBN calculations and the relative abundances of the light element isotopes (D, ^{3}He, ^{4}He, and ^{7}Li). This is shown in Figure 2 as a function of T'/T with a fixed number of dark sectors, $N_{DM} = 5$. The shaded bands include the uncertainty in the observed values. In this case, we notice that observations of primordial elements of D, ^{3}He, and ^{4}He are compatible with $T'/T \sim 0.2 - 0.3$.

The ^{7}Li problem remains because if $T'/T \sim 1$ then ^{7}Li comes out right, but the other

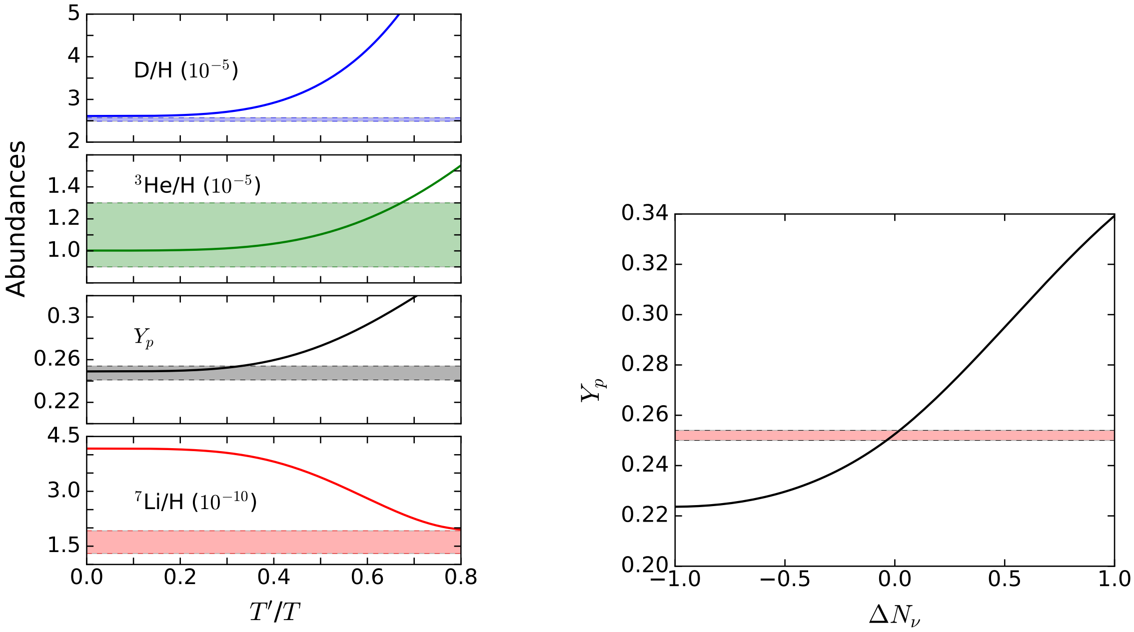

Figure 2. *Left:* Calculated relative abundances of D, ^{3}He, ^{4}He (mass fraction, Y_p) and ^{7}Li as a function of T'/T, with $N_{DM} = 5$ compared to observations. The bands represent uncertainties in the observations [44]. *Right:* Predictions for the primordial ^{4}He mass fraction as a function of extra neutrino families, with $T' = 0.3T_{BBN}$ and $N_{DM} = 5$. The horizontal band represents the observed mass fraction [44].

abundances will be completely off the observations. $\bar{g}_*(T)$ is much more sensitive to T' than it is to N_{DM}. Using $T' = 0.3T$ for cold dark sectors, we obtain a large range of values for $N_{DM} = 1 - 50$ compatible with the D, ^{3}He and ^{4}He abundances [44]. Figure 2 also shows the predictions for the primordial ^{4}He mass fraction as a function of extra neutrino families, ΔN_ν, with $T' = 0.3T_{BBN}$ and $N_{DM} = 5$. The horizontal band represents the observed mass fraction [44]. The model is thus compatible with the number of neutrino families $N_\nu = 3$. We thus conclude that there is no incompatibility with the observed primordial abundances and a universe composed with more than one sector of dark matter, e.g. $N_{DM} = 5$ and temperatures of the dark sectors of the order of $T' \sim 0.2 - 0.3T$.

4. Non-extensive statistics

The Maxwell-Boltzmann (MB) distribution is widely known to reproduce extremely well the distribution of velocities of particles in a thermal bath. The MB distribution is a result of the Boltzmann-Gibbs statistics, based on the assumptions that (a) the time between collisions among particles is much larger than their interaction time, (b) the interaction is short-ranged, (c) no correlation exists between the particle velocities, and (d) the collision energy is conserved without transfer to internal degrees of freedom. These very constraining assumptions are not expected to be always valid in thermodynamical equilibrium. In fact, alternatives to the Boltzmann-Gibbs (BG) statistics are known to exist [45, 46, 47]. In Ref. [48], one of these non-extensive statistics, namely, the Tsallis statistics [46, 47] has been used to describe the relative velocities of particles during the BBN. The effect on the lithium abundance was again the motivation for this work. The Tsallis statistics was used [46, 47], because it represents a family of entropies depending on a parameter q, which measures the departure from Boltzmann statistics. The Boltzmann

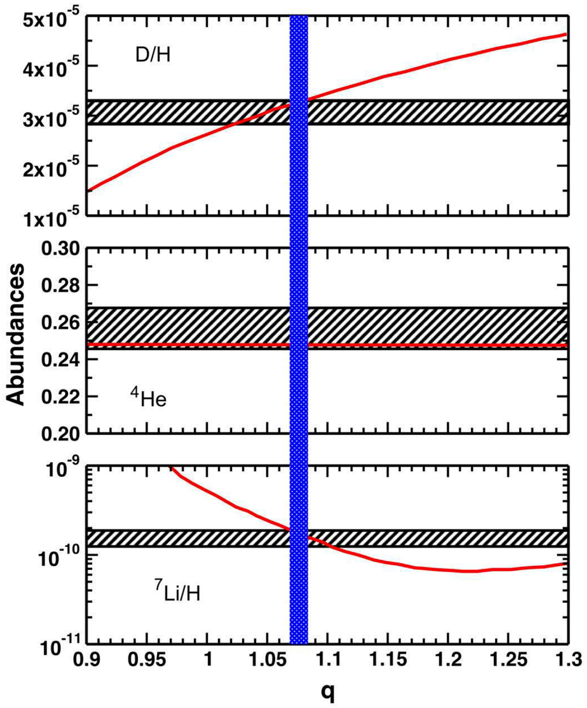

Figure 3. Predicted abundances D, ^{4}He and ^{7}Li (red curves) as a function of the Tsallis parameter q [53]. The observed primordial abundances including 1σ uncertainties are indicated by hatched horizontal bands [54, 8, 55]. The vertical (blue) band refers to the parameter q within the interval $1.069 < q < 1.082$.

statistics is recovered when $q = 1$.

In all previous applications of non-extensive statistics, it has been found that the non-extensive parameter q does not depart appreciably from the Boltzmann value $q = 1$. Non-extensive Maxwellian velocity distributions have previously been applied to study stellar nuclear burning, e.g. in Refs. [49, 50, 51, 52]. In Ref. [48] the Tsallis statistics was used to deduce reaction rates during the BBN and predictions were made for the ^{4}He, D, ^{3}He, and ^{7}Li abundances which are based on the reaction rates for p(n,γ)d, d(p,γ)^{3}He, d(d,n)^{3}He, d(d,p)t, ^{3}He(n,p)t, t(d,n)^{4}He, ^{3}He(d,p)^{4}He, ^{3}He(α,γ)^{7}Be, t(α,γ)^{7}Li, ^{7}Be(n,p)^{7}Li and ^{7}Li(p,α)^{4}He and their available experimental data [48]. The conclusion from Ref. [48] is that if either $q > 1$ of $q < 1$, the abundances of all elements are affected but that of ^{7}Li always increases. Therefore, it was inferred that the lithium problem always seems to get worse with the use of the Tsallis statistics.

However, there was a small, but relevant point neglected in the calculations of Ref. [48], namely, the proper inclusion of the reaction Q-values in the reaction rates obtained with the Tsallis statistics. This was fixed in Ref. [53] and shown that, when the Q-values for the reverse reactions are properly accounted for, a beautiful result emerges for a relatively small departure of the parameter q from unity. The abundances of H, D, ^{3}H, ^{3}He, and ^{4}He, do not change, but that of ^{7}Li does change appreciably, and in the correct direction to solve the ^{7}Li puzzle. In fact, an excellent agreement was found between the calculated and the primordial abundances observed for D, ^{4}He, and ^{7}Li for $1.069 < q < 1.082$, indicating that a possible solution to the cosmological lithium problem might arise from a fine tuning of the physics involved. This is shown in Figure 3 with the predicted abundances D, ^{4}He and ^{7}Li (red curves) as a function of the Tsallis parameter q. The observed primordial abundances including 1σ uncertainties are indicated by hatched horizontal bands [54, 8, 55]. The vertical (blue) band refers to the parameter q within the interval $1.069 < q < 1.082$.

The work published in Ref. [53] was cited as a research highlight by the American Astronomical Society [56]. It attests the relevance of the lithium puzzle and the anxiety that its solution entails for the astronomical community. The puzzle has been around the literature for a few decades already. The exercise played in Ref. [53] shows that a solution might be the outcome of a fine tuning of the physics during the BBN. The Tsallis statistics might be one possible departure from the standard physics during the big bang epoch. The question remains on the physical meaning for the value of $q \neq 1$, and its relation to other physical processes.

5. Acknowledgments

This work was supported in part by the U.S. DOE grant DE- FG02-08ER41533 and the U.S. National Science Foundation Grant No. 1415656. The author also thanks the support of the Brazilian funding agencies FAPESP, CNPq and CAPES.

References

[1] Bertulani C A and Kajino T 2016 *Prog. Part. Nucl. Phys.* **89** 56
[2] Komatsu E et al. 2011 *Ap. J.* **192** 18
[3] Ade P A R et al. 2016 *Astron. Astrophys.* **594** A13
[4] The ALEPH Collaboration, The DELPHI Collaboration, The L3 Collaboration, The OPAL Collaboration, The SLD Collaboration, The LEP Electroweak Working Group, The SLD Electroweak and Heavy Flavor Groups 2006 *Phys. Reports* **427** 257
[5] Patrignani C et al. (Particle Data Group) 2016 *Chinese Phys.* **C 40** 100001
[6] Spite M and Spite F 1982 *Nature* **297** 483; Spite F and Spite *A&A* **115** 357
[7] Aoki W et al. 2009 *Ap. J.* **698** 1803
[8] Sbordone L et al. 2010 *A&A* **522** A26
[9] Coc A et al. 2012 *Ap. J.* 744 **158**
[10] Pizzone R G et al. 2014 *Ap. J.* **786** 112
[11] Bertulani C A 2003 *Comput. Phys. Commun.* **156** 123
[12] Mukhamedzhanov A M, Shubhchintak and Bertulani C A 2016 *Phys. Rev.* **C 93** 045805
[13] Anders M et al. 2014 *Phys. Rev. Lett.* **113** 042501
[14] Asplund M, Lambert D L , Nissen P E, Primas F and Smith V V 2006 *Ap. J.* **644** 229
[15] Lind K, Melendez J, Asplund M, Collet R and Magic Z 2013 *A&A* **554** A96
[16] Wagoner R V 1969 *Ap. J. Suppl. Ser.* **18** 247
[17] Kawano L 1992 Let's Go: Early Universe. Primordial Nucleosynthesis: The Computer Way *NASA Technical Reports Server (NTRS): Hampton, VA, USA*
[18] Izotov Y I and Thuan T X 2010 *Ap. J. Lett.* **710** L67
[19] Salpeter E E 1954 *Aust. J. Phys.* **7** 373; Salpeter E E and Van Horn H M 1969 *Ap. J.* **155** 183
[20] Wang B, Bertulani C A and Balantekin A B 2011 *Phys. Rev.* **C 83** 018801
[21] Spitaleri C et. al. 2016 *Phys. Lett.* **B 755** 275
[22] Riemer-Sorensen S and Sem Jenssen E 2017 *Universe* **2** 44
[23] Cooke R J, Pettini M and Steidel C C 2017 *arXiv:1710.02730*
[24] Bania T M, Rood R T and Balser D S 2002 *Nature* **415** 54
[25] Broggini C et al. 2012 *JCAP* **6** 30
[26] Hou S Q et al. 2015 *Phys. Rev.* **C 91** 055802
[27] Barbagallo M et al. 2016 *Phys. Rev. Lett.* **117** 152701
[28] Kawabata T et al. 2017 *Phys. Rev. Lett.* **118** 052701
[29] Lamia L et. al. 2017 *Ap. J.* **850** 175
[30] Hartos M, Bertulani C A, Shubhchintak, Mukhamedzhanov A M, and Hou S 2018 *Astrop. J.* **862** 62
[31] Feng J L 2010 *arXiv:1003.0904*
[32] Bertone G, Hopper D and Silk J 2005 *Phys. Rep.* **405** 279
[33] Bertone G 2010 *Nature* **468** 389
[34] Lee T D and Yang C N 1956 *Phys. Rev.* **104** 254
[35] Kobzarev Y, Okun L and Pomeranchuk I 1966 *Yad. Fiz.* **3** 1154
[36] Pavsic M 1974 *Int. J. Theor. Phys.* **9** 229

[37] Foot R, Lew H and Volkas R 1991 *Phys. Lett.* **B 272** 67
[38] Akhmedov E, Berezhiani Z and Senjanovic G 1992 *Phys. Rev. Lett.* **69** 3013
[39] Oliveira O et al. 2011 *arXiv:1108.2723*
[40] Bertulani C A et. al. 2013 *AIP Proc.* **1498** 134
[41] Oliveira O et al. 2016 *Braz. J. Phys.* **46** 721
[42] Berezhiani Z G, Dolgov A D and Mohapatra R N 1996 *Phys. Lett.* **B375** 26
[43] Oliv K A (Particle Data Group - Review of Particle Physics) 2014 *Chin. Phys.* **C 38** 090001
[44] Bertulani C A, Challa V, He J J, Hou S and Kumar R 2017 *arXiv:1704.07803*
[45] Rényi A 1960 *Proc. of the 4th Berkeley Symposium on Mathematics, Statistics and Probability* 547
[46] Tsallis C *J. Stat. Phys.* **52** 479
[47] Gell-Mann M and Tsallis C eds. 2004 *Nonextensive Entropy-Interdisciplinary Applications, (Oxford University Press, New York)*
[48] Bertulani C A, Fuqua J and Hussein M S 2013 *Ap. J.* **767** 67
[49] Lissia M and Quarati P 2005 *Europhys. News* **36** 211
[50] Haubold J and Kumar D 2008 *Astroparticle Phys.* **29** 70
[51] Degl'Innocenti S et al. 1998 *Phys. Lett.* **B 441** 291
[52] Coraddu M et al. 1999 *Braz. J. Phys.* **29** 153
[53] Hou S et. al. 2017 *Ap. J.* **834** 165
[54] Aver E, Olive K A and Skillman E D 2010 *JCAP* **5** 003
[55] Olive K A, Petitjean P, Vangioni E and Silk J 2012 *MNRAS* **426** 1427
[56] Kohler S 2017 *AAS-NOVA* Fixing the Big Bang Theory's Lithium Problem, 15 February

IOP Conf. Series: Journal of Physics: Conf. Series **1291** (2019) 012003 doi:10.1088/1742-6596/1291/1/012003

Status and activities of the LAFN (*Laboratório Aberto de Física Nuclear*)

J R B Oliveira

Instituto de Física da Universidade de São Paulo, DFN, São Paulo, SP, Brazil

zero@if.usp.br

Abstract. A brief panorama is given about the status and the research activities of the LAFN - *Laboratório Aberto de Física Nuclear* (the "Open Nuclear Physics Laboratory"). The LAFN is an internal organization of the Nuclear Physics Department of the Institute of Physics of the University of São Paulo, São Paulo, SP, Brazil, which was created in the late 90's in order to facilitate the participation of users from other institutions in Brazil or abroad. Presently the Laboratory has more than 70 registered users, most of them active in proposing and performing experiments with the 8MV Pelletron-Tandem particle accelerator, which is a mayor nuclear physics research facility in Brazil. The experiment proposals are evaluated by a project advisory committee. It is characteristically a University based facility, with abundant participation of students, and production of several MSc and PhD theses regularly. The organizational structure of the Laboratory, and the characteristics of the Accelerator and peripherals will be described, as well as selected topics of the ongoing research both on basic and applied nuclear physics, such as nuclear structure and reaction mechanism studies with stable and radioactive beams, and tests of irradiation damage and other effects on electronic devices. Presently, the LAFN is part of the INCT-FNA ("Instituto Nacional de Ciência e Tecnologia - Física Nuclear e Aplicações"), supported by several Federal and State institutions from Brazil.

1. Introduction

The main facility of the LAFN is the 8UD Pelletron-Tandem heavy-ion accelerator, developed by NEC – Nuclear Electrostatics Corp., and installed at IFUSP in the early seventies [1]. It is the only one of its kind in Brazil, and with its akin facility TANDAR [2] in Argentina, the only ones in Latin America. Presently its ion source is a multicathode SNICS (NEC) capable of producing ions from ^{6}Li to ^{108}Ag or, in principle, even heavier ions. Typically, energies of around 5 MeV per nucleon are used. The Experimental Hall has 7 beam lines dedicated to various experimental setups. Presently one line is deactivated, and another is transporting the beam to the LINAC post-accelerator (under construction). The other lines are used for basic nuclear structure and reaction research, as well as physical applications.

At the 90's the LAFN was created as an organizational structure responsible for the maintenance of the Accelerator, and for making the facility available for users from inside or outside the University of São Paulo.

2. The LAFN organization

The organization of LAFN is defined in its statute, last revised in 2016. Its integral version is available at the at the Laboratory web site under the IFUSP website.

2.1. The Superior Council

The Superior Council is composed of the members of the Nuclear Physics Department (DFN) of IFUSP. It nominates the Director from a list of names provided by the Users Board.

2.2. The Director.

The Laboratory Director administrates the budget and operations of the Laboratory for a mandate of 2 years, allowed one extension.

2.3. The Program Advisory Committee.

The PAC is composed of eminent nuclear physics researchers chosen by the Director, the Superior Council and the Users Board. It yearly evaluates the experiment proposals and allocates time of Accelerator use for each based on merit and technical feasibility. The approved projects are publicly available at the Laboratory website.

2.4. The Users Board.

The users board is composed of all graduate researchers which have approved experiments evaluated by the PAC in the last 4 years, and which manifests interest in composing the board. It elects its own President, and discusses any issue relevant for the research at the laboratory and proposes improvements to the Direction. Presently, about 75 users are officially listed from a variety of countries, including Argentina, Canada, Colombia, France, Germany, Italy, Spain, and USA.

2.5. The Technical Coordinator

Coordinates the operation of the staff distributed in the executive sectors of the Laboratory: Development and Maintenance (Ion Optics, Vacuum, Machine shop), Electronics, Target Making, Data Acquisition, Secretary, and User Support. The staff is composed of 11 technicians in total.

3. The facility and peripherals

The research equipment available for the LAFN users consists of the accelerator and peripherals installed at the Oscar Sala 9-floor building at IFUSP, São Paulo, SP.

3.1. The accelerator

The 8UD Pelletron-Tandem is an 8MV electrostatic Tandem accelerator developed by NEC, and described in [1]. Figure 1 presents an overall view of the facility. Originally, the voltage distribution along the accelerator tube and equipotential rings was made by corona needles. Near the end of 2010 the corona needles were substituted by passive resistors which improved a lot the reliability and stability of the accelerator by preserving the SF6 gas quality. Shortly after that, the steel contact blades of the charging pulleys, which was causing erosion of the pellets and chain break downs, was eliminated. As a consequence of this, the original 8MV terminal voltage of the Accelerator has been routinely available ever since. Presently the analog control devices of the ion optics is being gradually replaced by digitally controlled devices (interfaced with PXI, with Labview). New constant current magnet power supplies of the mass and energy magnetic selectors were installed. The 32 cathode MC-SNICS provides the negative ions, accelerated to about 90 keV to be injected into the accelerator. The Carbon stripper foils at the terminal center are about 10μg/cm² thick, and are produced by the Target Laboratory of the LAFN. Typical beam intensities of 100 nA to 1μA are available for the users at their scattering chamber, depending on the ion species. An updated list is available at the LAFN website.

3.2. The experimental hall lines

Presently 6 of the 7 beam lines at the experimental hall are operational and dedicated to special research lines, comprising different scattering chamber and detector arrays.

3.2.1. The RIBRAS system. The Radioactive Ion Beams Brasil (RIBRAS) system is dedicated to the production of radioactive ion beam (RIB) species [3,4]. It consist of two identical superconducting solenoids with a maximum magnetic field of about 6 T. The radioactive species are produced by an intense primary beam (usually ^{7}Li) on a primary target (usually ^{9}Be) and the secondary beam of interest is separated and purified by a system of slits and lollipops, and focused by the solenoids onto a secondary target surrounded by an array of silicon detectors. Typical RIB intensities of 10^5 particles/s can be produced. The reaction mechanisms of light weakly bound unstable nuclei are investigated with this system.

3.2.2. The Saci-Perere spectrometer. This is a gamma-ray spectrometer [5] composed of 4 GeHP detectors with Compton suppressors, with a total photopeak efficiency of about 0.5%, and an ancillary system of *phoswich* plastic scintillators (ΔE-E telescopes) covering about 83% of the 4π solid angle of the sphere. It was designed for high-spin nuclear structure studies, but has also been used for reaction mechanism investigation by charged particle-gamma coincidence method [6].

3.2.3. The Enge Split-pole Spectrograph. This magnetic dipole spectrometer has a maximum field of 17kGauss, an acceptance angle of 2.7 msr and an excellent energy resolution of 1/2750 [7]. Its typically used for Coulomb-nuclear interference measurements and investigation of shape transitions and coexistence in mid-mass transitional nuclei [8].

3.2.4. The 30B multipurpose chamber. This is a 1 m diameter camera equipped with a goniometer for the positioning of particle detectors. Presently a particle detector telescope array (SATURN) is installed for nuclear reaction mechanism studies with stable weakly-bound beams [9,10].

3.2.5. The SAFIIRA line (0 degrees). This is the newest beam line built at the LAFN. Its set of beam scatterer/collimators allows for the production of a wide, low intensity uniform beam for irradiation of electronic devices. It is used for radiation tolerance tests as well as Single Event Upset and similar effects on electronic components and chips [11]. A large collaboration of many national institutions (CITAR project) is involved in this research, and has strategical importance for satellite/aerospace technology in Brazil.

3.2.6. The LINAC injection line. This line is intended for the injection of the Pelletron accelerated beam into the LINAC post-accelerator, under construction. Presently a scattering chamber after the superbuncher system is installed, which will allow for pulsed beam measurements. A LYSO(Ce) with Silicon Photomultipliers (SiPM) scintillator array [12], insensitive to magnetic fields, is being mounted in this line together with plastic scintillators for gamma-particle coincidence measurements dedicated to the study of nuclear reaction mechanisms with stable weakly-bound beams, and which can also be used with the RIBRAS radioactive beam facility.

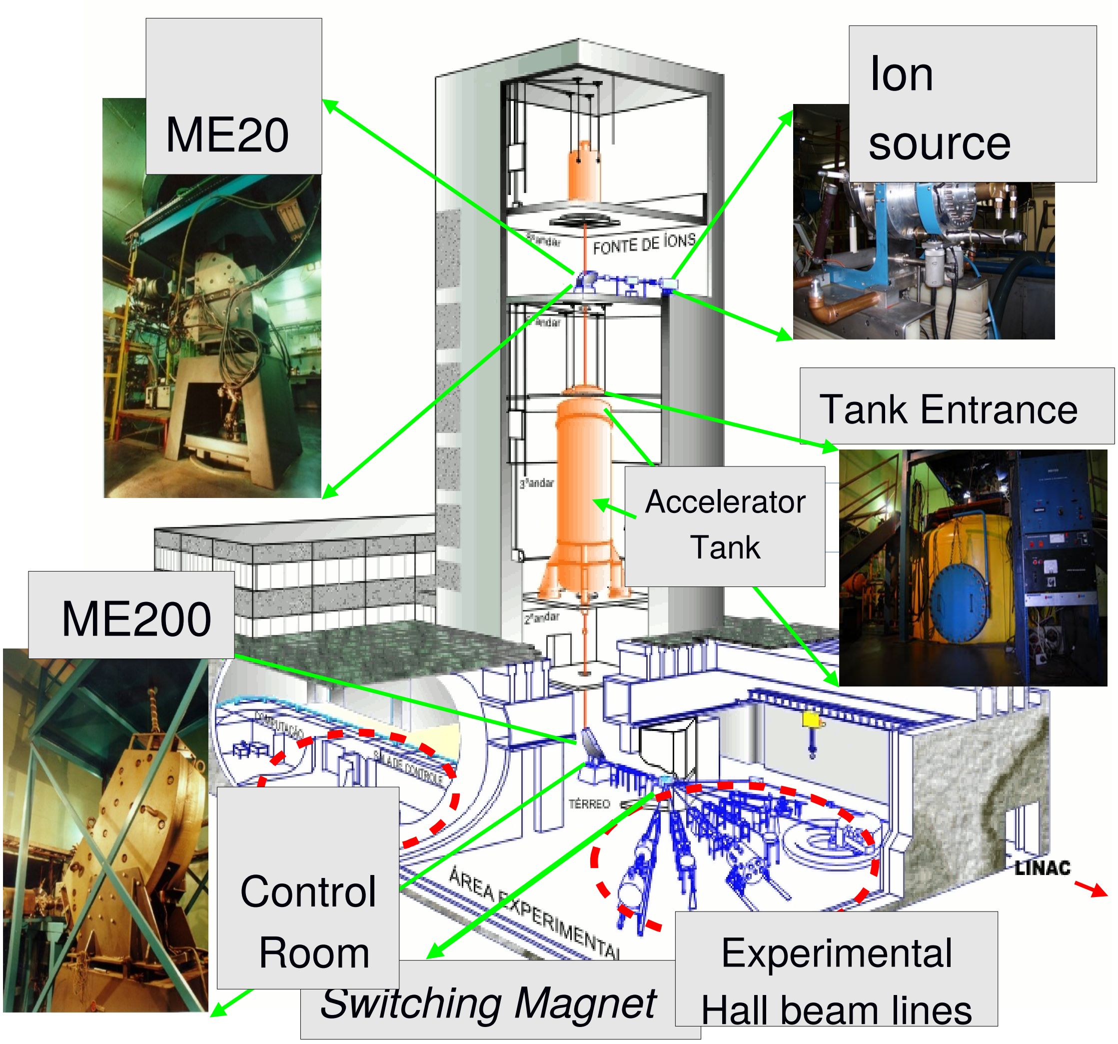

Figure 1. The 8UD Pelletron Tandem Facility of LAFN.

4. Statistical records

The simplest indicator of accelerator activity is the Pelletron chain hour counter. Figure 2 presents the number of hours of operation per year since 1980. The average value for this period is about 2300 hours per year. In spite of its age, there is no clear trend of reduction of activity of the Accelerator over the 40 year time span of the data, particularly considering the apparent recovery of the last two years.

The number MsC and PhD theses and of refereed articles published every year, with use of the LAFN equipment, is shown in Fig. 3. A change of pattern seems to have occurred around 1989, with a predominance of theses productions in the early periods, and a rather steady production of articles afterwards, with an average of 9 per year, with a standard deviation of 3. This rather stable production happened in spite of a reduction of more than 50% in University staff associated with experimental nuclear physics with accelerators which gradually occurred during the same period of time.

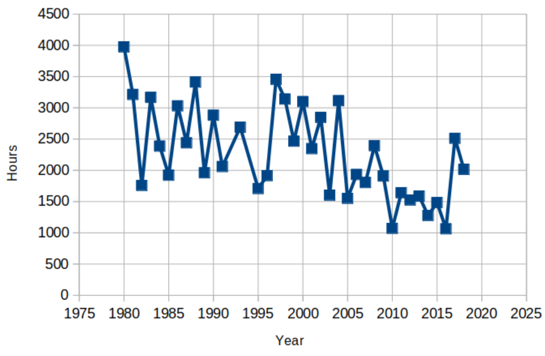

Figure 2. Hours of accelerator operation over the years since 1980, as measured by the Pellet chain motors hour counting.

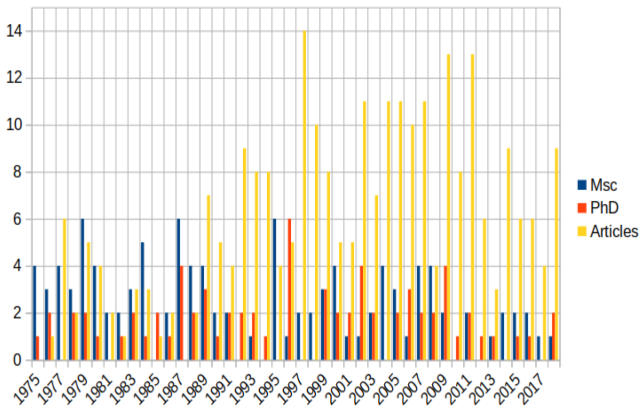

Figure 3. Production of graduate student theses (MSc and PhD) and refereed articles involving data taken with LAFN equipment, since 1975.

5. Recent research topics

In the last PAC meeting, held in October, 2018, 24 different projects were approved for a total use of 179 days of Accelerator beam with high priority, and 141 with low priority. The themes of these projects related to applied nuclear physics involve ion beam analysis of materials (by ERDA and PIXE techniques, -1 project each), irradiation with ion beams, such as of electronic devices (1 project), analysis and material modification (1 project), or development of instrumentation or experimental techniques (3 projects). Most of this research is important for aerospace technology and other engineering areas, and some for biology. The other projects are related to basic nuclear physics research, 10 of which with the use of radioactive beams (RIBRAS), and 7 with use of stable beams. Most of the basic nuclear physics research have great importance to astrophysics or to the general understanding of nuclear structure and reactions.

6. Final remarks

The LAFN has strategical importance for the field of low energy basic and applied nuclear physics in Brazil, and in Latin America to a large extent. Its structure, which allows for experiment proposals from external institutions from inside or outside Brazil, has motivated collaborations and helped to maintain an active production with use of the 8UD Pelletron Accelerator in its long lifetime, in spite of the funding instability which has accompanied its story. The recent association of the Laboratory to the INCT-FNA- "Instituto Nacional de Ciência e Tecnologia - Física Nuclear e Aplicações" - has helped with the basic maintenance of the equipment, and an indication of increase of activity has appeared in the last two years. There are perspectives of growth of the low energy nuclear physics field at an international level in face of the recent theoretical and computational advances, as well as the large investments in accelerator and detection systems, mostly involving radioactive beams [13]. It is generally recognized that small and mid-size facilities such as LAFN are important for their specific programs, for the development of instrumentation and formation of the new generation of qualified researchers. It is hoped that the scientific community and society in general can recognize the importance of maintaining and improving such a structure in order to keep up with the challenges and discoveries that lie ahead in the development of nuclear science.

Acknowledgments

The technical staff of the Laboratory is greatly acknowledged for their dedication, as well as the collaboration of all the researchers which have contributed either for the organization or the performance and analysis of the experiments. Support from various Brazilian agencies over the years is also acknowledged, such as CNPq, FINEP, FAPESP, CAPES individually and lately, through the INCT-FNA.

References

[1] Sala O and Spalek G 1974 *Nucl. Instr. Meth.* **122** 213
[2] Fazzini N *et al.* 1985 *Nucl. Instr. Meth.* A **244** 20
[3] Lichtenthäler R *et al.* 2005 *Eur. Phys. J.* A **25** 733
[4] Lichtenthäler R *et al.* 2016 *Few-Body Syst.* **57** 15
[5] Alcántara-Núñez J A *et al.* 2013 *Nucl. Inst. Meth.* A **497** 429
[6] Zagatto V A B *et al.* 2014 *Nucl. Inst. Meth.* A **749** 19
[7] Spencer J E and Enge H A 1967 *Nucl. Instr. Meth.* **49** 81
[8] Zhang X X *et al.* 2015 *J. Phys.: Conf. Ser.* **630** 012025
[9] Gasques L R et al. 2018 *Phys. Rev.* C **97** 034629
[10] Alvarez M A G, *et al.* 2018 *Phys. Rev.* C **98** 024621
[11] Medina N H *et al.* 2016 *J. of Nucl. Phys., Material Science, Radiation and Applications* **4** 13
[12] Oliveira J R B *et al.* 2018 *J. Phys.: Conf. Ser.* **1056** 012040
[13] NuPECC Long Range Plan 2017 (http://www.nupecc.org/pub/lrp17/lrp2017.pdf)

IOP Conf. Series: Journal of Physics: Conf. Series **1291** (2019) 012004 doi:10.1088/1742-6596/1291/1/012004

Recent results from RIBRAS (Radioactive Ion Beams in Brasil)

R Lichtenthäler[a], A Lépine-Szily[a], V Guimarães[a], S Appannababu[b], O C B Santos[a], U Umbelino[a], A Serra[a], K C C Pires[a], A L de Lara[a], E O N Zevallos[a], V Scarduelli[a], M Assunção[c], J Alcántara-Núñez[a].

[a]Instituto de Física, Universidade de São Paulo, 05508-090, São Paulo, Brazil.
[b] Department of Nuclear Physics, Andhra University, Visakhapatnam, India - 530 003.
[c]Departamento de Física, Universidade Federal de São Paulo -UNIFESP-, CEP 09913-030, Diadema Brazil.

E-mail: `rubens@if.usp.br`

Abstract. An overview of the experiments performed at RIBRAS over the last year is presented. Elastic scattering and breakup reactions induced by light exotic projectiles on different targets have been measured and some results are presented here for the ^{120}Sn(^{6}He,α) reaction. Resonant scattering experiments have been performed with ^{10}Be and ^{12}C secondary beams on a CH$_2$ thick target and the well known ^{12}C+p resonance was identified. A gamma-particle experiment using a new system of LYSO scintillators to detect gammas was done.

1. Introduction

Light nuclei far from the line of stability usually present a cluster like structure formed by a core surrounded by one or more weakly bound nucleons. Several examples, such as ^{6}He(α+2n), ^{11}Li(^{9}Li+2n), ^{11}Be(^{10}Be+n), ^{14}Be(^{12}Be+2n) and others have been found mainly in the neutron rich side of the nuclide chart. Owing to their small breakup energies and the low angular momentum of the valence neutrons, their wave functions extend to large distances from the core, forming a kind of neutron halo [1]. As a result, reactions such as projectile breakup and neutron transfer may be strongly favored in the interaction between these projectiles and different targets, which enhances their total reaction cross sections [2–11].

RIBRAS (Radioactive Ion Beams in Brasil) system is capable to produce low energy secondary beams of some of these light exotic nuclei [12–14].

Here we present results for the ^{120}Sn(^{6}He,α) reaction as well as several other scattering and resonant scattering experiments performed over the last year. A new setup for gamma-particle measurements using LYSO cristals was tested.

2. RIBRAS system

The RIBRAS (Radioactive Ion Beams in Brasil) consists of two superconducting solenoids in line [12–14]. A scheme of the RIBRAS setup is shown in Fig. 1. The secondary beams of ^{6}He, ^{8}B, ^{8}Li, ^{7}Be, ^{12}B and others are selected in-flight by the double solenoid system. The primary beams of the 8UD-Pelletron accelerator impinge on production targets such as ^{9}Be, LiF, ^{3}He. Nucleon transfer and fusion-evaporation reactions produce the secondary beams with intensities ranging from 10^4 to 10^6 pps for primary beam intensities around $300 - 500$ enA. The large acceptance of the first solenoid (30 msr) allows to collect most of the secondary particles produced at forward angles which partially compensates the low production cross sections due to the low primary beam energies.

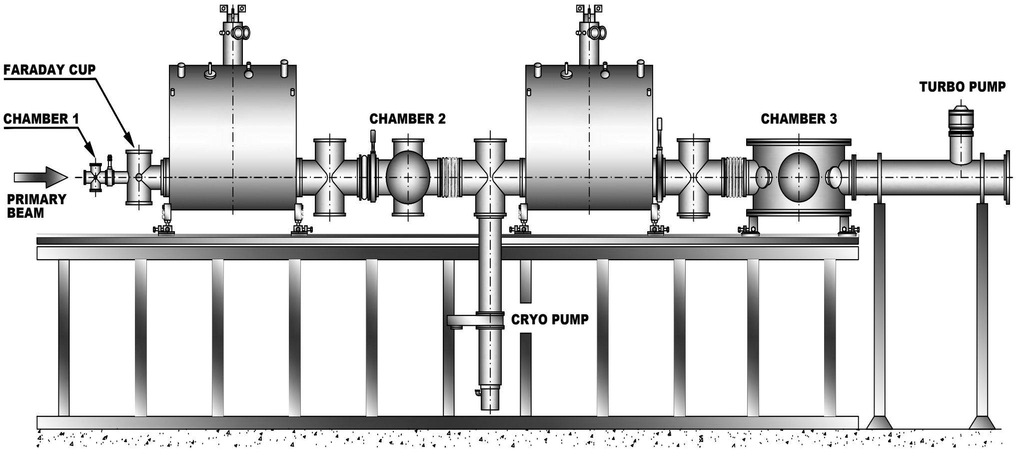

Figure 1. Scheme of RIBRAS.

The secondary particles from the primary target are selected by the first solenoid and focused in the scattering chamber 2 located just after the first solenoid. The secondary beam at this position is contaminated with p,d,t,α and degraded primary beam particles. A degrader foil can be placed in the scattering chamber 2 in order to provide differential energy loss and subsequent purification of the secondary beam by the second solenoid. In this way, a secondary beam with purity better than 92% can be achieved in the secondary scattering chamber 3.

The secondary beam production rates are maximized in the beginning of the experiment by varying the currents of the solenoids and monitoring the elastic scattering on a ^{197}Au target.

The measurements are usually carried out by using ΔE(25-50 μm)-E(1000 μm) silicon detector telescopes mounted on a rotating plate inside the secondary chambers 2 or 3, to perform angular distribution measurements.

Absolute cross sections are obtained by normalizing the elastic scattering data by using a Gold target, for which the scattering is pure Rutherford.

2.1. The ^{120}Sn(^{6}He,α) reaction.

Fig. 2 shows a bi-dimensional ΔE-E spectrum of the ^{120}Sn(^{6}He,α) reaction at E_{lab} = 24.5 MeV in scattering chamber 2.

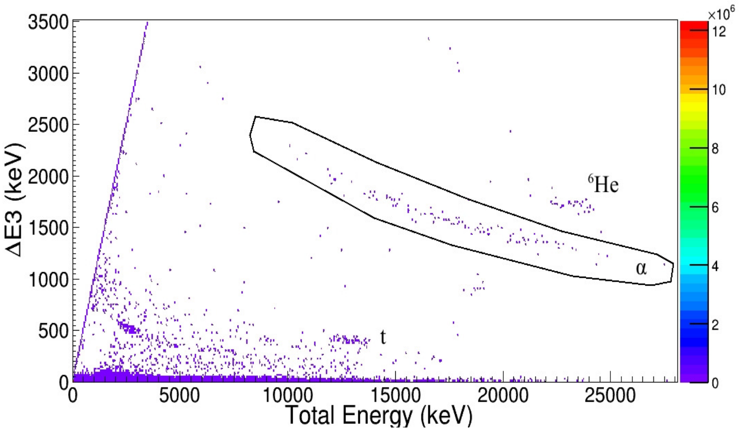

Figure 2. ΔE-E_{total} spectrum for the reaction ^{6}He + ^{120}Sn at $E_{^6He}$ = 24.5 MeV ($\theta_{lab} = 60^0$) [15].

The ^{6}He beam is produced by the ^{9}Be(^{7}Li,^{6}He) reaction and scattered on a ^{120}Sn target placed in the center of chamber 2.

We can clearly see that the elastically scattered ^{6}He peak is well separated from the α-particles. A broad α-particles energy distribution lie around and below the elastic peak energy. These α-particles are produced in the ^{6}He +^{120}Sn collision and are not seen in the runs with Gold target. One can also observe in Fig. 2 the light particles tritons, deuterons and protons well separated from the α.

In Fig. 3 we show the energy distribution corresponding to the projection of the α-cut of Fig.2. One can also see that the α distribution has a centroid located around 18 MeV, above the expected energy for a pure breakup at $\frac{2}{3}E_{6He}$ with E_{6He}=24.5 MeV, which would be around 16.3 MeV.

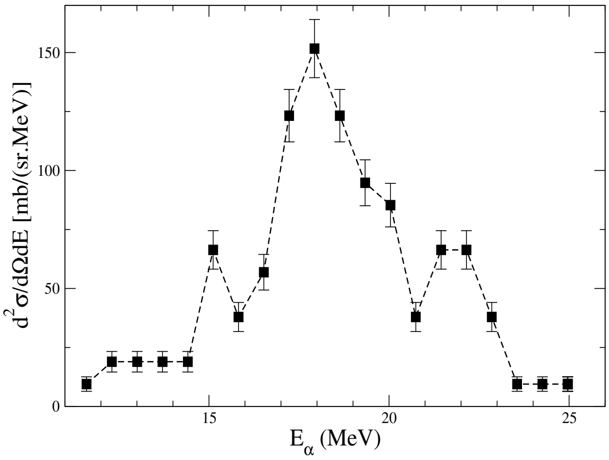

Figure 3. Energy distribution of the α-particles emitted from the ^{120}Sn(^{6}He,α)X reaction at 24.5 MeV ($\theta_{lab} = 60^0$).

α-particle energy distributions were measured at eight different bombarding energies from 17.4 MeV up to 24.5 MeV, the Coulomb barrier being around 13 MeV. An analysis as a function of the Q-value for the ^{120}Sn(^{6}He,α)^{122}Sn* reaction was performed. The $E_\alpha \rightarrow Q_\alpha$ transformation was performed by considering the two-body kinematics of the 2n-transfer reaction and adjusting the total reaction Q-value to reproduce the measured E_α energies. As a result, an interesting effect was observed in the behavior of the centroid of the Q-distributions with the bombarding energies. The centroid of the Q-value distribution decreases from slightly positive values ($Q_{reac} \approx$ 0.3 MeV) up to negative values around $Q_{reac} \approx -5.5 MeV$, as the incident energy increases from 17.4 to 24.5 MeV. Since $Q_{gs} = +14.01$ MeV is highly positive for this reaction, the residual nucleus ^{122}Sn must be formed in a highly excited state around $E_{exc} \approx 14$ MeV and above. At these high excitation energies, the 2n-transfer reaction populates states in the continuum of ^{122}Sn, well above the one-neutron emission threshold at $E_{exc} = 8.81$ MeV. More details of this analysis can be found in Ref. [15].

3. Elastic scattering measurements.

Several elastic scattering experiments have been performed in RIBRAS over the last year which will be described below. These experiments have been performed in scattering chamber 2 using only the first solenoid. Most of these experimental data is under analysis and no results will be presented here. More details about the experiments and results can be found in the other contributions to this proceedings.

3.1. The ^{12}B + ^{58}Ni scattering

The elastic scattering ^{12}B + ^{58}Ni been measured at $E_{lab} = 30$ and 33 MeV, above the Coulomb barrier (V$_B \sim$ 24 MeV). The secondary beam has been produced by the ^{9}Be(^{11}B,^{12}B)^{8}Be transfer reaction using ^{12}B primary beam produced by the Pelletron accelerator at 37 and 40 MeV with intensities of 300 enA. The intensity of the ^{12}B secondary beam was of 2×10^{5} pps. The secondary target was a 2.1 mg/cm^{2} isotopically enriched ^{58}Ni foil. The detection system consisted of two E-ΔE telescopes of 1000 μ m and 25 μ m thickness and one 1000 μm single detector at backward angles. The detection solid angles ($\sim$ 16 msr) were defined by circular collimators placed in front of the detectors. More details can be found in one of the contributions (E. Zevallos) in this proceedings.

3.2. The ^{8}Li scattering on ^{9}Be, ^{58}Ni and ^{120}Sn targets.

The ^{8}Li scattering has been measured on the light ^{9}Be, intermediate mass ^{58}Ni and heavy ^{120}Sn targets. The ^{8}Li secondary beam was produced by the ^{9}Be(^{7}Li,^{8}Li)^{8}Be transfer reaction using the ^{7}Li beam produced by the 8UD-Pelletron accelerator. Four silicon E($1000\mu m$) -ΔE($25\mu m$) telescopes with areas of 150 mm^{2} were used as detection system. For the ^{9}Be target one angular distribution was measured at $E_{lab} = 23.7$ MeV. This corresponds to about 7 times the Coulomb barrier $V_B = 3.5$ MeV. For the ^{58}Ni targets four angular distributions were measured at 23.9 MeV, 26.1 MeV, 28.7 MeV, and 30.0 MeV laboratory energies, the Coulomb barrier being at $V_B = 13.1$ MeV [16]. Two angular distributions on ^{120}Sn were measured at $E_{lab} = 21.7$ and 26.8 MeV, the Coulomb barrier being at $V_B = 20.5$ MeV

3.3. The ^{10}Be + ^{9}Be scattering.

The ^{10}Be beam has been produced by the ^{9}Be(^{11}B,^{10}Be) transfer reaction with a ^{11}B primary beam of 34 MeV. In Fig.4 we show a spectrum of the secondary beam particles produced in the reaction ^{9}Be(^{11}B,^{10}Be) detected in the scattering chamber 2. An angular distribution for the ^{10}Be+^{9}Be reaction was measured at $E_{lab} = 21.7$ MeV.

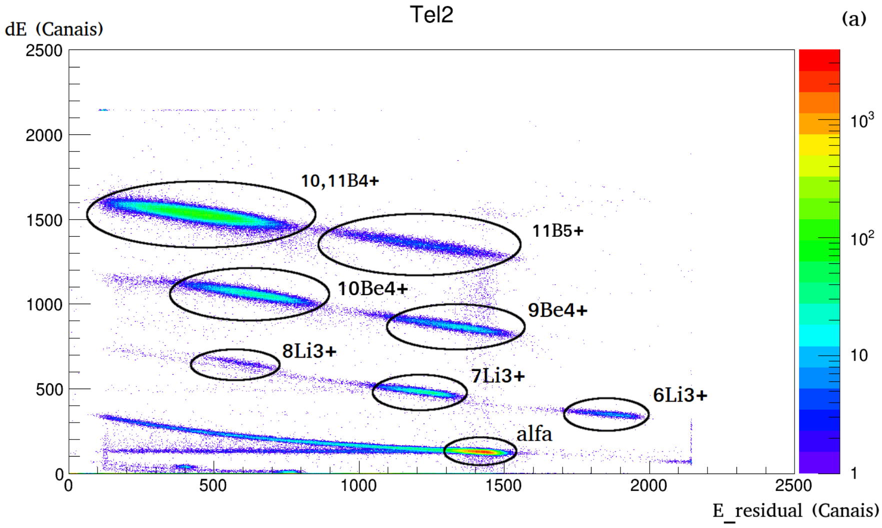

Figure 4. E-ΔE spectrum of the cocktail beam in the ^{9}Be(^{11}B,^{10}Be) production reaction.

4. Resonant scattering measurements

Measurements of resonant scattering of exotic beams such as ^{8}Li [17] and ^{6}He on CH_2 thick targets have been performed over the last year using the double solenoid system. In the thick target method one uses a CH_2 foil, thick enough to stop the projectile in the target. The recoil protons resulting from the interaction with the beam are detected at forward angles where silicon telescopes were mounted to identify the particles and measure their energy distributions. This technique allows the measurement of an excitation function and the identification of resonances in the p+projectile composed system. Over the last year, two resonant scattering experiments have been performed in RIBRAS, the ^{12}C+p and ^{10}Be+p, both using CH_2 solid targets (thick target method). The ^{12}C+p reaction was measured to identify a well known resonance [18] and use it for a precise energy calibration, see Fig. 5. In this case a primary ^{12}C beam scattered in the primary target foil was selected by the RIBRAS solenoids and used as the secondary beam.

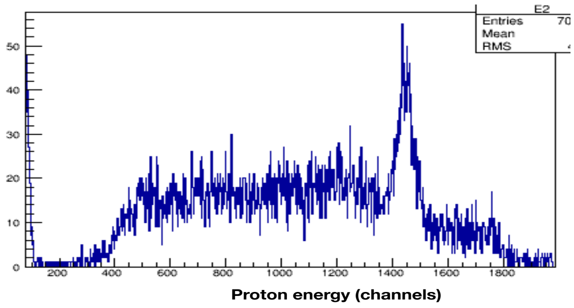

Figure 5. Proton spectrum from ^{12}C+p scattering measured at RIBRAS.

5. Gamma-particle coincidence measurements.

One of the difficulties in performing gamma measurements in RIBRAS comes from the residual magnetic field around the solenoid and inside the scattering chambers, which prevents the operation of photo-multipliers vacuum tubes based detectors. In addition to this, an intense neutron secondary beam comes from the RIBRAS primary target causing serious damage to germanium detectors. More recently, LYSO (Lutetium-yttrium oxyorthosilicate) scintillators are being used to detect gammas in association with silicon diodes which are not sensitive to magnetic fields. We purchased LYSO crystals and four gamma detectors were mounted by J.R.B. de Oliveira group (see contribution to this proceedings). A ^{8}Li+^{120}Sn test experiment was performed in RIBRAS using these LYSO detectors. The particles were detected in four silicon telescopes fixed at forward angles and the gammas were detected in the LYSO crystals placed around the target. A TDC peak was measured from the gammas in coincidence with light particles, which gave cross sections of the order of the expected for fusion reactions.

We expect this setup to be enlarged with more LYSO detectors and plan to use it in the future for fusion and other reactions using the RIBRAS facility.

6. Summary

A summary of the experiments performed in RIBRAS over the last year is presented. Elastic scattering and reactions involving light exotic projectiles such as ^{6}He, ^{8}Li, ^{10}Be, ^{12}B on several targets are reported. A new setup for gamma measurements using LYSO crystals is described.

7. Acknowledgments

This work has been supported by FAPESP (Brazil), contracts nos. 2013/22100-7 and 2014/19666-1. RL acknowledges CNPq (Conselho Nacional de Desenvolvimento Científico e Tecnológico) grant no. 305836/2014-5.

8. References

[1] Tanihata I, Hamagaki H, Hashimoto O, Shida Y, Yoshikawa N, Sugimoto K, Yamakawa O, Kobayashi T and Takahashi N 1985 *Phys. Rev. Lett.* **55** 2676
[2] de Faria P N et al. 2010 *Phys. Rev.* C **81** 044605
[3] de Faria P N et. al. 2010 *Phys. Rev.* C **82** 034602
[4] Pires K C et al. 2011 *Phys. Rev.* C **83** 064603
[5] Pires K C C et al. 2014 *Phys. Rev.* C **90** 027605
[6] Pires K C , Appannababu S, Lichtenthäler R, and Santos O C B 2018 *Phys. Rev.* C**98** 014614
[7] Morcelle V et al. 2017 *Phys. Rev. C* **95** 014615
[8] Morcelle V et al. 2014 *Phys. Lett.* B **732** 228
[9] Morcelle V et al. 2014 *Phys. Rev.* C **89** 044611
[10] Mohr P, Galaviz D, Fülöp Zs, Gyürky Gy, Kiss G G and Somorjai E 2010 *Phys. Rev.* C **82** 047601
[11] Mohr P et al. 2010 *Phys. Rev.* C **82** 044606
[12] Lichtenthäler R et al. 2016 *Few-Body Systems* **57** 157
[13] Lépine-Szily A, Lichtenthäler R, Guimarães V 2014 *Eur. Phys. J.* A **50** 128
[14] Lichtenthäler R, Lépine-Szily A, Guimarães 2005 *Eur. Phys. J.* A **25** 733
[15] Appannababu S et al. 2019 *Phys. Rev.* C **99** 014601
[16] Freitas A S , Marques L, Zhang X X , Luzio M A , Guillaumon P, Pampa Condori R and Lichtenthäler R 2016 *Braz. Jou. Phys.* **46** 120
[17] E. Leistenschneider et al. 2018 *Phys. Rev.* C **98** 064601
[18] Jingai Liu, Tianbao Xie and Fischbeck H J 1993 *Nucl. Instrum. and Methods in Phys. Res.* B **79** 468-470

XLI Brazilian Meeting on Nuclear Physics (RTFNB) IOP Publishing
IOP Conf. Series: Journal of Physics: Conf. Series **1291** (2019) 012005 doi:10.1088/1742-6596/1291/1/012005

Ab initio calculations of p-shell nuclei up to N^{2}LO in chiral Effective Field Theory

Pieter Maris
Dept. of Physics and Astronomy, Iowa State University, Ames, IA 50011, USA
E-mail: `pmaris@iastate.edu`

Abstract. Nuclear structure and reaction theory are undergoing a major renaissance with advances in many-body methods, realistic interactions with greatly improved links to Quantum Chromodynamics, the advent of high performance computing, and improved computational algorithms. State-of-the-art two- and three-nucleon interactions obtained from chiral Effective Field Theory provide a theoretical foundation for nuclear theory with controlled approximations. With highly efficient numerical codes, tuned to the current generation of supercomputers, we can perform ab-initio nuclear structure calculations for a range of nuclei to a remarkable level of numerical accuracy, with quantifiable numerical uncertainties. Here we present an overview of recent results for No-Core Configuration Interaction calculations of p-shell nuclei using these chiral interactions up to next-to-next-to-leading order, including three-body forces. We show the dependence of the ground state energies on the chiral order; we also present excitation spectra for selected nuclei and compare the results with experimental data.

1. Ab Initio Nuclear Structure and High Performance Computing

A microscopic theory for the structure and reactions of atomic nuclei poses formidable challenges for high-performance computing. A nucleus with Z protons and N neutrons is a self-bound quantum many-body system with $A = N + Z$ strongly interacting nucleons. The interactions feature both attractive and repulsive contributions along with significant spin and angular momentum dependence. Furthermore there are both short-range and long-range terms in the interaction, and in addition to nucleon-nucleon (NN) interactions, one also needs suitable three-nucleon forces (3NFs), and possibly even higher many-body interactions. The corresponding Hamiltonian can be written as

$$\hat{\mathbf{H}} \;=\; \sum_{i<j} \frac{(\vec{p}_i - \vec{p}_j)^2}{2\,m\,A} + \sum_{i<j} V_{ij} + \sum_{i<j<k} V_{ijk} + \ldots \tag{1}$$

where m is the nucleon mass, which we take to be equal for protons and neutrons. The nuclear wave functions are the solutions of the many-body Schrödinger equation

$$\hat{\mathbf{H}}\,\Psi(\vec{r}_1, \ldots, \vec{r}_A) \;=\; E\,\Psi(\vec{r}_1, \ldots, \vec{r}_A) \tag{2}$$

at discrete energy levels E.

In No-Core Configuration Interaction (NCCI) nuclear structure calculations [1] the wave function Ψ of a nucleus consisting of A nucleons is expanded in an A-body basis of Slater determinants Φ_k of single-particle wave functions $\phi_{nljm}(\vec{r})$. Here, n is the radial quantum number, l the orbital motion, j the total spin from orbital motion coupled to the intrinsic nucleon spin, and m the spin-projection. The Hamiltonian $\hat{\mathbf{H}}$ is also expressed in this basis and thus the many-body Schrödinger equation becomes a matrix eigenvalue problem; for $A > 4$ and NN plus 3N interactions, this matrix is sparse. The eigenvalues of this matrix are approximations to the energy levels, to be compared to the experimental binding energies and spectra, and the corresponding eigenvectors to the nuclear wave functions. Although the wave functions themselves are not observable, they can be employed to evaluate additional physical observables.

Conventionally, one uses a harmonic oscillator (HO) basis with energy parameter $\hbar\omega$ for the single-particle wave functions. A convenient and efficient truncation of the complete (infinite-dimensional) basis is a truncation on the total number of HO quanta: the basis is limited to many-body basis states with $\sum_A N_i \leq N_0 + N_{\max}$, with N_0 the minimal number of quanta for that nucleus and $N_{\max}$ the truncation parameter. (Even (odd) values of $N_{\max}$ provide results for natural (unnatural) parity.) Numerical convergence toward the exact results for a given Hamiltonian is obtained with increasing $N_{\max}$, and is marked by approximate $N_{\max}$ and $\hbar\omega$ independence. In practice we use extrapolations to estimate the binding energy in the complete (but infinite-dimensional) space [2, 3, 4, 5, 6], based on a series of calculations in finite bases.

The rate of convergence depends both on the nucleus and on the interaction. For realistic interactions, the dimension of the matrix needed to reach a sufficient level of convergence is in the billions, and the number of nonzero matrix elements is in the tens of trillions, which saturates available storage on current computing facilities. All NCCI calculations presented here were performed on the Cray XC30 Edison and Cray XC40 Cori at NERSC and the IBM BG/Q Mira at Argonne National Laboratory, using the code MFDn [7, 8].

2. Nuclear Interactions from Chiral Effective Field Theory

Chiral Effective Field Theory (χEFT) allows us to derive nuclear interactions (and the corresponding electroweak current operators) in a systematic way [9, 10, 11]. The chiral expansion is by no means unique: e.g. different choices for the functional form of the regulator and/or different choices for the degrees of freedom lead to different χEFT interactions. With the LENPIC collaboration [12, 13, 14] we use the same χEFT interactions for ab initio calculations ranging from nucleon-nucleon and nucleon-deuteron scattering to the structure of medium-mass nuclei. Specifically, here we use the semilocal coordinate-space regularized chiral potentials of Refs. [15, 16] to calculate the binding energies and spectra of p-shell nuclei. The leading order (LO) and next-to-leading order (NLO) contributions are given by NN-only potentials while 3NFs appear first at next-to-next-to-leading order (N^{2}LO) in the chiral expansion [10, 11]. Four-nucleon forces are even more suppressed and start contributing at N^{3}LO. The chiral power counting thus provides a natural explanation of the observed hierarchy of nuclear forces.

The Low-Energy Constants (LECs) in the NN-only potentials of Refs. [15, 16] have been fitted to nucleon-nucleon scattering, without any input from nuclei with $A > 2$. The 3NFs at N^{2}LO involve two LECs which govern the strength of the one-pion-exchange-contact term and purely contact 3NF contributions. Conventionally, these LECs are expressed in terms of two dimensionless parameters c_D and c_E. Obviously, these LECs cannot be fixed from nucleon-nucleon scattering; they have to be fitted to select 3-body (or higher A-body) observables. We follow the commonly adopted practice [17, 18, 19, 20] and use the ^{3}H binding energy as one of the observables; this gives us a correlation between c_D and c_E.

A wide range of observables has been considered in the literature to constrain the remaining LEC. In Ref. [14] different ways to fix this LEC in the 3-nucleon sector were explored, and it was shown that it can be reliably determined from the minimum in the differential cross section in elastic nucleon-deuteron scattering at intermediate energies. This allows us to make parameter-free calculations for $A \geq 4$ nuclei. In these proceedings we present an overview of the ground state energies for all stable p-shell nuclei (excluding mirror nuclei), as well as excitation spectra for selected nuclei up to $A = 12$, all obtained with the same semilocal regulator $R = 1.0$ fm and the same LECs. Specifically, the LECs values for the 3NFs at N^{2}LO are $c_D = 7.2$ and $c_E = -0.671$, as determined in Ref. [14]. Application of these interactions to nucleon-deuteron scattering can be found in Refs. [12, 13] for NN-only potentials, along with selected properties of light- and medium-mass nuclei, and in Ref. [14] including the 3NFs at N^{2}LO.

3. Ground State Energies for p-shell Nuclei

Here we present our results for the ground state energies of the stable p-shell nuclei, excluding mirror nuclei, all obtained with the same semilocal chiral interactions up to N^{2}LO. In Fig. 1 we show the ground state ($J^P = 1^+$) energy of ^{6}Li as function of the HO basis parameter $\hbar\omega$ for a range of $N_{\rm max}$ values. With NN-only potentials, we can perform calculations up to $N_{\rm max} = 18$ for $A = 6$ nuclei. This is sufficient to achieve a reasonable level of convergence, as can be seen from the left three panels of Fig. 1. With 3NFs however, we are limited to significantly smaller bases, and in order to improve the numerical convergence with basis size we therefore first perform a Similarity Renormalization Group (SRG) transformation [21, 22, 23] on the Hamiltonian. The right-most panel of Fig. 1 shows results for the ground state energy of ^{6}Li at N^{2}LO including 3NFs at a very modest SRG flow parameter $\alpha = 0.02$ fm^4 (note that $\alpha = 0$ correspond to the original Hamiltonian, without SRG), for calculations up to $N_{\rm max} = 12$. Indeed, the convergence with increasing $N_{\rm max}$ is significantly improved with this SRG-evolved interaction compared to the bare NN-only interactions at NLO and N^{2}LO. At $N_{\rm max} = 12$ the level of convergence is already comparable to that of the bare NLO and N^{2}LO potentials at $N_{\rm max} = 16$. Also note that the variational minimum in $\hbar\omega$ shifts to lower values due to the SRG evolution.

In Fig. 2 we show the ground state energies of ^{7}Li (left, $J^P = \frac{3}{2}^-$) and ^{10}B (right, $J^P = 3^+$) as function of $N_{\rm max}$ at fixed $\hbar\omega$ values close to the variational minimum with the N^{2}LO interaction with and without explicit 3NFs. Based on these results in finite bases, we can use extrapolations to the complete (infinite-dimensional) basis. Here we use a three parameter fit at fixed $\hbar\omega$ at or just above the variational minimum

$$E(N_{\rm max}) \approx E_\infty + a \exp\left(-bN_{\rm max}\right), \tag{3}$$

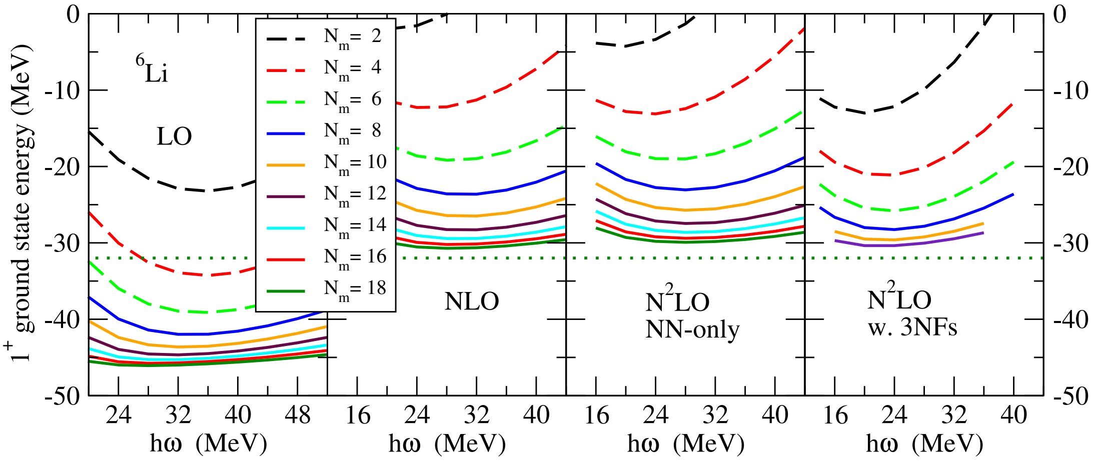

Figure 1. (Color online) Calculated ground state energy of ^{6}Li using chiral LO, NLO, and N^{2}LO interactions at $R = 1.0$ fm as function of the basis HO parameter $\hbar\omega$ for $N_{\rm max} = 2$ to 18 for NN-only potentials (left 3 panels) and at N^{2}LO w. 3NFs, SRG-evolved to $\alpha = 0.02$ fm^4 for $N_{\rm max} = 2$ to 12 (right-most panel). The dotted horizontal line is the experimental value.

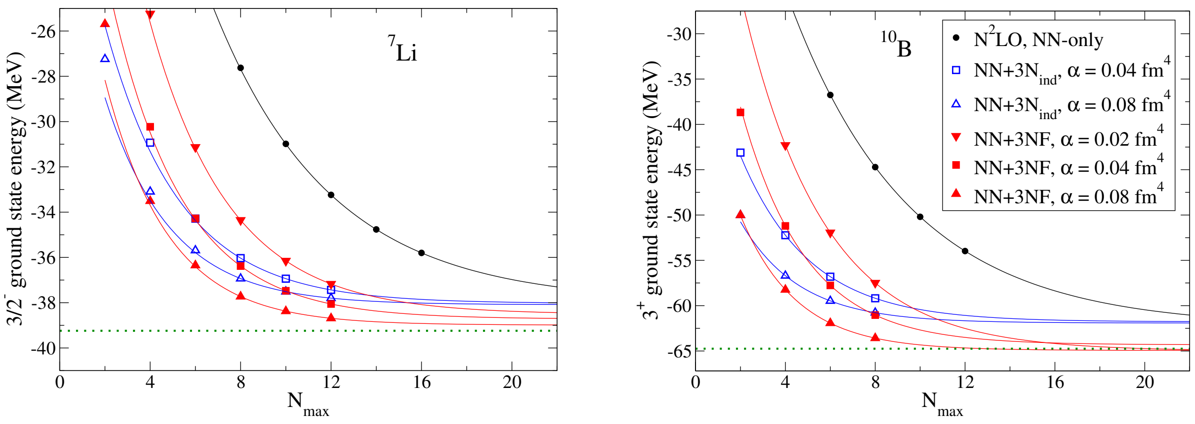

Figure 2. (Color online) Calculated ground state energies using chiral N^{2}LO interactions at $R = 1.0$ fm as function of $N_{\rm max}$ at the variational minimum in $\hbar\omega$ for ^{7}Li (left) and ^{10}B (right). The dotted horizontal line is the experimental value.

which seems to work well for a range of interactions and nuclei [2, 24, 25]. The lines in Fig. 2 correspond to the extrapolating function fitted to the three highest available $N_{\rm max}$ values.

Again, with the SRG-evolved interactions the ground state energies converge more rapidly with $N_{\rm max}$ than with the bare (black dots and curves) NN-only N^{2}LO interaction. However, as a consequence of the SRG transformation, our results do depend on the SRG flow parameter α, because we do not incorporate any induced interactions beyond 3NFs. Without explicit 3NFs, this dependence seems to be negligible, and typically less than the extrapolation uncertainty – the bare NN-only N^{2}LO interaction and the two SRG-evolved interaction with induced 3NFs extrapolate to approximately the same value. On the other hand, with explicit 3NFs there is a weak but noticeable dependence on the SRG parameter α, as can be seen by the spread of the red extrapolation curves in Fig. 2. This α dependence is due to induced 4-body (and higher-body) interactions which we have neglected.

In Table 1 we summarize our results up to N^{2}LO for the ground state energies of stable p-shell nuclei, excluding mirror nuclei, extrapolated to the complete basis. Our estimate of the extrapolation uncertainty is based on the difference with smaller $N_{\rm max}$ extrapolations, as well as the basis $\hbar\omega$ dependence over an 8 to 12 MeV span in $\hbar\omega$ values around the variational minimum, adjusted to be at least 20% of the difference with the variational minimum [13].

With NN-only potentials we use the bare interaction up to $A = 10$, for which we can perform calculation at $N_{\rm max} = 12$ or higher. For select nuclei with $11 \leq A \leq 16$ we use the SRG-evolved interaction at $\alpha = 0.04$ fm^4 with induced 3NFs for NN-only potentials up to $N_{\rm max} = 8$. At N^{2}LO with explicit 3NFs we present results with SRG-evolved interactions at both $\alpha = 0.04$ fm^4 and $\alpha = 0.08$ fm^4. As expected, the calculations at $\alpha = 0.08$ fm^4 are betted converged, and have therefore a smaller extrapolation uncertainty than those at $\alpha = 0.04$ fm^4. The anticipated α dependence appears to be of the same order of magnitude as the extrapolation uncertainty.

Generally, the agreement with the experimental binding energies improves as one goes from LO to NLO to N^{2}LO. At LO all p-shell nuclei are significantly overbound, but at N^{2}LO the binding energies of nuclei up to $A = 12$ are within few percent of the experimental values. As A increases beyond $A = 12$, the nuclei become more and more overbound – ^{12}C is overbound by about 3% whereas ^{16}O is overbound by about 13%. The overbinding of ^{16}O is significantly larger than the estimated chiral truncation uncertainty [13], even with the inclusion of the explicit 3NFs [14], and it is as of yet unclear what the origin of this overbinding is.

At NLO and higher, we obtain the correct spin and parity for the ground states of most p-shell

Table 1. Ground state energies of stable $A = 4$ to 16 nuclei with χEFT interactions up to N^{2}LO using $R = 1.0$ fm [13, 14]. The uncertainty estimate is only the extrapolation uncertainty in the many-body calculation, and does not include the chiral truncation error, nor uncertainties in the LECs. Entries with an asterix * indicate excited states for nuclei where the calculated and experimental ground states have different J^P. Experimental values are extracted from Ref. [26].

Nucleus		LO	NLO	N^{2}LO	N^{2}LO including 3NFs		
	J^P	NN-only	NN-only	NN-only	$\alpha = 0.04$ fm^4	$\alpha = 0.08$ fm^4	expt.
^{4}He	0^+	$-45.453(6)$	$-28.533(4)$	$-28.11(1)$	$-28.202(5)$	$-28.298(2)$	-28.296
^{6}He	0^+	$-43.2(2)$	$-28.7(2)$	$-27.9(2)$	$-28.55(15)$	$-28.79(8)$	-29.27
^{6}Li	1^+	$-46.7(1)$	$-31.6(2)$	$-31.0(2)$	$-31.49(16)$	$-31.72(6)$	-31.99
^{7}Li	$\frac{3}{2}^-$	$-57.1(2)^*$	$-38.7(3)$	$-38.0(4)$	$-38.72(16)$	$-38.99(6)$	-39.24
^{8}He	0^+	$-39.8(6)$	$-29.7(5)$	$-27.8(6)$	$-29.5(3)$	$-29.9(2)$	-31.41
^{8}Li	2^+	$-55.7(5)$	$-40.3(7)$	$-39.0(8)$	$-40.4(4)$	$-40.7(2)$	-41.28
^{8}Be	0^+	$-87.7(4)$	$-56.0(7)$	$-55.4(9)$	$-55.6(5)$	$-56.1(3)$	-56.50
^{9}Li	$\frac{3}{2}^-$	$-57.1(4)$	$-43.9(7)$	$-41.7(8)$	$-43.9(4)$	$-44.0(2)$	-45.34
^{9}Be	$\frac{3}{2}^-$	$-84.7(7)$	$-58.0(1.4)$	$-56.4(1.5)$	$-57.5(5)$	$-58.0(3)$	-58.16
^{10}Be	0^+	$-92.2(8)$	$-65.2(1.5)$	$-62.8(1.7)$	$-64.1(9)$	$-64.9(5)$	-64.98
^{10}B	3^+	$-88.1(1.2)^*$	$-64.6(1.5)^*$	$-62.3(1.7)^*$	$-64.3(8)$	$-64.9(5)$	-64.75
^{10}B	1^+	$-93.9(8)$	$-64.9(1.8)$	$-63.1(1.9)$	$-63.1(1.0)^*$	$-64.1(8)^*$	-64.03^*
		SRG evolved to $\alpha = 0.04$ fm^4			$\alpha = 0.04$ fm^4	$\alpha = 0.08$ fm^4	
^{11}Be	$\frac{1}{2}^+$	—	—	—	$-64.7(1.3)^*$	$-65.4(8)^*$	-65.48
^{11}Be	$\frac{1}{2}^-$	—	—	—	$-65.8(1.2)$	$-65.7(8)$	-65.16^*
^{11}B	$\frac{3}{2}^-$	$-108.(1.)$	$-76.8(6)$	$-73.9(7)$	$-77.2(9)$	$-77.7(5)$	-76.21
^{12}Be	0^+	—	—	—	$-68.9(1.4)$	$-69.8(9)$	-68.65
^{12}B	1^+	$-111.(1.)^*$	$-82.6(8)$	$-78.6(8)$	$-81.9(9)^*$	$-82.5(5)^*$	-79.58
^{12}B	2^+	$-111.(1.)^*$	$-82.3(9)^*$	$-77.8(7)^*$	$-82.8(9)$	$-83.2(5)$	-78.63^*
^{12}C	0^+	$-139.(1.)$	$-95.5(7)$	$-92.7(6)$	$-94.7(1.0)$	$-95.5(5)$	-92.16
^{13}B	$\frac{3}{2}^-$	—	—	—	$-89.5(1.0)$	$-90.3(7)$	-84.45
^{13}C	$\frac{1}{2}^-$	—	—	—	$-104.7(1.0)$	$-104.4(4)$	-97.11
^{14}C	0^+	—	—	—	$-116.0(1.3)$	$-116.1(5)$	-105.28
^{14}N	1^+	—	—	—	$-117.3(1.3)$	$-117.4(4)$	-104.66
^{15}N	$\frac{1}{2}^-$	—	—	—	$-130.4(1.6)$	$-131.0(6)$	-115.49
^{16}O	0^+	$-223.2(4)$	$-152.(1.)$	$-146.(1.)$	$-144.(2.)$	$-145.2(8)$	-127.62

nuclei – the exceptions are ^{10}B, ^{11}Be, and ^{12}B, for which we include both the experimental and the calculate ground states in Table 1. For ^{10}B, the NN-only interactions produce a $J^P = 1^+$ ground state, whereas the experimental ground state has $J^P = 3^+$. With the consistent explicit 3NFs at N^{2}LO we are able to reproduce the experimental ground state for ^{10}B, in agreement with previous studies of ^{10}B with χEFT interactions [19, 25]. For ^{12}B the situation is the opposite: at NLO and N^{2}LO without the 3NFs we do find the correct ground state, $J^P = 1^+$, but adding the 3NFs to the N^{2}LO NN potential leads to a ground state with $J^P = 2^+$, and the $J^P = 1^+$ state becomes the first excited state, with an excitation energy of about 1 MeV. It remains to be seen whether or not this discrepancy gets resolved at higher order in the chiral expansion.

The situation in ^{11}Be is different: here we have a nucleus with *parity inversion*, that is, the ground state has the opposite parity of what one would expect based on the shell-model. In NCCI calculations the 'natural' and 'unnatural' parity states are expressed in bases with even or odd $N_{\rm max}$ values respectively. For ^{11}Be that means the negative parity states are calculated in bases with even $N_{\rm max}$ and the positive parity states states in bases with odd $N_{\rm max}$. We then perform an extrapolation to the complete basis for the lowest state with even $N_{\rm max}$ as well as for the lowest state with odd $N_{\rm max}$. This leads to the energies listed in Table 1 for the $\frac{1}{2}^+$ state (the experimental ground state) and for the the $\frac{1}{2}^-$ state (the lowest natural parity state). Although the latter has a lower energy in our calculations, the difference with that of the $\frac{1}{2}^+$ is less than the extrapolation uncertainty, and within their uncertainties, both energies agree with the experimental values. In order to reliably determine which of these two states is the ground state we should use more sophisticated calculational methods for this system and follow e.g. the approach discussed in Ref. [27] for ^{11}Be.

4. Excitation Spectra for p-shell Nuclei

In addition to the ground state energies, we also obtain the energy levels of excited states. The energy differences with the ground state generally converge significantly better than the actually binding energies of excited states, at least for states of the same parity. In Fig. 3 we show the low-lying spectra of ^{6}Li and ^{7}Li as function of the HO basis parameter $\hbar\omega$ for several of $N_{\rm max}$ values. Again, with NN-only potentials we achieve a reasonable level of convergence, in particular for narrow excited states like the 3^+ state in ^{6}Li and the $\frac{1}{2}^-$ and $\frac{7}{2}^-$ states in ^{7}Li. The persistent increase of the excitation energies of with increasing $\hbar\omega$ for the higher excited states suggest that these are (significantly) broader, and therefore poorly converging in a HO basis. Indeed, the two 2^+ states in ^{6}Li are broad; and although the 0^+ in ^{6}Li (the analog state of ^{6}He) is narrow, in our calculations with NN-only interactions up to N^{2}LO, ^{6}He is not or barely bound, see Table 1; hence, with these interactions this state will be broad and poorly converging.

At LO the spectra do not agree with experiment – most excitation energies are too large, and often the order of the states is incorrect: e.g. in ^{7}Li the ground state, $\frac{3}{2}^-$, and the first excited state, $\frac{1}{2}^-$, are essentially degenerate. Indeed, the LO potential is not very realistic – not only is it significantly too attractive (it overbinds all p-shell nuclei by up to a factor of two), it is also missing e.g. essential spin-orbit couplings. However, starting at NLO the spectra tend to be in qualitative agreement with data. At N^{2}LO with explicit 3NFs we use SRG evolution to improve convergence of the NCCI calculations. The dependence of the excitation energies on the SRG parameter α is negligible, much smaller than the $\hbar\omega$ dependence, as can be seen in the the right-most panels of Fig. 3. Generally, inclusion of the 3NFs improves agreement with experiment (see also Fig. 9 of Ref. [14]). In particular, we see in Fig. 3 that the excitation energy of the 3^+ state of ^{6}Li moves slightly closer to experiment; and in ^{7}Li the $\frac{7}{2}^-$ also moves slightly closer to experiment. Furthermore the second $\frac{5}{2}^-$ state becomes much better converged while the first $\frac{5}{2}^-$ exhibits a persistent $\hbar\omega$ dependence, suggesting that the first $\frac{5}{2}^-$ is broad, and the second narrow, both in agreement with data.

In Fig. 4 we show the low-lying positive-parity spectra for ^{8}Li, ^{8}Be, and ^{10}Be at N^{2}LO with explicit 3NFs, SRG evolved to $\alpha = 0.04$ fm^4 (solid) and 0.08 fm^4 (dashed). Again, the SRG dependence is negligible compared to the $\hbar\omega$ dependence, except for the high-lying pairs of 2^+, 1^+, and 3^+ states in ^{8}Be; given this SRG dependence, the spectrum of ^{8}Be is in quite reasonable agreement with the data. For ^{8}Li we do find the known narrow 1^+, 3^+, and 4^+ states, as well as two poorly converged (i.e. broad) 1^+ states, all in reasanoble agreement with experiment; in addition we find one 0^+ state, as well as two 2^+ states, all poorly converged.

The first excited state in ^{10}Be, with $J^P = 2^+$, is quite well converged, and in excellent agreement with the experimental excitation energy. We also do find two additional 2^+ states among the lowest five states in qualitative agreement with data, but not as well converged. However, we do not find any low-lying 0^+ state in our calculations, in contrast to experiment; we will come back to this when discussing ^{12}C below. Furthermore, our calculations suggest that there is a 1^+ state between the second and third 2^+ excited state.

The low-lying spectra for ^{10}B up to N^{2}LO are shown in Fig. 5; in addition to the ground state 3^+, two low-lying 1^+ states, and a low-lying 2^+, there is also the 0^+ analog state of the ground state of ^{10}Be which is not shown. At LO the calculated spectrum does not look like the experimental spectrum at all: the lowest state is a 1^+ state, followed by three nearly degenerate states, with $J^P = 2^+$, 3^+, and 1^+, respectively, at excitation energies of about 6 MeV. At NLO and NN-only N^{2}LO the agreement with experiment is noticeably better, except for the ordering of the 3^+ ground state and the lowest 1^+ state. This is a known issue, and the general consensus

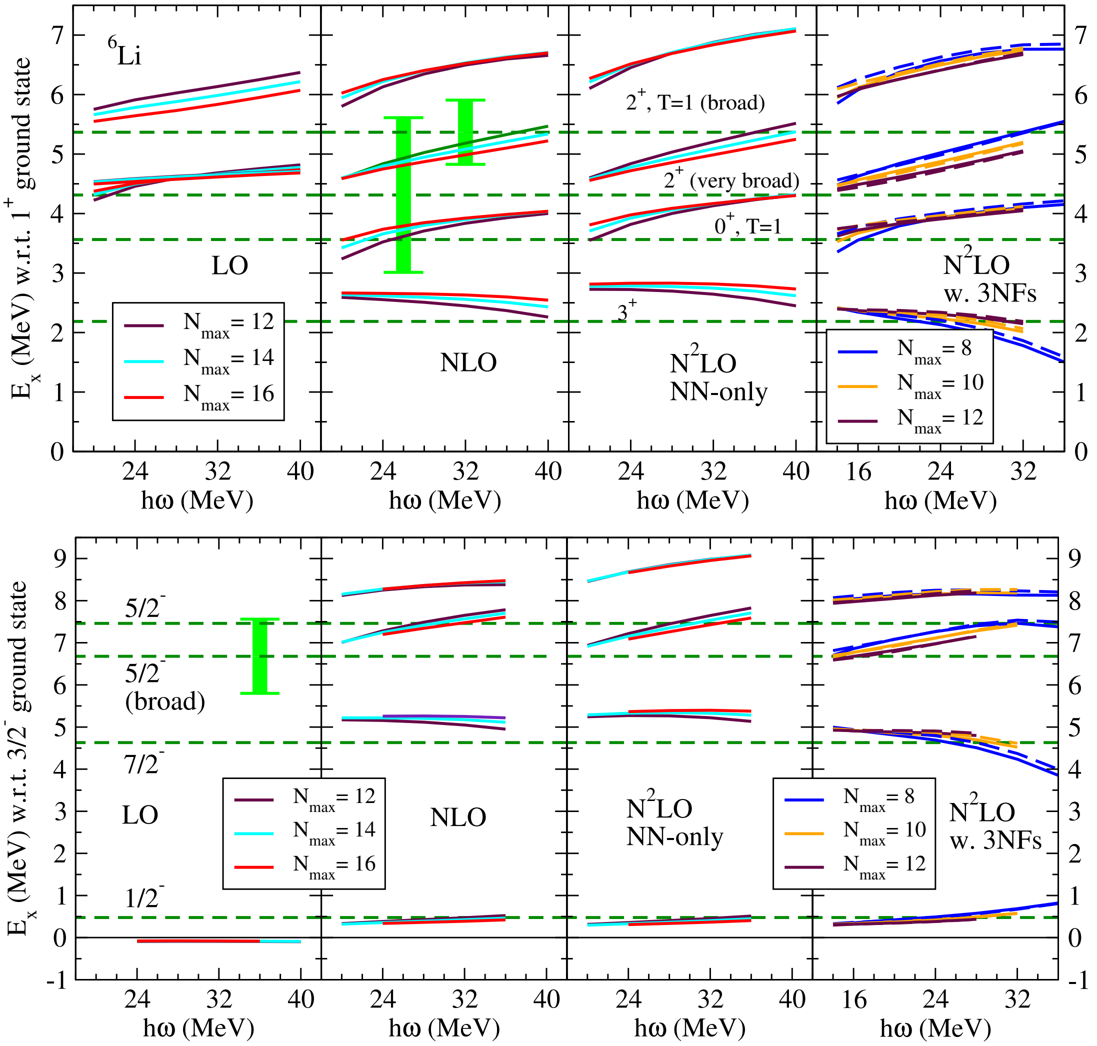

Figure 3. (Color online) Calculated excitation spectrum of ^{6}Li (top) and ^{7}Li (bottom) using chiral LO, NLO, and N^{2}LO interactions at $R = 1.0$ fm as function of the basis HO parameter $\hbar\omega$ for $N_{\max} = 12$ to 16 for NN-only potentials (left 3 panels) and at N^{2}LO w. 3NFs, SRG-evolved to $\alpha = 0.04$ fm^4 (solid) and $\alpha = 0.08$ fm^4 (dashed) for $N_{\max} = 8$ to 12 (right-most panels). The dashed horizontal lines are the experimental values [28].

is that 3NFs are needed to achieve the proper 3^+ ground state for ^{10}B [19, 25]. Indeed, adding the 3NFs at N^{2}LO does give the correct ground state, followed by two 1^+ states with excitation energies of a few MeV. However, these two low-lying 1^+ states mix, with the amount of mixing strongly dependent on the basis $\hbar\omega$ and $N_{\rm max}$ parameters, which makes it difficult to extract actual excitation energies for these two states [25]. The lowest 2^+ is in reasonable agreement with the data at N^{2}LO with 3NFs.

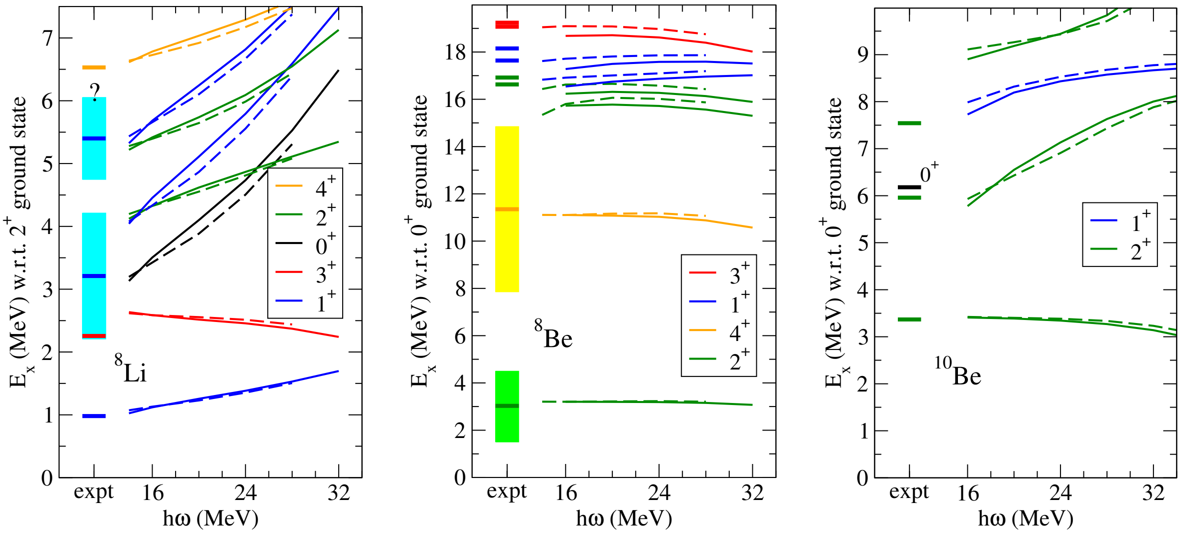

Figure 4. (Color online) Positive-parity excitation spectra of ^{8}Li, ^{8}Be, and ^{10}Be using the chiral N^{2}LO interaction w. 3NFs, SRG-evolved to $\alpha = 0.04$ fm^4 (solid) and $\alpha = 0.08$ fm^4 (dashed), as function of the basis HO parameter $\hbar\omega$, with $N_{\rm max} = 10$ for ^{8}Li and ^{8}Be and $N_{\rm max} = 8$ for ^{10}Be. Experimental levels from ENSDF, Ref. [29].

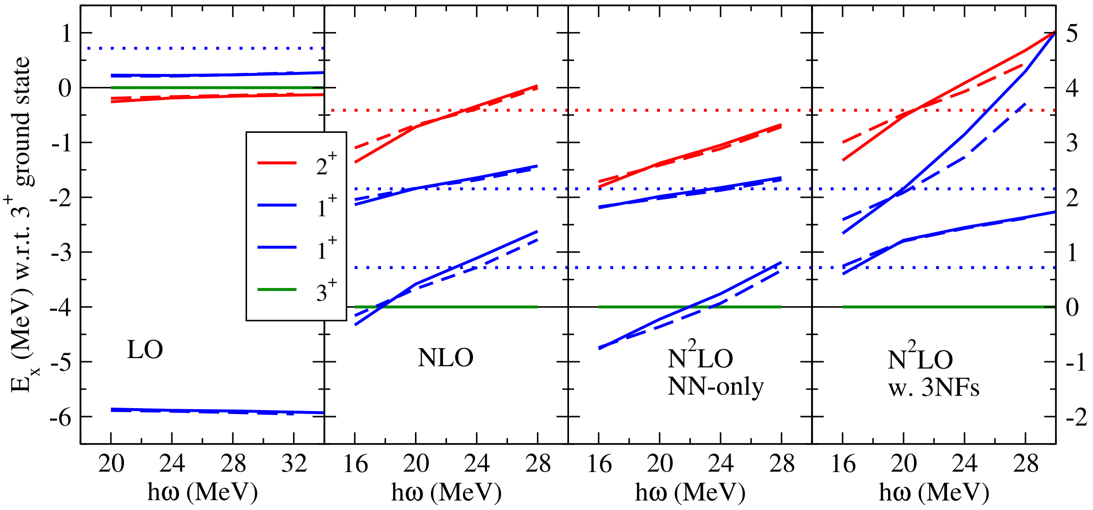

Figure 5. (Color online) Calculated positive-parity excitation spectrum of ^{10}B using chiral LO, NLO, and N^{2}LO interactions at $R = 1.0$ fm as function of the basis HO parameter at $N_{\rm max} = 8$ for NN-only potentials (left 3 panels) and for N^{2}LO w. 3NFs (right-most panel), all SRG-evolved to $\alpha = 0.04$ fm^4 (solid) and $\alpha = 0.08$ fm^4 (dashed). Note the different vertical offset for the LO panel. The dotted horizontal lines are the experimental values [29].

Finally, in Fig. 6 we show the low-lying positive-parity spectra for ^{12}B and ^{12}C. Again, at LO the spectra do not agree with experiment; furthermore, we do not find the Hoyle state in ^{12}C (nor any of its rotational excitations) due to the known limitations of the HO basis [31]. Furthermore, our spectra at NLO and N^{2}LO show a significant sensitivity to the chiral order, as well as the 3NFs at N^{2}LO, for both of these two nuclei.

In particular, at N^{2}LO with 3NFs the first excited 2^+ state in ^{12}B becomes the ground state in our calculations, and the splitting between this state and the other excited states is significantly too large. On the other hand, the energy differences of the 0^+, the second 2^+, the 1^+, and the 3^+ relative to the lowest 1^+ state are in better agreement with 3NFs than without 3NFs at N^{2}LO. Possibly even more puzzling, though not surprising, is the lowest 1^+ excited state in ^{12}C [32]. At NLO it is in reasonable agreement with experiment, just below the 4^+ rotational excitation of the ground state; at N^{2}LO without 3NFs, the order of the 1^+ and the 4^+ is reversed; and

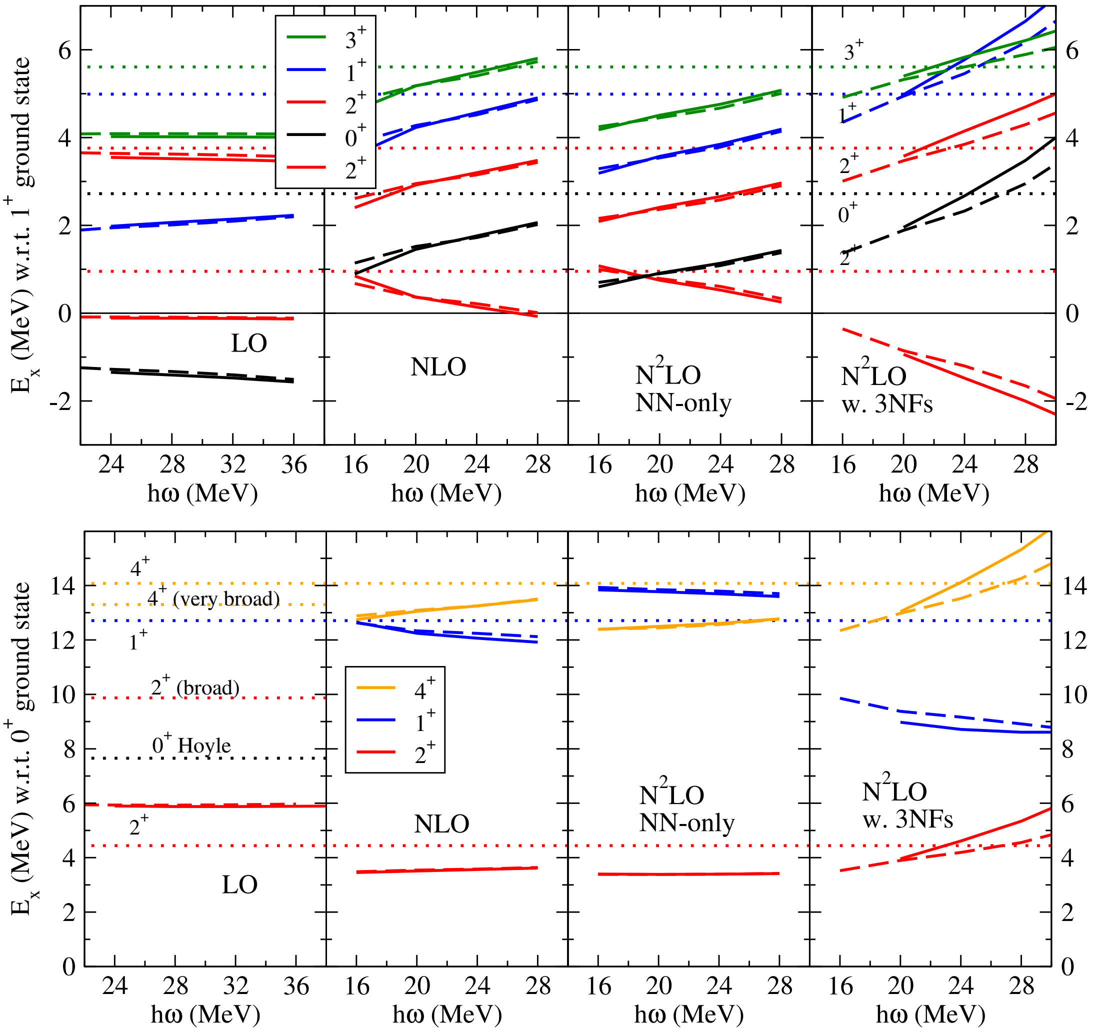

Figure 6. (Color online) Calculated positive-parity excitation spectrum of ^{12}B (top) and ^{12}C (bottom) using chiral LO, NLO, and N^{2}LO interactions at $R = 1.0$ fm as function of the basis HO parameter at $N_{\max} = 8$ for NN-only potentials (left 3 panels) and for N^{2}LO w. 3NFs (rightmost panel), all SRG-evolved to $\alpha = 0.04$ fm^4 (solid) and $\alpha = 0.08$ fm^4 (dashed). The dotted horizontal lines are the experimental values [30].

including the 3NFs at N^2LO reduces the excitation energy of the 1^+ by about 5 MeV, destroying the qualitative agreement with expemiment. Note that this shift due to the 3NFs is significantly larger than that for the 2^+ state in ^{12}B, which is of the order of 2 MeV.

In conclusion most spectra for p-shell nuclei up to to $A = 12$, calculated at N^2LO with 3NFs, agree reasonably well with the experimental data, in particular for narrow states. The exceptions are two states, in ^{12}B and ^{12}C respectively. The low-lying spectra of ^{10}B and ^{12}B, together with the excitation energy of the lowest 1^+ state in ^{12}C, could play a critical role in determining accurate NN and 3N interactions for the upper p-shell and beyond. Indeed, both the 2^+ state in ^{12}B and the 1^+ state in ^{12}C are sensitive to e.g. the LECs c_D and c_E.

Acknowledgments

This work was supported by the US Department of Energy under Grant No. DE-SC0018223 (SciDAC-4/NUCLEI) and the Fundação de Amparo à Pesquisa do Estado de São Paulo, Brazil (FAPESP) under Grant No. 2017/19371-0. This research used resources of the National Energy Research Scientific Computing Center (NERSC) and the Argonne Leadership Computing Facility (ALCF), which are US Department of Energy Office of Science user facilities, supported under Contracts No. DE-AC02-05CH11231 and No. DE-AC02-06CH11357, and computing resources provided under the INCITE award 'Nuclear Structure and Nuclear Reactions' from the US Department of Energy, Office of Advanced Scientific Computing Research.

References

[1] Barrett B R, Navrátil P and Vary J P 2013 *Prog. Part. Nucl. Phys.* **69** 131
[2] Maris P, Vary J P and Shirokov A M 2009 *Phys. Rev.* **C79** 014308
[3] Coon S A, Avetian M I, Kruse M K G, van Kolck U, Maris P and Vary J P 2012 *Phys. Rev.* **C86** 054002
[4] Furnstahl R J, Hagen G and Papenbrock T 2012 *Phys. Rev.* **C86** 031301
[5] More S N, Ekström A, Furnstahl R J, Hagen G and Papenbrock T 2013 *Phys. Rev.* **C87** 044326
[6] Wendt K A, Forssén C, Papenbrock T and Sääf D 2015 *Phys. Rev.* **C91** 061301
[7] Aktulga H M, Yang C, Ng E G, Maris P and Vary J P 2014 *Concurrency Computat.: Pract. Exper.* **26** 2631
[8] Shao M, Aktulga H, Yang C, Ng E G, Maris P and Vary J P 2018 *Comput. Phys. Commun.* **222** 1
[9] Weinberg S 1990 *Phys. Lett.* **B251** 288
[10] Epelbaum E, Hammer H W and Meißner U G 2009 *Rev. Mod. Phys.* **81** 1773
[11] Machleidt R and Entem D R 2011 *Phys. Rept.* **503** 1
[12] Binder S *et al.* (LENPIC) 2016 *Phys. Rev.* **C93** 044002
[13] Binder S *et al.* (LENPIC) 2018 *Phys. Rev.* **C98** 014002
[14] Epelbaum E *et al.* (LENPIC) 2018 *Preprint* `arXiv:1807.02848 [nucl-th]`
[15] Epelbaum E, Krebs H and Meißner U G 2015 *Eur. Phys. J.* **A51** 53
[16] Epelbaum E, Krebs H and Meißner U G 2015 *Phys. Rev. Lett.* **115** 122301
[17] Epelbaum E, Nogga A, Gloeckle W, Kamada H, Meißner U G and Witała H 2002 *Phys. Rev.* **C66** 064001
[18] Nogga A, Navrátil P, Barrett B and Vary J P 2006 *Phys. Rev.* **C73** 064002
[19] Navrátil P, Gueorguiev V G, Vary J P, Ormand W E and Nogga A 2007 *Phys. Rev. Lett.* **99** 042501
[20] Gazit D, Quaglioni S and Navrátil P 2009 *Phys. Rev. Lett.* **103** 102502
[21] Bogner S K, Furnstahl R J, Maris P, Perry R J, Schwenk A and Vary J P 2008 *Nucl. Phys.* **A801** 21
[22] Bogner S K, Furnstahl R J and Schwenk A 2010 *Prog. Part. Nucl. Phys.* **65** 94
[23] Roth R, Calci A, Langhammer J and Binder S 2014 *Phys. Rev.* **C90** 024325
[24] Maris P and Vary J P 2013 *Int. J. Mod. Phys.* **E22** 1330016
[25] Jurgenson E D, Maris P, Furnstahl R J, Navrátil P, Ormand W E and Vary J P 2013 *Phys. Rev.* **C87** 054312
[26] Audi G, Wapstra A and Thibault C 2003 *Nucl. Phys.* **A729** 337
[27] Calci A, Navrátil P, Roth R, Dohet-Eraly J, Quaglioni S and Hupin G 2016 *Phys. Rev. Lett.* **117** 242501
[28] Tilley D *et al.* 2002 *Nucl. Phys.* **A708** 3
[29] Tilley D, Kelley J, Godwin J, Millener D, Purcell J, Sheu C and Weller H 2004 *Nucl. Phys.* **A745** 155
[30] Kelley J, Purcell J and Sheu C 2017 *Nucl. Phys.* **A968** 71
[31] Chernykh M, Feldmeier H, Neff T, von Neumann-Cosel P and Richter A 2007 *Phys. Rev. Lett.* **98** 032501
[32] Maris P, Vary J P, Calci A, Langhammer J, Binder S and Roth R 2014 *Phys. Rev.* **C90** 014314

IOP Conf. Series: Journal of Physics: Conf. Series **1291** (2019) 012006 doi:10.1088/1742-6596/1291/1/012006

The Bethe-Salpeter approach to bound states: from Euclidean to Minkowski space

A Castro [1], E Ydrefors[1], W de Paula[1], T Frederico[1], J H de Alvarenga Nogueira[1,2], P Maris[3]

[1]Instituto Tecnológico da Aeronáutica, DCTA, 12.228-900 São José dos Campos, SP, Brazil
[2]Università di Roma La Sapienza, INFN, Sezione di Roma, P.le A. Moro 5, 00187 Roma, Italy
[3]Department of Physics and Astronomy, Iowa State University, Ames, IA 50011, USA

E-mail: `abigailalbuquerque27@gmail.com`

Abstract. The challenge to obtain from the Euclidean Bethe–Salpeter amplitude the amplitude in Minkowski is solved by resorting to un-Wick rotating the Euclidean homogeneous integral equation. The results obtained with this new practical method for the amputated Bethe–Salpeter amplitude for a two-boson bound state reveals a rich analytic structure of this amplitude, which can be traced back to the Minkowski space Bethe–Salpeter equation using the Nakanishi integral representation. The method can be extended to small rotation angles bringing the Euclidean solution closer to the Minkowski one and could allow in principle the extraction of the longitudinal parton density functions and momentum distribution amplitude, for example.

1. Introduction

Techniques to solve the Bethe–Salpeter Equation (BSE) in Minkowski space have been developed for bound state of bosons [1, 2, 3, 4, 5] and fermions [6, 7, 8, 9, 10], at the expense of being algebraically quite involved, either by use of the Nakanishi integral representation (NIR) [11] or by direct integration. On the other hand, calculations done in Euclidean space after performing the Wick rotation of the BSE are conceptually straigthforward [12, 13], but it is nontrivial to obtain structure observables that are defined on the light-front, such as e.g. parton distributions, from Euclidean solutions. It is desirable to be able to undo the Wick rotation and obtain the Minkowski space solutions from the Euclidean solutions, such that one could extract Minkowski space observables. The first steps in this direction are provided in this contribution.

Our goal here is to present solutions of the BSE for two-bosons close to the Minkowski space, by introducing a rotation into the complex plane of $k_0 \to k_0 \exp(\imath\theta)$, where $\theta = \pi/2$ is the standard Wick-rotation associated with the Euclidean space formulation, while the Minkowski space formulation corresponds to $\theta = 0$. We present solutions of the BSE for small angles and show that the rich analytic structure is accessible numerically by such technique [14]. The branch-points obtained from the integral representation of the vertex function are exhibited by our accurate numerical solutions, for the two-boson bound state in ladder approximation. We present an initial study with angles small as $\theta = \pi/128 \approx 1.4^\circ$, where we also explore different masses μ of the exchanged boson, as well as binding energies.

2. Two-body BSE in Euclidean space

A two-body bound state with total four-momentum p with $p^2 = -M^2$ can be described by the amputated Bethe–Salpeter vertex function Γ, which is a solution of the two-body bound state equation

$$\Gamma(k^2, k\cdot p; p^2 = -M^2) \;=\; \int \frac{d^4k'}{(2\pi)^4}\, K(k-k';p)\, \Delta(\tfrac{p}{2}+k')\, \Gamma(k'^2, k'\cdot p; p^2=-M^2)\, \Delta(\tfrac{p}{2}-k')\,. \tag{1}$$

Here, K is the two-body scattering kernel, and Δ are the (dressed) propagators for the constituent particles. In ladder truncation, the kernel reduces to $\frac{g^2}{(k-k')^2+\mu^2}$. Using bare propagators in the rest frame with 3-dimensional spherical coordinates, $p = (iM, \vec{p}=0)$, we have for the scalar bound state in the Euclidean metric

$$\begin{aligned}\Gamma(k_0, k_v; i\,M) \;=\;& -\frac{m^2\,\alpha}{\pi^2}\int_{-\infty}^{+\infty} dk_0' \int_0^{+\infty} dk_v'\, \frac{k_v'}{k_v}\, \ln\left(\frac{(k_0-k_0')^2+(k_v-k_v')^2+\mu^2}{(k_0-k_0')^2+(k_v+k_v')^2+\mu^2}\right)\\ &\times \frac{\Gamma(k_0', k_v'; i\,M)}{[(\frac{i}{2}M+k_0')^2+{k_v'}^2+m^2]\,[(\frac{i}{2}M-k_0')^2+{k_v'}^2+m^2]}\,,\end{aligned} \tag{2}$$

where $k_v \equiv |\vec{k}_v\,|$ and $k_v' \equiv |\vec{k}_v'\,|$, and $\alpha = g^2/(16\pi m^2)$. The standard normalization condition is applied to our BS amplitude model [15].

Although BSE is usually solved in the rest frame of the bound state, it should be noted that the (amputated) vertex $\Gamma(k^2, k\cdot p; p^2 = -M^2)$ is a function of the Lorentz scalar variables k^2 and $k\cdot p$ at fixed p^2. As long as the truncation of the BSE does not break Lorentz invariance (including any regularization schemes of divergences), the obtained solution is frame independent, and therefore does not need to be boosted for e.g. form factor calculations. Indeed, it has been demonstrated that meson observables, including form factors, calculated in the ladder truncation, are indeed frame-independent [16, 17].

3. Un-Wick rotation towards Minkowski space

Starting with the Euclidean space ladder BSE the rest frame, Eq. (2), we can make a change of variables $k_0 \to k_0\,\mathrm{e}^{i\delta}$ and $k_0' \to k_0'\,\mathrm{e}^{i\delta}$ with the rotation angle $\delta = \theta - \pi/2$, where θ is the rotation angle with respect to the usual Minkowski definition of the zero component of the momentum. Thus the un-Wick rotated BSE becomes

$$\begin{aligned}\Gamma(\mathrm{e}^{i\delta}k_0, k_v; i\,M) \;=\;& -\frac{m^2\,\alpha\,\mathrm{e}^{i\delta}}{\pi^2}\int_{-\infty}^{+\infty} dk_0' \int_0^{+\infty} dk_v'\, \frac{k_v'}{k_v}\, \ln\left(\frac{\mathrm{e}^{2i\delta}(k_0-k_0')^2+(k_v-k_v')^2+\mu^2}{\mathrm{e}^{2i\delta}(k_0-k_0')^2+(k_v+k_v')^2+\mu^2}\right)\\ &\times \frac{\Gamma(\mathrm{e}^{i\delta}k_0', k_v'; i\,M)}{[(\frac{i}{2}M+\mathrm{e}^{i\delta}k_0')^2+k_v'^2+m^2]\,[(\frac{i}{2}M-\mathrm{e}^{i\delta}k_0')^2+k_v'^2+m^2]}\,,\end{aligned} \tag{3}$$

which can be solved numerically, e.g. by iteration. In particular, starting from the Euclidean solution ($\delta = 0$), one can increase δ in small steps, and at each step use the solution at the previous step as the initial guess for solving the BSE iteratively, as is illustrated in the left panel of Fig. 1. Of course, as one approaches the Minkowski axis ($\delta \to \pi/2$, or equivalently, $\theta \to 0$), the numerical challenges in order to obtain a stable solution increase. Although we cannot solve the BSE at $\theta = 0$ exactly, we may be able to extrapolate to $\theta = 0$.

4. Two-body BSE in Minkowski space

Alternatively, one can use the NIR to solve the BSE in Minkowski space formulation. Following Ref. [1], we make use of the uniqueness assumption of the Nakanishi weight function in the

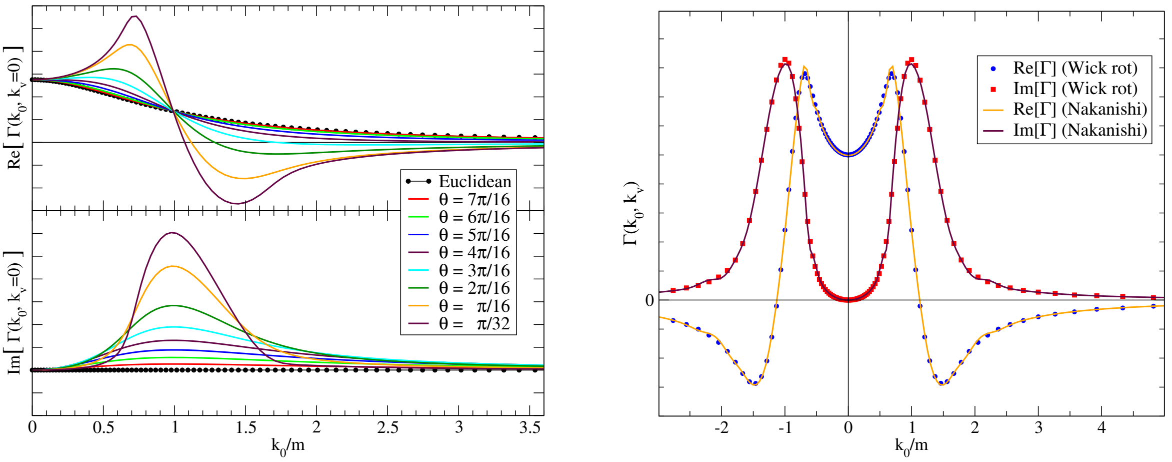

Figure 1. Numerical solutions for $\Gamma(k_0, k_v)$ for $\mu/m = 0.2$ and $M/m = 1.0$ in arbitrary units. Left: Solutions of the un-Wick rotated Euclidean BSE for a range of θ; Right: Comparison of the un-Wick rotated Euclidean BSE and the NIR at $\theta = \pi/16 \approx 11^\circ$.

non-perturbative domain. We have to remind that for the Bethe–Salpeter amplitude itself, the uniqueness assumption can be overcome, using the method of Light-Front projection [18], followed by the application of the inverse generalized Stieltjes transform [19].

The integral representation of the vertex function Γ is

$$\Gamma(k^2, k\cdot p; p^2 = M^2) \;=\; \int_{-1}^{+1} dz \int_{\gamma_{\min}}^{\infty} d\gamma \, \frac{g_\Gamma(\gamma,\, z)}{\gamma + m^2 - \frac{p^2}{4} - k^2 - k\cdot p\, z - \imath\epsilon} \,. \tag{4}$$

A task we have to undertake is to determine the minimum value of γ by checking for the adequacy of the solution in the form above for the BSE, which can in principle depend on z [20]. After introducing the one-boson exchange kernel in the BSE, and using uniqueness, we find that [1]

$$g_\Gamma(\gamma,\, z) = \frac{g^2}{(4\pi)^2} \int_{-1}^{+1} dz' \int_0^1 d\alpha_2 \int_0^1 d\alpha_3 \, \frac{(1-\alpha_3)}{(1+z')\,\bar{s}} \theta(\bar{s})\,\theta(1-\bar{\alpha})\,\theta(\bar{\alpha})\,\theta(\gamma_0 - \gamma_{\min}) \left.\frac{\partial g_\Gamma(\gamma',\, z')}{\partial \gamma'}\right|_{\gamma'=\gamma_0} ,$$

where

$$\begin{aligned} \bar{s} &= \frac{(1+z) + 2z'(\alpha_2+\alpha_3) + \alpha_3(1-z)}{1+z'} \\ \bar{\alpha} &= \frac{\alpha_2(1-z') + (z'-z)(1-\alpha_3)}{1+z'} \\ \gamma_0 &= \frac{\alpha_3(1-\alpha_3)\gamma - (1-\alpha_3)^2 \left(m^2 + (z^2-1)\,\frac{p^2}{4}\right) - \alpha_3\,\mu^2}{\bar{s}} \\ \gamma_{\min} &= \mu \left(2\sqrt{m^2 + (z^2-1)\,\frac{p^2}{4}} + \mu \right) . \end{aligned}$$

After a redefinition of the parameter γ, the integral equation for $g_\Gamma(\gamma,\, z)$ can be solved numerically using basis expansion (see e.g. [21]), and from that the observables like parton distributions can be calculated.

As a consistency check, we can also apply the (un-)Wick rotation to the NIR, and calculate the vertex function $\Gamma(e^{i\theta} k_0, k_v; M)$ from $g_\Gamma(\gamma,\, z)$. We do indeed find good agreement between the un-Wick rotated solution of the Euclidean BSE and the solution at arbitrary angles θ from the NIR, as can be seen in the right panel of Fig. 1.

5. Analytic structure of the Bethe–Salpeter amplitude

Our numerical solutions shown in the left panel of Fig. 1 strongly suggest the existence of singularities in the amputated vertex function Γ. A detailed analysis of the NIR, Eq. (4), shows that there are indeed branch-points in the amputated vertex function, located for $z = \pm 1$ at

$$\gamma_{\min} + m^2 - \frac{p^2}{4} - k^2 \pm k \cdot p \;=\; (m+\mu)^2 - \frac{p^2}{4} - k^2 \pm k \cdot p \;=\; 0\,, \tag{5}$$

which in the rest frame gives the branch-points at

$$|k_0| \;=\; k_0^{\pm} \;\equiv\; \sqrt{(m+\mu)^2 + k_v^2} \pm \frac{M}{2}\,. \tag{6}$$

The positive and negative branch-points in k_0 closest to the origin are separated by $2\sqrt{(m+\mu)^2 + k_v^2} - M$, which allows the rotation of the arguments of the vertex function in the complex k_0 plane without crossing singularities. This non-analytic behavior of the vertex function at these branch-points should be corroborated by the numerical results found for $\Gamma(k;p)$ in the k_0 plane.

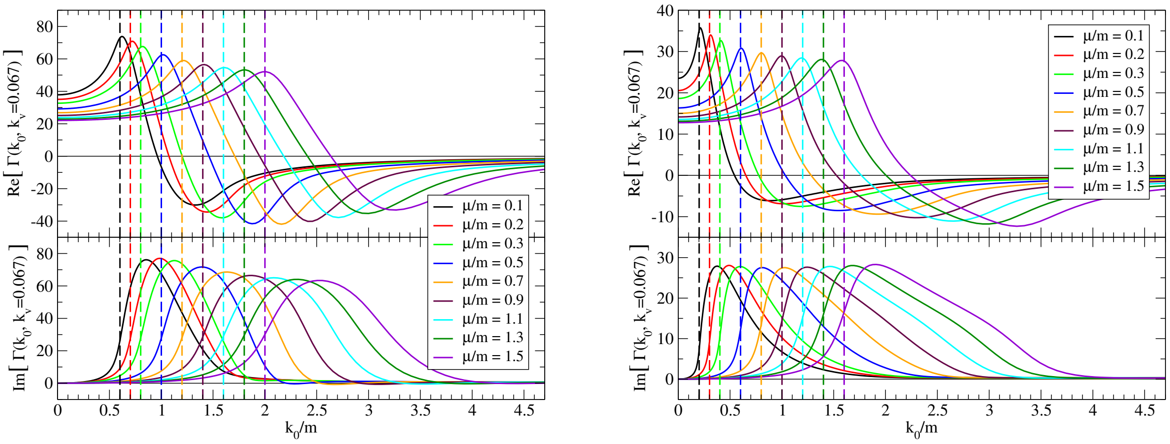

Figure 2. Numerical solutions for $\Gamma(k_0, k_v)$ at $\theta = \pi/32 \approx 5.6^\circ$ for a range of exchange masses μ. Left: for moderate binding, $M/m = 1.0$. Right: for weak binding, $M/m = 1.8$. The dashed vertical lines indicate the location of the first branch-point in $\Gamma(k_0, k_v)$.

In Fig. 2, we present our results with $0.1 \le \mu/m \le 1.5$ at an angle $\theta = \pi/32 \approx 5.6^\circ$ for two different bound state masses: $M/m = 1$, corresponding to moderate binding, and $M/m = 1.8$, corresponding to weak binding. The vertical bars show the location of the branch-points k_0^-, see Eq. (6), in the limit $\theta \to 0$. For $\theta = \pi/32 \approx 5.6^\circ$ the real part of $\Gamma(k_0, k_v)$ has a peak for $|k_0| \approx k_0^-$. Furthermore, the imaginary part of $\Gamma(k_0, k_v)$ is (almost) zero for $|k_0| < k_0^-$, but rises sharply near for $|k_0| \approx k_0^-$. At fixed binding energy, these peaks are more pronounced as the mass of the exchange particle decreases to zero.

As one decreases the angle θ to approach the Minkowski axis, both the peak in the real part of $\Gamma(k_0, k_v)$ and the sharp rise in the imaginary part of $\Gamma(k_0, k_v)$ become more pronounced, see the left panel of Fig. 3, suggesting that this is indeed a branch-point. These high-precision numerical calculations also confirm that there are no singularities closer to $k_0 = 0$ in $\Gamma(k_0, k_v)$ than those at $|k_0| = k_0^-$. Furthermore, the kink in both the real and the imaginary parts of $\Gamma(k_0, k_v)$ indicate the location of the non-analytic points at $|k_0| = k_0^+$.

Finally, in the right panel of Fig. 3 we show the Bethe–Salpeter amplitude with the external propagator legs

$$\chi(k_0, k_v; p) \;=\; \Delta(\tfrac{p}{2} + k')\, \Gamma(k_0, k_v; p)\, \Delta(\tfrac{p}{2} - k)\,, \tag{7}$$

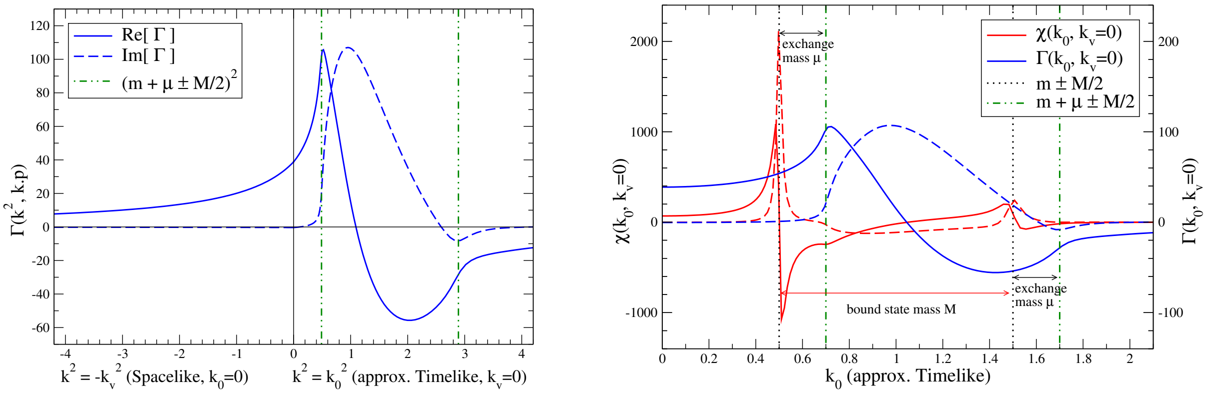

Figure 3. Numerical solution of the BSE for $\mu/m = 0.2$ and $M/m = 1.0$ at $\theta = \pi/128 \approx 1.4°$. Left: $\Gamma(k^2, k\cdot p)$ as function of k^2 in both the spacelike and (approximate) timelike region; Right: results for both Γ (blue) and $\chi = \Delta\Gamma\Delta$ (red) as function of k_0.

in addition to $\Gamma(k_0, k_v; p)$. Here we clearly see that the analytic structure of $\chi(k_0, k_v; p)$ is dominated by the poles in the constituent propagators Δ; the additional non-analytic structure at $|k_0| = k_0^-$ is reduced to relatively minor kinks in the real and imaginary parts of $\chi(k_0, k_v; p)$ at $|k_0| = k_0^-$, and the non-analyticity of $\chi(k_0, k_v; p)$ at $|k_0| = k_0^+$ is not even visible in this plot.

6. Concluding remarks

In this work we present a method to solve the BSE for two-bosons close the timelike axis in Minkowski space. To this end we perform an un-Wick rotation of the Euclidean BSE into the k_0 complex plane. Our solutions of this un-Wick rotated BSE are in good agreement with solutions obtained by solving the BSE in Minkowski space using the Nakanishi Integral Representation and a posteriori rotation into the complex plane. The numerical solutions suggest the existence of branch-points as one approaches the timelike region. Indeed, a detailed analysis of the Minkowski space Bethe–Salpeter equation using the Nakanishi Integral Representation reveals a rich analytic structure of the Bethe–Salpeter amplitude.

In conclusion, the un-Wick rotation captures the main physics of the vertex function, and it can be a valuable tool in the study of the Bethe–Salpeter amplitude close to the timelike region. We expect that this method can be useful to obtain structure observables that are defined on the light-front, such as e.g. parton distributions, and to further explore the phenomenology of strongly relativistic bound state systems.

Acknowledgments

We thank FAPESP Thematic grants no. 13/26258-4 and no. 17/05660-0. AC thanks CAPES; EY thanks FAPESP grant no. 2016/25143-7; WP thanks CAPES, Grant 88881.309870/2018-01 and CNPQ, Grants 313236/2018-6 and 438562/2018-6; TF thanks Conselho Nacional de Desenvolvimento Científico e Tecnológico (Brazil) and Project INCT-FNA Proc. No. 464898/2014-5; JHAN thanks FAPESP grant no. 2014/19094-8; PM thanks the Visiting Researcher Fellowship from FAPESP, grant no. 2017/19371-0. This study was financed in part by CAPES - Finance Code 001.

References

[1] Kusaka K and Williams A G 1995 *Phys. Rev.* D **51** 7026
[2] Kusaka K, Simpson K and Williams A G 1997 *Phys. Rev.* D **56** 5071

[3] Sauli V and Adam J 2001 *Nucl. Phys.* A **689** 467
[4] Frederico T, Salmè G and Viviani M 2012 *Phy. Rev.* D **85** 036009
[5] Pimentel R and de Paula W 2016 *Few-Body Syst.* **57** 491
[6] Carbonell J and Karmanov V A 2010 *Eur. Phys. J.* A **46** 387
[7] de Paula W, Frederico T, Salmè G and Viviani M 2016 *Phys. Rev.* D **94** 071901
[8] de Paula W, Frederico T, Salmè G, Viviani M and Pimentel R 2017 *Eur. Phys. J.* C **77** 764
[9] Salmè G, de Paula W, Frederico T and Viviani M 2017 *Few-Body Syst* **58** 118
[10] de Paula W, Frederico T, Salmè G and Viviani M 2018 *J. Phys.: Conf. Series.* **981** 012020
[11] Nakanishi N 1969 *Suppl. Prog. Theor. Phys.* **43** 1
[12] Maris P and Roberts C D 1997 *Phys. Rev.* C **56** 3369
[13] Maris P and Roberts C D 2003 *Int. J. Mod. Phys.* E **12** 297
[14] Castro A *et al*, in preparation
[15] Itzykson C and Zuber J B 1985 Quantum Field Theory (McGraw-Hill)
[16] Maris P and Tandy P C 2006 *Nucl. Phys. Proc. Suppl.* **161** 136
[17] Bhagwat M S and Maris P 2008 *Phys. Rev.* C **77** 025203
[18] Karmanov V A and Carbonell J 2006 *Eur. Phys. J.* A **27** 1
[19] Carbonell J, Frederico T and Karmanov V A 2017 *Phys. Lett.* B **769** 418
[20] Wanders G 1957 *Helvetica Physica Acta* **30** 417
[21] Frederico T, Salmè G and Viviani M 2014 *Phy. Rev.* D **89** 016010

XLI Brazilian Meeting on Nuclear Physics (RTFNB) IOP Publishing
IOP Conf. Series: Journal of Physics: Conf. Series **1291** (2019) 012007 doi:10.1088/1742-6596/1291/1/012007

The low energy physics of quarkonium suppression in heavy ion collisions

L Abreu, F S Navarra and M Nielsen

Instituto de Física, Universidade de São Paulo, Rua do Matão Travessa R, 187, 05508-090 São Paulo, SP, Brazil

E-mail: `navarra@if.usp.br`

Abstract.
In the late stage of relativistic heavy ion collisions there is a hadron gas phase, where particles interact at energies of the order of the temperature, i.e., $\simeq 100 - 150$ MeV. We discuss heavy quarkonium production and dissociation in this hot hadron gas. We review the theory giving special emphasis to our recent works on J/ψ and Υ suppression in interactions with pions.

1. Introduction

It is now a well accepted fact that in high energy heavy ion collisions a deconfined medium is created: the quark gluon plasma (QGP) [1, 2]. Indeed, a significant part of the RHIC and LHC physics program is devoted to determine and understand the properties of the QGP. This is the result of a long history.

In 1986, in a famous paper by Matsui and Satz [3] charmonium suppression was proposed as a signal of quark gluon plasma formation. Soon after, bottomonium suppresion was also considered as a tool to study the properties of QGP. At that point, all the accumulated experience with particle production indicated that the multiplicities of all kinds of particles tend to increase with the energy. Therefore the suppression of charmonium was an extremely novel and unfamiliar idea. The physics behind the suppression was simple. In a plasma there is color charge screening and so the would-be quark and anti-quark partners can not "see" themselves and bind together.

In the nineties, charmonium suppression was searched for in heavy ion collisions at the CERN-SPS. Some signs of suppression were found and hence for some authors the credit for the discovery of quark-gluon plasma had to be given to the CERN NA-35 and NA-50 Collaborations.

In 2001, in a very influential paper, Thews, Schroedter and Rafeslki [4] proposed that, in contrast to previous expectations, *charmonium enhancement* was the real signature of QGP. This enhancement would be essentially due to the residual screened Coulomb binding potential and to the large number of charm quarks and antiquarks coexisting in the QGP.

From the experimental side, RHIC started to operate in 2000 and the new data showed no extra suppression with respect to the SPS data, although the cms energy was ten times higher. At this point the community started to believe that both processes were happening. The suppression of the initially formed bound states was stronger and at the same time the recombination was responsible for an enhancement of the $c - \bar{c}$ bound states. Thus the net result was a suppression very similar to that previously observed but produced by a very different dynamics. In particular there was a prediction that, at even higher energies regeneration would take over and eventually we would see at the LHC an absence of suppression or "unsuppression". Ten years later this expectation would be confirmed by the LHC data.

In parallel to the evolution of the ideas about the dynamics of the quark gluon plasma, some work was also dedicated to understand what happens to all produced particles and also to heavy quarkonium, after the reconfinement phase transition, or hadronization. In a high energy heavy ion collision the QGP is formed, expands, cools, hadronizes and is converted into a hadron gas, which lives up to 10 fm/c and then freezes out. The particles formed during the QGP phase or at its end have to evolve in the middle of a strongly interacting hadronic medium. During this phase heavy quarkonium can be destroyed in the interaction with light mesons and then can be reformed again. For example, in the case of the J/ψ we can have

$$J/\psi + \pi \to D + \bar{D} \tag{1}$$

and also

$$D + \bar{D} \to J/\psi + \pi \tag{2}$$

Similar equations can be written for vector mesons (D^*), for excited charmonium states (ψ') and also for bottom mesons (Υ, B, B^*, ...etc). An interesting aspect of these reactions is that they happen at relatively low energies, tipically of the order of the temperature, i. e., $100 - 150$ MeV. Hence these final state interactions show that high energy collisions contain also low energy subprocesses.

Already in 1998, in a paper by Matinyan and Mueller [5] the theory of the interactions between charmonium and ordinary hadrons was developed to give a precise estimate of how strongly the charmonium is absorbed by a hadronic medium. Hadronic absorption was considered as a background for the most important suppression, which happened in the QGP, as a result of the color screening effect. This theory was based on effective Lagrangians with SU(4) symmetry and since then it has been improved by different authors. A very important improvement was the introduction of "anomalous parity interactions" (or simply anomalous interactions) done by Oh, Song and Lee in 2001 [6]. These interactions were shown to change the cross sections by two orders of magnitude. A subsequent improvement was to extend this kind of theory to the SU(5) symmetry and treat the analogous problem of the interaction between an Υ and a light meson. This was done in 2001 by Lin and Ko [7].

In this contribution we briefly review the theory of hadron interactions applied to heavy quarkonium and discuss the results obtained in our recent publications. In the next sections we present the development of the calculations for charmonium. The calculation steps for the bottomonium are essentially the same and, for the sake of conciseness, we only show the results. In the end we present some concluding remarks.

2. The cross sections

Now we briefly describe the calculation of the cross sections for the $\varphi - J/\psi$ interactions, where φ denotes a pseudoscalar or vector meson. For more details we refer the reader to [8]. The relevant Lagrangians are given by:

$$\begin{aligned}
\mathcal{L}_{PPV} &= -ig_{PPV}\langle V^{\mu}[P, \partial_{\mu}P]\rangle, \\
\mathcal{L}_{VVV} &= ig_{VVV}\langle \partial_{\mu}V_{\nu}\,[V^{\mu}, V^{\nu}]\rangle, \\
\mathcal{L}_{PPVV} &= g_{PPVV}\langle PV^{\mu}[V_{\mu}, P]\rangle, \\
\mathcal{L}_{VVVV} &= g_{VVVV}\langle V^{\mu}V^{\nu}[V_{\mu}, V_{\nu}]\rangle,
\end{aligned} \tag{3}$$

where the indices PPV and VVV, $PPVV$ and $VVVV$ denote the type of vertex incorporating pseudoscalar (P) and vector (V) meson fields in the couplings and g_{PPV}, g_{VVV}, g_{PPVV} and g_{VVVV} are the respective coupling constants. The symbol $\langle \ldots \rangle$ stands for the trace over $SU(4)$-matrices. In the derivation of the SU(4) theory of meson interactions, one works first with mathematical states. The physical states are combinations of the mathematical states. Usually one assumes what is called "ideal mixing", which means that the physical states are just described by their most important components. The matrix V_μ is parametrized by 16 vector-meson fields including the 15-plet and singlet of $SU(4)$. P is a matrix containing the 15-plet of the pseudoscalar meson fields, written in the physical basis in which η, η' mixing is taken into account.

In addition to the terms given above, we also consider anomalous parity terms. The anomalous parity interactions with vector fields can be described in terms of the gauged Wess-Zumino action [6], which can be summarized as

$$\begin{aligned}
\mathcal{L}_{PVV} &= -g_{PVV}\varepsilon^{\mu\nu\alpha\beta}\langle \partial_\mu V_\nu \partial_\alpha V_\beta P\rangle, \\
\mathcal{L}_{PPPV} &= -ig_{PPPV}\varepsilon^{\mu\nu\alpha\beta}\langle V_\mu(\partial_\nu P)(\partial_\alpha P)(\partial_\beta P)\rangle, \\
\mathcal{L}_{PVVV} &= ig_{PVVV}\varepsilon^{\mu\nu\alpha\beta}\Big[\langle V_\mu V_\nu V_\alpha \partial_\beta P\rangle \\
&\quad + \frac{1}{3}\langle V_\mu(\partial_\nu V_\alpha)V_\beta P\rangle\Big]. \qquad (4)
\end{aligned}$$

The g_{PVV}, g_{PPPV}, g_{PVVV} are the coupling constants of the PVV, $PPPV$ and $PVVV$ vertices, respectively [6]. The couplings given by the effective Lagrangians in Eqs. (3) and (4) allow us to study the following $\varphi J/\psi$ absorption processes

$$\begin{aligned}
(1)\ \varphi J/\psi &\to D_{(s)}\bar{D}, \\
(2)\ \varphi J/\psi &\to D^*_{(s)}\bar{D}^*, \\
(3)\ \varphi J/\psi &\to D^*_{(s)}\bar{D}, \\
(4)\ \varphi J/\psi &\to D_{(s)}\bar{D}^*, \qquad (5)
\end{aligned}$$

where the final states with strange charmed mesons stand for the initial states with K and K^* mesons, while final states with unflavored charmed mesons appear for the initial states with pions and ρ mesons. The diagrams considered to compute the amplitudes of the processes above are of two types: one-meson exchange and contact graphs. They are shown in Fig. 1 of Ref. [6].

We define the invariant amplitudes for the processes (1)-(4) in Eq. (5) involving $\varphi = \pi, K$ mesons as

$$\begin{aligned}
\mathcal{M}_1^{(\varphi)} &= \sum_i \mathcal{M}_{1i}^{(\varphi)\mu}\epsilon_\mu(p_2), \\
\mathcal{M}_2^{(\varphi)} &= \sum_i \mathcal{M}_{2i}^{(\varphi)\mu\nu\lambda}\epsilon_\mu(p_2)\epsilon^*_\nu(p_3)\epsilon^*_\lambda(p_4), \\
\mathcal{M}_3^{(\varphi)} &= \sum_i \mathcal{M}_{3i}^{(\varphi)\mu\nu}\epsilon_\mu(p_2)\epsilon^*_\nu(p_3), \\
\mathcal{M}_4^{(\varphi)} &= \sum_i \mathcal{M}_{4i}^{(\varphi)\mu\nu}\epsilon_\mu(p_2)\epsilon^*_\nu(p_4). \qquad (6)
\end{aligned}$$

In the above equations, the sum over i represents the sum over all diagrams contributing to the respective amplitude; p_j denotes the momentum of particle j, with particles 1 and 2 standing for initial state mesons, and particles 3 and 4 for final state mesons; $\epsilon_\mu(p_j)$ is the polarization vector related to the respective vector particle j. The explicit expressions of amplitudes $\mathcal{M}^{(\pi)}$ and $\mathcal{M}^{(K)}$ may be found in Ref. [6].

In the case of processes involving $\varphi = \rho, K^*$ mesons, we must add on the right hand side of each expression in Eq. (6) the contraction of the amplitude with the polarization vector of a vector meson, i.e. for the reaction (1) we have $\mathcal{M}_1^{(\varphi)\mu\nu}\epsilon_\mu(p_1)\epsilon_\nu(p_2)$ and so on. The explicit expressions of the amplitudes $\mathcal{M}^{(\rho)}$ and $\mathcal{M}^{(K^*)}$ used here are those published in Refs. [6] and [9, 10].

We are interested in the determination of the isospin-spin-averaged cross section for the processes in Eq. (5), which in the center of mass (CM) frame is defined as

$$\sigma_r^{(\varphi)}(s) = \frac{1}{64\pi^2 s}\frac{|\vec{p}_f|}{|\vec{p}_i|}\int d\Omega \overline{\sum_{S,I}}|\mathcal{M}_r^{(\varphi)}(s,\theta)|^2, \tag{7}$$

where $r = 1, 2, 3, 4$ labels $\varphi - J/\psi$ absorption processes according to Eq. (6); $\sqrt{s}$ is the CM energy; $|\vec{p}_i|$ and $|\vec{p}_f|$ denote the three-momenta of initial and final particles in the CM frame, respectively; the symbol $\overline{\sum_{S,I}}$ represents the sum over the spins and isospins of the particles in the initial and final state, weighted by the isospin and spin degeneracy factors of the two particles forming the initial state for the reaction r, i.e.

$$\overline{\sum_{S,I}}|\mathcal{M}_r|^2 = \frac{1}{g_1 g_2}\sum_{S,I}|\mathcal{M}_r|^2, \tag{8}$$

with $g_1 = (2I_{1i,r}+1)(2S_{1i,r}+1), g_2 = (2I_{2i,r}+1)(2S_{2i,r}+1)$ being the degeneracy factors of the initial particles 1 and 2.

We employ the isospin-averaged masses: $m_\pi = 138.1$ MeV, $m_\rho = 775.2$ MeV, $m_K = 495.6$ MeV, $m_{K^*} = 893.7$ MeV, $m_D = 1867.2$ MeV, $m_{D^*} = 2008.6$ MeV, $m_{D_s} = 1968.3$ MeV, $m_{D_s^*} = 2112.1$ MeV, $m_{J/\psi} = 3096.9$ MeV. Besides, the values of coupling constants appearing in the expressions of the amplitudes have been taken from Ref. [6] for $\mathcal{M}^{(\pi)}$; from Refs. [9, 10] for $\mathcal{M}^{(K)}$ and $\mathcal{M}^{(K^*)}$; and from Ref. [6] for the couplings involving ρ meson in $\mathcal{M}^{(\rho)}$. We have also included form factors in the vertices when evaluating the cross sections. They were taken from [6] and are:

$$F_3 = \frac{\Lambda^2}{\Lambda^2 + \mathbf{q}^2}; \quad F_4 = \frac{\Lambda^2}{\Lambda^2 + \bar{\mathbf{q}}^2}\frac{\Lambda^2}{\Lambda^2 + \bar{\mathbf{q}}^2}, \tag{9}$$

where F_3 and F_4 are the form factor for the three-point and four-point vertices, respectively; $\mathbf{q} = (\mathbf{p_1} - \mathbf{p_3})^2$ or $(\mathbf{p_2} - \mathbf{p_3})^2$ for a vertex involving a t- or u-channel meson exchange; and $\bar{\mathbf{q}} = [(\mathbf{p_1} - \mathbf{p_3})^2 + (\mathbf{p_2} - \mathbf{p_3})^2]/2$. The cutoff parameter Λ was chosen to be $\Lambda = 2.0$ GeV for all vertices [6].

As one can see, the Lagrangian theories suffer from two main deficiencies: i) the coupling constants are not known and ii) to regularize the theory and to account for the finite extension of hadrons one is forced to introduce form factors. The functional form of these form factors is unknown. Moreover they contain a cut-off parameter (usually called Λ) which is completely unknown.

The coupling constants can be determined if we use the SU(4) symmetry and some experimental input, such as the $g_{D^*D\pi}$ coupling constant, which is measured in the $D^* \to D\pi$ decay. Other needed coupling constants and also all the form factors can be evaluated with QCD sum rules [11]. Moreover one can compare the results obtained with effective Lagrangian with the cross sections directly computed with QCD sum rules [12]. After five years (1998 - 2003) of combined efforts the community arrived at a consensus on the values of certain cross sections, such as the $J/\psi - \pi$ cross section.

How the existence of a hot hadron gas phase affects the production of J/ψ ? In Eqs. 1 and 2 we show the possible reactions which may change the multiplicity of J/ψ's. They are related by detailed balance. The matrix element is the same in both directions but the spin-isospin factors are different and also the phase-space is different. For this reason absorption and production do not have the same probabilities. A comparison between both processes is shown in Fig. 1.

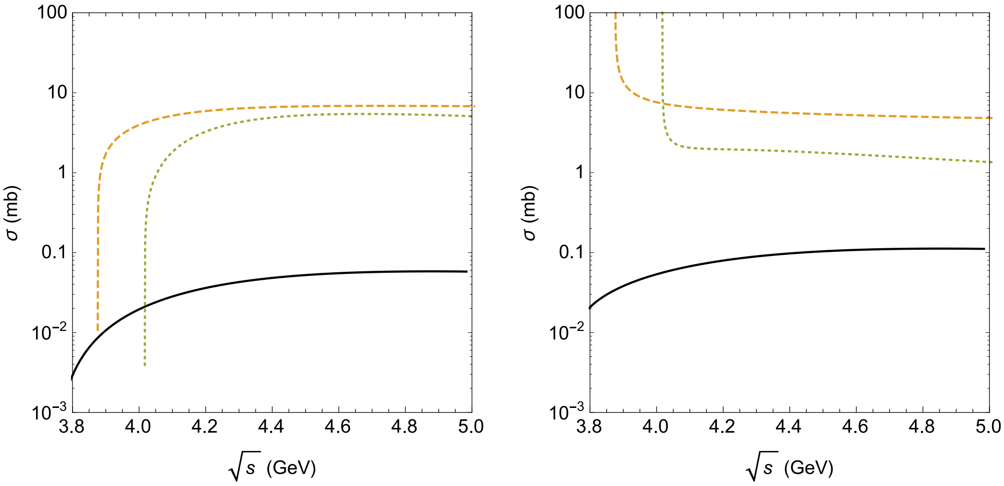

Figure 1. J/ψ absorption and production cross sections in different processes as a function of the CM energy $\sqrt{s}$. Left panel: $\pi J/\psi$ in the initial state. Solid, dashed and dotted lines represent the $\pi J/\psi \to D\bar{D}$, $\pi J/\psi \to D^*\bar{D}$ and $\pi J/\psi \to D^*\bar{D}^*$ reactions, respectively. Right panel: $\pi J/\psi$ in the final state. Solid, dashed and dotted lines represent the $D\bar{D} \to \pi J/\psi$, $D^*\bar{D} \to \pi J/\psi$ and $D^*\bar{D}^* \to \pi J/\psi$ reactions, respectively.

From these curves we can see that, excluding the low energy region (which will be much less relevant for phenomenology), the J/ψ production and absorption cross sections are very close to each other in almost all channels. Since the J/Ψ absorption and production cross sections have comparable magnitudes, what will determine the final yield of J/Ψ's will be the thermally averaged cross sections, which, reflecting the physical aspects of the hadron gas, will select the range of energies which are more important.

3. The role of exotic charmonium

In 2003 a new class of charmonium was discovered, the so-called exotic charmonium states (for recent reviews on the subject see Refs. [13, 14]). They are multiquark states composed by two quarks and two antiquarks ($c\bar{c}q\bar{q}$). As new members of the family they have a direct impact on the quarkonium - light hadron cross section, as it is illustrated in Fig. 2, where we show a new way to destroy (and also to regenerate) a J/ψ. In principle, the existence of these resonances in the s-channel could drastically change the $J/\psi - \pi$ cross section. Recently [8] we have calculated this effect and it turned out to be significant only in the energy region close to the reaction thresholds, being negligible elsewhere. This can be attributed to the narrow width of the resonances. These effects are illustrated in Fig. 3. On the left panel we see the J/Ψ absorption cross section by π's. The solid line represents the cross section obtained without including the Z_c (3900) exchange in the s-channel. The dashed line shows the result with the exchange of Z_c (3900) in the s-channel included. The right panel shows the J/Ψ absorption cross section by ρ. The solid line shows the cross section obtained without including the Z_c

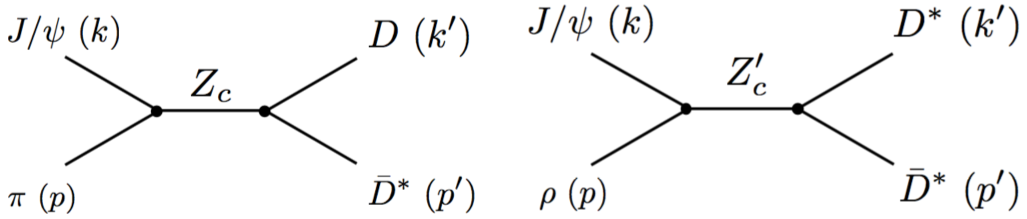

Figure 2. $J/\psi - \pi$ (left) and $J/\psi - \rho$ (right) reactions mediated by Z resonances in the s-channel.

(4025) exchange in the s-channel. The dashed line shows the result obtained by including the $Z_c(4025)$ exchange in the s-channel.

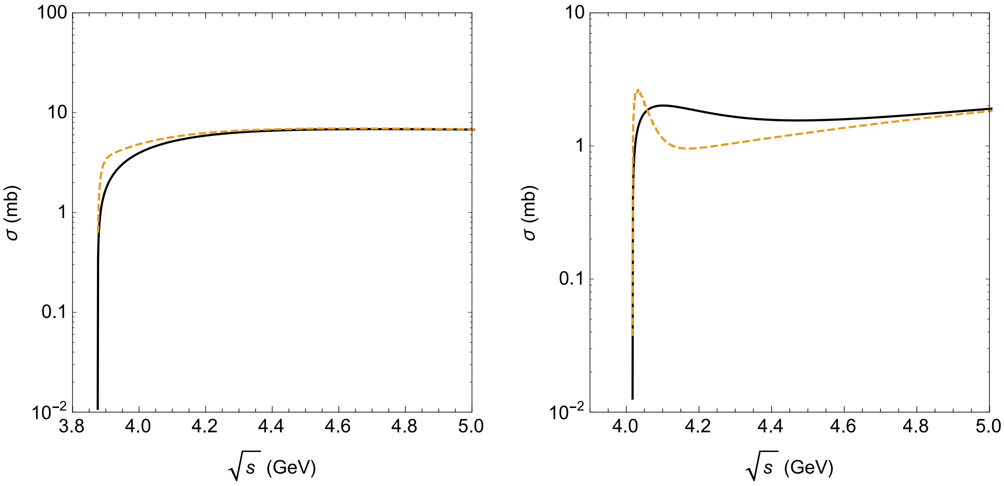

Figure 3. The left panel shows the J/Ψ absorption cross section by π's. The solid lines represent the cross sections obtained without including the Z_c (3900) exchange in the s-channel. The dashed lines show the results with the exchange of Z_c (3900) in the s-channel included. The right panel shows the J/Ψ absorption cross section by ρ. The solid line shows the cross sections obtained without including the Z_c (4025) exchange in the s-channel. The dashed line shows the results obtained by including the $Z_c(4025)$ exchange in the s-channel.

4. The effect of temperature

We define the thermally averaged cross section for a given process $ab \to cd$ as:

$$\langle \sigma_{ab\to cd}\, v_{ab} \rangle = \frac{\int d^3\mathbf{p}_a\, d^3\mathbf{p}_b\, f_a(\mathbf{p}_a)\, f_b(\mathbf{p}_b)\, \sigma_{ab\to cd}\ v_{ab}}{\int d^3\mathbf{p}_a\, d^3\mathbf{p}_b\, f_a(\mathbf{p}_a)\, f_b(\mathbf{p}_b)} \tag{10}$$

where v_{ab} represents the relative velocity of the two interacting initial particles a and b and the function $f_i(\mathbf{p}_i)$ is the Bose-Einstein distribution (of particles of species i), which depends on the temperature T.

In the two panels of Fig. 4 we plot the thermally averaged cross sections for $\pi J/\psi$ absorption (on the left) and production (on the right) via the processes discussed in previous section. We can see that for all processes the production reactions are larger than the absorption ones.

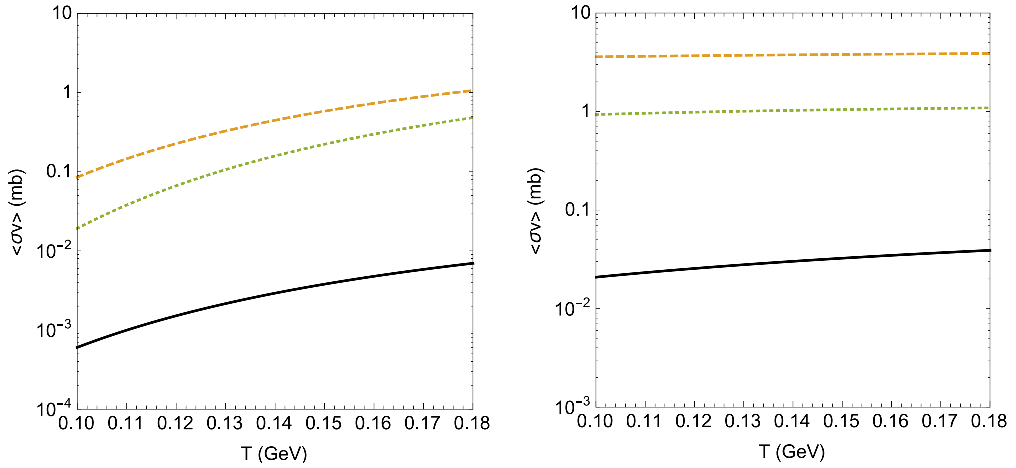

Figure 4. J/Ψ absorption and production cross sections by π's as a function of the temperature. Left panel: absorption reactions with $\pi J/\Psi$ in the initial state. $\pi J/\Psi \to D\bar{D}$ (solid line), $\pi J/\Psi \to D^*\bar{D}$ (dashed lines) and $\pi J/\Psi \to D^*\bar{D}^*$ (dotted lines). Right panel: production reactions with $\pi J/\Psi$ in the final state. The line convention is the same as in the left panel.

5. Time evolution of the J/ψ abundance

We complete this study by addressing the time evolution of the J/ψ abundance in hadronic matter, using the thermally averaged cross sections estimated in the previous section. We make use of the evolution equation for the abundances of particles included in processes discussed above. The momentum-integrated evolution equation has the form [15, 16, 17, 18]:

$$\begin{aligned}
\frac{dN_{J/\psi}(\tau)}{d\tau} = & \sum_{\varphi=\pi,\rho K,K^*} \Big[\langle\sigma_{D_{(s)}\bar{D}\to\varphi J/\psi}v_{D_{(s)}\bar{D}}\rangle n_{D_{(s)}}(\tau)N_{\bar{D}}(\tau) - \langle\sigma_{\varphi J/\psi\to D_{(s)}\bar{D}}v_{\varphi J/\psi}\rangle n_{\varphi}(\tau)N_{J/\psi}(\tau) \\
& +\langle\sigma_{D^*_{(s)}\bar{D}^*\to\varphi J/\psi}v_{D^*_{(s)}\bar{D}^*}\rangle n_{D^*_{(s)}}(\tau)N_{\bar{D}^*}(\tau) - \langle\sigma_{\varphi J/\psi\to D^*_{(s)}\bar{D}^*}v_{\varphi J/\psi}\rangle n_{\varphi}(\tau)N_{J/\psi}(\tau) \\
& +\langle\sigma_{D^*_{(s)}\bar{D}\to\varphi J/\psi}v_{D^*_{(s)}\bar{D}}\rangle n_{D^*_{(s)}}(\tau)N_{\bar{D}}(\tau) - \langle\sigma_{\varphi J/\psi\to D^*_{(s)}\bar{D}}v_{\varphi J/\psi}\rangle n_{\varphi}(\tau)N_{J/\psi}(\tau) \\
& +\langle\sigma_{D_{(s)}\bar{D}^*\to\varphi J/\psi}v_{D_{(s)}\bar{D}^*}\rangle n_{D_{(s)}}(\tau)N_{\bar{D}^*}(\tau) - \langle\sigma_{\varphi J/\psi\to D_{(s)}\bar{D}^*}v_{\varphi J/\psi}\rangle n_{\varphi}(\tau)N_{J/\psi}(\tau)\Big] \\
& + \sum_{\varphi=\bar{\pi},\bar{\rho},\bar{K},\bar{K}^*} \Big[\langle\sigma_{\bar{D}_{(s)}D\to\varphi J/\psi}v_{\bar{D}_{(s)}D}\rangle n_{\bar{D}_{(s)}}(\tau)N_{D}(\tau) - \langle\sigma_{\varphi J/\psi\to\bar{D}_{(s)}D}v_{\varphi J/\psi}\rangle n_{\varphi}(\tau)N_{J/\psi}(\tau) \\
& +\langle\sigma_{\bar{D}^*_{(s)}D^*\to\varphi J/\psi}v_{\bar{D}^*_{(s)}D^*}\rangle n_{\bar{D}^*_{(s)}}(\tau)N_{D^*}(\tau) - \langle\sigma_{\varphi J/\psi\to\bar{D}^*_{(s)}D^*}v_{\varphi J/\psi}\rangle n_{\varphi}(\tau)N_{J/\psi}(\tau) \\
& +\langle\sigma_{\bar{D}^*_{(s)}D\to\varphi J/\psi}v_{\bar{D}^*_{(s)}D}\rangle n_{\bar{D}^*_{(s)}}(\tau)N_{D}(\tau) - \langle\sigma_{\varphi J/\psi\to\bar{D}^*_{(s)}D}v_{\varphi J/\psi}\rangle n_{\varphi}(\tau)N_{J/\psi}(\tau) \\
& +\langle\sigma_{\bar{D}_{(s)}D^*\to\varphi J/\psi}v_{\bar{D}_{(s)}D^*}\rangle n_{\bar{D}_{(s)}}(\tau)N_{D^*}(\tau) - \langle\sigma_{\varphi J/\psi\to\bar{D}_{(s)}D^*}v_{\varphi J/\psi}\rangle\Big], \qquad (11)
\end{aligned}$$

where $n_{\varphi}(\tau)$ are $N_{\varphi}(\tau)$ denote the density and the abundances of π, ρ, K, K^*, charmed mesons and their antiparticles in hadronic matter at proper time τ. From Eq. (11) we observe that the J/ψ abundance at a proper time τ depends on the $\varphi J/\psi$ dissociation rate as well as on the $\varphi J/\psi$ production rate. We remark that in the rate equation we have also considered the processes involving the respective antiparticles, i.e. $\bar{\varphi} J/\psi \to \bar{D}_{(s)}^{(*)} D^{(*)}$ and $\bar{D}_{(s)}^{(*)} D^{(*)} \to \bar{\varphi} J/\psi$. We assume that π, ρ, K, K^*, D and D^* are in equilibrium. Therefore the density $n_i(\tau)$ can be written as [15, 16, 17, 18]

$$n_i(\tau) \approx \frac{1}{2\pi^2}\gamma_i g_i m_i^2 T(\tau) K_2\left(\frac{m_i}{T(\tau)}\right), \tag{12}$$

where γ_i and g_i are respectively the fugacity factor and the degeneracy factor of the relevant particle. The abundance $N_i(\tau)$ is obtained by multiplying the density $n_i(\tau)$ by the volume $V(\tau)$. The time dependence is introduced through the temperature $T(\tau)$ and volume $V(\tau)$ profiles appropriate to model the dynamics of relativistic heavy ion collisions after the end of the quark-gluon plasma phase. The hydrodynamical expansion and cooling of the hadron gas is modeled as in Refs. [15, 16, 17, 18] by a boost invariant Bjorken flow with an accelerated transverse expansion:

$$\begin{aligned} T(\tau) &= T_C - (T_H - T_F)\left(\frac{\tau - \tau_H}{\tau_F - \tau_H}\right)^{\frac{4}{5}}, \\ V(\tau) &= \pi\left[R_C + v_C(\tau - \tau_C) + \frac{a_C}{2}(\tau - \tau_C)^2\right]^2 \tau_C. \end{aligned} \tag{13}$$

In the equation above, R_C and τ_C fm/c denote the final transverse and longitudinal sizes of the quark-gluon plasma, while v_C and a_C are its transverse flow velocity and transverse acceleration at this time. $T_C = 175$ MeV is the critical temperature for the quark-gluon plasma to hadronic matter transition; $T_H = T_C = 175$ MeV is the temperature of the hadronic matter at the end of the mixed phase, occurring at the time τ_H. The freeze-out temperature $T_F = 125$ MeV then leads to a freeze-out time τ_F. In addition, we assume that the total number of charmed quarks in charmed hadrons is conserved during the processes. This number can be calculated with perturbative QCD and yields the charm quark fugacity factor γ_C in Eq. (12) [15, 16, 17, 18]. The total number of pions and ρ mesons at freeze-out was taken from Refs. [19, 20]. In the case of $K^{(*)}$ and $\bar{K}^{(*)}$ mesons [15], we work with the assumption that strangeness reaches approximate chemical equilibrium in heavy ion collisions due to the short equilibration time in the quark-gluon plasma and the net strangeness of the QGP is zero.

We will study the J/ψ evolution in the hadron gas formed in two types of collisions: central $Au - Au$ collisions at $\sqrt{s_{NN}} = 200$ GeV at RHIC and central $Pb - Pb$ collisions at $\sqrt{s_{NN}} = 5$ TeV at the LHC. The parameters which we need as input in Eqs. (13) are listed in Table 3.1 of Ref. [15] and, for convenience, are reproduced in Table 1.

Table 1. Parameters used in the parametrization of the hydrodynamical expansion, given by Eqs.(13).

	v_C (c)	a_C (c^2/fm)	R_C (fm)	τ_C (fm/c)	τ_H (fm/c)	τ_F (fm/c)	γ_c	$N_{J/\psi}$
RHIC	0.4	0.02	8	5	7.5	17.3	6.4	0.017
LHC	0.6	0.044	13.11	5	7.5	20.7	15.8	1.67

In Fig. 5 we present the time evolution of the J/ψ abundance as a function of the proper time for the two types of collisions discussed above: at RHIC (on the left panel) and at the LHC (on the right panel). Looking at the evolution equation, Eq. (11), we can see that the fate of the J/ψ population will be determined by the production and absorption cross sections and by the multiplicities of the other mesons, especially the pion multiplicity. While the cross sections alone would favor an enhancement of the J/ψ yield, the relative multiplicities favor its reduction, since in the hadron gas there are much more pions and kaons (which hit and destroy the charmonium states) than D's, $\bar{D}$'s, D_s's and $\bar{D}_s$'s (which can collide and create them). The result of this competition is a decrease of the J/ψ yield of approximately 20 % at RHIC and 24 % at the LHC. From the solid line in the figure we can see that if there were only pions in the gas, there would be a small suppression of the J/ψ yield. This comes from a cancellation between a difference in the cross sections favoring production with a large difference in multiplicities, as pions are much more abundant than open charm mesons. The same competition occurs if the gas would include ρ's, kaons and K^*'s.

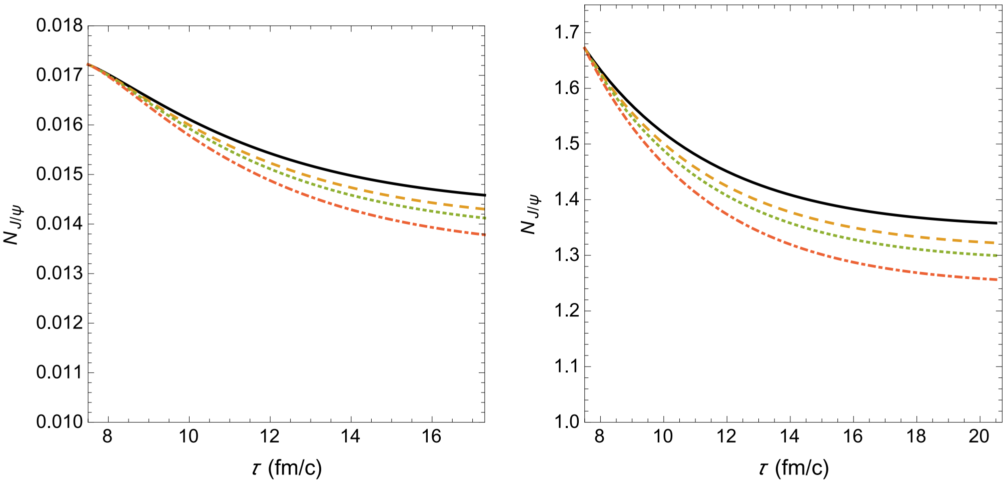

Figure 5. Left: Time evolution of J/ψ abundance as a function of the proper time in central Au-Au collisions at $\sqrt{s_{NN}} = 200$ GeV. Solid, dashed, dotted, dot-dashed lines represent the situations with only $\pi - J/\psi$ interactions and also adding the $\rho - J/\psi$, $K - J/\psi$ and $K^* - J/\psi$ contributions, respectively. Right: the same as on the left for LHC conditions.

6. Time evolution of the Υ abundance

While charmonium states have been extensively studied as QGP probes, bottomonium states were not explored so much, even though the $b\bar{b}$ family of states provides experimentally more robust and theoretically cleaner probes. Moreover, bottomonium states are regarded as better probes because recombination effects are believed to be much less significant than in the charmonium case. Although the recombination effect is expected to increase for bottomonia from RHIC to LHC energies, it is predicted to remain small [21, 22, 23, 24, 25, 26, 27].

From the experimental side, the CMS detector has excellent capabilities for muon detection and provides measurements of the Υ family which enable the accurate analysis of bottomonium [28] production. For this reason, the main interest may be shifted to the suppression of bottomonium states at LHC energies. The first indication of Υ suppression in heavy ion collisions was reported by CMS in 2011 [29]. Later it was also observed by the STAR Collaboration at RHIC [30]. The $\Upsilon(2S)$ and $\Upsilon(3S)$ resonances in PbPb collisions were seen to be more strongly suppressed than the $\Upsilon(1S)$ (compared with the pp result), showing the expected sequential suppression pattern [28].

The most recent data on prompt J/ψ [31] and Υ [28, 32, 33, 34] suppression in the most central Pb Pb collisions at small rapidities and small p_T, show that:

$$R_{AA}(J/\psi) \simeq 0.28 \pm 0.03 \tag{14}$$

and

$$R_{AA}(\Upsilon(1S)) \simeq 0.38 \pm 0.05 \tag{15}$$

These factors are very weakly dependent on the collision energy $\sqrt{s}_{NN}$. Although they are close to each other, they may be the result of a quite different dynamics.

After the QGP cooling and hadronization there is a hadron gas (HG) phase. Apart from being a reasonable assumption, the existence of this phase seems to be necessary to correctly reproduce [35] the multiplicities of K^* and ρ measured by the ALICE Collaboration [36, 37, 38]. Heavy quarkonium is produced at the beginning of the heavy ion collision. Then it may be destroyed and regenerated both in the quark gluon plasma and in the subsequent hadron gas. The observed Υ suppression has been explained mostly with models which take into account only what happens during the QGP phase. In [39] we addressed the contribution of the hadron gas phase to the Υ production and absorption.

In the literature, there is a large number of works on quarkonium interactions with light mesons in a hot hadron gas using different approaches (for a short and recent compilation of references on charmonium interactions, see [40]). Many of these works investigate the J/ψ-light meson reactions based on effective hadron Lagrangians [40, 41, 6, 42]. After a long series of works, different groups found a similar value of the $J/\psi - \pi$ cross section, which is close to the value obtained with QCD sum rules [12]. In [40], we have used all the known charmonium-light hadron absorption cross sections (together with the inverse interactions in which charmonium is produced) as input to solve the rate equation which governs the time evolution of J/ψ abundance in a hadron gas.

In contrast to the J/ψ case, the number of studies about the Υ interactions with light hadrons is much smaller [43]. In fact, to the best of our knowledge, the paper by Lin and Ko, Ref. [7], is the only one to give an estimate of the cross sections for scattering of Υ by pions and ρ mesons in a hot hadron gas. In that work the authors used a hadronic Lagrangian based on the SU(5) flavor symmetry. Including form factors with a cutoff parameter of 1 or 2 GeV at the interaction vertices, they found that the values of $\sigma_{\pi\Upsilon}$ and $\sigma_{\rho\Upsilon}$ are about 8 mb and 1 mb, respectively. However their thermal averages at a temperature of 150 MeV are both around only 0.2 mb. The reason for this reduction comes from the momentum average made in the thermal average. The kinematical threshold plays an important role since the sum of the masses of the initial state is $\simeq$ 9597 MeV and the sum of the masses of the final $B\bar{B}$ state (the lightest one) is $\simeq$ 10558. Hence their difference is $\simeq$ 960 MeV, which is still much larger than the temperature, $\simeq$ 150 MeV, and it is responsible for the strong reduction from 8 mb to 0.2 mb. They then conclude speculating that the absorption of directly produced Υ by comoving hadrons is unlikely to be important. In [39] we contributed to this subject extending the analysis performed in Ref. [40] to the bottomonia sector: we investigated the interactions of Υ with the surrounding hadronic medium composed of the lightest pseudoscalar meson (π) and the lightest vector meson (ρ). We calculated the cross sections for processes such as $\bar{B}^{(*)} + B^{(*)} \to \Upsilon + (\pi, \rho)$ scattering and their inverses, within the effective hadron Lagrangian framework. We improved the previous calculation introducing anomalous interactions. The obtained cross sections were used as input to solve the rate equation which allows us to follow the time evolution of the Υ multiplicity.

The importance of the anomalous vertices has been earlier mentioned in different contexts. For example, in Ref. [6] the J/ψ absorption cross sections by pions and ρ mesons were evaluated for several processes producing D and D^* mesons in the final state. The authors found that the $J/\psi\pi \to D^*\bar{D}$ cross section obtained with the exchange of a D^* meson in the t-channel, which involves the anomalous $D^*D^*\pi$ coupling, was around 80 times bigger than the one obtained with a D meson exchange in the t-channel.

As it was pointed out in [39], the introduction of anomalous interactions leads to a strong hadronic suppression of Υ instead of the weak suppression expected in [7]. If confirmed these results indicate that, in contrast to the J/ψ case, the Υ's are produced in the QGP, their number remains nearly constant throughout the plasma phase and their suppression takes place in the hadron gas phase.

The diagrams representing the Υ interactions are shown in Figs. 6 and 7. Repeating the steps described above for the case of the charmonium, we can compute the cross sections for absorption and production of Υ, their thermal averages and finally the evolution equation for the Υ abundance.

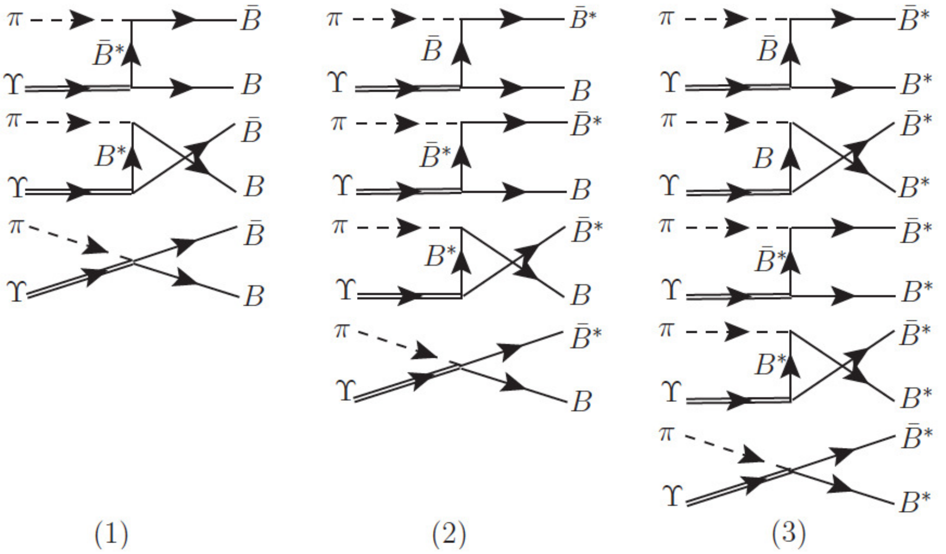

Figure 6. Diagrams contributing to the processes: (1) $\pi\Upsilon \to \bar{B}B$, (2) $\pi\Upsilon \to \bar{B}^*B$, and (3) $\pi\Upsilon \to \bar{B}^*B^*$.

From Fig. 8 we can see that excluding the low energy region (which will be much less relevant for phenomenology), the Υ production and absorption cross sections are close to each other. Therefore, taking into account that the Υ absorption and production cross sections have comparable magnitudes, the computation of thermally averaged cross sections is an essential step to determine the final abundance of Υ's.

In Fig. 9 we plot the thermally averaged cross sections for $\pi\Upsilon$ absorption (left panel) and production (right panel) via the processes discussed above. As can be seen, in general, the production reactions have larger cross sections than the corresponding inverse reactions.

The range of temperatures which is relevant for our discussion corresponds to a very narrow range of energies $\sqrt{s}$, not far from the reaction reaction thresholds. The lines in Fig. 9 preserve the relative importance of the channels and they reproduce what is observed in Fig. 8. In other words, the thermal averaging does not change the relative ordering of the cross sections.

The time evolution of the Υ abundance is plotted in Fig. 10 as a function of the proper time, for the two types of collisions discussed above: at RHIC (on the upper panel) and at the LHC (on the lower panel).

The behavior of the Υ multiplicity observed in Fig. 10 is not difficult to understand. Due to the assumption that the hadronic stage at LHC is longer compared to that at RHIC, more

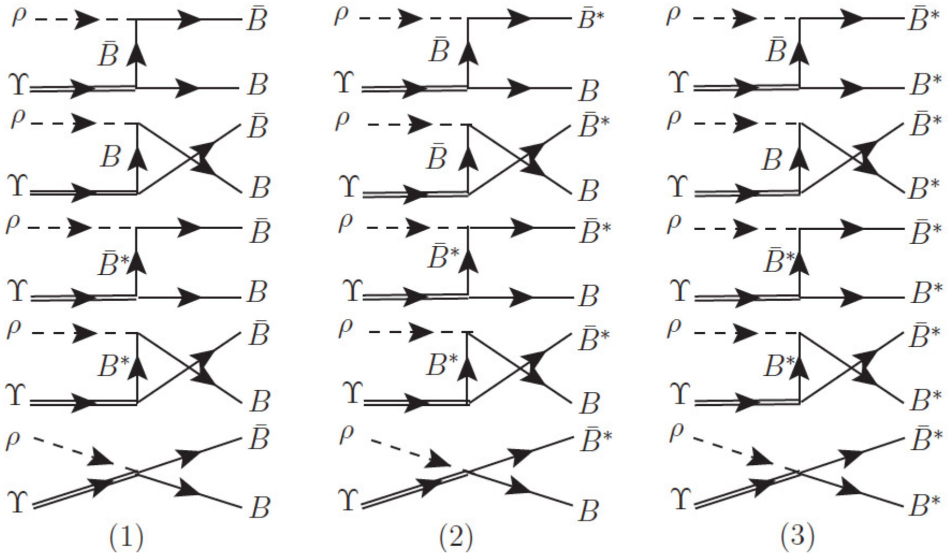

Figure 7. Diagrams contributing to the processes: (1) $\rho\Upsilon \to \bar{B}B$, (2) $\rho\Upsilon \to \bar{B}^*B$, and (3) $\rho\Upsilon \to \bar{B}^*B^*$.

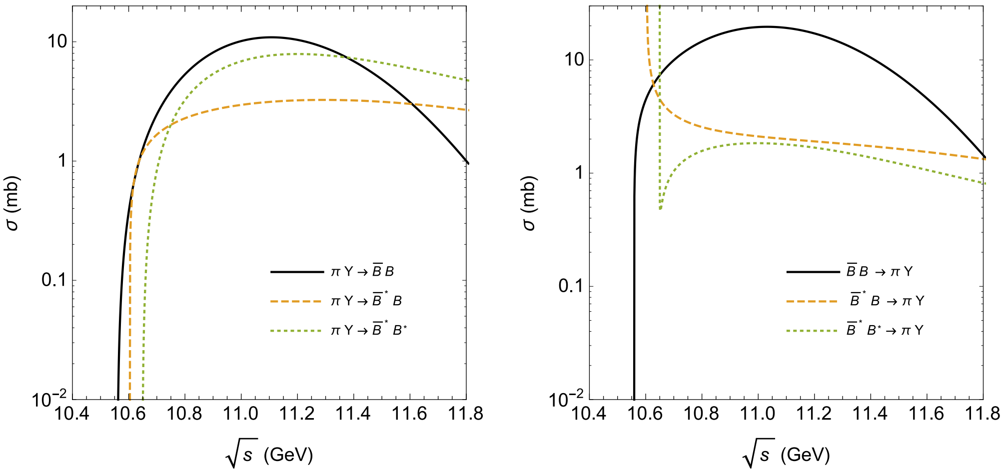

Figure 8. Υ absorption and production cross sections in different processes as a function of the CM energy $\sqrt{s}$. Left panel: $\pi\Upsilon$ in the initial state. Solid, dashed and dotted lines represent the $\pi\Upsilon \to \bar{B}B$, $\pi\Upsilon \to \bar{B}^*B$ and $\pi\Upsilon \to \bar{B}^*B^*$ reactions, respectively. Right panel: $\pi\Upsilon$ in the final state. Solid, dashed and dotted lines represent the $\bar{B}B \to \pi\Upsilon$, $\bar{B}^*B \to \pi\Upsilon$ and $\bar{B}^*B^* \to \pi\Upsilon$ reactions, respectively.

bottomonium states are lost in the hadronic medium at LHC. Also, it can be noticed, from Eq. (11), that the evolution of the Υ multiplicity depends on the production and absorption cross sections and also on the abundances of the other mesons. Although the production cross sections are greater than the absorption ones, which would enhance the Υ yield, the relative meson multiplicities lead to its reduction, since there are much more light mesons (especially pions) in the hadron gas to collide and destroy the bottomonium states than $B^{(*)}$'s and $\bar{B}^{(*)}$'s

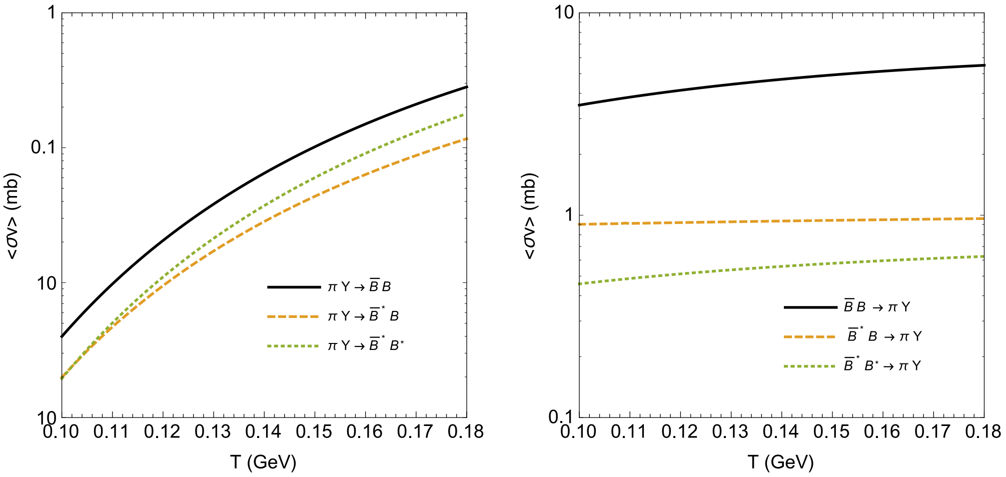

Figure 9. Thermally averaged cross sections for $\pi\Upsilon$ absorption and production as a function of the temperature. Left panel: $\pi\Upsilon$ in the initial state. Right panel: $\pi\Upsilon$ in the final state. Solid, dashed and dotted lines represent the reactions with $\bar{B}B$, $\bar{B}^{*}B$ and $\bar{B}^{*}B^{*}$, respectively, in final or initial state.

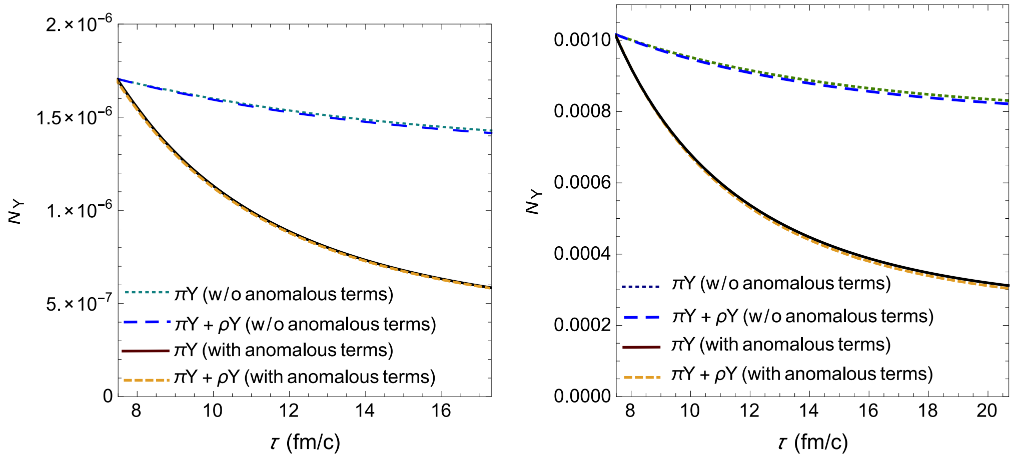

Figure 10. Left: Time evolution of Υ abundance as a function of the proper time in central Au-Au collisions at $\sqrt{s_{NN}} = 200$ GeV. Solid and dashed lines represent the situations with only $\pi - \Upsilon$ interactions and also adding the $\rho - \Upsilon$, respectively. Upper (lower) curves are calculated without (with) the anomalous interactions. Right: the same as on the left for LHC conditions.

to interact and create them. Besides, from the solid and dotted lines in Fig. 10 we can infer that the role of the ρ mesons in the gas is not relevant when compared to that of the pions. This comes from a cancellation between the terms associated to the production and absorption reactions: the different magnitudes of production and absorption processes are compensated by the relative multiplicities. Moreover we can see how important are the anomalous interactions. In both pannels, when we include them the upper curves move to the lower curves and the suppression increases by a factor $\simeq 3$.

The results shown in Fig. 10 suggest a decrease of the Υ yield of almost $\simeq 66$ % at RHIC and $\simeq 70$ % at the LHC. These numbers are compatible with (15). Taken literally, they would suggest that all the suppression comes from the hadron gas phase. However we are not yet in the position of sustaining this strong statement. Before that, there is a number of points to be discussed. First the interactions in the reactions are naturally dependent on the effective formalism considered, which determines the magnitudes of the cross sections. A change in the magnitude of the production reactions will modify those of the absorption in the same proportion. This will lead to an overall multiplicative factor in the right hand side of rate equation, Eq. (11), modifying the curves in Fig. 10. Besides, our results are strongly dependent on the form factors and cutoff values: different choices would modify the slope of the curves in Fig. 10. Furthermore, the relevance of the parametrization of the hydrodynamical expansion exhibited in Eq. (13) can not be underestimated. Different parameters can make the system cool faster or slower and accordingly change the multiplicities of the distinct particles.

Notwithstanding the points raised above, we stress the main result: a reduction of the number of Υ's in the hadron gas, which seems to be larger than in the case of J/ψ reported in Ref. [40]. Before closing this section, we show in Fig. 11 a comparison between the Υ and J/ψ multiplicities as a function of the proper time. For the sake of comparison we have rescaled them to the unity at the initial time. The J/ψ suppression is only of $\simeq 25$ %, whereas it is of $\simeq 70$ % in the case of the Υ.

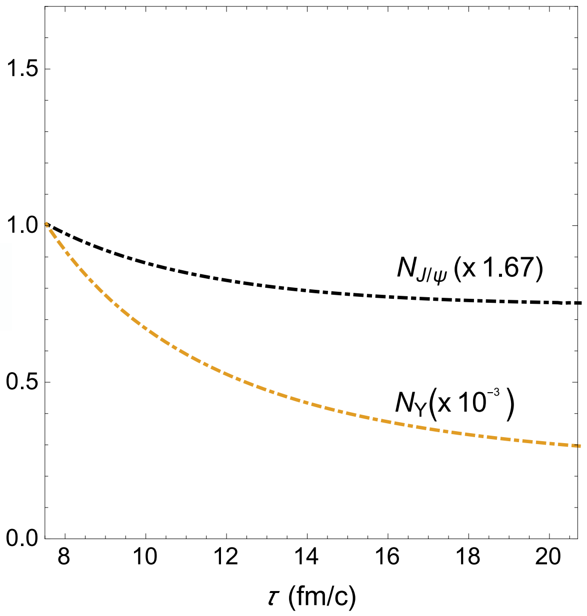

Figure 11. Time evolution of J/ψ (upper line) and Υ (lower line) abundances as a function of the proper time in central Pb-Pb collisions at the LHC.

7. Conclusions

Precise measurements of J/ψ abundancies in heavy ion collisions are an important source of information about the properties of the quark-gluon plasma phase. During this phase J/ψ is produced by recombination of charm-anticharm pairs. However, after hadronization the J/ψ's interact with other hadrons in the expanding hadronic matter. Therefore, the J/ψ's can be destroyed in collisions with other comoving mesons, but they can also be produced through the inverse reactions. In order to evaluate the hadronic effects on the J/ψ abundance in heavy ion collisions one needs to know the J/ψ cross sections with other mesons.

We have studied J/ψ dissociation and production reactions, making use of effective field Lagrangians to obtain the cross sections for the processes $(\pi, \rho, K, K^*) + J/\psi \rightarrow D_{(s)}\bar{D}, D^{(*)}_{(s)}\bar{D}, D_{(s)}\bar{D}^{(*)}, D^*_{(s)}\bar{D}^*$ and the corresponding inverse processes. We have then computed the thermally averaged cross sections for the dissociation and production reactions, the latter being larger. Finally, we have used the thermally averaged cross sections as input in a rate equation and have followed the evolution of the J/ψ abundance in a hadron gas.

With respect to the existing calculations, the improvements introduced in [8] are the inclusion of K and K^*'s in the effective Lagrangian approach (and the computation of the corresponding cross sections) and the inclusion of processes involving the new exotic charmonium states $Z_c(3900)$ and $Z_c(4025)$.

We conclude that the interactions between J/ψ and all the considered mesons reduce the original J/ψ abundance (determined at the end of the quark gluon plasma phase) by 20 % and 24 % in RHIC and LHC collisions respectively. Consequently, any really significant change in the J/ψ abundance comes from dissociation and regeneration processes in the QGP phase.

We have also discussed here the hadronic effects on the Υ abundance in heavy ion collisions. Effective Lagrangians have been used to calculate the cross sections for the Υ-production processes $\bar{B}^{(*)} + B^{(*)} \rightarrow \Upsilon + (\pi, \rho)$, and also for the corresponding inverse processes associated to the Υ absorption. We have also computed the thermally averaged cross sections for the dissociation and production reactions. Finally, we have employed the thermally averaged cross sections as inputs in the rate equation and have determined the time evolution of the Υ abundance in a hadron gas. In Ref. [39] we introduced the following improvements: inclusion of reactions which start or end with $\bar{B}B$ and $\bar{B}^*B^*$ in the case of the pion-Υ scattering, and $\bar{B}^*B$ in that involving ρ meson; inclusion of the anomalous parity interactions processes in the effective Lagrangian approach.

Our results suggest that the interactions between Υ and light mesons reduce the Υ abundance at the end of the quark gluon plasma phase by $\simeq 70$ %, which is more than in the case of the J/ψ reported in Ref. [40].

In conclusion, despite the fact that there are points to be improved to obtain a more realist description of the HIC phenomenology, we believe that our findings are important for the physics of both the quark gluon plasma and hadronic phases. Our result should encourage further studies of the Υ suppression in the hadron gas phase of relativistic heavy ion collisions.

8. Acknowledgments

This work was partially supported by FAPESP and CNPq.

9. References

[1] Adams J *et al.* 2005 *Nucl. Phys.* **A757** 102 ; Aarts G *et al.* 2017 *Eur. Phys. J.* **A53**, 93
[2] For a recent review, see Braun-Munzinger P, Koch V, Schafer T and J. Stachel 2016 *Phys. Rept.* **621** 76
[3] Matsui T and Satz H 1986 *Phys. Lett.* **B178** 416
[4] Thews R L, Schroedter M and Rafelski J 2001 *Phys. Rev.* **C63** 054905; Braun-Munzinger P and Stachel J 2000 *Phys. Lett.* **B490**, 196
[5] Matinyan S G and B. Müller B 1998 *Phys. Rev.* **C58** 2994
[6] Oh Y, Song T and Lee S H 2001 *Phys. Rev.* **C63** 034901
[7] Lin Z and Ko C M 2001 *Phys. Lett.* **B503** 104

[8] Abreu L M, Khemchandani K P, Martinez Torres A, Navarra F S and Nielsen M 2018 *Phys. Rev.* **C97** 044902
[9] Azevedo R S and Nielsen M 2004 *Phys. Rev.* **C69** 035201; Azevedo R S and Nielsen M 2004 *Braz. J. Phys.* **34** 272
[10] Azevedo R S and Nielsen M (*Preprint* nucl-th/0407080)
[11] Bracco M E, Chiapparini M, Navarra F S and Nielsen M 2012 *Prog. Part. Nucl. Phys.* **67** 1019; Osorio Rodrigues B, Bracco M E, Nielsen M and Navarra F S 2011 *Nucl. Phys.* **A852** 127; Bracco M E, Chiapparini M, Navarra F S and Nielsen M 2008 *Phys. Lett.* **B659** 559; Bracco M E, Chiapparini M, Navarra F S and Nielsen M 2005 *Phys. Lett.* **B605** 326; Navarra F S, Nielsen M and Bracco M E 2002 *Phys. Rev.* **D65** 037502 ; Navarra F S, Nielsen M, Bracco M E, Chiapparini M and Schat C L 2000 *Phys. Lett.* **B489** 319; Bracco M E, Chiapparini M, Lozea A, Navarra F S and M. Nielsen 2001 *Phys. Lett.* **B521** 1; Bracco M E, Navarra F S and M. Nielsen 1999 *Phys. Lett.* **B454** 346
[12] Duraes F O, Kim H c, Lee S H, Navarra F S and Nielsen M 2003 *Phys. Rev.* **C68** 035208; Duraes F O, Lee S H, Navarra F S and Nielsen M 2003 *Phys. Lett.* **B564** 97; Navarra F S, Nielsen M, Marques R S de Carvalho and Krein G 2002 *Phys. Lett.* **B529** 87
[13] For a review on charged exotic charmonium states, see Nielsen M and Navarra F S 2014 *Mod. Phys. Lett.* **A29** 1430005
[14] For a very recent review, see Albuquerque R M, Dias J M, Khemchandani K P, Martinez Torres A, Navarra F S, Nielsen M and Zanetti C (*Preprint* arXiv:1812.08207)
[15] Cho S *et al.* 2011 *Phys. Rev.* **C84** 064910
[16] Cho S *et al.* 2017 *Prog. Part. Nucl. Phys.* **95** 279
[17] Cho S *et al.* 2011 *Phys. Rev. Lett.* **106** 212001
[18] Cho S and Lee S H 2018 *Phys. Rev.* **C97** 034908
[19] Chen L W, Ko C M, Liu W and M. Nielsen 2007 *Phys. Rev.* **C76** 014906
[20] Cho S and Lee S H 2013 *Phys. Rev.* **C88** 054901
[21] Aarts G *et al.*, 2017 *Eur. Phys. J.* **A53** 93
[22] Du X, Rapp R and He M 2017 *Phys. Rev.* **C96** 054901
[23] Andronic A, Braun-Munzinger P, Redlich K and Stachel J 2007 *Phys. Lett.* **B652**, 259; Gorenstein M I, Kostyuk A P, Stoecker H and Greiner W 2001 *Phys. Lett.* **B509** 277
[24] Liu Y et al. 2011 *Phys. Lett.* **B697** 32; Zhou K, Xu N and Zhuang P 2014 *Nucl. Phys.* **A931** 654
[25] Emerick A, Zhao X and Rapp R 2012 *Eur. Phys. J.* **A48** 72
[26] Krouppa B and Strickland M 2016 *Universe* **2** 16
[27] Krouppa B, Ryblewski R and Strickland M 2015 *Phys. Rev.* **C92** 061901
[28] Hu Z, Leonardo N T, Liu T and Haytmyradov M 2017 *Int. J. Mod. Phys.* **A32** 1730015
[29] Chatrchyan S et al. 2011 *Phys. Rev. Lett.* **107** 052302; Hu Z 2011 *J. Phys.* **G38** 124071; Chatrchyan S et al. 2012 *J. High Energy Phys.* **05** 063
[30] Adamczyk L et al. 2014 *Phys. Lett.* **B735** 127; Erratum: 2015 *Phys. Lett.* **B743** 537
[31] Khachatryan V *et al.* 2017 *Eur. Phys. J.* **C77** 252
[32] A. M. Sirunyan et al. 2019 *Phys. Lett.* **B790** 270
[33] Khachatryan V et al. 2017 *Phys. Lett.* **B770** 357
[34] Khachatryan V et al. 2017 *Phys. Lett.* **B764** 031
[35] Shapoval V M, Braun-Munzinger P and Sinyukov Y M 2017 *Nucl. Phys.* **A968** 391
[36] Adam J et al. 2017 *Phys. Rev.* **C95** 064606
[37] Abelev B B et al. 2015 *Phys. Rev.* **C91** 024609
[38] Riabov V G et al. 2017 *J. Phys. Conf. Ser.* **798** 012054; Markert C et al. 2017 *J. Phys. Conf. Ser.* **878** 012003
[39] Abreu L M, Navarra F S and Nielsen M 2018 *Preprint* arXiv:1807.05081
[40] Abreu L M, Khemchandani K P, Martínez Torres A , Navarra F S and Nielsen M 2018 *Phys. Rev.* **C97** 044902
[41] Matinyan S G and Müller B 1998 *Phys. Rev.* **C58** 2994; Bourque A and Gale C 2009 *Phys. Rev.* **C80** 015204; Bourque A and Gale C 2008 *Phys. Rev.* **C78** 035206; Bourque A, Gale C and Haglin K L 2004 *Phys. Rev.* **C70** 055203; Lin Z and Ko C M 2000 *Phys. Rev.* **C62** 034903; Lin Z and Ko C M 2001 *J. Phys.* **G27** 617; Navarra F S, Nielsen M and Robilotta M R 2001 *Phys. Rev.* **C64** 021901; Haglin K L and Gale C 2001 *Phys. Rev.* **C63** 065201; Haglin K L 2000 *Phys. Rev.* **C61** 031902; Carvalho F, Duraes F O, Navarra F S and Nielsen M 2005 *Phys. Rev.* **C72** 024902
[42] Khemchandani K P, Martinez Torres A, Nielsen M and Navarra F S 2014 *Phys. Rev.* **D89** 014029
[43] Ferreiro E G and Lansberg J P 2018 *JHEP* **1810** 094

Proton- and neutron-halo breakups: Similarities and differences

B Mukeru[1,2]

[1]Department of Physics, University of South Africa, P.O. Box 392, Pretoria 0003, South Africa
[2]Instituto de Física Teórica, Universidade Estadual Paulista, Rua Dr. Bento T. Ferraz 271, 01140-70, São Paulo, Brazil

E-mail: `mukerb1@unisa.ac.za`

Abstract. It is shown in this paper that the decrease of the projectile ground state binding energy in a neutron-halo nucleus and the removal of the Coulomb barrier in the proton-halo nucleus, produce a similar qualitative effect on the elastic scattering cross sections. The variation of the binding energy produces opposite effects on elastic scattering and breakup cross sections. A strongly destructive Coulomb-nuclear interference owing to the decrease of the binding energy is also obtained.

1. Introduction

Despite the tremendous progress in tackling nuclear reactions induced halo and other loosely bound nuclei over the past decades [1, 2, 3, 4, 5, 6, 7], there still a number of issues that need to be addressed and new data are revealing new phenomena. Among the outstanding issues, one mentions the dynamic difference between the breakups of proton-halo and neutron-halo nuclei and their influence on other reaction channels, such as elastic scattering, fusion, among others. It is not fully understood how the absence of the core-neutron Coulomb interaction affects the breakup dynamics. There have been efforts to address this question [8, 10, 12, 13]. For example, the difference in the elastic scattering cross sections of ^{8}B and ^{11}Be induced reactions was attributed to the Coulomb and centrifugal barriers in ^{8}B [8, 9]. It was shown in these works that the removal of the Coulomb barrier greatly improves the disagreement between the different elastic scattering cross sections, despite the fact that the ground state binding energies of this two nuclei are significantly different. Similar results were reported in [10], where a strong suppression of the neutron-halo elastic scattering cross sections was obtained in the $^{7}\mathrm{Be}+p$ and $^{7}\mathrm{Be}+n$ reactions on the lead. On the other hand, in [11], where the same $^{7}\mathrm{Be}+p$ and $^{7}\mathrm{Be}+n$ reactions on a Nickel target were analyzed, it was shown that the neutron-halo breakup cross section is larger than its proton-halo counterpart, especially when the same binding energy was considered. The disagreement between the two breakup cross sections was significantly improved by increasing the $^{7}\mathrm{Be}+n$ binding energy. A conclusion that was also drawn in [12, 13]. This amounts to saying that the absence of the Coulomb barrier in the core-neutron potential can be, to some extend, compensated by the increase of its ground state binding energy. Intuitively, one would expect the opposite in the elastic scattering case. That is, the effect obtained in [8] by removing the Coulomb barrier in the proton-halo breakup, can also be obtained in the neutron-halo breakup by decreasing the ground state binding energy. One of the aims of this paper is to investigate this aspect.

Another important aspect as far as breakup reactions induced by loosely bound projectiles are concerned, is the importance of the Coulomb-nuclear interference. We recently analyzed its dependence on the proton-and neutron-halo ground state binding energies [11], and showed that when these energies increase, the Coulomb-nuclear interference is substantially reduced. However, this study was restricted to a single incident energy around the Coulomb barrier. It is interesting to investigate whether this conclusion holds for other reactions, as well as its dependence on the incident energy. In this paper, we analyze the breakup of ^{8}Li on the lead at incident energies below, around and well above the barrier. On one hand, we are particularly interested in verifying whether the decrease of the ground state binding energy in this neutron-halo nucleus can produce a similar effect as the removal of the Coulomb barrier in the ^{8}B proton-halo nucleus. Such study is crucial as it will further highlight the similarities and differences in the proton-halo and neutron-halo breakups. On the other hand, study the dependence the Coulomb-nuclear interference on ground state binding energy, considering a range of incident energy in an effort to extend the conclusion drawn in [11], and test its universality in breakup reactions induced by loosely bound projectiles. To this end, we consider five different ground state binding energies, which are obtained by adjusting the depth of the central part the Woods-Saxon $^7\text{Li} + n$ potential. The choice of ^{8}Li is motivated, on one have by the fact that it has the same ground state quantum numbers as ^{8}B, meaning that the only structural difference is the Coulomb barrier. On the other hand, the study of this nucleus has revealed unusual behavior [17, 18]. To obtain the elastic scattering and breakup cross sections, the three-body Schrödinger equation is first transformed into coupled differential equations by means of the continuum discretized coupled-channels (CDCC) method [19]. The latter are numerically solved using Fresco computer codes [20]

2. Results and Discussion

The projectile ^{8}Li modeled as $^7\text{Li} + n$, has a ground state binding energy of $\varepsilon_0 = 2.03\,\text{MeV}$, with $j^\pi = 2^+$, and a first excited state of $\varepsilon_{\text{ex}} = 0.88\,\text{MeV}$, with $j^\pi = 1^+$ [14]. The bound and continuum wave functions are obtained using a Woods-Saxon potential whose parameters were taken from [14]. The depth (V_0) of the central component was adjusted to give the ground and bound excited energies. On the other hand, both the depths of the central and spin-orbit

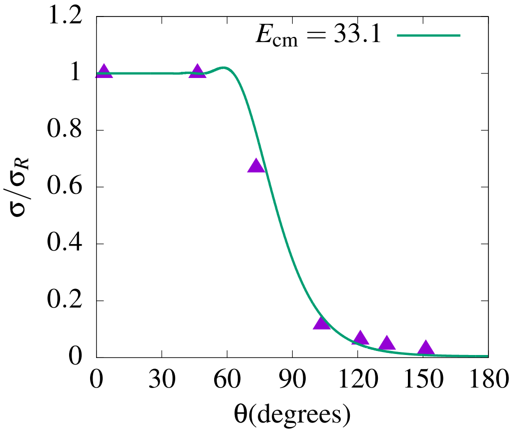

Figure 1. Elastic scattering cross section. The data points were taken from [21]

(V_{SO}) components were adjusted to obtain the other different ground state binding energies

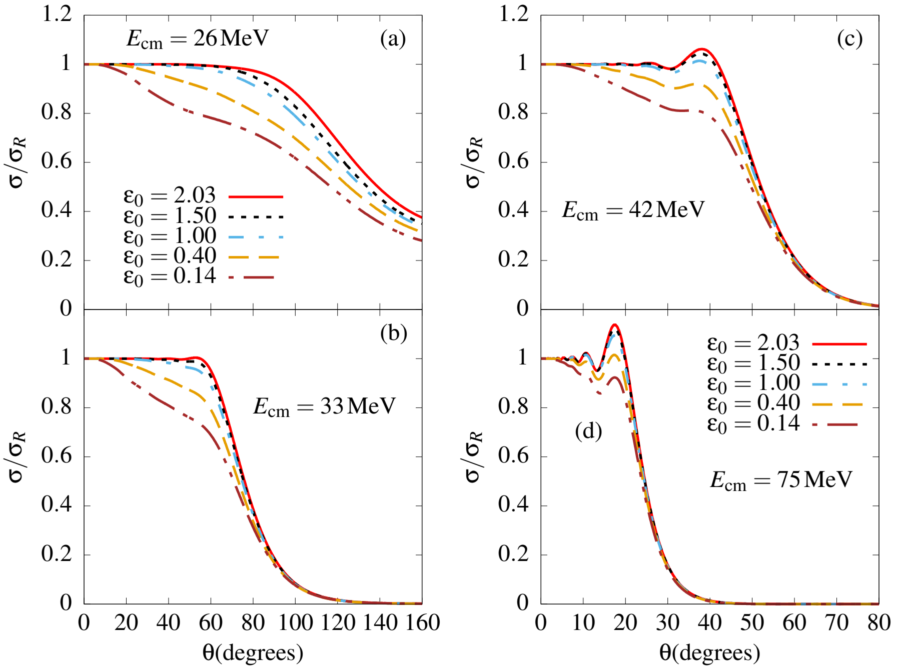

Figure 2. Elastic scattering cross sections for different ground state binding and incident energies.

(0.14 MeV, 0.40 MeV, 1.0 MeV, 1.50 MeV, randomly selected) well as the corresponding bound and continuum wave functions. The ^{7}Li global parametrization of [15], was used to obtain the core-target optical potential parameters. A slight adjustment of the depth of the real part results in a satisfactory fit the experimental data (see Fig.1). The $n+^{208}$Pb optical potential parameters were taken from [16]. The other various integration parameters were chosen in accordance with the convergence requirement.

The elastic scattering cross sections for $0.14\,\text{MeV} \leq \varepsilon_0 \leq 2.03\,\text{MeV}$ are presented in Fig.2, for incident energies below, around and well above the Coulomb barrier. Firstly, one notices that indeed, the elastic scattering cross sections are suppressed as the ground state binding energy decreases. Specifically, this suppression becomes substantial for binding energies below 1 MeV and $E_{\rm cm} \leq 42\,$MeV. A closer look at Fig.2(d), indicates that the position of the Coulomb rainbow is not affected by the variation of the binding energy. Taking a look at Fig. 4(b) of [9], it is also noticed that the position of the Coulomb rainbow is not affected by the removal of the Coulomb barrier in the ^{8}B nucleus. Therefore, one may conclude that the removal of the Coulomb barrier in the ^{8}B nucleus and the decrease of the binding energy in the ^{8}Li nucleus produce a similar qualitative effect in the elastic scattering cross sections. Furthermore, one may suggest that the lack of a Coulomb barrier in the neutron-halo nucleus can be compensated by the decrease of its binding energy. Given the fact that the breakup cross section increases with the decrease of the projectile ground state binding energy, these results reveal that a variation of the binding energy produces opposite effects on the elastic scattering and breakup cross sections.

To generalize the conclusion of [11], regarding the dependence of the Coulomb-nuclear interference on ground state binding energy, this interference is plotted in Fig.3, for the different ground state binding energies and incident energy of $E_{\rm cm} = 26\,$MeV [Fig.3 (a)] and

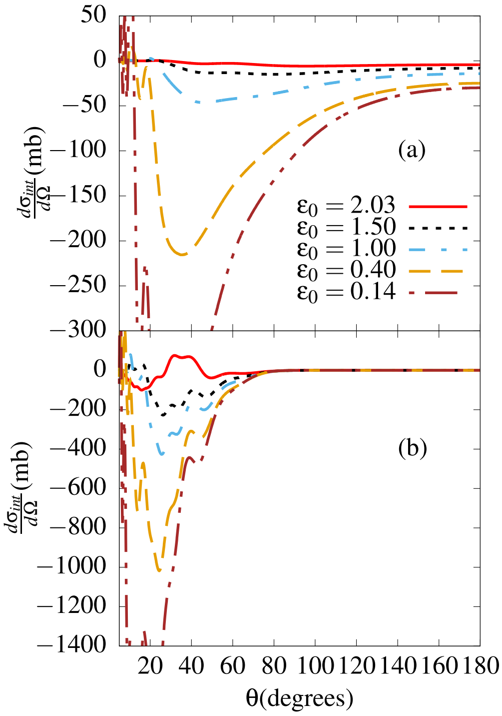

Figure 3. Coulomb-nuclear interferences for different ground state binding energies.

$E_{\rm cm} = 75\,\rm MeV$ [Fig.3 (b)]. It is calculated as follows

$$\frac{d\sigma_{\rm int}}{d\Omega} = \frac{d\sigma_{\rm tot}}{d\Omega} - \left(\frac{d\sigma_{\rm Coul}}{d\Omega} + \frac{d\sigma_{\rm nucl}}{d\Omega}\right), \tag{1}$$

where $\sigma_{\rm tot}$, $\sigma_{\rm Coul}$ and $\sigma_{\rm nucl}$ are total, Coulomb and nuclear breakup cross sections, respectively. This figure clearly shows that the Coulomb-nuclear interference is strongly enhanced and destructive as the binding energy decreases, in line with the findings of [11]. For a better analysis of Fig.3, the integrated Coulomb-nuclear interference is plotted in Fig.4, as function of the incident energy. One clearly notices in this figure that this interference is exclusively destructive where the destructiveness is strengthened with the decrease of the binding energy. These results depict a clear picture of some dynamic differences between the breakups of loosely bound and tightly bound projectiles, as far as the Coulomb-nuclear interference is concerned. In the latter case, one would expect this interference to either weaker or insignificant.

Even though Fig.4 displays unambiguously the dependence of Coulomb-nuclear interference on ε_0, it does not reveals where does this strong destructiveness come from. Based of the assessment in [11], one can attribute this to the fact that the Coulomb breakup cross section grows quickly with lowering of ε_0 that both total and nuclear breakup cross sections, such that $\sigma_{\rm tot} - (\sigma_{\rm Coul} + \sigma_{\rm nucl}) \ll 0$ as ε_0 decreases. To picture this, we define the ratios

$$\beta = \frac{\sigma_{\rm Coul} - \sigma_{\rm nucl}}{\sigma_{\rm Coul}} \tag{2}$$

$$\gamma = \frac{\sigma_{\rm Coul} - \sigma_{\rm tot}}{\sigma_{\rm Coul}}. \tag{3}$$

They are displayed inf Figs.5(a) and (b), respectively. Inspecting Fig.5(a), it is noticed that $0.93 \leq \beta \leq 0.97$. In other words, $\sigma_{\rm Coul} - \sigma_{\rm nucl} \to \sigma_{\rm Coul}$ as ε_0 decreases. Also, Fig.5(b) indicates

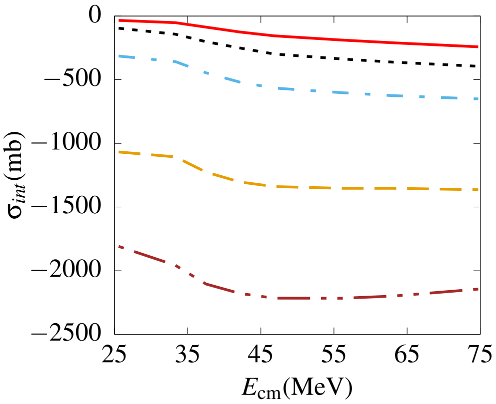

Figure 4. Integrated Coulomb-nuclear interferences for different ground state binding and incident energies.

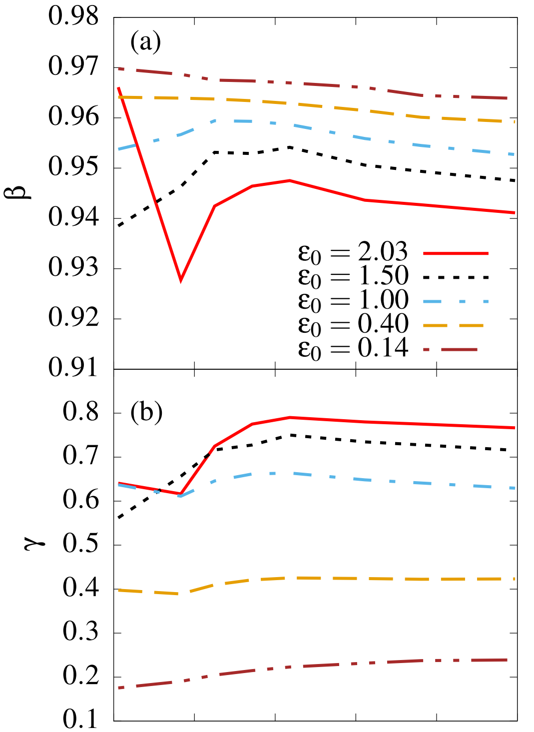

Figure 5. Ratios of Coulomb and nuclear breakup cross sections (a) and total breakup cross sections (b), as explained in the text.

that $0.1 \leq \gamma \leq 0.8$, meaning that $\sigma_{\rm Coul} \geq \sigma_{\rm tot}$. Therefore, this results in a destructive Coulomb-nuclear interference.

3. Summary

Analyzing the ^{8}Li+^{208}Pb reaction, we have shown in this paper that the decrease of the projectile ground state binding energy in a neutron-halo nucleus and the removal of the Coulomb barrier in the proton-halo nucleus, produce a similar qualitative effect on the elastic scattering cross sections. The variation of the binding energy produces opposite effects on elastic scattering and breakup cross sections. A strongly destructive Coulomb-nuclear interference owing to the decrease of the binding energy is also obtained. This might be a general feature in reactions induced by loosely bound nuclei.

Acknowledgment

I would like to thank FAPESPgrant 2016/01343-7 for financial support during my visit to ICTP-SAIFR in September 2018 where part of this work was done.

References

[1] Tanihata I, Savajols H and Kanungo R 2013 Prog. Part. Nucl. Phys. **68** 21
[2] Dasgupta M *et al* 2004 Phys. Rev. **C 70** 024606
[3] Mukeru B and Lekala M L 2015 Phys. Rev. **C 91** 064609
[4] Hussein M S, Lichtenthaler R, Nunes F M and Thompson I J 2006 Phys. Lett. **B 640** 91
[5] Ogata K *et al* 2013 Phys. Rev. **C 88** 024616
[6] Canto L F, Gomes P R S, Donangelo R, Lubian J, and Hussein M S 2015 Phys. Rep. **596**, 1
[7] Parkar V V *e*t al 2016 Phys. Rev. **C 94**, 024609.
[8] Yang Y Y, Liu X and Pang D Y 2016 Phys. Rev. **C 94** 034614
[9] Yang Y Y *et al* 2018 Phys. Rev. **C 98** 044608
[10] Rangel J, Lubian J, Canto L F and Gomes P R S 2016 Phys. Rev. **C 93** 054610
[11] Mukeru B 2018 J. Phys. G: Nucl. Part. Phys. **45** 065201 (15pp)
[12] Kumar R and Bonaccorso A 2011 Phys. Rev. **C 84** 014613
[13] Kucuk Y and Moro A M 2012 Phys. Rev. **C 86** 034601
[14] A. M. Moro *et al* 2003 Phys. Rev. **C 68** 034614
[15] Cook J 1982 Nucl. Phys. **A 388** 153-172.
[16] Mukeru B, Lekala M L and Denikin A S 2015 Nucl. Phys. **A 935** 1827
[17] Cook K J *et al* 2018 Phys. Rev. **C 97** 021601(R)
[18] Pakou A *et al* 2015 Eur. Phys. J. A **51** 55
[19] N. Austern *et al.*, Phys. Rep. **154** (1987) 125.
[20] www.fresco.org.uk.
[21] http://nrv.jinr.ru/nrv/

The role of nucleon knockout in pre-equilibrium reactions

E V Chimanski^{1,2}**, B V Carlson**^{1}**, R Capote**^{2}**, A J Koning**^{2}
^{1}Aeronautics Institute of Technology, São José dos Campos, Brazil
^{2}NAPC-Nuclear Data Section, International Atomic Energy Agency, Vienna, Austria

E-mail: `brett@ita.br`

Abstract. Nucleon-induced pre-equilibrium reactions are predominantly direct reactions. At low incident energies, excitation of all but the lowest energy collective states can be well described in terms of one-step reactions that produce particle-hole pairs. As the incident energy increases, the probability of exciting a nucleon to the continuum rather than to a bound particle state also increases. These knockout nucleons can escape the nucleus or induce secondary collisions that create still other continuum or bound particle-hole pairs. We discuss their role in pre-compound nuclear reactions here, first in a semiclassical Monte Carlo description of the reaction and then in a quantum one-step calculation.

1. Introduction

Above an incident energy of about 20 MeV, nucleon-induced pre-equilibrium reactions are dominated by direct reactions. Excitation of all but the lowest energy collective states can be well described in terms of one-step reactions that produce particle-hole pairs for smaller incident energies in this range. As the incident energy is increased, more complex excitations involving two or more particle-hole pairs become accessible through multi-step reactions. Quantum mechanical models of such multi-step direct reactions were developed many years ago [1, 2, 3] and have been studied and improved many times over since then [4, 5, 6, 7]. In these models, a leading continuum particle initiates the reaction and remains in the continuum as it scatters repeatedly from the nucleus to produce successive particle-hole pairs. However, as the incident energy increases, the probability of exciting a nucleon to the continuum rather than to a bound particle state also increases [8]. These knockout nucleons can escape the nucleus or induce secondary collisions that create still other continuum or bound particle-hole pairs. They are not taken into account in the MSD models developed until now.

The calculation of knockout to the continuum is a relatively straightforward extension of actual MSD calculations. However, here we would like to obtain a more general idea of the importance of this mechanism in pre-equilibrium reactions. This would require an extension of the existing MSD models codes to an arbitrary number of interactions leading to both bound and continuum configurations. As this is unfeasible, we will make use of the semiclassical DDHMS pre-equilibrium simulation model of Blann and Chadwick [9, 10]. As well as being the most conceptually sound semiclassical model, it is also the closest in correspondence to the quantum mechanical MSD models.

As a first step toward a quantum MSD calculation of excitation to continuum states, we also perform simple one-step DWBA calculations of the same knockout reactions studied using the semiclassical DDHMS simulations and compare the two. Although the two furnish results that are to a large extent quite similar, we also find puzzling differences between the two that we have not yet been able to explain.

We note that most of the semiclassical results analyzed here have been discussed previously in Ref. [11].

2. Method

An important characteristic of nucleon-induced pre-equilibrium reactions is that their early stages are dominated by collisions that increase the number of particle-hole pairs [12, 3]. This implies that the equal occupation of states with the same particle-hole number, assumed in the semiclassical exciton and hybrid models, is not justified. This limits their applicability to low energies, for which configurations above the two particle - one hole one are not extremely important.

As an alternative, Blann proposed the "hybrid Monte Carlo simulation" (HMS) model [9], in which a sequence of independent particle-hole pairs is excited during a reaction. Each excited particle and hole is considered an independent degree of freedom. Particles can be emitted and particles and holes with sufficient energy can create subsequent particle-hole pairs. Emission occurs in accord with the particle emission widths and excitation in accord with the particle and hole damping widths. At each step of the Monte Carlo simulation, an emission or particle-hole excitation is chosen based on the relative weight of the widths. The process continues until no particle or hole possesses sufficient energy to be emitted or to excite another particle-hole pair. Blann and Chadwick later extended the model to the DDHMS one, which calculates angular distributions as well as spectra [10].

While the equal occupation assumption of the exciton and hybrid models requires a strong residual interaction between states with the same particle-hole number, the independent particle and hole modes of the HMS model require that there be no residual interaction at all. Comparisons with complete simulations performed using an interaction consistent with the shell model show the HMS model to provide excellent agreement with the more complete calculations while the exciton model does not[13].

Since all active particles and holes can be followed in an HMS calculation, we can tag them according to the number of collisions that have occurred. Collision 1 is induced by the incident particle and initially labels this particle as well as the particle-hole pair it produces. Collision 2 is induced by one of these three and labels it as well as the particle-hole pair produced. The labelling continues for higher collision numbers.

The average number of collisions before formation of a residual compound nucleus is quite small on the average, as can be seen in Fig. 1, where, for a proton incident on ^{58}Ni, it increases from a value of about two at 10 MeV to about four at 200 MeV. The standard deviation also grows slowly, from a value of about one at 10 MeV to about three at 200 MeV. Interestingly, the difference between the average value and the standard deviation appears to be fixed at a value of one at all energies. In contrast, the maximum number of collisions before compound nucleus formation grows approximately linearly with the energy and reaches a value close to 50 at 200 MeV.

We label the emited particles according to their collision numbers as follows:

- **inel** - particles emitted after one collision in which the second particle is in a bound state;
- **ko** - particles emitted after one collision in which the second particle is also emitted;
- **1** - particles emitted after on collision independently of hat happens to the collision partner;

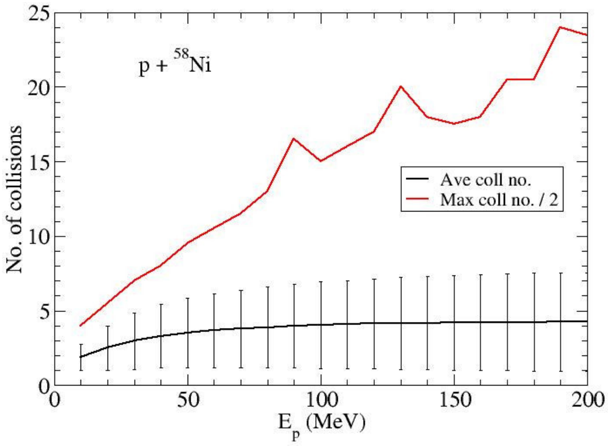

Figure 1. Average and total number of collisions before compound nucleus formation for the collision p + ^{58}Ni

- **2** - particles emitted after two collisions (although the second collision might be the emitted particles first collision) independently of what happens to the collision partner;
- **all** - particles emitted after any number of collisions.

The particles labelled **inel** correspond most closely to the leading particle of a usual one-step MSD reaction. In all cases, the residual nucleus might still emit other particles.

3. Semiclassical Calculations

To relate our calculations to experimental data, we compare our inclusive proton and neutron emission spectra for 90 MeV proton-induced reactions with the data of Refs. [14] and [15]. Our calculations were obtained using the HMS module in the EMPIRE-3 neutron reaction code [16]. All pre-equilibrium and compound nucleus emission has been taken into account. The quasi-elastic peak has not been included.

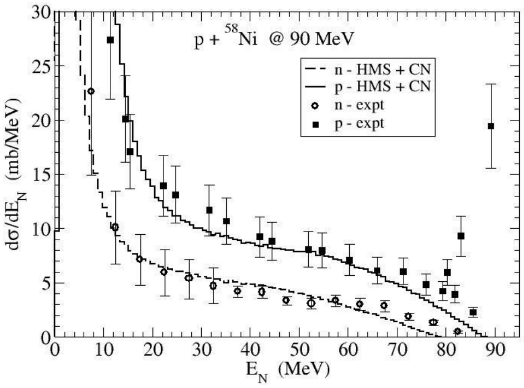

Figure 2. Calculated inclusive neutron and proton emission spectra compared with the experimental data of Refs. [14] and [15] for the collision p + ^{58}Ni.

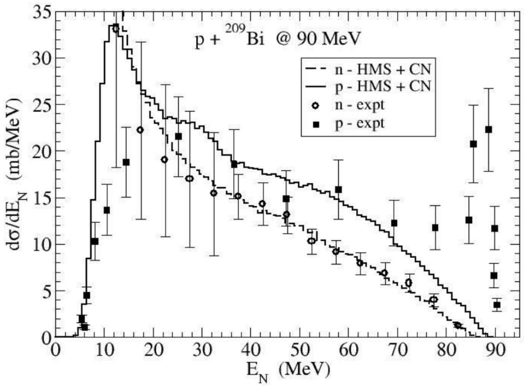

Figure 3. Calculated inclusive neutron and proton emission spectra compared with the experimental data of Refs. [14] and [15] for the collision p + ^{209}Bi.

In Figs. 2 and 3, we display the calculated inclusive emission spectra for ^{58}Ni and ^{209}Bi together with the experimental data. The agreement between the two is quite good, except for the lower energy proton emission from ^{209}Bi, which is overestimated by the calculations.

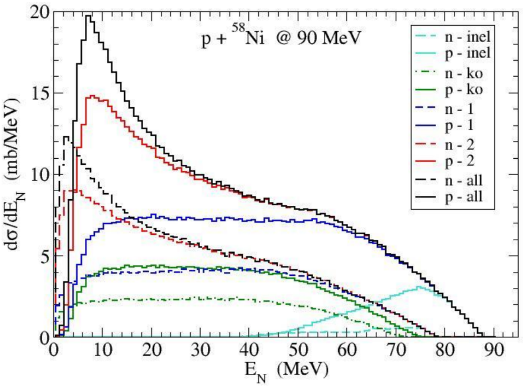

Figure 4. Contributions to the inclusive nucleon emission cross sections from the collision p + ^{56}Ni.

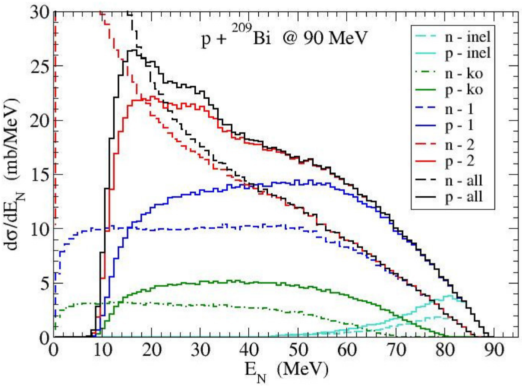

Figure 5. Contributions to the inclusive nucleon emission cross sections from the collision p + ^{209}Bi.

In Figs. 4 and 5, we show the decomposition of the inclusive emission cross spectra for ^{58}Ni and ^{209}Bi into their inelastic (inel), knockout (ko), first collision (1) and second collision (2) components. We observe that the emissions resulting in inelastic excitation exhaust the emission spectra for only a small range of about 10 MeV of the most energetic emissions. They then fall slowly, reaching zero at an energy corresponding to an excitation of the residual nucleus of about 50 MeV. Each of the first emission spectra minus the corresponding inelastic spectrum increases roughly in parallel with the corresponding knockout spectrum as the emission energy is reduced from its maximum value. The first emission and knockout spectra saturate at an energy corresponding to an excitation of the residual nucleus of about 25 to 30 MeV and remain flat until decreasing to zero at the Coulomb barrier for protons and at zero energy for neutrons. Finally, we observe that the particles emitted after at most two collisions (2) exhaust the spectra except at very low excitation energies. As we have seen in Fig. 1, the average number of collisions at 90 MeV is between three and four. We can thus conclude, to a good approximation, that the collisions beyond the first two lead on the average to the formation and subsequent decay of a compound nucleus.

The similar behavior of the knockout and first emission spectra as a function of energy suggests a simple relation between the two. The definitions of the two types of emissions also suggest such a relation: in knockout, both nucleons leave the nucleus after only one collision, while in first collision emission, the emitted nucleon suffers only one collision. The difference between the two thus refers to the first collisions in which the second nucleon suffers a second collision (or more) before escaping. Since the number of collisions a nucleon participates in is roughly proportional to the nuclear matter through which it passes, we can associate knockout emission with superficial collisions with the target and the remaining first emission nucleons with more central collisions. The simplest estimate we might make is that the knockout cross section should be restricted to an outer ring of width ΔR of the total first emission cross section πR^2. We would then have for the ratio

$$\sigma(ko)/\sigma(1) = (\pi R^2 - \pi(R - \Delta R)^2)/\pi R^2 = 1 - (1 - \Delta R/R)^2.$$

We plot the ratio of the two cross sections as a function of the incident energy for three nuclei: ^{27}Al, ^{58}Ni and ^{209}Bi in Fig. 6. We observe that the ratios for neutron and proton knockout

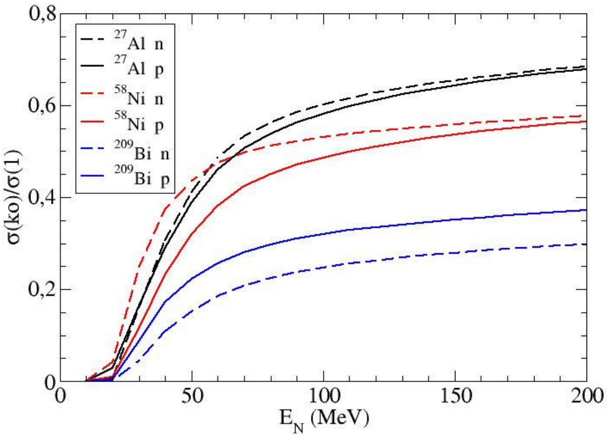

Figure 6. Ratio of knockout to one interaction neutron and proton emission cross sections for p + ^{27}Al, ^{58}Ni and ^{209}Bi.

are very similar for each nucleus. The ratios increase fairly rapidly below about 50 MeV, in the region of excitation energy in which inelastic excitation still contributes, and much more slowly above. The ratios decrease with increasing mass of the target nucleus as would be expected from the discussion above.

Table 1. Average ratio of knockout to first emission cross sections at 200 MeV and the corresponding effective surface thickness ΔR for the given nuclei.

Nucleus	Ratio	ΔR (fm)
^{27}Al	0.7	1.7
^{58}Ni	0.55	1.6
^{209}Bi	0.35	1.4

In the table, we give an estimate of the cross section ratio at an incident energy of 200 MeV and of the ring thickness ΔR in which knockout dominates. We observe that the value of ΔR is not constant but decreases slowly as the mass number of the nucleus increases. We argue that this does not invalidate the interpretation but simply reflects the increasing thickness of the matter that must be traversed as the mass number increases.

Although knockout nucleons tend to be produced in peripheral collisions, they are not the most energetic nucleons on the average. This can be seen in Figs. 4 and 5, by mentally subtracting the knock-out spectra from the corresponding one-step spectra. For low emission energies, the knockout spectra and one step spectra without knockout are similar in form, with the knockout spectra slightly large in the reaction induced on ^{56}Fe and the one step spectra without knockout slightly larger in the reaction induced on ^{209}Bi. In both cases, the one step spectra without knockout clearly dominate at higher energies, where they at first remain more or less constant while the knockout spectra decrease to zero, before decreasing to zero as well.

The difference in average energy can also be seen when energy-integrated angular distributions are compared, as in Fig. 7, for the reaction p + ^{58}Ni. The one step and knockout angular distributions are roughly parallel, but only on a log scale. In Fig. 8, the one step angular distributions without knockout clearly dominate at forward angles while the knockout angular distributions are dominant at backward angles. The flatter angular distributions of the knockout nucleons are due to their lower average energy.

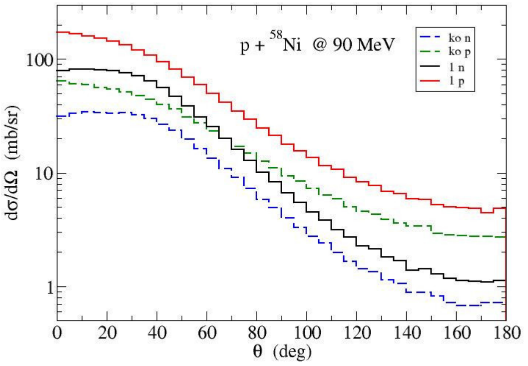

Figure 7. Energy-integrated knockout and one-step nucleon emission angular distributions from the collision p + ^{56}Ni.

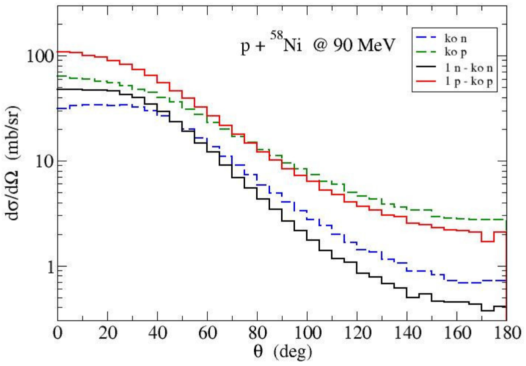

Figure 8. Energy-integrated knockout and one-step without knockout nucleon emission angular distributions from the collision p + ^{56}Ni.

4. Quantal Calculations

Although semiclassical multistep calculations can easily be performed to all orders, that is not the case for quantum calculations. Taking advantage of the iterative form of the multistep contributions in the Feshbach-Kerman-Koonin model[1], Koning and Chadwick[4] extended such calculations up to fourth order. Calculations using the more fundamental Tamura-Udagawa-Lenske[2] or Nishioka-Weidenmüller-Yoshida[3] quantum models have yet to be extended beyond two steps. We will discuss only the first step of a knockout reaction, which is included in none of these models.

The double differential energy-angular distribution for a knockout reaction can be written in terms of a T-matrix element $T_{i\rightarrow f}$ as

$$d\sigma_{i\rightarrow f} = \frac{2\pi}{\hbar v_i}\frac{d^3k_{f_1}}{(2\pi)^3}\frac{d^3k_{f_2}}{(2\pi)^3} f_{rec}\left|\left\langle \vec{k}_{f_1},\, \vec{k}_{f_2}\left|T_{i\rightarrow f}\right|\vec{k}_i\right\rangle\right|^2 \delta\left(E_{f_1}+E_{f_2}+\varepsilon^*-E_i-Q\right)\,, \tag{1}$$

where k_i refers to the incident nucleon momentum and k_{f_1}, k_{f_2} to the emitted nucleon momenta, with the corresponding kinetic energies being E_i and E_{f_1}, E_{f_2}, respectively. The energy-conserving δ function takes into account the Q value for emission of the second nucleon as well as the residual excitation energy ε^*. The factor f_{rec} takes into account the recoil of the residual nucleus.

After rearranging and integrating over the energy E_{f_2}, this can be rewritten as

$$\frac{d\sigma_{i\rightarrow f}}{dE_{f_1}d\Omega_{f_1}d\Omega_{f_2}} = \frac{1}{(2\pi)^5}\frac{\mu_i M_{f_1} M_{f_2}}{\hbar^6}\frac{k_{f_1}k_{f_2}}{k_i} f_{rec}\left|\left\langle \vec{k}_{f_1},\, \vec{k}_{f_2}\left|T_{i\rightarrow f}\right|\vec{k}_i\right\rangle\right|^2\,, \tag{2}$$

where μ_i is the reduced mass of the initial channel and M_{f_1}, M_{f_2} are the masses of the emitted nucleons.

We evaluate this amplitude in a simple single-particle shell-model basis, in which all levels are occupied by a single nucleon up to the Fermi level. The squared T-matrix amplitude can then be written as

$$\left|\left\langle \vec{k}_{f_1},\, \vec{k}_{f_2}\left|T_{i\rightarrow f}\right|\vec{k}_i\right\rangle\right|^2 = \frac{1}{2}\sum_{\mu_i\mu_{f_1}\mu_{f_2}}\sum_{h}\left|\left\langle \vec{k}_{f_1},\mu_{f_1}\,\vec{k}_{f_2},\mu_{f_2};h\left|T_{i\rightarrow f}\right|\vec{k}_i,\mu_i\right\rangle\right|^2 \tag{3}$$

where each of the terms in the sum takes the form

$$\left\langle \vec{k}_{f_1},\mu_{f_1}\,\vec{k}_{f_2},\mu_{f_2};h\left|T\right|\vec{k}_i\right\rangle = \int d^3r\, d^3r'\, \tilde{\psi}^{(-)\dagger}_{k_{f_1}\mu_{f_1}}(\vec{r})\; \tilde{\psi}^{(-)\dagger}_{k_{f_2}\mu_{f_2}}(\vec{r}')\; V\left(\vec{r}-\vec{r}'\right)\; \phi_h\left(\vec{r}'\right)\; \psi^{(+)}_{k_i\mu_i}(\vec{r})\,. \tag{4}$$

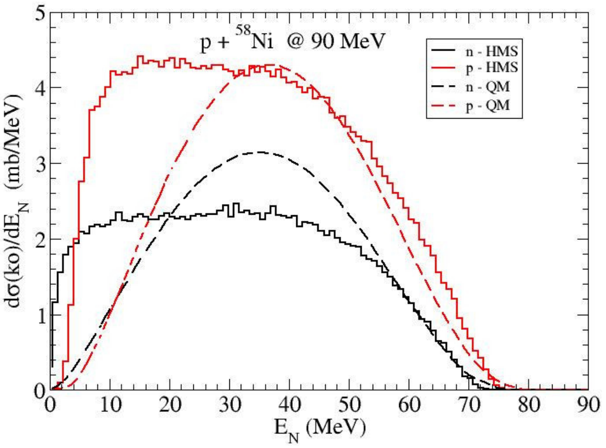

Figure 9. Comparison of the knockout spectra from the semiclassical and quantum calculations for the case of p + ^{58}Ni.

We present calculations of the reaction p + ^{58}Ni performed using the independent particle states of a harmonic oscillator basis with standardized spin-orbit splittings and the Koning-Delaroche optical potentials[17]. We use a contact interaction with spin and charge-exchange terms corresponding to a_{et}=1.0 and a_{es}=0.6 [18] and a total strength given by the parametrization of Ref. [19].

In Fig. 9, we compare the angle-integrated spectra of the quantum knockout calculation to the semiclassical HMS results for the case of p + ^{58}Ni. We note that both the proton and neutron emission spectra agree at the highest energies, where the emission spectra are decreasing to zero. The quantum proton spectrum accompanies the HMS one to its peak, while the quantum neutron spectrum overshoots the corresponding HMS spectrum, but follows the Quantum proton spectrum in form. Both quantum spectra then decrease to zero as the energy decreases and grossly underestimate the low energy spectrum predicted by the HMS simulations. The reason for the large discrepancy between the quantum and semiclassical knockout spectra at low emission energies is a mystery to us at them moment.

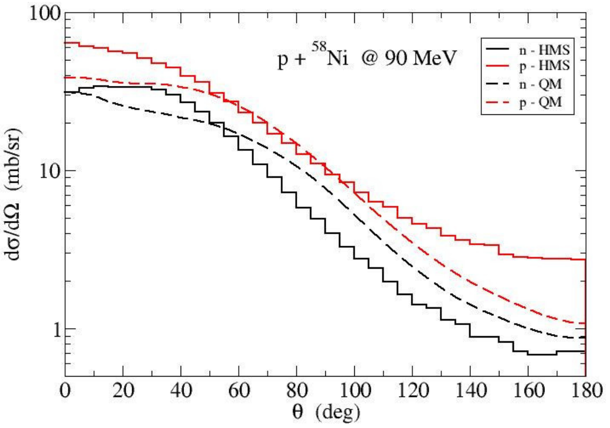

Figure 10. Comparison of the energy-integrated knockout angular distributions from the semiclassical and quantum calculations for the case of p + ^{58}Ni.

The difference in the spectra is reflected in the energy-integrated angular distributions, which we compare in Fig. 10. Due to their higher average emission energy, the quantum knockout calculations are slightly more forward peaked than the semiclassical HMS ones. They are roughly similar in magnitude, with the quantum angular distributions being flatter at forward angles but falling more rapidly at backward angles.

5. Conclusions

Nucleon-induced pre-equilibrium reactions are dominated by direct reactions. Quantum mechanical multi-step direct models of these reactions have treated them as being exclusively inelastic excitations. Using the semiclassical HMS model, we have shown here that nucleon knockout - direct excitation to the continuum - makes an important contribution to the emission cross section at incident energies above about 20 to 30 MeV.

We have also calculated knockout spectra and cross sections using a quantum DWBA formalism with a harmonic oscillator basis of states and a contact interaction. Our quantum and semiclassical calculations agree to large extent at high knockout emission energies but are radically different at low emission energies. We are currently working to either eliminate or understand the physical approximations behind these discrepancies in order to extend the quantum mechanical MSD model to explicitly include knockout reactions reactions in a consistent manner.

Acknowledgements

EVC acknowledges financial support from grants 2016/07398-8 and 2017/13693-5 of the São Paulo Research Foundation (FAPESP). BVC acknowledges financial support from grant 2017/05660-0 of the São Paulo Research Foundation (FAPESP) and grant 306433/2017-6 of CNPq. EVC and BVC acknowledge support from the INCT-FNA project 464898/2014-5.

References

[1] Feshbach H, Kerman A and Koonin S 1980 *Ann. Phys (N.Y.).* **125** 429.
[2] Tamura T, Udagawa T and Lenske H 1982 *Phys. Rev.* C **26** 379.
[3] Nishioka N, Weidenmüller H A and Yoshida S 1988 *Ann. Phys. (N.Y.)* **183** 166.
[4] Koning A and Chadwick M 1997 *Phys. Rev.* C **56** 970.
[5] Kawano T and Yoshida S 2001 *Phys. Rev.* C **64** 024603.
[6] Dupuis M, Kawano T, Delaroche J P and Bauge E 2011 *Phys. Rev.* C **83** 014602.
[7] Dupuis M, Bauge E, Hilaire S, Lechaftois S F, Péru S, Pillet N and Robin C 2015 *Eur. Phys. J.* A **51** 168.
[8] Carlson B V, Escher J E and Hussein M S 2014 *J. Phys.* G **41** 094003.
[9] Blann M 1996 *Phys. Rev.* C **54** 1341.
[10] Blann M and Chadwick M 1998 *Phys. Rev.* C **57** 233.
[11] Chimanski E V, Carlson B V, Capote R and Koning, A J 2018, *Proceedings of the 15th Varenna Conference on Nuclear Reaction Mechanisms*, to be published as a CERN Proceedings.
[12] Bisplinghoff J 1986 *Phys. Rev.* C **33** 1569.
[13] Pompeia C A and Carlson B V 2006 *Phys. Rev.* C **74** 054609.
[14] Wu J R, Chang C C and Holmgren H D 1973 *Phys. Rev.* C **19** 698.
[15] Kalend A M, Anderson B D, Baldwin A R, Madey R, Watson J W, Chang C C, Holmgren H D, Koontz R W, Wu J R and H. Machner H 1983 *Phys. Rev.* C **28** 105.
[16] Herman M, Capote R, Carlson B V, Oblozinský P, Sin M, Trkov A, Wienke H and Zerkin V 2007 *Nuclear Data Sheets* **108** 2655.
[17] Koning A J and Delaroche J P 2003 *Nucl. Phys.* A **713** 231.
[18] Ring P and Schuck P 1980 *The Nuclear Many-Body Problem* Springer-Verlag.
[19] Bonetti R, Koning A J, Akkermans J M and Hodgson P E 1994 *Phys. Rep.* **247** 1.

Fusion barrier distribution and superheavy elements

K Hagino[1,2] **and T Tanaka**[3,4]
[1] Department of Physics, Tohoku University, Sendai 980-8578, Japan
[2] Research Center for Electron Photon Science, Tohoku University, 1-2-1 Mikamine, Sendai 982-0826, Japan
[3] RIKEN Nishina Center for Accelerator-Based Science, Saitama 351-0198, Japan
[4] Department of Physics, Kyushu University, Fukuoka 819-0395, Japan

E-mail: `hagino@nucl.phys.tohoku.ac.jp`

Abstract. The barrier distribution, originated from channel coupling effects in heavy-ion fusion reactions, has been extracted experimentally for many systems using either a fusion excitation function or an excitation function of large-angle quasi-elastic scattering. In this article, we discuss an application of the latter method to the ^{48}Ca+^{248}Cm system, which is relevant to hot fusion reactions to synthesize superheavy elements. To this end, we carry out coupled-channels calculations for this system, taking into account the deformation of the target nucleus, and discuss the role of deformation in a formation of evaporation residues.

1. Introduction

Fusion reactions play an important role in several phenomena in physics. Those include the energy production in stars, nucleosyntheses, and formations of superheavy elements. Yet, from the theoretical point of view, fusion reactions, as well as fission, are typical examples of large amplitude collective motions of quantum many-body systems, and their microscopic understanding has still been far from complete.

In order to understand the dynamics of nuclear fusion, the Coulomb barrier between two nuclei plays an important role. This is a potential barrier formed as a result of cancellation between the long-ranged repulsive Coulomb interaction and a short ranged attractive nuclear interaction. The height of the Coulomb barrier defines the energy scale of a system, and here in this article, we shall mainly consider the energy region around the Coulomb barrier.

It has by now been well known that heavy-ion fusion cross sections are largely enhanced at energies below the Coulomb barrier, as compared to a prediction of a simple potential model. It has been understood that channel coupling effects, that is, the couplings of the relative motion between two nuclei to several collective excitations of the colliding nuclei, as well as particle transfer channels, play an essential role in enhancing subbarrier fusion cross sections [1, 2, 3, 4, 5]. The coupled-channels approach has been developed in order to take into account such channel coupling effects [6].

In the eigen-channel representation of the coupled-channels method, fusion cross sections in the presence of channel couplings can be represented as a weighted sum of fusion cross sections for each eigen-channel [7]. In this picture, a single Coulomb barrier is replaced by a distribution of multitude of barriers due to the channel coupling effects. A way to extract the barrier distribution directly from experimental fusion cross sections has been proposed by

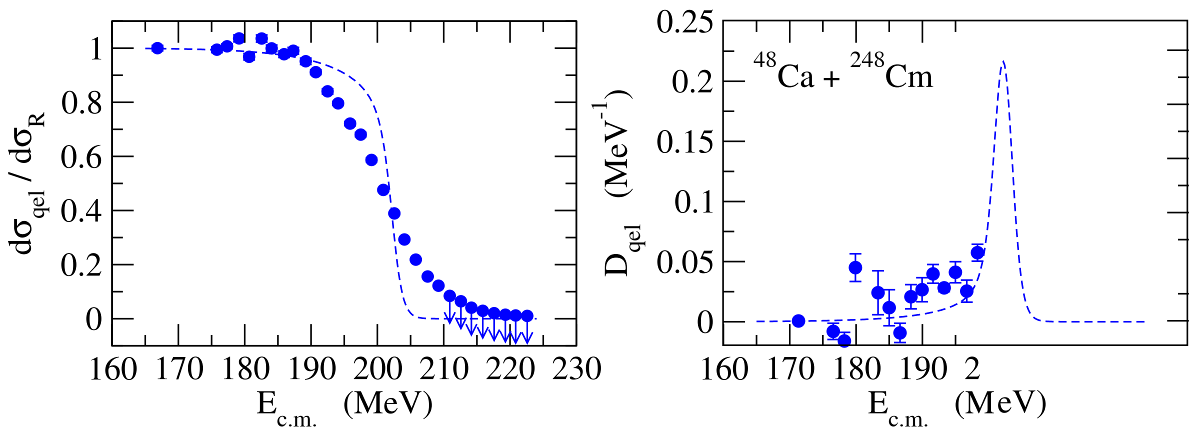

Figure 1. The quasi-elastic cross sections (the left panel) and the corresponding barrier distribution (the right panel) for the ^{48}Ca+^{248}Cm system. The experimental data are shown by the filled circles, where the arrows indicate the upper limit of cross sections. For comparison, the result of a potential model calculation is also shown by the dashed lines. The experimental data are taken from Ref. [14].

Rowley, Satchler, and Stelson [8]. In this method, the barrier distribution is extracted by taking the second energy derivative of the product of fusion cross sections, $\sigma_{\rm fus}$, and incident energies in the center of mass frame, E, that is, $d^2(E\sigma_{\rm fus})/dE^2$. The fusion barrier distribution has been extracted with this method for many systems [2, 9], which in general show that the shape of barrier distribution is sensitive to details of channel couplings, thus providing a good tool to understand the underlying dynamics of subbarrier fusion reactions.

It has been shown that a similar barrier distribution can be obtained also by using quasi-elastic scattering at backward angles [10, 11]. This is because quasi-elastic scattering corresponds to a reflection of flux at the barrier and thus it is complementary to fusion, which corresponds to a transmission of flux through the barrier. Very recently, the quasi-elastic barrier distribution was extracted for the ^{48}Ca+^{248}Cm system [14], the system which had been used to synthesize superheavy elements $Z = 116$ (Lv) [12, 13]. Using the GARIS ion separator at RIKEN, which has been used to synthesize the $Z = 113$ element (Nihonium) [17], quasi-elastic cross sections have been successfully measured, which are almost free from contamination of deep-inelastic cross sections. The barrier distribution extracted from such data is thus much better defined as compared to the previous attempts [15, 16] for systems relevant to the superheavy nuclei.

In this article, in order to discuss the reaction dynamics for superheavy elements, we present the coupled-channels analyses for the quasi-elastic barrier distribution for the ^{48}Ca+^{248}Cm system [14]. We consider the deformation of the target nucleus, ^{248}Cm, as well as a neutron transfer channel. We also discuss the connection of the barrier distribution to the measured evaporation residue cross sections.

2. Quasi-elastic barrier distribution

Quasi-elastic scattering is defined as a sum of elastic, inelastic, transfer, and breakup processes. That is, it is an inclusive process, being complementary to fusion. The quasi-elastic barrier distribution, $D_{\rm qel}$, is defined as [10, 11],

$$D_{\rm qel}(E) = -\frac{d}{dE}\left(\frac{\sigma_{\rm qel}(E,\pi)}{\sigma_R(E,\pi)}\right), \tag{1}$$

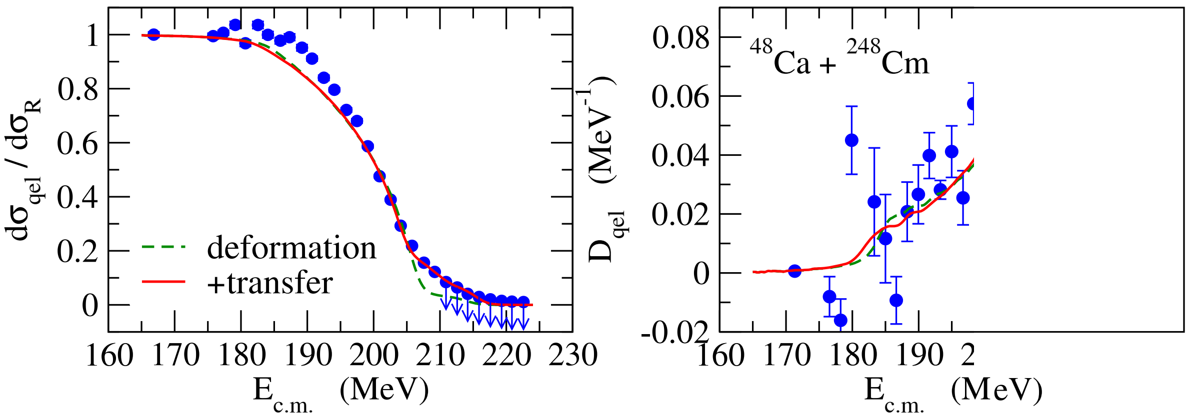

Figure 2. The quasi-elastic cross sections (the left panel) and the barrier distribution (the right panel) for the ^{48}Ca+^{248}Cm system. The dashed lines show the result of coupled-channels calculations which take into account the deformation of the target nucleus, ^{248}Cm, as well as the octupole phonon excitation in the projectile nucleus, ^{48}Ca. The solid lines are obtained by including in addition the neutron transfer channel. The experimental data are taken from Ref. [14].

where $\sigma_{\rm qel}(E,\pi)$ is a quasi-elastic cross section at the scattering angle π and $\sigma_R(E,\pi)$ is the Rutherford cross section. In previous measurements, quasi-elastic scattering was measured by detecting projectile-like particles at the scattering angle θ (in the center of mass frame) and the cross sections were mapped on those at $\theta=\pi$ using the effective energy defined by [10, 11],

$$E_{\rm eff} = 2E\,\frac{\sin(\theta/2)}{1+\sin(\theta/2)}. \tag{2}$$

The mapping has been shown to work well as long as the scattering angle θ is close to π [11]. In the new measurement with GARIS, on the other hand, the recoiled target-like particles were measured at π and the mapping of the quasi-elastic cross sections was not required [14]. This was not possible in the previous measurements, as it would have required to put a detector along the beam line. The measured quasi-elastic cross sections and the corresponding barrier distribution are shown in Fig. 1. The filled circles with arrows indicate the upper limit of cross sections, for which the deep-inelastic component may contaminate to some extent. For comparison, the figure also shows the result of a potential model. To this end, we use a Woods-Saxon potential with the depth parameter of $V_0 = -105$ MeV, the range parameter of $r_0 = 1.18$ fm, and the surface diffuseness parameter of $a = 0.6$ fm. The imaginary part of the potential is set to be well localized inside the barrier. It is clearly seen that the experimental barrier distribution is much more structured as compared to the result of the potential model, indicating the importance of channel coupling effects.

3. Coupled-channels calculations for the ^{48}Ca+^{248}Cm system

Let us then perform coupled-channels calculations and discuss the role of channel coupling effects, in particular the role of deformation of the target nucleus, ^{248}Cm. For a well deformed nucleus, for which the excitation energies of the ground state rotational band are small, cross sections for quasi-elastic scattering can be computed as [11],

$$\frac{d\sigma_{\rm qel}}{d\Omega} = \sum_I \frac{d\sigma_I}{d\Omega} = \int_0^1 d(\cos\theta)\left(\frac{d\sigma_{\rm el}}{d\Omega}\right)_\theta, \tag{3}$$

where σ_I is the cross section to populate the state with spin I in the ground state rotational band (including the ground state with $I = 0$). $(d\sigma_{\rm el}/d\Omega)_\theta$ is the cross section for elastic scattering for a fixed orientation angle θ for the target nucleus. This is calculated with a deformed potential for each θ, $V(r, \theta)$, where r is the relative distance between the two colliding nuclei. Notice that in this approximation the coupled-channels equations are completely decoupled and the cross sections are given as a weighted sum of cross sections for a single-channel system labeled by θ (for which there are only elastic scattering and absorption).

The dashed lines in Fig. 2 show the result of a coupled-channels calculation so obtained. To this end, we use the deformation parameters of $\beta_2 = 0.297$ and $\beta_4 = 0.04$ together with the radius parameter of $R_T = 1.2 \times 248^{1/3}$ fm [18]. We also take into account the octupole vibrational excitation in ^{48}Ca at 4.51 MeV with the (dynamical) deformation parameter of $\beta_3 = 0.175$, although the excitation energy is large and the excitation simply renormalizes the internucleus potential [3, 19]. One can see that a large part of the structure in the barrier distribution is well reproduced by this calculation. Especially, the asymmetric shape of the barrier distribution is well accounted for.

A further improvement can be achieved by taking into account the neutron transfer channel. The solid lines in Fig. 2 show the results with the 1 neutron pick-up channel, whose ground-state-to-ground-state Q value is $Q_{\rm gg} = -1.06$ MeV. We adjust the coupling strength for the transfer channel in order to reproduce the experimental quasi-elastic cross sections. This calculation slightly improves the cross sections around $E = 210$ MeV, and the main peak in the barrier distribution is somewhat altered. However, the modification is minor, and one can conclude that the main effect still comes from the deformation of the target nucleus.

4. Connection to evaporation residue formations

The barrier distribution discussed in the previous sections provides information on the Coulomb barrier in the entrance channel, that is, before the colliding nuclei reach the touching configuration. For medium-heavy systems, a compound nucleus is formed almost automatically once the touching configuration is achieved [3]. In contrast, in the superheavy region, there is a huge probability for the touching configuration to re-separate without forming a compound nucleus, that is, quasi-fission, due to a strong Coulomb repulsion between the two nuclei. Furthermore, even if a compound nucleus is formed with a small probability, it decays most likely by fission. Because quasi-fission characteristics significantly overlap with fission of the compound nucleus, a detection of fission events itself does not guarantee a formation of the compound nucleus. Therefore, a formation of superheavy elements is usually identified by detecting evaporation residues. A question then arises: what is the connection between the barrier distribution in the entrance channel and evaporation residue cross sections?

Figure 3 answers this question. This figure compares the quasi-elastic barrier distribution with the measured evaporation residue cross sections for the ^{48}Ca+^{248}Cm system. For the barrier distribution, the figure also shows the result of the coupled-channels calculation (the solid line). The contribution of the side collision ($\theta = \pi/2$) is denoted by the dashed curve. The figure clearly indicates that the maximum of the evaporation residue cross sections originates from the side collision. This is a clear confirmation of the notion of compactness proposed by Hinde *et al.* [20], who argued that the side collision leads to a compact touching configuration, for which the effective barrier height for the diffusion process is low, enhancing the formation probability of a compound nucleus.

This notion has further been confirmed theoretically using an extended version of the fusion-by-diffusion model [18]. The fusion-by-diffusion model is a simple one-dimensional model for the diffusion process proposed by Swiatecki *et al.* [21, 22, 23]. In this model, the potential for the diffusion process is parameterized as a parabolic function of s, that is the surface separation between the two spheres. Assuming the overdamped limit, the diffusion probability, $P_{\rm CN}$, is

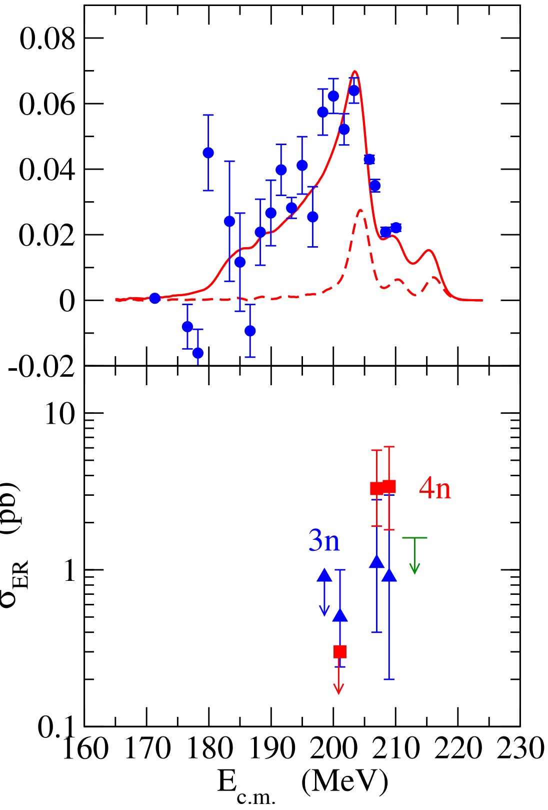

Figure 3. The experimental quasi-elastic barrier distribution (the upper panel) and the evaporation residue cross sections (the lower panel) for the ^{48}Ca+^{248}Cm system. For the barrier distribution, the figure also shows the results of the coupled-channels calculation (the solid line), for which the contribution of the side collision ($\theta = \pi/2$) is denoted by the dashed line. The experimental data are taken from Refs. [12, 13, 14].

then computed as [24],

$$P_{\rm CN} = \frac{1}{2}\left[1 - {\rm erf}\left(\sqrt{\frac{\Delta V}{T}}\right)\right], \tag{4}$$

where erf(x) is the error function, T is the temperature of the system, and $\Delta V = V_{\rm fiss}(s_{\rm sd}) - V_{\rm fiss}(s_{\rm inj})$ is the difference between the potential energy at the saddle configuration, $s_{\rm sd}$, and that at the injection point, $s_{\rm inj}$. In the fusion-by-diffusion model, the fission potential, $V_{\rm fiss}(s)$, as well as the saddle configuration, $s_{\rm sd}$, are globally parameterized according to Refs. [21, 22, 23], and the injection point, $s_{\rm inj}$, is treated as an adjustable parameter. In Ref. [18], this model has been extended by introducing the angle dependence to the injection point as,

$$s_{\rm inj}(\theta) = s_{\rm inj}^{(0)} + R_T \sum_\lambda \beta_{\lambda T} Y_{\lambda 0}(\theta). \tag{5}$$

The solid lines in Fig. 4 show the evaporation residue cross sections for the ^{48}Ca+^{248}Cm system obtained with this model [18]. The contributions of the side ($\theta = \pi/2$) and the tip ($\theta = 0$) collisions are denoted by the dashed and the dotted lines, respectively. At energies around 211 MeV, that is, the energies slightly above the barrier height for the side collision (see Fig. 3), the side collision gives the main contribution. At these energies, the contribution of the tip

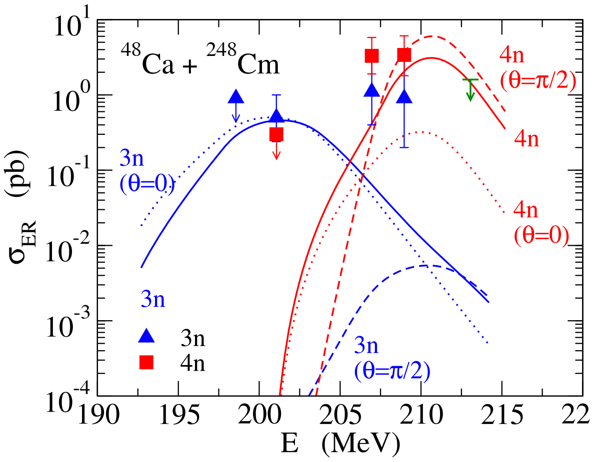

Figure 4. The evaporation residue cross sections for the ^{48}Ca+^{248}Cm system obtained with the extended fusion-by-diffusion model. The solid lines show the orientation averaged cross sections, while the dotted and the dashed lines denote the contributions of the tip ($\theta = 0$) and the side ($\theta = \pi/2$) collisions, respectively. The experimental data are taken from Refs. [12, 13].

collision is much smaller, since the injection point is large, and thus the diffusion probability is small. On the other hand, the side collision is largely suppressed at lower energies due to the small capture probability originated from a high capture barrier. The contribution of the tip collision then becomes dominant, for which the capture probability is not suppressed, even though the diffusion probability is small. In this way, the maximum of the evaporation residue cross sections are obtained at energies slightly above the barrier height for the side collision, at which the energy is high enough so that the capture probability is not suppressed and at the same time one can take advantage of large diffusion probabilities for the side collision.

5. Summary

The fusion barrier distribution has provided useful information on the reaction dynamics for heavy-ion sub-barrier fusion reactions for many systems. This continues to be the case also for systems relevant to superheavy elements. In this article, we have discussed the quasi-elastic barrier distribution for the ^{48}Ca+^{248}Cm system, that is, the system to synthesize the element 116 (Lv) with hot fusion reaction. The coupled-channels analyses for the recently measured data have clearly indicated that the side collision plays an important role in forming evaporation residues and that the maximum of the evaporation residue cross sections appears at energies slightly above the height of the Coulomb barrier for the side collision. This has made a clear confirmation of the notion of compactness for the side collision, which has also been confirmed theoretically using the extended fusion-by-diffusion model.

Of course, there still remain many challenges in nuclear reaction studies for superheavy elements, such as a clarification of shape evolution towards a compound nucleus with a deformed target, a role of quantum friction, and to understand the reaction dynamics of neutron-rich nuclei [25]. Apparently much more theoretical and experimental works will be required in order to gain a deeper insight into reaction dynamics for superheavy elements.

Acknowledgments

The authors thank K. Morita for useful discussions. K.H. also thanks V. Guimarães for his hospitality during his stay in Sao Paulo.

References

[1] Balantekin A B and Takigawa N 1998 *Rev. Mod. Phys.* **70** 77
[2] Dasgupta M, Hinde D J, Rowley N and Stefanini A M 1998 *Annu. Rev. Nucl. Part. Sci.* **48** 401
[3] Hagino K and Takigawa N 2012 *Prog. Theor. Phys.* **128** 1061
[4] Back B B, Esbensen H, Jiang C L and Rehm K E 2014 *Rev. Mod. Phys.* **86** 317
[5] Montagnoli G and Stefanini A M 2017 *Eur. Phys. J.* A**53** 169
[6] Hagino K, Rowley N and Kruppa A T 1999 *Comp. Phys. Comm.* **123** 143
[7] Dasso C H, Landowne S and Winther A 1983 *Nucl. Phys.* A**405** 381; 1983 *Nucl. Phys.* A**407** 221
[8] Rowley N, Satchler G R and Stelson P H 1991 *Phys. Lett.* B**254** 25
[9] Leigh J R, Dasgupta M, Hinde D J, Mein J C, Morton C R, Lemmon R C, Lestone J P, Newton J O, Timmers H, Wei J X and Rowley N 1995 *Phys. Rev.* C**52** 3151
[10] Timmers H, Leigh J R, Dasgupta M, Hinde D J, Lemmon R C, Mein J C, Morton C R, Newton J O and Rowley N 1995 *Nucl. Phys.* **A584** 190
[11] Hagino K and Rowley N 2004 **Phys. Rev.** C**69** 054610 ; 2005 *Brazilian J. of Phys.* **35** 890
[12] Oganessian Yu Ts *et al.* 2004 *Phys. Rev.* C**70** 064609; 2000 *Phys. Rev.* C**63** 011301
[13] Hofmann S *et al.* 2012 *Eur. Phys. J.* A**48** 62
[14] Tanaka T, Narikiyo Y, Morita K, Fujita K, Kaji D, Morimoto K, Yamaki S, Wakabayashi Y, Tanaka K, Takeyama M, Yoneda A, Haba H, Komori Y, Yanou S, Gall B J.-P., Asfari A, Faure H, Hasebe H, Huang M, Kanaya J, Murakami M, Yoshida A, Yamaguchi T, Tokanai F, Yoshida T, Yamamoto S, Yamano Y, Watanabe K, Ishizawa S, Asai M, Aono R, Goto S, Katori K and Hagino K 2018 *J. Phys. Soc. Jpn.* **87** 014201
[15] Mitsuoka S *et al.* 2007 *Phys. Rev. Lett.* **99** 182701
[16] Ntshangase S S *et al.* 2007 *Phys. Lett.* B**651** 27
[17] Morita K *et al.* 2004 *J. of Phys. Soc. Jpn.* **73** 2593; 2007 **76** 5001; 2012 **81** 3201
[18] Hagino K 2018 **Phys. Rev.** C**98** 014607
[19] Takigawa N, Hagino K, Abe M and Balantekin A B 1994 *Phys. Rev.* C**49** 2630
[20] Hinde D J *et al.* 1995 *Phys. Rev. Lett.* **74** 1295
[21] Swiatecki W J, Siwek-Wilczynska K and Wilczynski J 2003 *Acta Phys. Pol.* B **34** 2049
[22] Swiatecki W J, Siwek-Wilczynska K and Wilczynski J 2005 *Phys. Rev.* C**71** 014602
[23] Cap T, Siwek-Wilczynska K and Wilczynski J 2011 *Phys. Rev.* C**83** 054602
[24] Abe Y, Boilley D, Giraud B G and Wada T 2000 *Phys. Rev.* E**61** 1125
[25] Hagino K 2019 *AAPPS Bulletin* **29** 31

Sulfur status in judo athletes by XRF

M R Almeida[1], C B Zamboni[1], D N S Giovanni[1*], M R A Azevedo[2]

[1]Instituto de Pesquisas Energéticas e Nucleares, IPEN – CNEN/SP, São Paulo-SP, 05508000, Brasil.
[2] Universidade de Santo Amaro, UNISA/SP São Paulo - SP, 04743-030, Brasil

Email: czamboni@ipen.br, almeida.mramos@gmail.com

Abstract. The human biomonitoring, measurement of chemical and/or their metabolites in human fluids, is an important tool for assessing the health condition of subjects, included athletes. In this study, sulfur levels were investigated in blood of judo athletes using Energy Dispersive X-ray Fluorescence (EDXRF) technique. Twenty athletes participated of this study. Two groups of athletes were selected: judo with a balanced diet with multivitamin/mineral supplements consumption and judo with diet not controlled. These data were compared with the control group (subjects of the same age but not involved with physical activities). There was a significant increase of S levels in athletes with diet not controlled. These data can be useful to a well-planned nutritional proposition that can contribute to better performance of athletes.

1. Introduction

Many amateur athletes would like to have a specialized accompaniment program to improve their performance, but today this is still restricted to only a few of them. The training program used consists of long periods, often years, of monitoring by a technical team composed if doctor, nutritionist, and other necessary professionals. Them into accont individual and routine assessments, the focus is on pursuing improvements to benefit and enhance each athlete's performance. Of these programs that, in this area of activity, ‘‘little is a lot’’, which means that any benefit that may add advantages in performance of an athlete should be considered for a better competitiveness. Based on this need, in the last years, the Laboratório de Espectroscopia e Espectrometria das Radiações (LEE) at IPEN (CNEN-SP, Brazil) had performed investigations in sport medicine, focusing on the clinical follow-up of athletes, such as biochemical evaluation in body fluids, using the X-ray Fluorescence (XRF) and Neutron activation Analyses (NAA) techniques as an alternative for clinical practices [1-6]. These alternative procedures are capable to determine elements concentration in whole blood using an efficient, fast and non-destructive analysis. The results led to an increased interest in using this alternative methodology in several sports activities.

Specifically, sulfur plays an important role in training effects: it is present in all cells (representing approximately 0.25% of our weight), having an important role in the growth and metabolic processes, defense and detoxification. Besides, sulfur is present in cartilage and it is essential for collagen synthesis. In Sports Medicine a shortage of sulfur can cause the syndrome of physical fatigue after activity (muscle injury and decreased elasticity of the lung tissue) while excess can cause ulcerative colitis, acidosis and diarrhea. The major source of inorganic sulfate for humans derive from proteins and of several organic and inorganic sulfur compounds present in food. However, athletes usually make use of supplements rich in amino acids, most of them rich in sulfur composts, such as methionine ($C_5H_{11}NO_2S$), cysteine ($C_3H_7NO_2S$) and taurine ($C_2H_7NO_3S$). In this study, sulfur levels were investigated in blood of judo athletes submitted to different diet using EDXRF technique. The data from athletes were compared with those obtained from a group of same age and weight, but not involved in intense physically activities. These results of this comparison useful for evaluating the performance of athletes during the preparation period of competitions, as well as to propose new nutritional evaluation protocols in sport medicine.

2. Experimental

Twenty physically healthy professional (9 woman and 11 men) that were in constant training for the last 2 years, with average age of 20.2 ± 4.4 years, average weight of 73.2 ± 26.0 kg and training intensity of 8–10 h/ week participated in the study. Two groups of athletes were selected: judo athletes with multivitamin and mineral supplements consumption added to the diet for a period of 6 months (G1: 07 man and 05 woman) and judo athletes with not controlled diet (G2: 04 man and 04 woman). The blood samples were collected before the physical training with the approval of the Ethical Committee (CAAE: 15388713.0.0000.0081). Venous blood was collected (before the training) in a vacuum tube. About 50 μL of whole blood is transferred to the filter paper (~2.2 cm^2), in duplicate. The control group (CG) was composed of 20 health subjects, (10 man and 10 woman) selected from Paulista Blood Bank (at São Paulo city, Brazil) with the same range of age and weight, but not involved in intense physical activities. The CG sample preparation was the same as described for the athletes. A mini-X spectrometer with Ag target (XR-100SDD model, Amptek) was used to perform the EDXRF measurements. Each whole blood sample was irradiated for 900 s using 30 kV and 5 μA of excitation conditions and the analysis of the spectrum was performed using the WinQxas Software.

3. Results and discussion

The sulfur blood concentration, mean value (MV), standard deviation (±1SD), minimum value (min), and maximum value (max) for judo athletes and control group are show in Table 1.
The XRF whole blood spectrum is presented in Figure 1.

Table 1. Whole blood sulfur concentrations

g/L	Control Group *[range]**	Groups of Athletes	
	CG *[0.23 – 0.59]*	G1	G2
MV	0.41	0.46	0.59
±1SD	0.09	0.04	0.11
min	0.30	0.39	0.44
max	0.64	0.52	0.70

*considering a confidence interval of 95% (adopted in clinical practices)

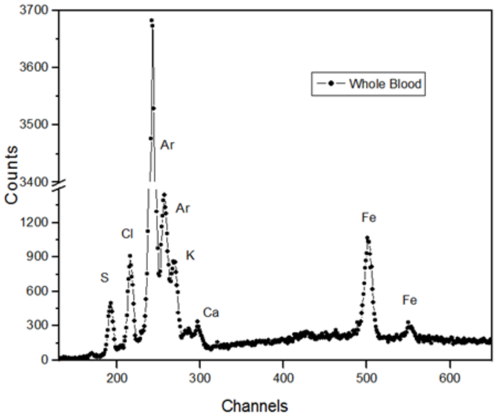

Figure 1. Spectrum of whole blood sample after 900 s of the excitation time

Figure 2 shows the sulfur concentration in whole blood of athletes (G1 and G2). In this figure, the indicate interval of control group, considering ± 1SD and ± 2SD, were also included for comparison.

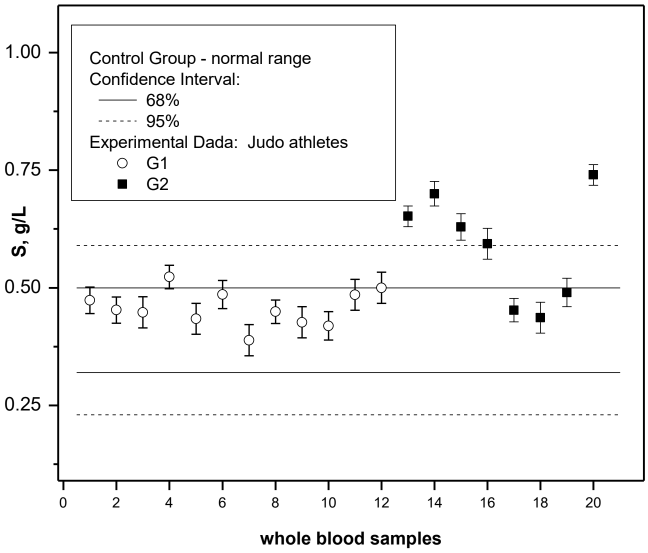

Figure 2. Comparison between the individual concentrations of S (g/L) in whole blood of judo athletes groups (G1 and G2) with the indicate interval of Control Group (CG)

According to the statistical analysis (Student *t-test*), there is a significant difference ($p < 0.05$) increase in the sulfur level in the G2 (athletes with diet not controlled) when compared with G1 group (diet controlled). These data can be useful to a well-planned diet proposition that could contribute to the performance of athletes.

Related to the Portable XRF Spectrometer it has shown to be appropriate for S blood analyses and offers a new contribution for studies in Sports Medicine related to biochemical analyses of blood.

4. Conclusions

The imbalance of S (increase) in athletes (G2) emphasizes the need of balanced diet and suggests that its blood level must be monitored during the training. Moreover, these results may be useful in other areas of research such as health and nutrition.

5. Acknowledgments

The authors thank the CNPq (305373/17-0) and FAPESP (15/01750-9) supported this work.

References

[1] Zamboni C B, Metairon S, Kovacs L, Macedo D and Rizzutto M 2016 *Journal of Radioanalytical and Nuclear Chemistry* **307** 1641.
[2] Zamboni C B, Kovacs L, Metairon S, Azevedo M, Furholz C and Uchida M 2016 *Journal of Radioanalytical and Nuclear Chemistry* **309** 45.
[3] Kovacs L, Zamboni C B, Lourenço T and Macedo D 2015 *In* Journal of Physics: Conference Series *IOP Publishing*, p. 012009.
[4] Oliveira L C and Zamboni C B 2013 *In* AIP Conference Proceedings *AIP*, pp. 73.
[5] Kovacs L, Zamboni C B, Nunes L, Lourenço and T Macedo D 2013 *Journal of Radioanalytical and Nuclear Chemistry* **297** 393.
[6] Kovacs L, Zamboni C B, Lourenço T F, Nunes L A and Macedo D V 2011 *In* AIP Conference Proceedings *AIP*, pp. 336.

Using pulsar's braking indices to estimate changes in their moments of inertia with age-related considerations

H O Oliveira [1], **N S Magalhaes** [1,2], **R M Marinho, Jr** [1], **G A Carvalho** [1,3,4] **and C Frajuca** [5],

[1]Graduate Program in Physics, Technological Institute of Aeronautics, Praça Marechal Eduardo Gomes 50, Sao Jose dos Campos, SP 12228-900, Brazil.

E-mail: `heitoroliveiradeoliveira@gmail.com`
[2]Federal University of Sao Paulo, Department of Physics, Rua Sao Nicolau 210, Diadema, SP 09913-030, Brazil.

E-mail: `nadja.magalhaes@unifesp.br`
[3]Dipartimento di Fisica and ICRA, Sapienza Università di Roma, P.le Aldo Moro 5, I–00185 Rome, Italy.
[4]ICRANet, P.zza della Repubblica 10, I–65122 Pescara, Italy.
[5]Federal Institute of Education, Science and Technology of Sao Paulo, R. Pedro Vicente 625, Sao Paulo, SP 01109-010, Brazil.

Abstract. Pulsars are modeled as neutron stars originated from the collapse of a progenitor one. In the canonical model they are described by spherical magnetized dipoles that rotate with the magnetic axis usually misaligned relative to the rotation axis, and such misalignment would explain the observation of radiation emitted in pulses in a certain direction rendering the typical observational characteristic of this kind of star. The frequency of such pulses decays with time and it can be quantified by the *braking index* (n). In the canonical model $n = 3$ for all pulsars but observational data show that $n \neq 3$. In this work we present a model for the understanding of the frequency decay of the rotation of a pulsar adapting the canonical one. We consider the pulsar a star that rotates in vacuum and has a strong magnetic field but, in contrast to the canonical model, we assume that its moment of inertia changes in time due to a uniform variation of a displacement parameter in time. We found that the old pulsars that present high values of the braking index tend to present smaller internal displacements of mass, in particular the superfluid neutron matter in the core. We relate this trend to neutron vortices' creep in rotating superfluids, indicating a possible reason for this coincidence.

1. Introduction

Pulsars are considered neutron stars that emit electromagnetic radiation in well-defined time intervals, rotate rapidly and are highly magnetized. The observed magnetic radiation is generated from its magnetosphere and is emitted due to the misalignment of the axis of rotation with respect to the magnetic axis of the star in the pattern from a rotating beacon [1].

The model to explain the frequency of the neutron stars' pulses [2], which we will call the canonical model, predicts a gradual deceleration of the rotation of these stars, quantified by a dimensionless parameter known as braking index, represented by "n". In that model this parameter has a theoretical value equal to 3 [3], but results derived from the observation are different from that predicted in the theoretical model, indicating that the canonical model needs improvement.

To this end the pulsar wind model [4] was presented in recent times yielding $n = 1$ such that, when combined with the contribution due to the magnetic dipole ($n = 3$), has presented interesting results although insufficient. A similar reasoning is followed in the work by [5].

In another investigation a phenomenological function was proposed in the energy conservation formula with the introduction of parameters which, although unrelated to known physical variables, allowed the prediction of ranges for braking indices [6]. A different approach by [7] proposed an increase in the angle between the magnetic moment and rotation axis as the cause of the evolution of the torque, while[8] investigated the possibility of an effective force acting on the star which varies with the first power of the tangential velocity of the crust of the pulsar.

In this work we focus on the internal dynamics of the pulsar: the interior of these stars present a significant amount of matter in the form of superfluid neutrons [9] and it is also expected that the coupling and decoupling of this matter alter the long-term dynamics that leads to the measurement of the braking index and therefore producing changes in the pure dipole model or deviations in the “normal” dipolar deceleration [10].

We present an approach to investigate the decay of the rotational frequency of pulsars that leads to the star's core and its evolution modifying an assumption of the canonical model. We introduce a time-varying parameter that accounts for an increasing moment of inertia in the pulsar core and relate it to the motion of superfluid vortices. Details on the results reported here can be found elsewhere, as a longer paper was accepted for publication during the preparation of this article [11].

2. Pulsar as a rotating magnetized conducting sphere: summary of the canonical model

For a rotating sphere the kinetic energy of rotation is equal to [12]:

$$E_{rot} = \frac{1}{2} I \Omega^2, \tag{1}$$

whose time derivative is

$$\dot{E}_{rot} = I \Omega \dot{\Omega}, \tag{2}$$

where Ω is the star's angular velocity and I is its moment of inertia.

The star'a magnetic radiation energy is believed to originate from the rotating magnetic dipole [12]

$$\dot{E}_{mr} = \frac{2}{3c^3} |\ddot{m}|^2, \tag{3}$$

with the magnetic dipole moment being given by

$$\vec{m} = \frac{B_P R^3}{2} (\cos\alpha \hat{k} + \sin\alpha \cos(\Omega \cdot t) \hat{\imath} + \sin\alpha \sin(\Omega \cdot t) \hat{\jmath}), \tag{4}$$

where B_P is the magnetic dipole field in the pole, R is the radius of the pulsar and α is the angle between the magnetic dipole axis and the rotation axis.

The angular velocity of the pulsar varies with time, as shown in Table 1. This could reflect on the behavior of the magnetic field with time since in this model it has the following expression when $\sin\alpha = 1$ [3]:

$$B_P = \sqrt{\frac{12 c^3 M}{5 R_0^4}} \sqrt{\frac{-\dot{\Omega}}{\Omega^3}}. \tag{5}$$

Table 1. Rotation frequency (ν) and its first and second time derivatives for the sample of pulsars.

Name	J name	ν (s^{-1})	$\dot{\nu}$ ($\times10^{-10}$ s^{-2})	$\ddot{\nu}$ ($\times10^{-21}$ s^{-3})	n	Refs.
B 0531+21	J0534+2200	29.946923	-3.77535	11.147	2.342(1)	[13]
B 0540-69	J0540-6919	19.7746860321	-1.8727175	3.772	2.13(1)	[14]
B0833-45	J0835-4510	11.200	-0.15375	0.036	1.7(2)	[15]
J1119-6127	J1119-6127	2.4512027814	-0.2415507	0.6389	2.684(2)[a]	[16]
J1208-6238	J1208-6238	2.26968010518	-1.6842733	0.33	2.598(1)	[17]
B1509-58	J1513-5908	6.611515243850	-0.6694371307	1.9185594	2.832(3)	[18]
J1734-3333	J1734-3333	0.855182765	-0.0166702	0.0028	0.9(2)	[19]
J1833-1034	J1833-1034	16.15935711336	-0.52751130	0.3197	1.857(1)	[20]
J1846-0258	J1846-0258	3.059040903	-0.665131	3.17	2.64(1)[b]	[21]

Notes. Besides these references, information regarding associations and most rotational parameters were taken from the ATNF Pulsar catalogue (http://www.atnf.csiro.au/research/pulsar/psrcat/; Manchester et al. 2005). Uncertainties (1σ) on the last quoted digit are shown between parentheses.

[a] A possible reduction of about 15% is observed after a large glitch [22].

[b] The braking index was found to decrease to $n = 2.19$ after a large glitch [23, 24].

In the canonical model, its rotating energy changes into electromagnetic energy:

$$\dot{E}_{rot} = -\dot{E}_{mr}, \tag{6}$$

implying

$$\dot{\Omega} = -k\Omega^3, \tag{7}$$

where k a positive constant.

The canonical model predicts a gradual slowdown of the star's rotation, which can be quantified by a dimensionless parameter, the the braking index n, defined by:

$$n \equiv \frac{\Omega\ddot{\Omega}}{\dot{\Omega}^2}. \tag{8}$$

In the canonical model this parameter assumes a single value ($n = 3$) for all pulsars. However, all the observational values for n are different from the one given by the canonical model (see table 1).

3. Inside a neutron star: summary of the dynamics of superfluid cores

3.1. Motion of neutron vortices

In order to characterize the flow type of a fluid it is important to analyze the circulation, defined as the line integral along a path C that surrounds the vortex circulation [25]:

$$\kappa = \oint_C \vec{v}_s \cdot d\vec{l}, \tag{9}$$

where v_s is the fluid velocity and dl is the line element along κ.

The polar decomposition ansatz for the condensate wave function allows us to describe the general shape of the Cooper pair [26], from which the velocity of the fluid can be found:

$$\psi(\vec{R}) = |\psi| e^{i\theta(\vec{R})}, \tag{10}$$

where $|\psi|$ is a thermodynamic state variable and the phase θ is a scalar.

Consequently the superfluid velocity is [27]

$$\vec{v_s} = \frac{\hbar}{2m_n}\vec{\nabla}\theta, \tag{11}$$

with $2m_n$ being the mass of a pair of neutrons and $\hbar$ being Planck's constant divided by 2π.

A velocity field described by the gradient of a function is called the potential flow, and it is found that the flow of a superfluid is irrotational:

$$\vec{\nabla} \times \vec{v_s} = \frac{\hbar}{2m_n}\vec{\nabla} \times (\vec{\nabla}\theta) = 0. \tag{12}$$

This indicates that the condensate cannot withstand a circulation except at certain points (singularities) within the fluid [26], generating an isolated configuration of singularities known as vortex lines, where the circulation does not need to disappear [27]. In this configuration with non-zero circulation the vortex lines carry angular momentum.

3.2. Dynamics of fluid rotation inside neutron stars

The angular velocity Ω of a rotating superfluid is determined by distribution of quantized vortex lines in relation to an azimuthal symmetry about the rotation axis. In this case the linear velocity

$$v_s(r) \equiv r\Omega(r) \tag{13}$$

at distance r from the rotation axis is determined from equation 9 as

$$\oint \vec{v} \cdot d\vec{l} = 2\pi\Omega(R_n)R_n^2 = \kappa_0 \int_0^{R_n} 2\pi r' n(r')dr', \tag{14}$$

being κ_0 the vorticity quantum carried by each vortex line.

In fluid mechanics the mass conservation analog for vortices is called the vortex conservation law [27]:

$$\frac{\partial n_v}{\partial t} + \vec{\nabla} \cdot (n_v v_R \hat{r}) = 0, \tag{15}$$

where n_v is the density of vortices and v_R is the radial velocity in relation to the rotation axis of the neutron star. When this law is associated to other superfluid properties [26, 28] one finds an expression for the brake in the superfluid rotation, $\dot{\Omega}_s$:

$$\dot{\Omega}_s = -\frac{\kappa_0 n_v v_R}{R_n}. \tag{16}$$

Therefore, when the superfluid rotation decays in time the vortices move outward with velocity v_R. One can show that [29] $n_v \kappa_0 = 2\Omega_s$, allowing the above equation to be rewritten as

$$\frac{\dot{\Omega}_s}{\Omega_s} = -\frac{2v_R}{R_n}. \tag{17}$$

It is expected that the star's core and crust reach the same angular velocity at large time scales [30].On such scales the magnetic torque about the crust is then transmitted to the core, implying $\dot{\Omega}_s \equiv \dot{\Omega}$. Therefore the equation 17 can be rewriten as

$$\frac{\dot{\Omega}}{\Omega} = -\frac{2v_R}{R_n}. \tag{18}$$

We assume that the crust of a pulsar is thin, with the core occupying approximately 80% of its radius, allowing for 1.4 $M_\odot$ stars with physical equations of state. Then for a total radius of 10 km the core's radius is $R_n \approx 8$ km.

In the next section we will use this physical mechanism and the radiation due to the rotating magnetic dipole to present a new model to v_R that allows the calculation of the radial velocity of the flow of the superfluid vortices without using vortex conservation hypotheses. In particular, this variation is of the order of neutron vortices creep in rotating superfluids.

4. Magnetic dipole radiation and the displacement parameter

The possibility of the stretching of a pulsar in response to rotation [31] inspired this investigation of the behavior of the braking index in the presence of a variation in time of a displacement parameter, which we will argue that is the radial velocity flow discussed in the previous section. This flow of vortices would promote the transfer of the angular momentum of the star's core generating the variation of the moment of inertia between the core and the crust of the neutron star. This assumption differs from the canonical models approach [32].

As in the canonical model we assume that the pulsar changes its rotational energy (E_{rot}) into electromagnetic dipole radiation (E_{mr}) as in equation 6 and that it consists of a thin, solid crust with *constant* moment of inertia I_c. However, differently from that model we will consider that its large spherical core with total constant mass, M_n, made basically of superfluid neutrons, has moment of inertia given by

$$I_n(t) \equiv \lambda M_n R^2(t). \tag{19}$$

In this expression R is a *displacement parameter* that summarizes in its mathematical behavior all physical factors that influence the moment of inertia other than the core's total mass. We assume that the core's moment of inertia may change with time but not due to a change in its total mass or physical radius; instead, any change in I_n will be due to *internal displacements* of mass that are quantified by $R(t)$.

We can perform a Taylor expansion of the displacement parameter and we will assume that this expansion can be truncated after its second term due to negligible higher R derivatives:

$$R(t) \approx R_n + t\dot{R}. \tag{20}$$

Physically this implies that the displacement parameter varies at a nearly constant rate in time, $\dot{R}$. This constant with units of speed is expected to vary from pulsar to pulsar as it informs about the inner dynamics of the star.

Differentiating the expression for the rotational energy, equation (1), with respect to time, in view of the assumptions of our model results in

$$\dot{E}_{rot} = \frac{1}{2}\frac{d}{dt}(I_c\Omega_c^2 + I_n\Omega_n^2). \tag{21}$$

Since any changes in the angular velocity of the crust, Ω_c, are rapidly transmitted to the core, in practice the angular velocity of the latter, Ω_n, will be considered equal to $\Omega_c \equiv \Omega$. As the moment of inertia of the thin crust is expected to be much less than the moment of inertia of the large, heavy core, we approximate $I_c + I_n \approx I_n$. Similarly, we consider M_n practically equal to the total mass of the pulsar, M. We will further admit that for the duration of typical observational time intervals, τ, the condition $\tau\dot{R} << R_n$ holds such that equation (20) yields the typical value for R:

$$R = R_n\left(1 + \tau\frac{\dot{R}}{R_n}\right) \Rightarrow R \approx R_n. \tag{22}$$

Finally, assuming a core that occupies the vast majority of the pulsar's volume we have $R_n \approx R_0$ and the expression for the rotation power becomes

$$\dot{E}_{rot} = \lambda M R_0^2 \Omega^2 \left(\frac{\dot{\Omega}}{\Omega} + \frac{\dot{R}}{R_0} \right). \tag{23}$$

The above assumptions regarding our model can be used to find the following expression for the magnetic radiation power from equations (3) and (4)

$$\dot{E}_{mr} = \frac{\sin^2 \alpha B_P^2 R_0^6 \Omega^4 + 24 \sin^2 \alpha B_P^2 R_0^4 \dot{R}^2 \Omega^2 + 36 B_P^2 R_0^2 \dot{R}^4}{6c^3}. \tag{24}$$

Therefore, we are again assuming that the quantity $\dot{R}$, which does not correspond physically to a change in the star's radius, describes mathematically all unknown physical influences that may affect the magnetic radiation power.

Substituting equations (23) and (24) in equation (6) yields

$$\begin{aligned} \lambda M R^2 \Omega^2 \left(\frac{\dot{\Omega}}{\Omega} + \frac{\dot{R}}{R} \right) &= -\frac{\sin^2 \alpha B_P^2 R^6 \Omega^4}{6c^3} \\ &- \frac{24 \sin^2 \alpha B_P^2 R^4 \dot{R}^2 \Omega^2 + 36 B_P^2 R^2 \dot{R}^4}{6c^3}, \end{aligned} \tag{25}$$

where we dropped the sub index 0 in R_0 such that R henceforth corresponds to the typical star radius.

Solving this equation for the time variation of the angular velocity, $\dot{\Omega}$, we can obtain the braking index n using the definition (8):

$$n = \frac{(3 \sin^2 \alpha B_P^2 R^5 \Omega^2)}{(12 \lambda c^3 \dot{R} M + \sin^2 \alpha B_P^2 R^5 \Omega^2)}. \tag{26}$$

Solving this equation for $\dot{R}$ we find the expression for the time variation of the displacement parameter:

$$\dot{R} = -\frac{\sin^2 \alpha B_P^2 (n-3) R^5 \Omega^2}{12 \lambda c^3 n M}. \tag{27}$$

We will estimate the values of $\dot{R}$ assuming the following typical values, applied to the pulsars given in Table 1: star radius R = 10 km; total mass M = 1.4 $M_\odot$ (where $M_\odot$ denotes one solar mass). These values imply a moment of inertia $I_0 = 2MR^2/5 = 56\ M_\odot\ km^2$ when the pulsars were born.

The expression for the magnetic field for pulsars in our model is biven by

$$B_P = \sqrt{\frac{6 \lambda c^3 M}{R^4 sin^2(\alpha)}} \sqrt{\frac{-\dot{\Omega}}{\Omega^3} - \frac{\dot{R}}{R \Omega^2}}. \tag{28}$$

In this expression, when $\dot{R} = 0$ and $\sin \alpha = 1$ the canonical expression (5) is recovered. The second term under the second square root of this equation, which has the contribution of the $\dot{R}$, will be negligible when

$$|\dot{R}| \ll |\frac{\dot{\Omega}}{\Omega} R|. \tag{29}$$

Table 2. Time variation of the radius ($\dot{R}$) and magnetic field at the pole according to our model (B_P) for our sample of pulsars.

Pulsar	$\dot{R}$ (cm s^{-1})	B_P (G)
B0531+21	1.2×10^{-6}	1.1×10^{13}
B0540-69	1.3×10^{-6}	1.4×10^{13}
B0833-45	3.0×10^{-7}	9.0×10^{12}
J1119-6127	4.4×10^{-7}	1.2×10^{14}
J1208-6238	3.8×10^{-7}	1.2×10^{14}
B1509-58	2.4×10^{-7}	4.8×10^{13}
J1734-3333	8.6×10^{-7}	1.1×10^{14}
J1833-1034	6.1×10^{-7}	9.8×10^{12}
J1846-0258	2.7×10^{-6}	1.4×10^{14}

Substituting (28) in (26) yields

$$n = 3\frac{\dot{\Omega}/\Omega + \dot{R}/R}{\dot{\Omega}/\Omega - \dot{R}/R}. \tag{30}$$

This equation can be inverted, yielding an expression for the variation in time of the displacement parameter:

$$\dot{R} = \frac{\dot{\Omega}}{\Omega} R \frac{n-3}{n+3}. \tag{31}$$

We used this equation to obtain the values of $\dot{R}$ presented in Table 2, which show that for this sample of pulsars the condition (29) is not completely fulfilled. The values of the magnetic field given by the canonical model have the same order of magnitude of the values obtained with our model from equation (28). Nevertheless, canonical values of the magnetic field should not be used in equations (26) and (27), as they would yield canonical results. The small difference between the values of the magnetic field in the two models is essential to yield observational braking indices.

4.1. When angular momentum is conserved

From the angular momentum definition, $L = I\Omega$, when angular momentum is conserved then $\dot{L} = \dot{I}\Omega + I\dot{\Omega} = 0$. In our case the moment inertia of the core (I_n) is changing in time and is much larger than the crust's moment of inertia (I_c, which is constant). Therefore, angular momentum conservation implies:

$$\dot{I}_n \Omega = -I_n \dot{\Omega}. \tag{32}$$

As I_n is given by equation 19 we can rewrite this equation as:

$$\frac{\dot{\Omega}}{\Omega} = \frac{-2\dot{R}}{R_n}, \tag{33}$$

which allows us to identify: $\dot{R} = v_R$.

5. Inferring age from the displacement parameter

A study that may in the future lead to an age calculation for pulsars with a nucleus of superfluid matter different from the characteristic age may be: to estimate the order of the displacement parameter according to the possible age of the pulsar. As there is an estimated rotation frequency at birth of the pulsar [15] it may be possible to calculate a pulsars age from the superfluid displacement parameter and the braking index. We will find the range of the displacement parameter according to the age of the pulsars between 0.5 and 100 thousand years.

From the equation 31 and of the characteristic age (t_c): $t_c = -\Omega/2\dot{\Omega}$, we can write:

$$\dot{R} = \frac{(3-n)}{(3+n)}\frac{R}{2t_c}, \tag{34}$$

from this equation we made the figures 1, 2 and 3.

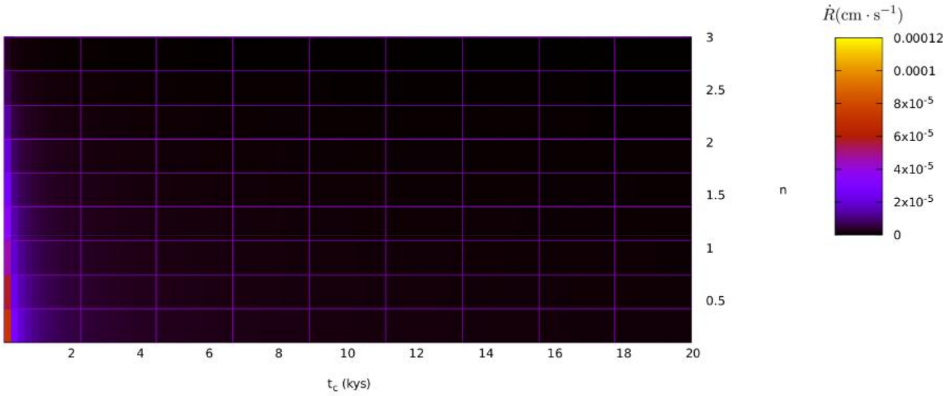

Figure 1. In the figure the displacement parameter is the axis represented by the right bar in cms^{-1}, while the braking index is represented by the vertical axis with "n" from 0 to 3, and the age is on the horizontal axis of 0.5 to 20 thousand years.

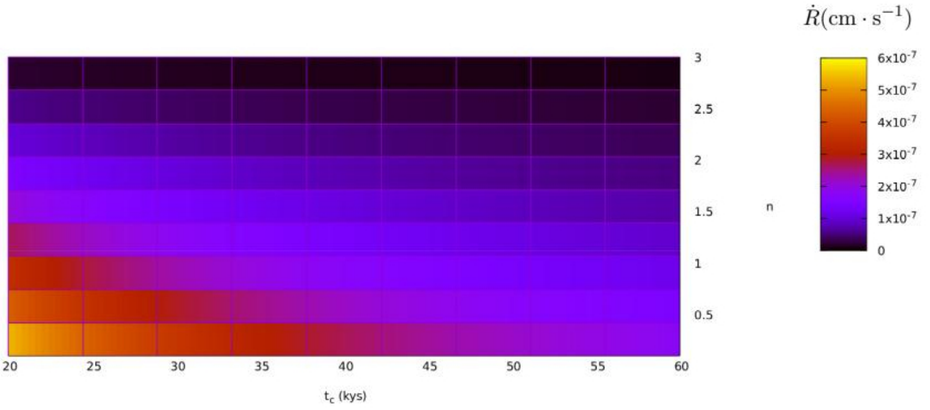

Figure 2. In the figure the displacement parameter is the axis represented by the right bar in cms^{-1}, while the braking index is represented by the vertical axis with "n" from 0 to 3, and the age is on the horizontal axis of 20 to 60 thousand years.

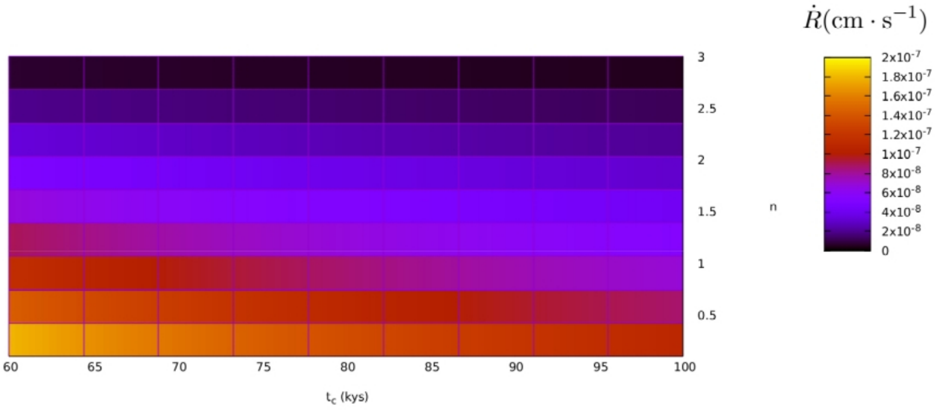

Figure 3. In the figure the displacement parameter is the axis represented by the right bar in cms^{-1}, while the braking index is represented by the vertical axis with "n" from 0 to 3, and the age is on the horizontal axis of 60 to 100 thousand years.

The figures represent the same but for different age ranges for better visualization. We observe from the figures that when the braking index approaches the value of 3 the variation of the parameter decreases tending to zero. We note that the greater age the values of the displacement parameter become lower. In addition to this trend note that the higher the age and the braking index the lower the displacement parameter values.

6. Conclusions

In this work we modified the canonical model for pulsars including changes in moment of inertia, expecting to provide a better explanation for pulsars' braking indices. The moment of inertia would change due to mass motions inside the star, quantified by a displacement parameter. We found that the displacement parameter relates to the velocity of superfluid neutron vortices when n=1. Our model assumes that the a time-varying moment of inertia changes uniformly in the radial direction which coincides with the direction of motion of neutron superfluid vortex lines. In this work we introduced the displacement parameter $\dot{R}$ and its estimates were found based on observational data.

We conjecture that the increase in moment of inertia in this model may be related to the dynamics of superfluid vortex lines in the pulsars core due to the coincidence between the estimated value for $\dot{R}$ and the approximate speed of travel of vortex lines in the core (less than the cm/day).

As consequences of this study other questions are unfolding, such as calculation of pulsars' ages and the relation between torque and the angle between magnetic moment and rotation axis, which are under investigation.

Acknowledgments

HOO thanks *Coordenação de Aperfeiçoamento de Pessoal de Nível Superior* (CAPES) for the financial support. NSM acknowledges the National Institute of Science and Technology in Astrophysics (INCT-A, Brazil; a joint CNPq and FAPESP project, FAPESP grant # 2008/57807-5) for support. GAC thanks CAPES for financial support under the process PDSE # 88881.188302/2018-01. CF thanks CPNQ for support, CNPQ grant # 309098/2017-3. The authors acknowledge FAPESP for support under the thematic project # 2013/26258-4.

References

[1] Gold T 1968 *Nature* **218** 731
[2] Gunn J and Ostriker J P 1969 *Nature* **221** 454
[3] Glendenning N K 2000 Compact stars: Nuclear physics, particle physics, and general relativity (New York: ed Springer)
[4] Xu R and Qiao G 2001 *Astrophys. J. Lett.* **561** L85
[5] Kou F and Tong H 2015 *Mon. Not. R. Astron. Soc.* **450** 1990
[6] Magalhaes N S *et al.* 2012 *Astrophys. J.* **755** 54
[7] Allen M P and Horvath J E 1997 *Mon. Not. R. Astron. Soc.* **287** 615
[8] Magalhaes N S *et al.* 2016 *Mon. Not. R. Astron. Soc.* **461** 3993
[9] Baym G *et al.* 1969 *Nature* **224** 673
[10] Ho W C G and Andersson N 2012 *Nature Phys.* **8** 787
[11] de Oliveira H O *et al.* 2018 *JCAP* 11 025. See also arXiv:1807.11474v3 [astro-ph.HE] 13 Aug 2018
[12] Shapiro S L and Teukolsky S A 2008 Black holes, white dwarfs and neutron neutron stars: the physics of compact objects, (New York: ed John Wiley & Sons)
[13] Lyne A *et al.* 2015 *Mon. Not. R. Astron. Soc.* **446** 857
[14] Ferdman R D *et al.* 2015 *Astrophys. J.* **812** 95
[15] Espinoza C M *et al.* 2016 *Mon. Not. R. Astron. Soc.* **466** 147
[16] Weltevrede P *et al.* 2011 *Mon. Not. R. Astron. Soc.* **411** 1917
[17] Clark C J *et al.* 2016 *Astrophys. J. Lett.* **832** L15
[18] Livingstone M A and Kaspi V M 2011 *Astrophys. J.* **742** 31
[19] Espinoza C M *et al.* 2011 *Astrophys. J.* **741** L13
[20] Roy J *et a.* 2012 *Mon. Not. R. Astron. Soc.* **424** 2213
[21] Livingstone M A *et al.* 2007 *Astrophys. Space Sci.* **308** 317
[22] Antonopoulou D *et al.* 2015 *Mon. Not. R. Astron. Soc.* **447** 3924
[23] Livingstone M A *et al.* 2011 *Astrophys. J.* **730** 66
[24] Archibald R F *et al.* 2015 *Astrophys. J.* **810** 67
[25] Landau L and Lifshitz E 1980 Course of theoretical physics Vol. 9: Statistical physics (Oxford: ed Pergamon Press)
[26] Sauls J A 1989 Superfluidity in the interiors of neutron stars In: Timing neutron stars (Dordrecht: ed Springer)
[27] Ghosh P 2007 Rotation and accretion powered pulsars, (Singapore: ed World Scientific)
[28] Alpar M A *et al.* 1984 *Astrophys. J.* **276** 325
[29] Hall H E 1960 *Adv. Phys.* **9** 89
[30] Paschalidis V and Stergioulas N 2017 *Living Rev. Relativ.* **20** 7
[31] Hartle J B Thorne K S 1968 *Astrophys. J.* **153** 807
[32] Ostriker J P and Gunn J 1969 *Astrophys. J.* **157** 1395

XLI Brazilian Meeting on Nuclear Physics (RTFNB) IOP Publishing
IOP Conf. Series: Journal of Physics: Conf. Series **1291** (2019) 012013 doi:10.1088/1742-6596/1291/1/012013

Bethe-Salpeter approach to three-body bound states with zero-range interaction

E Ydrefors[1], **J H Alvarenga Nogueira**[1,2], **V A Karmanov**[3] **and T Frederico**[1]

[1]Instituto Tecnológico de Aeronáutica, DCTA, 12228-900 São José dos Campos, Brazil
[2]Dipartimento di Fisica, Università di Roma “La Sapienza” & INFN, Sezione di Roma Piazzale A. Moro 5 - 00187 Roma, Italy
[3]Lebedev Physical Institute, Leninsky Prospekt 53, 119991 Moscow, Russia

E-mail: `ydrefors@kth.se`

Abstract. The Bethe-Salpeter equation for three scalar bosons, with zero-range interaction, is solved in Minkowski space by direct integration of the four-dimensional integral equation. The singularities occuring in the propagators are treated properly by standard analytical and numerical methods, without relying on any ansatz for the Bethe-Salpeter amplitude. The results for the binding energies and transverse amplitudes are compared with the results computed in Euclidean space. A fair agreement between the calculations is obtained.

1. Introduction

The Bethe-Salpeter (BS) equation [1, 2] comprises a reliable tool for the description of relativistic few-body systems in the non-perturbative regime. From the numerical point of view, the most straightforward way to solve this integral equation is to carry out its analytic continuation to the Euclidean space, through the Wick rotation [3]. Some physical quantities, e.g. binding energies, are unaltered under this transformation. However, as shown in [4], the Euclidean BS amplitude cannot be naively used to compute some dynamical observables. For such applications one needs the BS amplitude solution in Minkowski space. The two-scalar BS equation, with one-boson-exchange interaction, was solved successfully in Minkowski space by several research groups, see e.g. [5, 6, 7, 8]. The Nakanishi integral representation [9, 10] was then adopted to put the BS equation in a non-singular solvable form.

Unraveling the structure of relativistic three-body systems has important implications for applications in subatomic physics, but it is more difficult if compared to two-body systems. Most of the comprehensive studies in the three-body context have, so far, been carried out for the zero range interaction framework, which, despite of its simplicity, is quite useful. Investigations of the structure of three-body systems with short-range interactions are also important for Efimov physics which dominates the properties of the energy eigenstates with total vanishing angular momentum, composed by the maximally symmetric configuration. The low-energy properties of such systems are given by model independent correlations with few physical scales, namely the large scattering lengths and one characteristic three-body scale. Such universal correlations are limit cycles repeating themselves geometrically in the limit where the scattering length goes to infinity, as happens to the Efimov states with binding energies geometrically separated. For a more comprehensive discussion of the universality in few-body systems, see e.g. Ref. [14]. The mentioned properties are retained in a relativistic description of the three-boson equation considering a low momentum expansion with respect to the individual mass. The Efimov phenomena from the point of view of a relativistic model is associated with the infrared behavior of the associated momentum space integral equations. However, it is well-known that in non-relativistic three-body systems with zero-range interaction the binding energy is not bounded from below, i.e. they have a so-called Thomas collapse, which can be related to the Efimov effect due to the scale invariance of the ultraviolet form of the non-relativistic equations [11]. On the contrary, it was shown in Refs. [12, 13] that in a relativistic framework the Thomas collapse is not anymore equivalent to the Efimov effect, as the mass is a scale breaks the equivalence between the infrared region (non-relativistic) and the ultraviolet region. Furthermore, the Thomas collapse is eliminated by the appearance of an effective short-range repulsion due to the relativistic propagation of the constituents. Consequently, it is important to study the structure of such systems within fully relativistic frameworks.

The BS and Light-Front (LF) equations for the three-boson system with zero-range interaction were derived in [12]. The LF equation, which is obtained by performing the integration over k^- of the BS amplitude, only preserves the valence component of the BS amplitude, and was solved by Frederico in a limited range and the solution was subsequently generalized in Ref. [13]. Recently, in [15], we solved the BS equation, introduced in [12], in Euclidean space and it was then deduced that higher-Fock components beyond the valence have a great impact on the structure of the three-body system. As already pointed out, it is crucial to acquire the BS amplitude directly in Minkowski space. To this end, we solved in the recent work [17] the BS equation by direct integration in Minkowski space and some of the results are presented in this contribution. The results for the binding energies and transverse amplitudes are also compared with the ones obtained in Euclidean space.

2. Three-body Bethe-Salpeter equation

We consider a system of three bosons, with constituent masses m, with zero-range interaction. The BS equation for the Faddeev component of the vertex function then reads [12]

$$v(p,q) = 2iF(M_{12}) \int \frac{d^4k}{(2\pi)^4} \frac{i}{[k^2 - m^2 + i\epsilon]} \frac{i}{[(p-q-k)^2 - m^2 + i\epsilon]}, \tag{1}$$

where p denotes the total four momentum of the three-body system and q is the four momentum of the spectator particle. Furthermore, $F(M_{12})$ is the two-body scattering amplitude and the squared mass of the two-body subsystem is given by $M_{12}^2 = (p-q)^2$.

The BS equation (1) comprises a highly-singular integral equation and is thus challenging to solve numerically. If the purpose simply is to compute well-defined quantities, such as binding energies, one can transform Eq. (1) to the complex plane through the Wick rotation. In the rest frame ($\vec{p} = \vec{0}$), the Euclidean BS equation is given by [15]

$$v_E(q'_4, q'_v) = 2F(-M'^2_{12}) \int_{-\infty}^{\infty} dk'_4 \int_0^{\infty} \frac{dk'_v}{(2\pi)^3} \frac{\Pi_E(q'_4, q'_v, k'_4, k'_v)}{(k'_4 - \frac{i}{3}M_3)^2 + k'^2_v + m^2}, \tag{2}$$

with the kernel

$$\Pi_E(q'_4, q'_v, k'_4, k'_v) = \frac{k'_v}{2q'_v} \log \frac{(k'_4 + q'_4 + \frac{i}{3}M_3)^2 + (q'_v + k'_v)^2 + m^2}{(k'_4 + q'_4 + \frac{i}{3}M_3)^2 + (q'_v - k'_v)^2 + m^2}. \tag{3}$$

In the derivation of (2), we performed the change of variables $k = k' + \frac{p}{3}$ and $q = q' + \frac{p}{3}$, so that the Wick rotation could be accomplished without crossing any singularities of the integrand in Eq. (1).

The three-body LF equation, introduced in [12], is completely defined in Minkowski space, but it only gives access to the valence component. For realistic calculations of dynamical observables, it is thus essential to also study the full solution of Eq. (1) directly in Minkowski space. Following the technique introduced in [16], we write the propagator $[k^2 - m^2 + i\epsilon]^{-1}$ as

$$\frac{1}{k^2 - m^2 + i\epsilon} = PV\frac{1}{k_0^2 - \varepsilon_k^2} - \frac{i\pi}{2\varepsilon_k}[\delta(k_0 - \varepsilon_k) + \delta(k_0 + \varepsilon_k)], \tag{4}$$

with $\varepsilon_k = \sqrt{k_v^2 + m^2}$ and $k_v = |\vec{k}|$.

Eq. (1) can then transformed to the partially non-singular form [17]

$$\begin{aligned} v(q_0, q_v) = \frac{\mathcal{F}(M_{12})}{(2\pi)^4} \int_0^\infty k_v^2 dk_v \Bigg\{ & \frac{\pi i}{\varepsilon_k} \left[\Pi(q_0, q_v; \varepsilon_k, k_v) v(\varepsilon_k, k_v) + \Pi(q_0, q_v; -\varepsilon_k, k_v) v(-\varepsilon_k, k_v)\right] \\ & - 2\int_{-\infty}^0 dk_0 \left[\frac{\Pi(q_0, q_v; k_0, k_v) v(k_0, k_v) - \Pi(q_0, q_v; -\varepsilon_k, k_v) v(-\varepsilon_k, k_v)}{k_0^2 - \varepsilon_k^2}\right] \\ & - 2\int_0^\infty dk_0 \left[\frac{\Pi(q_0, q_v; k_0, k_v) v(k_0, k_v) - \Pi(q_0, q; \varepsilon_k, k_v) v(\varepsilon_k, k_v)}{k_0^2 - \varepsilon_k^2}\right] \Bigg\}, \end{aligned} \tag{5}$$

where the propagator singularities have been eliminated by subtractions. The kernel Π has now only weak (logarithmic) singularities which will be treated numerically and is given explicitly in [17].

It is not possible to directly compare the Minkowski vertex function $v(q_0, q_v)$ with the corresponding Euclidean one. However, one can use, in the BS amplitude, instead of $k = (q_0, q_v)$ the LF variables $q = (q_-, q_+, \vec{q}_\perp)$, with $q_\mp = q_0 \mp q_z$ and $\vec{q}_\perp = (q_x, q_y)$. The double integrals of the Minkowski BS amplitude over q_+ and q_-, and of the corresponding Euclidean ones over q_0, q_z, are then the same.

The contribution $L_1(\vec{k}_{1\perp}, \vec{k}_{2\perp})$ to the transverse amplitude takes the form [17]

$$\begin{aligned} & L_1(\vec{k}_{1\perp}, \vec{k}_{2\perp}) = \\ & \quad - i\int_{-\infty}^\infty dk_{1z} \Bigg\{ \frac{i\pi}{2\tilde{k}_{10}} \left[\chi(\tilde{k}_{10}, k_{1z}; \vec{k}_{1\perp}, \vec{k}_{2\perp}) v_M(\tilde{k}_{10}, k_{1v}) + \chi(-\tilde{k}_{10}, k_{1z}; \vec{k}_{1\perp}, \vec{k}_{2\perp}) v_M(-\tilde{k}_{10}, k_{1v})\right] \\ & \quad - \int_0^\infty dk_{10} \frac{\chi(-k_{10}, k_{1z}; \vec{k}_{1\perp}, \vec{k}_{2\perp}) v_M(-k_{10}, k_{1v}) - \chi(-\tilde{k}_{10}, k_{1z}; \vec{k}_{1\perp}, \vec{k}_{2\perp}) v_M(-\tilde{k}_{10}, k_{1v})}{k_{10}^2 - \tilde{k}_{10}^2} \\ & \quad - \int_0^\infty dk_{10} \frac{\chi(k_{10}, k_{1z}; \vec{k}_{1\perp}, \vec{k}_{2\perp}) v_M(k_{10}, k_{1v}) - \chi(\tilde{k}_{10}, k_{1z}; \vec{k}_{1\perp}, \vec{k}_{2\perp}) v_M(\tilde{k}_{10}, k_{1v})}{k_{10}^2 - \tilde{k}_{10}^2} \Bigg\}, \end{aligned} \tag{6}$$

where

$$\tilde{k}_{10} = \sqrt{k_{1z}^2 + \vec{k}_{1\perp}^2 + m^2}. \tag{7}$$

Similarly to the treatment of the BS equation, we have here used subtractions to eliminate the propagator singularities at $k_0 = \pm\tilde{k}_{10}$.

3. Results and discussion

In Ref. [17], we solved Eq. (5) by adopting a bi-cubic spline decomposition of the vertex function $v(p, q)$. In Table 1 is shown the computed eigenvalue λ, which multiplies the right-hand side of the BS equation, for three different values of the two-body scattering length. In the calculations we used also as input the three-body binding energy obtained by solving the Euclidean BS equation derived in [15]. In the table, an eigenvalue of $\lambda = 1.0$ indicates that Minkowski and

Euclidean solutions are consistent. It is seen that for all three cases that the real part of λ is close to one. For reasons of numerical stability, we used in the Minkowski-space computations cut-offs on the variables q_0 and q_v. On the contrary, in the solution of the Euclidean BS equation the full integration domain was retained. This could explain the small imaginary parts and the error in the real parts.

am	B_3/m	λ
-1.280	0.006	$0.999 - 0.054i$
-1.500	0.395	$1.000 + 0.002i$
-1.705	1.001	$0.997 + 0.106i$

Table 1. Eigenvalues of the three-body ground state for three scattering lengths, a, computed by using the Euclidean three-body binding energies.

Furthermore, in Fig. 1 it is shown as an example the calculated vertex function, $v(q_0, q_v = 0.5m)$, for the three-body binding energy $B_3/m = 0.395$. As discussed in more detail in [17], the vertex function has peaks at the values of q_v and q_0, corresponding to that $M_{12}^2 = 0$ or $M_{12}^2 = 4m^2$. In the figure these positions are indicated with dashed lines.

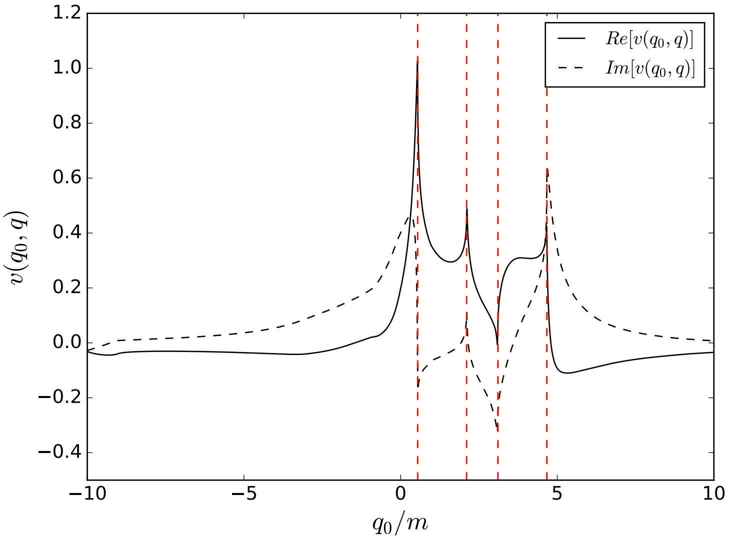

Figure 1. The vertex function, $v(q_0, q_v = 0.5m)$ with respect to q_0 for the parameters $am = -1.5$ and $B_3/m = 0.395$.

As already mentioned, we use for the three-body vertex function an expansion in terms of a finite number of spline functions. It is then important to make sure that the adopted number of basis functions is enough. To this end, we display in Fig. 2 the real and imaginary parts of $v(q_0, q_v = 0.5m)$, calculated by using different number of subintervals N_{qv} and N_{q0}, corresponding to the variables q_v and q_0. The results in the figure corresponds to the parameters $am = 1.5$ and $B_3/m = 0.395$. It is clearly visible in the figure that for $N_{q_v} \geq 40$ and $N_{q_0} \geq 80$, the solution is well-converged.

Moreover, in Fig. 3 we show the modulus of the contribution $L_1(k_{1\perp}, k_{2\perp} = 0)$ to the transverse amplitude for $B_3/m = 0.395$, calculated by using Eq. (6). The results are also compared with the corresponding Euclidean ones. It is visible in the figure that the results are

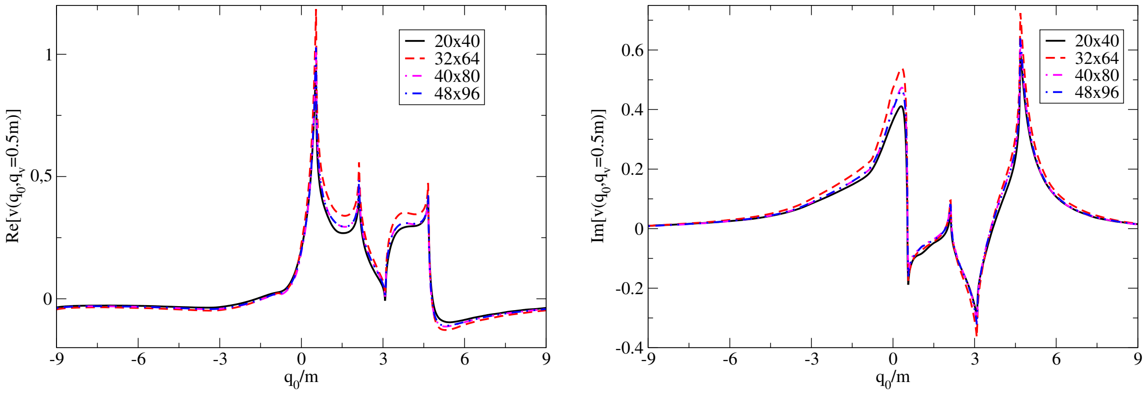

Figure 2. Convergence of the real (left panel) and imaginary (right panel) parts of the vertex function $v(q_0, q_v = 0.5m)$ with respect to the size of the basis, $N_{q_v} \times N_{q0}$. The results correspond to the case $B_3/m = 0.395$.

in fair agreement with each other. As is clearly seen in Fig. 1, the vertex $v(q_0, q_v)$ with respect to q_0 is a non-smooth function. Despite of this, the computed transverse amplitude versus $k_\perp$ is smooth, which makes the coincidence even more remarkable.

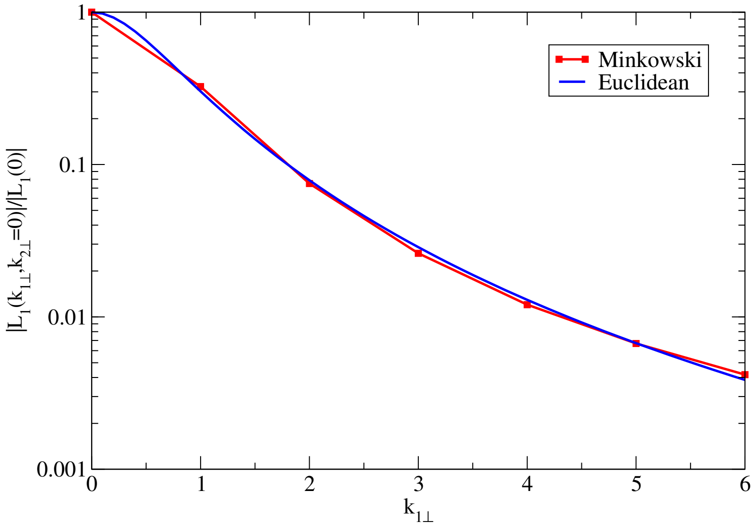

Figure 3. Transverse contribution, $L_1(k_{1\perp}, k_{2\perp} = 0)$, obtained in Minkowski space compared with the one computed in Euclidean space, for the parameters $am = -1.5$ and $B_3/m = 0.395$.

4. Conclusions

We have in this work, solved, directly in Minkowski space, the three-body BS equation derived in [12] for scalar bosons interacting by the two-body zero-range interaction. Our results show that both the three-body binding energies and transverse amplitudes, derived by direct integration of the Minkowskian BSE, agree with the Euclidean ones. However, the method is rather demanding from the numerical perspective, because of the appearance of many singularities which have to be treated properly. One possible way to the improve the numerical accuracy and also to be able to treat more realistic kernels is to transform the BS equation into a non-singular form by using the Nakanishi integral representation [9, 10]. This is a work in progress and calculations based on this method will be undertaken soon.

Acknowledgments

We are grateful to Jaume Carbonell for stimulating discussions. This study was financed in part by Conselho Nacional de Desenvolvimento Científico e Tecnológico (CNPq) and by Coordenação de Aperfeiçoamento de Pessoal de Nível Superior - Brasil (CAPES) - Finance code 001. J.H.A.N. acknowledges the support of the grants #2014/19094-8 and #2017/14695-1 and V.A.K. of the grant #2015/22701-6 from Fundação de Amparo à Pesquisa do Estado de São Paulo (FAPESP). E.Y. thanks for the financial support of the grant #2016/25143-7 from FAPESP. We thank the FAPESP Thematic Projects grants #13/26258-4 and #17/05660-0. V.A.K. is also sincerely grateful to the group of theoretical nuclear physics of ITA, São José dos Campos, Brazil, for kind hospitality during his visit.

References

[1] Salpeter E E and Bethe H 1951 *Phys Rev* **84** 1232
[2] Gell-Man M and Low F 1951 *Phys Rev* **84** 350
[3] Wick G C 1954 *Phys Rev* **96** 1135
[4] Carbonell J and Karmanov V A 2011 *Few-Body Syst* **49** 205
[5] Kusaka K and Williams A G 1995 *Phys Rev D* **51** 7026
[6] Kusaka K, Simpson K and Williams A G 1997 *Phys Rev D* **56** 5071
[7] Karmanov V A and Carbonell J 2006 *Eur Phys J A* **27** 1
[8] Frederico T, Salmè G and Viviani M 2014 *Phys Rev D* **89** 016010
[9] Nakanishi N 1963 *Phys Rev* **130** 1230
[10] Nakanishi N 1969 *Prog Theor Phys Suppl* **43** 1
[11] Thomas L H 1935 *Phys Rev* **47** 903.
[12] Frederico T 1992 *Phys Lett B* **282** 409
[13] Carbonell J and Karmanov V A 2003 *Phys Rev C* **67** 037001
[14] Frederico T et al 2012 *Prog Part Nucl Phys* **67** 939
[15] Ydrefors E et al 2017 *Phys Lett B* **770** 131
[16] Carbonell J and Karmanov V A 2014 *Phys Rev D* **90** 056002
[17] Ydrefors E et al 2019 *Phys Lett B* **791** 276.

IOP Conf. Series: Journal of Physics: Conf. Series **1291** (2019) 012014 doi:10.1088/1742-6596/1291/1/012014

Phase transitions of cold and dense quark matter in an external magnetic field

D C Duarte[1] **and R L S Farias**[2]

[1]Departamento de Física, Instituto tecnológico de Aeronáutica, 12228-900 São José dos Campos, SP, Brazil

[2]Departamento de Física, Universidade Federal de Santa Maria, 97105-900 Santa Maria, RS, Brazil

E-mail: `dyana@ita.br`

Abstract. In this work we study the effects of an external magnetic field in the competition of chiral and diquark order parameters in cold and dense quark matter, using a SU(2) version of the NJL model. We verify the influence of the magnetic field in the phase diagram, and perform a comparison of the results obtained using a Fermi-Dirac form factor regularization with ones obtained by using a method that makes a full separation of the finite magnetic contributions and the divergencies, the Magnetic Field Independent Regularization.

1. Introduction

One of the most intriguing problems in physics currently is the description of the quantum chromodynamics (QCD) phase diagram in $T \times \mu_B$ plane. Mainly in the region of intermediate to high baryon density, many efforts have been devoted in an attempt to understand the transition between hadronic and deconfined phases, but this mechanism is still poorly understood. One of the reasons for this scenario is that lattice first principle calculation, using Monte Carlo method, have serious problems in to deal with the region of nonzero chemical potential, since the fermion determinant that becomes complex [1]. Moreover, motivated by the fact that strong magnetic fields may be produced in noncentral heavy-ion collisions [2], might have played an important role in the physics of the early universe [3] and also may be present in the surface and core of magnetars [4], investigations of the effects produced by a magnetic field in the phase diagram of strongly interacting matter became a subject of great interest in recent years. Results from lattice simulation of three color QCD at zero baryon density shows that the background magnetic field strengthens the chiral symmetry breaking region at zero temperature, phenomenon called magnetic catalysis (MC) [5], while an inverse magnetic catalysis (IMC) takes place at finite temperature [6].

The astrophysical scenario may occur in regions of low temperature and intermediate density, where color superconducting phases are expected to exist. Due to the already mentioned sign problem, the most part of the knowledge of QCD phase structure at finite baryon density comes from effective models that preserves some of its symmetries. One of the most popular effective model used to study the color superconducting phases is the Nambu–Jona-Lasinio (NJL) model [7, 8], due to its simplicity to implementate and possibility to include and analyze different color pairing configurations. Many works have been dedicated to study the effects of magnetic fields in color superconducting phases (see [9, 10, 11, 12] and references therein), through chiral effective models in different contexts and approximations. In this paper we argue that the use of a nonrenormalizable model must be performed carefully, and devoting special attention to the regularization of divergencies. In this sense, the negligence in to cut medium contributions might lead to spurious results and interpretations, as we will discuss in Sec. 3.

This work is organized as follows. In Sec. 2 we present the NJL model in the presence of a constant external magnetic field, focusing in the parametrization and discussing two different regularization schemes. Sec. 3 is dedicated to present the results obtained and compare these two schemes, and in Sec. 4 we show some final remarks.

2. NJL Model and Parameters

We consider a NJL model including scalar-pseudoscalar and color pairing interactions, whose standard Lagrangian density in the presence of an external magnetic field is given by

$$\mathcal{L} = \bar{\psi}\left(i\not{D} - m_c\right)\psi + G_s\left[\left(\bar{\psi}\psi\right)^2 + \left(\bar{\psi}i\gamma_5\tau\psi\right)^2\right] + G_d\left(i\bar{\psi}\epsilon_f\epsilon_c^3\gamma_5\psi\right)\left(i\bar{\psi}\epsilon_f\epsilon_c^3\gamma_5\psi^C\right) \,. \qquad (1)$$

where G_s and G_d are the scalar and diquark coupling constants, m_c is the current quark mass (that we choose to take the exact isospin symmetry limit, i.e., $m_u = m_d = m_c$), $\vec{\tau}$ are Pauli matrices in flavor space, $(\epsilon_c^3)^{ab} = (\epsilon_c)^{3ab}$ and $(\epsilon_f)_{ij}$ are the antisymmetric matrices in color and flavor spaces, and $D_\mu = \partial_\mu - i\tilde{e}\tilde{Q}\tilde{\mathcal{A}}_\mu$. The rotated charge matrix $\tilde{Q}$ is given by

$$\tilde{Q} = Q_f \otimes 1_c - 1_f \otimes \left(\frac{\lambda_8}{2\sqrt{3}}\right)$$

where $Q_f = \mathrm{diag}(q_u, q_d)$, λ_8 is the color quark matrix $\lambda_8 = \mathrm{diag}(1,1,-2)/\sqrt{3}$ and $\mathcal{A}_\mu = \delta_{\mu 2}x_1 B$. It results in the different rotated charges $\tilde{q}$ for each quark colors, namely, $u_r = 1/2$, $u_g = 1/2$, $u_b = 1$, $d_r = 1/2$, $d_g = 1/2$ and $d_b = 0$. In the presence of an external magnetic field the corresponding mean field thermodynamical potential in $T \to 0$ limit is given by [13]

$$\Omega(eB, \mu, \Delta) = \frac{(M - m_c)^2}{4G} + \frac{\Delta^2}{4G_d} + \sum_{\tilde{q}=0,\frac{1}{2},1} \Omega_{\tilde{q}} \qquad (2)$$

where we have defined

$$\Omega_0 = 2\int \frac{d^3k}{(2\pi)^3}\left[E_{k,0} + (\mu - E_{k,0})\theta(\mu - E_{k,0})\right] \qquad (3)$$

$$\Omega_1 = \frac{eB}{2\pi}\sum_{l=0}^{\infty}\alpha_l \int_{-\infty}^{\infty}\frac{dk_3}{2\pi}\left[E_{k,1} + (\mu - E_{k,1})\theta(\mu - E_{k,1})\right] \qquad (4)$$

$$\Omega_{\frac{1}{2}} = -\frac{eB}{2\pi}\sum_{l=0}^{\infty}\alpha_l \int_{-\infty}^{\infty}\frac{dk_3}{2\pi}\left(E_\Delta^+ + E_\Delta^-\right) \qquad (5)$$

In these expressions, α_l takes into account the degeneracy of Landau levels, and dispersion relations are given by

$$\begin{aligned} E_{k,0}^{\pm} &= \sqrt{\vec{k}^2 + M^2} \pm \mu & \qquad E_{k,\frac{1}{2}}^{\pm} &= \sqrt{k_3^2 + M^2 + eBl} \pm \mu \\ E_{k,1}^{\pm} &= \sqrt{k_3^2 + M^2 + 2eBl} \pm \mu & \qquad E_{\Delta}^{\pm} &= \sqrt{\left(E_{k,\frac{1}{2}} \pm \mu\right)^2 + \Delta^2} \end{aligned}$$

Due to its nonrenormalizability, NJL needs a proper regularization scheme to avoid the ultraviolet divergences. As a consequence it is necessary to introduce a cutoff parameter Λ, that becomes a scale of the model. Together with the scalar and diquark coupling constants G_s and G_d and the current quark mass m_c, Λ is a parameter that must be specified to obtain the numerical results. These parameters are usually fixed such as to reproduce the empirical values of the pion mass m_π, the pion decay constant f_π and the quark condensate $\langle \bar{q}q \rangle_0$. Besides that, Fierz transformation gives the value of $G_d = 0.75G_s$, but to investigate the competition between scalar and diquark condensates we choose to treat G_d as a free parameter.

2.1. Regularization

Most part of the studies of magnetic field effects in color superconducting phases are based on form factors U_Λ [10, 14, 15], that are implementated through the prescription

$$\sum_{l=0}^{\infty} \int_{-\infty}^{+\infty} \frac{dk_3}{2\pi} \to \sum_{l=0}^{\infty} \int_{-\infty}^{+\infty} \frac{dk_3}{2\pi} U_\Lambda \left(\sqrt{k_3^2 + 2l \left| q_f \right| B} \right) \tag{6}$$

in the momentum integrals. Different smooth form factors have been used in the literature, as discussed in [13] and references therein. One of the most frequently used is the Fermi-Dirac type, given by

$$U_\Lambda^\alpha(x) = \frac{1}{2} \left[1 - \tanh\left(\frac{x/\Lambda - 1}{\alpha} \right) \right] \tag{7}$$

where α is a smoothness parameter.

By the other hand, many works have been claiming that the separation of medium contributions from divergent integrals is crucial to obtain the correct description of phase structure and behavior of physical quantities [16, 17, 12, 18, 19]. In this context we use the Magnetic Field Independent Regularization (MFIR), based in the complete separation of magnetic field dependent contributions and divergent terms [20, 13, 21, 22, 23, 24, 25, 26], whose implementation is based in to add and subtract the $eB = \mu = 0$ contribution in Ω_1, and $\mu = 0$ contributions in and $\Omega_{\frac{1}{2}}$. After some algebraic manipulations we obtain

$$\begin{aligned}
\Omega_0 &= 2 \int \frac{d^3k}{(2\pi)^3} \left[2E_{k,0} + (\mu - E_{k,0}) \theta(\mu - E_{k,0}) \right] && (8) \\
\Omega_1 &= \frac{(eB)^2}{2\pi^2} \left[\zeta'(-1, \chi) - \frac{(\chi^2 - \chi)}{2} \ln(\chi) + \frac{\chi^2}{4} \right] \\
&+ \sum_{l=0}^{l_{max}} \alpha_l \frac{eB}{4\pi^2} \left[\mu \sqrt{\mu^2 - s^2} - s^2 \ln\left(\frac{\mu + \sqrt{\mu^2 - s^2}}{s} \right) \right] && (9)
\end{aligned}$$

and also

$$\begin{aligned}
\Omega_{\frac{1}{2}} &= 4 \sum_{j=\pm 1} \int \frac{d^3k}{(2\pi)^3} \sqrt{(E_k + j\mu)^2 + \Delta^2} \\
&- \frac{(eB)^2}{2\pi^2} \left[\zeta'(-1, x) + \frac{1}{2} \left(x^2 - x \right) \ln(x) + \frac{x^2}{4} \right] \\
&+ \frac{eB}{\pi^2} \int_0^\infty dk_3 \frac{F(k_3^2)}{2} + \frac{eB}{\pi^2} \int_0^\infty dk_3 \left\{ \sum_{l=1}^{\infty} F\left(k_3^2 + eBl \right) + \int_0^\infty dy \; F\left(k_3^2 + eBy \right) \right\} && (10)
\end{aligned}$$

with $\chi = M^2/2eB, s = \sqrt{M^2 + 2eBl}, l_{max} = (\mu^2 - M^2)/2eB, x = (M^2 + \Delta^2)/eB$ and

$$F\left(z^2\right) = \sum_{j=\pm 1}\left[\sqrt{\left(\sqrt{z^2+m^2}+j\mu\right)^2+\Delta^2} - \sqrt{z^2+m^2+\Delta^2}\right]$$

Note that from Ω_1 and $\Omega_{\frac{1}{2}}$ we extract purely magnetic contribution, ensuring that no eB contribution will be regularized with the divergences of the theory[1].

3. Numerical results and discussion

In this work we have obtained $G_s = 4.75$ GeV$^{-2}, m_c = 4.99$ MeV and $\Lambda = 660$ MeV, that reproduces $m_\pi = 135$ MeV, $f_\pi = 92.3$ MeV and $\langle \bar{q}q \rangle_0^{1/3} = -250$ MeV. For both regularization schemes the vacuum quark mass $M_0 \sim 302$ MeV, and we use the smoothness parameter $\alpha = 0.01$ for FD. Numerical results are obtained by minimizing the thermodynamical potential (2) in each regularization scheme with respect to Δ and M.

It is well known that at zero chemical potential (and consequently $\Delta = 0$) the chiral condensate and constituent quark mass increases with the magnetic field presents a magnetic catalysis. From Fig. 1 one may see that for both schemes the magnetic catalysis is observed, but when using FD there are strong non-physical oscillations that becomes more pronounced with the increase of the magnetic field, which does not happen in MFIR case. These oscillations are usually confused with the well-known Van Alphen-de Haas oscillations, that are related with discontinuities in the densities. Clearly this is not the case here, since $\mu = 0$. By examining the thermodynamic potential, the only contribution that can generate these oscillations is Ω_1, that contains the theta function whose argument depends on eB, stablishing a upper limit to the Landau levels sum. While $q = 0$ contribution does not depends on the magnetic field, in $q = 1/2$ the coupling of quark species to Δ eliminates the theta function from the sum, i.e., the density is nonzero for all Landau levels while $\Delta \neq 0$.

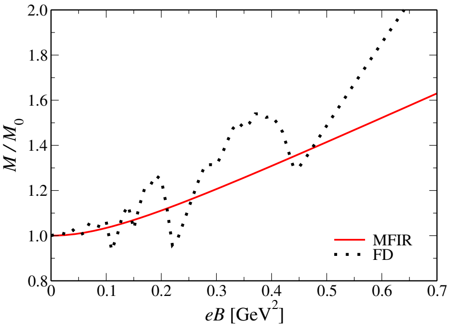

Figure 1. Constituent quark mass M as a function of eB for $G_d = \mu = 0$, comparing MFIR and FD.

In Figs. (2) and (3) we compare the order parameters obtained with FD and MFIR as functions of the magnetic field for $\mu = 0.4$ GeV. One may see now the vAdH oscillations also in MFIR, but note that the behavior of the curves is quite different for both schemes. In MFIR both Δ and M are decreasing functions of the magnetic field (IMC) and present smooth oscillations, while using FD both quantities seems to increase with eB, besides the strong non-physical oscillations. Figs. (4) and (5) shows the MFIR results for Δ and M as functions of eB, using $\mu = 0.4$ GeV and for different values of the diquark coupling constant. It is possible to see from both panels that the vAdH oscillations becomes smaller and curves becomes smooth with the increase of G_d. This is related to the fact that the value of diquark condensate increase while chiral condensate decreases with G_d, causing a supression of the oscillations even with the increase of the magnetic field.

---

[1] For more details relative to MFIR implementation see [13, 12]

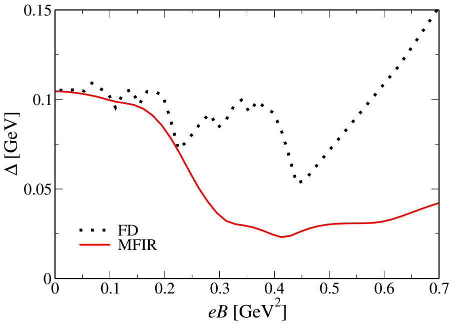

Figure 2. Order parameter Δ as a function of the magnetic field, comparing MFIR and FD.

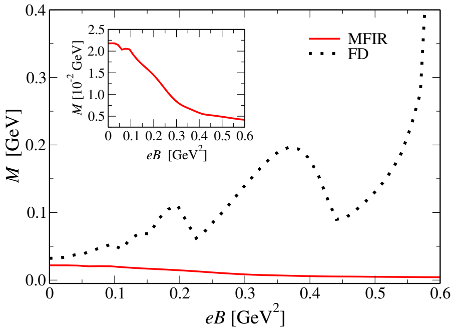

Figure 3. Constituent quark mass M as a function of the magnetic field, comparing MFIR and FD.

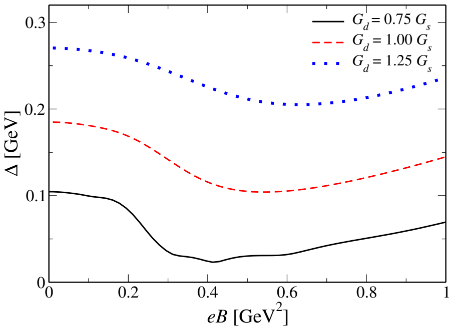

Figure 4. Order parameter Δ as a function of the magnetic field for different values of the diquark coupling G_d using MFIR.

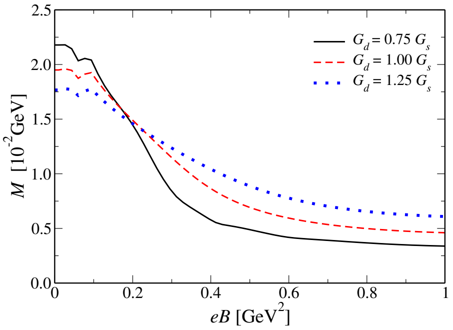

Figure 5. Constituent quark mass M as a function of the magnetic field for different values of the diquark coupling G_d using MFIR.

4. Final Remarks

We study the effects of the inclusion of an external magnetic field in the phase structure and in the behavior of order parameters in a SU(2) version of the NJL model with diquark interaction, giving special attention to the regularization scheme. From the results obtained one may see that FD produces strong non physical oscillation in Δ and M, that are not related to the well known Van Alphen-de Haas, but to the incorrect regularization of integrals that depends on the magnetic field. When these oscillations are present they have a physical meaning, and are related with discontinuities in the density, represented by the theta functions. Using MFIR we were able to observe the real vAdH oscillations and obtain the correct behavior of the aforementioned quantities, and also notice that the oscillations becomes less pronounced with the increasing of the diquark coupling constant G_d. This is related to the increase of the value of Δ and decreasing of M with G_d, that supress the oscillations when the magnetic field increases. Ref. [27] has shown that increase of G_d causes the first-order transition of the chiral and diquark gaps becomes crossover through a second-order phase transition at $eB = 0$, while Ref. [15] shows, using FD, that the presence of the external magnetic field also provokes the change from a smooth crossover to a first order phase transition, and also changes the critical baryon chemical potential. It would be useful to perform a complete study of the phase diagram in the presence of an external magnetic field using MFIR, to verify and compare these results.

Acknowledgments

This work was partially supported by Fundação de Amparo à Pesquisa do Estado de São Paulo (FAPESP) under grant 2017/26111-4 (DCD) and by Conselho Nacional de Desenvolvimento Científico e Tecnológico (CNPq) under grant Nos. 304758/2017-5 (RLSF).

References

[1] Karsch F 2002 Lattice QCD at High Temperature and Density *Lectures on Quark Matter* (*Lecture Notes in Physics* vol 583) ed Plessas W and Mathelitsch L (Springer Berlin Heidelberg) pp 209–249 ISBN 978-3-540-43234-0
[2] Fukushima K, Kharzeev D E and Warringa H J 2008 *Phys. Rev. D* **78**(7) 074033
[3] Vachaspati T 1991 *Physics Letters B* **265** 258–261 ISSN 0370-2693
[4] C K, S D, T S and J v P e a 1998 *Nature* **393** 235–237 ISSN 0028-0836 10.1038/30410
[5] Shovkovy I 2013 Magnetic Catalysis: A Review *Strongly Interacting Matter in Magnetic Fields* (*Lecture Notes in Physics* vol 871) ed Kharzeev D, Landsteiner K, Schmitt A and Yee H U (Springer Berlin Heidelberg) pp 13–49 ISBN 978-3-642-37304-6
[6] Bali G S, Bruckmann F, Endrődi G, Fodor Z, Katz S D and Schäfer A 2012 *Phys. Rev. D* **86**(7) 071502
[7] Klevansky S P 1992 *Rev. Mod. Phys.* **64**(3) 649–708
[8] Buballa M 2005 *Physics Reports* **407** 205–376 ISSN 0370-1573
[9] Noronha J L and Shovkovy I A 2007 *Phys. Rev. D* **76**(10) 105030
[10] Fukushima K and Warringa H J 2008 *Phys. Rev. Lett.* **100**(3) 032007
[11] Ferrer E J and de la Incera V 2013 *Magnetism in Dense Quark Matter* (Berlin, Heidelberg: Springer Berlin Heidelberg) pp 399–432 ISBN 978-3-642-37305-3
[12] Duarte D C, Allen P G, Farias R L S, Manso P H A, Ramos R O and Scoccola N N 2016 *Phys. Rev. D* **93**(2) 025017
[13] Allen P, Grunfeld A G and Scoccola N N 2015 *Phys. Rev. D* **92**(7) 074041
[14] Fayazbakhsh S and Sadooghi N 2010 *Phys. Rev. D* **82**(4) 045010
[15] Mandal T and Jaikumar P 2017 *Adv. High Energy Phys.* **2017** 6472909
[16] Farias R L S, Dallabona G, Krein G and Battistel O A 2006 *Phys. Rev. C* **73**(1) 018201
[17] Farias R L S, Dallabona G, Krein G and Battistel O A 2008 *Phys. Rev.* **C77** 065201
[18] Farias R L S, Duarte D C, Krein G and Ramos R O 2016 *Phys. Rev. D* **94**(7) 074011
[19] Coppola M, Allen P, Grunfeld A G and Scoccola N N 2017 *Phys. Rev.* **D96** 056013
[20] Ebert D and Klimenko K 2003 *Nuclear Physics A* **728** 203–225 ISSN 0375-9474
[21] Menezes D P, Pinto M B, Avancini S S, Martínez A P and Providência C 2009 *Phys. Rev. C* **79**(3) 035807
[22] Farias R L S, Gomes K P, Krein G I and Pinto M B 2014 *Phys. Rev.* **C90** 025203
[23] Farias R L S, Timoteo V S, Avancini S S, Pinto M B and Krein G 2017 *Eur. Phys. J.* **A53** 101
[24] Avancini S S, Farias R L S, Benghi Pinto M, Tavares W R and Timóteo V S 2017 *Phys. Lett.* **B767** 247–252
[25] Avancini S S, Dexheimer V, Farias R L S and Timóteo V S 2018 *Phys. Rev.* **C97** 035207
[26] Avancini S S, Farias R L S and Tavares W R 2018 (*Preprint* `1812.00945`)
[27] Huang M Z P C W 2002 *Physical Review D* **65**(7)

XLI Brazilian Meeting on Nuclear Physics (RTFNB) IOP Publishing
IOP Conf. Series: Journal of Physics: Conf. Series **1291** (2019) 012015 doi:10.1088/1742-6596/1291/1/012015

Neutral meson properties in hot and magnetized quark matter

R L S Farias[1], **S S Avancini**[2] **and W R Tavares**[2]
[1]Departamento de Física, Universidade Federal de Santa Maria, 97105-900 Santa Maria, RS, Brazil
[2]Departamento de Física, Universidade Federal de Santa Catarina, 88040-900 Florianópolis, Santa Catarina, Brazil

E-mail: `ricardo.farias@ufsm.br`

Abstract. In this work we evaluate the π^0 pole-mass in the RPA approximation at finite magnetic field and temperature in the NJL SU(2) model. To this end, we employ an alternative version of the Magnetic Field Independent Regularization based on the Riemann-Hurwitz zeta function. To employ this formalism, we present a set of equations applied to the gap equation and pseudo-scalar polarization loop at the mean field approximation and random phase approximation.

1. Introduction

The importance of understanding the behavior of the pole-mass of neutral mesons at finite magnetic field and $T = 0$ in the context of the NJL SU(2) model has been the subject of some previous studies[1, 2, 3, 4]. Also, the importance of adopting an appropriate regularization scheme in NJL-type models has been calling the attention [5, 6, 7, 8, 9] in recent years. In a magnetized medium, it has been clearly demonstrated the importance of the regularization scheme, where the choice of some prescriptions may give rise to spurious solutions [6, 7]. These problems can be avoided if one chooses regularization schemes where the explicit separation of the vacuum and magnetized medium contributions are done. Recently, these methods have been baptized as MFIR (magnetic field independent regularization) in ref [6].

In this work, we wish to show an alternative way to explore this separation, introducing the formalism of ref. [10] where a study of a magnetized relativistic electron gas was made in terms of the Hurwitz-Riemann zeta function. Some works studying Bose-Einstein condensation of relativistic fermions at finite magnetic field have applied some similar ideas [11, 12]. We apply this formalism for the regularization of the quark mass gap equation and polarization loop integral within the SU(2) Nambu-Jona-Lasinio model in the mean field approximation in a hot and magnetized medium.

2. Formalism

2.1. zMFIR - a regularization scheme based on the Hurwitz-Riemann zeta function

The Grand canonical potential and the thermodynamical properties, in general, can be derived in a variety of effective models. We can start with the general structure of this quantity, which is:

$$I = \sum_f \sum_{s=\pm 1} \int \frac{d^3p}{(2\pi)^3} f(E_f) \quad , \quad E_f = \sqrt{p^2 + M_f^2} \quad , \tag{1}$$

We can make use for the following prescription, to pass from non-magnetized to magnetized system

$$\begin{aligned} I_f(0) &= I_f(B=0) = \sum_{s\pm 1} \int \frac{d^3p}{(2\pi)^3} f(E_f) \to I_f(B) = \beta_f \sum_{n=0}^{\infty} g_n \int_{-\infty}^{\infty} \frac{dp_3}{(2\pi)^2} f(E_n) \quad , \\ E_f &= \sqrt{\vec{p}^{\,2} + M_f^2} \quad \to \quad E_n = \sqrt{p_3^2 + M_f^2 + 2\beta_f n} \ , \end{aligned} \tag{2}$$

The key ingredient in this formalism is the non-normalized density of states, that will allow us to formulate the new regularization scheme, given by:

$$g_f(E,B) = \frac{\beta_f}{(2\pi)^2} \sum_{n=0}^{\infty} g_n \int_{-\infty}^{\infty} dp_3 \ \delta(E - E_n) \quad , \tag{3}$$

where the integral $I_f(B)$ can be rewrited as:

$$I_f(B) = \int_{M_f}^{\infty} dE \ g_f(E,B) \ f(E) \ . \tag{4}$$

Following the analytical procedures of [10, 13], we can obtain after some straightforward steps:

$$g_f(E,B) = E \ \frac{(2\beta_f)^{1/2}}{(2\pi)^2} \ \left\{ 2 \left[\zeta(\frac{1}{2}, \{q_E\}) - \zeta(\frac{1}{2}, q_E + 1) \right] - \frac{1}{q_E^{1/2}} \right\}, \tag{5}$$

where $\{q_E\} \equiv q_E - [q_E]$ is the fractional part of q_E and $\zeta(x,y)$ is the Riemann-Hurwitz zeta function.

Now, we can separate $g_f(E,B) = g_f(E) + \bar{g}_f(E,B)$, where $g_f(E)$ is the non-magnetic contribution:

$$g_f(E) = \frac{E\sqrt{E^2 - M_f^2}}{\pi^2}, \tag{6}$$

and $\bar{g}_f(E,B)$ is the purely magnetic contribution:

$$\bar{g}_f(E,B) = E \ \frac{(2\beta_f)^{1/2}}{2\pi^2} \ \left[\zeta(\frac{1}{2}, \{q_E\}) - \zeta(\frac{1}{2}, q_E) - 2q_E^{1/2} + \frac{1}{2q_E^{1/2}} \right]. \tag{7}$$

Now, we can rewrite the integral in terms of these two contributions $I_f(B) = I_f(0) + \tilde{I}_f(B)$, where from eq.(6) we can obtain the vacuum contribution of the model and the pure magnetic contribution. Applying these results in eq.(4), and defining:

$$\tilde{\mathcal{H}}_{1/2}(q_E) = \left[\zeta(\frac{1}{2}, \{q_E\}) - \zeta(\frac{1}{2}, q_E) - 2q_E^{1/2} + \frac{1}{2q_E^{1/2}} \right]. \tag{8}$$

we can obtain the gap equation for the magnetized NJL model, using $f(E_n) = (p_3^2 + M^2 + 2\beta_f n)^{-1/2}$ applied to eq.(2) by [13]:

$$\frac{M-m}{2MG} = I_{vac} + I_G(T,\mu) + I(B) + I(B,T)\ . \tag{9}$$

where each quantity is given by

$$\begin{aligned}
I_G &= \frac{N_c}{\pi^2}\left[\Lambda\epsilon_\Lambda - M^2 \ln\left(\frac{\Lambda+\epsilon_\Lambda}{M}\right)\right], \\
I_G(T,\mu) &= -2N_cN_f \int \frac{d^3p}{(2\pi)^3}\frac{n(E)+\bar{n}(E)}{\sqrt{p^2+M^2}}, \\
I_G(B) &= N_c \sum_{f=u,d} \int_0^\infty dq_E\ \frac{(2\beta_f)^{3/2}}{(2\pi)^2}\tilde{\mathcal{H}}_{1/2}(q_E)\frac{1}{E(q_E)}\ , \qquad (10) \\
I_G(B,T,\mu) &= -N_c \sum_{f=u,d} \int_0^\infty dq_E\ \frac{(2\beta_f)^{3/2}}{(2\pi)^2}\tilde{\mathcal{H}}_{1/2}(q_E)\frac{[n(E(q_E))+\bar{n}(E(q_E))]}{E(q_E)}\ . \qquad (11)
\end{aligned}$$

in the last expression, $n(x)$ is the Fermi-Dirac distribution and $E(q_E) = \sqrt{M_f^2 + 2\beta_f q_E}$.

2.2. zMFIR applied to the π^0 pole mass in a magnetized medium

Making use of the usual RPA approximation, and selecting the quantum numbers associated to the neutral pion, one can show that the pole-mass of the π^0 meson is given by the relation:

$$1 - 2G\Pi_{ps}(k^2)|_{k^2=m_{\pi^0}^2} = 0\ . \tag{12}$$

where one obtains

$$m_{\pi^0}^2 = -\frac{m}{M}\frac{1}{4GN_cN_f I(m_{\pi^0}^2)}\ , \tag{13}$$

where in previous equation $k = (k_0 = m_{\pi^0}^2, \vec{k} = \vec{0})$ and after using the Matsubara formalism in the latter integral, one obtains:

$$I(k_0^2) = \int \frac{d^3p}{(2\pi)^3}\frac{1}{E(k_0^2 - 4E^2)}\left[1 - n(E) - \bar{n}(E)\right]\ , \tag{14}$$

To use the alternative zMFIR scheme, we apply the formalism presented in the last section for the polarization integral at finite magnetic field and temperatures, and one obtains [13]:

$$I(k_0^2, B, T) = I_{vac}(k_0^2) + I(k_0^2, B) + I_{T,\mu}(k_0^2) + I_{T,\mu}(k_0^2, B)\ , \tag{15}$$

where, we can identify each quantity as:

$$\begin{aligned}
I_{vac}({k_0}^2) &= \int \frac{d^3p}{(2\pi)^3}\frac{1}{E\,(k_0^2 - 4E^2)}\ , \qquad (16) \\
I(k_0^2, B) &= -\sum_{f=u,d} \frac{(2\beta_f)^{1/2}}{32\pi^2}\int_0^\infty dx x \mathcal{H}_{1/2}(x^2)\frac{1}{\bar{E}_f\,(x^2 - \bar{x}_0^2)}\ , \qquad (17) \\
I_{T,\mu}(k_0^2, B) &= \sum_{f=u,d} \frac{(2\beta_f)^{1/2}}{32\pi^2}\int_0^\infty dx x \mathcal{H}_{1/2}(x^2)\frac{n(E)+\bar{n}(E)}{\bar{E}_f\,(x^2 - \bar{x}_0^2)}\ , \qquad (18)
\end{aligned}$$

where $\bar{x}_0^2 = (k_0^2/4 - M^2)/(2\beta_f)$, $x_f \equiv M^2/(2\beta_f)$ and $I_{T,\mu}(k_0^2)$ is given by equation (14). Of course, the latter expressions also have to be interpreted as Cauchy principal values when $\bar{x}_0^2$ is greater than zero or, equivalently, when $k_0 > 2M$.

3. Numerical Results

The parameters used in this work are $\Lambda = 664.3$ MeV, $m_0 = 5.0$ MeV and $G = \frac{2.06}{\Lambda^2}$ [15]. In the figures 1 and 2 we show the numerical equivalence between the MFIR and zMFIR formalism, using as an example the evaluation of the gap equation at $T = 0$ and at $T \neq 0$. Also, in the figures 3 and 4 we evaluate the normalized pressure $P_N = P(eB, T) - P(eB, 0)$ in both formalisms (more details see Ref [13]).

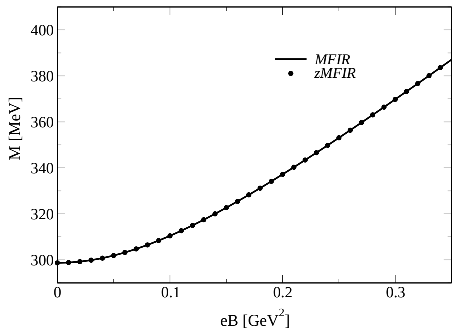

Figure 1: The effective quark mass as a function of magnetic field at $T = 0$.

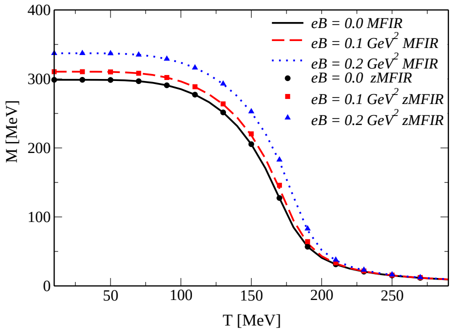

Figure 2: Effective quark mass as a function of temperature for different values of magnetic field.

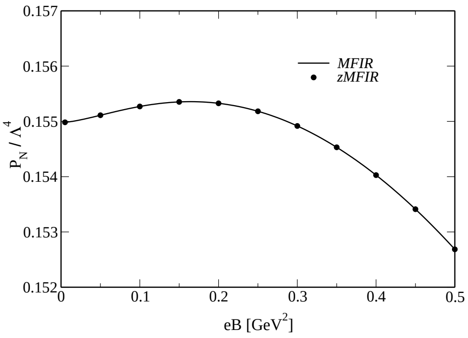

Figure 3: The normalized Pressure at $T = 0$ as a function of magnetic field.

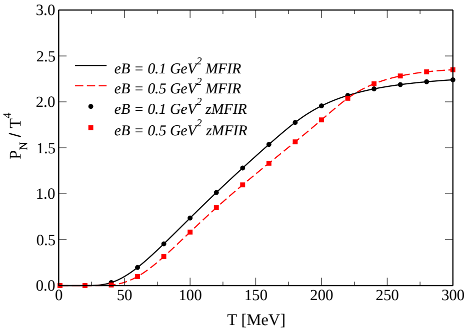

Figure 4: Normalized pressure P_N as a function of temperature for different values of magnetic field.

In Fig. 5 we show the results for the effective quark mass and the pole-mass of neutral meson π_0 at finite temperature and the $eB = 0$. At low temperatures the effective quark masses are, in a very good approximation, the same as the calculated in the vacuum, i.e, $M(T) \approx M(0)$. In this phase, the neutral meson is the pseudo-goldstone boson, that has a finite mass $m_\pi \approx 135$ MeV. At the pseudo-critical temperature, the effective quark masses becomes almost the current quark mass $M \approx m_0$. In this region when the temperature increases we achieve $m_{\pi^0} = 2M$ which defines the Mott temperature [14]. At this point the equations (14) should be interpreted as its Principal Value, when $p = \sqrt{\frac{m_{\pi^0}^2}{4} - M^2}$ [16, 17]. As can be seen from our results, the neutral meson becomes a thermal excitation.

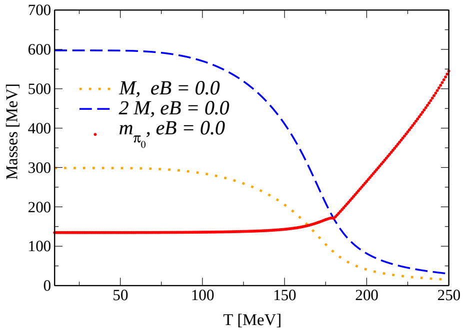

Figure 5: Masses of π_0 meson and quarks as a function of the temperature for $eB = 0$.

The effective quark and pion masses at finite temperature at $eB = 0.1\mathrm{GeV}^2$ can be seen in the Fig. 6. The pole-mass of the neutral collective excitations are showed in the same figure as well. At low temperatures, the magnetic field enhances the chiral condensate and the effective quark masses becomes stronger (magnetic catalysis [18]). When the temperature is greater than the pseudo-critical temperature, the chiral symmetry partially restores and the effective quark masses becomes weaker. At high enough temperatures, i.e , $T > T_{Mott}$ the neutral meson enters in the Wigner-Weyl phase. In this phase, the neutral meson is a thermal excitation with a finite decay width, but the increase of the magnetic field causes the thermal excitation to become more energetic when compared with the zero magnetic field case. The dimensional reduction [18, 19] play a main role in the “jump” of the thermal excitation at T_{Mott}. At temperatures above the Mott dissociation, $T > T_{Mott}$, the thermal energy is not sufficient to excite all possible states in the phase space due the dimensional reduction caused by the strong magnetic field. The resonant $q - \bar{q}$ pair in this case has less states to occupy. Hence, the “jump” in the resonant mass is just the π_0 mass going to its lowest possible energy state, when all other states are not accessible anymore. In Fig. 7 we sketch the results with $eB = 0.2\, GeV^2$ and as expected the previous qualitative analysis still can be used, however, the thermal excitations beyond T_{Mott} becomes even more energetic.

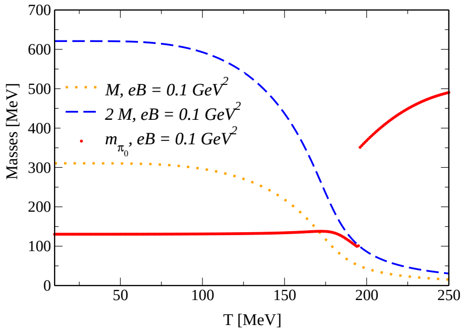

Figure 6: Effective quark mass and π_0 pole-mass as a function of the temperature at $eB = 0.1\mathrm{GeV}^2$.

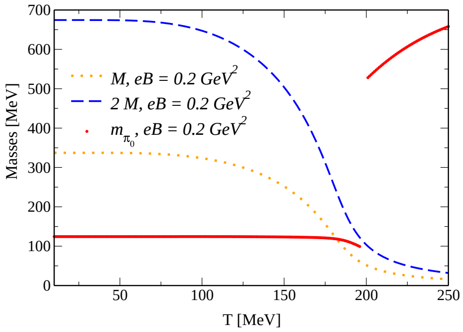

Figure 7: Effective quark mass and π_0 pole-mass as a function of the temperature at $eB = 0.2\mathrm{GeV}^2$.

4. Conclusions

We have investigated some properties of the magnetized NJL SU(2) model at finite temperature in the mean field approximation. The regularization of the model was performed by using a new procedure based on the Riemann-Hurwitz zeta function. We have shown that the new formalism is equivalent to the usual MFIR one. We derived the gap equation and the pseudo-scalar polarization loop through this formalism. As an direct application of the formalism, we have evaluated the π^0 pole-mass within the standard random phase approximation. Although both the MFIR and the zMFIR are completely equivalent, the new method has shown to be more appropriate for the study of the neutral meson properties.

Acknowledgments

This work was partially supported by Conselho Nacional de Desenvolvimento Científico e Tecnológico (CNPq) under grants 304758/2017-5 (R.L.S.F) and 6484/2016-1 (S.S.A.), and as a part of the project INCT-FNA (Instituto Nacional de Ciência e Tecnologia - Física Nuclear e Aplicações) 464898/2014-5 (SSA) and Coordenação de Aperfeiçoamento de Pessoal de Nível Superior (CAPES) (W.R.T).

[1] Avancini S S, Tavares W R, and Pinto M B 2016 *Phys. Rev. D* **93** 014010
[2] Avancini S S, Farias R L S, Benghi Pinto M, Tavares W R and Timóteo V S 2017 *Phys. Lett.* **B767** 247-252
[3] Farias R L S, Avancini S S, Pinto M B, Tavares W R and Timóteo V S 2017 *Int. J. Mod. Phys. Conf. Ser.* **45** 1760060
[4] Gómez D G, Izzo Villafae M F and Scoccola N N 2018, *Phys. Rev. D* **97** 034025
[5] Kohyama H, Kimura D and Inagaki T 2015 *Nucl. Phys. B* **896** 682
[6] Allen P G, Grunfeld A G and Scoccola N N 2015 *Phys. Rev. D* **92** 074041
[7] Duarte D C, Allen P G, Farias R L S, Manso P H A, Ramos R O and Scoccola N N 2016 *Phys. Rev. D* **93**(2) 025017
[8] Farias R L S, Duarte D C, Krein G and Ramos R O, *Phys. Rev. D* **94**(7) 074011
[9] Duarte D C, Farias R L S and Ramos R O, Regularization issues for a cold and dense quark matter model in β equilibrium *Preprint* arXiv:1811.10598 [hep-ph]
[10] Dib C O and Espinosa O 2001 *Nucl. Phys. B* **612** 492
[11] Feng B, Hou D F and Ren H C 2015 *Phys. Rev. D* **92** 065011
[12] Feng B, Hou D F, Ren H C and Wu P 2016 *Phys. Rev. D* **93**, 085019
[13] Avancini S S, Farias R L S and Tavares W R 2018 Neutral meson properties in hot and magnetized quark matter: a new magnetic field independent regularization scheme applied to NJL-type model *Preprint* arXiv:1812.00945 [hep-ph]
[14] Wergieluk A, Blaschke D, Kalinovsky Y L and Friesen A V 2013 *Phys. Part. Nucl. Lett.* **10** 660
[15] Buballa M 2005 *Phys. Rep.* **407** 205-376
[16] Florkowski W and Friman A V 1994 *Acta Physica Polonica* **B 25** 49
[17] Asakawa M and Yazaki K 1989 *Nucl. Phys. A* **504** 668
[18] Miransky V A and Shovkovy I A 2015 *Phys. Rep.* **576** 1
[19] Gusynin V P, Miranski V A and Shovkovy I A *Nucl. Phys. B* **462** 249 (1996).

IOP Conf. Series: Journal of Physics: Conf. Series **1291** (2019) 012016 doi:10.1088/1742-6596/1291/1/012016

Deep inelastic scattering from string/gauge duality with soft IR cutoff and exponentially small Bjorken parameter

E F Capossoli[1,2] **and H Boschi-Filho**[2]

[1]Departamento de Física and Mestrado Profissional em Práticas da Educação Básica (MPPEB), Colégio Pedro II, 20.921-903 - Rio de Janeiro - RJ - Brazil

[2]Instituto de Física, Universidade Federal do Rio de Janeiro, 21.941-972 - Rio de Janeiro - RJ - Brazil

E-mail: `eduardo_capossoli@cp2.g12.br`

E-mail: `boschi@if.ufrj.br`

Abstract. In this work we use the string/gauge duality within the Softwall Model (SW). In this model a dilaton field is introduced in the action for the fields playing the role of a soft infrared (IR) cutoff. The SW model is very useful as it provides linear Regge trajectories for mesons. Here, using a $10-$dimensional SW model, we calculate the corresponding structure functions for deep inelastic scattering (DIS) in which electrons are scattered off hadrons in a kinematical regime where the hadrons are broken apart, with high virtuality q, in the exponentially small x (Bjorken parameter) regime. Our results for this regime are consistent with those achieved using other holographic and non-holographic approaches.

1. Introduction

Deep Inelastic Scattering (DIS) has an important role in high energy experimental physics since using it we could access the internal structure of protons or other hadrons.

The DIS can be described by a scattering between a lepton ℓ and a target hadron with momentum P producing a diversity of other hadrons. During this scattering a virtual photon of momentum q is exchanged.

The relevant parameters for DIS are the virtuality of the photon, given by $q^2 = q_\mu q_\nu \eta^{\mu\nu} = -Q^2$, with metric signature $\eta^{\mu\nu} = (-,+,+,+)$, the mass M of the initial hadron, such that $M^2 = -P^2$, the squared center-of-mass energy $s = -P_X^2 = -(P+q)^2$ and the Bjorken variable x, defined by $x \equiv -q^2/2.P.Q$.

For our purposes, the differential cross section for DIS is given by $d\sigma \propto (\alpha^2/q^4) L^{\mu\nu} W_{\mu\nu}$, where α is the fine structure constant, $L^{\mu\nu}$ is the leptonic tensor, and $W_{\mu\nu}$ is the hadronic tensor, which is the quantity of interest here. In the case where the initial hadronic state is not polarized, the hadronic tensor can be written as [1]:

$$W^{\mu\nu} = i \int d^4y \; e^{iq\cdot y} \langle P, \mathcal{Q} | [J^\mu(y), J^\nu(0)] | P, \mathcal{Q} \rangle \tag{1}$$

where $|P, \mathcal{Q}\rangle$ represents a normalizable hadronic state with 4-momentum P^μ and electric charge $\mathcal{Q}$ of the initial hadron and J^μ is the electromagnetic hadronic current.

Using gauge invariance, which implies $q_\mu W^{\mu\nu} = 0$, together with the Lorentz covariance, the hadronic tensor in (1) can be decomposed as in the following:

$$W^{\mu\nu} = W_1 \left(\eta^{\mu\nu} - \frac{q^\mu q^\nu}{q^2} \right) + \frac{2x}{q^2} W_2 \left(P^\mu + \frac{q^\mu}{2x} \right) \left(P^\nu + \frac{q^\nu}{2x} \right), \tag{2}$$

where $W_1(x, q^2)$ e $W_2(x, q^2)$ are the unpolarized structure functions, which describe the quark distribution of momenta inside the hadrons.

For a particular combination between x and q^2, one can see an approximate relation between these functions called the Callan-Gross relation, so that:

$$W_2(x, q^2) \approx 2x \, W_1(x, q^2). \tag{3}$$

The canonical approach to deal with strong interactions is based on QCD. However QCD fails in the low energy limit when $g_{YM} > 1$. In this context we have to choose another approach to overcome this difficulty.

The AdS/CFT correspondence [2], also known as string/gauge duality, proposed by Juan Maldacena, brought new ways to study strong interactions where QCD cannot be treated perturbatively.

This correspondence or duality relates a conformal Super Yang-Mills (SYM) theory with extended supersymmetry $\mathcal{N} = 4$ and the symmetry group $SU(N)$ for $N \to \infty$ (large N) in a flat Minkowski space-time in $3 + 1$ dimensions with a type IIB superstring theory in a $10-$dimensional curved space, which is a five dimensional anti de Sitter space times a five dimensional hypersphere, or simply, $AdS_5 \times S^5$.

Due to the conformal invariance one cannot use the correspondence directly. In order to break this invariance one can use, for instance, two fruitful bottom-up approaches known as the hardwall and softwall models. In the first one, a hard cutoff is introduced in the AdS space and a slice of this space in the region $0 \leq z \leq z_{\max}$ is considered, with a boundary condition at $z = z_{\max}$. For more information one can see [3–8]. In the context of DIS, using the hardwall, one can see [9–14].

In the second bottom-up approach, or the softwall model, a soft infrared cutoff is introduced in the action. This is done by using a decreasing exponential related to the dilatonic field. For more information one can see [15–21]. Other studies for DIS have been discussed within the softwall model, finding results consistent with the literature [22, 23]. For other DIS studies using holographic models see for instance [24–37].

Here, in this work, we discuss the exponentially small x regime within the softwall model and calculate the corresponding structure functions. More details related to these calculations can be seen in [38].

2. The DIS within the Softwall Model

Let us start this section describing the DIS within the softwall model [22, 38]. In this approach the action for the fields in the $AdS_5 \times S^5$ is given by:

$$S = \int d^{10}x \sqrt{-g}\, e^{-\phi(z)} \mathcal{L} \tag{4}$$

where $\mathcal{L}$ is the Lagrangean density, $\phi = kz^2$ is a scalar field related to the dilaton, g is the determinant of the metric g_{MN} of the $AdS_5 \times S^5$ space:

$$ds^2 = g_{MN} dx^M dx^N = \frac{R^2}{z^2}(dz^2 + \eta_{\mu\nu} dy^\mu dy^\nu) + R^2 d\Omega_5^2, \tag{5}$$

z is the holographic coordinate, $d\Omega_5^2$ is the angular measure on S^5, and R is the AdS_5 space radius.

In order to deal with the DIS within the softwall model it is convenient to split the action Eq.(4) in different parts. The first part, with 5-dimensional gauge fields $A_m = (A_\mu, A_z)$, which does not depend on the coordinates of S^5 space, is given by:

$$S = -\int d^{10}x\sqrt{-g}\; e^{-\phi(z)}\frac{1}{4}F^{mn}F_{mn}. \tag{6}$$

The second one, with scalar fields Φ, which describe the initial and final hadrons, which for simplicity are considered both as spinless, is given by:

$$S = \int d^{10}x\sqrt{-g}\; e^{-\phi(z)}(\partial_m\Phi\partial^m\Phi + m_5^2\Phi^2). \tag{7}$$

From the EOM of the action Eq. (6), with a convenient choice of a Lorentz-like gauge [22], one gets:

$$A_\mu(y^\mu, z) = \eta_\mu\; k\;\Gamma(1+\frac{q^2}{4k})\; e^{iq\cdot y}\; z^2\,\mathcal{U}(1+\frac{q^2}{4k};2;kz^2)\;, \tag{8}$$

$$A_z(y^\mu, z) = \frac{iq.\eta}{2}\;\Gamma(1+\frac{q^2}{4k})\; e^{iq\cdot y}\; z\,\mathcal{U}(1+\frac{q^2}{4k};1;kz^2). \tag{9}$$

where $\Gamma(x)$ is the Gamma function and $\mathcal{U}(a;b;c)$ is the Tricomi confluent hypergeometric function.

From the EOM of the action Eq. (7), with the ansatz, $\Phi(y_\mu,\ z,\ \Omega) = e^{iP\cdot y}\psi(z,\Omega)$, one gets for the initial state of the hadron:

$$\Phi_i(y_\mu,\ z,\ \Omega) = \left[\frac{2k^{\Delta-1}}{\Gamma(\Delta-1)}\right]^{1/2}\frac{1}{R^4}\; e^{iP.y}\; z^\Delta\;\psi(\Omega). \tag{10}$$

For the final state, one has:

$$\Phi_X(y_\mu,\ z,\ \Omega) = \left[\frac{2k^{\Delta-1}\Gamma(\frac{s}{4k}-\frac{\Delta}{2}+1)}{\Gamma(\frac{s}{4k}+\frac{\Delta}{2}-1)}\right]^{1/2}\frac{1}{R^4}\; e^{iP_X\cdot y}\; z^\Delta\; L_{n_X}^{\Delta-2}(kz^2)\;\psi(\Omega), \tag{11}$$

where Δ is the conformal dimension of an operator associated with the initial and final hadrons [22] and $L_n^m(y)$ are the associated Laguerre functions.

3. The exponentially small$-x$ regime in the Softwall Model

The DIS in the exponentially small x regime is characterized by multiple pomeron exchange represented by gravitons in the AdS/CFT correspondence [9].

The dominant contribution at high energies to the string scattering amplitude in the 10$-$dimensional SW model is given by:

$$S_{\text{string}} = \int d^{10}x\sqrt{-g}\; e^{-\phi(z)}\mathcal{L}_{\text{eff,string}} \tag{12}$$

which is identified with the amplitude of the forward Compton scattering in four dimensions and can be written as:

$$\eta_\mu\eta_\nu T^{\mu\nu}(2\pi)^4\delta^4(q-q') = S_{\text{string}}, \tag{13}$$

where $T^{\mu\nu}$ is a tensor which has the same decomposition of the hadronic tensor $W^{\mu\nu}$ presented in Eq.(2) and S_{string} is in the following:

$$\begin{aligned} S_{\text{string}} &= \frac{1}{8}\int d^{10}x\sqrt{-g}\; e^{-\phi(z)}\Big\{4v^a v_a \partial_m \Phi F^{mn} F_{pn} \partial^p \Phi \\ &\quad - \Big(\partial^M \phi \partial_M \Phi v^a v_a + 2v^a \partial_a \Phi v^b \partial_b \Phi\Big)\, F^{mn} F_{mn}\Big\} G|_{t=0} \end{aligned} \tag{14}$$

where v^a are the Killing vectors of the compact S^5 space (or more generically W), F^{mn} is associated with an incoming photon with 4−momentum q_μ and an outgoing one with 4−momentum q'_μ and Φ represents the incoming and outgoing scalars state with 4−momentum P^μ and P^μ_X, respectively.

After some manipulations, the imaginary part of S_{string} takes the form:

$$\begin{aligned} \operatorname{Im} S_{\text{string}} &= (2\pi)^4 \delta(q-q')\; \eta_\mu \eta\nu\; \frac{\pi\rho R^8 (x)^{\alpha'|\xi|/2}}{4s}\; a^2\, \Gamma^2\left(1+\frac{q^2}{4k}\right) \\ &\times \left\{\sum_{m=1}^{\infty} e^{-kz_m^2}\, \frac{z_m^{2\Delta+2}}{4}\, \mathcal{U}^2\left(1+\frac{q^2}{4k};1;kz_m^2\right)(-q^2)\left[p^\mu - \frac{p.q}{q^2}q^\mu\right]\left[p^\nu - \frac{p.q}{q^2}q^\nu\right]\right. \\ &+ k^2 \sum_{m=1}^{\infty} e^{-kz_m^2}\, z_m^{2\Delta+4}\, \mathcal{U}^2\left(1+\frac{q^2}{4k};2;kz_m^2\right)(p.q)^2 \\ &\times \left.\left[\eta^{\mu\nu} - \frac{(p^\nu q^\nu + p^\nu q^\mu)}{p.q} + \frac{q^2}{(p.q)^2} p^\mu p^\nu\right]\right\}. \end{aligned} \tag{15}$$

Comparing with Eq. (13), one has:

$$\begin{aligned} \operatorname{Im} T^{\mu\nu} &= \frac{\pi\rho R^8 (x)^{\alpha'|\xi|/2}}{4s}\; a^2\, \frac{q^4}{4x^2}\left\{\left[\eta^{\mu\nu} - \frac{q^\mu q^\nu}{q^2}\right]\mathcal{I}_2\right. \\ &\quad + \left.\left[p^\mu + \frac{q^\mu}{2x}\right]\left[p^\nu + \frac{q^\nu}{2x}\right] 4x^2 \left(\mathcal{I}_1 + \frac{\mathcal{I}_2}{q^2}\right)\right\} \end{aligned} \tag{16}$$

where

$$\mathcal{I}_1 \equiv \frac{1}{4}\Gamma^2(j) \sum_{m=1}^{\infty} e^{-kz_m^2}\, z_m^{2\Delta+2}\, \mathcal{U}^2\left(j;1;kz_m^2\right) \tag{17}$$

$$\mathcal{I}_2 \equiv k^2\, \Gamma^2(j) \sum_{m=1}^{\infty} e^{-kz_m^2}\, z_m^{2\Delta+4}\, \mathcal{U}^2\left(j;2;kz_m^2\right) \tag{18}$$

Consequently, one can write the structure functions for DIS within the softwall model in the exponentially small x regime, so that:

$$\begin{aligned} W_1(x,q^2) &= \frac{\pi^2 \rho k^{\Delta-1}}{4\Gamma(\Delta-1)}\, \frac{q^4 (x)^{\alpha'|\xi|/2}}{sx^2}\, \mathcal{I}_2 \\ W_2(x,q^2) &= \frac{\pi^2 \rho k^{\Delta-1}}{4\Gamma(\Delta-1)}\, \frac{q^4 (x)^{\alpha'|\xi|/2}}{sx^2}\, (2xq^2)\left(\mathcal{I}_1 + \frac{\mathcal{I}_2}{q^2}\right). \end{aligned} \tag{19}$$

In order to compare our results with ref.[9] one can use Hypergeometric functions' properties and consider the approximations in which x is exponentially small and q^2 is large [38], so that one can rewrite Eqs.(19) as:

$$W_1(x,q^2) \approx \frac{\pi^2 \rho\ (x)^{-2+\alpha'|\xi|/2}}{8\ (4\pi g_s N)^{1/2}\ \Gamma(\Delta-1)} \left(\frac{k}{q^2}\right)^{\Delta-1} \mathcal{I}_{1,\,2\Delta+3} \tag{20}$$

$$W_2(x,q^2) \approx \frac{\pi^2 \rho\ (x)^{-1+\alpha'|\xi|/2}}{4\ (4\pi g_s N)^{1/2}\ \Gamma(\Delta-1)} \left(\frac{k}{q^2}\right)^{\Delta-1} (\mathcal{I}_{0,\,2\Delta+3} + \mathcal{I}_{1,\,2\Delta+3})\,, \tag{21}$$

where

$$\mathcal{I}_{r,s} \equiv \int_0^\infty dw\ w^s\ K_r^2(w) = 2^{(s-2)}\ \frac{\Gamma(\frac{s+1}{2}+r)\ \Gamma(\frac{s+1}{2}-r)\ \Gamma^2(\frac{s+1}{2})}{\Gamma(s+1)}. \tag{22}$$

Computing the ratio of these structure functions one finds:

$$\frac{W_2(x,q^2)}{W_1(x,q^2)} \approx 2x\ \left(\frac{2\Delta+3}{\Delta+2}\right). \tag{23}$$

Finally, one can see that this ratio is in agreement with the one found in [9] within the hardwall model.

4. Last comments

In this work we have used the AdS/CFT correspondence to study DIS with an exponentially small Bjorken parameter within the Softwall model. The correspondence proved itself to be an excellent tool to tackle QCD out of the perturbative regime. Furthermore we reproduced the results found within the hardwall model.

The exponentially small x regime is also important to study the QCD phase diagram. This problem was discussed within the hardwall model in [11]. Since the hardwall and softwall models have different spectra, in particular leading to different Regge trajectories, we studied the saturation line in the softwall model to see if it leads to any different behavior. The complete details and references can be found in [38].

For recent discussions on holographic approaches to DIS, see for instance [39–42].

5. Acknowledgments

H. B.-F. is partially supported by Conselho Nacional de Desenvolvimento Científico e Tecnológico (CNPq) and Coordenação de Aperfeiçoamento de Pessoal de Nível Superior (Capes) (Brazilian Agencies).

References

[1] Manohar A V 1992 *lake louise 1992, symmetry and spin in the standard model* (*Preprint* `hep-ph/9204208`)
[2] Maldacena J M 1998 *Adv. Theor. Math. Phys.* **2** 231
[3] Polchinski J and Strassler M J 2002 *Phys. Rev. Lett.* **88** 031601
[4] Boschi-Filho H and Braga N R F 2003 *J. High Energy Phys* JHEP0305(2003)009
[5] Boschi-Filho H and Braga N R F 2004 *Eur. Phys. J. C* **32** 529
[6] Boschi-Filho H, Braga N R F and Carrion H L 2006 *Phys. Rev. D* **73** 047901
[7] Capossoli E F and Boschi-Filho H 2013 *Phys. Rev. D 88* **2** 026010
[8] Rodrigues D M, Capossoli E F and Boschi-Filho H 2017 *Phys. Rev. D 95* **7** 076011
[9] Polchinski J and Strassler M J 2003 *J. High Energy Phys* JHEP0305(2003)012
[10] Brower R C, Polchinski J, Strassler M J and ITan C 2003 *J. High Energy Phys* JHEP0712(2003)005
[11] Hatta Y, Iancu E and Mueller A H 2008 *J. High Energy Phys* JHEP0801(2008)026
[12] Bayona C A B, Boschi-Filho H and Braga N R F 2008 *J. High Energy Phys* JHEP0810(2008)088
[13] Gao J H and Xiao B W 2009 *Phys. Rev. D 80* 015025
[14] Brower R C, Djuric M, Sarcevic I and Tan C I 2010 *J. High Energy Phys* JHEP1011(2010)051
[15] Karch A, Katz E, Son D T and Stephanov M A 2006 *Phys. Rev. D 74* 015005
[16] Colangelo P, Fazio F D, Jugeau F and Nicotri S 2007 *Phys. Lett. B* **652** 73

[17] Li D and Huang M 2013 *J. High Energy Phys* JHEP1311(2013)088
[18] Capossoli E F and Boschi-Filho H 2016 *Phys. Lett. B* **753** 419
[19] Capossoli E F and Boschi-Filho H 2016 *Phys. Lett. B* **760** 101
[20] Capossoli E F, Li D and Boschi-Filho H 2016 *Eur. Phys. J. C 76* **6** 320
[21] Rodrigues D M, Capossoli E F and Boschi-Filho H 2018 *EPL 122* **2** 21001
[22] Bayona C A B, Boschi-Filho H and Braga N R F 2008 *J. High Energy Phys* JHEP0803(2008)064
[23] Braga N R F and Vega A 2012 *Eur. Phys. J. C 72* 2236
[24] Bayona C A B, Boschi-Filho H, Braga N R F and Torres M A C 2010 *J. High Energy Phys* JHEP1010(2010)055
[25] Cornalba L and Costa M S 2008 *Phys. Rev. D 78* 096010
[26] Pire B, Roiesnel C, Szymanowski L and Wallon S 2008 *Phys. Lett. B* **670** 84
[27] Albacete J L, Kovchegov Y V and Taliotis A 2008 *J. High Energy Phys* JHEP0807(2008)074
[28] Bayona C A B, Boschi-Filho H and Braga N R F 2008 *J. High Energy Phys* JHEP0809(2008)114
[29] Yoshida Y 2010 *Prog. Theor. Phys.* **123** 79
[30] Hatta Y, Ueda T and Xiao B W 2009 *J. High Energy Phys* JHEP0908(2009)007
[31] Avsar E, Iancu E, McLerran L and Triantafyllopoulos D N 2009 *J. High Energy Phys* JHEP0911(2009)105
[32] Cornalba L, Costa M S and Penedones J 2010 *J. High Energy Phys* JHEP1003(2010)133
[33] Bayona C A B, Boschi-Filho H and Braga N R F 2010 *Phys. Rev. D 81* 086003
[34] Cornalba L, Costa M S and Penedones J 2010 *Phys. Rev. Lett. 105* 072003
[35] Koile E, Macaluso S and Schvellinger M 2014 *J. High Energy Phys* JHEP1401(2014)166
[36] Koile E, Kovensky N and Schvellinger M 2014 *J. High Energy Phys* JHEP1505(2015)001
[37] E Koile N K and Schvellinger M 2015 *J. High Energy Phys* JHEP1512(2015)009
[38] Capossoli E F and Boschi-Filho H 2015 *Phys. Rev. D 92* **12** 126012
[39] Jorrin D, Kovensky N and Schvellinger M 2016 *J. High Energy Phys* JHEP1604(2016)113
[40] Jorrin D, Schvellinger M and Kovensky N 2016 *J. High Energy Phys* JHEP1612(2016)003
[41] N Kovensky G M and Schvellinger M 2018 *J. High Energy Phys* JHEP1804(2018)118
[42] Amorim A, Quevedo R C and Costa M S 2018 *Phys. Rev. D 98* **2** 026016

IOP Conf. Series: Journal of Physics: Conf. Series **1291** (2019) 012017 doi:10.1088/1742-6596/1291/1/012017

Effect of the nucleon-nucleon interaction on the fusion cross-section within the relativistic mean field formalism

M Bhuyan[1,2], **Raj Kumar**[3], **and B V Carlson**[2]
[1]Department of Physics, Faculty of Science, University of Malaya, Kuala Lumpur 50603, Malaysia
[2]Instituto Tecnológico de Aeronáutica, São José dos Campos-12.228-900, São Paulo, Brazil
[2]School of Physics and Materials Science, Thapar Institute of Engineering and Technology, Patiala-147004, Punjab, India

E-mail: `bunuphy@um.edu.my`

E-mail: `rajkumar@thapar.edu`

E-mail: `brett@ita.br`

Abstract. We establish a relationship between the nucleon-nucleon interaction potential and the nuclear fusion reaction cross-sections at low energies. The axially deformed self-consistent relativistic mean field is used with the non-linear NL3* interaction parameter set. The Wong formula is used to estimate the fusion cross-section for ^{58}Ni + ^{58}Ni and ^{48}Ca + ^{238}U systems, which are known to display fusion hindrance phenomena. The results of the application of the nucleus-nucleus optical potential for the fusion cross-section from the recently developed effective relativistic NN-interaction (R3Y) potential is compared with the well-known, phenomenological M3Y potential. The results obtained from our present calculation for the R3Y interaction are reasonable good as compared to the M3Y potential concerning the available experimental at barrier energies. The present analysis pursues a full microscopic studies of fusion process at low energies by taking the R3Y potential along with the relativistic mean field density instead of taking the M3Y interaction within the double folding approach.

1. Introduction

In the last 70 years, a large body of theoretical and experimental work have been devoted to understanding the properties of atomic nuclei through the bare interaction between a pair of nucleons. Although a substantial development has been made to explain the nuclear force in terms of nucleon-nucleon (NN) interactions, remains an open problem at present. In principle, the central part of the NN-interaction is considered as a typical square-well, Gaussian or Yukawa potential of various ranges and strengths, which can be obtained from the observed phase shifts in an elastic-scattering processes [1]. A large number of interactions have been constructed by studying NN- scattering, but extensive modifications in the scattering behavior due to the presence of surrounding nucleons occur in a nucleus [2]. Further, the reconstruction of the NN-potential through particle exchanges is made possible by the development of quantum field theory [3]. The analytical derivation of a potential through particle exchange is important to understand the nuclear force as well as structural properties via the nucleus-nucleus optical potential for the study of many nuclear phenomena such as nuclear radioactivity, nuclear scattering, nuclear fission and fusion process [4, 5, 6]. An alternative approach to NN-interactions at low energies has been formulated by Ekström *et. al.*, [7] in terms of an effective theory for non-relativistic nucleons, which involves a few basic coupling constants to reproduce the nucleon scattering data. Furthermore, the relativistic effective NN-interaction R3Y potential [4, 6] analogous to the M3Y one [8] can be derived from the relativistic mean field Lagrangian, which depends on the coupling constant among the interacting mesons and their masses [4, 6].

The nucleus-nucleus optical potential is quite important in studies of elastic scattering of light and heavy-ion (HI) systems, in particular for the simple one-dimensional barrier penetration model (BPM) of a fusion reaction, which is significantly influenced by the NN-potential, nuclear matter density distributions and the Coulomb potential [9, 6]. A microscopic description is required for calculating the nuclear potential that incorporates the physical process, especially fusion, in terms of the NN interaction [6]. At low energy, the system can fuse either by penetrating the interaction barrier or it must have sufficient energy to overcome the Coulomb barrier to be absorbed. In the present study, we consider reactions from different mass regions i.e ^{58}Ni + ^{58}Ni, and ^{48}Ca + ^{238}U, as their fusion excitation functions are available experimentally and also known for fusion hindrance [10, 11]. Below the Coulomb barrier, nuclear structure effects dominate the fusion dynamics, whereas the centrifugal potential suppresses the structure effects at above barrier energies. Here, one of the points of interest is to observe the ability of the relativistic R3Y potential along with the microscopic relativistic mean field density to estimate the nuclear interaction potential for the study of fusion reactions at low energies.

The paper is organized as follows: the relativistic mean-field formalism and the analytical expressions for the R3Y potential are given in Sec. 2. This section also including a brief description of the Wong formula. Sec. 3 presents the results of our calculations and discussions. A brief summary of the results obtained, together with concluding remarks, are given in Sec. 4.

2. The relativistic mean-field Theory

In the last few decades, the relativistic mean field theory has been applied successfully to study the structural properties of finite nuclei over the nuclear chart, including the unknown island of superheavy nuclei [6, 12, 13, 14]. We have used the microscopic self-consistent relativistic mean field (RMF) theory as a standard tool to study fusion using the Wong formula. The form of a typical relativistic Lagrangian density for a nucleon-meson many body system is, [6, 14, 15]

$$\begin{aligned}\mathcal{L} &= \overline{\psi}\{i\gamma^{\mu}\partial_{\mu} - M\}\psi + \frac{1}{2}\partial^{\mu}\sigma\partial_{\mu}\sigma - \frac{1}{2}m_{\sigma}^{2}\sigma^{2} - \frac{1}{3}g_{2}\sigma^{3} - \frac{1}{4}g_{3}\sigma^{4} - g_{s}\overline{\psi}\psi\sigma \\ &\quad -\frac{1}{4}\Omega^{\mu\nu}\Omega_{\mu\nu} + \frac{1}{2}m_{\omega}^{2}\omega^{\mu}\omega_{\mu} - g_{\omega}\overline{\psi}\gamma^{\mu}\psi\omega_{\mu} - \frac{1}{4}\vec{B}^{\mu\nu}.\vec{B}_{\mu\nu} + \frac{1}{2}m_{\rho}^{2}\vec{\rho}^{\mu}.\vec{\rho}_{\mu} \\ &\quad -g_{\rho}\overline{\psi}\gamma^{\mu}\vec{\tau}\psi\cdot\vec{\rho}^{\mu} - \frac{1}{4}F^{\mu\nu}F_{\mu\nu} - e\overline{\psi}\gamma^{\mu}\frac{(1-\tau_{3})}{2}\psi A_{\mu}. \end{aligned} \qquad (1)$$

The ψ are the Dirac spinors for the nucleons. The iso-spin and its third component are denoted by τ and τ_3, respectively. Here g_σ, g_ω, g_ρ and $\frac{e^2}{4\pi}$ are the coupling constants for $\sigma-$, $\omega-$, $\rho-$ mesons and photon, respectively. The constant g_2, and g_3 are coupling constants for the self-interacting non-linear $\sigma-$meson fields. The masses of the $\sigma-$, $\omega-$, $\rho-$ mesons and nucleons are m_σ, m_ω, m_ρ, and M, respectively. The quantity A_μ stands for the electromagnetic field. The vector field tensors for the ω^μ, $\vec{\rho}_\mu$ and photon are given by, $F^{\mu\nu} = \partial_\mu A_\nu - \partial_\nu A_\mu$, $\Omega_{\mu\nu} = \partial_\mu\omega_\nu - \partial_\nu\omega_\mu$, and $\vec{B}^{\mu\nu} = \partial_\mu\vec{\rho}_\nu - \partial_\nu\vec{\rho}_\mu$, respectively. From the above Lagrangian density we obtain the field equations for the Dirac nucleons, and the meson fields, as

$$\Big(-i\alpha.\bigtriangledown + \beta(M + g_\sigma\sigma) + g_\omega\omega + g_\rho\tau_3\rho_3\Big)\psi = \epsilon\psi,$$

$$\left(-\bigtriangledown^2+m_\sigma^2\right)\sigma(r)=-g_\sigma\rho_s(r)+g_2\sigma^2(r)+g_3\sigma^3(r),$$
$$\left(-\bigtriangledown^2+m_\omega^2\right)\omega(r)=g_\omega\rho(r);\left(-\bigtriangledown^2+m_\rho^2\right)\rho(r)=g_\rho\rho_3(r). \tag{2}$$

In the limit of one-meson exchange, in a static baryonic medium, the single nucleon-nucleon potential for scalar (σ), and vector (ω, ρ) fields are given by,

$$V_\sigma=-\frac{g_\sigma^2}{4\pi}\frac{e^{-m_\sigma r}}{r}+\frac{g_2^2}{4\pi}re^{-2m_\sigma r}+\frac{g_3^2}{4\pi}\frac{e^{-3m_\sigma r}}{r};V_\omega(r)=+\frac{g_\omega^2}{4\pi}\frac{e^{-m_\omega r}}{r};V_\rho(r)=+\frac{g_\rho^2}{4\pi}\frac{e^{-m_\rho r}}{r}. \tag{3}$$

The relativistic effective nucleon-nucleon interaction (V_{eff}^{R3Y}) taking into account the single-nucleon exchange effects can be written as, [4, 6],

$$V_{eff}^{R3Y}(r)=\frac{g_\omega^2}{4\pi}\frac{e^{-m_\omega r}}{r}+\frac{g_\rho^2}{4\pi}\frac{e^{-m_\rho r}}{r}-\frac{g_\sigma^2}{4\pi}\frac{e^{-m_\sigma r}}{r}+\frac{g_2^2}{4\pi}re^{-2m_\sigma r}+\frac{g_3^2}{4\pi}\frac{e^{-3m_\sigma r}}{r}+J_{00}(E)\delta(r). \tag{4}$$

The effective R3Y *NN*-interaction is obtained from the scalar and vector parts of the meson fields, analogous to the M3Y potential [8]. Here the R3Y potential is derived for the NL3* force, which can predict nuclear matter properties as well as the properties of the finite nuclei at very high isospin asymmetries [6]. It is worth mentioning that the analytical expression for the R3Y interaction is only possible for interaction parameters that contain only linear and/or non-linear self-coupling terms. In the case of relativistic forces with cross-coupling terms (i.e., FSUGold, G1, G2, etc.), one has to obtain a numerical solution to generate *NN*-interactions. On the other hand, the M3Y effective interaction, obtained from a fit of the G-matrix elements based on the Reid-Elliott soft-core *NN*-interaction [8], in an oscillator basis, is the sum of three Yukawa's (M3Y) with ranges 0.25 fm for a medium-range attractive part, 0.4 fm for a short-range repulsive part and 1.414 fm to ensure the long-range tail of the one-pion exchange potential (OPEP). The widely used M3Y effective interaction ($V_{eff}^{M3Y}(r)$) is given by

$$V_{eff}^{M3Y}(r)=7999\frac{e^{-4r}}{4r}-2134\frac{e^{-2.5r}}{2.5r}+J_{00}(E)\delta(r), \tag{5}$$

where the strength is in MeV. One can find more details in Refs. [4, 5, 6]. The nuclear interaction potential, $V_n(R)$, between the projectile (p) and the target (t) nuclei is calculated from the RMF (NL3*) matter densities ρ_p and ρ_t using the well known double folding procedure [8] for the M3Y and the R3Y interaction potential, as

$$V_n(\vec{R}) \;=\; \int\rho_p(\vec{r}_p)\rho_t(\vec{r}_t)V_{eff}\left(|\vec{r}_p-\vec{r}_t+\vec{R}|\equiv r\right)d^3r_pd^3r_t. \tag{6}$$

Adding the Coulomb potential $V_C(R)$ ($=Z_pZ_te^2/R$) results in a nucleus-nucleus interaction potential $V_T(R)$ [$=V_n(R)+V_C(R)$], used for calculating the fusion properties.

Wong Formula: In terms of the partial waves ℓ, the fusion cross-section for two nuclei colliding with a center-of-mass energy ($E_{c.m.}$), is given by [16]

$$\sigma(E_{c.m.})=\frac{\pi}{k^2}\sum_{\ell=0}^{\ell_{max}}(2\ell+1)P_\ell(E_{c.m.}), \tag{7}$$

with $k=\sqrt{\frac{2\mu E_{c.m.}}{\hbar^2}}$ and μ is the reduced mass. P_ℓ is the transmission coefficient for each ℓ which describes the penetration of the barrier V_T^ℓ (R). Using the Hill-Wheeler [17, 18] approximation, the penetrability P_ℓ, in terms of the barrier height $V_B^\ell(E_{c.m.})$ and curvature $\hbar\omega_\ell(E_{c.m.})$, is

$$P_\ell=\left[1+\exp\left(\frac{2\pi(V_B^\ell(E_{c.m.})-E_{c.m.})}{\hbar\omega_\ell(E_{c.m.})}\right)\right]^{-1}. \tag{8}$$

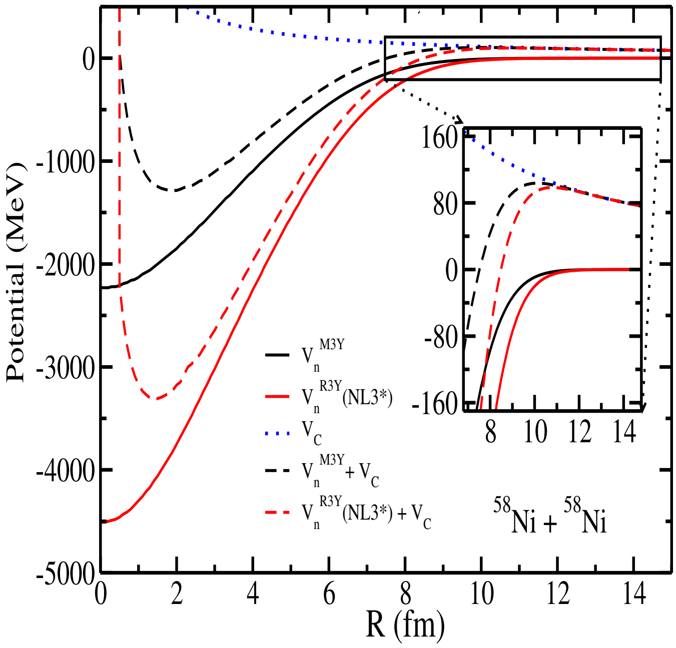

Figure 1. (Color online) The total nucleus-nucleus optical potential V_T (R) and the individual contributions (the nuclear V_n (R) (M3Y) and V_n (R) (R3Y) for the NL3* parameter set, and the Coulomb V_C (R) potential) as a function of radial distance for ^{58}Ni + ^{58}Ni. See text for details.

Here, $\hbar\omega_\ell = \hbar\left[|d^2V_T^\ell(R)/dR^2|_{R=R_B^\ell}/\mu\right]^{1/2}$ is evaluated at the barrier position $R = R_B^\ell$ corresponding to the barrier height V_B^ℓ, and the R_B^ℓ obtained from the condition, $|dV_T^\ell(R)/dR|_{R=R_B^\ell} = 0$. Instead of solving Eq. (7) explicitly, which requires the complete ℓ-dependent potentials $V_T^\ell(R)$, Wong [16] carried out the ℓ-summation in Eq. (7) approximately under specific conditions: (i) $\hbar\omega_\ell \approx \hbar\omega_0$, and (ii) $V_B^\ell \approx V_B^0 + \frac{\hbar^2\ell(\ell+1)}{2\mu {R_B^0}^2}$, which assumes $R_B^\ell \approx R_B^0$ too. In other words, both V_B^ℓ and $\hbar\omega_\ell$ are obtained for $\ell = 0$. Using these approximations, and replacing the ℓ-summation in Eq. (7) by an integral, gives, on integration, the $\ell = 0$ barrier-based Wong formula [16],

$$\sigma(E_{c.m.}) = \frac{{R_B^0}^2\hbar\omega_0}{2E_{c.m.}}.\ln\left[1 + \exp\left(\frac{2\pi}{\hbar\omega_0}(E_{c.m.} - V_B^0)\right)\right]. \tag{9}$$

This is the simple formula used in the present work to calculate the fusion cross-section using the barrier characteristics, V_B^0, R_B^0 and $\hbar\omega_0$ within the barrier penetration model. For details see Ref. [6, 19].

3. Details of the calculations and Results

The RMF calculations furnish the effect of fusion hindrance using the self-consistent relativistic mean field formalism via the Wong formula. In this regards, in the first step, we calculate the M3Y (using Eq. 5) and the microscopic R3Y (using Eq. 4) *NN*-potential for the NL3* interaction parameter set. The details of the relativistic effective *NN*-interactions for various forces and the phenomenological M3Y potential can be found in the Refs. [4, 5, 6]. In the second step, we calculate bulk properties such as the binding energy, quadrupole moment Q_{20}, the total matter density distribution, nuclear radii, and the single particle energy levels for nucleons. Instead of concentrating on the nuclear structure output profiles, we use the monopole component of the

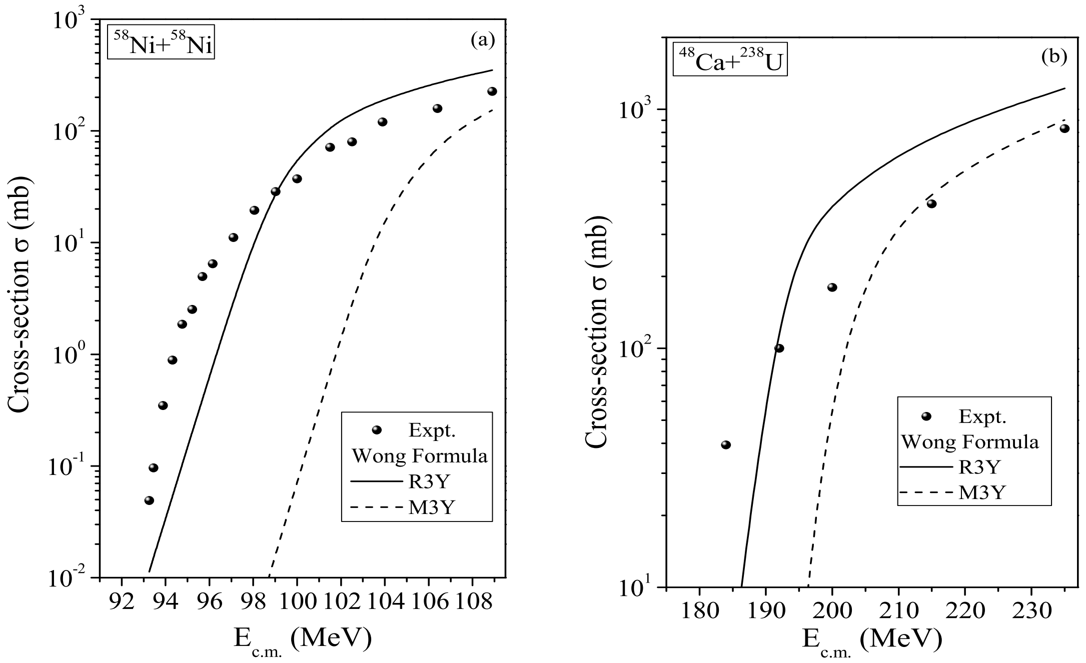

Figure 2. Fusion-evaporation cross-section as a function of the center-of-mass energy $E_{c.m.}$, for the R3Y using NL3* (solid line), and the M3Y (dashed line) potential along with the experimental data for (a) ^{58}Ni + ^{58}Ni [10] and (b) ^{48}Ca + ^{238}U [11]. See the text for details.

mean field densities for the target (t) and projectile (p) as the input to estimate the nuclear interaction potential using Eq. (6). The total interaction potentials $V_T(R) = V_n(R) + V_C(R)$ for the ^{58}Ni + ^{58}Ni, and ^{48}Ca + ^{238}U systems are obtained for the M3Y and R3Y interactions for NL3* densities. As a representative case, the results for the nucleus-nucleus interaction potentials without Coulomb for the M3Y (solid black line), and the R3Y interactions for NL3* (solid red line) interaction parameters are displayed in Fig. 1. The total interaction potential (corresponding dashed line) along with the Coulomb potential V_C (blue dotted line) are also shown in Fig. 1. From the figure, we note that the nuclear potentials obtained from the M3Y differ significantly from the R3Y (NL3*), particularly in the central region while this difference decreases simultaneously with respect to the radial distance. Further, the heights of the barrier for M3Y interaction are a bit higher as compare to the R3Y (NL3*) case (seen more clearly in the inset of Fig. 1). For example, the R3Y (NL3*) is about 1 MeV more attractive compared to the M3Y as is illustrated in the inset of Fig. 1.

The barrier characteristics of the nuclear interaction potential i.e. the barrier height, position and frequency from the total interaction potential are used in the Wong formula for estimating the fusion reaction cross-section for the systems ^{58}Ni + ^{58}Ni, and ^{48}Ca + ^{238}U, known for fusion hindrance phenomena. Fig. 2 (a) shows the comparison of the fusion cross-section obtained for ^{58}Ni + ^{58}Ni around the Coulomb barrier with the experimental data [10]. The solid and dashed line are for the fusion cross-section from R3Y and M3Y potentials, respectively within the Wong formula for NL3* densities. From the figure, one can see that the fusion cross-section calculated using M3Y underestimates that of the R3Y interaction and the experimental data. In other words, the cross-section obtained for R3Y interaction with the NL3* interaction parameters is relatively superior to M3Y interaction when compared with the experimental data [10] at below barrier energies. Motivated by the observation, calculations are then pursued for ^{48}Ca + ^{238}U along with the experimental data [11], shown in Fig. 2 (b). From Fig. 2 (b), a similar conclusion can be drawn for the R3Y and M3Y potentials for this reaction system, as found for ^{58}Ni +

^{58}Ni at below barrier energies. At above barrier energies, the M3Y interaction is slightly better than the R3Y interaction. However the estimate of the R3Y interactions, at energies above the barrier, can be improved by adopting the ℓ-summed Wong formula. More details of the ℓ-summed Wong formula for various fusion cross-sections can find in Refs. [6, 19, 20].

4. Summary and Conclusions

We have shown the effect of the nucleon-nucleon interaction potential on the fusion reaction cross-sections for ^{58}Ni + ^{58}Ni, and ^{48}Ca + ^{238}U, known for fusion hindrance phenomena. The axial deformed relativistic mean field with the NL3* force has been used along with the Wong formula to provide a transparent and analytic way to calculate the fusion cross-section by means of a convenient approach to the nucleus-nucleus optical potential. The RMF (NL3*) matter densities for target and projectile are used for calculating the corresponding nuclear potential within a double folding procedure, for the study of fusion at low energies. We find the R3Y interaction to be a better choice than the M3Y one for prediction of the cross-section of fusion reactions below the barrier. The present analysis pursues a full microscopic study by taking the R3Y potential along with the relativistic mean field densities within the Wong formula. More details of the work can be found in Refs. [6, 20].

Acknowledgments

This work was supported by FAPESP Project Nos. 2014/26195-5 & 2017/05660-0, INCT-FNA Project No. 464898/2014-5, Seed Money Project of Thapar Institute of Engineering and Technology, Department of Science and Technology (DST), Govt. of India Project No. YSS/2015/000342 under Young Scientist Scheme, and by the CNPq - Brasil.

References

[1] Brueckner K A and Watson K M 1953 *Phys. Rev.* **92** 1023.
[2] Stoks V G J, Klomp R A M, Terheggen C P F and Swart J J de 1994 *Phys. Rev. C* **49** 2950.
[3] Garcon M and Orden J W Van 2001 *Adv. Nucl. Phys.* **26** 293.
[4] Singh B B, Bhuyan M, Patra S K and Gupta Raj K 2012 *J. Phys. G: Nucl. Part. Phys.* **39** 025101.
[5] Sahu B B, Singh S K, Bhuyan M, Biswal S K and Patra S K 2014 *Phys. Rev. C* **89** 034614.
[6] Bhuyan M and Kumar Raj 2018 *Phys. Rev. C* **98** 054610.
[7] Ekström A, Baardsen G, Forssn C, Hagen G, Hjorth-Jensen M, Jansen G R, Machleidt R, Nazarewicz W, Papenbrock T, Sarich J and Wild S M 2013 *Phys. Rev. Lett.* **110** 192502.
[8] Satchler G R and Love W G 1979 *Phys. Reports* **55** 183.
[9] Stiliarid E, Bohlen H G, Frobrich P, Gebauer B, Kolbert D, Oertzen W von, Wilpert M and Th Wilpert 1989 *Phys. Lett. B* **223** 291.
[10] Beckerman M *et al.* 1981 *Phys. Rev. C* **23** 1581.
[11] Kozulin E M, Knyazheva G N, Itkis I M, Itkis M G, Bogachev A A, Chernysheva E V, Krupa L, Hanappe F, Dorvaux O, Stuttgé L, Trzaska W H, Schmitt C and Chubarian G 2014 *Phys. Rev. C* **90** 054608.
[12] Serot B D and Walecka J D 1986 *Advances in Nuclear Physics* ed Negele J W and Vogt Erich vol 16 (Plenum Press, New York) p 1.
[13] Carlson B V and Hirata D 2000 *Phys. Rev. C* **62** 054310.
[14] Lalazissis G A, Karatzikos S, Fossion R, Arteaga D Pena, Afanasjev A V and Ring P 2009 *Phys. Lett. B* **671** 36.
[15] Boguta J and Bodmer A R 1977 *Nucl. Phys. A* **292**, 413.
[16] Wong C Y 1973 *Phys. Rev. Lett.* **31** 766.
[17] Hill D L and Wheeler J A 1953 *Phys. Rev.* **89** 1102.
[18] Thomas T D 1959 *Phys. Rev.* **116** 703.
[19] Kumar Raj, Bansal M, Arun S K and Gupta Raj K 2009 *Phys. Rev. C* **80** 034618.
[20] Bhuyan M, Kumar Raj, Jain D, Patra S. K and Carlson B V 2019 **under preparation**.

IOP Conf. Series: Journal of Physics: Conf. Series **1291** (2019) 012018 doi:10.1088/1742-6596/1291/1/012018

Searching signature of neutrino-nucleus coherent scattering with Mössbauer Spectroscopy

C Marques[1,3] **G S Dias**[1] **H H Chavez Sanchez**[2] **S B Duarte**[3]

[1]Instituto Federal do Espírito Santo-Grupo de Física Teórica e Aplicada-IFES/GFTA
Av. Vitória 1729, Jucutuquara, Vitória, ES, Brazil, CEP 29040-780
[2]UCL-Faculdade do Centro Leste, Rodovia ES 010, Km 6
BR 101, Serra-ES, Brazil
[3]Centro Brasileiro de Pesquisas Físicas (CBPF) Rua Dr. Xavier
Sigaud 150, Urca, RJ, Brazil, CEP 22290-180

E-mail: `cmarques@ifes.edu.br`, `gilmar@ifes.edu.br`, `helderch@hotmail.com`, `sergio@cbpf.br`

Abstract. The Mössbauer spectroscopy is proposed as an alternative experimental technique to be pursued in the detection of Coherent Elastic ν-Nucleus Scattering (CENNS). The neutrino transferred energy in the neutrino-nucleus interaction causes a perturbation at the nuclear level structure of the Mössbauer isotope, leading to a displacement of the isomeric peak of the electromagnetic resonance. We calculate this isomeric shift correction due to the occurrence of CENNS and show that this quantity can be measured with enough precision in a typical Mössbauer spectroscopic experiment. We also shown that a reasonable number of events is expected and allow to extract the correction in the isomeric shift in a typical neutrino reactor flux. This isomeric shift correction is pointed out as a figure of merit for signature of CENNS in our proposal.

1. Introduction

A direct evidence of the Coherent Elastic ν-Nucleus Scattering (CENNS) has been considered an experimentally challenging task to better understand weak neutral current in the context of the Standard Model of Particle Physics(SM) [1, 2, 3, 4]. An evidence of the process has been intensively pursued by many experimental collaborations in the last four decades [5, 6, 2, 3, 7] developing a great effort to the direct detection of this weak process, which has the largest predicted cross section in the energy range below 50 MeV.

Recently, the COHERENT collaboration report the first undoubtedly measurement of the CENNS process[8]. An efficient scintillator detector was used in the experiment carried out at the Oak Ridge National Laboratory. With a Spallation Neutron Source it was produced an extremely intense neutron beam, which was scattered by a mercury target generating a secondary pion beam. Produced pions decays into an intense neutrino flux ($\approx 10^{11}$/s) with energy in the range of 16 to 53 MeV [8]. The pulsed neutrino flux was scattered by 14.6 kg crystal made of CsI doped with Sodium atoms. The experimental setup was properly structured to prevent any contamination from external sources of neutrons and neutrinos, like atmospheric or solar and galactic neutrinos. This experiment accumulate CENNS events during fifteen months produced in accordance to the SM prediction.

Here we are searching for a signature of the CENNS using Mössbauer nuclear spectroscopy(MS) [10, 9]. The great domain of the technique all over the world makes possible a broad experimental check of our predictions and confirm results obtained by different laboratories.

As it is well known the main characteristic of Mössbauer technique is the recoil less interaction of the electromagnetic radiation with the nucleus in a crystal sample. This aspect is assumed to be preserved in the CENNS process with absorber nucleus used in Mössbauer measurement. The nucleus maintain its fixed position in the local minimum of the crystal potential lattice. The effect of the energy transferred by neutrinos to the nucleus is to induce a perturbation in the inner degree of nuclear structure. We assume that the quantum state of the valence neutron is modified. Consequently, the nuclear volume is changed and the consequent change in the isomeric shift can be observed with the typical accuracy of this spectroscopic technique. To determine our prediction, we assume that only the valence neutron is perturbed at the structure of a characteristic nucleus of Mössbauer machine (a typical one is ^{57}Fe). With this transition between single particle states of the valence neutron in the CENNS process, we calculate the change in isomeric shift. Pauli blocking prevent transitions at the inner structure of the nuclear core.

In next section of this letter, we summarize the main characteristics of CENNS. Our proposal of use Mössbauer technique to observe CENNS is presented in more details in section III. The isomeric shift correction due to CENNS process is calculated in section IV. In Section V it is estimated the event rates for some Mössbauer isotopes used as absorber. Section VI presents our main conclusions.

2. The Main Characteristic of CENNS

The CENNS was proposed theoretically by Freedman [1]in 1974. A Feynman diagram of this weak process is shown in Fig. 3. The effective Lagrangian to describe the process is given by

$$L = G_F L^{\mu} J_{\mu}, \tag{1}$$

where G_F is the Fermi constant, L^{μ} the lepton current, and J_{μ} is the hadron current inside the nucleus. Experimental efforts have been developed in the detection of CENNS, some of them represented by large scientific collaborations namely, COHERENT [11, 8], CONNIE [12] and TEXONO [13], among others. As mentioned before, after decades of searching only in the last year the COHERENT Collaboration [8] announced the first irrefutable detection of CENNS.

It is well known that the coherence aspect of CENNS, requires $qR \ll 1$, with q being the transferred momentum and R the nuclear radius. This implies that the wavelength of neutrinos will be comparable to the nuclear radius. Detailed discussions about the phenomena can be found in Refs. [1, 14, 4, 6, 3] and references therein. We stress the fact that the cross section of this process has the largest value ($\sigma \approx 10^{-38}$ cm^2) at least four orders of magnitude larger than other neutrino interactions in the same low-energy regime [6].

The Freedman differential cross section for this process is [1, 2, 15]

$$\frac{d\sigma_{\text{CENNS}}}{dT} = \frac{G_F^2}{4\pi} Q_w^2 M_A F^2(q^2)\left(1 - \frac{M_A T}{2E_\nu^2}\right), \tag{2}$$

where T is the transferred energy to the nucleus, A is the target mass, E_ν is the neutrino energy and $Q_w = N - Z(1 - 4\sin^2\theta_w)$ is the weak charge, which depends on the number of neutrons

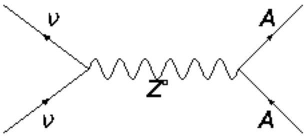

Figure 1. Feymann diagram of the CENNS process.

(N) and protons (Z). Here θ_w is the Weinberg angle satisfying $\sin^2\theta_w \approx 1/4$ and the proton contribution is negligible. The last fact made CENNS a very sensitive probe to nuclear neutron density [16]. The form factor $F(q^2) \to 1$ as $q \to 0$ define the coherence condition.

We remind that as a weak process, the interaction involved in the CENNS should be many order of magnitude greater than the gravitational phenomena. Even so, the MS was successfully employed to measure the gravitational red shift of light by Pound and Rebka [17, 18] at the end of the fifties. Thus, we hopefully expect that a properly MS array could be used in the study of eletroweak phenomena.

3. The Mössbauer Technique Applied to Detect CENNS

One of the main characteristics of the MS is that the nuclei in the absorber material of the machine are recoil less when interacting with gamma photons becoming from the source decay. This condition is fundamental for the resonant radiation absorption in the MS. We considered that the recoil less feature was preserved for the CENNS because the transferred energy to the nucleus is in the same range of the gamma photon. The transferred momentum by the Z^0 exchange is assumed to be transmitted to the valence neutron slightly modifying the neutron distribution in the nuclear surface and promoting a typical isomeric shift correction in the MS experiment. In addition, it is straightforward to show that the recoil less nuclei in the source and absorber is consistent for both processes, the resonant condition of the electromagnetic radiation and for the coherent neutrino scattering by the nuclei. The fraction f of the recoil less nuclei in Z^0 exchange between neutrino and nuclei in the CENNS can be analyzed similarly to the case of the gamma radiation interaction. It can be shown that the fraction of recoil less events can be put in the form of Debye-Waller factor [19], which, for the CENNS, takes the form

$$f = \exp\left(-\frac{T^2}{Mc^2\hbar\omega}\right), \tag{3}$$

where $T = E_\nu^2/2Mc^2$ is the energy transferred by the Z^0 to target nucleus of mass M. Here $\hbar\omega \approx 10^{-3}$ eV for Fe, Co etc, is the order of magnitude of energy lattice vibrations. In the range of neutrino energies below ≈ 50 MeV the recoil less f factor is essentially unity. Therefore, we argue that this small energy fraction is accommodated by a perturbed change in valence neutron levels.

4. Isomeric Shift Correction due to the CENNS Interaction

We consider that the energy transferred to the valence neutron is considered as a first-order perturbation term in the the valence neutron state of a shell model non-perturbed base. We assume that the perturbed neutron wave functions acquire a small projection in the next state of the unperturbed system. This model is similar to that proposed in the reference[8] in which weak force produces low energy electron states mixtures. This picture allows us to consider the problem as a two-level system, with neutron state fluctuating between the two unperturbed state levels. In the present case we will focus on ^{57}Fe because it is the most common in the literature, but many other nuclei can be studied with this technique, e.g., La, Te, Cd and Sm [10]. The unperturbed ^{57}Fe valence neutron is at a state of definite angular momentum, given by the common distribution of the neutron and proton content [20] in nuclear shell model – its wave function is regular at the origin (typically a Bessel function). Thus the perturbed valence neutron states, after the Z^0 interaction are

$$\Phi^+ = \frac{-\lambda j_{3/2}(kr)}{\sqrt{1+\lambda^2}} + \frac{j_{5/2}(kr)}{\sqrt{1+\lambda^2}}, \tag{4}$$

$$\Phi^- = \frac{j_{3/2}(kr)}{\sqrt{1+\lambda^2}} + \frac{\lambda j_{5/2}(kr)}{\sqrt{1+\lambda^2}}. \tag{5}$$

The λ parameter in the above equations appears in the perturbed treatment and is associated to the ratio between the square of the transferred energy and the energy difference of the non-perturbed energy states [21] of the valence neutron. Explicitly we have,

$$\lambda = \lambda(E_\nu) = \frac{3E_\nu^2}{8Mc^2(E_{5/2} - E_{3/2})}. \tag{6}$$

The term $(E_{5/2} - E_{3/2})$ is the difference between the energy of the non-perturbed states of the valence neutron. In ^{57}Fe case, this is responsible for the emission of 14.4 KeV photon which is emitted and absorbed resonantly without nuclear recoil.

In the context of the shell model for Woods-Saxon potential with spin orbit term[22, 20, 23, 24], the two states of valence neutron for the ^{57}Fe can be described by spherical Bessel functions, $j_{3/2}(kr)$ and $j_{5/2}(kr)$. We have used for the wave number of the valence neutrons $k \approx 0.5$ fm^{-1}, which is, as usually, approximately the inverse of twice neutron radius.

The isomeric shift can be calculated [10] as being

$$\delta I_s^* = \frac{4\pi Z e^2 R_{gs}^2}{5}\Big(\frac{R_{exc} - R_{gs}}{R_{gs}}\Big)[\psi^2_{l=0}(0)_a - \psi^2_{l=0}(0)_s], \tag{7}$$

where Z is the number of protons in the nucleus, R_{gs} is the mean radius of the charge distribution at the ground state of nucleus and R_{exc} for the Z^0 excited nuclear radius, respectively, the $\psi's$ are the s electrons wave functions, evaluated at the origin [19, 10] for the absorber and the source of gamma radiation. In the literature, the difference between nuclear radius of the excited nucleus and the ground state is $(R_{exc} - R_{gs})$, which in conventional gamma resonance is reported to be $\approx 10^{-3} R_{gs}$ [19, 10]. Our estimate for $\frac{R_{exc}-R_{gs}}{R_{gs}}$, calculated using the perturbed neutron wave functions $\Phi_{+/-}$ above is $\approx 10^{-4} R_{gs}$. With this result and Eq. 7, we can obtain the correction at isomeric shift induced by the weak process (Z^0 exchange) in CENNS. As we can see only one order of magnitude smaller than the typical characteristic γ measurements. This value for $\delta_{I_s^*}$ is perfectly solved with the MS technique accuracy, namely 10^{-10} eV [17, 18, 10]. Consequently, we point out that if we take subtraction of a MS measurement without the neutrino flux and other result of identical measure with the reactor neutrino beam, we would reveal the contribution of the CENNS interactions.

5. Event Rates for Mössbauer Isotopes

In this section we estimate the expected event rate n, for some nuclei of interest in Mössbauer Spectroscopy. This number could be given by the expression 8.

$$n = N_t \int_{E_{min}}^{E_{max}} dE_\nu \Phi(E_\nu) \frac{d\sigma(E_\nu)}{dE_\nu}, \tag{8}$$

Where N_t is the number of target nuclei, which we assume of order 10^{23}, E_ν is the energy of neutrinos at incident flux, Φ is the reactor flux of neutrinos, σ is the cross section of CENNS. $E_{max/min}$ is the maximum/minimum energy at the spectrum of neutrinos. In the case of Möessbauer nuclei, the energy exchange of Z and the target nucleus is integrally absorbed by the neutron field, and the overall nucleus has no momentum inside the crystal lattice. Then the cross section is maximal and given by:

$$\sigma_{cenns} = \frac{G_F^2 E_\nu^2 N^2}{4\pi}, \tag{9}$$

In this expression G_F is the Fermi constant and N is the neutron number, E_ν is the energy of neutrinos. The proton contents contribution is ignored due its tiny weak charge. The energy distribution of the neutrino flux from the reactor neutrinos is not well established in complete details[25]. However some estimations can be used in order to have a practical definition of the rate and number of events in an experimental test.

The reactor neutrino flux is not well theoretically understood in its full extent. As we see at the figure 2 below, it presents a bump of anti neutrinos at 4.5 Mev, which is not yet well explained. We know that it holds a very high quantity of neutrinos/cm^2s, of order 10^{13}. It ranges between 0 to $E_{max} = 10$ Mev.

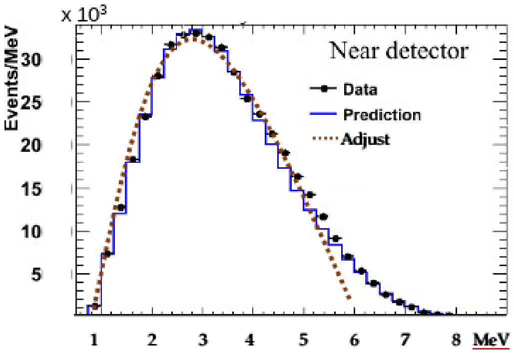

Figure 2. Reactor Anti-neutrino flux from Daya Bay(top). **There is an** Anti-neutrino excess around 4.5 Mev(middle). Comparison of predicted and measured prompt energy spectra(botton). This figure was taken from [26].

In our estimation we use the normalized function$\Phi(E_\nu) = 22.6 * 10^{-3}(E_\nu - \frac{1}{6} \cdot 10^{-6} E_\nu^2)$ as the mostly simple curve that fits approximately the spectrum for the reactor showed at figure 2. With these assumptions, the event rates n for some Mössbauer isotopes are displayed in the graph below and more specifically for three MS isotopes at table 1.

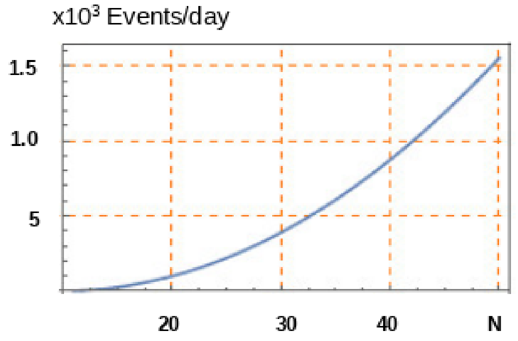

Figure 3. Events calculated from expression 8. We are considering $\approx 10^{23}$ nucleus subjected to an integrated reactor anti neutrino flux of order $10^{13}/cm^2s$

Table 1. Event rates for nuclides of interest

Nucleus	N	Cross Section($10^{-38}cm^2$)	Event rate
Fe	30	3, 8	$\approx 10^2/day$
Rh	58	14	$\approx 10^3/day$
Bk	150	9600	$\approx 10^5/day$

The isotopes Bk and Rh present higher event rates than the Fe, however there are some difficulties in CENNS observation in the use of them. The separation of the valence levels energy, are some hundreds of keV, making the parameter λ in Eqs.$(4-5)$ almost null. Additionally the measure of the spectra of these elements is hard to calculate, due to their tiny relative abundance. This appoints the conventional Iron isotope as a favorable choice of the CENNS experiment using the Mössbauer Technique.

6. Conclusions

This work develops model calculation to determine some estimate of the rate and number of events to give support for the use of MS spectroscopy as a suitable technique to see the CENNS process.

The isomeric shift correction obtained when the machine is exposed to a neutrino flux of reactors is the signature of contribution at the MS experiment. Our estimate is a correction of the order $\sim 10^{-7}$ eV for a system using ^{57}Fe isotope, this value is greater than the typical energy resolution of this technique,$\sim 10^{-10}$ eV. We then guess, that future MS experiments could be suitable to integrate the neutrino experimental plants.

Acknowledgements: S. B. Duarte acknowledge financial support from CNPq. The authors are also grateful to Pedro Cavalcanti Malta, Gustavo Pazzini de Brito, Jos A. Helayël-Neto, Hélio da Motta and Arthur M. Kós for the encouragement and for clarifying discussions during the development of this work.

[1] Freedman D Z 1974 Coherent effects of a weak neutral current Physical Review D V 9
[2] Giunt C and Studenikin A 2015 Neutrino Eletromagnetic Interactions: A Window to New Physics Reviews of Modern Physics 87 531
[3] Brice S J et al 2013 A new Method for measuring Coherent Elastic Neutrino Nucleous Scattering at an Off-Axis High-Energy Beam Target arXiv:1311.5958v1
[4] Krauss L M et al 1984 Antineutrino astronomy and geophysics Nature 310 5974 191-198
[5] Drukier A and Stodolsky L 1984 Principles and applications of a neutral-current detector for neutrino physics and astronomy PRD 30 11
[6] Formaggio J A and Zeller G P 2012 From eV to EeV: Neutrino cross sections across energy scales Reviews of Modern Physics
[7] Collar J I 2014 arXiv: 1047.7524v2[physics.ins-det]
[8] Akimov D et al 2017 Observation of coherent elastic neutrino-nucleus scattering Science 357 6356 1123-1126
[9] Gruverman I J 2013 Mssbauer Effect Methodology: Proceedings of the Fifth Symposium on Mssbauer Effect Methodology New York City (Springer Science and Business Media)
[10] Greenwood N N 2012 Mssbauer spectroscopy (Springer Science Business Media)
[11] Akimov D et al 2015 The COHERENT Experiment at the Spallation Neutron Source arXiv preprint arXiv:1509.08702
[12] CONNIE collaboration 2016 arXiv:1608.01565v3 [physics.ins-det]
[13] Singh V and Wong H T 2006 Phys Atom Nuclei 69: 1956 https://doi.org/10.1134/S1063778806110214
[14] Mosel U and Lalakulich O 2012 Neutrino-nucleus Interactions arXiv: 1211.1977 vI[nucl-th]
[15] Scholberg K 2012 Prospects for Measuring NeutrinoNucleus Coherent Scattering with a Stopped-Pion Neutrino Source Nuclear Physics B-Proceedings Supplements 229 505
[16] Balantekin A B 2017 Facets of Neutrino-Nucleus Interactions arXiv preprint arXiv:1711.03667
[17] Pound R V and Rebka Jr G A 1959 Resonant absorption of the $14.4-$keV γ ray from $0.10-\mu$sec Fe57. Physical Review Letters 3 12 554
[18] Pound R V and Snider J L 1964 Effect of gravity on nuclear resonance Physical Review Letters 13 18 539
[19] Marfunin A S 2012 Spectroscopy luminescence and radiation centers in minerals (Springer Science Business Media)
[20] Blatt J M and Weisskopf V F 2012 Theoretical nuclear physics (Springer Science Business Media)
[21] Yu K M and Flambaum V V 2002 Influence of perturbations on the electron wavefunction inside the nucleus Journal of Physics B: Atomic, Molecular and Optical Physics 35 19 4101
[22] Wong S S M Introduction to Nuclear Physics Prentice Hall Englewood Cliffs New Jersey 07632.
[23] Jonker M et al 1982 Experimental study of differential cross sections in charged-current neutrino and antineutrino interactions Phys Lett B 109 1/2 133-140
[24] Hamzavi M and Rajabi A A Generalized nuclear Woods-Saxon potential under relativistic spin symmetry limit ISRN High Energy Physics
[25] Kopeikin V I 2002 Flux and spectrum reactor antineutrinos Physics of Atomic Nuclei 7 52 143152 doi:10.134/s1063778812020123
[26] Vorobel V and Daya Bay Collaboration 2017 J Phys Conf Ser 873 012031

XLI Brazilian Meeting on Nuclear Physics (RTFNB) IOP Publishing
IOP Conf. Series: Journal of Physics: Conf. Series **1291** (2019) 012019 doi:10.1088/1742-6596/1291/1/012019

Ionizing radiation effects in a rectifier circuit

A C V Bôas[1], M A Guazzelli[1], R C Giacomini[1] and N H Medina[2]

[1] Departamento de Física, Centro Universitário FEI, São Bernardo do Campo, Brazil.
[2] Instituto de Física da Universidade de São Paulo, São Paulo, Brazil.

E-mail: [1] alexiscvb.fei@gmail.com

Abstract. This work aims to study the effects of ionizing radiation on a half-wave rectifier circuit. The diodes of the circuit, rectifier and Zener, were exposed to X-rays of 10 keV of effective energy. The characteristic curves of both diodes were evaluated before and after being subjected to cumulative total ionizing dose (TID) effects. The accumulation of charges in the dielectric structures of the diodes alter their individual functionalities, but the changes verified in the rectification were irrelevant. In this study, three irradiation methods were used to correlate the physical mechanisms responsible for the effects caused by radiation with variations in the electrical parameters of the devices and the efficiency of the rectifier circuit.

1. Introduction

In the mid-19th century, little was known about semiconductors and devices made with these materials. There were, however, some empirical work, as was the case with the invention of the solid-state rectifier, presented by F. Braun, in 1874 [1]. This rectifier was made with PbS crystal, welded with a metal wire (contact tip diode). This diode showed to be very unstable and it was temporarily abandoned until it was necessary to resume it, since the valve diodes were not attending the demand for high-frequency usage. The beginning of the 20th century in turn was fundamental for microelectronics, since there was a huge progress in theoretical Physics, with the development of quantum mechanics [2]. Semiconductor devices generally are separated into two categories: majority-carrier devices and minority-carrier devices. Field-effect transistors (FET's) and Schottky barrier diodes are the primary representatives of the majority-carrier device category. Most other semiconductor devices including bipolar transistors, solar cells, diodes, rectifiers, and silicon-controlled devices are in the categories of the minority carrier devices [3]. On the other hand, the damage provoked in the electronic devices by the effects of exposure to ionizing radiation is basically defined by three main mechanisms: 1) the accumulation of charges in the dielectric structures and semiconductor interfaces defined by Total Ionizing Dose (TID); 2) the incidence of high energy linear transfer (LET) ionizing particles in a sensitive region of the circuit or device defined by Single Event Effect (SEE); 3) the interaction between an incident particle and the crystalline lattice of the material, damaging its crystalline structure, known as Displacement Damage (DD) [4]. The device chosen to analyze the radiation effects was a diode because, due to its sensitivity to radiation and the quantities required in today's circuitry, have received considerable attention to determine the effects of radiation on their electrical properties. This attention has included exposure to various radiation environments, with measurements of electrical characteristics before, after, and/or during the irradiation processes. Results of these investigations have shown permanent changes in the diode characteristics, including increases in forward-voltage drop and reverse current and decreases in reverse-recovery time [3]. There are several applications for the diodes, they can be part of logic gates (AND/OR), they can comprise gyros circuits, stapler circuits, voltage multipliers, protection circuits of any kind, led displays.

However, they are primarily important for application as voltage rectifiers [5]. Although, all rectifier circuits need diodes, it can come in many topologies, such as half-wave rectifier, full-wave rectifier, central bypass rectifier [5]. This work aims to study the effects of ionizing radiation on a half-wave rectifier circuit. A typical application of the rectifier circuit is the cellphone charger, which converts the AC voltage of the power outlet into a continuous 5 V. Nevertheless, the most impressive application could be considered the use as rectifier for the various rectifying voltage circuits required by a satellite in space [2, 5]. Due to the great variety and importance of the applications, the rectifier circuit was chosen to be studied in this work. The effects of radiation, and its variations are considered individual changes of a particular component, and it may modify the functionality of the circuit, for example the rectification of the signal [1, 4].

1.1. Half-wave rectifier circuit

The half-wave rectifier circuit has the function of transforming an alternating voltage supply into a direct voltage signal. In the circuit of Figure 1, capacitor C1 and a Zener diode are used for output voltage regulation [6].This circuit operates with the interaction between the diodes. The junction diode (DR) has the function of eliminating all the negative part of the incoming signal. The Zener diode (DZ) limits the output voltage, working in the avalanche region and bringing a certain stability and precision to the circuit output. This circuit is simple to analyze and robust to external interference, allowing a study of the individual behavior of each diode [5, 6]. In addition, it is possible to verify how much the alterations of each characteristic parameter of the diodes can affect the circuit behavior. Figure 1 shows the half-wave rectifier circuit used in this work. Figure 2 presents the input and output signals from the numeric circuit simulation (SPICE).

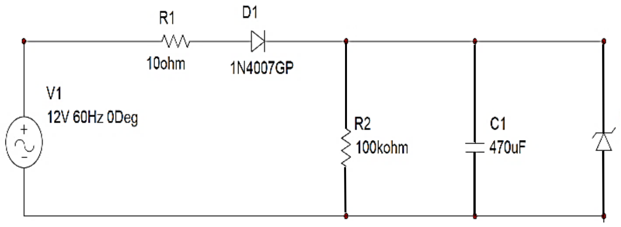

Figure 1. Half-wave rectifier circuit scheme.

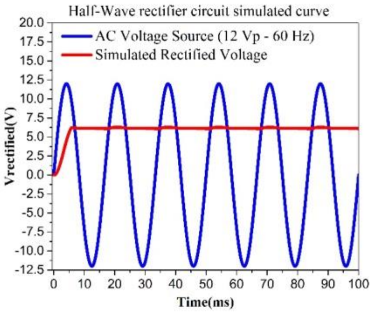

Figure 2. circuit response simulation.

2. Methodology

The circuit exposure to ionizing radiation was carried out at the Laboratory of Ionizing Radiation Effects (LERI – Laboratório de Efeitos da Radiação Ionizante) at Centro Universitário FEI, using a Shimadzu XRD-6100 diffractometer. The diodes were de-encapsulated in FEI Materials Laboratory and characterized through a PXI-NI platform [2]. The set-up programming was done in LabView to operate in conjunction with the PXI-NI platform. The modules work variating voltage and measure point to point the current on the diode. The device was under test (DUT) placed perpendicular to the X-ray beam. Both diodes were de-encapsulated with chemical processes to avoid the X-ray absorption by the epoxy cover.

2.1. Three methods of irradiation

In order to understand the behavior of the rectifier circuit after the irradiation of the two diodes, which have different functions in the circuit, three different test methodologies were performed. In the first method, both diodes were subjected to accumulated TID of about 3.5 krad (100 rad = 1 Gy), performed in two irradiation procedures with a time interval of one week between them, using a dose rate of 3.2 rad(Si)/min. In the second method, five irradiation steps were performed with a 24 hour time interval between them, in this method both diodes were exposed at a dose rate of 566 rad(Si)/min, totaling an accumulated dose of 250 krad. In the third method, only the junction diode was exposed to eight irradiation steps with a time interval of 10 minutes between them, at a dose rate of 1204 rad(Si)/min, totaling a total dose of 96 krad. Table 1 shows the summary of the three methods.

Table 1. Summary to the three-irradiation procedures.

MEHOD	1º	2º	3°
DOSE RATE (rad(Si)/min)	(3.2±0.2)	(566±30)	(1204±60)
TOTAL DOSE (krad)	(3.49±0.17)	(250±12)	(96±5)

The DUTs were characterized before and after each irradiation method, in order to establish some correlation between the effects of the radiation of each device individually and the general effect caused in the signal of the rectifier circuit. To study the behavior of the rectifier circuit, several combinations were made using the diodes DR and DZ that underwent the effects of different TIDs through the three methods of irradiation posed in this study.

3. Results and Discussion

Only one representative characteristic I_d versus V curve for each method will be presented as a way of exemplifying the results. In Figures 3 and 4 the junction diode (DR) and Zener diode (DZ) characteristic curves after the first method are shown. Figure 5 and 6 shows the DR and DZ diode characteristic curves after the second method and in Figure 7 the DR diode characteristic curve after the third method is shown.

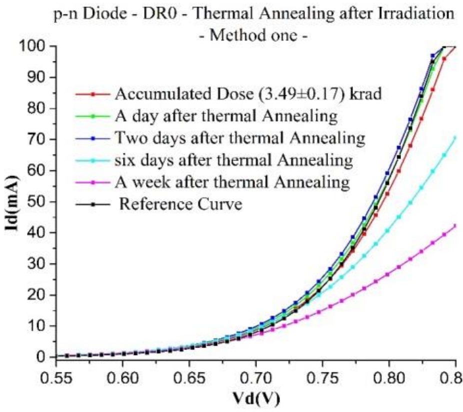

Figure 3. Characteristic curve I_dxV_d to the junction Diode on the first irradiation procedure

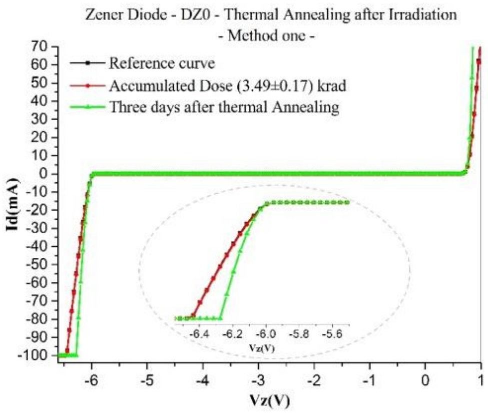

Figure 4. Characteristic Curve I_dxV_z to the Zener Diode on the first irradiation procedure.

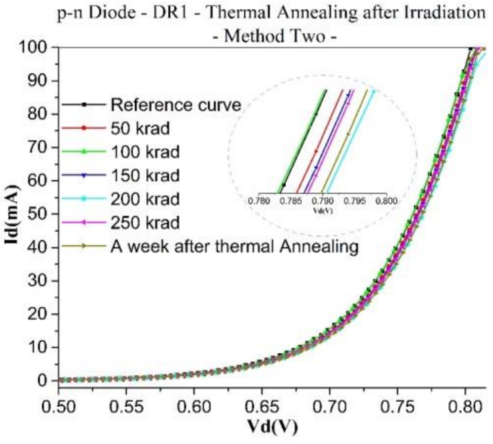

Figure 5. Characteristic curve I_dxV_d to the junction Diode on the second irradiation procedure.

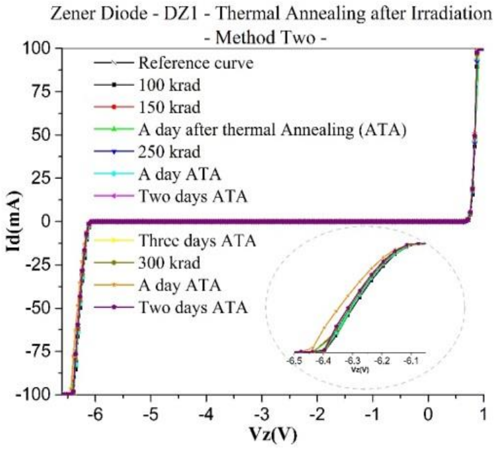

Figure 6. Characteristic Curve I_dxV_z to the Zener Diode on the second irradiation procedure.

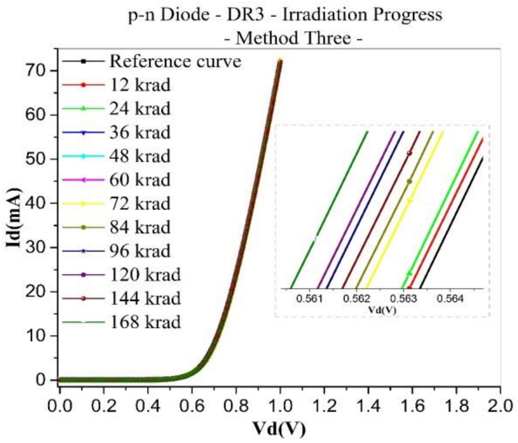

Figure 7. Characteristic Curve I_dxV_d to the junction Diode on the third irradiation procedure.

Table 2. Rectified Voltages in the three applied methods

METHOD	DIODE	RECTIFIED VOLTAGE (± 2%)
FIRST	DR0/DZ0	5.90 V
SECOND	DR1/DZ	5.95 V
SECOND	DR2/DZ	6.06 V
SECOND	DR/DZ1	5.93 V
SECOND	DR/DZ2	5.94 V
SECOND	DR1/DZ1	5.92 V
SECOND	DR1/DZ2	5.91 V
SECOND	DR2/DZ2	5.94 V
THIRD	DR3/DZ	6.10 V
THIRD	DR3/DZ1	5.95 V
THIRD	DR3/DZ2	5.96 V

The results indicate the junction diodes with the first irradiation method present the higher variation in its characteristic curve parameters, as shown in Figure 3, while the Zener diode with all other irradiation procedures fluctuated very little. In order to obtain the various rectifying voltages of the circuit, several tests were performed, with several irradiated diode combinations. Table 2 shows the rectified voltage for each of these circuit configuration, where DR represents the rectifier diode and DZ the Zener diode, the number after the diode type represents the order in which it was irradiated. For example, DR2 was irradiated after DR1, but both belong to the second applied method. When only DR or DZ is used it means that a non-irradiated diode was used. The rectified reference voltage measured is 5.90 V.

4. Conclusion

Considering a rectifying voltage, without irradiation, of 5.9 V and observing the characterization of eleven diode combinations in the rectified circuit, the rectified voltages are very close to the reference value, the lower voltage was obtained using the first method and was about 5.9 V and the highest voltage was about 6.10 V obtained with the third irradiation method. The mean rectifier voltage after all irradiation procedures is (5.96 ±0.02) V, indicating the rectifier circuit is tolerant to radiation taking into account the X-ray doses the diodes were submitted. Even with the effect of the accumulated radiation (TID), the junction region, modified by the entrapment of charges, and the variation of the work function (ϕ) of the semiconductor, there were small variations in the rectified voltage, due to the fact that it is the Zener diode that dictates the rectifying voltage in the circuit, and for all irradiation methods the Zener diode suffered little variation in its functionality.

5. References

[1] Swart J 2009 *Semicondutores – Fundamentos, técnicas e aplicações* Editora da Unicamp (São Paulo: Campinas)
[2] Cirne K H 2011 *Estudo e fabricação de MOSFET's robustos à radiação para aplicações espaciais de circuitos integrados* Dissertação de Mestrado (Centro Universitário da FEI)
[3] C L Hanks and D J Hamman 1971 *Radiation effects design handbook* (Washington D.C.)
[4] Johnston A 2010 *Reliability and radiation Effecs inCompound Semiconductors* World Scientific Publishing Co. Pte. Ltd (California: Institute of Technology)
[5] Boylestad R and Nashelsky L 2012 *Electronic Devices and Circuit Theory* Pearson 11th ed
[6] Sedra A S and Smith K C 2004 *Microelectronics Circuits* Pearson 5th ed (New York/Oxford)

Acknowledgments

This work was supported by Centro Universitário FEI; FAPESP Proc. No. 2017/18181-2; CNPq, FINEP Proc. No. 01.12.0224.00; INCT-FNA Proc. No. 464898/2014-5.

XLI Brazilian Meeting on Nuclear Physics (RTFNB) IOP Publishing
IOP Conf. Series: Journal of Physics: Conf. Series **1291** (2019) 012020 doi:10.1088/1742-6596/1291/1/012020

A proposal to study long-lived isotopes produced by thermal neutron irradiation of digital devices

G S Zahn[1], F A Genezini[1], M Moralles[1], P T D Siqueira[1], N H Medina[2], V A P Aguiar[2], E L A Macchione[2], N Added[2], M A G da Silveira[3]

[1] Instituto de Pesquisas Energéticas e Nucleares - IPEN-CNEN/SP
[2] Instituto de Física da Universidade de São Paulo
[3] Centro Universitário FEI, São Bernardo do Campo, Brazil

E-mail: `gzahn@ipen.br`

Abstract. In this work, we present a facility to study errors in digital devices exposed to thermal neutrons from a beam hole in the IEA-R1 nuclear reactor, as well as the long-lived isotopes produced in the irradiation of digital electronic devices under a slow neutron field. Preliminary results obtained with the analysis of a 28nm SRAM-based Xilinx Zynq-7000 FPGA are presented.

1. Introduction

Exposure of digital devices to radiation may induce several types of effects. Directly ionizing radiation will deposit charge within the system, while indirectly ionizing radiation will, by interaction with the device's material, produce directly ionizing radiation.

While the effects of photons, heavy ions, electrons and fast neutrons have been thoroughly studied [1, 2], studies on the influence of slow neutrons are scarce. These neutrons have kinetic energies around 0.02 eV, thus they are unable to break chemical bounds or even to excite individual electrons, so they will produce directly ionizing radiation only by means of nuclear reactions. The most common reactions for low-energy neutrons are $^{10}B(n,\alpha)^{7}Li$ and the neutron capture (n,γ) reactions, with considerably large cross sections ($\sigma > 1b$) for most metals and rare-earth elements. These capture reactions, in turn, will frequently produce radioactive nuclides that will emit delayed directly ionizing radiation (either β^- or β^+), aside from rendering the system radioactive.

Recently, new ultra-high-current accelerators have been proposed (e.g., the *NUMEN* accelerator in Italy [3]) that should create strong ($10^5 cm^{-2} \cdot s^{-1}$) slow neutron fields in the positions where nuclear ionstrumentation must reside, thus requiring the study of the effect of such neutron fluxes in data acquisition digital systems.

In this work, we have studied the built-up radioactivity in a Xilinx Zynq-7000 FPGA board subjected to neutron irradiation in beam holes of a nuclear reactor.

2. Induced Radioactivity

In the case of exposure of N nuclides of a given type to a particle flux of ϕ ($cm^{-2} \cdot s^{-1}$), the rate at which a given nuclear reaction with a cross section σ happens is given by:

$$\frac{dN}{dt} = N \cdot \sigma \cdot \phi \tag{1}$$

If the produced nuclide is radioactive and decays with a half-life $T_{1/2}$, the activity of these nuclides (A^*) present in the sample after an irradiation period t will not be a linear function of t:

$$A^* = N \cdot \sigma \cdot \phi \left(1 - e^{-\lambda \cdot t}\right) \tag{2}$$

where $\lambda = ln(2)/T_{1/2}$. This means that for irradiation times up to a single half-life the growth is approximately linear, while after 7-10 half-lives the activity saturates at $N \cdot \sigma \cdot \phi$. Therefore, for a device that should star under irradiation for a long period of time (up to several years), the build-up of long-lived radionuclides ($T_{1/2} > 100$ days, for instance) could present a real issue, both in terms of radiological protection and for the integrity of the device itself. Moreover, for these long-lived radionuclides, the activity build-up can be simulated by increasing the irradiation flux, as when $t << T_{1/2}$, $(1 - e^{-\lambda \cdot t}) \approx t$.

3. Experimental Procedure

In a preliminary test to check for signals of activity build-up in digital acquisition systems, a 28nm SRAM-based Xilinx Zynq-7000 FPGA board was irradiated in the IEA-R1 nuclear reactor. As the test also intended to check the suitability of the available facilities for this type of test, irradiations were performed in distinct beam-holes in the IEA-R1 reactor.

Initially, the board was irradiated in the monochromatic low-energy facility installed in beam-hole number 6, where the neutron flux is $\sim 6 \times 10^4 cm^{-2} \cdot s^{-1}$ for two 8-hour periods (as the reactor operates on an 8 hour per day basis, these irradiations were carried out for two consecutive days). Then, in order to check the suitability of the other facility, in the next day the board was irradiated in beam-hole number 3, under a mixed neutron field (mostly thermal, but epithermal and fast neutrons are also present); during this test the reactor's operational power was progressively raised so that, in the last hour, the flux reached approximately $10^8 cm^{-2} \cdot s^{-1}$.

The residual radioactivity was then studied by gamma spectrometry, both after 18h of the end of irradiation and after 6 days of decay. These measurements were performed using an Ortec HPGe detector, with the spectra analysed using Canberras Genie-2000 software. A rough efficiency calibration was performed using point sources (^{166m}Ho and ^{152}Eu) placed at approximately the same distance as the board – an exact calibration was not possible for these tests, as the board is very heterogenous and the exact position where each nuclide was produced cannot be determined.

4. Preliminary Results and Discussion

In the first measurement, after 18 h of decay, the total gamma activity was estimated to be around 30 kBq. The strongest individual contribution came from the annihilation peak at 511 keV ($\sim$ 6 kBq), followed by noticeable contributions ($\sim$ 0.5 kBq) from ^{198}Au ($T_{1/2} = 65$ h), ^{82}Br ($T_{1/2} = 35$ h), ^{64}Cu ($T_{1/2} = 13$ h) and ^{24}Na ($T_{1/2} = 15$ h). All of the identified radionuclides have half-lives below 3 days and shouldn't present relevant issues.

In the second measurement, after 6 days of decay, total gamma activity was estimated around 5 kBq, with noticeable contributions ($\sim$ 500 Bq) from the annihilation peak and also from ^{198}Au ($T_{1/2} = 65$ h), ^{82}Br ($T_{1/2} = 35$ h), and ^{64}Cu ($T_{1/2} = 13$ h), all of which have half-lives short enough to be considered irrelevant in long-term exposition studies. Minor relevant contributions ($\sim$ 5 Bq), though, were noticed for the activation of ^{60}Co ($T_{1/2} = 1925$ days), ^{182}Ta ($T_{1/2} = 115$ days), ^{65}Zn ($T_{1/2} = 244$ days) and ^{124}Sb ($T_{1/2} = 60$ days) – these radionuclides have longer half-lives and, specially in the cases of ^{65}Zn and ^{60}Co, may present really relevant issues if the board is to be irradiated for a period of time of several years.

5. Conclusions

Both facilities tested in this work proved to be suitable for the irradiation of electronic devices. The results of the preliminary tests showed that at least some long-lived nuclides – most noticeably ^{60}Co and ^{65}Zn – were produced during these tests, emphasizing the importance of further studies. A shortcoming noticed in these studies resides in the definition of a reasonable gamma-detection efficiency value, which will only be possible by splitting the board in its individual components or by using restrictive collimators during irradiation or counting. Nevertheless, if the aim of the study is simply to assess the production of isotopes that may pose a safety threat after long irradiations, the large uncertainties that would come from the gamma-counting efficiency should not be a problem.

References

[1] Ferlet-Cavrois V, Massengill L W, Gouker P 2013 *IEEE Trans. Nucl. Sci.* **60**, 1767
[2] Aguiar V A P et al. 2014 *Nucl. Instrum. Meth. Phys. Res. B*, **332**, 397
[3] Cappuzzello F et al. 2018 *Eur. Phys. J. A* **54** 72

Sodium analysis in sweeteners by neutron activation analyses technique

I M M A Medeiros[1,2], C B Zamboni[1], D N S Giovanni[1], J A G Medeiros[2]

[1]Centro do Reator de Pesquisa – CRPq, Instituto de Pesquisas Energéticas e Nucleares, IPEN – CNEN/SP, São Paulo-SP, 05508000, Brasil.
[2]Universidade Cidade de São Paulo – UNICID, São Paulo-SP, 03071000, Brasil

Email: jageiros@ipen.br, ilca.medeiros@ipen.br, czamboni@ipen.br, daltongiovanni@gmail.com

Abstract. Evaluation of Sodium in sweeteners is important in nutritional investigations and for consumers: excessive sodium consumption is one of the major risk factors, responsible for hypertension and cardiovascular diseases. In this study, twelve brands acquired in markets of São Paulo city were analysed by Instrumental Neutron Activation Analyses technique (INAA). The aim was to verify compliance with ANVISA recommendation in relation to sodium level. The results were compared with the amounts recommended and with the tolerable intake limit (< 0.4 g/kg). The sodium concentration in sweeteners samples showed low content for most of the brands. The results shown that for the general population, it is not risk.

1. Introduction

The body needs only a small amount of sodium (less than 500 milligrams per day) to function properly (this amount is less than ¼ teaspoon). According to the World Health Organization (WHO), sodium intake should not exceed 2 grams per day. However, no one even comes close to eating that amount. Sodium content more than 75% comes from processed and prepackaged products, such as sweeteners, condiments, sauces and soft drinks may contain high doses. Sodium may appear in labels such as sodium benzoate, saccharin sodium, and monosodium glutamate.

O In 2010, it was proposed by the Ministry of Health and ANVISA (representative entities of the public health of Brazil) an increase in the efforts to reduce sodium consumption by the Brazilian population to less than 1700 mg / person / day [1]. Since then, processed foods have been evaluated intensively based on sodium content (more than 75 % of the sodium in food comes from processed and prepackaged products). Among the processed products, sweetener intake has increased significantly in the last decade: sweetener consumption in the American population (adult) increased from 27% to 41%; among children, it was 9% to 25% (an increase of more than 200%). In Brazil, there are no official statistics, but according to "*Food Guide for the Brazilian Population"* (Guia Alimentar para a População Brasileira [2], the trend is the same.

Evaluation of this ion in sweeteners is important in nutritional investigations and for consumers: excessive sodium consumption is one of the major risk factors, responsible for hypertension and cardiovascular diseases [3]. In this study, twelve brands acquired in markets of São Paulo city were analyzed by Instrumental Neutron Activation Analyses technique (INAA).

2. Experimental

Each sample was sifted and homogenized. Each sample (mass ~80 mg) was prepared in triplicate. Each sample was sealed into individual polyethylene bags, together with the Certified Reference Material Sample and Standard and were irradiated for 300s, in a pneumatic station at the nuclear reactor (IEA-R1, 3.5-4.5 MW, pool type), IPEN/CNEN-SP, Brazil, with a thermal neutron flux (ranging from 5.6 x 10^{12} to 6.2 x$\cdot10^{12}$ n cm^{-2} s^{-1}). After the irradiation, the activated materials were gamma-counted for 900s using an HPGe (Model GEM-6019), coupled to an MCA ORTEC (Model 919E). The gamma ray spectra analysis was performed using the ATIVAÇÃO software. The NIST 1573a reference material was used as standard and for analytical quality control.

3. Results and Discussion

The INAA method was validated using reference material (NIST 1573a): the accuracy of the method was evaluated by Zscore test [4] and the repeatability of the methods was evaluated by RSD values. These results are presented in Table1.

Table 1. The analysis of the reference material

Reference Material (Mean ± 1SD, mg kg^{-1})	136 ± 4
Present Study (Mean ± 1SD, mg kg^{-1})	135 ± 9
RSD, %	6.7
Z-score values	0.3

The Na concentrations were presented in Table 2. The results were expressed by: Mean Value (MV), Standard Deviation (±1SD), Minimum (min) and Maximum (max). Figure 1 was elaborated to show the comparison with the tolerable intake limit.

Table 2. Na concentrations in Sweetener brands by INAA

	Sweetener Brands	
Na, gkg^{-1}	Aspartame n= 6	Sucralose n=6
MV	0.739	0.207
±1SD	1.508	0.204
min	0.013	0.019
max	3.811	0.493

n: number of samples

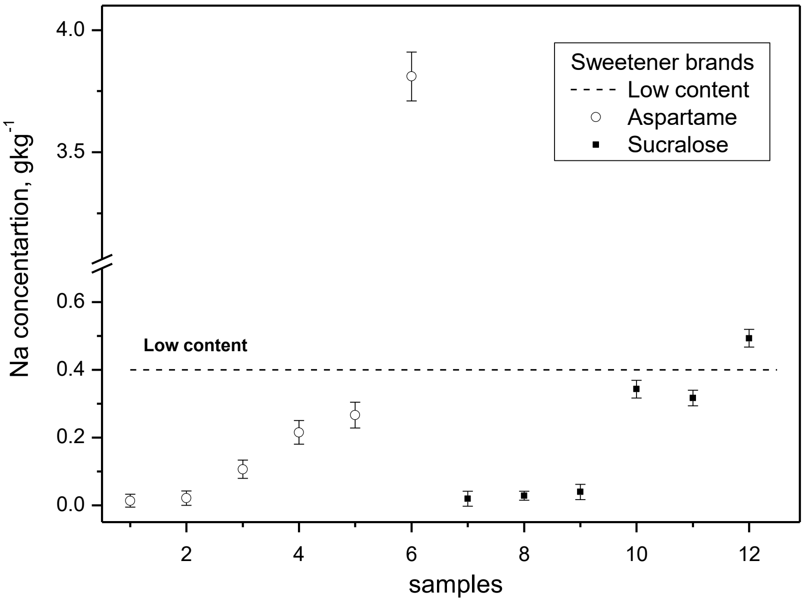

Figure 1. Na concentration in sweeteners samples

According to Table 1, the Z value = 0.3 indicated that our result was satisfactory (|Z score| < 2) and is within the range of certified data at 95% confidence level as well as the repeatability of the method, RSD = 6.7 % (RSD < 10 %). Related to Table 2, the Na concentration in sweeteners samples showed a low content (‹0.4 g kg^{-1}) according to ANVISA recommendations. Only two brands (sucralose) are above the recommended (0.4 g kg^{-1}), but only one (3.8 g kg^{-1}) shows significant difference, about 10 times above the recommended. However, patients with Metabolic Syndrome (~ 2000 million people in Brazil) may be at risk [5,6].

4. Conclusion

The sodium concentration in sweeteners samples showed to be low content. The results shown that for the general population, it is not risk.

5. Acknowledgments

The authors would like to acknowledge the CNPq and FAPESP for the financial support.

References

[1] Redução de Sódio, Açúcar e Gordura Trans, http://dab.saude.gov.br/portaldab/ape_promocao_da_saude.php?conteudo=reducao (Accessed 12/12 2018).
[2] Brasil 2006 Guia alimentar para a população brasileira: promovendo a alimentação saudável Ministério da Saúde Brasilia
[3] Cogswell M E, Mugavero K, Bowman B A, Frieden T R 2016 *N Engl J Med* 375 580. doi:10.1056/NEJMsb1607161.
[4] Eurachem/CITAC 2012 In guide: Quantifying Uncertainty in Analytical Measurement Edited by S. L. R. Ellison, and A. E. Williams
[5] Sherling D H, Perumareddi P, Hennekens C H 2017 *J Cardiovasc Pharmacol Ther* 22 365. doi:10.1177/1074248416686187.
[6] Penalva D Q F 2008 *Revista de Medicina* 87 245.

XLI Brazilian Meeting on Nuclear Physics (RTFNB) IOP Publishing
IOP Conf. Series: Journal of Physics: Conf. Series **1291** (2019) 012022 doi:10.1088/1742-6596/1291/1/012022

Study of the elemental composition of plants and extracts of medicinal plants through X-ray fluorescence

T H P Estanagel[1], J M Oliveira Jr.[1,2], W Bonventi Jr.[2], N Aranha[2], M V Chaud[1,2], M M D C Vila[1], V M Balcão[1,2] and V M H Yoshida[2]

[1] Graduate Program in Pharmaceutical Sciences, University of Sorocaba, Rod. Raposo Tavares Km 92.5, 18023-000, Sorocaba, São Paulo, Brazil.
[2] Graduate Program in Technological and Environmental Processes, University of Sorocaba, Rod. Raposo Tavares Km 92.5, 18023-000, Sorocaba, São Paulo, Brazil.
Corresponding author: jose.oliveira@prof.uniso.br

Abstract. Medicinal plant extracts are mostly used in different kinds of products in different areas, such as pharmaceutical, cosmetic, food and veterinary, being employed in different dosages and applications. It is known that the metabolism of the human body is regulated by the presence or absence of certain chemical elements. Some elements enter vital functions, such as potassium and calcium. Potassium helps in muscle contractions, especially of the heart muscle, and calcium enters as an specific element in the bone composition. Some other elements like heavy metals (As, Hg, Cd, and Pb) are highly toxic to the human body, even at quite low concentrations. Therefore, there is the need to investigate the chemical composition of plants and medicinal extracts, because the presence of some elements in levels concentrations, as well as the deficiency of others, can lead to a series of metabolic disorders in the human body. The main objective of this study was to evaluate the chemical composition of plants and extracts of medicinal plants, using the Energy Dispersive X-Ray Fluoresce (EDXRF) technique, to assessing the chemical composition of plants and extracts. The qualitative and quantitative chemical elements investigated in the plants and extracts were: As, Cr, Cu, Fe, Ni, Zn, Si, P, S, Cl, K, Ca, Ti, V, Mn, Co, Rb, Zr, Cd, Sn, Ba, Hg, Pb, Bi, Mo, Pd, and Pt.

1. Introduction

Medicinal plants and extracts of medicinal plants are mostly used in different kinds of products in different areas, such as pharmaceutical, cosmetic, food and veterinary, being employed in different dosages and applications. It is known that the metabolism of the human body is regulated by the presence or absence of certain chemical elements. Some elements aid in vital functions like potassium and calcium. Potassium helps in muscle contractions, especially of the heart muscle, and calcium enters as a specific element in the bone composition [1,2,3]. Some other elements like heavy metals (As, Hg, Cd and Pb) are highly toxic to the human body, even at quite low concentrations [4]. Therefore, there is a need to investigate the chemical composition of plants and extracts of medicinal plants, to verify the presence of some elements in levels concentrations, as well as the deficiency of others, that can lead to a series of metabolic disorders in living organisms [5,6]. Heavy metals even in extremely low doses can cause some damages to the human body. The origin of plants and methods of obtaining of extracts can influence such phytochemical compositions. With this in mind, it is necessary to investigate the chemical composition of these extracts as a way to avoid the presence of contaminating elements harmful to health, above levels established by regulatory agencies, mainly contamination by the heavy metals As, Pb, Hg and Cd. Thus, the main objective of this study was to evaluate the chemical composition of plants and plant extracts, using the Energy Dispersive X-Ray Fluoresce (EDXRF) technique [7], to evaluate the final chemical composition of the extracts, and also as production and purification processes, which may interfere with the final chemical composition of the product. The qualitative and quantitative chemical elements investigated in the plants and extracts were: As, Cr, Cu, Fe, Ni, Zn, Si, P, S, Cl, K, Ca, Ti, V, Mn, Co, Rb, Zr, Cd, Sn, Ba, Hg, Pb, Bi, Mo and Pt.

2. Material and methods

Fourteen extracts of medicinal plants, as well as six samples of crushed medicinal plants used in this study were acquired commercially. The EDXRF technique was chosen because it allows the simultaneous determination of several elements over a wide range of concentrations and requires minimal sample preparation. The identification and quantification of each chemical element can be done using EDXRF, because each chemical element has a unique set of atomic energy levels, it emits a unique set of X-rays after excitation, which is characteristic of each emitter element, and the intensity of an X-ray line depends on the number of corresponding atoms which were excited. The laboratory setup used in this work includes: a) a 25 mm^2 SDD X-ray detector with a resolution of 136 eV and b) an X-ray tube with Ag target, both manufactured by Amptek Inc. (Bedford, Massachusetts, USA). The equipment settings used in the data acquisition were: a) an irradiation timeframe of 300 s, b) peak time of 11.2 µs and c) dead time of 30%. The X-ray excitation source was set at 30 kV, an electric current of 10 µA of intensity and no filter was used in front of X-ray source or detector. For the fluorescence analyzes, tablets of the extracts and of the crushed plants were made (about 3g of each), using compression machine adjusted to 15 tons loading, producing tablets of 22 mm of diameter by 3 mm of height. The fluorescence system was calibrated using calibration samples containing known amounts of the major elements of interest. The calibration showed limits of detection, for several elements, less than 1 µg/g. The fluorescence system has enough sensitivity to indicate the presence of chemical elements and their respective concentrations, from the element Aluminum to Fermion. The analyses were performed in the Laboratory of Applied Nuclear Physics of Sorocaba University (LAFINAU). Amptek's ADMCA software for data acquisition and Amptek's XRS-FP™ software for spectrum processing and quantitative analysis were used.

3. Results and Discussion

Tables 1 and 2 show the concentrations of the identified elements and their respective deviations for the different medicinal extracts and crushed medicinal plants. The measurements were made in triplicate and the error is the standard deviation of the mean. To improve the manufacturing process used in the production of the extracts, known as spray drying, in some cases the use of adjuvants is necessary, for example, to reduce the humidity of the extract, thus preventing it from accumulating on the walls of the containers or to get better it appearance, color, etc. However, the use of these adjuvants may introduce contaminants in the extracts or add elements that were not originally present in the ground plants, such as the silicon element which, due to the use of the substance Silicon Dioxide as a secant, was introduced in some extracts, as in the Chá Verde and Espinheira Santa. In addition, by analyzing the elemental composition of these adjuvants, relatively high concentrations of some heavy metals, such as Hg, Pb and Cd were detected, contributing to increasing the contamination of the final product, with these harmful elements to the human body.

Table 1 (a). Chemical elements identified and quantified in the medicinal plants extracts.

Sample number	1	2	3	4	5	6	7
Scientific name	*Cynara scolymus L.*	*Myrciaria Dubia*	*Solanum Sessiliflorum*	*Camellia sinensis L.*	*Rhamus purshiana*	*Camellia Sinensis L.*	*Malpighia glabra L.*
Popular name	Alcachofra	Camu Camu	Mana Cubiu	Chá Verde	Cascara Sagrada	Matchá	Acerola
Elements	C (µg/g)	C (µg/g)	C (µg/g)	C (µg/g)	C (µg/g)	C (µg/g)	C (µg/g)
As	-	-	-	-	0.2 ± 0.1	-	-
Cr	23.0 ± 1.3	13.0 ± 0.8	16.0 ± 0.9	15.0 ± 0.8	22.0 ± 1.2	14.0 ± 0.8	12.0 ± 0.7

Cu	28.0 ± 0.9	17.0 ± 0.5	16.0 ± 0.5	16.0 ± 0.5	27.0 ± 0.9	16.0 ± 0.5	14.0 ± 0.5
Fe	104.0 ± 3.4	65.0 ± 2.1	65.0 ± 2.1	61 ± 2	94.0 ± 3.1	62.0 ± 2.0	57.0± 1.8
Ni	46.0 ± 3.4	25 ± 2	26.0 ± 2.1	25.0 ± 1.9	44.0 ± 3.3	25.0 ± 1.9	22.0 ± 1.8
Zn	25.0 ± 1.4	14.0 ± 0.7	14.0 ± 0.8	14.0 ± 0.7	25.0 ± 1.3	13.0 ± 0.7	12.0 ± 0.7
Si	-	(27.3 ± 4.0) 10^3	(17.6 ± 2.8) 10^3	(45.3 ± 6.2) 10^3	-	(28.3 ± 4.1) 10^3	(46.4 ± 0.2) 10^3
P	150 ± 11	-	-	-	192 ± 16	-	-
S	(3.6 ± 0.2) 10^3	(5.4 ± 0.3) 10^3	-	(5.2 ± 0.3) 10^3	(2.0 ± 0.1) 10^3	(3.6 ± 0.3) 10^3	751 ± 143
Cl	(3.0 ± 0.1)10^3	(2.5 ± 0.1) 10^3	(2.1 ± 0.1) 10^3	(3.9 ± 0.2) 10^3	175 ± 45	(3.4 ± 0.2) 10^3	(1.1 ± 0.1) 10^3
K	(9.3 ± 0.2)10^3	690 ± 103	(1.9 ± 0.1) 10^3	708 ± 113	(1.2 ± 0.1) 10^3	148 ± 71	762 ± 92
Ca	38 ± 4	33 ± 2	19 ± 2	11 ± 9	16.0 ± 2.4	4.4 ± 1.4	2.0 ± 0.6
V	15 ± 2	6 ± 1	9.0 ± 1.4	5 ± 1	18 ± 2	6 ± 1	6 ± 1
Mn	142 ± 9	71 ± 6	72 ± 6	76 ± 6	106 ± 9	72 ± 6	58 ± 6
Co	2.0 ± 0.5	2.0 ± 0.3	1.0 ± 0.3	2 .0± 0.3	2.0 ± 0.4	1.0 ± 0.3	1.0 ± 0.3
Rb	13 ± 2	4.0 ± 1.5	4.0 ± 1.3	3 ± 1	2 ± 2	4 ± 1	4 ± 1
Zr	6 ± 2	5.0 ± 1.2	2.0 ± 0.7	5.0 ± 1.2	7 ± 2	4 ± 1	6.0 ± 1.3
Cd	2 .0± 0.2	5.0 ± 0.5	5.0 ± 0.4	-	1.0 ± 0.2	-	2.0 ± 0.2
Sn	14 ± 7	5 ± 3	8 ± 4	6.0 ± 3.3	15 ± 8	7 ± 4	7 .0± 3.4
Ba	4.0 ± 1.2	2.0 ± 0.7	5.0 ± 1.2	4 ± 1	2 ± 1	4 ± 1	2.3 ± 0.7
Hg	3.0 ± 0.5	1.0 ± 0.2	1.0 ± 0.2	1.0 ± 0.2	2.0 ± 0.4	1.0 ± 0.2	0.4 ± 0.2
Pb	3.0 ± 0.5	2.0 ± 0.3	2.0 ± 0.3	2.0 ± 0.3	4.0 ± 0.6	1.4 ± 0.2	1.8 ± 0.3
Bi	1.0 ± 0.4	1.0 ± 0.2	-	-	1.0 ± 0.5	0.5 ± 0.2	0.3 ± 0.2
Mo	-	-	0.3 ± 0.1	-	-	-	-
Pt	1.0 ± 0.3	2.3 ± 0.3	0.6 ± 0.2	0.8 ± 0.2	1.1 ± 0.5	0.6 ± 0.2	0.5 ± 0.2

Table 1 (b). Continuation

Sample number	8	9	10	11	12	13	14
Scientific name	*Paulina Cupana K.*	*Illex Paraguariensis*	*Maytenus Ilicifolia L.*	*Equinacea purpúrea L.*	*Melissa Officinalis L.*	*Passiflora incarnata L.*	*Aesculus Hippocastanum L.*
Popular name	Guaraná	Mate Verde	Espinheira Santa	Equinácea	Melissa	Passiflora	Castanha da Índia
Elements	C (μg/g)	C (μg/g)	C (μg/g)	C (μg/g)	C (μg/g)	C (μg/g)	C (μg/g)
As	-	-	0.2 ± 0.1	1.3 ± 0.2	2.0 ± 0.2	-	-
Cr	19.6 ± 1.1	16 ± 1	18 ± 1	24.0 ± 1.5	23.0 ± 1.4	25.0 ± 1.5	12.0 ± 0.7
Cu	22.0 ± 0.7	20.6 ± 0.7	21.0 ± 0.7	35 ± 1	36 ± 1	35 ± 1	20.0 ± 0.6
Fe	90 ± 3	94 ± 3	78.0 ± 2.5	120 ± 4	108 ± 4	127 ± 4	60 ± 2
Ni	39 ± 3	32 ± 3	33.3 ± 2.4	51 ± 4	49 ± 4	51 ± 4	25 ± 2
Zn	21.0 ± 1.2	19.9 ± 0.9	18.3 ± 1.0	33.2 ± 1.5	29.4 ± 1.4	30.6 ± 1.4	14.5 ± 0.7
Si	-	(35.1 ± 5.1) 10^3	(20.3 ± 3.3) 10^3	-	-	-	(214.7 ± 26.9) 10^3
P	42 ± 38	(1.3 ± 0.2) 10^3	989 ± 464	222 ± 170	873 ± 359	204 ± 224	(5.9 ± 1.4) 10^3
S	(2.3 ± 0.1) 10^3	(4.3 ± 0.3) 10^3	(6.8 ± 0.3) 10^3	153 ± 29	499 ± 50	(2.0 ± 0.1) 10^3	(1.2 ± 0.2) 10^3
Cl	(1.9 ±0.1) 10^3	(2.6 ± 0.1) 10^3	(4.9 ± 0.2) 10^3	(1.00 ± 0.04) 10^3	(1.73 ± 0.06) 10^3	(4.7 ± 0.1) 10^3	989 ± 52
K	490 ± 117	(12.5 ± 0.3) 10^3	(8.9 ± 0.2) 10^3	(19.5 ± 0.4) 10^3	(33.9 ± 0.6) 10^3	(25.1 ± 0.5) 10^3	(31.2 ± 0.6) 10^3
Ca	101 ± 11	228 ± 19	532 ± 25	289 ± 13	51 ± 16	(1.07 ± 0.04) 10^3	88 ± 18
V	8.0 ± 1.4	7.0 ± 1.2	12 ± 2	10 ± 2	17.0 ± 2.5	13 ± 2	6 ± 1
Mn	102 ± 8	385 ± 11	94 ± 7	187 ± 10	127 ± 11	137 ± 10	59 ± 8
Co	2.0 ± 0.4	1.5 ± 0.4	1.7 ± 0.3	4.0 ± 0.6	3.0 ± 0.5	2.4 ± 0.5	1.2 ± 0.3
Rb	5.0 ± 1.7	9.0 ± 1.1	10.0 ± 1.1	21.0 ± 1.5	26.0 ± 1.5	14.0 ± 1.7	7.0 ± 0.9
Zr	8.8 ± 2.1	7.1 ± 1.7	10.0 ± 2.2	8.0 ± 2.1	6.5 ± 1.9	16.0 ± 3.5	3.1 ± 0.9
Cd	1.0 ± 0.1	2.0 ± 0.3	4.0 ± 0.4	2.0 ± 0.4	2.0 ± 0.3	3.0 ± 0.4	1.0 ± 0.1
Sn	10.1 ± 5.3	13.8 ± 6.5	11.1 ± 5.5	14.6 ± 7.7	20.3 ± 9.9	11.8 ± 6.4	6.9 ± 3.6
Ba	1.3 ± 0.7	0.9 ± 0.7	2.9 ± 1.0	-	-	-	1.1 ± 0.9
Hg	1.0 ± 0.3	1.2 ± 0.3	2.5 ± 0.4	5.3 ± 0.7	18.0 ± 1.2	4.4 ± 0.7	0.5 ± 0.2
Pb	3.1 ± 0.5	2.0 ± 0.3	1.6 ± 0.3	3.6 ± 0.5	2.5 ± 0.5	4.2 ± 0.6	1.4 ± 0.2
Bi	1.0 ± 0.4	0.6 ± 0.3	0.5 ± 0.3	1.5 ± 0.5	1.1 ± 0.5	0.4 ± 0.4	0.3 ± 0.2
Mo	-	-	-	-	-	-	-
Pt	0.4 ± 0.3	1.5 ± 0.3	0.6 ± 0.3	1.5 ± 0.5	1.1 ± 0.3	2.2 ± 0.5	0.4 ± 0.2

Table 2. Chemical elements identified and quantified in the crushed medicinal plants.

Sample number	15	16	17	18	19	20
Scientific name	*Equinacea purpurea L.*	*Maytenus ilicifolia L.*	*Camellia sinensis L.*	*Rhamus purshiana*	*Cynara scolymus L.*	*Paulina cupana K.*
Popular name	Equinácea	Espinheira Santa	Chá Verde	Cascara Sagrada	Alcachofra	Guaraná

Elements	(µg/g)	(µg/g)	(µg/g)	(µg/g)	(µg/g)	(µg/g)
As	-	-	-	0.5 ± 0.2	-	-
Cr	14.0 ± 1.1	21.6 ± 1.4	21.2 ± 1.3	23.9 ± 1.6	12.1 ± 1.0	24.2 ± 1.4
Cu	32.7 ± 1.1	34.7 ± 1.1	41.7 ± 1.3	37.2 ± 1.2	31.7 ± 1.0	40.9 ± 1.3
Fe	412 ± 8	180 ± 5	339 ± 7	215 ± 6	505 ± 9	228 ± 5
Ni	47.0 ± 4.2	51.5 ± 3.9	53.6 ± 4.2	56.8 ± 4.5	45.8 ± 4.5	49.9 ± 3.6
Zn	30.8 ± 1.5	33.1 ± 1.5	40.0 ± 1.6	34.1 ± 1.7	32.1 ± 1.5	34.3 ± 1.5
Si	(6.1 ± 1.5) 10^3	-	-	-	(3.6 ± 1.1) 10^3	-
P	(3.4 ± 0.4) 10^3	(2.0 ± 0.3) 10^3	(2.1 ± 0.3) 10^3	576 ± 331	(1.8 ± 0.3) 10^3	(1.9 ± 0.3) 10^3
S	(1.4 ± 0.1) 10^3	(1.10 ± 0.08) 10^3	(1.7 ± 0.1) 10^3	288 ± 39	(2.3 ± 0.1) 10^3	(1.1 ± 0.1) 10^3
Cl	155 ± 10	(4.5 ± 0.1) 10^3	472 ± 25	-	(12.0 ± 0.3) 10^3	449 ± 25
K	(30.1 ± 0.5) 10^3	(18.6 ± 0.4) 10^3	(18.9 ± 0.4) 10^3	(4.2 ± 0.1) 10^3	(50.3 ± 0.9) 10^3	(12.3 ± 0.3) 10^3
Ca	(21.5 ± 0.6) 10^3	(12.8 ± 0.3) 10^3	(8.5 ± 0.2) 10^3	(18.7 ± 0.5) 10^3	(25.4 ± 0.7) 10^3	170 ± 7
Ti	214 ± 22	-	112 ± 30	189 ± 51	231 ± 19	72 ± 23
V	5.5 ± 1.4	4.2 ± 1.1	5.8 ± 1.3	4.5 ± 3.3	6.0 ± 1.6	9.9 ± 1.8
Mn	214 ± 10	170 ± 10	(1.85 ± 0.04) 10^3	413 ± 14	165 ± 10	143 ± 10
Co	3.5 ± 1.1	2.5 ± 0.6	2.5 ± 1.0	1.9 ± 0.7	3.7 ± 1.2	3.7 ± 0.8
Rb	19.0 ± 1.5	14.7 ± 1.9	41.8 ± 1.7	19.6 ± 1.9	37.7 ± 1.6	16.1 ± 1.6
Zr	28.8 ± 4.0	21.6 ± 4.4	22.1 ± 4.7	39.0 ± 3.5	31.1 ± 3.4	18.7 ± 3.9
Cd	1.8 ± 0.2	1.9 ± 0.2	0.5 ± 0.1	2.0 ± 0.3	1.1 ± 0.2	1.8 ± 0.2
Sn	17.3 ± 8.7	16.7 ± 8.5	20.8 ± 10.2	23.2 ± 11.5	13.5 ± 7.1	14.1 ± 7.4
Ba	-	-	-	35.9 ± 4.4	-	3.6 ± 1.3
Hg	6.4 ± 0.8	2.8 ± 0.6	1.5 ± 0.6	1.4 ± 0.5	8.2 ± 0.8	2.9 ± 0.6
Pb	2.7 ± 0.4	3.1 ± 0.5	4.0 ± 0.6	3.9 ± 0.6	3.3 ± 0.5	4.0 ± 0.6
Bi	0.5 ± 0.4	1.8 ± 0.5	1.4 ± 0.5	0.5 ± 0.4	0.8 ± 0.4	0.6 ± 0.4
Mo	-	-	-	-	0.8 ± 0.3	-
Bi	-	0.5 ± 0.4	-	-	-	3.1 ± 0.6

Analyzing the concentrations of the different elements present in the medicinal plants extracts (Table 1) and the corresponding crushed medicinal plants (Table 2), one can notice that on average, the extraction process used (infusion of the crushed plant in cold, hot water or alcohol) has low efficiency for the extraction of most of the elements, as an example, compare the concentrations of Calcium, Potassium, Iron, etc. in the extracts with their respective levels in the crushed plants. On the other hand, the extraction process also decreases the concentration of some elements that are harmful to the human health, like Lead and Mercury, that even after the extraction process shows concentrations levels above those allowed by the Brazilian Pharmacopoeia [8]. The values provided in Table 3 are example of concentration limits for components (drug substances and excipients) of drug products dosed at a maximum daily dose of 10 g/day for the oral intake, predicted by the Brazilian Pharmacopeia [8]. These values serve as default concentration limits to aid discussions between drug product manufacturers and the suppliers of the components of their drug products.

Table 3. Concentration limits for components of drug products with a 10 g maximum daily dose, according to the Brazilian Pharmacopoeia [8].

Elements	C (µg/g)
Arsenic (As)	1.5
Cadmium (Cd)	0.5
Lead (Pb)	1.0
Mercury (Hg)	1.5
Chromium (Cr)	25
Copper (Cu)	250
Manganese (Mn)	250
Molybdenum (Mo)	25
Nickel (Ni)	25
Platinum (Pt)	10
Vanadium (V)	25

Analyzing the maximum limits allowed by the Brazilian Pharmacopoeia for heavy metals, it is observed that the Arsenic element appears in few samples, having presented concentrations a little above the allowed only by the extracts of the Melissa and Equinácea plants. In the case of the element Lead, all samples analyzed showed concentration above the limits established by the Brazilian Pharmacopoeia

[8]. For the Cadmium element, with the exception of the extracts of Chá Verde and Matchá the other extracts and all the ground plants presented concentrations above the limit established for this element, which is extremely low of only 0.5 μg/g. In the case of the element Mercury some plants and extracts presented concentration above the allowed limit, but a relatively large group also was below the limit concentration or very close to this one. However, it is worth noting the concentration of Mercury found in some extracts that were far above the limit, as is the case of the Melissa extract where the concentration measured was (18.0 ± 1.2) μg/g. As we did not have the corresponding ground plants to compare, it was not possible to verify if there was interference of the productive process in the production of this extract. For the other elements shown in Table 3, the concentrations obtained are within the acceptable limits for these elements.

4. Conclusions

EDXRF was used successfully for the determination of the elemental composition of medicinal plants and medicinal extracts. The EDXRF technique proved to be very versatile when compared to the technique recommended for this type of analysis by the Brazilian Pharmacopoeia [8], which is the Atomic Absorption Spectroscopy. The results show that the EDXRF technique can be recommended as a useful tool in the qualitative and quantitative control of medicinal drugs.

References

[1] Stuart I F 1991 Perspectives on Human Biology (Brown Publisher: Dubuque)
[2] Campbell N A 1996 Biology (The Benjamin, Cummings Publishing Company, Inc.: California)
[3] Jacob A 1996 Textbook of Clinical Chemistry (Counders WB Co.: Philadelphia, PA) p 965
[4] Ennever F1994 Principles and Methods of Toxicology (Hayes, Raven Press: New York) p 417
[5] Tolonen M 1990 Vitamins and Minerals in Health and Nutrition (Ellis Horwood Limited: Chichester, England)
[6] Sivarajan V V and Balachandran I 1994 Ayurvedic Drugs and Their Plant Sources (Oxford & IBH Publishing Co. Pvt. Ltd: New Delhi)
[7] Jenkins R, Gould R W and Gedcke D 1995 Quantitative X-Ray Spectrometry. 2nd ed. (New York: Marcel Dekker, Inc., 2nd ed.)
[8] Agência Nacional de Vigilância Sanitária and Fundação Oswaldo Cruz 2010 Brazilian Pharmacopeia (Vol. I, ISBN: 978-85-88233-40-9, 548p and Vol. II, ISBN: 978-85-88233-41-6, 904p, 5º ed.)

Acknowledgements

Project funding by Fundação de Amparo à Pesquisa do Estado de São Paulo (FAPESP, São Paulo, Brazil; Grant nº 2018/06801-9). Support from CNPq (Brazil) to V.M. Balcão (Ref. n°. 308208/2017-0).

Ions concentration in blood samples of SJL/J dystrophic mice strains using X-ray fluorescence spectrometry

D N S Giovanni[1], M R Almeida[1], C B Zamboni[1], S Metairon[1], K N Balduino[1], M F Suzuki[1] and C R Bueno Jr[2]
[1]Instituto de Pesquisas Energéticas e Nucleares, IPEN – CNEN/SP São Paulo-SP, 05508000, Brasil.
[2]Centro de Estudos do Genoma Humano, Instituto de Biociências - USP, São Paulo – SP, 05508000, Brasil

E-mail: daltongiovanni@usp.br; almeida.mramos@gmail.com

Abstract. Star This study proposes an investigation of ions in whole blood of the dystrophic animal model SJL/J (mice strain with dysferlin protein deficiency) and in the control group (C57BL/6J) using the Energy Dispersive X-ray Fluorescence (EDXRF) spectrometry technique. The comparison between control and dystrophic mice results shown an increase in blood for P, S, K and Fe ($p < 0.05$) while a decrease in Ca ($p < 0.05$). This elemental analysis will contribute to evaluate the best diagnostic, care and treatment procedures, for the Progressive Muscular Dystrophy.

1. Introduction

The Progressive Muscular Dystrophies (PMDs) are genetic diseases that affect muscular groups. More than thirty different forms of muscular dystrophies have been identified and, all of them have a hereditary character and has no cure [1-3]. This study proposes an investigation of ions of clinical relevance (such as, Ca, Cl, Cu, K, Fe, P and S) in whole blood of the dystrophic animal model (SJL/J mice strain - dysferlin protein deficiency) [4,5], using the Energy Dispersive X-ray Fluorescence (EDXRF) technique. The advantages of using this alternative procedure are the facilities that can be introduced, that is, the measurements can be carried out in a few minutes using small amounts of blood (few microliters), which is an important abridgment when the biological material is scarce. The conventional procedure performed in serum (using at least a 1.0 mL)[6], which requires the euthanize of this small animal model (the total mice body blood ~ 1.2 mL). Blood analyses was also performed in a healthy mouse strain (C57BL/6J), adopted as control group, with the intent to check differences among these groups.

2. Experimental Procedure

The mice strains came from Jackson Laboratory (Maine, USA) [5] and were later inbred at IPEN (São Paulo, Brasil). Whole blood samples from SJL/J (n=6) and C57BL/6J (n = 12) male mice were collected. The blood collection was performed according to the rules approved by the Animal Research Ethics Committee (087/99). For sample preparation aliquots of 50 μL whole blood (duplicate), from each animal model collected by the retro-orbital venous plexus, were transferred to filter paper (Whatman, nº 41) using a calibrated micropipette. The EDXRF analyses were performed using a portable XRF Spectrometer (PXRFS), composed by an Amptek detector X-123 SDD and an X-ray tube with Ag target.

The characteristic of the fluorescence intensity of K_α line was measured with a Si Drift detector (25 mm^2 x 500 µm) with Be window (12.5 µm). Each biological sample was irradiated for 300 to 900 s using 5µA and 30kV. The analyses were performed using WinQxas software program (IAEA, version 1.3).

3. Results and discussion

For the PXRFS calibration, standard solutions for each reference control sample, containing varying concentrations were prepared. For example, the calibration curve for Fe Kα line is presented in Figure 1.

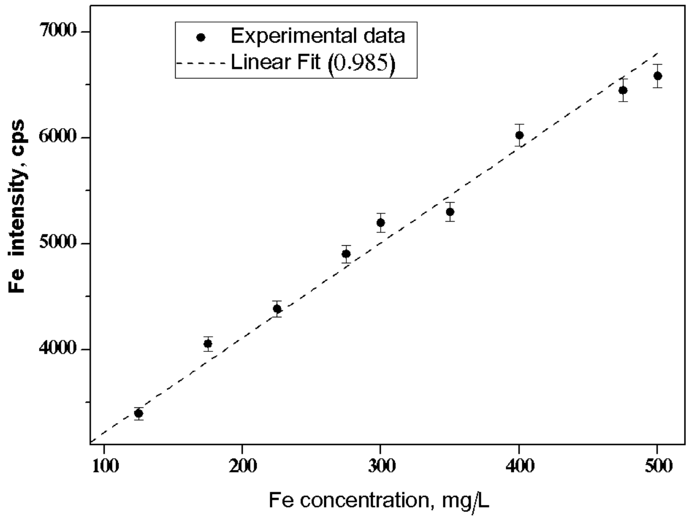

Figure 1. Calibration curve for Fe Kα line

The results for elements concentrations in whole blood mice strains samples using EDXRF technique are shown in Table 1. The results were expressed by mean value (MV), standard deviation (±1SD) and by the range for a confidence interval of 95% usually adopted in clinical evaluation. To visualize, in Figure 2 are shown the results (duplicate) of SJL/J species whole blood by using EDXRF analysis. A comparison between control and dystrophic animal models results are presented in Figure 3

Table 1. Elements concentrations in whole blood by EDXRF analysis

	SJL/J n=6	C57BL/6J n=12
Elements	MV ± 1SD [range]	
P, mg/L	1192 ± 243 [706 – 1678]	781 ± 185 [411 – 1051]
S, mg/L	1519 ± 312 [895 – 1863]	1229 ± 200 [829– 1629]
Cl, mg/L	2933 ± 380 [2173 – 3693]	2954± 442 [2070 – 3838]
K, mg/L	2488 ± 283 [1922- 3054]	2001± 513 [975 – 3027]
Ca, mg/L	142 ± 61 [20 – 134]	186±20 [146 – 226]
Mn, µg/L	0.68 ± 0.10 [0.48 – 0.88]	nd

Fe, mg/L	324 ± 29	187± 13
	[266 – 382]	[161 – 213]
Cu, µg/L	3.90± 0.45	3.44 ± 0.33
	[3.00 - 4.80]	[2.78 – 4.10]

n: number of samples
nd: not determined

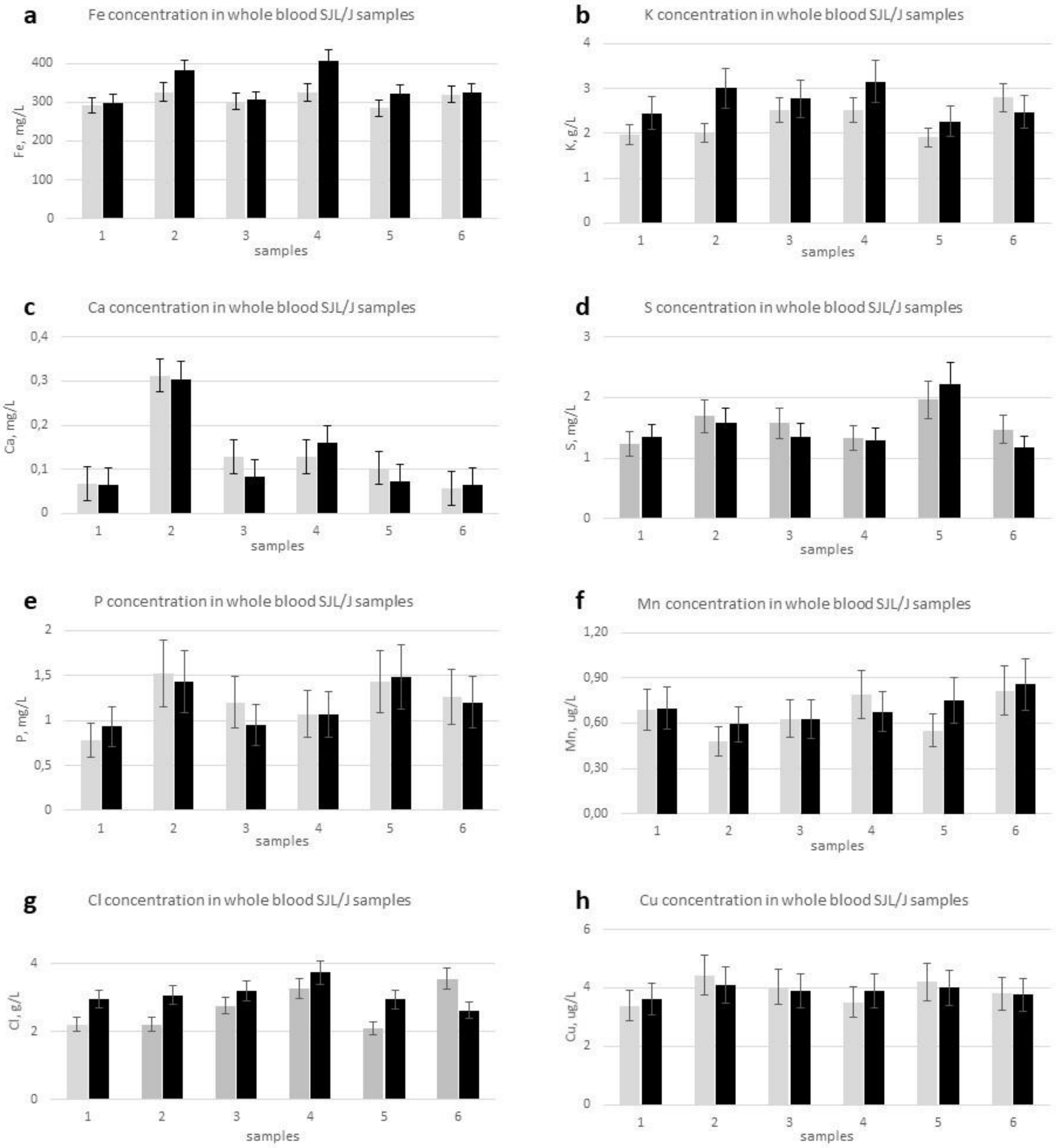

Figure 2. Elements Fe (a), K(b), Ca(c), S(d), P(e), Mn(f), Cl(g) and Cu(h) concentration for SJL/J whole blood mice samples analyzed in duplicate

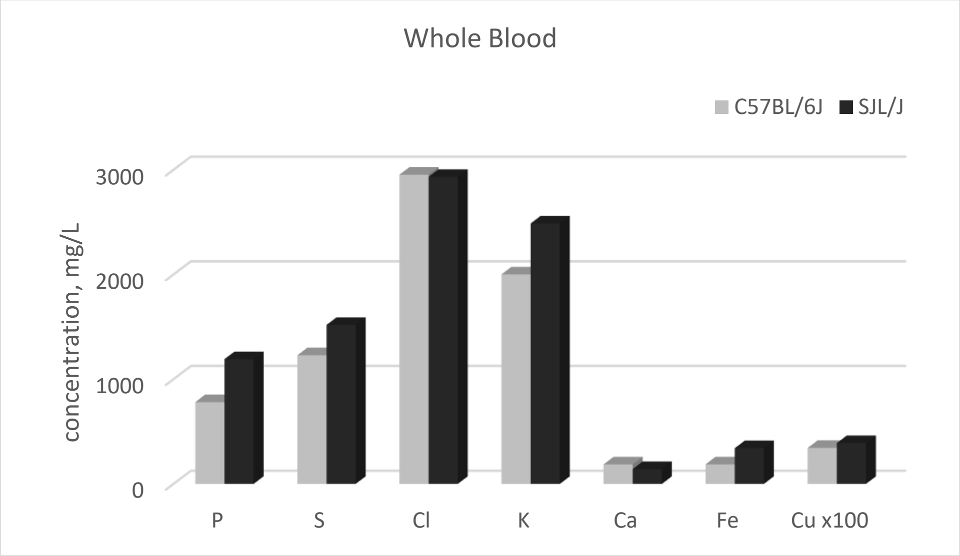

Figure 3. Whole blood concentrations results for SJL/J & C57BL/6J

By establishing an indicative interval for ions in whole blood of SJL/J dystrophic mice strain enable to verify differences among them (dystrophic and control), which is an important condition to the animal model selection in the investigation of muscular dystrophy. According to t-test, there is agreement between the species only for Cl. The comparison between control and dystrophic mice emphasizes an increase in blood for P, S, K and Fe ($p < 0.05$) while a decrease in Ca is more accentuated ($p < 0.05$) in the absence of dysferlin protein.

4. Conclusion

The elements concentration in whole blood for the SJL/J dystrophic animal model emphasize some significant differences for several ions when compared with the control group (C57BL/6J). Besides, the study of ions behavior in in whole blood this dystrophic specie contribute for a more accurate evaluation on the diagnoses.

5. Acknowledgments

The authors thank the financial support of Fundação de Amparo à Pesquisa do Estado de São Paulo (FAPESP) and Conselho Nacional de Desenvolvimento Científico e Tecnológico (CNPq).

References

[1] Emery A E H 2002 *The Lancet* **359** 687. doi:10.1016/S0140-6736(02)07815-7.
[2] Zatz M 2005 *Science* **308** 55.
[3] Chelly J and Desguerre I 2013 *Handb Clin Neurol* **113** 1343. doi:10.1016/B978-0-444-59565-2.00006-X.
[4] Blake D J,Weir A,Newey S E and Davies K E 2002 *Physiol Rev* **82** 291. doi:10.1152/physrev.00028.2001.
[5] SJL/J dystrophic mice strain - Jackson Laboratory, https://www.jax.org/strain/000686.
[6] Zamboni C B,Azevedo M R and Metairon S 2018 *In* Raio-X para dosagem de ferro no sangue: Prática Clínica *Novas Edições Acadêmicas* Mauritius p.^pp. 19

XLI Brazilian Meeting on Nuclear Physics (RTFNB) IOP Publishing
IOP Conf. Series: Journal of Physics: Conf. Series **1291** (2019) 012024 doi:10.1088/1742-6596/1291/1/012024

Study of induced activity of ^{167}Ho from different neutron capture paths

T S L Morais[1] **and M S Dias**[2]

Nuclear and Energy Research Institute (IPEN-CNEN/SP)
Nuclear Metrology Laboratory (LMN) – Research Reactor Center (CRPq)
Av. Professor Lineu Prestes 2242, Cidade Universitária, 05508-000
São Paulo, SP, Brazil

[1]thales.morais@usp.br, [2]msdias@ipen.br

Abstract. The main purpose of this study is to predict the induced activity of ^{167}Ho produced by ^{165}Ho(n,γ)^{166m}Ho(n,γ)^{167}Ho, ^{165}Ho(n,γ)^{166}Ho(n,γ)^{167}Ho and ^{166m}Ho(n,γ)^{167}Ho reactions to choose the best path to measure the cross section with lowest uncertainty. The activation and decay scheme was established starting from the ^{165}Ho target and considering single, double and triple neutron capture reactions. The activity results were deduced from differential activation equations and decay rates for all reaction products. The calculations were performed considering samples which were taken from a stock solution supplied by the Electrotechnical Laboratory (Japan) for purposes of an international comparison.

1. Introduction

To predict the induced activity from neutron capture reactions is an important step in planning a neutron cross section measurement. The Nuclear Metrology Laboratory (LMN) at the IPEN, in São Paulo, has been involved in improving the accuracy of neutron cross sections by irradiations at the IEA-R1 research reactor. For the measurement of the thermal neutron cross section and the resonance integral of the ^{166m}Ho(n,γ)^{167}Ho reaction it is necessary to know all the different paths that ^{167}Ho can be produced by neutron capture reactions. As a result, the best method of irradiation can be chosen in order to reduce the uncertainties in the measurements. The difficulty of conducting experiments with radioactive targets is due to the complex decay and activation schemes. This is one of the reasons why the thermal neutron cross section and the resonance integral data are scarce in the literature for the ^{166m}Ho(n,γ)^{167}Ho reaction, when compared with reactions with stable isotopes.

2. Methodology

The activation and decay scheme was established starting from ^{165}Ho considering single, double and triple neutron capture reactions (see Figure 1) and the calculations were performed considering samples with 20 MBq/g of Ho and 0.31 g/ml of $HoCl_3$ in 1N HCl according to stock solutions supplied by the Electrotechnical Laboratory (Japan) for purposes of an international comparison[3].

The variation in the number of atoms of the target nucleus ^{165}Ho (N_5) is given by:

$$\frac{dN_5}{dt} = -N_5\sigma_{5,6m}\phi - N_5\sigma_{5,6}\phi \tag{1}$$

Where:
$\sigma_{5,6m}$ = cross section for ^{165}Ho(n,γ)^{166m}Ho reaction;
$\sigma_{5,6}$ = cross section for ^{165}Ho(n,γ)^{166}Ho reaction;
ϕ = neutron flux.

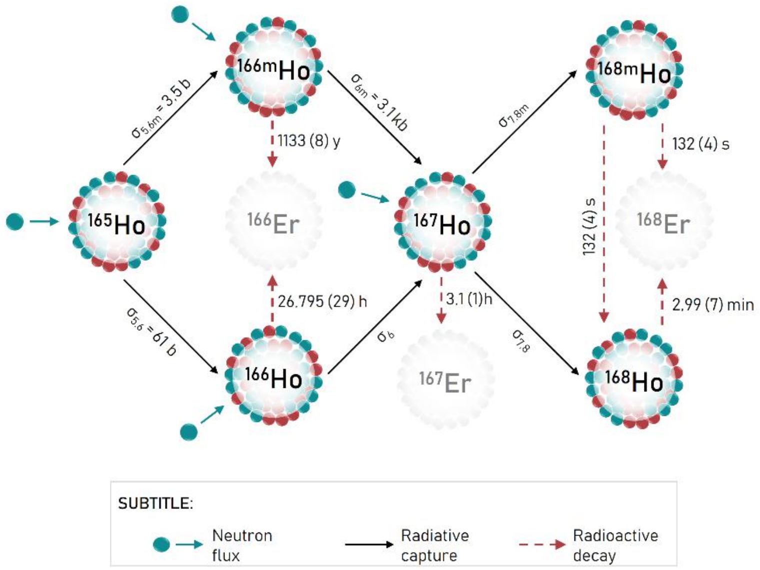

Figure 1. Activation and decay scheme starting from ^{165}*Ho* [1][2]

The first term refers to the production rate of ^{166m}Ho and the second refers to the production rate of ^{166}Ho. Solving the differential equation (1) by the method of separation of variables, the result is:

$$N_5(t) = e^{-(\sigma_{5,6m}+\sigma_{5,6})\phi t} \cdot e^{K_1} \tag{2}$$

Where K$_1$ is a constant and ***t*** is the irradiation time. When ***t = 0***, $N_5 = N_5^0$. Where N_5^0 is the number of atoms of ^{165}Ho in the sample at the beginning of the irradiation. Replacing this information in the equation (2) one obtains $e^{K_1} = N_5^0$, therefore:

$$N_5(t) = N_5^0 e^{-(\sigma_{5,6m}+\sigma_{5,6})\phi t} \tag{3}$$

The variation of ^{166m}Ho atoms in the sample, must consider the formation of ^{166m}Ho atoms through the activation of ^{165}Ho, the decay of the ^{166m}Ho, and its activation forming ^{167}Ho, as follows:

$$\frac{dN_{6m}}{dt} = N_5\sigma_{5,6m}\phi - \lambda_{6m}N_{6m} - N_{6m}\sigma_{6m}\phi \tag{4}$$

Where:
λ_{6m} = decay constant of ^{166m}Ho;
σ_{6m} = cross section for ^{166m}Ho(n,γ)^{167}Ho reaction.

Replacing equation (3) into equation (4), multiplying both sides by $e^{(\lambda_{6m}+\sigma_{6m}\phi)t}$ and solving the differential equation, the result is:

$$N_{6m}(t) = \frac{N_5^0\sigma_{5,6m}\phi e^{-(\sigma_{5,6m}+\sigma_{5,6})\phi t}}{\lambda_{6m} - (\sigma_{5,6m} + \sigma_{5,6} - \sigma_{6m})\phi} + K_2 e^{-(\lambda_{6m}+\sigma_{6m}\phi)t} \tag{5}$$

Where K_2 is a constant.

Considering that initially (***t* = *0***) there was a certain amount of ^{166m}Ho atoms (N_{6m}^{0}), one obtains:

$$N_{6m}(t)=\frac{N_5^0\sigma_{5,6m}\phi}{\lambda_{6m}-(\sigma_{5,6m}+\sigma_{5,6}-\sigma_{6m})\phi}\left[e^{-(\sigma_{5,6m}+\sigma_{5,6})\phi t}-e^{-(\lambda_{6m}+\sigma_{6m}\phi)t}\right]+N_{6m}^0 e^{-(\lambda_{6m}+\sigma_{6m}\phi)t} \tag{6}$$

The number of ^{166}Ho atoms in the sample can be calculated in a similar way, as follows:

$$N_6(t)=\frac{N_5^0\sigma_{5,6m}\phi}{\lambda_6-(\sigma_{5,6m}+\sigma_{5,6}-\sigma_6)\phi}\left[e^{-(\sigma_{5,6m}+\sigma_{5,6})\phi t}-e^{-(\lambda_6+\sigma_6\phi)t}\right] \tag{7}$$

Where:
λ_6 = decay constant of ^{166}Ho;
σ_6 = cross section for ^{166}Ho(n,γ)^{167}Ho reaction.

Analyzing the production of ^{167}Ho from ^{166}Ho and ^{166m}Ho.

$$\frac{dN_7}{dt}=N_{6m}\sigma_{6m}\phi+N_6\sigma_6\phi-\lambda_7N_7-N_7\sigma_7\phi \tag{8}$$

Where:
λ_7 = decay constant of ^{167}Ho;
σ_7 = sum of cross sections for ^{167}Ho(n,γ)^{168}Ho and ^{167}Ho(n,γ)^{168m}Ho reactions.

The first term refers to the activation of ^{166m}Ho, the second refers to the activation of ^{166}Ho, the third refers to the radioactive decay of ^{167}Ho and the fourth refers to the activation of ^{167}Ho.

Analogously to what has already been presented and replacing the values of N_{6m} and N_6 according to equations (6) and (7), we have:

$$\begin{aligned}N_7(t)={}&\frac{N_5^0\sigma_{5,6}\sigma_6\phi^2}{\lambda_6-\left(\sigma_{5,6m}+\sigma_{5,6}-\sigma_6\right)\phi}\left[\frac{e^{-\left(\sigma_{5,6m}\phi+\sigma_{5,6}\phi\right)t}-e^{-\left(\lambda_7+\sigma_7\phi\right)t}}{\lambda_7-\left(\sigma_{5,6m}+\sigma_{5,6}-\sigma_7\right)\phi}+\frac{e^{-\left(\lambda_6+\sigma_6\phi\right)t}-e^{-\left(\lambda_7+\sigma_7\phi\right)t}}{\lambda_6-\lambda_7+\left(\sigma_6-\sigma_7\right)\phi}\right]+\\&+\frac{N_5^0\sigma_{5,6m}\sigma_{6m}\phi^2}{\lambda_{6m}-\left(\sigma_{5,6m}+\sigma_{5,6}-\sigma_{6m}\right)\phi}\left[\frac{e^{-\left(\sigma_{5,6m}\phi+\sigma_{5,6}\phi\right)t}-e^{-\left(\lambda_7+\sigma_7\phi\right)t}}{\lambda_7-\left(\sigma_{5,6m}+\sigma_{5,6}-\sigma_7\right)\phi}+\frac{e^{-\left(\lambda_{6m}+\sigma_{6m}\phi\right)t}-e^{-\left(\lambda_7+\sigma_7\phi\right)t}}{\lambda_{6m}-\lambda_7+\left(\sigma_{6m}-\sigma_7\right)\phi}\right]+\\&+N_{6m}^0\sigma_{6m}\phi\left[-\frac{e^{-\left(\lambda_{6m}+\sigma_{6m}\phi\right)t}-e^{-\left(\lambda_7+\sigma_7\phi\right)t}}{\lambda_{6m}+\sigma_{6m}\phi-\lambda_7-\sigma_7\phi}\right]\end{aligned} \tag{9}$$

Since the induced activity of ^{167}Ho is given by,

$$A_7(t)=A_7^{5,6}(t)+A_7^{5,6m}(t)+A_7^{6m}(t) \tag{10}$$

The terms in equation (10) are the activities of ^{167}Ho from ^{165}Ho(n,γ)^{166}Ho(n,γ)^{167}Ho, ^{165}Ho(n,γ)^{166m}Ho(n,γ)^{167}Ho and ^{166m}Ho(n,γ)^{167}Ho reactions, respectively.

Multiplying the equation (9) by λ_7 we get $A_7(t)$, so the following equations were determined:

$$A_7^{5,6}(t)=\frac{\lambda_7 N_5^0\sigma_{5,6}\sigma_6\phi^2}{\lambda_6-(\sigma_{5,6m}+\sigma_{5,6}-\sigma_6)\phi}\left[\frac{e^{-(\sigma_{5,6m}\phi+\sigma_{5,6}\phi)t}-e^{-(\lambda_7+\sigma_7\phi)t}}{\lambda_7-(\sigma_{5,6m}+\sigma_{5,6}-\sigma_7)\phi}+\frac{e^{-(\lambda_6+\sigma_6\phi)t}-e^{-(\lambda_7+\sigma_7\phi)t}}{\lambda_6-\lambda_7+(\sigma_6-\sigma_7)\phi}\right] \tag{11}$$

$$A_7^{5,6m}(t)=\frac{\lambda_7 N_5^0\sigma_{5,6m}\sigma_{6m}\phi^2}{\lambda_{6m}-(\sigma_{5,6m}+\sigma_{5,6}-\sigma_{6m})\phi}\left[\frac{e^{-(\sigma_{5,6m}\phi+\sigma_{5,6}\phi)t}-e^{-(\lambda_7+\sigma_7\phi)t}}{\lambda_7-(\sigma_{5,6m}+\sigma_{5,6}-\sigma_7)\phi}+\frac{e^{-(\lambda_{6m}+\sigma_{6m}\phi)t}-e^{-(\lambda_7+\sigma_7\phi)t}}{\lambda_{6m}-\lambda_7+(\sigma_{6m}-\sigma_7)\phi}\right] \tag{12}$$

$$A_7^{6m}(t)=\lambda_7 N_{6m}^0\sigma_{6m}\phi\left[-\frac{e^{-(\lambda_{6m}+\sigma_{6m}\phi)t}-e^{-(\lambda_7+\sigma_7\phi)t}}{\lambda_{6m}+\sigma_{6m}\phi-\lambda_7-\sigma_7\phi}\right] \tag{13}$$

3. **Results**

Figure 2 shows the activity (in Bq) of ^{167}Ho as a function of irradiation time, considering samples with 10 mg from a solution with 20 MBq/g of ^{166m}Ho and 0.31 g/ml of $HoCl_3$ in 1N HCl[3]. As can be seen, the predominant contribution comes from the ^{166m}Ho(n,γ)^{167}Ho reaction.

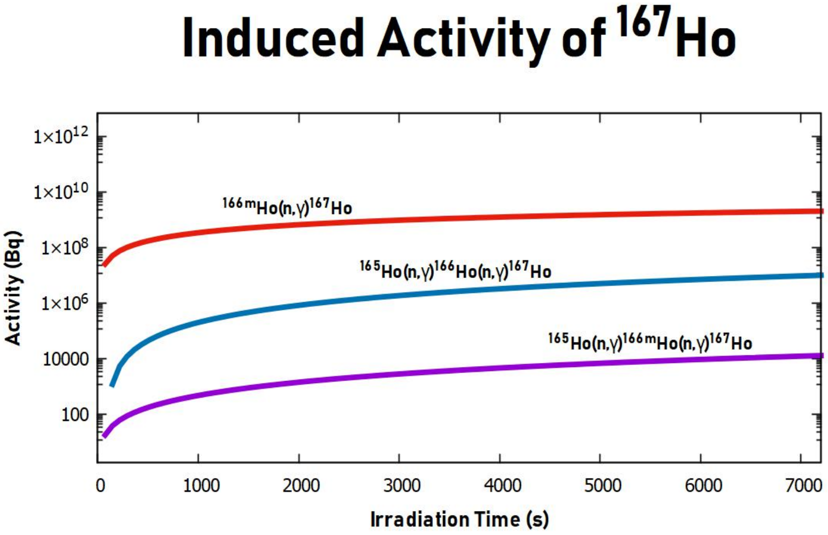

Figure 2. Induced Activity of ^{167}Ho as a function of irradiation time.

Acknowledgments

The authors are indebted to the National Counsel of Technological and Scientific Development (CNPq), from Brazil, for partial support of the present research work.

References

[1] International Atomic Energy Agency IAEA (2018) The Live Chart of Nuclides. https://www-nds.iaea.org/relnsd/vcharthtml/VChartHTML.html

[2] Harada H, Wada H, Nakamura S , Furutaka K and Katoh T (2000) “Measurement of Effective Neutron Capture Cross Section of ^{166m}Ho using Two Step Irradiation Technique”, Journal of Nuclear Science and Technology, 37:9, 821-823.

[3] Hino, Matui, Yamada, Takeuchi S, Onoma, Iwamoto and Kogure. “Absolute measurement of ^{166m}Ho radioactivity and development of sealed sources for standardization of gamma-ray emitting nuclides”, Applied radiation and isotopes, 52:3 (2000) 545-549.

XLI Brazilian Meeting on Nuclear Physics (RTFNB) IOP Publishing
IOP Conf. Series: Journal of Physics: Conf. Series **1291** (2019) 012025 doi:10.1088/1742-6596/1291/1/012025

Thermal neutron induced upsets in 28nm SRAM

V A P Aguiar[1], N H Medina[1], N Added[1], E L A Macchione[1], S G Alberton[1], C L Rodrigues[1], T F Silva[1], G S Zahn[2], F A Genezini[2], M Moralles[2], F Benevenuti[3] and M A Guazzelli[4]

[1] Instituto de Fisica da Universidade de Sao Paulo - Brazil
[2] Instituto de Pesquisas Energeticas e Nucleares - IPEN-CNEN/SP - Brazil
[3] Universidade Federal do Rio Grande do Sul - Brazil
[4] Centro Universitario FEI, Sao Bernardo do Campo, Brazil

E-mail: `vitor.angelo.aguiar@usp.br`

Abstract. In this work, we present the first results of static tests in a 28nm SRAM under thermal neutron irradiation from the IPEN/IEA-R1 research reactor. The SRAM used was the configuration memory of a Xilinx Zynq-7000 FPGA and the ECC frame was used to detect bit-flips. It was obtained a SEU cross-section of $9.2(21) \times 10^{-16}$ cm^2/bit, corresponding to a FIT/Mb of 12(5), in accordance with expected results. The most probable cause of SEU in this device are ^{10}B contamination on tungsten contacts.

1. Introduction

Single-event effects on eletronic devices are described as system events triggered by a single particle's charge deposition in a sensitive node of a device. This charge deposition may cause a current-pulse transient in a transistor that can lead to a bit-flip in a digital system, or even trigger a high-current state capable of destroying the device. Single-event effects are caused mainly by heavy-ions and protons [1], although there are also observations with electrons and neutrons [1, 2].

In the case of electronic components of aerospace use, embedded control devices used in avionics are exposed to a neutron spectrum from the interaction of cosmic rays with the atmosphere. This neutron spectrum is fairly intense around 10 MeV in the region of the South Atlantic Anomaly [3].

Laboratory irradiation of devices allow the study of the effects of single events (SEE) caused by neutrons, such as bit-flips in digital devices [4], or even effects of displacement damages of atoms in the crystalline lattice, which alter the electrical characteristics of the devices, like solar cells whose gain factor changes after neutron exposure. Controlled studies in each range of neutron energies provide better prediction capability of failures and optimization of embedded system designs. In recent years, the observation of single-event burnout, a destructive effect, caused by neutrons is also a concern for high-reliability applications [5]

Due to the absence of electrical charge, neutron-induced effects are result of neutron interactions with nuclei present in the medium. For neutrons with energies ranging from thermal (25 meV) up to tens of MeV, the most commom reactions are the neutron capture reactions, suceeded in most cases by gamma or beta emissions. However, in the presence of ^{10}B the $^{10}B(n,\alpha)^7Li$ reaction may take place, with cross-section values as large as 3838 barn, and which products alpha particle (1.78 MeV and 1.47 MeV[1]) and lithium recoil (about 1 MeV) are much more capable of triggering an effect [1].

For semiconductor devices, it was common the presence of insulating layers made of borophosposilicate-glass (BPSG), which contains ^{10}B in natural abundance of 19.9%, and, as its location was very close to the sensitive nodes, was a serious issue for soft errors in digital circuits. Despite the manufacturers have eliminated the presence of BPSG layers, the interconnect processing method uses B_2H_6 carrier gas, resulting in an accumulation of ^{10}B in the sidewalls of tungsten contact holes [6, 7].

In order to improve manufacturing processes and/or mitigation techniques, it is crucial to understand all the process involved in neutron soft-error generation and precise measurements of neutron SEU cross-sections.

This paper presents some of the first results of thermal neutron irradiation studies at IEA-R1 research reactor, where the thermal neutron single-event upset cross-section for 28nm SRAM was determined.

2. Experimental Procedure

Nuclear reactors are strong sources of thermal, epithermal and fast (up to 5-10 MeV) neutrons. The nuclear fission process produces fast neutrons in the few-MeV range, and the reactor moderator (usually water) reduces the neutrons' energies by means of scattering progressively until they reach thermal equilibrium with the medium (with energies around 0.025 eV). These neutrons can be then extracted from the reactor pool through *beam holes* and these neutron beams can then be filtered and/or separated from the accompanying gamma-rays by using different materials. One of the most effective ways to do so is to use crystal monochromators, where neutrons with the right energy are diffracted towards the sample.

The device under test was irradiated in the monochromatic low-energy facility installed at IEA-R1 research reactor at IPEN, where the neutron flux is $\sim 6{\times}10^4 cm^{-2}{\cdot}s^{-1}$, for approximately 7 hours. Figure 1 shows the beam exit and sample holder.

The testing was carried out in a 28 nm configuration SRAM (CRAM) of a Xilinx Zynq-7000 FPGA. An aleatory pattern of "0"s and "1"s was loaded in the CRAM and the device was configured to report bit-flips detected by the Error Correction Code instance by means of a logic signal in a digital output. A scaler was used to count the bit-flips.

3. Results and Discussion

To determine device's sensitvity, single-event upset cross-section and failures in time (FIT/Mb) were calculated. SEU cross-section is given by equation 1, were N represents the number of events observed with fluence Φ. Uncertainties are calculated assuming a Poisson distribution for single-event upsets. Failures-in-time represents the expected number of events recorded for one billion device-hours of operation, per megabit, and it is expressed in terms of cross-section as in equation 2, where ϕ is the neutron flux ($[n/s/cm^2]$) and N_{bits} is the total number of memory bits.

$$\sigma = \frac{N}{\Phi} \tag{1}$$

$$FIT/Mb = \frac{\sigma \times \phi \times 3.6 \times 10^{12}}{N_{bits}} \tag{2}$$

Were observed 24 bit-flips under a $\sim 10^9$ n/cm^2 fluence, resulting in a SEU cross-section of 9.2(21) $\times$ 10^{-16} cm^2/bit and FIT/Mb of 12(5), in accordance with the expected order of magnitude, although somewhat below the reported value of 29(3) FIT/Mb [8].

---

[1] Corresponding to lithium recoil in ground and excited states, respectively.

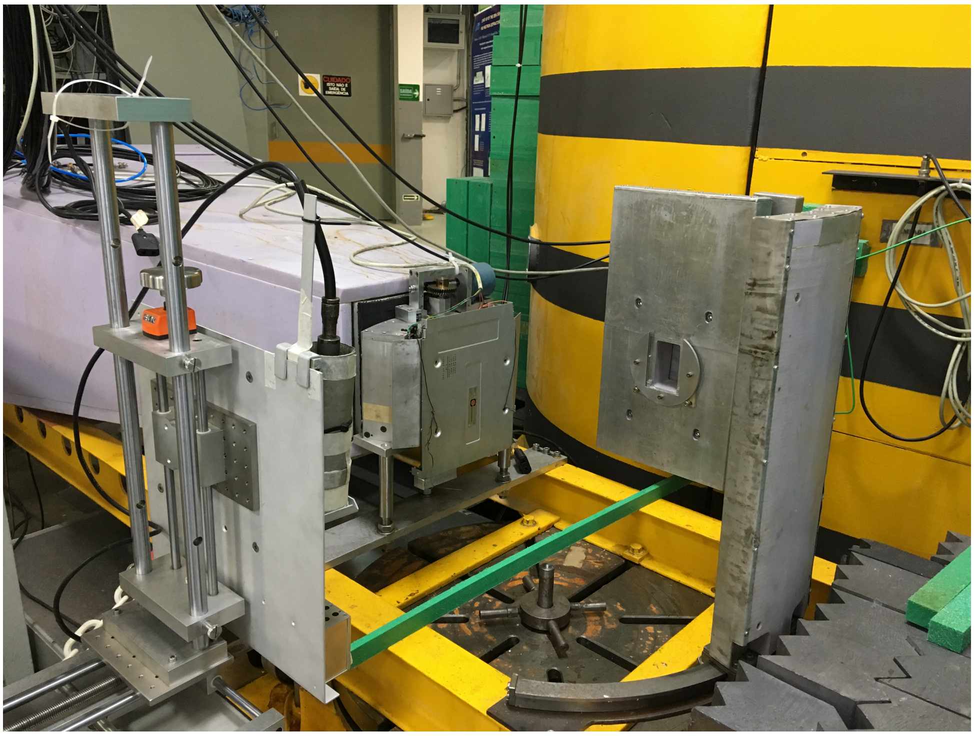

Figure 1. Thermal neutron irradiation setup

In order to determine the boron content present in the sample, Rutherford Back-Scattering and Nuclear Reaction Analysis were performed at LAMFI-USP, with alpha and proton beams at several energies. For NRA, proton energies from 2.0 to 3.2 MeV and detection angle of 170^o, and the reaction considered was $^{11}B(p,\alpha)^8Be$[2] The data were analyzed using MultiSIMNRA software [9], and the boron content was below the detection limit of the setup, estimated in about $10^{17}\ atoms/cm^2$. The complex structure of the device also has influenced on the analysis. The absence of detectable amount of boron together with information on manufacturing processes leads to the conclusion that contaminant boron in tungsten contacts is responsible for the SEU observed, in accordance to ref. [6], which also states that such boron content should be detectable only by secondary-ion-mass-spectrometry (SIMS) technique. Dopping boron concentration should not be an issue in modern devices [1]. Further analysis are being conducted.

4. Conclusions

In this work we measured the thermal neutron upset cross section for a 28nm SRAM using the ECC frame of a Zynq-7000 SRAM FPGA and thermal neutrons from a setup installed in IPEN/IEA-R1 research reactor. The results obtained were a SEU cross-section of $9.2(21) \times 10^{-16}\ cm^2/bit$ and FIT/Mb of 12(5). More studies should be made to determine the composition of the FPGA and the upset cross-section for different voltage/neutron energy configurations.

Acknowledgments

Authors would like to thank CNEN for financial support.

---

[2] ^8Be is an unbound nucleus and decays in two alfa particles, but only the alfa particle from the reaction (p,α) has a defined energy from reaction Q-value and kinematics - around 6.0 MeV for the experimental condition.

References

[1] Baumann R C 2005 *IEEE Transactions on Device and Materials Reliability* **5** 305–316
[2] Barak J, Murat M and Akkerman A 2012 *Nuclear Instruments and Methods in Physics Research B* **287** 113–119
[3] Federico C, Goncalez O, Fonseca E, Martin I and Caldas L 2010 *Radiation measurements* **45** 1526–1528
[4] Sierawski B D, Warren K M, Reed R A, Weller R A, Mendenhall M M, Schrimpf R D, Baumann R C and Zhu V 2010 *Reliability Physics Symposium* (IEEE International)
[5] Shoji T, Nishida S, Hamada K and Tadano H 2015 *IEEE Transactions on Power Electronics* **30** 2474–2480
[6] Fang Y P and Oates A 2014 *IEEE Transactions on Device and Materials Reliability* **14** 583–586
[7] Gasiot G, Soussan D, Autran J L, Malherbe V and Roche P 2015 *Reliability Physics Symposium* (IEEE International)
[8] Xilinx 2018 Device reliability report Tech. rep. Xilinx Inc.
[9] Silva T, Rodrigues C, Mayer M, Moro M, Trindade G, Aguirre F, Added N, Rizzutto M and Tabacniks M 2016 *Nuclear Instruments and Methods in Physics Research B* **371** 86–89

IOP Conf. Series: Journal of Physics: Conf. Series **1291** (2019) 012026 doi:10.1088/1742-6596/1291/1/012026

Investigation of ions in human whole saliva by analytic techniques

V M Miura[1], C B Zamboni[1], O G Tasso[1], H R Lewgoy[1], K A Jesus[2] and R Y R Silva[3]

[1] Centro do Reator de Pesquisa – CRPq, Instituto de Pesquisas Energéticas e Nucleares, IPEN – CNEN/SP, São Paulo-SP, 05508000, Brazil.
[2] Faculdade de Odontologia da Universidade de São Paulo, São Paulo-SP, 05508000, Brazil
[3] Universidade de São Paulo, Hospital Universitário, HU-USP, São Paulo-SP, 05508000, Brazil

E-mail: vivi_takamiura@hotmail.com, czamboni@ipen.br

Abstract. In this study, ions of clinical relevance in non-stimulated human whole saliva obtained from healthy subject's donors (adults and children) at São Paulo city (Brazil), were investigated. The Instrument Neutron Activation Analysis (INAA) and Energy Dispersive X-Ray Fluorescence (EDXRF) techniques were used. The comparison concentration between adults and children for Cl, K, Ca and Fe showed significant differences for all elements, emphasizing the need of adopting different reference values.

1. Introduction

Saliva is a body fluid comprising 95 % of water and 0.5 % of ions and molecules. This fluid has multiple functions, such as antibacterial, antiviral and antifungal action. It also performs the control of the quantity of water of the organism, the maintenance of the acidity of the mouth (which prevents tooth decay), the maintenance of the balance that regulates the excretion of body fluids, as well secretes hormones that play an important role in the development of the palate. In the past years, the use of saliva as a diagnostic fluid has presented significant progress in clinical testing of several diseases [1-3]. The main advantage of using saliva as a diagnostic tool is that the biomarkers present in serum and urine are also found in saliva. In addition, it is easy and quick to collect (non-invasive procedure).

The salivary secretion occurs into the salivary glands (in a flow around 1.5 ml/min) from parotid (~50 %), submandibular (~ 35 %), sublingual (7 – 8 %) and from several smaller glands (< 7 %). The whole saliva is the mixture of these glandular secretions and other components (such as bacteria and epithelial cells) and its collection can be done using stimulating agents or without stimulation. The availability of accurate reference values for inorganic elements in human whole saliva represents an important indicator of the health status. Nowadays, the evaluation of ions in saliva can identify drug intake, cardiovascular dysfunctions and problems in the thyroid gland [1,2]. Studies with the Brazilian population (adults) have already been performed using Neutron Activation Analysis (NAA) and X-Ray Fluorescence (XRF) techniques generating promising results for the diagnosis of oral diseases [4-6]. Now we intend to investigate saliva obtained from adults and children. In this study, non-stimulated human whole saliva obtained from healthy subject's donors (adults and children) at São Paulo city (Brazil), was investigated. The Instrument Neutron Activation Analysis (INAA) and Energy Dispersive X-Ray Fluorescence (EDXRF) techniques were used. The elements Cl, K, Ca and Fe were selected because they can be used as biomarkers: Ca is used as a parameter to determine the susceptibility of dental caries; Cl, Ca and Fe, increase the resistance of enamel to caries; K and Cl are responsible for maintaining the osmolarity and Fe can be a predictive marker of iron deficiency [5,7-9].

2. Experimental Procedure

SAMPLE PREPARATION**:** saliva obtained from donors, adults (18 – 60 y) and children (2 – 17 y) at São Paulo city (Brazil). Adults (20 samples): ~ 2 mL were collected in dental office by a dentist directly in sterilized plastic containers. For children (15 samples): ~ 1 mL was collected in pediatric hospital (HU - USP). The samples were lyophilized. Considering that the INAA and EDXRF procedures are non destructive, the same sample was used for both analyses.

INAA: Samples of adults and standard solution (Cl, K, Ca and Fe) were irradiated at IEA-R1 (4.5 MW, pool type) nuclear reactor at IPEN in a thermal neutron flux, for minutes to hours, and gamma counting using HPGe (GEM-60195) detector connected to a MCA ORTEC -919E.

EDXRF: Samples (adults and children) were excited and measured using a portable X-Ray Spectrometer: Ag X-Ray target and Si Drift detector (25 mm^2 x 500 µm / 12.5 µm Be window) and counting time of 300 s measured with 30 kV and 5 µA. The spectrometer was calibrated for Cl, K, Ca and Fe using linear regression method for concentration up to 500 ppm.

3. Results and Discussion

The elements concentrations determined in non-stimulated whole saliva samples are presented in Table 1 (adults) and Table 2 (children). The results were expressed by: Mean Value (MV), Standard Deviation (± 1 SD), Minimum (min) and Maximum (max). Figure 1 was elaborated to show the comparison between whole saliva samples of adults and children. The data was subjected to a statistical analyses by the students *t-test.*

Table 1. Elements concentration in adults non- stimulated whole saliva

Elements mg/kg	MV	± SD	Min	Max
Cl				
EDXRF	776	299	350	1332
INAA	620	168	290	1030
K				
EDXRF	817	278	406	1417
INAA	612	90	299	702
Ca				
EDXRF	131	62	54	247
INAA	112	34	64	224
Fe				
EDXRF	151	47	77	286
INAA	193	81	49	201

Table 2. Elements concentration in children non-stimulated whole saliva by EDXRF

Elements, mg/kg	MV	±1SD	Min	Max
Cl	497	303	62	941
K	495	284	91	944
Ca	57	41	17	138
Fe	85	32	42	153

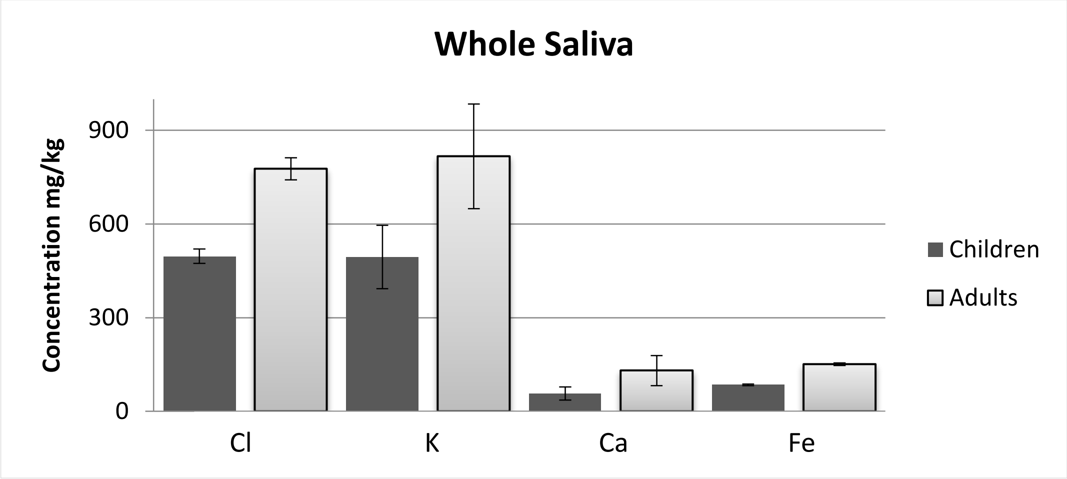

Figure 1. Comparison between the inorganic elements, in whole saliva samples of adults and children

According to the Student's *t-test* the comparison between the INAA and EDXRF techniques (Table 1) showed the discrepancy of results to be insignificant at 95 % confidence level for all element while the comparison concentration between adults and children (Table 2) emphases statistically differences ($p<0.05$) for all elements. However, more large-scale studies are needed to establish the normal range for these elements in saliva aiming its application in biochemistry tests.

Through these investigations, we also found that portable XRF spectrometer is suitable for the rapid and highly sensitive analysis of saliva.

4. Conclusion

The reference values presented in this study emphasizing the need of adopting different recommendations of specifics ions (Ca, Cl, Fe and K) in whole saliva for adults and children.

5. Acknowledgments

Financial support: FAPESP and CNPq

References

[1] Kaufman E and Lamster I B 2002 *Crit Rev Oral Biol Med* 13 197.
[2] Pfaffe T, Cooper-White J, Beyerlein P, Kostner K and Punyadeera C 2011 *Clin Chem* 57 675. doi:10.1373/clinchem.2010.153767.
[3] Lima D P, Correia A S C, Anjos A L and d Boer N P 2014 *Revista Odontológica de Araçatuba* 35 55.
[4] De Medeiros J, Zamboni C, Kovacs L and Lewgoy H 2015 *In* Journal of Physics: Conference Series *IOP Publishing*, p. 012006.
[5] Lewgoy H R, Zamboni C B, Metairon S, Medeiros I M and de Medeiros J A 2013 *Journal of Radioanalytical and Nuclear Chemistry* **296** 573.
[6] Poles Jr A A, Balcão V M, Chaud M V, Vila M M, Aranha N, Yoshida V M and Oliveira Jr J M 2016 *Applied Radiation and Isotopes* **118** 221.
[7] Costa E M, Azevedo J A, Martins R F, Rodrigues V P, Alves C M and Ribeiro C C Thomaz E B 2017 *Rev Bras Ginecol Obstet* **39** 94. doi:10.1055/s-0037-1599217.
[8] Jagannathan N Thiruvengadam C Ramani P Premkumar P Natesan A Sherlin H J 2012 *J Clin Pediatr Dent* **37** 25.
[9] Ghathwan K H, Abd S T, Jwad S K and Saadi A H A 2016 *Int. J. Adv. Res. Biol. Sci* **3** 18.

XLI Brazilian Meeting on Nuclear Physics (RTFNB) IOP Publishing
IOP Conf. Series: Journal of Physics: Conf. Series **1291** (2019) 012027 doi:10.1088/1742-6596/1291/1/012027

The influence of superfluid core cooling in the braking index of Pulsars.

C Frajuca[1,], F S Bortoli[1], G A Santos[1], F Y Nakamoto[1] and M A Souza[1]
[1] Sao Paulo Federal Institute – Sao Paulo, SP, Brazil

E-mail: Frajuca@gmail.com

Abstract: Pulsars are stars from which electromagnetic radiation is observed to pulsate in well-defined time intervals as the star rotates and the emission of eletromagnetic signal is located in a place different from the rotation center. The frequencies of the pulses decay with time, quantified by the braking index (n). In the canonical model n = 3, in general, for all pulsars, but observational data shows that n is lower than 3. In this work a new model is presented, based on a modification of the canonical one incorporating the influence of neutron and proton density that appear in the superfluid core and, as the star cools down, the density of the superfluid core increases making the star to shrink with time and temperature, making the inertia moment to decrease. The difference ot this model from the canonical one is that the star moment of inertia decreases with time (what would accelerate the rotation of the star) what makes the star to not slow down as fast as it should without this process.

1. Introduction

The Graviton Group is a researgh Brazilian group dedicated to the study of Gravitational Waves, Neutron Stars is a candidate source of Gravitational Waves, that is the reason the group is devoted in the study of Pulsars. The detection of gravitational waves came after a long road of experiments planned in 2010 [1], in 2016 finally the detection was made [2,3]. A very strong evidence of the existence of Gravitational Waves appeared in the **PSR B1913+16** (also known as **PSR J1915+1606**, **PSR 1913+16**, and the **Hulse–Taylor binary** named after its discoverers) is a pulsar (a radiating neutron star) binary system. PSR 1913+16 was the first binary pulsar to be discovered and its orbital period is decreasing with time due the emission of gravitational waves [4]. The first attempts to gravitational wave detection starts in the early sixties [5] with the resonant mass gravitational wave detection [6,7,8,9].

The Brazilian efforts towards the detection of gravitational waves are centered on the Schenberg detector. In the Schenberg detector six sensors are connected to the surface of the sphere, arranged according to the distribution of Merkowitz and Johnson [10,11]. These transducers are located as if they were in the center of 6 pentagons connected in a surface corresponding to half dodecahedron. Each transducer amplifies the motion occurring on the region of the sphere in which it is connected. The already amplified movement excites the membrane of one resonant cavity. In this resonant cavity microwaves are pumped, which generate the electronic signal that will return taking all the information of the OG's. Intensity and direction of the OGs can be obtained from the analysis of the output signal of these 6 transducers [12,13,14].

To reach the resonant cavities, first the microwaves are conducted from the outside of the dewar (thermo flask where every antenna system is contained) by cabling to microstrip antennas. These antennas, located in front of the parametric transducers, conduct the microwaves into the resonant cavity and another set of antennas pick up the returned signal. The Brazilian efforts on the field can be summarized in [15-26]. Much of this work is made using Finite Element Modellind (FEM) [27,28].

2. The neutrons stars

Pulsars are astrophysical objects normally modeled as neutron stars originated from the collapse of a progenitor star [29]. In a model, which we will refer as the canonical one, pulsars are described by spherical rotating magnetized dipoles, usually with the magnetic axis misaligned relatively to the rotation axis. This misalignment would be responsible for the observation of radiation emitted in well-defined time intervals in a certain direction, which is the typical observational characteristic of this kind of star.

Observation shows that the rotation frequency of pulsars is slowly decaying with time, implying a gradual decrease of the angular velocity, according to the canonical model [30]. Such decay can be quantified by a dimensionless parameter known as the braking index, n. The canonical model predicts that this index has only one value for all pulsars, equal to 3. However, observational data shows that actual braking indices are different from 3, indicating that the canonical model requires some corrections [31, 32].

3. The modified URCA process

Murca process can work with a slight modification at lower densities from the Durca process. The modified Urca process can cool the star

$$n+N \rightarrow p+N+l+\nu_l \, , \qquad (1)$$

$$p+N+l \rightarrow n+N+\nu_l \qquad (2)$$

where N is a nucleon - a proton or a neutron, l is a lepton and ν_l is the neutrino or antineutrino of the lepton. This process, can work at much lower densities, but produces 7 orders of magnitude more emissivity than the Urca process. As a result, it's the dominant process in the superfluid core.

4. The neutron star density increases as the temperature decreases

As the neutrino emission takes place, the neutron star superfluid core cools down and its density increases This can be seen on Figure 1 [33]. If there is only this process happening, the rotation of the star should increase to keep the angular momentum constant, but there is other process happening, the one described as the canonical, then the star braking index should be less than 3.

5. The cooling down of the superfluid core

The superfluid core cools down in complex ways, but in a period 100 to 100 thousand years it cools down in a very especific way as can be seen on Figure 2, see reference [34].

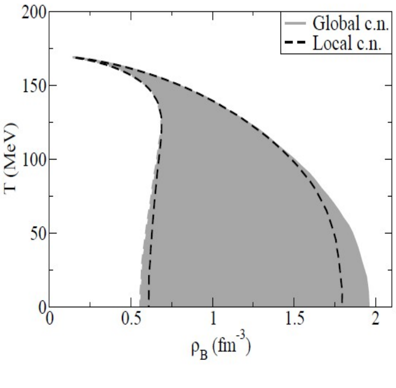

Figure 1: Temperature versus baryon density for neutron star matter assuming local and global charge neutrality. Souce [33].

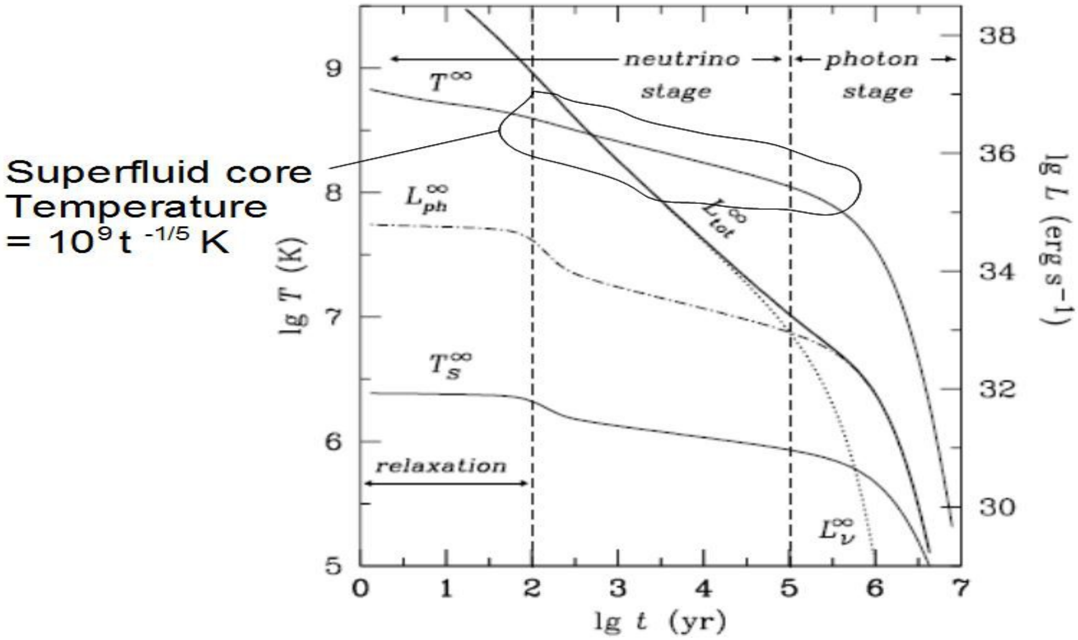

Figure 2: The region circulate on the curve shown as T $^\infty$ is the period where the star cool down, the approximated expression for the superfluid core temperature from time equal to 100 to 100,000 years is also shown. Souce [34].

6 The neutron potential

The neutron potential in the core of the neutron star can be approximated to the neutron potential in a nucleous [35], this potential can be seen on Figure 3. This potential is a non-relativistic one, as the neutron star core is relativistic, this potential is used only as an approximation. In the same figure, there is a line tangential to the curve at the temperature of 1 Billion Kelvin, what means a thermic energy of approximately 0.1 MeV, the slope of this line is 0.001 fm/MeV. What will happen to the curve if the temperature drops to 0.1 billion Kelvin? The curve will shift to the left proportional to the slope of the curve at 0.1 MeV. Then the neutron will move closer to the other neutron by 0.0001 fm. As the distance is close to one fm, the neutron will move closer to the other neutron by a factor of 10^{-4}. As the diameter of the neutron star is approximately 10 km, the neutron star will shrink by one meter in diameter.

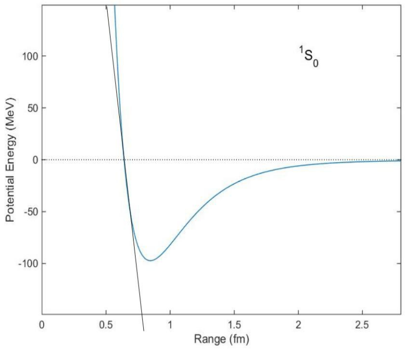

Figure 3: Neutron potential ploted against the distance from another neutron.

7 Conclusions

In the scenario presented the density of the superfluid core of the neutron star increases with time.The results presented here corroborates that the neutron star shrinks as it cools down, this makes the star to decelerate slower and, then, makes the braking index lower than 3. Neverthless the result is too small to make a difference, as this decreasing in size happens during a very long time. This also justify the use of a non relativistic potential because the difference in the bracking index is very small, it won´t justify the use of a much more complex potential to reach the same conclusion.

Acknowledgements

Carlos Frajuca acknowledges FAPESP for grant #2013/26258-4 and grant #2006/56041-3.

References

[1] The Gravitational Waves International Committee Roadmap (GWIC). A global pan. June 2010. Glasgow: Univerty of Glasgow - Department of Physics and Astronomy - Kelvin Building (G12 8QQ), 117p.
[2] Taylor J H, Hulse R A, Fowler L A, Gullahorn GE, Rankin J M 1976 *Astrophysical Journal* **206** L53
[3] Weber J 1960 *Physical Review* **117** 306
[4] Thorne K S 1987 “300 years of gravitation”. Cambridge: Cambridge University Press: 1987, p.330.
[5] Blair D G “The detection of Gravitational Waves.” 1991 Cambridge: Cambridge University Press
[6] Richard J P 1984 *Physical Review Letters* **167** 165
[7] Aguiar O D *et al.* 2006 *Journal Class. Quantum Grav.* **23**, 239
[8] Frajuca C *et al.* 2004 *Class. Quantum Grav.* **21** 1107
[9] Velloso W F, Aguiar OD and Magalhaes NS *Proc. First International Workshop for an Omnidirectional Gravitational Radiation Observatory* 1997 Singapore:World Scientific
[10] Merkowitz S M and Johnson W W 1997 *Phys. Rev. D* **56** 7513
[11] Merkowitz S M and Johnson W W 1993 P*hys. Rev. Lett.* **70**, 2367
[12] Locke C R, Tobar M E and Ivanov E N 2000 *Rev. Sci. Instrum.* **71,** 2737
[13] Ribeiro K L *et al.* 2004 *Class. Quantum Grav.* **21,** 1225
[14] Andrade L A *et al.* 2004 *Class. Quantum Grav.* **21,** 1215
[15] Aguiar O D et al. 2011 *Journal of Physics: Conference Series* **363,** 012003
[16] Aguiar O D et. al. 2005 *Class. Quantum Grav.* **22**, 209
[17] Frajuca *et al* 2002 *Class. Quantum Grav.* **19** 1961
[18] Magalhaes N S *et al.* 1997 *Astrophysical Journal* **475**, 462
[19] Magalhaes N S *et al.* 1995 *MNRAS* **274**, 670
[20] Frajuca C, Bortoli F S, Magalhaes N S 2005 *Brazilian Journal of Physics* **35** 1201
[21] Frajuca C, Bortoli F S, Magalhaes N S 2006 *Journal of Physics: Conference Series* **32** 319
[22] Aguiar O D et al. 2004 *Class. Quantum Grav.* **21** 457
[23] Frajuca C, Magalhaes N S, Bortoli, F S, Horiguti A M 2008 *Journal of Physics: Conference Series* **122** 012029
[24] Bortoli F S *et al* 2010 *Journal of Physics: Conference Series* **228** 012011.
[25] Magalhaes N S *et al* 1997 *Gen. Relat. Grav.* **29** 1511
[26] Aguiar O D *et al 2002 Brazilian Journal of Physics* **32** 866
[27] Bathe, K-J, “Finite Element Procedures”, New Jersey: Prentice Hall, 1996.
[28] Filho A A, “Elementos Finitos”, Sao Paulo: Erica, 2000
[29]Wu F, Xu R X and Gil, J *Astron. Astrophys.* **409** 641
[30]Chukwude, AE, Baiden, AA, Onuchukwu, CC 2010 *Astron. Astrophys.* **515** A21
[31]Chen, WC, Li XD 2010 *Astron. Astrophys.* **450** L1
[32]Ho, W C G, Anderson, N 2015 *Nature Phys.* **8** 787
[33]Dexheimer V, Negreiros R, Schramm S and Hempel M 2012 a*rXiv: 1208.1320v1* [astro-ph.He] 07 Aug 2012
[34]Yakolev D G et. Al 2004 *ArXiv:astro-ph/0409751v1* 30 Sep 2004
[35]Machleidt R and Slaus I 2001 *J. Phys.G* **27** R69

Neutrino emission from neutron star crusts

S V C Ramalho, G S Vicente and S B Duarte
Centro Brasileiro de Pesquisas Físicas, Rio de Janeiro, RJ, Brazil.
E-mail: `saulovcr@cbpf.br`

Abstract. Neutrino production is the dominant cooling process in neutron stars. After the rapid cooling during the protoneutron star stage, the neutron star crust is formed. Neutrinos continue to be produced in the crust, which can escape from the surface. This neutrino production is an important process to the final cooling phase of the star. They are produced in the crystalline lattice formed by nuclei permeated by an electronic gas. Quantum oscillations of the electron density with respect to the lattice of nuclei generates plasmons, which decay in a pair of neutrinos. Many works have studied the plasma of the nucleus in the star, however, without incorporating the effect of the lattice in the crust of the neutron star. The objective of this work is to include the lattice in the calculation of the plasmon decay rate using quantum field theory at finite temperature. It is not common to find studies on the crystalline lattice of the star using quantum field theory and the calculations generally used for neutrino emissivity consider a homogeneous and isotropic medium, which can not be directly applied in the context of neutron star crust.

1. Introduction

Neutron stars are the most fascinating stars in the universe. In fact, these small stars have an estimated radius of $R \simeq 10$ Km, measured masses of $M \simeq 1.5\ M_{\odot}$ and average densities of $\rho \simeq 7 \times 10^{14}\ \mathrm{g \cdot cm^{-3}}$, which is often greater than the standard nuclear density, $\rho_0 \simeq 2.8 \times 10^{14}\ \mathrm{g \cdot cm^{-3}}$. The crust is a small portion of the neutron star, approximately $0.3 - 0.5$ Km (see [2]), however, process which occur is the crust are important for the understanding of the thermal relaxation and cooling of the star. The crust has a variety of structures containing free electrons, neutrons, screened nuclei, being partially ionized atoms or fully ionized nuclei. Nuclei are structured in a crystal lattice (Coulomb crystal), permeated by an electron gas in a valence band of the coulomb crystal.

Our objective in this work is to include the effects of the lattice on the plasmon decay in a pair of neutrino and antineutrino. There are some papers and books [1] with calculations in the case of a free electron plasma. However, the presence of the crystalline lattice in the plasma may change the plasmon decay rate due to the Coulomb interaction of this lattice, which can be introduced as an external field.

2. Methods

We observe that the highest stability structure of a one-component-plasma (OCP) crystalline lattice is reached by a body-centered cubic (bcc) or face-centered-cubic (fcc) lattice [1]. We adopt the bcc configuration for the neutron star's crust. This lattice forms a Coulomb crystal, which the ion coupling parameter has the lower limit $\Gamma > 172$ [1] and depends on temperature

T, atomic number Z and the radius of Wigner-Seitz a_i, which depends of the ion density. The ion coupling parameter reads

$$\Gamma = \frac{Z^2 e^2}{a_i k_b T}. \tag{1}$$

This calculation is based on a crystalline lattice immersed in an homogeneous and isotropic gas of electrons. However in our case the local energy density inside the cells begin to have an important influence for the neutrino pair production mechanism.

A more realistic charge distribution in the plasma should be considered in the quantum field calculation of the neutrino production in the crust. In the case of a classical and non relativistic approach, we first calculate the electric potential $V_{\text{ext}}(x,y,z)$ generated by the lattice bcc, which is given by

$$\begin{aligned} V_{\text{ext}}(x,y,z) &= \frac{Q}{4\pi\epsilon_0}\sum_{n,m,p}\left\{\frac{1}{\sqrt{(a\ n-x)^2+(a\ m-y)^2+(a\ p-z)^2}}+\right. \\ &+ \left.\frac{1}{\sqrt{\left[a\left(n-\frac{1}{2}\right)-x\right]^2+\left[a\left(m-\frac{1}{2}\right)-y\right]^2+\left[a\left(p-\frac{1}{2}\right)-z\right]^2}}\right\}\Theta(r-R). \end{aligned} \tag{2}$$

Performing the Fourier transform of $V_{\text{ext}}(r)$ and considering non-stationary oscillations in this lattice we have

$$V_{\text{ext}}(r,t) = \sum_q V(q)e^{i(q.r-\omega t)}, \tag{3}$$

where ω is the optical longitudinal vibration [6] originating in the instantaneous displacement of the bcc lattice. At the high frequency limit of lattice vibrations, the ions are unable to keep pace with rapid field variations, so they remain virtually stationary.

We use the Lindhard-Mermin response function for a degenerate gas in which the ions are fully ionized, where the limit $\tau \to \infty$ gives the non-degenerate case of Lindhard dielectric function. For well-defined elementary excitations in the collisionless limit, $\omega\tau \gg 1$, when the lifetime of these excitations is long compared to the period of oscillations. we write the dielectric function $\epsilon(q,\omega)$ in the Lindhard-Mermin:

$$\epsilon(q,\omega) = 1 + \left(\frac{4\pi e^2}{q^2}\right)\frac{\delta n(q,\omega)}{U_{\text{sc}}(q)}, \tag{4}$$

where

$$\delta n(q,\omega) = \frac{B(q,\omega+i/\tau)U_{\text{sc}}(q)}{1-\frac{1}{(1-i\omega\tau)}\left(1-\frac{B(q,\omega+i/\tau)}{B(q,0)}\right)}. \tag{5}$$

The dielectric function in this case is used to generate the screening potential (6) and find the plasma frequency ω_{pl}, where the frequency depends on an effective electron mass of $m_e(r)$. When we work with a free electron plasma we can calculate the effective mass using $m_e^* = m_e\gamma_r$. However, in this case where at each position of the cell we have spatial dependent induced potentials $V_{\text{ind}}(r)$, which leads us to a mass dependent on the position in the cell. This method of calculating the effective mass can be done via [5]. The induced and screening potentials depends on the external potential and the dielectric function of gas, which are given as, respectively,

$$V_{\text{sc}}(q,\omega) = \frac{V_{\text{ext}}(q,\omega)}{\epsilon(q,\omega)}, \tag{6}$$

and

$$V_{\text{ind}}(r,t) = V_{\text{sc}}(r,t) - V_{\text{ext}}(r,t). \tag{7}$$

Writting the dielectric function by Lindhard's theory, we can find the plasmon dispersion relation to the quantum and non-relativistic case. From the dispersion relation we can calculate the decay rate of plasmons in pairs of neutrinos and antineutrinos. Using the linear response theory of quantum field theory at finite temperature, we can obtain how an electric field modifies an electron gas and write the periodic electrical potential generated by the crystalline lattice immersed in an electron gas. In this lattice configuration it is possible to observe phenomena such as Friedel's oscillations, which can also be seen in quantum mechanics, generating a non-homogeneity in the density of electrons on this surface from neutron stars.

The electric potential of the lattice enters as an external source to influence the Dirac fields of the electrons in that plasma, thus modifying the Dirac equation of motion. The linear response can be written as

$$\delta\langle A_\mu(x_i,t)\rangle = i\int_{t_0}^{t} dt\; Tr\left\{\hat{\rho}[H_{\text{ext}}(t), A_\mu(x,t)]\right\}. \tag{8}$$

The dispersion relation of collective excitations is necessary for calculating the decay rate. To find the dispersion relation it is necessary to obtain the field response (see [3]) that in this work is given by

$$\delta\langle A_\mu(x_i,t)\rangle = \int dt \int d^3x_i'\; \partial_\alpha F^{\alpha\nu}_{\text{ext}} D^R_{\nu\mu}, \tag{9}$$

where $\delta\langle A_\mu(x_i,t)\rangle$ describes the field response and the dispersion relation can be derived from this equation. The matrix $F^{\alpha\mu}_{ext}$ represents the external field generated from the lattice acting on the plasma of electrons and $D^R_{\nu\mu}$ is the real propagator of the photons, which reads

$$D_{\nu\mu} = \frac{1}{G-k^2}P_T^{\nu\mu} + \frac{1}{F-k^2}P_L^{\nu\mu} + \frac{\rho}{k^2}\frac{k_\nu k_\mu}{k^2}, \tag{10}$$

where P_T transverse projector and the P_L longitudinal projector. The oscillations of the charged particles produce quasi-particles with two modes of transverse oscillations and one longitudinal mode. Transverse oscillation modes are called phonons, which are quasi-acoustic vibration particles and the longitudinal modes are called plasmons, which are the quasi-particles representing the quantum of density of the charge oscillation in that medium. As is well known in the literature, such plasmons may decay into neutrinos. There is an important quantity to be calculated which is the emissivity, whose flux represents the energy density loss by the star at a given time. Emissivity can be calculated by making use of the polarization tensor $\Pi_{\mu\nu}(K)$ (see [4]) for which we can obtain the decay rate and thus write the emissivity Q:

$$Q = \sum_\nu \int \frac{d^3k}{(2\pi)^3}[2n_B(\omega_t(k))\omega_t(k)\Gamma_t(k) + n_B(\omega_l(k))\omega_l(k)\Gamma_l(k)] \tag{11}$$

in equation above Γ represent this case decay rate and n_B the Bose-Einstein distribution.

3. Results to be obtained

The determination of neutrino pair production to the neutrino luminosity of the crust is still in progress and as a first step we determine the electric field configuration inside a lattice cell. The energy density and the electron screening of the ions in the lattice is also determined. Friedel oscillations of electron density are considered and will have an important effect on the energy density inside the lattice cell.

Some developments of this work may be useful for future works with thermal relaxation of the neutron star crust, and applications in cores of white dwarfs, superconductivity in the crystalline lattice of their crusts.

Acknowledgments

Acknowledgment to financial support of CAPES and CBPF.

References

[1] Haensel P, Potekhin A Y and Yakovlev D G 2007 *Neutron Stars. 1. Equation of State and Structure* (Springer,New York)
[2] Yakovlev D G, Kaminker A D , Gnedin O Y and Haensel P 2001 *Phys. Rep.* **354** 1-115
[3] Kapusta J I and Gale C 2006 *Finite-Temperature-Field Theory Principles and Applications.*(Cambridge, New York)
[4] Braatem E and Segel D 1993 *Phys. Rev.* D **48** 1478-91
[5] Frahn W E and Lemmer R H 1957 *Nuo. Cim.* **5** 1564-72
[6] Slyom J 2007 *Fundamentals of the physics of solid. 1. Estructure and Dynamics* (Springer, Berlin)

XLI Brazilian Meeting on Nuclear Physics (RTFNB) IOP Publishing
IOP Conf. Series: Journal of Physics: Conf. Series **1291** (2019) 012029 doi:10.1088/1742-6596/1291/1/012029

Elastic scattering and total reaction cross sections for the ^{12}B+^{58}Ni system

E O N Zevallos[1], **V Guimarães**[1], **E N Cardozo**[2], **J Lubian**[2], **O C B Santos**[1] , **R Linares**[2], **M Assunção**[3], **J Alcantara-Núnez**[1], **A L de Lara**[1], **R Lichtenthaler Filho**[1], **K C C Pires**[1], **U Umbelino**[1], **S Appannababu**[1], **N Added**[1] , **D S Monteiro**[4,5], **V Morcelle**[6]

[1] Instituto de Física, Universidade de So Paulo, São Paulo, SP, Brazil
[2] Departamento de Física, Universidade Federal Fluminense, Niterói, RJ, Brazil
[3] Departamento de Física, Universidade Federal de São Paulo, Diadema, SP, Brazil
[4] Universidade da Integração Latino-Americana, UNILA, Foz do Iguaçu, PR, Brazil
[5] University of Notre Dame, Notre Dame, IN, USA
[6] Departamento de Física, Universidade Federal Rural do Rio de Janeiro, RJ, Brazil

E-mail: `valdir.guimaraes@usp.br`

Abstract. Angular distributions for elastic scattering of radioactive ^{12}B projectile on ^{58}Ni target have been measured for the first time. They were obtained at two energies, $\mathrm{E_{Lab}}$ = 30.0 and 33.0 MeV, close to the Coulomb barrier. These angular distributions were analyzed with the conventional optical model using Woods-Saxon shape and double-folding São Paulo potentials. The total reaction cross sections were extracted from this analysis and compared with other similar masses systems.

1. Introduction

The structure of stable nuclei has been extensively investigated through direct reactions. However, nowadays, a great interest has been devoted to the study of properties of light proton and neutron rich nuclei away from the stability valley. Some of these radioactive nuclei can be called exotic due to their anomalous structures. Nuclei such as ^{6}He, ^{8}B, ^{11}Li, ^{11}Be, and ^{15}C can exhibit large radial extension, as compared to the stable ones, in which the valence nucleons extend outside the binding potential, forming a halo structure [1]. Elastic scattering measurements at low energy are very useful tool to investigate the static effects (nuclear structure) of the nuclei involved and dynamic effects (coupling of reactions channels) in the collisions [2, 3]. In the recent past years, several experiments have been dedicated to the investigation of elastic scattering induced by these light radioactive nuclei [2, 4]. The elastic scattering of the proton-rich exotic nucleus ^{8}B on ^{58}Ni has been investigated and, from optical model analysis and continuum discretized coupled channels calculations, the halo structure for this weakly-bound nucleus (S_p=0.138 MeV) has been established [5, 6]. Recently, elastic scattering of the two stable and tightly-bound boron isotopes, ^{10,11}B, has also been investigated with interesting results in terms of deformation and spin-orbit effects [7, 8]. To complete the study on the boron isotope chain we investigate the elastic scattering of the neutron-rich ^{12}B on the same ^{58}Ni target. The ^{12}B nucleus is radioactive, with ground-state spin $J^{\pi} = 1^{+}$ and it has a small ground-state deformation of $Q = 1.321$ fm^2. This nucleus has a predominant configuration given by a ^{11}B+n, with separation energy of S_n=3.370 MeV. Due to this separation energy one can say this nucleus is in the border to be considered weakly or tightly bound nucleus. For weakly bound nuclei, the breakup channel may strongly complete with the elastic scattering and coupled-channel analysis would be required to describe the cross sections. For stable and tightly bound nuclei the optical model analysis of the elastic scattering angular distribution can be useful to extract some information such as radius and deformations. The optical model approach with Woods-Saxon (WS) and double-folding São Paulo potentials (SPP) were used to analyze the measured angular distributions.

2. The experiment

Angular distributions for the ^{12}B+^{58}Ni elastic scattering were measured for the first time at energies close to the Coulomb barrier, E_{Lab} = 30.0 and 33.0 MeV. These measurements were performed at Pelletron Laboratory of the University of So Paulo, Brazil. The ^{12}B secondary radioactive beam was produced with the ^{9}Be(^{11}B,^{12}B) transfer reaction in the RIBRAS facility [9]. The ^{9}Be production target and the ^{58}Ni reaction target had 14 μm and 2.1 mg/cm^2 of thickness, respectively. The ^{11}B primary beam had an intensity of about 300 nAe. The produced ^{12}B secondary radioactive beam was focused by the first solenoid of the RIBRAS in the ^{58}Ni target, which was mounted in the scattering chamber and had an average intensity of 2×10^5 pps. Runs with gold target, 4.6 mg/cm^2 thick, were also performed for the overall normalization purpose since, at these energies, the elastic scattering on gold target is purely Rutherford. The detection system consisted of two $\Delta E - E$ telescopes with silicon planar detectors of 25 and 1000 μm in thickness, for the measurements at forward angles, and one 1000-μm thick E planar silicon detector, for measurements at backward angles. The telescopes and the single E detector had circular apertures that subtended a solid angle of about 16 msr (±4.0°). Since only one solenoid was used for this measurement, some particles other than ^{12}B, such as ^{9}Be, ^{6,7}Li, ^{4}He and others were also present in the cocktail beam. However, these particles could be separated and identified in the $\Delta E - E$ spectrum, as shown in Fig. 1.

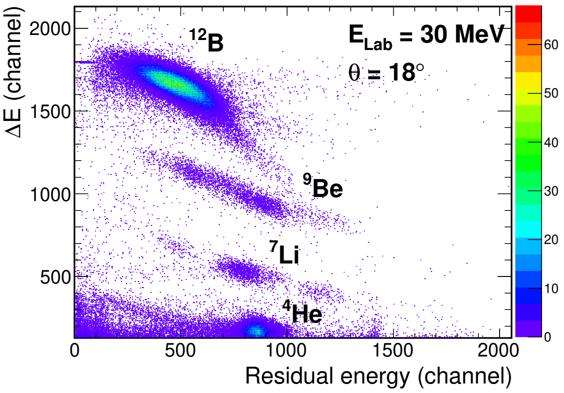

Figure 1. Typical $\Delta E - E$ energy spectrum for the ^{12}B+^{58}Ni system measured at 18° and 30.0 MeV. The scattered particles ^{12}B and the ^{9}Be, ^{7}Li and ^{4}He contaminants are indicated.

3. Analysis of the angular distributions

The measured angular distributions for the elastic scattering of ^{12}B+^{58}Ni ranged from θ_{Lab} = 18° to 65°, at 30.0 MeV, and θ_{Lab} = 26° to 68°, at 33.0 MeV. The uncertainties in the cross sections ranged from 1.5% to 12% starting from the most forward to the most backward angles. These angular distributions have been analyzed with optical model (OM). We performed optical model calculations using Woods-Saxon (WS) and double-folding São Paulo Potential (SPP) [10]. All the calculations were performed with code FRESCO [11]. The results of the OM analysis with the WS potential are shown in Figs. 2 and 3. The WS potentials were obtained by adjusting the parameters which best reproduced the elastic scattering data. The obtained parameters are listed in Table I. As can be seen in the Figs. 2 and 3 the agreement with the data is excellent, in particular at the Fresnel peak. The results of the analysis with the SPP are also show in Figs. 2 and 3. The SSP is a potential of double convolution on the nuclear densities of the projectile and target and it can then be used in association with the optical model, with $N_{\rm R}$ and $N_{\rm I}$ as the normalization for the real and imaginary part, respectively. From a large systematic, the values of $N_{\rm R}$=1.00 and $N_{\rm I}$=0.78 were adopted for nucleus with normal density (diffuseness a=0.56) [10]. By adopting these values for the normalization of the SPP we could not describe the experimental angular distributions, as can be seen in Figs. 2 and 3. By performing a searching procedure for the best values of these normalization which describe the data, we obtained: $N_{\rm R}$=0.99 and $N_{\rm I}$=0.36 for the angular distribution at 30.0 MeV and $N_{\rm R}$=0.66 and $N_{\rm I}$=0.28 for the one at 33.0 MeV. The departure from the systematic normalization is a clear indication of the influence of static and/or dynamic effects. Possible static effects could be checked by using a better value for the ^{12}B matter density, which could be obtained by measurement or detailed microscopic structure calculation. However, this is out of the scope of the present preliminary results. The dynamic effect could be investigated by the identification of the important channels, which by its turn can be obtained by a coupled-channel calculation. This coupled-channel analysis has already been performed for this system, with interesting results [12].

Table 1. Parameters for the Woods-Saxon potential used in the OM calculations.

$E_{\rm Lab}$ MeV	V_0 MeV	r_r fm	a_r fm	W_0 MeV	r_i fm	a_i fm	$\sigma_{\rm R}$ mbar
30.0	121.4	1.11	0.59	157.6	0.68	0.85	675
33.0	40.8	1.18	0.54	150.0	0.68	0.85	774

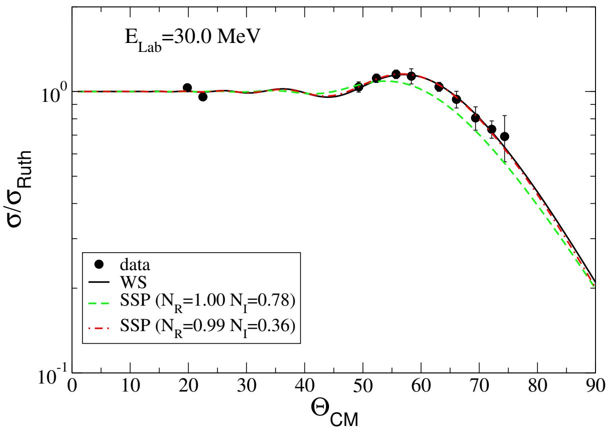

Figure 2. Angular distribution for the ^{12}B+^{58}Ni system at 30.0 MeV. The lines are the results for the optical model analysis with potentials indicated.

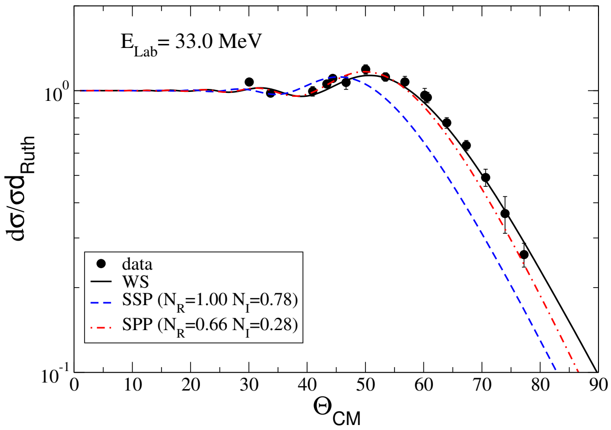

Figure 3. Angular distribution for the ^{12}B+^{58}Ni system at 33.0 MeV. The lines are the results for the optical model analysis with potentials indicated.

4. Total reaction cross section

The total reaction cross section can be extracted from the optical model analysis. These values can be used to compare with those obtained from other systems with similar target. However, to better compare the total reaction cross sections for the different systems we used the reduction procedure suggested by P. R. Gomes *et al.* in Ref. [13]. This prescription is valid when the compared systems has very similar masses [14, 15], as the case of the systems compared in the present work. In this proposed receipt, the reduced total reaction cross section and reduced energies are given by:

$$\sigma_{\rm red} = \sigma_{\rm R}/(A_{\rm P}^{1/3} + A_{\rm T}^{1/3}) \qquad \text{and} \qquad E_{\rm red} = E_{\rm CM} \times (A_{\rm P}^{1/3} + A_{\rm T}^{1/3})/(Z_{\rm P} Z_{\rm T}) \tag{1}$$

In these equations, $\sigma_{\rm R}$ is the total reaction cross section, $\rm E_{CM}$ is the energy in the center of mass framework and $\rm A_P(A_T)$ and $\rm Z_P(Z_T)$ stand for mass and charge of the projectile (target), respectively. With this normalization (reduction), the geometrical effects are, in principle, removed and the eventual anomalous values of the reduced radii ($\rm r_0$) in the radius definition for a normal nucleus, $\rm R=r_0 \times (A_P^{1/3}+A_T^{1/3})$, which should be related to physical processes, are not washed out. The obtained total reaction cross sections for ^{12}B with WS potential are listed in Table 1. These values are similar to those obtained with SPP. In Figure 4, we plotted the reduced total reaction cross sections for several systems as a function of the reduced energy. Considering this plot one can infer, for instance, about the role of the breakup in the elastic scattering, since projectiles with different breakup threshold energies are involved, from weakly bound nucleus (^{6}Li, ^{7}Li, ^{7}Be and ^{9}Be), tightly-bound (^{10}B, ^{11}B and ^{16}O) and exotic nuclei (^{6}He and ^{8}B). As we can see in the figure, the reduced cross sections for the exotic nuclei lie above those for the weakly-bound normal nuclei and much above than for the tightly-bound projectiles. For the ^{12}B nucleus, with binding energy of S_n=3.337 MeV, the reduced total reaction cross sections lie on the tightly-bound nuclei region.

5. Conclusion and summary

We have investigated the elastic scattering of the radioactive nucleus ^{12}B on ^{58}Ni target at energies close to the Coulomb barrier ($\rm V_B \approx 27$ MeV). The elastic scattering for this projectile has been measured for the first time. The angular distributions measured at 30.0 and 33.0 MeV were analyzed with the optical model using Woods-Saxon and double folding São Paulo potentials. The angular distributions were very well described with these potentials when the parameters were varied. However, the static effects of the projectiles and the dynamic

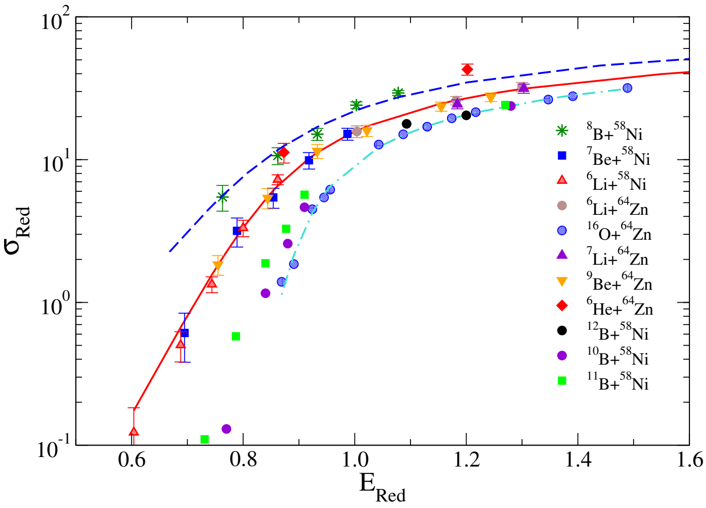

Figure 4. Reduced total reaction cross sections as a function of the reduced energies for the system indicated. The figure has been taken from Ref. [16] and updated with data from ^{10}B [7], ^{11}B [8], and ^{12}B from the present work. The curves are just to guide the eye joining sets of data with similar behavior.

effects of the process are embedded in these parameters. Considering the São Paulo Potential, the departure from the standard normalization (N_R=1.0 and N_I= 0.78) is an indication of the importance of coupling of other direct reactions channels in the elastic scattering. The identification of the important channels can be achieved only by coupled-channel calculation analysis. Total reaction cross sections could be extract from the OM analysis for the ^{12}B+^{58}Ni system, and from the comparison with the cross sections from some other light nuclei, in particular from boron isotopes (^{8}B, ^{10}B, ^{12}B) indicates that ^{12}B resembles more a tightly-bound nucleus.

Acknowledgments

The authors V. G. and K. C. C. P. would like to thank São Paulo Research Foundation (FAPESP) (Grant 2016/02864-4, 2016/17612-7 and 2016/21434-7) and the Conselho Nacional de Desenvolvimento Científico (CNPq) (Grant 304961/2017-5) for the financial support. V. M. thanks FAPERJ. The authors also thank INCT-FNA (Instituto Nacional de Ciência e Tecnologia- Física Nuclear e Aplicações).

References

[1] Tanihata I, Savajols S, Kanungo R 2013 *Prog. Part. Nucl. Phys.* **68** 215
[2] Canto L F, Gomes P R S, R. Donangelo, Lubian J, and Hussein M S 2015 *Phys. Rep.* 596 1
[3] Keeley N, Kemper K W, and Rusek K 2013 *Physical Review* C **88** 017602
[4] Kolata J J, Guimarães V, and Aguilera E F 2016 *The Eur. Physical Journal* A **52** 123
[5] Aguilera E F *et al.* 2009 *Physical Review* C **79**, 021601
[6] Lubian J, Correa T *et al* 2009 *Physical Review* C **79**, 064605
[7] Scarduelli V, Crema E, Guimarães *et al* 2017 *Physical Review* C **96** 054610
[8] Deshmukh N N, Guimarães V *et al.* 2015 *Physical Review* C **92** 054615
[9] Lepine-Szily A, Lichtenthaler R and Guimarães V 2014 *Eur. Phys. Journal* A **50** 128
[10] Chamon L C *et al.* 2002 *Physical Review* C **66** 014610
[11] Thompson I J 1988 *Comput. Phys. Rep.* **7** 167
[12] Zevallos E O N, Guimarães V, Cardozo E N *et al.* 2018 *Physical Review* **C** in press
[13] Gomes P R S, Lubian J, Padron I, Anjos R M 2005 *Physical Review* C **71** 017601
[14] Canto L F, Mendes Junior D R, Gomes P R S, Lubian J 2015 *Physical Review* C **92** 014626
[15] Deshmukh N N and Lubian J 2018 *Eur. Phys. J.* A **54** 101
[16] Guimarães V *et al.* 2011 *Journ. of Physics: Conference Series* **312** 082024

Spin-orbit effects in the ^{8}Li+^{58}Ni elastic scattering

O C B Santos[1], R Lichtenthäler[1], K C C Pires[1], A M Moro[2], U Umbelino[1], E O N Zevallos[1], M Assunção[3], S Appannababu[1], J Alcántara-Núñez[1], A L de Lara[1], V Scarduelli[1], V Guimarães[1], A Lépine-Szily[1], A. S. Serra[1], R Linares[4], V A B Zagatto[4], P N de Faria[4], V Morcelle[5], M C Morais[4], A Barioni[3], J M B Shorto[6]

[1]Instituto de Física, Universidade de São Paulo, São Paulo, Brazil
[2]Departamento de Física Atómica, Molecular y Nuclear, Universidad de Sevilla, Spain
[3]Universidade Federal de São Paulo, SP, Brazil
[4]Universidade Federal Fluminense, RJ, Brazil
[5]Universidade Federal Rural do Rio de Janeiro, Seropédica - RJ, Brazil
[6]IPEN, Comissão Nacional de Energia Nuclear, São Paulo, Brazil

E-mail: `osvaldo.santos@usp.br`

Abstract. In this work we present an elastic scattering angular distribution for the ^{8}Li+^{58}Ni system measured at $E_{\rm lab}$ = 26.1 MeV. The ^{8}Li beam was produced in the Radioactive Ion Beams in Brasil (RIBRAS) facility using the ^{7}Li primary beam delivered by the 8-UD Pelletron accelerator. The angular distribution covers the angular range from 20 to 85 degrees in the center of mass frame. The data have been analysed by optical model and coupled channels calculations, including couplings to low-lying states in ^{8}Li and the spin-orbit interaction. Our results indicate that the inclusion of the spin-orbit interaction in the calculations is important to describe the data at backward angles.

1. Introduction.

A large research field was opened with the possibility of producing secondary beams of nuclei out of the stability valley. Several facilities became operational all over the world making this field one of the most active in the low energy nuclear physics domain [1–5]. In particular, in the region of light nuclei there are several interesting phenomena to be explored [6–8]. Light nuclei, in general, present cluster structure with low breakup energies for certain configurations. ^{6,7}Li and ^{9}Be are examples of stable weakly bound light nuclei with breakup energies of $E_{\rm bu}$=1.47 MeV, 2.46 MeV and 1.67 MeV, for $\alpha + d$, $\alpha + t$ and $\alpha + \alpha + n$ configurations respectively. As one goes always of the valley of stability, there are radioactive species, with relatively long half-lives (≈800 ms), and they have even lower breakup energies. Exotic structures such as neutron halos can be found for instance in ^{6}He (α+n+n; $E_{\rm bu}$=0.975 MeV) and ^{11}Li (^{9}Li+n+n; $E_{\rm bu}$=0.37 MeV) among others.

Although ^{8}Li(^{7}Li+n; $E_{\rm bu}$=2.0 MeV) is not considered an exotic nuclei, its possible importance to astrophysics has attracted some interest in the investigation of its structure. The synthesis of heavy elements in stars has to overcome the A = 5 and 8 mass gaps for which there are no stable elements. For A = 8, there are only two bound nuclei, ^{8}Li and ^{8}B. They are mirror nuclei and have half-lives of 840 ms and 770 ms respectively, long enough to possibly affect the nucleosynthesis in stars and in the primordial Universe [9–12]. For this reason, studies involving

A = 8 nuclei are welcome since they can provide information of the interacting potential which is an important ingredient in calculations of cross sections involving these nuclei [13].

Here, we present an angular distribution of the ^{8}Li+^{58}Ni elastic scattering at 26.1 MeV, which corresponds to an energy twice the Coulomb barrier for this system V_b = 13.1 MeV [14, 15]. Analyses with optical model(OM) and coupled channels(CC) calculations were performed using a double folding Sao Paulo potential (SPP) [16] and an important contribution of the spin-orbit interaction was identified.

2. Experimental Setup.

The 28 MeV ^{7}Li primary beam was delivered by the 8-UD Pelletron accelerator with an intensity between 200 and 300 enA. The ^{8}Li secondary radioactive ion beam was produced by the RIBRAS system using the one neutron transfer reaction ^{9}Be(^{7}Li,^{8}Li). The ^{8}Li beam was selected and focused by the first solenoid in the central scattering chamber. The intensity of the secondary beam was around 2×10^5 pps (per 250 enA of primary beam) in the scattering chamber. To compensate for the relatively low intensity of the radioactive ion beam, thick targets (in order of mg/cm^2) and large detection solid angles $\approx$ 20 msr are usually applied. The thickness of the ^{58}Ni and ^{197}Au targets were of 2.1 mg/cm^2 and 4.6 mg/cm^2, respectively. The Gold target was used to normalize the data and to obtain the absolute cross sections, assuming the ^{8}Li+^{197}Au scattering as pure Rutherford, which is valid in the energy range of the present experiment.

The detection system consists of four ΔE-E telescopes formed by silicon surface barrier detectors of ΔE=25 μm and E=1000 μm thickness.

A typical E-ΔE spectrum at θ_lab = 26° with Gold target is presented in figure 1. We identify the ^{8}Li peak as well as the contaminants of the secondary beam. The contaminants are alphas, protons, deuterium, tritium and other particles such as the ^{9}Be, recoiling from the primary target, and ^{7}Li from the primary beam. A ^{6}He peak was identified as coming from the ^{9}Be(^{7}Li,^{6}He) reaction in the primary target.

Four ^{8}Li+^{58}Ni angular distributions at 23.9 MeV, 26.1 MeV, 28.7 MeV, and 30.0 MeV laboratory energies were measured. Figure 2 presents the ^{8}Li + ^{58}Ni distribution at 26.1 MeV.

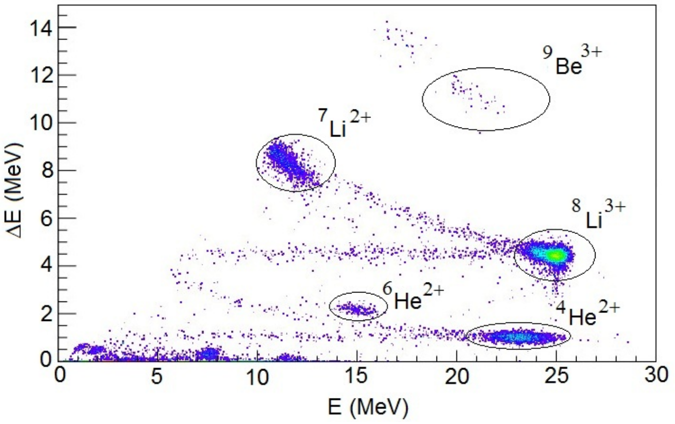

Figure 1. Typical bi-dimensional spectra obtained for ^{8}Li+^{197}Au system at $\theta_\mathrm{lab} = 26°$.

3. Monte Carlo simulation.

Due to the large detection solid angles and the intrinsic angular divergence of the RIBRAS beam, it is necessary to make a correction in the nominal detection angles. This was performed using a Monte Carlo simulation code (*RIBRAS*) [17]. The simulation generates aleatory events inside the beam spot and in the detector, tracing the ray between them and obtaining the scattering angle distribution of the events. It takes into account the angular divergence of the secondary beam, angular straggling and the geometry of the slits of the detectors. A folding between the Rutherford cross section and the angle distribution is performed to calculate the average detection angle. Cross sections different from Rutherford can be used as well. As the elastic cross section drops down quickly with angle, this correction causes a shift of the average angle to the forward direction, being more important at forward angles. An example of the corrections is shown in figure 2.

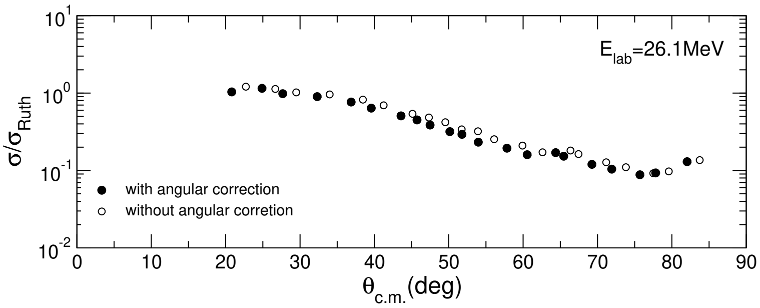

Figure 2. The ^{8}Li+^{58}Ni angular distribution with (black points) and without (white points) angular correction performed using the (*RIBRAS*) simulation.

4. Analysis and Results.

In figure 3 we present the ^{8}Li +^{58}Ni angular distribution compared with four different calculations. The blue line is an Optical Model (OM) calculation using the SPP with N_r=1 and N_i =0.78. Usually the angular distributions for exotic projectiles such as ^{6}He exhibit more absorption than optical model calculation with SPP and the calculations usually overestimate the experimental data at backward angles. Here, the results show the opposite, SPP calculation underestimates the experimental cross sections. This motivated us to consider different effects that could be causing this enhancement with respect to the SPP calculations. One possibility is the effect of the coupling to the first low lying ^{8}Li excited states on the elastic distribution. To estimate this effect we performed Coupled Channels (CC) calculations using the FRESCO program [18], including the coupling to the first 1^+ (980 keV), second 3^+ (2.26 MeV) and third 1^+ (3.21 MeV) excited states of ^{8}Li. Only nuclear excitation was considered with a deformation length of δ_2=1.75 fm [19]. The results of the CC calculations are shown as the green line in figure 3 which is a little above the OM calculation (blue line), but not sufficient to explain the data.

Another effect that could contribute to the enhancement of the cross sections comes from the fact that our energy resolution is not sufficient to separate the first excited state of ^{8}Li(980 KeV) from its ground-state. In this case a contamination from the inelastic excitation would be present in the elastic peak (quasi-elastic scattering) causing an enhancement of the cross section. The pink line in figure 3 corresponds to the sum of the inelastic and elastic cross section, obtained from the CC calculation. We see that there is a small effect but not sufficient to explain all the observed enhancement.

Finally, we considered the effect of the spin of the projectile in the calculation. The ^{6,7,8}Li isotope chain has, respectively, ground state spins of 1^+, $3/2^-$ and 2^+, ^{8}Li being the larger. Then we included the effect of the spin-orbit interaction (S.O.) in the OM calculations. The red line corresponds to the results of the calculations where the spin-orbit term was included. The form

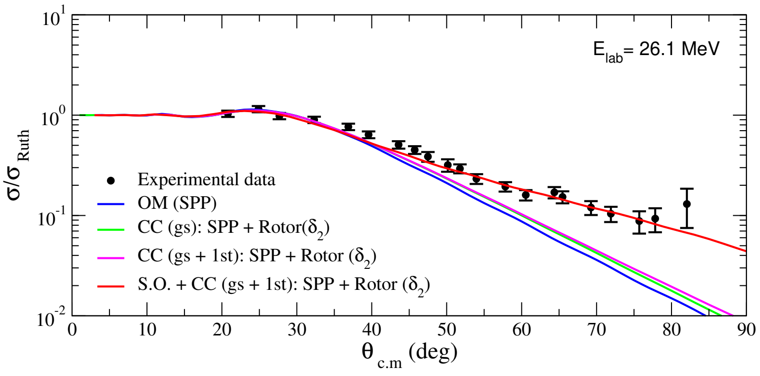

Figure 3. Angular distribution for ^{8}Li+^{58}Ni system measured at E_{lab}=26.1 MeV compared to calculations, as described in the text.

factor of the spin-orbit term was taken as the derivative of an Woods-Saxon, whose parameters are V_{0s}=1.96 MeV, r_{0s}=1.25 fm and a_{0s}=0.65 fm. The calculation were performed using the FRESCO code and V_{0s} was varied to best reproduce the data. The result is surprising and shows that the effect of spin-orbit interaction explains the data with reasonable S.O. parameters. We also performed calculations for ^{6,7}Li data but the spin-orbit interaction seems not to be as important as in the ^{8}Li case.

5. Conclusions

An elastic scattering angular distribution for the ^{8}Li+^{58}Ni system is presented. The experimental cross sections at backward angles show a considerable enhancement when compared to Optical Model calculations using the Sao Paulo Potential. Coupled channels calculations were performed to investigate the effect of the projectile excitation in the angular distribution. The results show that the projectile quasi-elastic excitation gives little effect in the backward angular distribution, not sufficient to explain the observed enhancement. The inclusion of the spin-orbit interaction in the calculations can account for the observed enhancement.

6. Acknowledgment

The authors would like to thanks the Coordenação de Aperfeiçoamento de Pessoal de Nível Superior (CAPES) and Fundação de Amparo à Pesquisa do Estado de São Paulo (FAPESP) proc. 2013/22100-7 and 2016/17612-7 for financial support.

References

[1] Lichtenthäler R, Lépine-Szily A and Guimarães V 2005 *Eur. Phys. J.* A **25** 1733
[2] Lépine-Szily A, Lichtenthäler R and Guimarães V 2014 *Eur. Phys. J.* A **50** 128
[3] Lépine-Szily A, Lichtenthäler R and RIBRAS collaboration 2007 *Nucl. Phys.* A **787** 94c
[4] Lichtenthäler R, Alvarez M A G, Lépine-Szily A, Appannababu S, Pires K C C, Da Silva U U, Scarduelli V, Condori R P and Deshmukh N 2016 *Few-Body Systems* **57**(3) 157163
[5] Blumenfeld Y, Nilsson T and Van Duppen P 2013 *Phys. Scr.* **T152** 014023
[6] Pires K C C *et al* 2014 *Phys. Rev.* C **90** 027605
[7] Morcelle V *et al* 2014 *Phys. Rev.* C **89** 044611
[8] Kolata J J, Guimarães V and Aguilera E F 2016 *Eur. Phys. J.* A **52** 123
[9] Claus E R and William S R 1988 *Cauldrons in the Cosmos* University of Chicago Press
[10] Camargo O *et al* 2007 *Phys. Rev.* C **75** 054602
[11] Mendes Jr D R *et al* 2012 *Phys. Rev.* C **86** 064321
[12] Leistenschneider E *et al* 2018 *Phys. Rev.* C **98** 064601
[13] Morcelle V *et al* 2017 *Phys. Rev.* C **95** 014615

[14] Freitas A S, Marques L, Zhang X X, Luzio M A, Guillaumon P, Pampa-Condori R and Lichtenthäler R 2016 *Braz. J. Phys.* **46** 120128
[15] Pires K C C, Appannababu S, Lichtenthäler R and Santos O C B 2018 *Phys. Rev.* C **98** 014614
[16] Chamon L C, Carlson B V, Gasques L R, Pereira D, De Conti C, Alvarez M A G, Hussein M S, Cândido Ribeiro M A, Rossi Jr E S and Silva C P 2002 *Phys. Rev.* C **66** 014610
[17] Lichtenthäler R *Ribras code Not Published*
[18] Thompson I J 1988 *Computer Physics Reports* **7**(4) 167212
[19] Tengborn E *et al* 2011 *Phys. Rev.* C **84** 064616

Confinement effects from a PNJL model at zero temperature regime

O A Mattos, O Lourenço and T Frederico

Departamento de Física, Instituto Tecnológico de Aeronáutica, DCTA, 12228-900, São José dos Campos, SP, Brazil

E-mail: `odilonam@ita.br` , `odilon@ita.br`, `tobias@ita.br`

Abstract. The Polyakov-Nambu-Jona-Lasinio (PNJL) model is a model that incorporates confinement effects in the Nambu-Jona-Lasinio (NJL) model through the addition of the Polyakov loop (Φ). These effects are studied at finite temperature regime. However, at zero temperature its modified Fermi-Dirac distributions become step functions and Φ disappears from the equations of state (EOS), as well as the Polyakov potential, leading the model to the conventional form of the NJL model. In this work we propose a variation of the PNJL model where all the couplings depend on Φ with the constraint that the interactions vanish at the deconfinement phase where Φ reaches its maximum value and the quarks behave as free particles. In this approach, coupling constants of original PNJL model become now dependent on Φ. As a consequence, all equations of state present a Φ dependence even at zero temperature regime. The thermodynamics of this new model is discussed.

1. Introduction

The NJL model is an effective quark model widely used to describe the mechanism of mass generation of quarks [1, 2] . An disadvantage of this model is its lack of the deconfinement effects. The PNJL model is an improved version of the NJL one in the sense that the confinement/deconfinement phenomenon is taken into account through the inclusion of the Polyakov loop (Φ) at finite temperature regime [3]. However, at zero temperature regime, the structure of the PNJL model completely loses information on Φ (Wilson loop at finite temperature [4]), since its equations become the same as the NJL model. We propose in this work a modification in the scalar and vector coupling strengths of the two flavor NJL model by making them dependent on Φ. As a constraint, we require that all interactions disappear in the deconfined phase (free quarks regime, $\Phi \sim 1$).

2. NJL model

The NJL model was initially proposed in Refs. [6, 7] basically as a model for elementary nucleons (point particles) interacting to each other through a contact interaction. By that time Quantum Chromodynamics (QCD) did not yet exist, but after it was developed, physicists realized that NJL model shares some conceptually important features with QCD such as chiral symmetry breaking and dynamical mass generation. It has been used as an effective model for QCD ever since. Since then, it is also used as a phenomenologial model for quarks. It can be used to study the SU(2) system where only two quarks (up and down) are considered in quark matter. In this context, the Lagrangian density of the model reads

$$\mathcal{L}_0 = \bar{\psi}(i\partial\!\!\!/ - m_0)\psi + G_s\left[(\bar{\psi}\psi)^2 - (\bar{\psi}\gamma_5\tau\psi)^2\right] - G_V\left[(\bar{\psi}\gamma_\mu\psi)^2 + (\bar{\psi}\gamma_\mu\gamma_5\psi)^2\right] , \tag{1}$$

with $m_0 = m_u = m_d$ being the current quark mass. G_s and G_v regulate the strength of the scalar and vector interactions, respectively. The T_{00} component of the energy-momentum tensor gives the energy density of the system (symmetric in our case), which in the mean-field approach is written as,

$$\mathcal{E} = G_s\rho_s^2 + G_V\rho^2 + \frac{\gamma}{2\pi^2}\int_0^{k_F} dkk^2(k^2+M^2)^{1/2} - \frac{\gamma}{2\pi^2}\int_0^{\Lambda} dkk^2(k^2+M^2)^{1/2} - \mathcal{E}_{vac}. \tag{2}$$

The chemical potential is given by $\mu = (k_F^2 + M^2)^{1/2} + 2G_V\rho$ and the pressure can then be defined as $P = \mu\rho - \mathcal{E}$. Its form is

$$P = G_V\rho^2 - G_s\rho_s^2 + \frac{\gamma}{6\pi^2}\int_0^{k_F} dk\frac{k^4}{(k^2+M^2)^{1/2}} + \frac{\gamma}{2\pi^2}\int_0^{\Lambda} dkk^2(k^2+M^2)^{1/2} - P_{vac} , \tag{3}$$

where λ is the cutoff parameter, and k_F is Fermi momentum related to the quark density ρ through $\rho = (\gamma/6\pi^2)k_F^3$. $\gamma = N_s \times N_f \times N_c = 12$ is the degeneracy factor due to the spin, flavor, and color numbers ($N_s = 2$, $N_f = 2$ and $N_c = 3$). The vacuum terms ($\mathcal{E}_{vac}$ and P_{vac}) are obtained when $k_F = 0$ and are inserted in the model in order to impose $\mathcal{E} = P = 0$ at $\rho = 0$. The constituent quark mass is

$$M = m_0 + \frac{G_s\gamma}{\pi^2}\int_{k_F}^{\Lambda}\frac{M}{(k^2+M^2)^{1/2}} , \tag{4}$$

with the quark condensate is given by $\rho_s = \langle\bar{\psi}\psi\rangle = (m_0 - M)/2G_s$.

In Fig. 1 we show the plots for the pressure and quark condensate (in units of its value in vacuum $\rho_{s(\mathrm{vac})}$) as a function of μ.

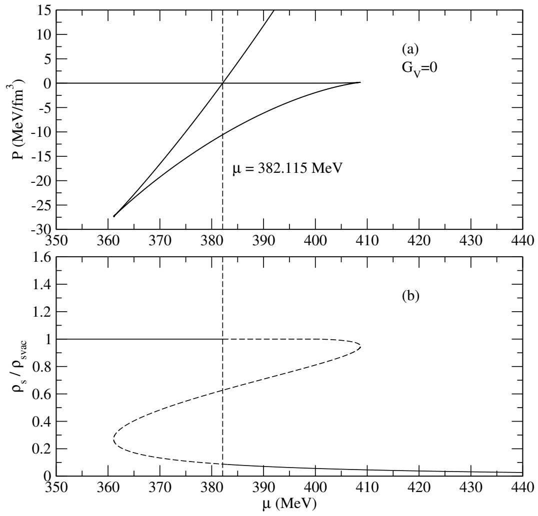

Figure 1. For NJL model, (a) $P \times \mu$ and (b) $\rho_s/\rho_{s(\mathrm{vac})} \times \mu$ for $G_V = 0$ with parametrization of table 2.2 of Ref. [5], where $\Lambda = 587.9$ Mev, $m_0 = 5.6$ Mev and $G_s\Lambda^2 = 2.44$.

Notice from the figure a clear signature of a first order phase transition, similar to that presenting in relativistic hadronic mean-field models [8, 9] at moderate temperatures [10].

3. Our results

The PNJL model [11, 12, 13, 14] is an extended version of the NJL in which the so called Polyakov loop Φ is is included in the Lagrangian density of the NJL model through a Polyakov potential constructed in order to adjust QCD lattice results of the pure gauge system. It is a phenomenological measure of the quark confinement, with $\Phi = 0$ ($\Phi = 1$) representing confinement (deconfinement). All the EOS of the NJL model are modified by the inclusion of Φ in the thermodynamical quantities. However, at $T = 0$, the Polyakov loop completely disappear of these EOS and the PNJL model is reduced to the conventional NJL model again.

In this work we propose the modification of the coupling constants of the NJL model by making them dependent on Φ, namely, $G_s \to G_s(1-\Phi^2)$ and $G_V \to G_V(1-\Phi^2)$ with the condition that the interactions regulated by them vanish at the deconfinement phase ($\Phi = 1$). The similar proposition for the constants can be seen in the references [15, 16, 17, 18]. These replacements give rise to the following energy density and pressure, respectively,

$$\begin{aligned}\mathcal{E} &= G_s\rho_s^2 + G_V\rho^2 + \frac{\gamma}{2\pi^2}\int_0^{k_F} dk k^2(k^2+M^2)^{1/2} - \frac{\gamma}{2\pi^2}\int_0^{\Lambda} dk k^2(k^2+M^2)^{1/2} \\ &+ \mathcal{U}(\Phi,\rho_s,\rho) - \mathcal{E}_{vac}\ , \end{aligned} \tag{5}$$

$$\begin{aligned}P &= G_V\rho^2 - G_s\rho_s^2 + \frac{\gamma}{6\pi^2}\int_0^{k_F} dk \frac{k^4}{(k^2+M_f^2)^{1/2}} + \frac{\gamma}{2\pi^2}\int_0^{\Lambda} dk k^2(k^2+M_f^2)^{1/2} \\ &- 2G_V\Phi^2\rho^2 - \mathcal{U}(\Phi,\rho_s,\rho) - P_{vac}, \end{aligned} \tag{6}$$

where it is possible to define a Polyakov loop potential as

$$\mathcal{U}(\Phi,\rho_s,\rho) = -G_s\Phi^2\rho_s^2 - G_V\Phi^2\rho^2 + a_3T_0^4\log\left[1-6\Phi^2+8\Phi^3-3\Phi^4\right], \tag{7}$$

with an explicit back reaction of the quark system into the gluonic one, since $\mathcal{U}$ is also a function of the quark quantities ρ_s and ρ besides Φ as well. In Eq. (7), we have included the logarithmic term in order to ensure Φ limited to $\Phi = 1$, see Ref [19]. Here, $T_0 = 190$ MeV and a_3 is taken as a free parameter.

This specific modification in the NJL model turn the model in a type of PNJL in which it is possible to investigate the deconfinement effects at zero temperature.. As an example we show in Fig. 2 the Φ dependence of $\mathcal{E}$ for ρ corresponding to a baryonic density of $\rho_B = 3\rho_0$ ($\rho_0 = 0.15$ fm^{-3}).

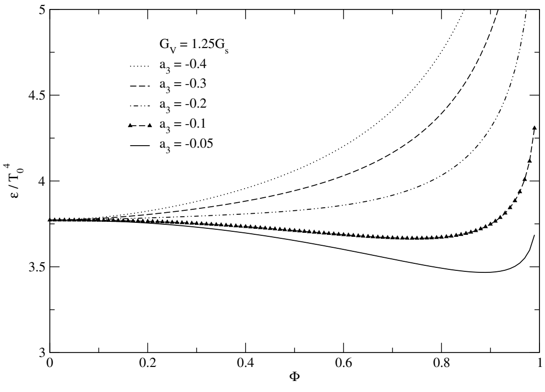

Figure 2. Energy density of Eq. (5) as a function of Φ for different a_3 values. G_V is fixed to $G_V = 1.25G_s$. The parameters is the same of the figure 1.

Notice from the Fig. 2 that there is a set of a_3 values that produce a minimum at $\Phi > 0$ for the energy density as a function of Φ. This feature is not present in the traditional PNJL model (G_s and G_V fixed) at zero temperature since in that case, energy density and pressure have no dependence on Φ, i. e., Φ in Eqs. (5) and (6).

4. Conclusions and perpectives

We could verify that our modification in the NJL model at zero temperature, namely, the replacements $G_s \to G_s(1-\Phi^2)$ and $G_V \to G_V(1-\Phi^2)$, ensures a nonvanishing contribution of Φ to the EOS of the model allowing the study the confinement/deconfinement phase transition, what is not possible in the traditional PNJL model. We intend to investigate in more details the thermodynamical quantities of this modified model in order to completely define the range of parameters for a_3 and G_V that leads to $\Phi \neq 0$ solutions.

5. Acknowledgments

This work was partially supported by CNPq under grants 310242/2017-7 (O.L.) and 308486/2015-3 (T.F.), by FAPESP under the thematic projects 2013/26258-4 (O.L.) and 2017/05660-0 (T.F.), and by INCT-FNA project 464898/2014-5. This study was also financed in part by the Coordenação de Aperfeiçoamento de Pessoal de Nível Superior - Brasil (CAPES) - Finance Code 001.

[1] Vogl U, Weise W 1991 *Prog. Part. Nucl. Phys* **27** 195-272
[2] Klevansky S P 1992 *Rev. Mod. Phys.* **64** 649-708
[3] Fukushima K, Skokov V 2017 *Prog. Part. Nucl. Phys.* **96** 154-199
[4] Wilson K G 1974 *Phys. Rev.* D **10** 2445-2459
[5] Buballa M 2005 *Phys. Rept.* **407** 205-376
[6] Nambu Y , Jona-Lasinio G 1961 *Phys. Rev.* **122** 345
[7] Nambu Y , Jona-Lasinio G 1961 *Phys. Rev.* **124** 246
[8] Lourenço O, Dutra M, Delfino A, Amaral R L P G 2007 *Int. J. Mod. Phys.* E **16** 3037; Lourenço O, Santos B M, Dutra M, Delfino A 2016 *Phys. Rev.* C **94** 045207; and Lourenço O, Dutra M, Menezes D P 2017 *Phys. Rev.* C **95** 065212
[9] Santos B M, Dutra M, Lourenço O, Delfino A 2015 *Phys. Rev.* C **92** 015210; 2014 *Phys. Rev.* C **90** 035203
[10] Silva J B , O Lourenço, A Delfino, Sá Martins J S, Dutra M 2008 *Phys. Lett.* B **664** 246-252
[11] Fukushima K 2004 *Phys. Lett.* B **591** 277–284
[12] Lourenço O, Dutra M, Delfino A, Malheiro M 2011 *Phys. Rev.* D **84** 125034
[13] Lourenço O, Dutra M, Frederico T, Delfino A, Malheiro M 2012 *Phys. Rev.* D **85** 097504
[14] Dutra M, Lourenço O, Delfino A, Frederico T, Malheiro M 2013 *Phys. Rev.* D **88** 114013
[15] Ferreira M, Costa P, Lourenço O, Frederico T, Providência C 2014 *Phys. Rev. D* **89** 116011
[16] Farias R L S, Gomes K P, Krein G, Pinto M B 2014 *Phys. Rev. C* **90** 025203; and Farias R L S, Timóteo V S, Avancini S S, Pinto M B, Krein G 2017 *Eur. Phys. J. A* **53** 101
[17] Timóteo V S, Farias R L S, Avancini S S, Pinto M B, Tavares W R 2018 *EPJ Web Conf.* **171** 20001
[18] Avancini S S, Farias R L S, Pinto M B, Tavares W R, Timóteo V S 2017 *Phys. Lett.* B **767** 247-252
[19] Dexheimer V A, Schramm S 2010 *Phys. Rev.* C **81** 045201

IOP Conf. Series: Journal of Physics: Conf. Series **1291** (2019) 012032 doi:10.1088/1742-6596/1291/1/012032

The gluonic halo of the nucleons

L A Trevisan[1], **C Mirez**[2] **and D I da Silva**[3]

[1] Department of Mathematics and Statistics, State University of Ponta Grossa, Parana, PR, Brazil
[2] Federal University of Jequitinhonha and Mucuri Valleys, Campus do Mucuri, Teófilo Otoni, Cep 3529-2700, Minas Gerais, MG, Brazil
[3] Youdigital, Rua Joao Gbur 861, Cep 82640-000, Curitiba, PR, Brazil

E-mail: `luisaugustotrevisan@uepg.br`

Abstract. On the scope of the nonextensive statistical model for the nucleon's structure function, we propose that gluons may occupy a bigger volume than the quarks, in nucleons. This correction is needed to fit the carry out momentum of each kind of particle. At the end of the work, we notice that the radius was not the only variable to be changed to get the goal of momentum adjustment and the another constraints.

1. Introduction

The use of statistical models to describe the structure function (unpolarized and polarized) of the nucleons was quite common at the end of the eighties and beginning of nineties [1–10]. These model were mainly based in the MIT bag models [11, 12], with some variations. More recently, Trevisan [13] and Trevisan and Mirez [14] proposed models that consider the nonextensive effects on the quarks statistics, for both cases. All these models suppose that the bag has a fixed radius, for the gluons and quarks. After an initial function is obtained, some corrections are needed to fit better the model, such as finite size corrections [9] or the QCD convolutions [3].

2. The model

In the present work, we show a model where the gluons may place in a bigger space than the quarks, since the quarks may emit gluons in all directions and therefore gluons may occupy more volume than the quarks. We notice that from this correction, some features of the model may be improved, such as the total momentum carried by gluon, that under the initial hypothesis of equal radius for quarks and gluons was below the observed values. Therefore, in the proposed model of the nucleon, the quarks have around them a gluonic cloud, the gluonic halo of the nucleons.

In our picture the nucleon (mass $M = 939$ MeV) consists of a gas of massless partons (quarks, antiquarks, gluons) in equilibrium at temperature T in the spherical volume V with radius R. Considering the usual sum rules for the proton and some experimental data for the polarized structure function E142 [15], E143 [16], E154 [17, 18], SMC [19] and HERMES [20], we have the following set of equations and constraints:

$$n_{u\uparrow} + n_{u\downarrow} - n_{\bar{u}\uparrow} - n_{\bar{u}\downarrow} = 2, \tag{1}$$

$$n_{d\uparrow} + n_{d\downarrow} - n_{\bar{d}\uparrow} - n_{\bar{d}\downarrow} = 1, \tag{2}$$

$$n_{s\uparrow} + n_{s\downarrow} - n_{\bar{s}\uparrow} - n_{\bar{s}\downarrow} = 0, \tag{3}$$

$$n_{u\uparrow} - n_{u\downarrow} + n_{\bar{u}\uparrow} - n_{\bar{u}\downarrow} = \Delta u, \tag{4}$$

$$n_{d\uparrow} - n_{d\downarrow} + n_{\bar{d}\uparrow} - n_{\bar{d}\downarrow} = \Delta d, \tag{5}$$

$$n_{s\uparrow} - n_{s\downarrow} + n_{\bar{s}\uparrow} - n_{\bar{s}\downarrow} = \Delta s, \tag{6}$$

$$\sum_{\text{all partons}} (\text{momentum fraction}) = 1, \tag{7}$$

Where the values are $\Delta u = 0.83 \pm 0.03$, $\Delta d = -0.43 \pm 0.03$, $\Delta s = -0.10 \pm 0.03$.

The parton number density dn^i/dx in the infinite-momentum frame (IMF) and the density dn/dE in the nucleon rest frame are related to each other by:

$$\frac{dn^i}{dx} = \frac{M^2 x}{2} \int_{xM/2}^{M/2} \frac{dE}{E^2} \frac{dn}{dE}, \tag{8}$$

where the superscript i refers to the IMF, M is the nucleon mass and E is the parton energy. For each particle α, we have:

$$\frac{dn_\alpha}{dx} = \frac{M^2 x V}{2} \int_{Mx/2}^{M/2} \frac{g f_\alpha(E) dE}{2\pi^2}, \tag{9}$$

where x is the Bjorken variable and g is the spin-color degeneracy factor. V is the nucleon volume and $f_\alpha(E)$ is the probability distribution, which is given by:

$$f_\alpha(E) = \frac{1}{[1 + (q-1)\beta(E - \mu_\alpha)]^{1/(q-1)} \pm 1}, \tag{10}$$

for the case $(E - \mu_\alpha) > 0$ and

$$f_\alpha(E) = \frac{1}{[1 + (1-q)\beta(E - \mu_\alpha)]^{1/(1-q)} \pm 1}, \tag{11}$$

The following relations among the chemical potentials are used to solve the system:

$$\mu_{\bar{\alpha}\downarrow} = -\mu_{\alpha\uparrow}, \tag{12}$$

and

$$\mu_{\bar{\alpha}\uparrow} = -\mu_{\alpha\downarrow}. \tag{13}$$

3. Preliminary Results

In order to fit the variables, two additional constraint are considered, as follow:

(i) The total momentum of quarks is around 0.54 [21].

(ii) The violation of Gottfried sum rule is around 0.118 That is difference

$$\int_0^1 \bar{d} - \bar{u}$$

in the proton [22].

The Preliminary results are shown in the table below:

Table 1. Some values for the Radius of gluons and quarks in the model. As predicted, gluons are *bigger* then the quarks. Rg and Mg are the gluon Radius and Momentun, respectively. Rq and Mq are related to the quarks. T is the temperature, and q is the Tsallis variable.

T(MeV)	q	Rg(fm)	Rq(fm)	Mg	Mq	Gott
31	0.94	4.58	2.8	0.43	0.57	0.144
32	0.94	4.4	2.6	0.43	0.57	0.122
33	0.94	4.2	2.5	0.43	0.58	0.118

Therefore we may conclude that, with the used data, the following relation is obtained:

$$\frac{Rg}{Rq} \approx 1.67$$

In comparison with the previous result, showed in [13], we notice that the temperature has changed from $T = 46$ MeV, with $q = 0.96$ and $R = 1.8$ fm. The total momentum of the quarks was about 80%. The physical interpretation may be the following: to decrease the quark momentum, the temperature must decrease also, but to keep the same violation of the Gottfried sum rule, the meson cloud must be big.

To consider the gluonic halo may help to understand the mesonic cloud and some interactions in nuclear medium [23]. Therefore, this study should be improved. More recent works, based on lattice QCD [24], obtained the gluon momentum fraction about 30%. Jahan and Choudhury [25] used the self similarity to obtain a relation among the gluon fraction and Q^2. The possible correlations among the temperature, gluon momentum, the violation of the Gottfried sum rule and the radius is also an interesting subject to be researched.

3.1. Acknowledgments

We thank to the Setor de Ciências Exatas e Naturais of the UEPG for the support.

References

[1] Angelini C and Pazzi R 1982 *Phys. Lett.* A **113B** 343. Angelini C and Pazzi R 1984 *Phys. Lett.* **135B** 473
[2] Cleymans J and Thews R L 1988 *Z. Phys.* C **37** 315
[3] Mac E and Ugaz E 1989 *Z. Phys.* C **43** 655
[4] Mirez C, Tomio L, Trevisan L A and Frederico T 2010 *Nucl. Phys.* B *(Proceed. Suppl.)* **199** 252-257. Mirez C, Tomio L, Trevisan L A and Frederico T 2010 *Int. J. M. Phys.* D **19** 1697-1701. Mirez C 2010 *AIP Conf. Proc.* **1245** 137-140. Mirez C, Trevisan L A, Tomio L and Frederico T 2009 *AIP Conf. Proc.* **1139** 202
[5] Trevisan L A, Mirez C, Tomio L and Frederico T 2008 *Eur. Phys. J.* C **56** 211. Trevisan L A, Frederico T and Mirez C 2007 *Nucl. Phys.* A **790** 522c-525c. Trevisan L A, Tomio L and Frederico T 1999 *Eur. Phys. J.* C **11** 351
[6] Bickerstaff R P and Londergan J T 1990 *Phys. Rev.* D **42** 3621
[7] Devanathan V, Karthiyayini S and Ganesamurthy K 1991 *Mod. Phys. Lett.* A **9** 3455
[8] Devanathan V and McCarthy J S 1996 *Mod. Phys. Lett.* A **11** 147
[9] Bhalerao R S 1996 *Phys. Lett.* B **380** 1
[10] Zhang Y, Shao L and Ma 2009 *Phys. Lett.* B **671** 30 *Preprint* nucl-th/0909.0454v1
[11] Chodos A, Jaffe R L, Johnson K, Thorn C B and Weisskopf V F 1974 *Phys. Rev.* D **9** 3471
[12] Jaffe R L 1975 *Phys. Rev.* D **11** 1953
[13] Trevisan L A 2016 *Int. J. Mod. Phys.* E **25** 165010
[14] Trevisan L A and Mirez C 2013 *Int. J. Mod. Phys.* E **22** 1350044
[15] E142, Anthony P L et al 1996 *Phys. Rev.* D **54** 6620
[16] E143, Abe k et al 1998 *Phys. Rev.* D **58** 112003

[17] E154, Abe k et al 1997 *Phys. Lett.* B **405** 180
[18] E154, Abe k et al 1997 *Phys. Rev. Lett.* **79** 26
[19] SMC, Adeva B et al 1998 *Phys. Rev.* D **58** 112002
[20] HERMES, Ackerstaff K et al 1997 *Phys. Lett.* B **404** 383
[21] Halzen F and Martin A D 1984 *Quarks and Leptons: An Introductory Course in Modern Particle Physics*, (John Wiley and Sons, Singapore) p 203
[22] New Muon Collaboration, Amaudruz P et al 1991 *Phys. Rev. Lett.* **66** 2712. Arneodo M et al 1994 *Phys. Rev.* D **50** R1
[23] NPLQCD Collaboration, Winter et al 2017 *Phys. Rev.* D **96** 9 094512
[24] Alexandrou et al 2017 *Phys. Rev.* D **96** 5 054503
[25] Jahan and Choudhury A 2013 *Mod. Phys. Lett.* A **27** 10.1142

XLI Brazilian Meeting on Nuclear Physics (RTFNB) IOP Publishing
IOP Conf. Series: Journal of Physics: Conf. Series **1291** (2019) 012033 doi:10.1088/1742-6596/1291/1/012033

Effects of dissipative hydrodynamics on elliptic flow and HBT interferometry in central collisions at RHIC

D S Lemos[1] **and O Socolowski Jr**[2]
[1]Instituto de Física Teórica, Universidade Estadual Paulista, Brazil
[2]Instituto de Matemática, Estatística e Física, Universidade Federal do Rio Grande, Brazil

E-mail: `dener.lemos@sprace.org.br`

Abstract. In this work, we study relativistic heavy ion collisions by using a hydrodynamic model for both ideal and viscous cases to investigate the influence of dissipative effects on the elliptic flow and HBT interferometry. We conclude that the bulk viscosity has small influence in hydrodynamic calculations. However, our results show that the shear effects are important for describing the experimental data in central collisions.

1. Introduction

Relativistic heavy ion collisions allow the study of the behavior of matter under extreme pressure and temperature conditions. Under these conditions it is possible to observe a transition from ordinary matter to a quark-gluon plasma (QGP) [1]. One possible tool for studying the system formed in these collisions is the hydrodynamic model [2, 3]. The application of this model is based on the assumption that the system reaches a state of local thermodynamic equilibrium and in the fact that the matter formed in these collisions shows a collective behavior.

Our aim in this work is to investigate the influence of shear and bulk viscosities on elliptic flow and HBT radii by using a hydrodynamic model with smooth initial conditions and an equation of state based on lattice QCD with a crossover transition between the QGP and the hadron gas. The calculations were performed for central Au+Au collisions (0-5%) with $\sqrt{s_{\rm NN}} = 200$ GeV in 2+1 dimensions (boost invariance).

2. Hydrodynamic Model

In the hydrodynamic model each fluid element can be characterized by its energy-momentum tensor and other conserved numbers (baryonic number, strangeness, etc.). In this work, we assumed that all conserved numbers are zero, so the hydrodynamic equations can be written as

$$\partial_{;\mu} T^{\mu\nu} = \partial_\mu T^{\mu\nu} + \Gamma^{\mu}_{\ \sigma\mu} T^{\sigma\nu} + \Gamma^{\nu}_{\ \sigma\mu} T^{\mu\sigma} = 0, \tag{1}$$

where $\Gamma^{\mu}_{\ \sigma\mu}$ are the Christoffel symbols and $T^{\mu\nu}$ the energy-momentum tensor given by [4, 5]

$$T^{\mu\nu} \;=\; \epsilon u^\mu u^\nu - (P + \Pi)\Delta^{\mu\nu} + \pi^{\mu\nu}. \tag{2}$$

Here ϵ, u^μ, P, Π, $\pi^{\mu\nu}$ and $\Delta^{\mu\nu}$ are, respectively, the energy density, the fluid four-velocity, the pressure, the bulk viscosity, the shear viscosity tensor and the ortogonal projector to u^μ. We solved Eq. (1) in Milne coordinates [4].

The second order viscous hydrodynamic equations are calculated for both shear and bulk viscosities, using the Israel-Stewart framework [6]

$$\Delta^{\mu\alpha}\Delta^{\nu\beta}u^{\gamma}\partial_{;\gamma}\pi_{\alpha\beta} = -\frac{1}{\tau_\pi}\left[\pi^{\mu\nu}-\eta\sigma^{\mu\nu}\right]-\frac{4}{3}\pi^{\mu\nu}\partial_{;\gamma}u^{\gamma}, \tag{3}$$

$$u^{\gamma}\partial_{;\gamma}\Pi = -\frac{1}{\tau_\Pi}\left[\Pi-\zeta\partial_{;\gamma}u^{\gamma}\right]-\frac{4}{3}\Pi\partial_{;\gamma}u^{\gamma}, \tag{4}$$

where $\sigma^{\mu\nu} = \Delta^{\mu\lambda}\partial_{;\lambda}u^{\nu} + \Delta^{\nu\lambda}\partial_{;\lambda}u^{\mu} - \frac{2}{3}\Delta^{\mu\nu}\partial_{;\lambda}u^{\lambda}$ and η, ζ, τ_π, τ_Π are, respectively, the shear coeficient, the bulk coeficient, the shear relaxion time, the bulk relaxion time. The relaxion times depend on the viscous coeficiets as $\tau_\pi = \frac{3}{T}\frac{\eta}{s}$ and $\tau_\Pi = \frac{6}{T}\frac{\zeta}{s}$ [3], where T is the temperature and s the entropy density. The η/s and ζ/s are parameters in our model. To perform the hydrodynamic evolution, we also have to provide the initial conditions (IC) and the equation of state (EoS).

When the mean free path becomes of the order of the system size, the hydrodynamic model is no longer valid and the particles decouple by traveling in straight line to the detector. Here, we employ the freeze-out framework [7] to calculate the decoupling by using the Cooper-Frye formula [8]

$$\frac{1}{2\pi}\frac{dN}{p_{\mathrm{T}}dp_{\mathrm{T}}dyd\phi} = \int_{\Sigma} d\Sigma_{\mu}p^{\mu}f(p_{\mu}u^{\mu}), \tag{5}$$

where N is the number of particles, p_{T} the transverse momentum, y the rapidity, ϕ the azimuthal angle, p^{μ} the four-momenta and $d\Sigma_{\mu}$ is the normal vector to the freeze-out surface. The distribution function is given by $f = f_0 + \delta f_\pi + \delta f_\Pi$, where f_0 is equilibrium distribution function [7]; δf_π and δf_Π are the corrections for shear and bulk viscosities, respectively [3].

3. Numerical Results

We used IC generated by T$_{\mathrm{R}}$ENTo [9]. The hydrodynamic equations were solved by using vHLLE [4] with the s95p EoS [10], and the decoupling calculated by using THERMINATOR2 [7]. We perform simulations for ideal fluids and different scenarios of viscous fluids. In viscous simulations we consider η/s constant in all the hydrodynamical evolution and ζ/s constant in the hadron gas phase and zero in the QGP phase [3].

3.1. Elliptic Flow

The collective behavior of the system formed in heavy ion collisions is described by the anisotropic flow [11], where the initial spacial anisotropy is reflected in the final state of particles. In order to calculate the anisotropic flow, we rewrite the azimuthal part in equation (5) using a Fourier tranform as

$$\frac{dN}{d\phi} = 1 + 2\sum_{n=0}^{\infty} v_n \cos\left(\phi - \psi_{\mathrm{R}}\right), \tag{6}$$

where v_n are the Fourier components and ψ_{R} is the reaction plane angle. Here, we calculated the second Fourier component (v_2), called elliptic flow, using the event plane method [12]. Figure 1 shows the p_{T} dependence of v_2 compared with data. The result for ideal hydrodynamics is shown in red line, the blue line is for viscous hydrodynamics with $\eta/s = 0.08$ and $\zeta/s = 0.04$, magenta line is for $\eta/s = \zeta/s = 0.08$, green line is for $\eta/s = 0.16$ and $\zeta/s = 0.04$, and black squares are experimental data. We see that the ideal hydrodynamics can describe the data for $p_T < 1$ GeV. However, for describing the data for higher values of p_T one has to include shear effects. Also, we can see that the bulk viscosity has no significant effects on v_2.

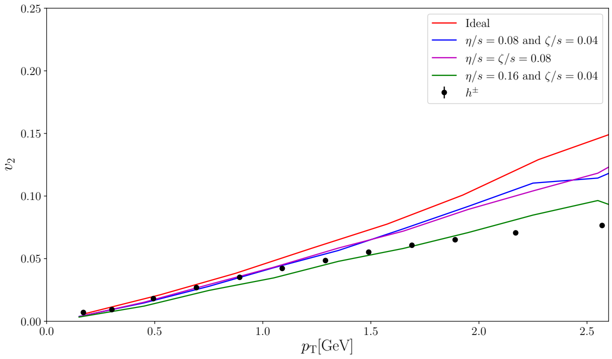

Figure 1. p_T dependence of v_2 for charged hadrons in central Au+Au collisions at 200 GeV. Comparison of ideal hydrodynamics and different viscous scenarios. Data from STAR collaboration [13]
.

3.2. HBT Interferometry

The HBT effect [15] allows measuring the space-time dimensions of the interacting region, at freeze-out, in a high energy collision. To calculate the so-called HBT radii, we used the correlation function defined, for a pair of pions with momentum p_1 and p_2, as

$$\mathcal{C}(p_1, p_2) = \frac{\mathcal{P}_2(p_1, p_2)}{\mathcal{P}_1(p_1)\mathcal{P}_1(p_2)}, \tag{7}$$

where $\mathcal{P}_2$ is the probability of detection of both particles simultaneously and $\mathcal{P}_1$ is the probability of detection of each particle individualy. We calculated the equation (7) using the Monte Carlo approach implemented in THERMINATOR2 by using the Berstch-Pratt coordinates [14]. The *long* coordinate is defined along the beam direction; the *out* coordinate is parallel to the average transverse momentum of the pair ($\vec{K}_\mathrm{T} = (\vec{p}_1 + \vec{p}_2)/2$) and the *side* coordinate is orthogonal to both *long* and *out*. We fitted the correlation function using a Gaussian function

$$\mathcal{C} = 1 + \lambda \exp\left\{-R^2_{out}q^2_{out} - R^2_{side}q^2_{side} - R^2_{long}q^2_{long}\right\}, \tag{8}$$

where $q = p_1 - p_2$ is the relative four-momentum of the pair in *out*, *side* and *long* directions and λ is the chaoticity parameter. Figure 2 shows K_T dependence of R_{out}, R_{side}, R_{long} and R_{out}/R_{side} for hydrodynamic simulations compared with data. The red-dashed line is the result for ideal hydrodynamics; the blue-dashed line is for viscous hydrodynamics with $\eta/s = 0.08$ and $\zeta/s = 0.04$; the magenta-dashed line is for $\eta/s = \zeta/s = 0.08$; the green-dashed line from $\eta/s = 0.16$ and $\zeta/s = 0.04$; black squares are experimental data. Although our results fail to reproduce the experimental data for R_{out}, R_{side}, and R_{long}, we can see no influence of bulk viscosity in HBT radii, analogously to v_2 results. We also have a better agreement with data for R_{out}/R_{side} when we increase the shear coeficient η/s.

4. Conclusions and Perspectives

In summary, we have used the hydrodynamic model in 2+1 dimensions for both ideal and viscous cases to calculate v_2 and HBT radii. We have shown that the effect of bulk viscosity is to small for both observables in central collisions. However, the inclusion of shear viscosity brings a better agreement with data for v_2 in higher p_T and for the ratio R_{out}/R_{side}. A more detailed study about the influence of dissipative effects can be found in [17]. Some improvements to this work can be made in the future: it includes hydrodynamic simulations in 3+1 dimensions, event-by-event initial conditions, viscous dependence on temperature.

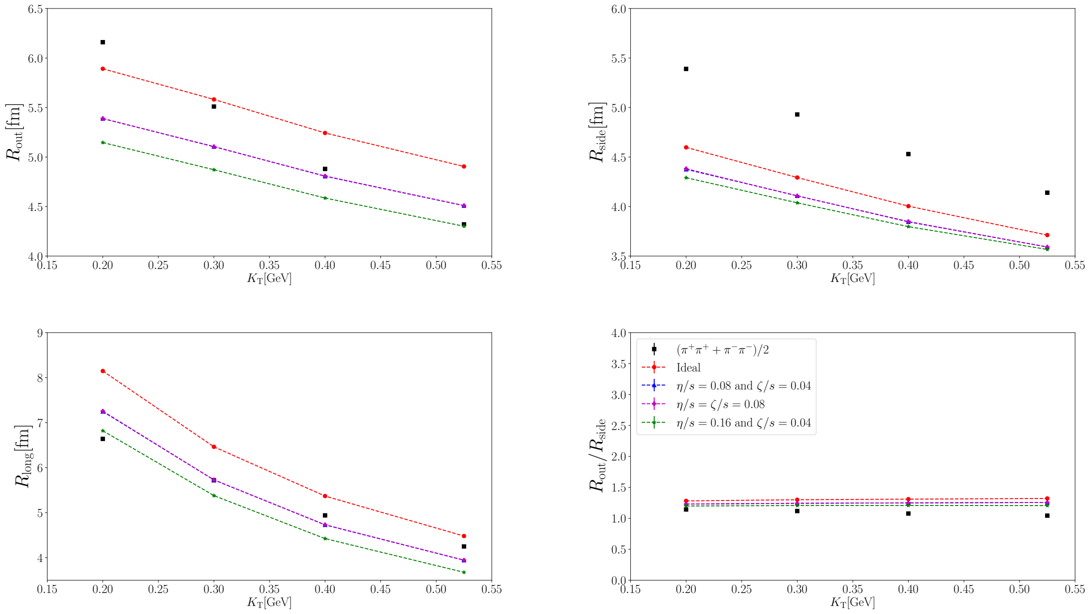

Figure 2. K_{T} dependence of HBT radii for charged pions in the Bertsch-Pratt system R_{out} (top left), R_{side} (top right), R_{long} (bottow left) and the ratio R_{out}/R_{side} (bottow right) for central Au+Au collisions at 200 GeV. Data from STAR collaboration [16].

5. Acknowledgments

This material is based upon work supported by the São Paulo Research Foundation (FAPESP) under Grant No. 2017/02675-6. This work was partially supported by CAPES (Brazilian research funding agency). This research was supported by computional resources supplied by the Center for Scientific Computing (NCC/GridUNESP) of the São Paulo State University (UNESP). DSL acknowledges the financial support by IFT/UNESP for participating in the XLI Brazilian Meeting on Nuclear Physics.

References

[1] Ludlam T and Aronson S 2005 Hunting the quark gluon plasma *BNL-73847-2005*.
[2] Hama Y, Kodama T and Socolowski Jr O 2005 *Braz. J. Phys.* **35** 24; Andrade R P G, Grassi F, Hama Y and Qian W L 2011 *Nucl. Phys.* A **854** 81; Noronha-Hostler J, Denicol G S, Noronha J, Andrade R P G and Grassi F 2013 *Phys. Rev.* C **88** 044916.
[3] Bozek P 2012 *Phys. Rev.* C **85** 034901.
[4] Karpenko Iu, Huovinen P and Bleicher M 2014 *Comp. Phys. Commun.* **185** 3016.
[5] Landau L D and Lifshitz E M 1987 Fluid Mechanics *Butterworth-Heinemann Ltd.*
[6] Israel W 1976 *Annals Phys.* **100** 310; Israel W and Stewart J M 1979 *Annals Phys.* **118** 341.
[7] Chojnacki M, Kisiel A, Florkowski W and Broniowski W 2012 *Comput. Phys. Commun.* **183** 746.
[8] Cooper F and Frye G 1974 *Phys. Rev.* D **10** 186;
[9] Moreland J S, Bernhard J E and Bass S A 2015 *Phys. Rev.* C **92** 011901.
[10] Huovinen P and Petreczky P 2010 *Nucl. Phys.* A **837** 26.
[11] Ollitrault J Y 1992 *Phys. Rev.* D **46** 229.
[12] Poskanzer A M and Voloshin S A 1998 *Phys. Rev.* C **58** 1671.
[13] STAR Collaboration 2005 *Phys. Rev.* C **72** 014904.
[14] Bertsch G F 1989 *Nucl. Phys.* A **498** 173C.
[15] Hanbury Brown R and Twiss R Q 1958 *Nature* **178** 4541; Padula Sandra S 2005 *Braz. J. Phys.* **35** 25;
[16] STAR Collaboration 2005 *Phys. Rev.* C **71** 044906.
[17] Lemos D S 2017 Efeitos da Hidrodinâmica Dissipativa e da Equação de Estado sobre o Fluxo Elíptico e a Interferometria HBT *Masters dissertation* FURG.

XLI Brazilian Meeting on Nuclear Physics (RTFNB) IOP Publishing
IOP Conf. Series: Journal of Physics: Conf. Series **1291** (2019) 012034 doi:10.1088/1742-6596/1291/1/012034

Geometry and multiplicity in high energy collisions of d-Au

K J C Gonçalves[1], **D G Torrieri**[1] **and R A de Souza**[1]
[1]Depto de Raios Cósmicos e Cronologia, DRCC/IFGW
E-mail: `kaymang@ifi.unicamp.br`

Abstract. In characterizing the strongly coupled QCD system produced in nuclear collisions an important uncertainity is the initial state, in particular the role of nuclear and subnuclear scale fluctuations in small systems. In this regard, the d-Au collision is a potentially unique probe since the deuterium nucleus contains only two nuclei, allowing potentially to separate nucleonic and sub-nucleonic dynamics from multiplicity cuts. We investigate this possibility via the PHOBOS Glauber Monte Carlo program. We calculate geometric quantities of the initial state of an ultra-relativistic collision between a deuterium and a gold nucleus , and systematically examine the relationship between geometry and experimental observables.

1. Introduction

Asymmetric collisions have a large fluctuation in the geometry of the initial conditions, thus providing a field of study where we can more accurately analyze their possible influences on the quantities observed with the number of charged particles produced. More specifically we have that in d-Au collisions we can separate classes of events with a nucleon of deuterium and two nucleons to study its probable influences in the observables.

2. The Glauber Monte Carlo Model

In Glauber's model the following assumptions are made: highly energetic ones are not deflected, in this way, they have a linear trajectory. The movement of the nucleons are independent of the nuclei. The total cross section is given in terms of the nucleon-nucleon cross section. The first step of the Glauber Monte Carlo Model is to prepare two nuclei randomly defining the position of the nucleons in each nucleus. The position of each nucleon in the transverse plane is determined by the probability density function as two parameters. The second step is to simulate the nuclear collision, where the impact parameter $\hat{\mathbf{b}}$ is randomly selected from the geometric distribution $\frac{d\sigma}{db} = 2\pi b$ [1]. It is assumed that two nucleons of different nuclei collided when the transverse distance is smaller than the "ball diameter" defined as $D = \sqrt{\sigma_{NN}/\pi}$ [2] where the σ_{NN} is the cross section.

3. Geometric Quantities

The geometric quantities are determined through many nucleon-nucleon collisions. Below we have the following geometric quantities produced in a collision of $\sqrt{s_{nn}} = 200$ GeV between deuterium and gold.

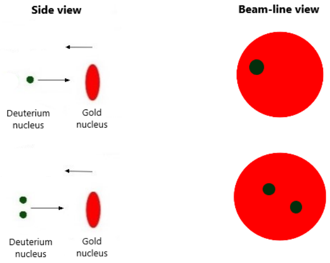

Figure 1. The figure above depicts the two types of events during the various collisions between d and Au.

The image above represents events with only one nucleon of deuterium as participant and with two nucleons of deuterium as participants. With this we can exemplify how through the d-Au collision we have two very different geometries.

Below is a graph that relates the N_{part}, is defined as the number of nucleons of different nuclei that have made at least one collision, to the distance between the nucleons of deuterium.

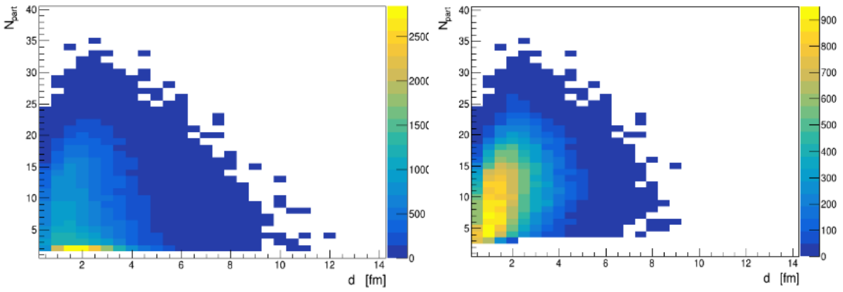

Figure 2. The figure on the right lists the number of participants with the distance between deuterium nucleons for all events and the second with the restriction that the two deuterium nucleons are always participants.

This relation to the components of the positions of the nucleus of deuterium with respect to the plane $x - y$ can best be understood from the figure below.

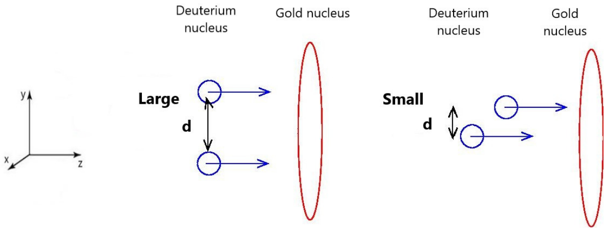

Figure 3. The figure above represents a schematic view of a d-Au collision and the possible arrangements of the deuterium nucleons.

In the figure 2, we see a clear correlation between the N_{part} and the distance between the nucleons, d, for events with two nucleons of deuterium as participants. This happens because depending on the configuration of the nucleons we will have a greater or smaller number of participants.

We can also determine the eccentricity of the participant plane from the MC Glauber model and we can include fluctuations in the shape of nucleon known as Glauber-Gribov fluctuations.

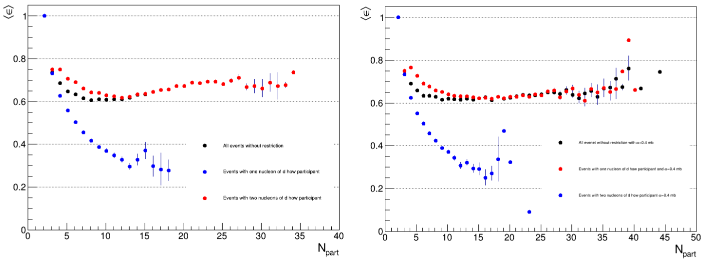

Figure 4. The graph above compares the eccentricities of the participant plane produced in a collision d-Au with one and two nucleons of deuterium as participant.

The graph above compares the eccentricities produced for a collision that has as participant only one nucleon of deuterium, represented by the blue plot, with events with two nucleons of deuterium as participants, represented by the red plot, and events without any restriction of number of deuterium nucleons as participants, represented by the black plot. The left plot was made using the MC Glauber model and the right plot using Glauber-Gribov fluctuations. From these graphs, we can see that classes of events with one nucleon of deuterium and two nucleons of deuterium have differents eccentricities of the participant plane and, therefore, differents geometric quantities. Thus we can study these classes separately and their influences in the observables, as for example the number charged particles.

4. Particle Production

We can use N_{coll}, that is defined as the number of binary nucleon-nucleon collisions, and N_{part} to determine the number of charged particles generated after interaction. These two values are incorporated into the model by the following $P(\mu, \kappa, n) \times N_{ancs}$ where $N_{ancs} = fN_{part} + (1-f)N_{coll}$ refers to the number of ancestors, f is a parameter and $P(\mu, \kappa, n)$ is the negative binomial distribution with n being the number of collisions per ancestor, μ the mean multiplicity and k controlling the width of the distribution

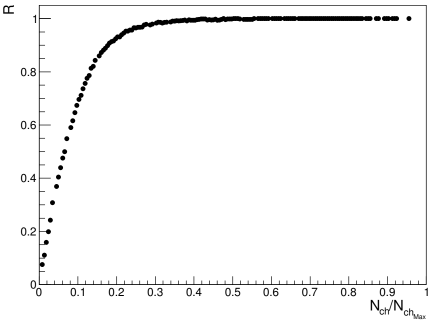

Figure 5. The histogram represents the fraction of events that generate charged particles and that have two nucleons of deuterium as participants.

We note that events with two nucleons of deuterium as participants are the ones that produce the largest amount of charged particles and, thus, events with only one nucleon deuterium produce a smaller amount of particles. The next step of this work is the comparison between simulations results and experimental data. We, for this, can utilize cuts of multiplicity using the zero degree calorimeter, where these measurements can be used to separate events with two nucleons of deuterium as participant.

5. Concluding Remarks

Collisions between deuterium and gold are important because we can separate classes of events with different geometries, for example, events with a nucleon of deuterium as participants and two nucleons of deuterium. In this way, we can verify theoretical models that depend on geometry.

6. References

[1] Miller M L et al 2007 Glauber Modeling in High-Energy Nuclear Collisions *Ann. Rev. Nucl. Part. Sci.* **57** p 205-243

[2] Loizides C, Nagle J and Steinberg P 2015 Improved version of the Phobos Glauber Monte Carlo *Elsevier BV* p 13-18

[3] Adam J et al 2016 Anisotropic Flow of Charged Particles in Pb-Pb Collisions at $\sqrt{s_{NN}}$=5.02 TeV. *Phys. Rev. Lett* **116** p 1-16

[4] Aamodt K et al 2011 Centrality Dependence of the Charged-Particle Multiplicity Density at Midrapidity in Pb-Pb Collisions at $\sqrt{s_{NN}} = 2.76$ TeV. *Phys. Rev. Lett* **106** p 1-10

[5] Broniwski W and Arriola E R 2014 Signatures of a Clustering in Light Nuclei from Relativistic Nuclear Collisions *Phys. Rev. Lett* **112** p 1-5

[6] Qin G and Mller B 2014 Elliptic and triangular flow anisotropy in deuteron-gold collisions at $\sqrt{s_{NN}}$ =200GeV at RHIC and in proton-lead collisions at $\sqrt{s_{NN}}$=5.02TeV at the LHC *Phys. Rev. Lett C.* **89** p 1-7

[7] Grosse O, Jan F and Reygers K 2010 Charged-particle multiplicity in proton–proton collisions *J. Phys. G.* **37** p 1-50

[8] Loizides C 2016 Glauber modeling of high-energy nuclear collisions at the subnucleon level *Phys. Rev. Lett C.* **94** p 1-12

[9] Nagle J L and Zajc W A 2018 Small System Collectivity in Relativistic Hadron and Nuclear Collisions *Ann. Rev.* p 1-36

[10] Adler S S et al 2008 Centrality dependence of charged hadron productionin deuteron+gold and nucleon+gold collisions at $\sqrt{s_{NN}}$= 200 GeV *Phys. Rev. Lett C.* **77** p 1-15

[11] Luzum M and Petersen H 2014 Initial State Fluctuations and Final StateCorrelations in Relativistic Heavy-Ion Collisions *J. Phys. G* **41** p 1-50

[12] Pruneau C Gavin S and Voloshin S 2002 Methods for the Study of Particle Production Fluctuations *Phys. Rev. Lett C.* **66** p 1-12

[13] Alver B et al 2007 The Importance of Correlations and Fluctuations on the Initial Source Eccentricity in High-Energy Nucleus-Nucleus Collisions *Phys. Rev. Lett C.* **77** p 1-18

[14] Bozek A 2012 Collective flow in p-Pb and d-Pb collisions at TeV energies *Phys. Rev. Lett C.* **77** p 1-10

[15] Qin G Y Mller B 2014 Elliptic and triangular flow anisotropy in deuteron-gold collisions at RHIC and proton-lead collisions at the LHC *Phys. Rev. Lett C.* **89** p 1-7

XLI Brazilian Meeting on Nuclear Physics (RTFNB) IOP Publishing
IOP Conf. Series: Journal of Physics: Conf. Series **1291** (2019) 012035 doi:10.1088/1742-6596/1291/1/012035

Standard Reference for Zero Temperature from Quantum Supersymmetry is Possible?

C Marques[1] **G S Dias**[1] **and H H Chavez Sanchez**[2]
[1]Instituto Federal do Espírito Santo-Grupo de Física Teórica e Aplicada-IFES/GFTA
Av. Vitória 1729, Jucutuquara, Vitória, ES, Brazil, CEP 29040-780
[2]UCL-Faculdade do Centro Leste, Rodovia ES 010, Km 6
BR 101, Serra-ES, Brazil

E-mail: `cmarques@ifes.edu.br`, `gilmar@ifes.edu.br`, `helderch@hotmail.com`

Abstract. Supersymmetry at a susy harmonic oscillator, $H(\omega_1, \omega_1)$, can be broken or restored in certain conditions and parameters, that are linked with thermal interaction and with a polynomial interactions of creation and annihilation operators. All possibles supersymmetric harmonic oscillators represented by a point (ω_1, ω_1) in the frequency space of the system, are in a two dimensional surface parametrized by the (ω_2, α_2), which we call s-surface, where α_2 is the interaction parameter. The temperature in the s-surface are intended to be zero. Interaction with the thermal bath represented by the tilde Hilbert space from the doubling Hilbert space, establishes thermal oscillations that push the system from the s-surface. In such a way we can define the set of all supersymmetric harmonic oscillator or in a equivalent way the s-surface as a global standard reference for zero temperature.

1. Introduction

Supersymmetry can be broken due thermal effects or due some interactions, as we demonstrated in the work: supersymmetry breaking at finite temperature in a SUSY harmonic oscillator with Interaction ref[1]. The statistical average of the Hamiltonian at finite positive temperature is not zero. So, considering this referred SUSY model, it is possible to define a s-surface, parameterized with two parameters, that maps all supersymmetric harmonic oscillators.

Although there are some controversies in the literature, refs [2], [3], [4], [5], [6] and [7], of whether supersymmetry is broken at finite temperature, in this paper we follow the viewpoint that supersymmetry (SUSY) is broken at positive temperature even when unbroken at $T = 0$, ref[2]; an example is the supersymmetric harmonic oscillator, that exists only in $T = 0$, as we can see by the ref [1]. We will consider this model here to define the s-surface.

2. zero temperature and the s-surface

Despite of the controversy question about Lorentz transformations of thermodynamic quantities [9, 10, 11], there is agreement that zero temperature is a Lorentz invariant. Also is invariant the condition to break the supersymmetry in the SUSY harmonic oscillator, or in an equivalent way, the condition of belonging in the s-surface; Which means that the bosonic frequency ω_b and fermionic frequencies ω_f can change by Lorentz transformation, but the equality $\omega_b = \omega_f$ remains, it is invariant. In such a way the set of all supersymmetric harmonic oscillators, or in an equivalent way, the s-surface, we define as a standard reference for zero temperature for all Lorentz referential. Each point P over the s-surface represents a supersymmetric harmonic oscillator (ω_1, ω_1), whose temperature is zero. The SUSY harmonic oscillator can be pushed out of s-surface, $(\omega_1, \omega_1) => (\omega_1, \omega_2)$ due to thermal fluctuations or by some polynomial interactions of creation and annihilation operators. Through similar interaction it is possible to move back the system to the s-surface (ω_3, ω_3) by a convenient choice of parameters; revealing an interesting magneto caloric effect at the supersymmetric harmonic oscillator.

3. The s-surface solution

The s-surface follow directly from the condition over $H = H_0 + H_{int}$ where
$\mathrm{H}_0 = \omega_1 a^\dagger a + \omega_2 b^\dagger b$, and

$$H_{int} = \alpha a^\dagger b^\dagger b - \alpha a b^\dagger b. \tag{1}$$

where $a^\dagger$ and $b^\dagger$ are respectively the bosonic and fermionic creation operators and the dual a and b, are respectively the annihilation operators. Though H is a supersymmetric oscillator for some parameter α, defined by $(\alpha)^2 = \omega_2\omega_1 - (\omega_1)^2$. H_0 is not a supersymmetric harmonic oscillator due to the fact that $\omega_1 \neq \omega_2$.

From H with no constrain in the parameter α, after we perform the Bogoliubov transformation ref[1],

$$\begin{aligned} a_2 &= a + \frac{\alpha}{\omega_1} b^\dagger b; & a_2^\dagger &= a^\dagger + \frac{\alpha}{\omega_1} b^\dagger b; \\ b_2 &= (\exp[\frac{\alpha}{\omega_1}(a^\dagger - a)])b; & b_2^\dagger &= b^\dagger(\exp[\frac{\alpha}{\omega_1}(a - a^\dagger)]). \end{aligned} \tag{2}$$

that preserves the algebra,
$\mathrm{a}^\dagger \wedge a = -1/2$; $a^\dagger \bullet a = n_b + 1/2$
$b^\dagger \bullet b = 1/2$; $b^\dagger \wedge b = n_f - 1/2$
$n_b \in N$ and $n_f \in \{0, 1\}$.
we obtain the harmonic oscillator with the bosonic and fermionic frequencies ω_1 and ω_3, respectively.

$$H = \omega_1 a^\dagger a + \omega_3 b^\dagger b \tag{3}$$

The condition to be supersymmetric harmonic oscillator is $\omega_3 = \omega_1$, leading the solution bellow that define the s-surface,

$$\omega_{1\pm} = \frac{1}{2}(\omega_2 \pm (\omega_2^2 - 4\alpha^2)^{1/2});$$

This summarize that supersymmetry can be broken or restored through some definition of parameters, from a polynomial interaction that could be a external magnetic field.

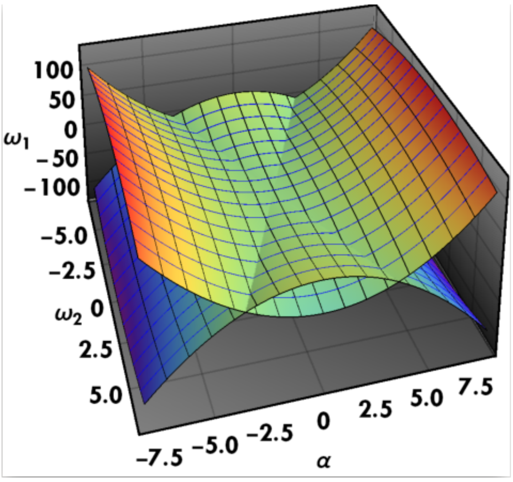

Figure 1. S- Surface showing the parameters which is consistent to unbroken SUSY($T = 0$K).

4. Susy Harmonic Oscillator at Finite Temperature by Thermo field Dynamics - TFD

To introduce the temperature following the algorithm of TFD, we double the Hilbert space ref[1], writing the generator of time translation by: $\hat{H} = \omega_1(a^\dagger a + b^\dagger b) - \omega_1(\widetilde{a}^\dagger \widetilde{a} + \widetilde{b}^\dagger \widetilde{b})$That allows us to calculate the thermal vacuum and then the statistical average of any operator in the thermal vacuum, in particular the Hamiltonian operator of the supersymmetric oscillator with interaction. The unitary transformation that leads the vacuum to the thermal vacuum and any operator to a thermal operator preserving the algebra in eq. in (3), is also called Bogoliubov transformation, $\mathrm{A}(\beta) = e^{-iG} A(0) e^{iG}$, $|0(\beta)\rangle = e^{-iG}|0\rangle$, where $G = -i\theta(\beta)(\widetilde{b}b - b^\dagger \widetilde{b}^\dagger) - i\theta(\beta)(\widetilde{a}a - a^\dagger \widetilde{a}^\dagger)$, is the generator of the Bogoliubov transformation, and $\beta = 1/\kappa T$, κ is the Boltzmann constant. with $\tan\theta(\beta) = e^{-\beta\omega_1/2}$.

The thermal energy of the thermal vacuum is given by $\mathrm{E}_0(\beta) = \langle 0(\beta)|\omega_1 a_2^\dagger a_2 + \omega_1 b_2^\dagger b_2|0(\beta)\rangle =$

$$\omega_1 \left(\frac{e^{-\beta\omega_1}}{1 - e^{-\beta\omega_1}} + \frac{e^{-\beta\omega_1}}{1 + e^{-\beta\omega_1}} \right). \tag{4}$$

This shows that the supersymmetric is broken at $T > 0$, Fig.2.

5. Conclusion

Supersymmetry is broken when temperature is introduced in the model, we try to use an interaction to restore the supersymmetry but it is possible only in some parts of the ensemble not in the whole ensemble. Although the fermionic and bosonic quantum corrections in a supersymmetric theory tend to cancel, the thermal effects are additive and the thermal energies are positive. Leading to non-zero statistical average of the Hamiltonian at finite temperature. All possibles supersymmetric harmonic oscillators represented by a point (ω_1, ω_1) in the frequency space of the system, are in a two dimensional surface, which we call s-surface. The temperature in the s-surface are intended to be zero. Interaction with the thermal bath represented by

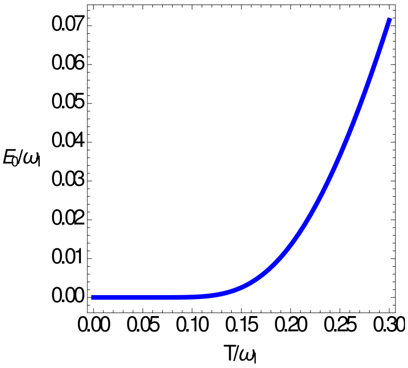

Figure 2. Plot of the vacuum energy E_0/ω_1, as function of T/ω_1.Taken from [1].

the tilde Hilbert space from the doubling Hilbert space, establishes thermal oscillations that push the system from the s-surface. Zero temperature is Lorentz invariant, which implies that supersymmetric Harmonic Oscillator and the s-surface is also Lorentz invariant. In such a way we can define the supersymmetric harmonic oscillator or in an equivalent way, the s-surface as a standard reference for zero temperature for all Lorentz referential. At $T \neq 0$ the supersymmetry is broken, and now we have a bosonic and fermionic oscillator model with the respective frequency (ω_1, ω_2). The susy harmonic oscillator was pushed out of the s-surface due to thermal fluctuations.

Another possible and interesting application of this model are the study of the break of symmetries perceived by the wave function of the valence neutron field, specially in some conditions like those appointed at the work Searching Neutrino-Nucleus interaction in Mössbauer Spectroscopy [12].

ACKNOWLEDGEMENTS

Professor Gilmar De Souza Dias is grateful to the University of Alberta, Canada for the office and other facilities, when he was visiting at UAlberta, when interesting works were made and interesting ideas were developed. This work started that time.

References

[1] Marques C et al 2018 Supersymmetry Breaking at Finite Temperature in a Susy Harmonic Oscillator with Inter- action. In: 14th International Workshop on Hadron Physics (Hadron Physics 2018) Florianopolis Santa Catarina Brazil March 18-23 2018
[2] Girardello L and Grisaru M T 1982 Soft breaking of supersymmetry Nuclear Physics B 1941 65-76
[3] Van Hove L C P 1982 Supersymmetry and positive temperature for simple systems Nuclear Physics B 207CERN-TH-3280 15-28
[4] Das A and Kaku M 1978 Supersymmetry at high temperatures Physical Review D 18 12 4540
[5] Teshima K 1983 Supersymmetry at finite temperatures Physics Letters B 123 3-4 226-230
[6] Umezawa H et al 1982 Thermo Field Dynamics North-Holland, Amsterdam
[7] Umezawa H 1995 Advanced field theory: Micro macro and thermal physics AIP
[8] Raghunathan K and Santhanam T S 1986 Supersymmetric oscillator and the phase problem Physical Review D 33 12 3790
[9] Schwartz H M 1977 Einsteins comprehensive 1907 essay on relativity part I American Journal of Physics 45 6 512-517

[10] Landsberg P T 1967 Does a Moving Body Appear Cool? Nature 214 5091 903
[11] Farias C et al 2017 What is the temperature of a moving body? Scientific reports 7 1 17657
[12] Marques C et al 2018 Searching evidences of Neutrino-Nucleus Coherent Scattering with M ossbauer Spectroscopy In: 14th International Workshop on Hadron Physics Hadron Physics 2018 Florianpolis Santa Catarina Brazil March 18-23 2018 arXiv:1804 05930

XLI Brazilian Meeting on Nuclear Physics (RTFNB) IOP Publishing
IOP Conf. Series: Journal of Physics: Conf. Series **1291** (2019) 012036 doi:10.1088/1742-6596/1291/1/012036

A Monte Carlo model of deuteron emission in pre-equilibrium nuclear reactions

E A Teixeira and B V Carlson

Dep. de Física, Instituto Tecnológico de Aeronáutica, São José dos Campos, SP, Brazil

E-mail: `estevao@ita.br`

Abstract. Nucleon-induced pre-equilibrium reactions are important in many applications of nuclear physics. About 20% of the particles emitted in such reactions are composites, such as deuterons and alpha particles. Deuterons are produced through emission from the compound nucleus, as well as through two important direct reaction mechanisms - “pick-up” and coalescence. Iwamoto and Harada developed a semi-classical pre-equilibrium model that describes both direct mechanisms as a generalization of coalescence. We have implemented the Iwamato and Harada unified model of deuteron emission in Blann and Chadwick’s hybrid Monte Carlo model. This implementation was made in order to analyse data of reactions of the type (p,d), that is, proton induced reactions having deuterons as emitted particles, but our previous results were not satisfactory. In order to find a new approach for the deuteron emission, we are investigating an eikonal approximation to the phase space of Iwamoto and Harada model. We are also comparing our angular distributions with the experimental ones using DWUCK4. Nevertheless, our results are not satisfactory yet and our work is under development.

1. Introduction

Nucleon-induced pre-equilibrium reactions are important in the description and modeling of fast reactors, accelerator-driven systems (ADS) and radiotherapy with particle beams. The exciton model of pre-equilibrium reactions assumes the excitation of a chain of particle-hole states of the pre-compound nucleus that results from the fusion of the incident particle with the target (two particles and one hole, three particles and two holes, etc.) [1]. To estimate emission from the stage of n+1 particles and n holes, it assumes that each state of this kind is equally probable. However, Bisplinghoff demonstrated that in general this hypothesis is satisfied only for the initial configuration of two particles and one hole states [2].

With the goal of defining a pre-equilibrium reactions model without this defect, Blann developed a model called the “hybrid Monte Carlo” model (HMS), which takes into account the chain of particles and holes states of the exciton model through independent excitations of two particles and one hole [3, 4]. A detailed comparison between both models shows that while the exciton model assumes that the interaction between the configuration of n+1 particle and n hole states is so strong that these reach equilibrium before making another transition, the “hybrid Monte Carlo” model neglects any interaction between the particle - hole states of each configuration. Obviously, the physical case should lie between these two extremes.

About 20% of the pre-equilibrium emissions in these reactions correspond to composite particles, such as deuterons and alpha particles. An important reaction mechanism for the production of deuterons is "pick-up", in which an incident nucleon takes another nucleon from the target nucleus. Another pre-equilibrium deuteron production mechanism is coalescence [5, 6, 7], in which a deuteron is formed from two fast nucleons that are emitted close to one another in phase-space. In the context of the exciton model of pre-equilibrium reactions, Iwamoto and Harada developed a model that unifies these two mechanism of deuteron emission [8, 9, 10].

2. Iwamoto and Harada unified model

We started with the model proposed in Ref. [9], in which deuteron formation is represented by a quasi-classical phase space factor. As we were trying to reproduce their results, we found some inconsistencies in their calculations. With that, we tried to improve this model by making the necessary adjustments to implement it in Blann and Chadwick's model, [4]. This implementation would allow us to obtain more realistic results in pre-equilibrium nuclear reactions.

Even with the treatment of the inconsistencies in the Iwamoto and Harada model, our results were not satisfactory. Our values did not fit with the experimental values and the results of the deuteron formation mechanisms did not follow the same pattern as the experimental data. As an example, our ratio of the deuteron pick-up partial emission widths and proton partial emission widths decreased with the increase of the target mass while the experimental data kept the same ratio.

3. Eikonal phase space

We decided to investigate an alternative approximation to the phase space as a way to improve our last results. With that, we have begun to investigate an eikonal phase space.

To begin, we calculate the one-step distorted-wave Born approximation (DWBA) amplitude of a proton-induced (p,d) reaction in the following way:

$$\langle \vec{K}_d; h|T^{(1)}|\vec{K}_p\rangle = \int d^3r_d \int d^3r_p \phi_d^\dagger \psi_d^{\dagger(-)} V(\vec{r}_d - \vec{r}_p)\phi_n \psi_p^{(+)}, \tag{1}$$

where $\psi_d^{(-)}$ is the outgoing deuteron wave function and $\psi_p^{(+)}$ is the incoming proton wave function. Both of these include the information of the plane wave plus the spherical wave that reach the detector. ϕ_n is the neutron wave function and ϕ_d is the internal wave function of the deuteron.

4. Preliminary results

We started analyzing the differential cross section for the (p, d) reaction on ^{40}Ca in the $1d3/2$ ground-state. However, our simulations did not achieve the same pattern as the experimental data [13].

In order to see why the differential angular cross section did not fit with the experimental data, we searched for the cause of the difference between the results. At first, we tested the $t\rho$ potential against the optical potential that Ref. [13] uses.

In our work, the incident proton is subject to a potential represented by the $t\rho$ approximation,

$$U(\vec{r}) = -\frac{\hbar v}{2}\left[\sigma_{pp}^T(i+\alpha_{pp})\frac{Z}{A} + \sigma_{pn}^T(i+\alpha_{pn})\frac{N}{A}\right]\rho_m(\vec{r}). \tag{2}$$

with $\sigma_{n_1n_2}^T$ being the total cross section and $\alpha_{n_1n_2}$ a scattering phase factor, both energy dependent. $\rho_m(\vec{r})$ is the target density distribution, $v = \hbar k/\mu$, Z and N are the proton and neutron number of the nucleus of mass number $A = Z + N$. We interpolated the values found in Ref. [14] to obtain α and σ.

In Ref [13], a phenomenological optical potential is used. It is given by

$$V(r) = V_C(r_C) - V(e^{x}+1)^{-1} - i\left[W - 4W_D a'\frac{d}{dr}\right](e^{x'}+1)^{-1} + \left[\frac{\hbar c}{m_p c^2}\right]^2 V_{SO}\frac{1}{r}\frac{d}{dr}(e^{x''}+1)^{-1}\sigma I, \quad (3)$$

where $x = (r - R_0)/a_0$, $x' = (r - R')/a'$, $x'' = (r - R'')/a''$, with $R_0 = r_0 A^{1/3}$, etc., and the Coulomb potential V_C is that for a uniformly charged sphere of radius $R_C = r_C A^{1/3}$. W_0 and W_D are the volume and surface parts, respectively, of the imaginary potential, and V_{SO} is the real part of the spin-orbit potential, σ is the projectile spin and I is the orbital angular momentum. The values of the parameters are given in Ref. [13].

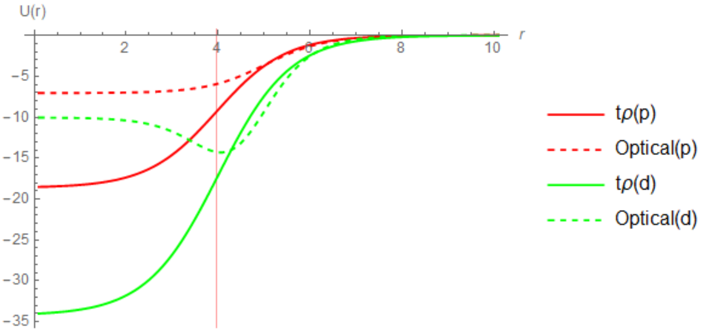

Figure 1. Comparison between the $t\rho$ approximation and the optical potential used in Ref. [13]. The abscissa represents the nucleus radius in fm and the ordinate represents the potential value in MeV. The red vertical line represents the target radius.

In Fig. 1, one can see that our potential is in a good agreement with the optical potential just at large radii but much deeper at smaller radii.

In Ref. [13], the distorted-wave Born approximation (DWBA) code DWUCK (Distorted Wave University of Colorado Kunz) [15] was used to analyze the differential cross section. As we are trying to build our code and using their experimental values as our source, we decided to compare results. In Fig. 2, one can see their experimental values (dots) and our calculations using their values input in DWUCK4 (line). In their work, they used an adiabatic potential for the deuteron channel but we did not include it in our input. It may be what causes the difference between our results, but such a conclusion is preliminary.

As our next step, we expect to conclude our comparison of the optical model potential and the $t\rho$ potential. With that, we expect to have a good idea of how the $t\rho$ approximation should behave in our differential cross section results. This step is important in order to validate the phase space that we are studying. Our hope is to improve the calculations of our model of deuteron emission in pre-equilibrium reaction.

5. Goal and Conclusion

Our ultimate goal is to implement a version of the Iwamoto and Harada model in the DDHMS module of the nuclear reaction code EMPIRE[11] which performs calculations of pre-equilibrium reactions within the HMS model, and then use it to analyze data of reactions of the type (p,d).

As our previous results using Iwamoto and Harada model were not satisfactory, we are analyzing the phase space of the “pick-up” reactions using an eikonal approximation. With that, we hope to get better results and to improve the Iwamoto and Harada model.

As next steps, we will investigate the relation between our transition matrix as function of the energy and of the nucleus radius. Achieving better results, we plan to implement the Iwamato and Harada unified model with our modifications in Blann and Chadwick’s “hybrid Monte Carlo”

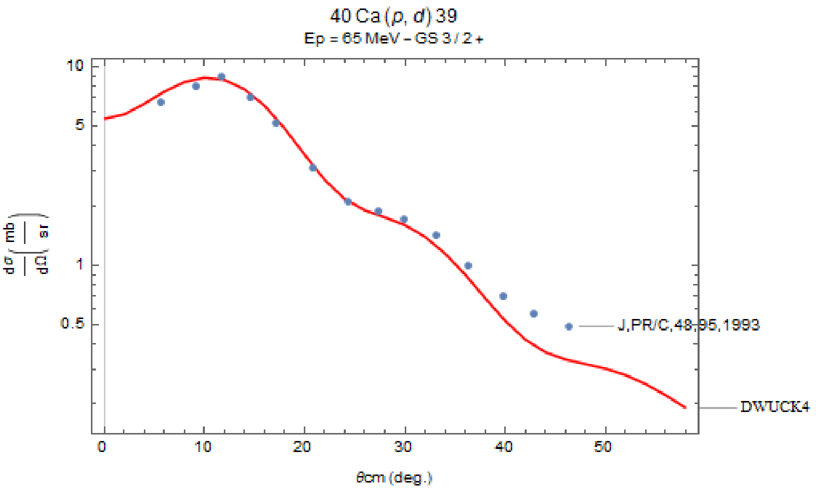

Figure 2. Angular distribution data of cross section for the ground state 3/2+ state in ^{40}Ca(p,d)^{39}Ca. The dots are the experimental values from Ref. [13] and the line are the predictions of the DWBA theory calculated using DWUCK [15].

model, to obtain a more physically-motivated description of pre-equilibrium deuteron emission. Inserting this result in the nuclear reactions code EMPIRE, we hope to improve the analysis of (p,d) reaction data.

Acknowledgments

E. A. Teixeira acknowledges support from the Coordenação de Aperfeiçoamento de Pessoal de Nível Superior - Brasil (CAPES) - Código de Financiamento 001. B. V. Carlson acknowledges support from grant 2017/05660-0 of the São Paulo Research Foundation (FAPESP) and grant 306433/2017-6 of the Brazilian National Council for Scientific and Technological Development (CNPq). The authors acknowledge support from the INCT-FNA project 464898/2014-5.

References

[1] Koning A and Duijvestijn M 2004 *Nucl. Phys.* A **744** (2004) 15.
[2] Bisplinghoff J 1986 *Phys. Rev.* C **33** 1569.
[3] Blann M 1996 *Phys. Rev.* C **54** 1341.
[4] Blann M and Chadwick M 1997 *Phys. Rev.* C **57** 233.
[5] Butler S and Pearson C 1961 *Phys. Rev. Lett.* **7** 69; 1963 *Phys. Rev* **129**, 836.
[6] Schwarzschild A and Zupancic C 1963 *Phys. Rev.* **129** 854.
[7] Nagle J, Kumar B, Kusnezov D, Sorge H and Mattiello R 1996 *Phys. Rev.* C **53** 367.
[8] Iwamoto A and Harada E 1982 *Phys. Rev.* C **26** 1821.
[9] Sato K, Iwamoto A and Harada E 1983 *Phys. Rev.* C **28** 1527.
[10] Konoboeyev A and Korovin Y 1996 *Kerntechnik* **61** 45.
[11] Herman M et al 2007 *Nucl. Dat. Sheets* **108** 2655.
[12] Hosono K et al 1980 *Nuclear Physics* A **343** p.234-248.
[13] Matoba M et al 1993 *Phys. Rev* C **48** p.95-104.
[14] Bertulani C, Campbell C and Glasmacher T 2003 *Computer Physics Communications* **152** p.317-340.
[15] Kunkz P, Maruhn J and Koonin E 1993 *Computational Nuclear Physics* 2 p.88-107.

α-cluster structure in ^{62,64}Ge described by the local potential approach

M A Souza[1,2], H Miyake[1], T Borello-Lewin[1], C A da Rocha[3,4] and C Frajuca[2]

[1] Instituto de Física, Universidade de São Paulo, Rua do Matão, 1371, CEP 05508-090, Cidade Universitária, São Paulo - SP, Brazil
[2] Departamento de Mecânica, Instituto Federal de Educação, Ciência e Tecnologia de São Paulo - Campus São Paulo, Rua Pedro Vicente, 625, CEP 01109-010, Canindé, São Paulo - SP, Brazil
[3] Departamento de Ciências e Matemática, Instituto Federal de Educação, Ciência e Tecnologia de São Paulo - Campus São Paulo, Rua Pedro Vicente, 625, CEP 01109-010, Canindé, São Paulo - SP, Brazil
[4] Universidade São Judas Tadeu (USJT) - Campus Mooca, Rua Taquari, 546, CEP 03166-000, Mooca, São Paulo - SP, Brazil

E-mail: `marsouza@if.usp.br`

Abstract. The unstable nuclei ^{62}Ge and ^{64}Ge are analyzed in terms of the α + core structure applying a nuclear potential with (1 + Gaussian)×(W.S. + W.S.^{3}) shape. The ground state bands of ^{62}Ge and ^{64}Ge and first negative parity band of ^{64}Ge are calculated and compared with experimental data. The calculated ^{64}Ge ground state band gives a good account of the experimental energies from 0^+ to 8^+ state. The rms intercluster separations and $B(E2)$ transition rates are obtained for the ^{64}Ge ground state band and a discussion is presented.

1. Introduction

The α-cluster model has been applied successfully to nuclei near the doubly closed shells assuming an α + core configuration [1,2]. Previous works [3–5] indicate that the α-cluster model with local potential approach is also adequate to describe the spectroscopic properties of nuclei farther from double shell closures. However, there are many nuclei not studied in this viewpoint yet, particularly in the region between ^{40}Ca and ^{90}Zr. The recent work of Souza and Miyake [4] discusses the α + core structure in ^{46}Cr and ^{54}Cr using the (1 + Gaussian)×(W.S. + W.S.^{3}) nuclear potential shape and a good account of the respective ground state bands and $B(E2)$ transition rates is obtained. The present work aims to apply the same potential shape in Ge isotopes to test its efficiency in different isotopic chains of this mass region.

2. Preferential Ge isotopes for α-clustering

The preferential nuclei for α-clustering were selected applying the same criterium used in previous work [3] focusing the intermediate mass region. The variation of binding energy per nucleon was revealed to be an appropriate quantity to pick the preferential α + core configuration among different nuclei. This value is given by Q_α/A_T, where Q_α is the Q-value for α-separation and A_T is the mass number of the total nucleus. The chain of even-even Ge isotopes is shown

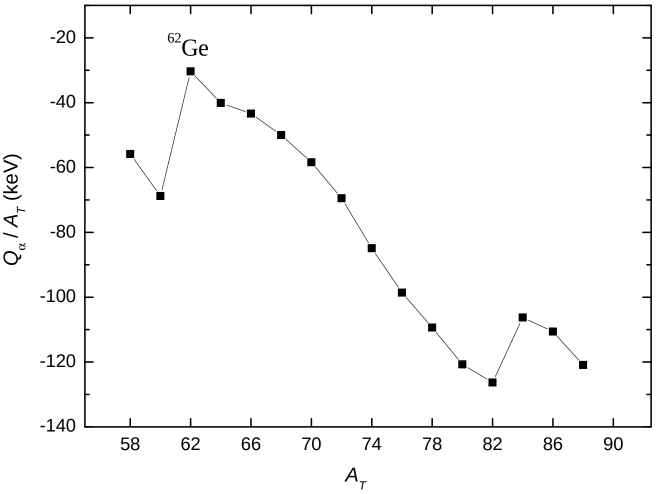

Figure 1. Q_α/A_T values obtained for the α + core decomposition of even-even Ge isotopes as a function of the mass number A_T. The Q_α/A_T maximum corresponding to ^{62}Ge is indicated.

in figure 1 pointing that ^{62}Ge is the preferential nucleus for α-clustering in this set followed by ^{64}Ge, with the second highest Q_α/A_T value.

3. The Model

The α-cluster model regards the total nucleus as an α-particle orbiting an inert core. The ^{62}Ge and ^{64}Ge nuclei are assumed as $\alpha+^{58}$Zn and $\alpha+^{60}$Zn systems, respectively. The α + core potential is the sum

$$V(r) = V_N(r) + V_C(r) \tag{1}$$

of nuclear and Coulomb terms. The Coulomb potential is described by an α-particle interacting with an uniformly charged spherical core of radius R. The nuclear potential is expressed by:

$$V_N(r) = -V_0 \left[1 + \lambda \exp\left(-\frac{r^2}{\sigma^2}\right)\right] \left\{\frac{b}{1+\exp[(r-R)/a]} + \frac{1-b}{\{1+\exp[(r-R)/3a]\}^3}\right\} , \tag{2}$$

where V_0, λ, a, and b are fixed parameters, and R and σ are variable parameters. The description of the ground state bands of the two nuclei is obtained with the fixed values $V_0 = 220$ MeV, $a = 0.65$ fm, $b = 0.3$, and $\lambda = 0.14$, while R and σ are fitted for each nucleus. The employed R and σ values are: $R = 4.621$ fm and $\sigma = 0.366$ fm for ^{62}Ge, and $R = 4.647$ fm and $\sigma = 0.278$ fm for ^{64}Ge. The values of V_0, λ, a, and b were adjusted previously to describe the ground state bands of the nuclei ^{20}Ne, ^{44}Ti, ^{94}Mo, and ^{212}Po, in which the α-cluster structure is recognized in preceding studies [1–3]. The depth V_0 is increased to 241 MeV only for the calculation of the ^{64}Ge negative parity band.

The nucleons of the α-cluster, according to Pauli principle, occupy shell-model orbitals out of the core. This restriction is defined by the global quantum number $G = 2N + L$, where N is the number of internal nodes in the radial wave function and L is the orbital angular momentum. In the case of the $\alpha+^{58}$Zn and $\alpha+^{60}$Zn systems we have $G \geq 12$, where $G = 12$ corresponds to the ground state band. This value is obtained from the Wildermuth condition [6] and yields an appropriate description of the ^{62}Ge and ^{64}Ge ground state bands. The two α + core systems are solved numerically to obtain the properties of the bound and quasi-bound states.

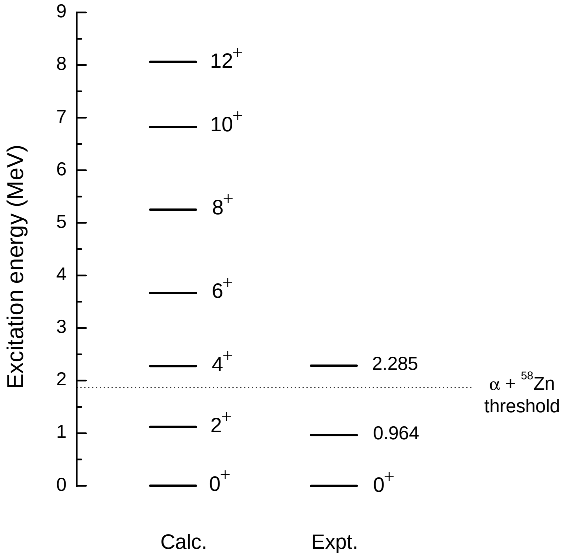

Figure 2. Calculated energy levels for the ground state band ($G = 12$) of the α+^{58}Zn system in comparison with experimental energies of ^{62}Ge [7]. A correspondence of the experimental energy levels 0.964 MeV and 2.285 MeV with the 2^+ and 4^+ states, respectively, is suggested.

Table 1. Calculated rms intercluster separations ($\langle R^2\rangle^{1/2}$) and $B(E2)$ transition rates for the ground state band of ^{64}Ge. The calculated $B(E2)$ values have been obtained without effective charges.

J^π	$\langle R^2\rangle^{1/2}$ (fm)	$B(E2; J \rightarrow J-2)$ (W.u.)
$0^{+\,a}$	4.350	
$2^{+\,a}$	4.354	6.574
$4^{+\,a}$	4.312	8.897
$6^{+\,a}$	4.234	8.542
$8^{+\,a}$	4.136	7.071
$10^{+\,b}$	4.016	
$12^{+\,b}$	3.921	

[a] Properties calculated with use of the experimental energy levels.

[b] Properties calculated with use of the theoretical energy levels.

4. Results and conclusions

The α-cluster model was applied to ^{62}Ge and ^{64}Ge; the energy levels of the ground state band ($G = 12$), in comparison with experimental data [7, 8], are presented in figures 2 and 3. The results show a good description of the ^{64}Ge ground state band from 0^+ to 8^+ state. One should take into account that the fixed parameters V_0, λ, a, and b are the same applied for nuclear spectra description of different mass regions [1, 3, 4]. The results for the negative parity band of ^{64}Ge are not conclusive, since the respective experimental levels have undefined assignments. Unfortunately there are few experimental data on ^{62}Ge for a consistent comparison; therefore we suggest a correspondence of the experimental energy levels 0.964 MeV and 2.285 MeV with the 2^+ and 4^+ states, respectively.

The calculated $B(E2)$ values for the ^{64}Ge ground state band are presented in table 1. The formulae used to determine the $B(E2)$ values are detailed in Ref. [3]. Ref. [9] presents the experimental value $B(E2) = 27(4)$ W.u. for the $2_1^+ \rightarrow 0_1^+$ transition, which implies an effective charge $\delta e \approx 0.5\,e$ so that the model reproduces the experimental value. However, more $B(E2)$ experimental data are needed for a complete evaluation of the theoretical values.

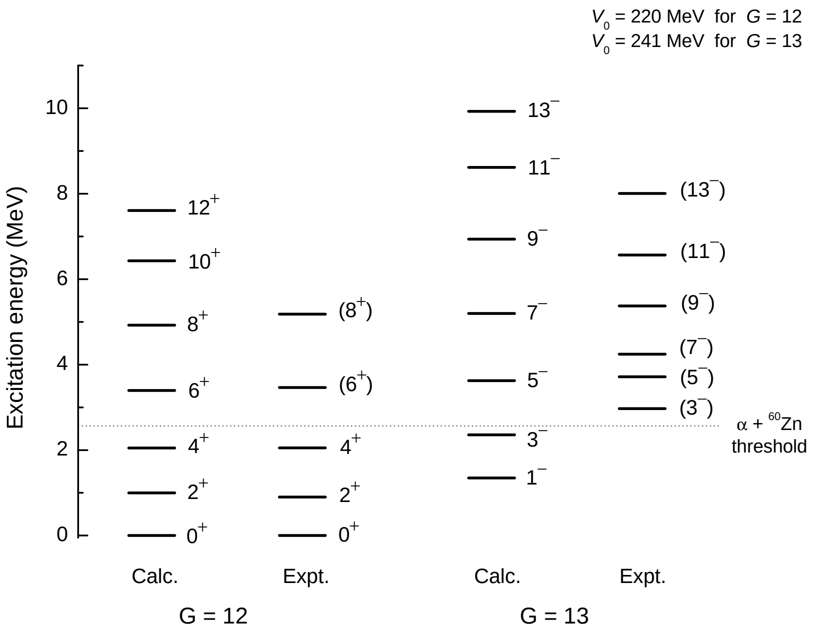

Figure 3. Calculated energy levels for the ground state band ($G = 12$) and negative parity band ($G = 13$) of the α+^{60}Zn system in comparison with experimental energies of ^{64}Ge [8].

The calculated intercluster rms radii for ^{64}Ge (see table 1) indicate that the α-cluster character is stronger for the first members of the ground state band. Such behavior (antistretching effect) has already been observed in the ^{46}Cr and ^{54}Cr ground state bands with the same α + core potential shape [4].

The present work, in addition to our previous article on Cr isotopes [4], indicates that the (1 + Gaussian)×(W.S. + W.S.^{3}) potential shape is suitable for a global description of the α-cluster structure in the nuclei of transition region. New experimental data, mainly from α-transfer reactions, will be welcome for comparison with our results.

Acknowledgments

M. A. Souza receives financial support from Coordenação de Aperfeiçoamento de Pessoal de Nível Superior (CAPES). Supports from HPC-STI of University of São Paulo and INCT-FNA are also acknowledged.

References

[1] Buck B, Merchant A C and Perez S M 1995 *Phys. Rev.* C **51** 559
[2] Michel F, Ohkubo S and Reidemeister G 1998 *Prog. Theor. Phys. Suppl.* **132** 7
[3] Souza M A and Miyake H 2015 *Phys. Rev.* C **91** 034320
[4] Souza M A and Miyake H 2017 *Eur. Phys. J.* A **53** 146
[5] Mohr P 2017 *Eur. Phys. J.* A **53** 209
[6] Wildermuth K and Tang Y C 1977 *A Unified Theory of the Nucleus* (New York: Academic Press)
[7] Nichols A L, Singh B and Tuli J K, ENSDF webpage: `http://www.nndc.bnl.gov/ensdf/`
[8] Singh B 2007 *Nuclear Data Sheets* **108** 197
[9] Starosta K *et al.* 2007 *Phys. Rev. Lett.* **99** 042503

The effect of the delta-rich hadronic stellar matter in the maximum neutron star mass using the nonlinear Walecka and Zimanyi-Moszkowski models

J C T Oliveira[1], H Rodrigues[2] and S B Duarte[3]

[1] Departamento de Física, Universidade Federal de Roraima, Campus do Paricarana s/n, 69310-270, Roraima, Brazil
[2] Centro Federal de Educação Tecnológica do Rio de Janeiro, Av. Maracanã 229, 20271-110, Rio de Janeiro, RJ, Brazil
[3] Centro Brasileiro de Pesquisas Físicas, Rua Dr. Xavier Sigaud 150, 22290-180, Rio de Janeiro, RJ, Brazil

E-mail: jose.oliveira@ufrr.br

Abstract. In this work, the delta-rich hadronic stellar matter condensate is studied in the context of a relativistic mean field calculation for hadrons and mesons using the nonlinear Walecka (NLW) and Zimanyi-Moszkowski (ZM) models. Considering different values of delta-mesons coupling constants we present the delta matter effect in the equation of state in each of these models. Solving numerically the Tolman-Oppenheimer-Volkoff (TOV) equation, we obtain the maximum neutron star mass. We note that the NLW model provides a stiffer equation of state when compared to the ZM model for the same values of delta-mesons coupling constants, and as a consequence gives more massive neutron stars.

1. Introduction

In the present work, the delta-rich hadronic stellar matter condensate is studied in the context of a relativistic mean field calculation for hadrons in beta-equilibrium with the leptons present in the medium. The baryonic sector includes the complete 1/2-spin octet and delta-resonances with 3/2-spin, which interact by exchange of scalar, vector and isovector mesons (σ, ω and ρ). For a given set of nucleon-mesons coupling constants ($g_{\sigma N}$, $g_{\omega N}$ and $g_{\rho N}$), which reproduces the nuclear matter properties at saturation density, it is discussed the neutron stars structure with respect to changes of the delta-mesons coupling constants ($g_{\sigma\Delta}$, $g_{\omega\Delta}$ and $g_{\rho\Delta}$).

2. The models

In the models studied in this work, the equations of state (EoS) consider the 1/2-spin baryon octet (n, p, Λ^0, Σ^-, Σ^0, Σ^+, Ξ^-, Ξ^0), the 3/2-spin baryonic resonances represented by the delta-matter (Δ^-, Δ^0, Δ^+, Δ^{++}) and Ω^-, in the baryonic sector [1, 2]. In the leptonic sector, we consider the electrons and the muons. We have adopted the nonlinear Walecka (NLW) and Zimanyi-Moszkowski (ZM) models with the Lagrangian densities [3-5] given by $\mathscr{L} = \mathscr{L}_F + \mathscr{L}_I$, where

$$\begin{aligned}\mathcal{L}_F = {} & \textstyle\sum_B \Psi_B (i\, \gamma_\mu \partial^\mu - m_B)\Psi_B + \sum_\zeta R_{\zeta\nu} (i\, \gamma_\mu \partial^\mu - m_\zeta)\, R^\nu{}_\zeta \\ & + 1/2\, (\partial_\mu \sigma\, \partial^\mu \sigma - m_\sigma{}^2 \sigma^2) - b/3\, m_N\, (g_{\sigma N} \sigma)^3 - c/4\, (g_{\sigma N} \sigma)^4 - 1/4\, \omega_{\mu\nu}\, \omega^{\mu\nu} \\ & + 1/2\, m_\omega{}^2\, \omega_\mu\, \omega^\mu - 1/4\, \rho_{\mu\nu} \,.\, \rho^{\mu\nu} + 1/2\, m_\rho{}^2\, \rho_\mu . \rho^\mu + \textstyle\sum_\lambda \Psi_\lambda (i\, \gamma_\mu \partial^\mu - m_\lambda)\Psi_\lambda,\end{aligned} \tag{1}$$

and

$$\begin{aligned}\mathcal{L}_I = {} & \textstyle\sum_B \Psi_B\, (g_{\sigma B}\, \sigma - g_{\omega B}\, \gamma_\mu\, \omega^\mu - 1/2\, g_{\rho B}\, \gamma_\mu\, \tau . \rho^\mu)\Psi_B \\ & + \textstyle\sum_\zeta R_{\zeta\nu}\, (g_{\sigma\zeta}\, \sigma - g_{\omega\zeta}\, \gamma_\mu\, \omega^\mu - 1/2\, g_{\rho\zeta}\, \gamma_\mu\, \tau . \rho^\mu) R^\nu{}_\zeta,\end{aligned} \tag{2}$$

which represents the nonlinear Walecka model, while that

$$\begin{aligned}\mathcal{L}_F = {} & \textstyle\sum_B \Psi_B (i\, \gamma_\mu \partial^\mu - M_B)\Psi_B + \sum_\zeta R_{\zeta\nu} (i\, \gamma_\mu \partial^\mu - M_\zeta)\, R^\nu{}_\zeta \\ & + 1/2\, (\partial_\mu \sigma\, \partial^\mu \sigma - m_\sigma{}^2 \sigma^2) - 1/4\, \omega_{\mu\nu}\, \omega^{\mu\nu} + 1/2\, m_\omega{}^2\, \omega_\mu\, \omega^\mu \\ & - 1/4\, \rho_{\mu\nu} \,.\, \rho^{\mu\nu} + 1/2\, m_\rho{}^2\, \rho_\mu . \rho^\mu + \textstyle\sum_\lambda \Psi_\lambda (i\, \gamma_\mu \partial^\mu - m_\lambda)\Psi_\lambda,\end{aligned} \tag{3}$$

and

$$\begin{aligned}\mathcal{L}_I = {} & \textstyle\sum_B \Psi_B\, (m^*{}_B\, g_{\sigma B}\, \sigma - g_{\omega B}\, \gamma_\mu\, \omega^\mu - 1/2\, g_{\rho B}\, \gamma_\mu\, \tau . \rho^\mu)\Psi_B \\ & + \textstyle\sum_\zeta R_{\zeta\nu}\, (m^*{}_\zeta\, g_{\sigma\zeta}\, \sigma - g_{\omega\zeta}\, \gamma_\mu\, \omega^\mu - 1/2\, g_{\rho\zeta}\, \gamma_\mu\, \tau . \rho^\mu) R^\nu{}_\zeta,\end{aligned} \tag{4}$$

represents the Zimanyi-Moszkowski model. In the equations above, $\mathcal{L}_F$ is the Lagrangian density for free baryons, electrons and muons. The σ, ω and ρ, and m_N stands for meson fields and nucleon mass, respectively. In addition, the interaction Lagrangian is specified in the $\mathcal{L}_I$ expression. Ψ_B represents the Dirac spinor describing the baryon octet, the $R_{\zeta\nu}$ is the Rarita-Schwinger spinor [6], with $\zeta = \Delta^-, \Delta^0, \Delta^+, \Delta^{++}$, describing the 3/2-spin baryonic resonances, B = n, p, Λ^0, Σ^-, Σ^0, Σ^+, Ξ^-, Ξ^0, and $\lambda = e^-, \mu^-$.

3. Results and conclusions

In Figs. (1-2) we show the behavior of the equations of state for stellar delta-matter calculated with the nonlinear Walecka and Zimanyi-Moszkowski models for different values of delta-mesons coupling constants. Using these equations of state obtained by the models, we have numerically solved the Tolman-Oppenheimer-Volkoff (TOV) structure equations [7, 8] in order to obtain the mass-radius relationship of a neutron star.

The Figs. (3-4) compare the mass versus radius for the neutron stars considering the set of values ($\alpha = \beta = \gamma = 1.0$) when calculated with the nonlinear Walecka and Zimanyi-Moszkowski models for different central densities. In the Figures, we have taken different values for the quantities $\alpha = g_{\omega\Delta}/g_{\omega N}$, $\beta = g_{\sigma\Delta}/g_{\sigma N}$ and $\gamma = g_{\rho\Delta}/g_{\rho N}$. Through these quantities, we find the allowed values of ratios of scalar, vector, and isovector coupling constants of the delta over those of the nucleon [9].

We note that the NLW model provides a stiffer equation of state for the case ($\alpha = \beta = \gamma = 1.0$) when compared to the ZM model, and so it tends to give more massive neutron stars as we can see in the Figs. (3-4). In conclusion, we remark that the neutron star has a maximum mass ($M = 1.8\ M_{sol}$) when we use the NLW model for the case ($\alpha = \beta = \gamma = 1.0$) with central density $\rho_C = 2.5 \times 10^{15}$ (g/cm^3) as we can see in the Fig. 4. This result for the maximum mass of a neutron star is compatible with the observational data [10, 11].

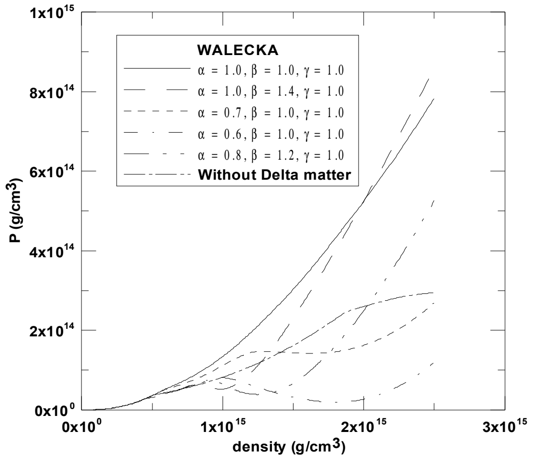

Figure 1. Pressure versus density for different values of delta-meson coupling constants calculated with the nonlinear Walecka model.

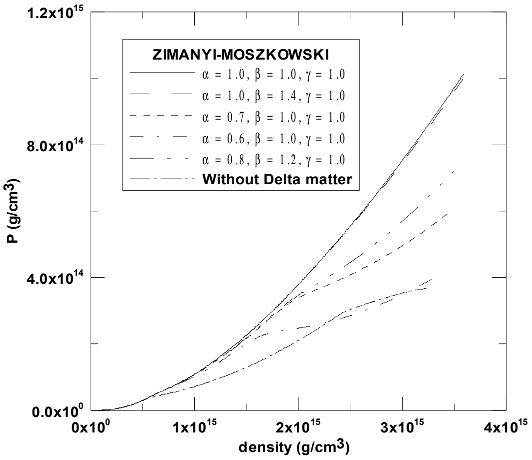

Figure 2. Pressure versus density for different values of delta-meson coupling constants calculated with the Zimanyi-Moszkowski model.

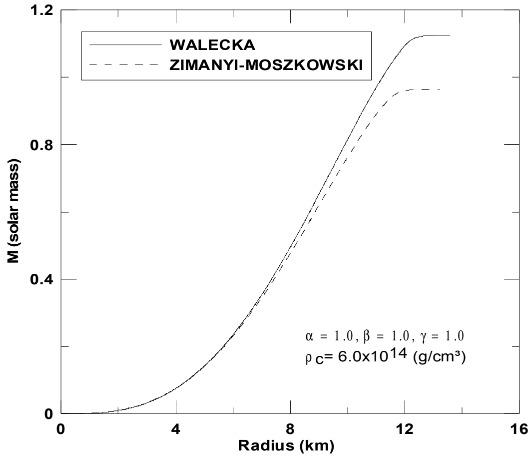

Figure 3. Mass-radius diagrams for the set of values ($\alpha = \beta = \gamma = 1.0$) with central density $\rho_C = 6.0 \times 10^{14}$ (g/cm^3).

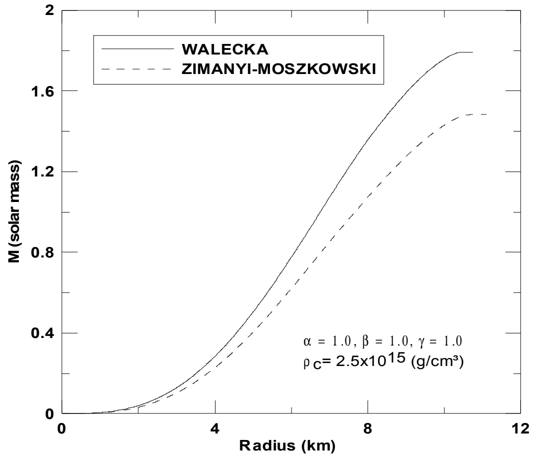

Figure 4. Mass-radius diagrams for the set of values ($\alpha = \beta = \gamma = 1.0$) with central density $\rho_C = 2.5 \times 10^{15}$ (g/cm^3).

References

[1] Oliveira J C T et al 2000 Mod. Phys. Lett. A **15** 1529
[2] Oliveira J C T et al 2007 Int. J. Mod. Phys. D **16** 175
[3] Walecka J D 1974 Ann. Phys. **83** 497
[4] Zimanyi J and Moszkowski S A 1990 Phys. Rev. C **42** (4) 1416
[5] Taurines A R et al 2001 Phys. Rev. C **63** (6) 065801
[6] Rarita W and Schwinger J 1941 Phys. Rev. **60** 61
[7] Tolman R C 1939 Phys. Rev. **55** 364
[8] Oppenheimer J R and Volkoff G M 1939 Phys. Rev. **55** 374
[9] Kosov D S et al 1998 Phys. Lett. B **421** 37
[10] Lattimer J M and Prakash M 2005 Phys. Rev. Lett. **94** 111101
[11] Lattimer J M 2012 Annu. Rev. Nucl. Part. Sci. **62** 485

Core longitudinal momentum distributions in the stripping reactions of two-neutron halo nuclei

L A Souza[1,2], **T Frederico**[3] **and C A Bertulani**[4]

[1] Instituto de Física, Universidade de São Paulo, 05508-090, São Paulo, SP, Brazil
[2] Departamento de Física, Universidade Federal de Lavras, 37200-000, Lavras, MG, Brazil
[3] Instituto Tecnológico de Aeronáutica, DCTA, 12228-900, São José dos Campos, SP, Brazil
[4] Department of Physics and Astronomy, Texas A&M University-Commerce, Commerce, TX 75429-3011, USA

E-mail: `lucasufsj@gmail.com`

Abstract. The core longitudinal momentum distributions in two-neutron stripping reactions for halo nuclei of ^{20}C and ^{22}C are computed and compared to the experimental data obtained by detecting the core nucleus. The three-body wave function from the zero-range renormalized model is used as input in our calculations. We approximate the wave function of the projectile with a three-body structure, namely neutron-neutron-core, to an effective two-body one by integrating over neutron-neutron relative distance, such that the one has a core-dineutron wave function. The eikonal approximation is used in the description of the fragment-target interactions where the São Paulo optical potential is used for modeling the core-target and a Woods-Saxon potential is used for the dineutron-target interaction.

1. Introduction

Thanks to technological developments particle beams of unstable neutron rich nuclei are produced in laboratories and it is now possible to measure reaction cross-sections of very short half-life halo nuclei. They are composed by a core plus one or two loosely bound nucleons like the neutron-rich carbon isotopes, which have been observed within last couple of years [1, 2, 3]. In addition to experimental efforts, theoretical groups, in the last decades, have been making efforts in order to obtain indirect informations about neutron halo from observables such as the core momentum distributions [4, 5, 6]. This is important since it provides model constraints to make possible the prediction of other halo-nuclei properties, like the matter radius, see for example [7].

The differential cross-sections for the stripping processes (inelastic breakup) for two-body projectile on a target was discussed in Ref. [8]. We follow the theory presented in that work and compute the core longitudinal momentum distribution of the bound neutron-rich carbon isotopes, in particular, for the collision of beams of ^{20}C and ^{22}C with energy of 240 A MeV, with a target of stable ^{12}C. We approximate the three-body projectile wave function by a two-body one, namely an effective core-dineutron wave function, by integrating the three-body wave function over the neutron-neutron relative coordinate.

2. Three-body zero-range wave function

To describe the two-neutron halo nucleus as a three-body system (for example $^{20}\mathrm{C} = {}^{18}\mathrm{C}+n+n$, where n represents one neutron of the halo), the wave function can be written as a possible set of the relative coordinates $\Psi(\mathbf{r},\mathbf{r}_{nn})$ as defined in Fig. 1. The wave function is an eigenstate of the three-body zero-range Hamiltonian where $S_{2n}=-E$ is the two-neutron separation energy. The neutrons are supposed to be in a spin singlet state and the configuration space zero-range model wave function [9, 10] is:

$$\Psi(\mathbf{r},\mathbf{r}_{nn}) = \int d\mathbf{q}\,\frac{e^{-\kappa_{nn}|\mathbf{r}_{nn}|}}{|\mathbf{r}_{nn}|}\,e^{i\mathbf{q}.\mathbf{r}}\,f_{nn}(\mathbf{q}) + \left\{\int d\mathbf{q}\,\frac{e^{-\kappa_{nc}|\mathbf{r}_{nc}|}}{|\mathbf{r}_{nc}|}\,e^{i\mathbf{q}.\mathbf{r}_{n',nc}}f_{nc}(\mathbf{q}) + (n\leftrightarrow n')\right\}, \quad (1)$$

where the last term $(n\leftrightarrow n')$ means the symmetry under exchange of the neutrons. The relative coordinate of the core to the neutron-neutron center of mass is $\mathbf{r}$. The absolute value for vector $\mathbf{r}_{nc}=\mathbf{r}+\frac{\mathbf{r}_{nn}}{2}$ is the distance between the core and the neutron. The relative coordinate of n' to the neutron-core center of mass is $\mathbf{r}_{n',nc}=\frac{A}{A+1}\mathbf{r}-\frac{A+2}{2(A+1)}\mathbf{r}_{nn}$ and the κ's in the two-body subsystems wave functions are: $\kappa_{nn}=\sqrt{2\frac{\mu_{nn}}{\hbar^2}\left(S_{2n}+\frac{\hbar^2q^2}{2\mu_{nn,c}}\right)}$, and $\kappa_{nc}=\sqrt{2\frac{\mu_{nc}}{\hbar^2}\left(S_{2n}+\frac{\hbar^2q^2}{2\mu_{nc,n}}\right)}$, with the reduced masses, $\mu_{nn}=\frac{m}{2}$, $\mu_{nn,c}=m\frac{2A}{A+2}$, $\mu_{nc}=m\frac{A}{A+1}$, $\mu_{nc,n}=m\frac{A+1}{A+2}$, where A is the mass number of the core and the neutron mass is m. The zero-range three-body wave function is obtained by solving the coupled integral equations for $f_{nn}(\mathbf{q})$ and $f_{nc}(\mathbf{q})$, which are spectator functions. These integral equations are solved having as inputs the $n-n$ and $n-c$ scattering lengths, and the value of S_{2n} (See details in Ref. [9]).

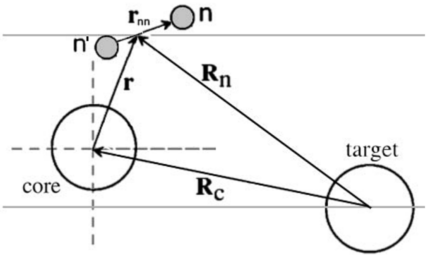

Figure 1. Coordinates for two-neutron stripping reaction.

3. Differential two-neutron stripping cross-section

The cross-section for the stripping reaction $(n+n+c)+target\rightarrow c+X$, where $(n+n+c)$ is the initial state of the projectile and c corresponds to a final state of the core, is given in [8]:

$$\frac{d\sigma_{str}}{d^3k_c}=\frac{1}{(2\pi)^3}\frac{1}{2l+1}\sum_m\int d^2b_n\;\left[1-|S_n(\mathbf{b}_n)|^2\right]\left|\int d^3r\;e^{i\mathbf{k}_c.\mathbf{r}}S_c(\mathbf{b}_c)\Psi_{lm}(\mathbf{r})\right|^2, \quad (2)$$

where $\mathbf{k}_c$ is the core momentum, $\mathbf{b}_c$ and $\mathbf{b}_n$ are the impact parameter vectors referring to the transverse components of $\mathbf{R}_c$ and $\mathbf{R}_n$ as in Fig. 1. S_c and S_n are the scattering matrix of the $c+target$ and $(n+n)+target$, respectively. We introduce the three-body bound state wave function, Eq. (1), which has the predominance of s-wave $\ell=0$. However, we approximate the wave function from three- to two-body by considering the two-neutron stripping. For that reduction to an effective core-dineutron wave function we integrate the three-body wave function over $\mathbf{r}_{nn}$ as follows:

$$\Psi(\mathbf{r}):=\int d^3r_{nn}\,\Psi(\mathbf{r},\mathbf{r}_{nn}). \quad (3)$$

3.1. Eikonal approximation

The Eikonal approximation is a semiclassical method to obtain the S-matrix, $S(b)$, as a function of the impact parameter b, where one neglects the excitation energies of the projectile which moves along a straight-line trajectory at high energy. By considering that the projectile beam propagate towards the target with the initial momentum on the z-axis, the S-matrix can be written as $S(b) = \exp[i\chi(b)]$, and the eikonal phase is given by:

$$\chi(b) = -\frac{1}{\hbar v}\int_{-\infty}^{\infty} U_{opt}(b,z)dz, \tag{4}$$

with v the fragment-target relative velocity and U_{opt} is the optical potential.

The São Paulo optical potential (SPP) is used to describe the interaction between the core and the carbon target. This potential consists on a theoretical energy-dependent model that has been successful in describing the elastic and inelastic scattering for weakly bound nuclei based on a double folding potential for target and the projectile [11, 12]. It is built with the fundamental nucleon-nucleon interaction folded into a product of the nucleon densities of the nuclei and a polarization potential that carries the nonelastic contributions.

The dineutron-target interaction is described by a Woods-Saxon potential that is given by:

$$V^{WS}(r) = \frac{V_0 - iV_{0_I}}{1 + \exp\left((r - R_0)/a\right)}, \tag{5}$$

where R_0 is the target nuclear radius of ^{12}C and $a = 0.676$ fm determines the diffuseness of the nuclear surface. The parameters used for real and imaginary parts are $V_{0_R} = 49.9395$ MeV and $V_{0_I} = 1.8256$ MeV, respectively [13].

4. Core longitudinal momentum distributions

We decompose the cross-section in momentum components and integrate over the perpendicular momentum component $k_{c_\perp}$ as,

$$\frac{d\sigma}{d\,k_{c_\parallel}} = \int \frac{d\sigma}{d^3k_c}\, d^2k_{c_\perp}, \tag{6}$$

the longitudinal momentum distribution is given by

$$\frac{d\sigma}{dk_{c_\parallel}} = \frac{1}{2\pi}\int_0^\infty d^2b_n\Big[1 - |S_n(b_n)|^2\Big]\int_0^\infty d^2\rho\, |S_c(\rho, b_n, \phi)|^2\left|\int_{-\infty}^{\infty} dz\, \exp[-ik_\parallel z]\Psi(\rho, z)\right|^2, \tag{7}$$

where ϕ is the core angle around the z-axis and $|\mathbf{b}_c| = \sqrt{b_n^2 + \rho^2 - 2\rho b_n\cos(\phi - \phi_n)}$, with the dineutron position vector was fixed at angle $\phi_n = 2\pi$.

The two-neutron differential stripping cross-sections for the momentum distributions of the core $P_\parallel = \hbar k_{c_\parallel}$ are shown in Fig. 2 for the projectiles of ^{22}C (left-frame) and ^{20}C (right-frame) colliding at 240 A MeV on the carbon target. The distributions have been convoluted with the experimental resolution and normalized to the cross-sections data. The distributions are convoluted as $n_{\text{conv}}(q) = \int_{-\infty}^{\infty} dq'\ \exp\big(-(q - q')^2/2\sigma^2\big)\ n(q')$, where $n(q')$ is the cross-sections calculated with Eq. (2) and are represented by full lines in both frames. The theoretical results for the ^{22}C are convoluted with the experimental resolution $\sigma = 27$ MeV/c and added to a wide experimental distribution $\sigma_{\text{wide}} = 89.6$ MeV/c (brown dashed line) associated to a full width at half maximum of FWHM = 211 MeV/c from Ref. [2]. The distribution for the ^{18}C core in the reaction ^{12}C(^{20}C,^{18}C)X is computed for an experimental resolution of $\sigma = 28$ MeV/c. The red dashed line in the right-frame represents the approximation so-called the "transparent limit" where S_c=1 and it neglects the effect of the interaction between the observed fragment and the target nucleus. The distribution without the experimental resolution is shown as well. The three-body wave functions for the halo nuclei are computed by using two-neutron separation energies with $S_{2n} = 3.5$ MeV($S_{2n} = 0.396$ MeV [3]) for the ^{20}C(^{22}C). The bound subsystem ^{19}C has one-neutron separation energy of $S_{1n} = 0.58$ MeV and for the borromean system ^{22}C, we use the neutron-core system in the unitary limit, where the neutron-core virtual state energy vanishes, $E_{nc}^{virtual} = 0$.

The wide distribution added in the case of ^{22}C is associated with neutrons in the inner orbits of the core. In the case of ^{20}C, we have not taken into account such contributions, but as one see in Fig. 2, our calculations lacks strength for $|P_{\|}| > 100$ MeV/c, due possibly to neutrons emitted from such inner configurations, which should be considered in a future investigation.

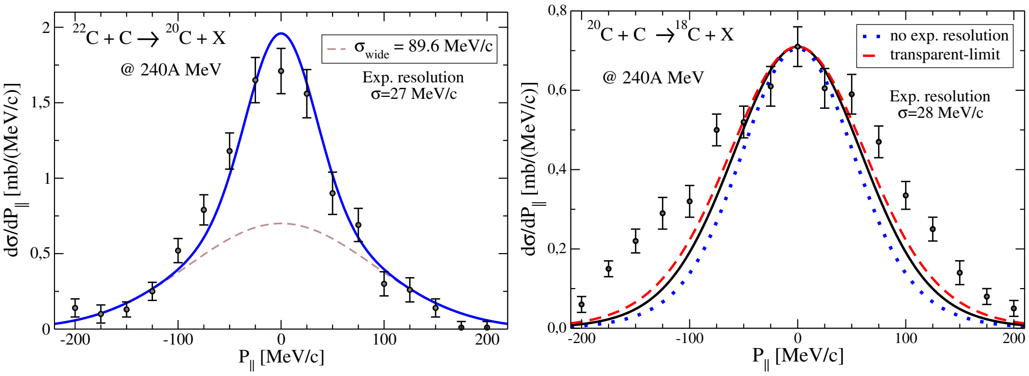

Figure 2. The core longitudinal momentum distributions of ^{22}C (left-frame) and ^{20}C (right-frame) obtained with a beam energy of 240 A MeV form the collision with the carbon target are represented by full lines in both panels. The distributions are convoluted with the experimental resolutions, and for ^{22}C it is added to a wide normal distribution represented by dashed line. The blue-dotted line is the distribution without the experimental resolution for ^{20}C. The red-dashed line is the transparent-limit in which S_c=1. The experimental results are from Ref. [2].

5. Discussion and Outlook

The theory of one-neutron halo stripping reaction has been extended to calculate the cross-sections of two-neutron stripping processes. The core momentum distribution of ^{22}C, computed by using the known low-energy parameters, shows a fair consistency with the experimental results. The nucleus ^{20}C requires a more accurate analysis, since we believe that a wider experimental resolution should be considered. In general, the results show that the zero-range model is appropriate to describe the three-body projectile in that stripping process. Despite we have only computed the momentum density for the neutron rich isotopes of carbon, we plan in the future calculate the breakup of other exotic two-neutron halo nuclei, using the same approximation to obtain the nuclear distortion of the fragments in the stripping reaction . In addition, Coulomb interaction should be taken account to complete this work when considering more heavier targets.

6. References

[1] Tanaka K *et al* 2010 *Phys. Rev. Lett.* **104**, 062701
[2] Kobayashi N *et al* 2012 *Phys. Rev.* C **86**, 054604
[3] Togano Y *et al* 2016 *Phys. Lett.* B **761**, 412
[4] Barranco F, Vigezzi E and Broglia R A 1996 *Z. Phys.* A **356**, 45
[5] Bertulani C A and Hansen P G 2004 *Phys. Rev.* C **70**, 034609
[6] Souza L A, Bellotti F F, Frederico T, Yamashita M T and Lauro Tomio 2016 *Phys. Lett.* B, **757**, 368
[7] Acharya B, Ji C, and Phillips D R 2013 *Phys. Lett. B* **723**, 196
[8] Hencken K, Bertsch G and H. Esbensen 1996 *Phys. Rev.* C **54**, 3043
[9] Amorim A E A, Frederico T and Lauro Tomio 1997 *Phys. Rev.* C **56**, R2378
[10] Souza L A, Garrido E and Frederico T 2016 *Phys. Rev.* C **94**, 064002
[11] Chamon L C *et al*2002 *Phys. Rev.* C **66**, 014610
[12] Alvarez M A G, *et al* 2003 *Nucl. Phys.* A **723**, 93
[13] Koning A and Delaroche J, *Nucl. Phys.* A **713**, 231
[14] Serber R 1947 *Phys. Rev.* **72**, 1008

Consistent Skyrme parametrization and its critical parameter values

M Dutra[1], **O Lourenço**[1] **and A Delfino**[2]

[1]Departamento de Física, Instituto Tecnológico de Aeronáutica, DCTA, 12228-900, São José dos Campos, SP, Brazil
[2]Instituto de Física - Universidade Federal Fluminense, Av. Litorânea s/n, 24210-150 Boa Viagem, Niterói RJ, Brazil

E-mail: `marianad@ita.br`

Abstract. A new Skyrme parametrization was developed based on a shortlist of Skyrme forces. These selected parameterizations, 16 in total, were found in a comprehensive study involving 240 parametrizations submitted to constraints related to nuclear matter properties. The critical parameters associated with the liquid-gas phase transition, critical density, critical pressure, and critical temperature are calculated for this new parametrization as well as its flash point.

1. Introduction

Properties of nuclear matter are reasonably well described by different versions of relativistic and non-relativistic models. The basic idea is to parameterize the NN and NNN interactions by zero range (Skyrme model) density-dependent functions to model ground state properties of finite nuclei and nuclear matter. In this perspective, the microscopic details of NN and NNN forces, such as meson exchange, are not explicitly considered and all the physically relevant information is carried by the parameters of the density-dependent phenomenological forces which include the spin, orbital angular momentum and isospin couplings. However, the parameterization of such forces is not unique and there exist, in principle, an infinite number of parameter sets, fitted to ground state properties of (doubly-or semi-magic) stable nuclei and symmetric and asymmetric nuclear matter (ANM). In this work, we presented the construction of a conventional non-relativistic Skyrme parameterization, called SkUFF, based on the set of consistent Skyrme parametrizations (CSkP), selected in Ref.[1].

2. Skyrme model

One of the advantages of the structure of the Skyrme density functional is that it allows the analytical expression of all variables characterizing infinite nuclear matter [2, 3, 4, 5, 6]. The CSkP models are: **GSkI, GSkII, KDE0v1, LNS, MSL0, NRAPR, Ska25s20, Ska35s20, SKRA, Skxs20, SQMC650, SQMC700, SkT1, SkT2, SkT3** and **SV-sym32** (for details see reference therein [1]). They satisfy all 11 constraints that describe the symmetric nuclear matter (SMN), the pure neutron matter (PNM), and a mixture of both related with the symmetry energy (MIX). The selection of these 16 parametrizations and their saturation properties are presented in Ref.[1].

The energy per particle of infinite nuclear matter, defined in terms of the energy density $\mathcal{E}$ and particle number density ρ of these parameterizations, is written as

$$\begin{aligned} E = \frac{\mathcal{E}}{\rho} &= \frac{3\hbar^2}{10M}\left(\frac{3\pi^2}{2}\right)^{2/3}\rho^{2/3}H_{5/3} + \frac{t_0}{8}\rho[2(x_0+2)-(2x_0+1)H_2] \\ &+ \frac{1}{48}t_3[2(x_3+2)-(2x_3+1)H_2]\rho^{\sigma+1} + \frac{3}{40}\left(\frac{3\pi^2}{2}\right)^{2/3}\rho^{5/3}\left(aH_{5/3}+bH_{8/3}\right), \quad (1) \end{aligned}$$

with $a = t_1(x_1+2)+t_2(x_2+2)$, $b = \frac{1}{2}\left[t_2(2x_2+1) - t_1(2x_1+1)\right]$, and $H_n(y) = 2^{n-1}[y^n+(1-y)^n]$. Where $y = Z/A$ is the proton fraction, and M is the nucleon mass. From Eq.(1) we can obtain others nuclear matter quantities like incompressibility, symmetry energy, slope, and volumetric isospin incompressibility.

3. Results

The SkUFF parametrization is a conventional Skyrme model and has up to 9 adjusting parameters. For this calculation, it was necessary to fix observables of matter nuclear, such as binding energy, saturation density, effective mass, incompressibility, the energy of symmetry and its derivatives. We established the values of these quantities as the simple arithmetic mean of the values presented by the 16 selected models. Such numbers are arranged in the Table 1.

Table 1. Observables values for SkUFF parametrization.

ρ_0 [fm^{-3}]	E_0 [MeV]	K_0 [MeV]	J [MeV]	L_0 [MeV]	K_{vs} [MeV]	m^*
0.163	15.87	227.85	32.56	59.18	−382.04	0.855

Note that we fixed only 7 observables. Due to the type of Skyrme EoS, we can not be able to write all constants as a function of the saturations quantities only [7]. Thus, we proceed to calculate t_0, x_0, t_1, x_1, t_3, x_3 and σ from the observables define in Table 1, and again, use an arithmetic mean for the CSkP to get the remaining data t_2 and x_2. After these procedures we find the following (Table 2) parameters for the SkUFF.

Table 2. SkUFF parameters. The dimensions are: t_0 [MeV.fm^3], $t_1 = t_2$ [MeV.fm^5], and t_3 [MeV.fm$^{3(\sigma+1)}$]. The others are dimensionless.

t_0	t_1	t_2	t_3	x_0	x_1	x_2	x_3	σ
−2030.31	193.50	−82.81	12756.77	0.127	0.036	−0.539	0.051	0.25

3.1. Behavior in the constraints

The values for the numerical constraints are shown in Table 3. Realize that the SkUFF model is approved in all of them and not only in those that have been fixed to find its constants. For more details, see [1].

In Figures (1) and (2) we illustrate how this new parameterization is consistent with the graphical constraints of SNM and PNM.

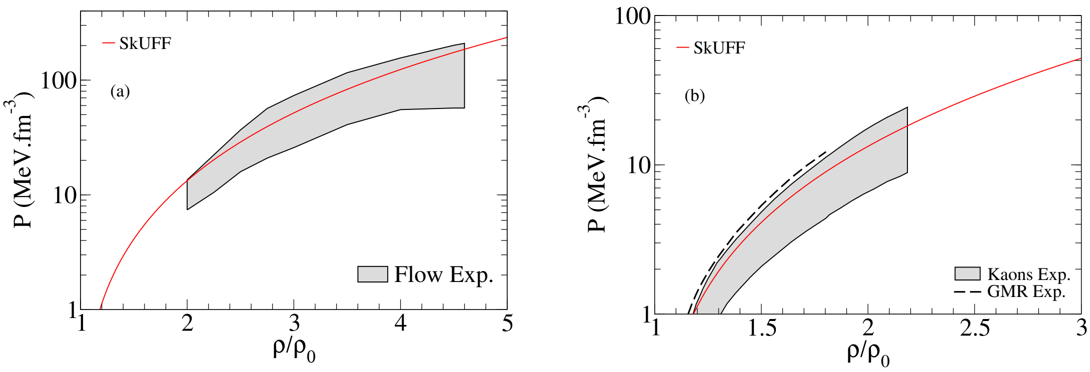

Figure 1. Behavior for the SMN. (a) SM3 and (b) SM4. Bands extracted from Ref.[1].

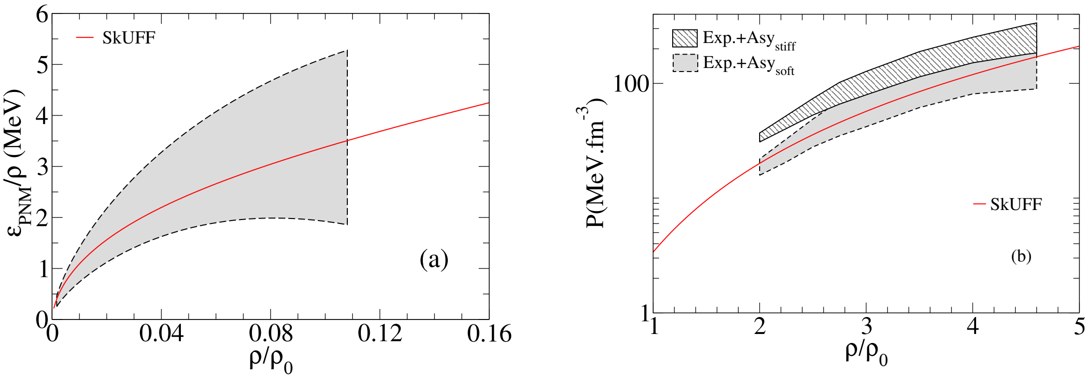

Figure 2. Behavior for the PNM. (a) PNM1 and (b) PNM2. Bands extracted from Ref.[1].

Table 3. Numerical constraints for SkUFF.

K_0 [MeV]	K' [MeV]	J [MeV]	L [MeV]	$K_{\rm vs}$ [MeV]	$\frac{E_{\rm sym}(\frac{\rho_0}{2})}{J}$	$\frac{3P_{\rm PNM}}{L\rho_0}$
227.84	384.42	32.56	59.18	−382.04	0.633	1.049

3.2. Application for SNM at Finite Temperature

The temperature inclusion was made using the expansion suggested by Ref. [8] for the Fermi gas. This expansion works well for T approximately greater than 5 MeV. The pressure, in this case, can be written

$$P = \frac{3t_0}{8}\rho^2 + \frac{1}{8}\left(\frac{3\pi^2}{2}\right)^{2/3}\rho^{8/3}(a+b) + \frac{3t_3}{48}(\sigma+1)\rho^{\sigma+2} + T\rho + \frac{T\lambda^3}{8\sqrt{2}\gamma}\rho^2, \tag{2}$$

where $\lambda = \left[\frac{2\pi(\hbar c)^2}{MT}\right]^{1/2}$ is the thermal wavelength and $\gamma = 2$.

The critical values can be obtained by

$$\left(\frac{\partial P}{\partial \rho}\right) = \left(\frac{\partial^2 P}{\partial \rho^2}\right) = 0, \tag{3}$$

and is given by

$$T_c = \frac{2}{9}\left(\frac{3\pi^2}{2}\right)^{2/3}(a+b)\rho_c^{5/3} + \frac{t_3}{16}\sigma(\sigma+1)(\sigma+2)\rho_c^{\sigma+1}, \tag{4}$$

for the "flash" values we used this condition

$$\left(\frac{\partial P}{\partial \rho}\right) = P = 0 \tag{5}$$

that produced

$$T_f = \frac{1}{12}\left(\frac{3\pi^2}{2}\right)^{2/3}(a+b)\rho_f^{5/3} + \frac{t_3}{16}\sigma(\sigma+1)\rho_f^{\sigma+1}. \tag{6}$$

The values for the critical and "flash" quantities are showed in Table 4.

Table 4. Critical and "flash" values for SkUFF. For comparison with experimental data, we showed the values from Ref.[9].

Model	T_c [MeV]	ρ_c [fm^{-3}]	P_c [MeV.fm^{-3}]	T_f [MeV]	ρ_f [fm^{-3}]
SkUFF	16.59	0.054	0.254	12.67	0.084
Ref.[9]	17.9 ± 0.4	0.06 ± 0.01	0.31 ± 0.07		

4. Summary

We presented the construction and the behavior of Skyrme SkUFF parameterization in nuclear matter. The SkUFF was consistent with all the constraints proposed in Ref.[1]. Besides, we studied its behavior at finite temperature, calculating its critical parameters. The calculated values for the SkUFF differ from the experimental ones by about 5% for T_c and 4% for P_c. The value for the critical density was within the margin of error.

5. Acknowledgments

This study was financed in part by the Coordenação de Aperfeiçoamento de Pessoal de Nível Superior - Brasil (CAPES) - Finance Code 001, by Conselho Nacional de Desenvolvimento Científico e Tecnológico (CNPq) under grants 310242/2017-7 and 406958/2018-1 (O. L.), 433369/2018-3 (M. D.) and 310205/2017-4 (A. D.), by Fundação de Amparo à Pesquisa do Estado de São Paulo (FAPESP) under thematic project 2013/26258-4 (O. L.), and by INCT-FNA project 464898/2014-5.

[1] Dutra M, Lourenço O, Martins J S S *et al.* 2012 *Phys. Rev.* C **85** 035201
[2] Chabanat E, Bonche P, Haensel P, Meyer J and Schaeffer R 1997 *Nucl. Phys.* A **627** 710
[3] Lourenço O, Dutra M, Delfino A and Amaral R L P G 2007 *Int. J. Mod. Phys.* E **16** 3037
[4] Lourenço O, Santos B M, Dutra M and Delfino A 2016 *Phys. Rev.* C **94** 045207
[5] Lourenço O, Dutra M and Menezes D P 2017 *Phys. Rev.* C **95** 065212
[6] Santos B M, Dutra M, Lourenço O and Delfino A 2015 *Phys. Rev.* C **92** 015210; 2014 *Phys. Rev.* C **90** 035203
[7] Agrawal B K, Shlomo S, Au K V 2004 *Phys. Rev.* C **70** 057302
[8] Huang K 1987 *Statistical Mechanics* (EUA: John Wiley, 2. ed.)
[9] Elliott J B, Lake P T, Moretto L G and Phair L 2013 *Phys. Rev.* C **87** 054622

Predictions on the α-cluster structure in ^{104}Te

M A Souza[1,2], **H Miyake**[1], **T Borello-Lewin**[1], **C A da Rocha**[3,4] **and C Frajuca**[2]

[1] Instituto de Física, Universidade de São Paulo, Rua do Matão, 1371, CEP 05508-090, Cidade Universitária, São Paulo - SP, Brazil
[2] Departamento de Mecânica, Instituto Federal de Educação, Ciência e Tecnologia de São Paulo - Campus São Paulo, Rua Pedro Vicente, 625, CEP 01109-010, Canindé, São Paulo - SP, Brazil
[3] Departamento de Ciências e Matemática, Instituto Federal de Educação, Ciência e Tecnologia de São Paulo - Campus São Paulo, Rua Pedro Vicente, 625, CEP 01109-010, Canindé, São Paulo - SP, Brazil
[4] Universidade São Judas Tadeu (USJT) - Campus Mooca, Rua Taquari, 546, CEP 03166-000, Mooca, São Paulo - SP, Brazil

E-mail: `marsouza@if.usp.br`

Abstract. The present work analyzes the α + core structure in ^{104}Te using the local potential model. The α + core interaction is described by a nuclear potential of (1 + Gaussian)×(W.S. + W.S.^{3}) shape. The energy levels, total α widths and rms intercluster separations are determined for the ground state band and compared with a previous calculation which uses a double-folding potential. The two potential forms produce similar spectra between the 0^+ and 14^+ states. The antistretching effect is predicted for the ^{104}Te ground state band, as is observed in previous α + core calculations in intermediate mass nuclei. An α-decay half-life $T_{1/2,\alpha} \approx 3$ ns is predicted for ^{104}Te in the α-decay energy $Q_\alpha \approx 5.36$ MeV using an α preformation factor $P = 1$. The calculated $T_{1/2,\alpha}$ value is compatible with the recently reported experimental result on α-decay of ^{104}Te.

1. Introduction

The α-cluster model has been able to describe satisfactorily properties as energy levels, α emission widths, electromagnetic transition rates and α elastic scattering data for light, intermediate and heavy nuclei [1–4]. In this context, there is a great interest in the ^{104}Te nucleus, since an α-decay experimental observation of this nucleus could indicate the presence of the α+^{100}Sn structure, as well as reinforce the influence of the double shell closure $N, Z = 50$ in the nuclear structure of this mass region. Recently, the observation of the $^{108}\text{Xe} \to {}^{104}\text{Te} \to {}^{100}\text{Sn}$ α-decay chain was reported [5], including the measurement of the α-decay energy and half-life of ^{104}Te. This experimental information motivates the comparison with nuclear models applied to ^{104}Te.

The work of P. Mohr [6] discusses the α-decay in Te isotopes and shows predictions on the α + core structure in ^{104}Te, such as energy levels and the α-decay half-life, using a double-folding potential for the nuclear α + core interaction. In the present work, the α + core structure in ^{104}Te is analyzed with a nuclear potential of (1 + Gaussian)×(W.S. + W.S.^{3}) shape, which was successful in the study of the same structure in ^{46}Cr and ^{54}Cr [2]. It is intended to verify the similarities or differences between the results obtained in this work and previous calculations as in Ref. [6].

2. The Model

The α-cluster model regards the total nucleus as an α-particle orbiting an inert core. Therefore, the ^{104}Te nucleus is assumed as an $\alpha+^{100}$Sn system. The α + core interaction is described through a local potential

$$V(r) = V_N(r) + V_C(r) \tag{1}$$

containing the nuclear and Coulomb terms. The Coulomb potential $V_C(r)$ is that of an α-particle interacting with an uniformly charged spherical core of radius R. The intercluster nuclear potential is proposed as

$$V_N(r) = -V_0\left[1+\lambda\exp\left(-\frac{r^2}{\sigma^2}\right)\right]\left\{\frac{b}{1+\exp[(r-R)/a]}+\frac{1-b}{\{1+\exp[(r-R)/3a]\}^3}\right\}\ , \tag{2}$$

where V_0, λ, a, and b are fixed parameters, and R and σ are variable parameters. The description of the ground state band of ^{104}Te is obtained with the fixed values $V_0 = 220$ MeV, $a = 0.65$ fm, $b = 0.3$, and $\lambda = 0.14$, while R and σ are fitted specifically for ^{104}Te. The R and σ values employed for the ground state band are: $R = 5.708$ fm and $\sigma = 0.44$ fm. The values of V_0, λ, a, and b were adjusted previously to describe the ground state bands of the nuclei ^{20}Ne, ^{44}Ti, ^{94}Mo, and ^{212}Po, in which the α-cluster structure is recognized in preceding studies [1, 3, 4]. The parameter R was fitted with 10^{-3} fm precision to give the bandhead closest to the value $E(0^+) = 5.354$ MeV, which is predicted by Mohr [6] in a study of the α + core potentials in neighboring Te isotopes. The fit criterion resulted in the energy $E(0^+) = 5.364$ MeV for the present calculation.

According to the Pauli principle, the nucleons of the α-cluster must lie in shell-model orbitals outside the core. This restriction is defined by the global quantum number $G = 2N + L$, where N is the number of internal nodes in the radial wave function and L is the orbital angular momentum. In the case of the $\alpha+^{100}$Sn system we have $G \geq 16$, where $G = 16$ corresponds to the ground state band. This value is determined from the Wildermuth condition [7]. The α + core system is solved numerically to obtain the properties of the resonant states. The energy eigenvalues provide the levels of the spectrum and the associated wave functions are used to calculate other nuclear properties.

3. Results

Applying the α-cluster model to ^{104}Te, we obtain the ground state band ($G = 16$) shown in figure 1 in comparison with the theoretical band calculated by Mohr [6] for the same nucleus. A similarity between the theoretical spectra calculated with the (1 + Gaussian)×(W.S. + W.S.^{3}) and double-folding potentials is observed, except for the spacing between the 14^+ and 16^+ levels. This result is gratifying, since the two potential forms were obtained independently.

Table 1 shows the results for the rms intercluster separations ($\langle R^2\rangle^{1/2}$) and total α-widths (Γ_α) referring to the ground state band of ^{104}Te. The α-widths were calculated using the semiclassical approximation proposed in Ref. [8]. The α-decay width calculated for the 0^+ state is $\Gamma_\alpha \approx 1.51 \times 10^{-13}$ MeV in the α-decay energy $Q_\alpha = 5.364$ MeV, using an α preformation factor $P = 1$; this width implies an α-decay half-life $T_{1/2,\alpha} \approx 3.02$ ns. However, by applying a factor $P = 10\,\%$, as suggested by Mohr [6], $T_{1/2,\alpha}$ is increased to ≈ 30.21 ns. For comparison, the α-decay half-life obtained by Mohr with the double-folding potential is $T_{1/2,\alpha} \approx 5$ ns in the

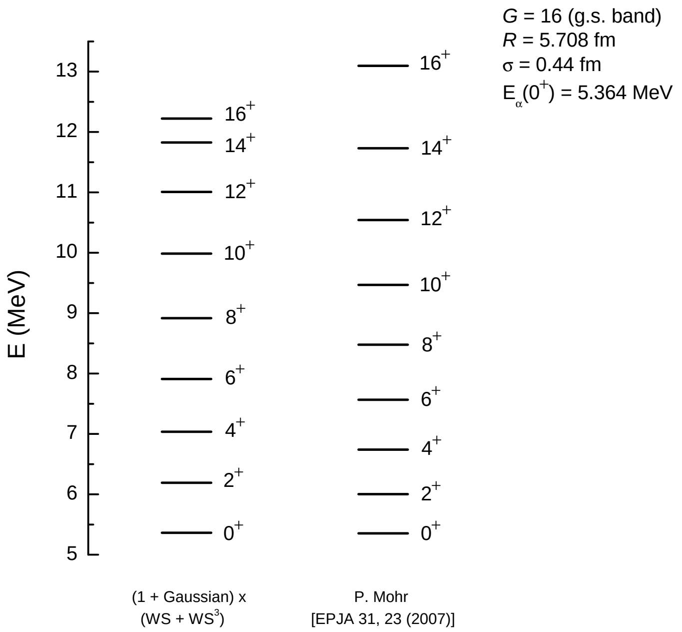

Figure 1. Calculated energy levels for the ground state band ($G = 16$) of the α+^{100}Sn system in comparison with the theoretical band calculated by Mohr [6] which uses a double-folding potential as the nuclear α + core interaction. The energy scale is given with reference to the α+^{100}Sn threshold.

α-decay energy $Q_\alpha = 5.42$ MeV. The $T_{1/2,\alpha}$ values obtained in this work with $P = 10\,\%$ and the Mohr's work are close with respect to the order of magnitude.

The recently published ^{104}Te α-decay experiment [5] obtained the measure $T^{\rm exp}_{1/2,\alpha} < 18$ ns in a decay energy $Q^{\rm exp}_\alpha = 5.1(2)$ MeV. Although the present calculation was made at an energy slightly above the experimental range, it should be noted that the calculated half-life with $P = 1$ is consistent with the experimental data. Therefore the present calculation suggests a high α preformation factor for the ^{104}Te decay.

The calculated intercluster rms radii for ^{104}Te indicate that the α-cluster character is stronger for the first members of the ground state band. Such behavior (antistretching effect) has already been observed in the ^{46}Cr and ^{54}Cr ground state bands with the same α + core potential shape [2]. Also, the antistretching effect is seen in other nuclei of the intermediate mass region with different α + core potentials [1, 3].

4. Conclusions

The present work shows that the (1 + Gaussian)×(W.S. + W.S.^{3}) and double-folding potentials produce similar spectra for the α+^{100}Sn system between the 0^+ and 14^+ states. This is a gratifying result and shows that the two potential forms are compatible in this aspect. The results obtained for rms intercluster separations indicate that the α-cluster character is stronger for the first members of the ground state band, as is predicted in other intermediate mass nuclei with the α + core structure. The α-decay half-life predicted for ^{104}Te is $T_{1/2,\alpha} \approx 3.02$ ns in the α-decay energy $Q_\alpha \approx 5.36$ MeV, using an α preformation factor $P = 1$. This result suggests a high preformation factor for the ^{104}Te α-decay, being able to reach $P \sim 1$.

The present work was developed mainly for a comparative study of the

Table 1. Calculated rms intercluster separations ($\langle R^2\rangle^{1/2}$) and total α-widths (Γ_α) for the ground state band of ^{104}Te. An α preformation factor $P = 1$ is applied. Note: $u\mathrm{E}v = u \times 10^v$

J^π	$\langle R^2\rangle^{1/2}$ (fm)	Γ_α (MeV)
0^+	5.255	1.51E−13
2^+	5.268	1.62E−11
4^+	5.238	2.50E−10
6^+	5.161	8.03E−10
8^+	5.059	1.09E−09
10^+	4.946	5.23E−10
12^+	4.836	7.28E−11
14^+	4.745	2.24E−12
16^+	4.695	7.58E−15

(1 + Gaussian)×(W.S. + W.S.^{3}) and double-folding nuclear potentials applied to ^{104}Te. The recent experimental results of Ref. [5] should be analyzed in more detail in our forthcoming publication.

Acknowledgments

M. A. Souza receives financial support from Coordenação de Aperfeiçoamento de Pessoal de Nível Superior (CAPES). Supports from HPC-STI of University of São Paulo and INCT-FNA are also acknowledged.

References

[1] Souza M A and Miyake H 2015 *Phys. Rev.* C **91** 034320
[2] Souza M A and Miyake H 2017 *Eur. Phys. J.* A **53** 146
[3] Michel F, Ohkubo S and Reidemeister G 1998 *Prog. Theor. Phys. Suppl.* **132** 7
[4] Buck B, Merchant A C and Perez S M 1995 *Phys. Rev.* C **51** 559
[5] Auranen K *et al.* 2018 *Phys. Rev. Lett.* **121** 182501
[6] Mohr P 2007 *Eur. Phys. J.* A **31** 23
[7] Wildermuth K and Tang Y C 1977 *A Unified Theory of the Nucleus* (New York: Academic Press)
[8] Gurvitz S A and Kalbermann G 1987 *Phys. Rev. Lett.* **59** 262

XLI Brazilian Meeting on Nuclear Physics (RTFNB) IOP Publishing
IOP Conf. Series: Journal of Physics: Conf. Series **1291** (2019) 012042 doi:10.1088/1742-6596/1291/1/012042

Comparison of saddle point and exact combinatorial level densities

N C da Fonseca e Oliveira, M Dutra, B V Carlson

Technological Institute of Aeronautics

E-mail: `natalie@ita.br`

Abstract. Accurate level densities are an important ingredient in the calculation of compound nucleus emission cross sections. They are often approximated numerically using the saddle point approximation to the canonical level density obtained from the grand canonical partition function using the inverse Laplace transform. Here, we use a modified version of the saddle-point approximation proposed by Rossignoli to obtain canonical level densities and average properties of a system. However, the level density needed in nuclear reaction calculations is actually the energy-conserving microcanonical one. For simple systems, the latter can be calculated combinatorially. Here we calculate microcanonical level densities using an evenly-spaced single particle density for one type of nucleon and compare these to saddle-point canonical level densities obtained from the same single-particle density. The simplest continuous approximation to the microcanonical level density describes it well near its peak but poorly at low excitation energies. The canonical level density obtained from the partition function fares somewhat better but is still not completely successful. It tends to exceed the exact result by a few percent. We discuss the differences between the canonical and microcanonical level densities and suggest how these might be reduced.

1. Introduction

The determination of nuclear densities of states is very important for the description of nuclear reactions and decays[1]. These can be estimated using a saddle point approximation to the inverse Laplace transform of the grand canonical ensemble, as was done by Bethe many years ago[2], using Monte Carlo techniques or, in certain simple cases, calculated exactly using combinatorial methods. A direct comparison of exact combinatorial calculations with the saddle point approximation to the density of states reveals that the latter systematically overestimates the exact density.

An intermediate quantity that is also useful in nuclear decay calculations is the canonical ensemble and the associated Helmholtz free energy. Here we compare the free energy, entropy and average excitation energy obtained in two manners: from a saddle point approximation to the inverse Laplace transform in number of the grand canonical ensemble and directly from the exact combinatorial calculation. We find the agreement between these to be excellent. However, a second saddle point approximation, this time to the inverse Laplace transform of the excitation energy, still does not provide us with a good approximation to the level density.

2. Statistical Ensembles

2.1. The Grand Canonical

The grand canonical ensemble describes a system which exchanges energy and particles with a larger reservoir [2,3]. Its partition function, in the case of a set of independent particles, is given by a product of a factor over each of the possible states E_k of the system,

$$Z_{GC}(\alpha,\beta) = \prod_K (1 + e^{\alpha - \beta E_k}) \,, \tag{1}$$

where β is the inverse of the temperature and $\alpha = \beta\mu$, with μ being the chemical potential. In terms of this, we can determine the expectation values of the number of particles and the energy, as well as the entropy, by

$$\langle N \rangle = \frac{\partial}{\partial \alpha} \ln Z_{GC}(\alpha,\beta) \,, \tag{2}$$

$$\langle E \rangle = -\frac{\partial}{\partial \beta} \ln Z_{GC}(\alpha,\beta) \,, \tag{3}$$

$$S = \ln Z_{GC}(\alpha,\beta) - \alpha\langle N \rangle + \beta\langle E \rangle \,. \tag{4}$$

The density of states can be expressed as the inverse Laplace transform of the partition function,

$$\omega(E,N) = \frac{1}{(2\pi i)^2} \int d\alpha d\beta Z_{GC}(\alpha,\beta) e^{(-\alpha N + \beta E)} \,, \tag{5}$$

which, in the saddle point approximation, can be estimated as

$$\omega(E,N) = \frac{\exp[\ln Z_{GC}(\alpha_0,\beta_0) - \alpha_0 N + \beta_0 E]}{2\pi \sqrt{\left[\frac{\partial^2 \ln Z_{GC}}{\partial \beta^2} \frac{\partial^2 \ln Z_{GC}}{\partial \alpha^2} - \left(\frac{\partial^2 \ln Z_{GC}}{\partial \beta \partial \alpha} \right)^2 \right] \Bigg|_{\alpha_0,\beta_0}}} \,, \tag{6}$$

where β_0 and α_0 are the values at the saddle point.

2.2. The Microcanonical

The microcanonical ensemble describes an isolated system with a well defined excitation energy and particle number[2,3]. For a fixed particle number, the density of states furnishes a description of the ensemble as a function of the excitation energy.

Here we will make use of a combinatorial calculation of the density of states for a fixed number of particles in a set of uniformly spaced states. In the case we show here, the density of states was calculated for 20 particles in 40 states. The density of states has 396 distinct energies and a total of 1.1×10^{11} states. This exact density of states is compared to the saddle point approximation in Fig. 1. We note that exact density of states possesses a maximum of 1.2×10^9 states at energy 198 and decreases at higher energies to a single state at energy 396. The saddle point approximation can describe the density of states only up to energy 198.

2.3. The Canonical Ensemble

The canonical ensemble describes a system with a fixed number of particles that only exchanges energy with a reservoir [2,3]. Its partition function can be defined exactly in terms of the density of states as

$$Z_C(\beta,N) = \int dE \quad \omega(E,N) e^{-\beta E}. \tag{7}$$

The partition function $Z_C(\beta, N)$ can also be obtained from the grand canonical ensemble as

$$Z_C(\beta, N) = \frac{1}{2\pi i} \int d\alpha Z_{GC}(\alpha, \beta) e^{-\alpha N}\,, \tag{8}$$

which, in the saddle point approximation, is

$$Z_C(\beta, N) = \frac{\exp[\ln Z_{GC}(\alpha_0, \beta) - \alpha_0 N]}{\sqrt{2\pi \left[\frac{\partial^2 \ln Z_{GC}}{\partial \alpha^2}\right]}\Bigg|_{\alpha_0}} \tag{9}$$

The Helmholtz free energy is defined as

$$F(\beta, N) = -\frac{1}{\beta} \ln Z_C(\beta, N)\,. \tag{10}$$

We can define the entropy and the expectation value of the energy in the canonical ensemble as

$$S(\beta, N) = \beta^2 \frac{\partial}{\partial \beta} F(\beta, N)\,, \tag{11}$$

$$E(\beta, N) = F(\beta, N) + \frac{1}{\beta} S(\beta, N)\,. \tag{12}$$

In Figs. 1a, 2a and 2b, we compare the Helmholtz free energy, entropy and energy obtained using the microcanonical density of states and the saddle point approximation with the grand canonical partition function for the same system of 20 particles in 40 states used in Fig. 1. We find that in this case, the saddle point approximation furnishes an excellent description of the canonical ensemble quantities.

We can also attempt an alternative approximation to the density of states, by using the fact that the latter can also be obtained as the inverse Laplace transform of the canonical partition function [8],

$$\omega(E, N) = \frac{1}{2\pi i} \int d\beta Z_C(\beta, N) e^{\beta E}. \tag{13}$$

The saddle point approximation to this expression is also displayed in Fig. 1. Unfortunately, although the Helmholtz free energy can easily be obtained from the exact combinatorial calculation of the level density, the inverse path, from the canonical partition function to the density of states through the saddle approximation, does not furnish the accuracy we would hope to obtain.

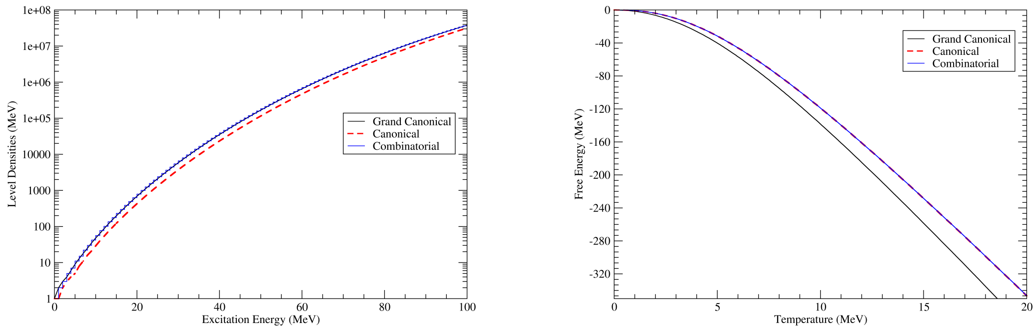

Figure 1. (Left)Density of states as a function of the excitation energy. (Right) Helmholtz free energy as a function of the temperature.

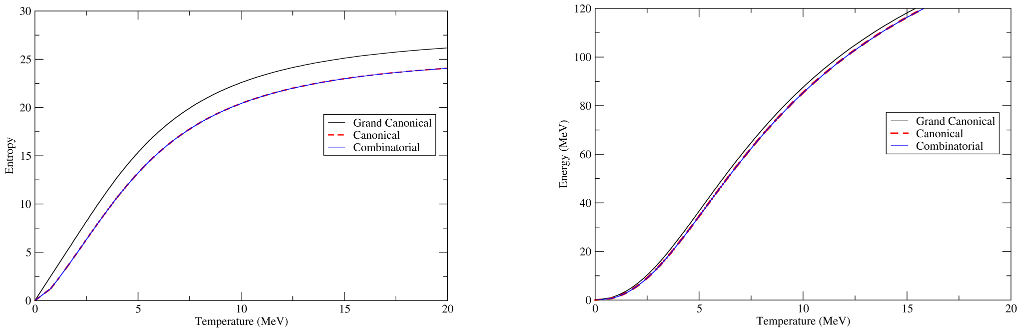

Figure 2. (Left)Entropy as a function of the temperature. (Right) Energy as a function of the temperature.

3. Conclusion

We have compared saddle point approximations to the density of states, Helmholtz free energy, entropy and excitation energy to their exact values for a system of 20 particles in 40 uniformly spaced states. We find the Helmholtz free energy and the canonical entropy and excitation energy to be in excellent agreement. However, the saddle point approximations to the density of states do not succeed in providing a similar level of agreement with the exact result.

4. Acknowledgments

This study was financed in part by the Coordenação de Aperfeiçoamento de Pessoal de Nivel Superior - Brasil (CAPES) - Finance Code 001. BVC acknowledges support from grant 2017/05660-0 of the São Paulo Research Foundation (FAPESP) and grant 306433/2017-6 of the CNPq. The authors acknowledge support from the INCT-FNA project 464898/2014-5.

References

[1] Rossignoli R 1995 *Phys. Rev.* C **51** 1772
[2] Cole A J 2000 *Statistical Models For Nuclear Decay* (Grenoble: CRC Press)
[3] Salinas S R A 2013 *Introdução à Fisica Estatistca* (São Paulo: EDUSP)
[4] Pathria R K, Beale P D 1996 *Statistical Mechanichs* (Oxford: Butterworth-Heinemann)

XLI Brazilian Meeting on Nuclear Physics (RTFNB) IOP Publishing
IOP Conf. Series: Journal of Physics: Conf. Series **1291** (2019) 012043 doi:10.1088/1742-6596/1291/1/012043

Consistent relativistic mean-field models: symmetry energy parameter

O Lourenço[1], **M Dutra**[1], **O Hen**[2], **E Piasetzky**[3] **and D P Menezes**[4]
[1]Departamento de Física, Instituto Tecnológico de Aeronáutica, DCTA, 12228-900, São José dos Campos, SP, Brazil
[2]Massachusetts Institute of Technology, Cambridge, Massachusetts 02139, USA
[3]School of Physics and Astronomy, Tel Aviv University, Tel Aviv 69978, Israel
[4]Departamento de Física - CFM - Universidade Federal de Santa Catarina, Florianópolis - SC - CP. 476 - CEP 88.040 - 900 - Brazil

E-mail: `odilon@ita.br`

Abstract. In this work, we revisit the study published in [Dutra *et al.*, Chinese Physics C 42, 064105 (2018)] where 34 consistent relativistic mean-field models were analyze at the nuclear matter constraints in relation to the role of short-range correlations in the calculation of the symmetry energy and its consequence on the value of the gamma parameter.

1. Introduction

Nuclear matter properties are reasonably well described by different versions of relativistic and non-relativistic models [1, 2, 3, 4]. We use the relativistic mean-field models to analyze the behavior of the symmetry energy in symmetric nuclear matter. The symmetry energy $\mathcal{S}(\rho)$ is a very important quantity in nuclear physics and it is related to different nuclear processes [5]. It can be written as the difference between the energy per nucleon of pure neutron matter ($y = 0$) and the energy per nucleon of symmetric matter ($y = 1/2$), where $y = Z/A$ is the proton fraction. This statement can be verified by using the expansion of the energy per nucleon in terms of $\delta = 1 - 2y$, around $\delta = 0$, at a given density as $E(\rho, \delta) \simeq E(\rho, 0) + \mathcal{S}_2(\rho)\delta^2 + \mathcal{O}(\delta^4)$. By taking this parabolic form for $E(\rho, \delta)$ it is possible to use $\mathcal{S}(\rho) \simeq \mathcal{S}_2(\rho) = E(\rho, 1) - E(\rho, 0)$ as a good approximation in order to compute the symmetry energy. Many nuclear and astrophysical properties are related to this quantity, as for example, the mass-radius diagram and the cooling process of neutron stars [6, 7]. At finite nuclei, the neutron skin thickness is related to the slope of the symmetry energy [8, 9]. Here, we revisit the study published in [10] to show the behavior of the γ parameter, related to the symmetry energy through its potential part when the short range correlations (SRC) are included in the calculations.

2. Relativistic Mean-Field models

The 34 consistent relativistic mean-field models (CRMF) used in this study (see Table 1) were extensively analyzed in the Ref. [11] under the nuclear matter point of view. These models have two different structures: non-linear and density dependent ones. We can find the expressions for the symmetry energy to both kinds of models through

$$\mathcal{S}(\rho) = \frac{1}{8}\frac{\partial^2 E(\rho,y)}{\partial y^2}\bigg|_{\rho,y=1/2} = \mathcal{S}^{kin}(\rho) + \mathcal{S}^{pot}(\rho). \tag{1}$$

The expressions are

$$\mathcal{S}_{\rm NL}(\rho) = \frac{k_F^2}{6E_F^*} + \frac{g_\rho^2}{8m_\rho^{*2}}\rho - \left(\frac{g_\delta}{m_\delta}\right)^2 \frac{M^{*2}\rho}{2E_F^{*2}[1+(g_\delta/m_\delta)^2 A(k_F,M^*)]}, \tag{2}$$

$$\mathcal{S}_{\rm DD}(\rho) = \frac{k_F^2}{6E_F^*} + \frac{\Gamma_\rho^2}{8m_\rho{}^2}\rho - \left(\frac{\Gamma_\delta}{m_\delta}\right)^2 \frac{M^{*2}\rho}{2E_F^{*2}[1+(\Gamma_\delta/m_\delta)^2 A(k_F,M^*)]}, \tag{3}$$

with

$$E_F^* = (k_F^2 + M^{*2})^{1/2}, \tag{4}$$

$$A(k_F,M^*) = \frac{2}{\pi^2}\int_0^{k_F}\frac{k^4dk}{(k^2+M^{*2})^{3/2}}, \quad \text{and} \tag{5}$$

$$m_\rho^{*2} = m_\rho^2 + g_\sigma g_\rho^2\sigma(2\alpha_2 + \alpha_2' g_\sigma\sigma) + \alpha_3' g_\omega^2 g_\rho^2 \omega_0^2. \tag{6}$$

The behavior of the symmetry energy for these models is shown in Fig 1.

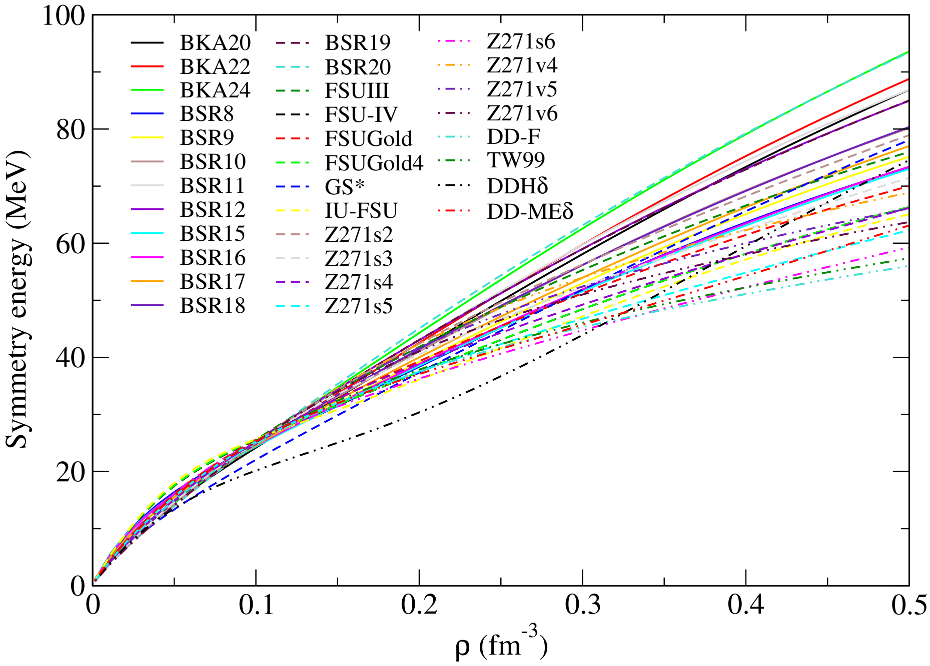

Figure 1. Symmetry energy versus density.

3. Results

We start by looking at the potential part of the symmetry energy. It can be related to the γ parameter through the following parabolic expression

$$\mathcal{S}^{pot}(\rho) = \mathcal{S}_0^{pot}(\rho/\rho_0)^\gamma. \tag{7}$$

Table 1. Some property values at saturation density for CRMF models: saturation density (ρ_0), binding energy (E_0), incompressibility (K_0), effective mass (m^*), symmetry energy (J), and slope of symmetry energy (L_0). For more details and references see [11].

Models	ρ_0 [fm^{-3}]	E_0 [MeV]	K_0 [MeV]	m^*	J [MeV]	L_0 [MeV]
non-linear model						
BKA20	0.146	−15.93	237.95	0.64	32.24	75.38
BKA22	0.147	−15.91	225.24	0.61	33.17	78.79
BKA24	0.147	−15.95	227.06	0.60	34.19	84.80
BSR8	0.147	−16.04	230.95	0.61	31.08	60.25
BSR9	0.147	−16.07	232.50	0.60	31.61	63.89
BSR10	0.147	−16.06	227.41	0.60	32.72	70.83
BSR11	0.147	−16.08	226.75	0.61	33.69	78.78
BSR12	0.147	−16.10	232.35	0.61	34.00	77.90
BSR15	0.146	−16.03	226.82	0.61	30.97	61.79
BSR16	0.146	−16.05	224.98	0.61	31.24	62.33
BSR17	0.146	−16.05	221.67	0.61	31.98	67.44
BSR18	0.146	−16.05	221.13	0.61	32.74	72.65
BSR19	0.147	−16.08	220.83	0.61	33.78	79.47
BSR20	0.146	−16.09	223.25	0.61	34.54	88.03
FSU-III	0.148	−16.28	229.54	0.61	33.89	71.72
FSU-IV	0.148	−16.28	229.54	0.61	31.43	52.16
FSUGold	0.148	−16.28	229.54	0.61	32.56	60.44
FSUGold4	0.147	−16.40	229.56	0.61	31.40	51.74
FSUGZ03	0.147	−16.07	232.48	0.60	31.54	63.98
FSUGZ06	0.146	−16.05	225.06	0.61	31.18	62.42
G2*	0.154	−16.07	214.77	0.66	30.39	69.68
IU-FSU	0.155	−16.40	231.33	0.61	31.30	47.21
Z271s2	0.148	−16.24	271.00	0.80	34.08	76.62
Z271s3	0.148	−16.24	271.00	0.80	33.27	67.81
Z271s4	0.148	−16.24	271.00	0.80	32.53	60.18
Z271s5	0.148	−16.24	271.00	0.80	31.84	53.57
Z271s6	0.148	−16.24	271.00	0.80	31.20	47.81
Z271v4	0.148	−16.24	271.00	0.80	34.29	77.00
Z271v5	0.148	−16.24	271.00	0.80	34.04	73.90
Z271v6	0.148	−16.24	271.00	0.80	33.80	70.94
density dependent models						
DD-F	0.147	−16.04	223.32	0.56	31.63	56.00
TW99	0.153	−16.25	240.27	0.55	32.77	55.31
DDHδ	0.153	−16.25	240.18	0.55	25.34	45.33
DD-MEδ	0.152	−16.08	219.60	0.61	32.18	51.43

By writing the slope as

$$L_0 = 3\rho_0 \left(\frac{\partial \mathcal{S}}{\partial \rho}\right)_{\rho=\rho_0} = 3\rho_0 \left[\left(\frac{\partial \mathcal{S}^{kin}}{\partial \rho}\right)_{\rho=\rho_0} + \frac{\gamma}{\rho_0}\mathcal{S}_0^{pot}\right] = L^{kin}(\rho) + L^{pot}(\rho), \tag{8}$$

we can find the γ parameter

$$\gamma = \frac{L_0 - L_0^{kin}}{3\,\mathcal{S}_0^{pot}} = \frac{L_0^{pot}}{3\,\mathcal{S}_0^{pot}}, \tag{9}$$

where the superscript refers to the kinetic part (kin) and potential part (pot) of these quantities and the subscript 0 means that all these quantities were calculated at the saturation density. For more details see Ref. [10].

There are two recent predictions for the γ parameters. The first one constrains the kinetic part of S at saturation obtained from free proton-to-neutron ratios measured at intermediate energy nucleus-nucleus collisions with SRC included and predicts the value 0.25 ± 0.05 [12]. The second one constrains S at saturation without SRC. These constraint was taken from ASY-EOS at GSI, where the elliptic flows of neutron and light-charged particles in an Au-Au reaction resulted in 0.72 ± 0.19 [13].

To obtain the γ value we use Equation (9) and calculate its value for three cases:

(i) complete kinetic term for the different models:

$$\mathcal{S}_i^{kin}(\rho) \quad = \quad \frac{k_F^2}{6E^*_{F\,i}} \tag{10}$$

where $i =$ NL, DD, with $E^*_{F\,i} = (k_F^2 + M_i^{*2})^{1/2}$ and

$$M^*_{\rm NL} = M - g_\sigma \sigma, \quad M^*_{\rm DD} = M - \Gamma_\sigma(\rho)\sigma, \tag{11}$$

for symmetric matter. The Fermi momentum is written in terms of density as $k_F = (3\pi^2\rho/2)^{1/3}$. The potential part for the symmetry energy, in this case, is given by the remaining terms in Eq. (2) for the NL model, and Eq. (3) for the density dependent one. This analysis shows that only 7 parametrizations have the γ value inside the interval $\gamma = 0.72 \pm 0.19$. They are: BKA20, BKA22, BKA24, BSR11, BSR19, BSR20, and G2*.

(ii) separation of the *really kinetic term*, the one without any dependence of the interaction with the mesons, from the rest of the symmetry energy:

$$\mathcal{S}_{\rm NL}^{kin}(\rho) = \mathcal{S}_{\rm DD}^{kin}(\rho) = \frac{k_F^2}{6E_F}, \tag{12}$$

with $E_F = (k_F^2 + M^2)^{1/2}$, for the kinetic part, and

$$\mathcal{S}_{\rm NL}^{pot}(\rho) \quad = \quad \frac{k_F^2}{6E^*_{F\,\rm NL}} - \frac{k_F^2}{6E_F} + \frac{g_\rho^2}{8m_\rho^{*2}}\rho, \tag{13}$$

$$\mathcal{S}_{\rm DD}^{pot}(\rho) \quad = \quad \frac{k_F^2}{6E^*_{F\,\rm DD}} - \frac{k_F^2}{6E_F} + \frac{\Gamma_\rho^2 \rho}{8m_\rho^2} - \frac{(\Gamma_\delta/m_\delta)^2 (M^*_{\rm DD})^2 \rho}{2E^{*2}_{F\ \rm DD}\left[1 + \left(\frac{\Gamma_\delta}{m_\delta}\right)^2 A_{\rm DD}\right]}, \tag{14}$$

for the potential one.

Here we found 20 parametrizations with γ coefficients in agreement with the range $\gamma = 0.72 \pm 0.19$. They are: BKA20, BKA22, BKA24, BSR8, BSR9, BSR10, BSR11, BSR12, BSR15, BSR16, BSR17, BSR18, BSR19, FSU-III, FSUGZ03, FSUGZ06, G2*, Z271s2, Z271s3, and Z271s4.

(iii) replace the kinetic part of the symmetry energy by the one proposed in Ref. [12]:

$$\mathcal{S}_i^{pot}(\rho) = \mathcal{S}_i(\rho) - \mathcal{S}_{\rm SRC}^{\rm kin}(\rho), \tag{15}$$

where $i =$ NL, DD. The expressions for the total symmetry energy $\mathcal{S}_i(\rho)$ are given by Eq. (2), or Eq. (3) for the nonlinear or density dependent models respectively.

$$\mathcal{S}_{\rm SRC}^{\rm kin}(\rho) = \left(2^{2/3} - 1\right)\frac{3k_F^2}{10M} - \Delta\mathcal{S}^{\rm kin}(\rho), \tag{16}$$

with

$$\Delta\mathcal{S}^{\rm kin}(\rho) \quad = \quad \frac{c_0 {k_F^0}^2}{2M\pi^2}\left[\lambda\left(\frac{\rho}{\rho_0}\right)^{1/3} - \frac{8}{5}\left(\frac{\rho}{\rho_0}\right)^{2/3} + \frac{3\rho}{5\lambda\rho_0}\right], \tag{17}$$

where the parameters $c_0 = 4.48$ and $\lambda = 2.75$ are also taken from Ref. [12].

In this case, only 6 parametrizations agree with the range $\gamma = 0.25 \pm 0.05$.

4. Summary

In this work, we reviewed the subject already analyzed in reference [10]. The behavior of the total symmetry energy was presented in Fig. 1. For the cases where the kinetic term does not contain the short-range correlations the CRMF predicts γ values in the interval 0.72 ± 0.19. More precisely, in cases 1 and 2, there are respectively 7 and 20 models within this interval. In case 3, where SRC was included, a decrease in the value of the range was observed and 6 parameterizations were able to describe the γ values within the intervals 0.25 ± 0.05.

5. Acknowledgments

This work was supported by Conselho Nacional de Desenvolvimento Científico e Tecnológico (CNPq) under grants 310242/2017-7 and 406958/2018-1 (O. L.), 433369/2018-3 (M. D.), and 301155/2017-8 (D. P. M.), by Fundação de Amparo à Pesquisa do Estado de São Paulo (FAPESP) under thematic project 2013/26258-4 (O. L.), and by INCT-FNA project 464898/2014-5.

[1] Lourenço O, Dutra M, Delfino A and Amaral R L P G 2007 *Int. J. Mod. Phys.* E **16** 3037
[2] Lourenço O, Santos B M, Dutra M and Delfino A 2016 *Phys. Rev.* C **94** 045207
[3] Lourenço O, Dutra M and Menezes D P 2017 *Phys. Rev.* C **95** 065212
[4] Santos B M, Dutra M, Lourenço O and Delfino A 2015 *Phys. Rev.* C **92** 015210; 2014 *Phys. Rev.* C **90** 035203
[5] Baldo M, Burgio G F 2016 *Prog. Part. Nucl. Phys.* **91** 203
[6] Providência C, Avancini S S, Cavagnoli R, Chiacchiera S, Ducoin C, Grill F, Margueron J, Menezes D P, Rabhi A and Vidaña 2014 *Eur. Phys. J.* **50** 44
[7] Horowitz C J and Piekarewicz J 2001 *Phys. Rev. Lett.* **86** 5647
[8] Tsang M B, Stone J, Camera F *et al.* 2012 *Phys. Rev. C* **86** 015803
[9] Krugmann A, Martin D, von Neumann-Cosel P, Pietralla N and Tamii A for the E350 Collaboration 2014 *EPJ Web of Conferences* **66** 02060
[10] Dutra M, Lourenço O, Hen O, Piasetzky E and Menezes D P 2018 *Chinese Physics* C **42** 064105
[11] Dutra M, Lourenço O, Avancini S S, Carlson B V, Delfino A, Menezes D P, Providência C, Typel S and Stone J R 2014 *Phys. Rev.* C **90** 055203
[12] Hen O, Li B-A, Guo W-J, Weinstein L B and Piasetzky E 2015 *Phys. Rev.* C **91** 025803
[13] Russotto P *et al.* 2016 *Phys. Rev.* C **94** 034608

AnalisaCAEN, a simple software suite to reduce and analyze coincidence data collected using CAEN v1724 digitizer

G S Zahn, F A Genezini, I Ribeiro Jr

Instituto de Pesquisas Energéticas e Nucleares - IPEN-CNEN/SP

E-mail: `gzahn@ipen.br`

Abstract. In this work a small software suite for the reduction and analysis of coincidence data collected using CAEN's proprietary software was developed. These software check the output files for coincidences, generate a single list mode file with the coincident events, build histograms for each input, plus a time difference histogram and a 2-detector data matrix, perform time gates and allows for the subtraction of accidental coincidences, and perform energy gating on the final data matrices, generating histograms with the gated spectra. Moreover, the suite has an integrator that guides the user through all the required steps.

1. Introduction

The CAEN v1724 is an 8-channel 14-bit 100MS/s digital pulse processing (DPP) digitizer that allows for quite flexible data acquisition arrangements. Pulse shaping parameters can be individually adjusted for each of the 8 inputs, and several data acquisition constraints can be set between any number of inputs, allowing for singles, coincidence and/or anticoincidence combinations for data acquisition, for instance. The data collection can be performed either in the form of individual histograms for each input or in list mode, which can be outputted either in ASCII or binary data formats.

The ASCII list mode output consists of one file for each input channel, with 5 header lines and then one line for each registered event with the absolute timestamp (in tens of nanoseconds, in the case of the v1724 digitizer) and the corresponding channel of the energy event; however, even when set to strict coincidence mode, the digitizer registers some unpaired events related to events registered in the same channel that set the "coincidence start" signal while the coincidence window was still open.

The digitizer comes with two distinct option of software. There is a very complex and technical option, called *DPP Runner*, which requires programming knowledge, and a very basic and simple option, *MC2 Analyzer*, which allows for simple set-up of the acquisition, but won't perform decent spectrum analysis.

To allow for the analysis of coincidence data acquired using this digitizer, a small software suite was developed that: 1) checks the output files for coincidences and generates a single list mode ASCII file with the coincident events and their time difference (nanoseconds); 2) for each detector pair, builds histograms for each input, plus a time difference histogram and a 2-detector data matrix; 3) performs time gates in the data and allows for the subtraction of accidental coincidences, also generating histograms and a matrix; and 4) performs the requested energy gates on the final data matrices, generating ASCII histograms with the gated spectra. In order to simplify the usage for non-experts, the suite also features an integrator that guides the user through all the required steps.

2. Software Design

The software suite was developed using the *Pascal* programming language, and at the present stage runs only in command-line mode. The compiler used was the open-source *FreePascal*, version 3.0 [1], and the software was only tested within the Windows operating system (though, as FreePascal is cross-platform, it should be reasonably easy to implement in Linux too, if required).

The conceptual design was to develop individual command-line utilities that perform each of the required steps, in order to allow for a latter integration into a graphical user interface (GUI). Each of the utilities should accept all required input via command-line parameters but, in order to simplify the usage, they can also ask for these inputs interactively.

3. The Software Suite

The suite consists of 5 pieces of software that perform simple tasks, plus an integrator to simplify the use of the suite.

3.1. LeCAENCoinc

It's the first piece, which at the present stage reads only the text-mode outputs, compiling them in a single ASCII output file – the next versions should also be able to deal with the binary data format. While reading, it checks for coincidences within a given coincidence gate time – this is done on-the-fly in a line-by-line basis (skipping the "unpaired" lines on each file), reading the whole inputs before doing so would be unfeasible due to the enormous number of events that can be present in each input file. The output file is in ASCII format, consisting of a list of coincidence events in the form (γ_1, γ_2, dT), where γ_1 and γ_2 are the amplitudes registered in channel 1 and 2, respectively, and dT is the time difference in ns between channels.

3.2. HistoCAEN

This program is the next in line, as it reads the output coincidence file and produces two 1-D histograms for the gamma channels, plus a time difference 1-D histogram and a 2-D gamma-gamma matrix. This software can also optionally perform time-gating, which is applied to all outputs, in order to allow for selection of total or accidental events. The output files are compressed to 4096 channels (energy histograms) in order to reduce memory and disk usage.

3.3. SomaMatriz

This is a program designed to sum or subtract two or more 2-D data matrices, allowing for the subtraction of accidental events from the total events gate, producing an output matrix that should only contain the real coincidence events. This sum is a simple matricial summation, with each matrix multiplied by a user-input weight in order to account for the difference in the number of time channels used in each gate – the weight should be the inverse of the number of time channels, and the accidental events matrices should have a negative weight. The results are output as one 2-D matrix and 2 1-D histograms, one for each channel.

3.4. FatiaMatriz

This is the final step so far, as it performs channel gating on a 2-D matrix, producing a gated 1-D histogram. Only a single gate can be performed at a time, and the software requires the detector in which to do the gating, as well as the initial and final channel of the gate. The output file contains an ASCII histogram of the gated events – at the present stage this is a simple 4096-line file with each line containing the number of counts in the respective channel.

3.5. AnalisaCAEN

This is a simple, command-line integrator for the suite, which performs the required steps, requesting for the necessary information. At the present stage, energy gating isn't yet implemented, and it has be performed manually using FatiaMatriz. In its present stage it requires the use of an external software (Cambio [2]) to display the time spectrum in order to allow for time-gating.

3.6. HistoSingles

This is an extra program which reads the original text-mode outputs and produces the full 1-D histogram for each input, which can be useful if acquisition was not performed in coincidence mode.

4. Programmed Future Implementations

In its present stage, the software suite is usable, having been thoroughly tested by a few non-technical users. Some upgrades are required, though, if these software are to be easily usable.

The first upgrade required is the implementation of energy gating into the AnalisaCAEN integrator. This task, albeit seemingly simple, isn't easy to implement as it requires knowledge on the spectrum analysis results in order to properly define the gates.

Another very important feature that should be added soon is the ability to automatically convert the output 1-D histograms in a more widespread format as Ortec's CHN [3] or the ANSI/IEEE N42.42 Standard [4]. This would allow for the inclusion of non-spectral data as energy calibration, counting times and so on.

Finally, a major step in making this software easily usable for non-technical users would be the implementation of a Graphical User Interface. It should be noted that, as of now, the inclusion of spectrum analysis into the suite is not foreseen, as this is the most delicate step in nuclear data analysis and there are quite a few excellent choices for that purpose [5].

5. Conclusions

The software suite developed proved to be useful, allowing users to perform coincidence data reduction in a quick and reliable manner. The most delicate step in the development of this software is the verification of coincidences within the initial list-mode output files, as it contains both paired and unpaired events. There are still some important features to be added, but in its present stage the suite is absolutely usable.

References

[1] Free Pascal team 2018 *Free Pascal – open source compiler for pascal and object pascal* available at https://www.freepascal.org/
[2] Sandia National Laboratories 2008 *Cambio v.080911* available at https://hekili.ca.sandia.gov/Cambio/
[3] ORTEC 2002 *Software File Structure Manual for DOS and Windows Systems* ORTEC Part No. 753800, Manual Revision E
[4] The N42.42 Working Group 2018 ANSI/IEEE N42.42 Standard, available at https://www.nist.gov/programs-projects/ansiieee-n4242-standard
[5] Zahn G S, Genezini F A, Moralles M 2015 Evaluation of Peak-fitting Software for Gamma Spectrum Analysis https://arxiv.org/abs/1511.04362v1

XLI Brazilian Meeting on Nuclear Physics (RTFNB) IOP Publishing
IOP Conf. Series: Journal of Physics: Conf. Series **1291** (2019) 012045 doi:10.1088/1742-6596/1291/1/012045

Single-event effects: experimental setup for power MOSFETs and diffusion model for cross section calculations in low-voltage MOSFETs

S G Alberton[1], **N H Medina**[1], **N Added**[1], **V A P Aguiar**[1], **R Menegasso**[1], **E L A Macchione**[1] **and M A G Silveira**[2]

[1] Institute of Physics, University of São Paulo, São Paulo, Brazil
[2] Centro Universitário da FEI, São Bernardo do Campo, Brazil

E-mail: `alberton@if.usp.br`

Abstract. MOSFETs are subject to different types of Single-Event Effects (SEEs) induced by heavy ions, with low-voltage MOSFETs being more susceptible to non-destructive effects, such as Single-Event Transients, than high-voltage MOSFETs which may also be susceptible to destructive effects. In this paper an experimental setup used to study SEEs in power MOSFETs at the São Paulo 8UD Pelletron accelerator and computational simulations for SEE cross section calculations in low-voltage MOSFETs are presented.

1. Introduction

Since the mid 1970s, it is known that electronic devices are subject to operational failures when exposed to radiation [1, 2]. These operational failures are very significant in environments where the exposure to radiation is quite intense, such as satellites, avionic systems, particle accelerators, and nuclear reactors. Single-Event Effects (SEEs) are a class of ionizing radiation effects in electronic devices that has been dominant in embedded space systems [3]. SEEs are caused by the incidence of a single ionizing particle with enough energy to create a large number of electron-hole pairs within a sensitive volume of the electronic device. Under conduction and drift movements within the device, the electron-hole pairs configure electric currents that are able to cause non-destructive effects (soft errors) like electric transients in analog circuits (Single-Event Transient - SET), logical state changes in digital circuits (Single-Event Upset - SEU), and even destructive effects (hard errors). Although computational methods are able to estimate the radiation effects caused on electronic devices [4], any such devices should be able to withstand particle accelerator testing in order to be considered safe for use in space applications [5].

Currently, a beam line named SAFIIRA ("*SistemA de Feixes Iônicos para IRradiações e Aplicações*") dedicated to studies of SEEs with heavy ions was developed at the São Paulo 8UD Pelletron accelerator [6]. This experimental setup has been used to study the radiation effects in power MOSFETs which, in radiation environments, are liable to suffer soft errors, such as SETs, and hard errors, such as Single-Event Burnout (SEB) and Single-Event Gate Rupture (SEGR) [7]. Recently, SET and SEB cross section measurements in power transistors were carried out using a non-destructive method for the ionic species available at the 8UD Pelletron accelerator and the data obtained are under analysis.

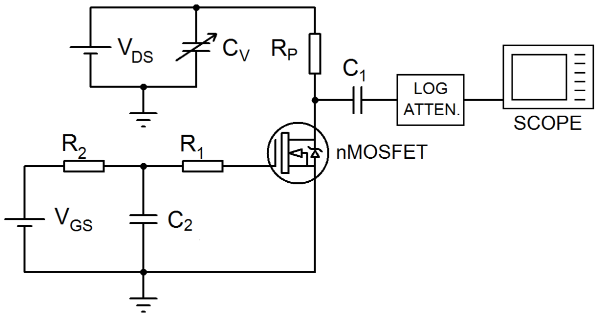

Figure 1. Schematic diagram of the test setup for SET, SEGR and protective SEB measurements.

In the first part of this paper we present a description of the experimental test setup that has been used for SEE studies in power MOSFETs. In this frame, the circuitry considerations are detailed in an updated perspective for accurate measurements. In the second part, a Monte Carlo routine based on a diffusion model for SEUs in memory devices was adapted to SETs in low-voltage MOSFETs and the results are shown.

2. Test Setup for MOSFET irradiation

The irradiation experiments in power MOSFETs has been conducted at SAFIIRA [6], located at the 8UD Pelletron accelerator of the ”*Laboratório Aberto de Física Nuclear da Universidade de São Paulo*” (LAFN-USP, Brazil). SAFIIRA was designed in order to obtain low-intensity highly-uniform heavy ion beams in the device under test (DUT) through the combination of Rutherford scattering and quadrupole defocusing techniques. The 8UD Pelletron accelerator is able to provide ion beams from ^{1}H up to ^{107}Ag with a surface Linear Energy Transfer (LET) in silicon ranging from 0.5 to 40 MeV.mg^{-1}.cm^{-2}.

Power MOSFETs may be subject to different effects (mainly SET, SEB and SEGR) and to measure them an electric circuit was developed taking into account modern circuitry considerations [7, 8]. Although SEBs are entirely destructive events, protective methods based on the current limiting technique are well known and used for cross section measurements in the usual way [9, 10]. In Figure 1 the proposed test setup for the SEE measurements in power MOSFETs, including protective electric circuit and the acquisition system, is shown.

SEE qualifications should be performed considering the worst case, *i.e.*, under conditions that maximize the SEE cross section. For non-destructive SEB measurements, the value of the protection resistor R_P (Figure 1) is responsible for the effectiveness of the protective method and for the accuracy of the measures taken. An appropriate value of R_P can be estimated if the characteristic curve for the avalanche regime is known, which can be obtained by direct measurements or quasi-stationary avalanche simulations [8]. In the absence of the high-voltage characteristic curve, the value for R_P can be estimated if the DUT drain-to-source leakage current i_{DSS} is known, since, for high values of R_P, the voltage drop in the protection resistor is not negligible with respect to the voltage drop through the DUT and the V_{DS} applied [11].

In SEB measurements, the capacitor C_1 is charged by the power supply V_{DS} while the MOSFET remains in the off state ($V_{GS} = 0$ e $V_{DS} > 0$). SEB can be triggered if the heavy ion strike turns on the *npn* parasitic bipolar transistor for a certain critical voltage $V_{DS_{th}}$ and a second breakdown occurs. Since the equivalent impedance between the oscilloscope and the attenuator is 50 Ω, C_1 is discharged to provide current to the MOSFET due to the fact that the protection resistor R_P limits the current provided by the power supply V_{DS}. The nominal value of C_1 must be chosen in accordance with the particle flux on the DUT area and the desired signal detection time. Although the electric current provided by C_1 depends on its nominal value, higher values can provide a large amount o charge to destroy the DUT and disable the limiting current technique [10].

Traditionally, in SEB measurements a stiffening capacitor C_V is used, which is ideally placed as close as possible to the DUT. Is assigned to the capacitor C_V the function of filtering high frequency noises, compensating voltage drops to the DUT and minimizing parasitic circuit effects. However, it is expected that small ion-induced transients can occur while V_{DS} is low enough to trigger a SEB. In this case, C_V can suppress the transient detection by quickly compensating these voltage drops in the DUT and its usage is not recommended for SET cross section measurements.

The electric circuit also allows identification of SEGR if a picoammeter monitors the current provided by the power supply V_{GS}. The network R_1-C_2-R_2 is used as a suppression filter to prevent electrical stress in the gate oxide. Its use is exclusively preventive because, unlike protective SEB measurements, to the present day there are no protective methods for SEGR cross section measurements.

3. DMSEE: Diffusion Model for Single-Event Effect Cross Section Calculations

In the occurence of a SEE, the electron-hole pairs created in the plasma filament can be collected by a sensitive region of the device through diffusion and drift transport. In the particular case where the electric field intensity inside the device is low enough, the diffusion transport is predominant.

Wrobel's diffusion method [13] is based on the calculation of the total collected charge Q_c by a sensitive region of an electronic device considering the diffusion of each elemental ion track produced by the ion strike. Thus, the deposited charge at a point Z of the ion track, Q_d(Z), is related to Q_c through the solid angle of the sensitive region viewed from point Z, denoted Ω(Z):

$$Q_c = Q_d(Z) \cdot \frac{\Omega(Z)}{4\pi} \tag{1}$$

The stopping power curves can be calculated for several ion species using the SRIM code [14] and a Monte Carlo routine simulates the ion beam incidence. In this method, the SEE cross sections are calculated using the critical charge criterion (or critical energy in silicon), i.e., a SEE occurs if Q_c exceeds a predefined critical value.

Based on Wrobel's method for SEU cross section calculations in memory devices [13], the DMSEE (Diffusion Model for Single-Event Effect cross section calculations) code was developed. DMSEE considers passivation and metallization layers of the device in its calculations and the solid angles are calculated for parallelepiped sensitive volumes by using analytical solutions rather than numerical approaches [15].

To explore DMSEE applications, a low-voltage pMOSFET, whose sensitive area and critical charge can be easily estimated (from reference [16]), was simulated. The sensitive volume size and the critical energy were estimated to be about $50\times50\times1\ \mu\text{m}^3$ and 11 MeV, respectively. In addition, 1 μm passivation (SiO_2) and metallization (Al) layers were considered. Figure 2 shows the geometry adopted and the resulting simulation.

The Weibull function shape could be obtained and the Weibull fit parameters resemble the experimental ones. As discussed in [13], the diffusion model is not able to perform predictions for LETs near the threshold. However, given the inaccurate estimates considered as input to DMSEE, this simplified methodology presents promising results and extends the application of Wrobel's method to SEUs only.

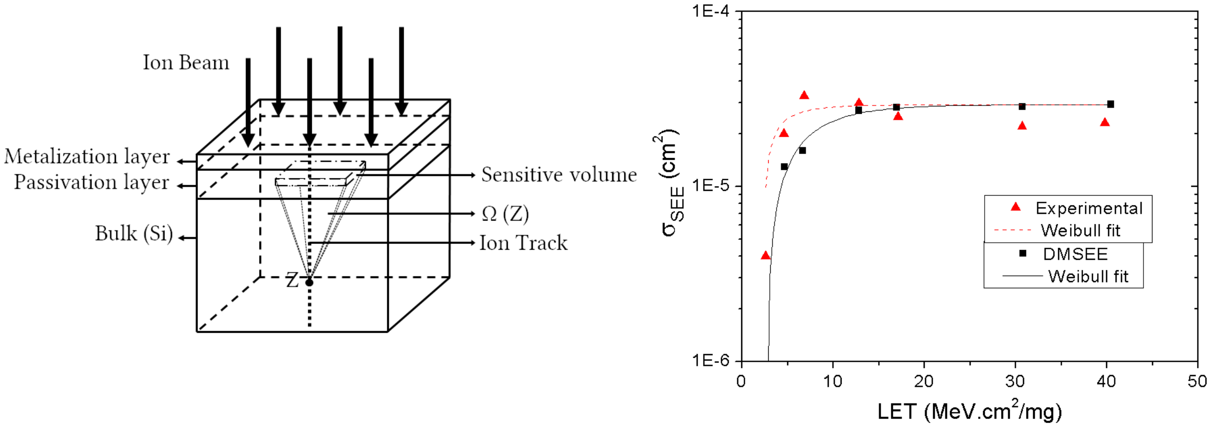

Figure 2. Geometry used for calculations and comparison between DMSEE and experimental results obtained in a pMOSFET (from [16]). The black solid line is a Weibull fit of the DMSEE data and the red dashed line is a Weibull fit of the experimental data.

4. Summary and Conclusions

In this work an experimental setup intended to study ionizing radiation effects in power MOSFETs and the basic framework of a Monte Carlo code for SEE cross section calculations in low-voltage MOSFETs, based on a diffusion model, were presented.

The test setup presented allows SET, SEGR and SEB measurements in MOSFETs. Although SEB is an entirely destructive effect, the proposed experimental setup allows SEB cross section measurements to be performed non-destructively due to the current limiting technique, reducing costs associated with destroyed DUT samples and lost facility test time. The main aspects for accurate SEE measurements in power transistors were presented and the considerations of circuitry were discussed in some detail.

DMSEE computational code was used for SEE cross section calculations in a low-voltage pMOSFET and the results obtained by computational simulation were compared to the experimental ones. Wrobel's diffusion method, used for SEU cross section calculations in SRAM memories, was successfully adapted to low-voltage MOSFETs, despite inherent differences related to the geometry, dimension sizes and critical energy of these devices.

References

[1] Binder D, Smith E C and Holman A B 1975 *IEEE Trans. Nucl. Sci.* **22** pp 2675-80
[2] Ziegler J F et al 1996 *IBM J. Res. Develop.* **40** pp 3-18
[3] Petersen E 2011 *Single Event Effects in Aerospace* (John Wiley & Sons)
[4] Dodd P 2005 *IEEE Trans. Device Mater. Rel.* **5** pp 343-57
[5] ESA/ESCC 2014 *Single Event Effects Test Method and Guidelines: Basic specification No. 25100*
[6] Medina N H et al 2016 *J. Nucl. Phy. Mat. Sci. Rad. A.* **4** pp 13-23
[7] Titus J L 2013 *IEEE Trans. Nucl. Sci.* **60** pp 1912-28
[8] Liu S et al 2012 *IEEE Trans. Nucl. Sci.* **59** pp 1125-29
[9] Oberg D L and Wert J L 1987 *IEEE Trans. Nucl. Sci.* **34** pp 1736-41
[10] Fischer T A 1987 *IEEE Trans. Nucl. Sci.* **34** pp 1786-91
[11] Luu A et al 2008 *IEEE Trans. Nucl. Sci.* **55** pp 2166-73
[12] Hohl J H and Galloway K F 1987 *IEEE Trans. Nucl. Sci.* **34** pp 1275-80
[13] Wrobel F, Hubert G and Iacconi P 2006 *IEEE Trans. Nucl. Sci.* **53** pp 3271-76
[14] Ziegler J F, Ziegler M D and Biersack J P 2008 *SRIM - The Stopping and Range of Ions in Matter* (Ion Implantation Press)
[15] Mathar R J 2015 *Solid Angle of a Rectangular Plate* Technical Note
[16] Medina N H et al 2014 *IEEE Rad. Eff. Data Workshop (REDW)* pp 272-4